The 2nd Meeting on the Physical Oceanography of Sea Straits,
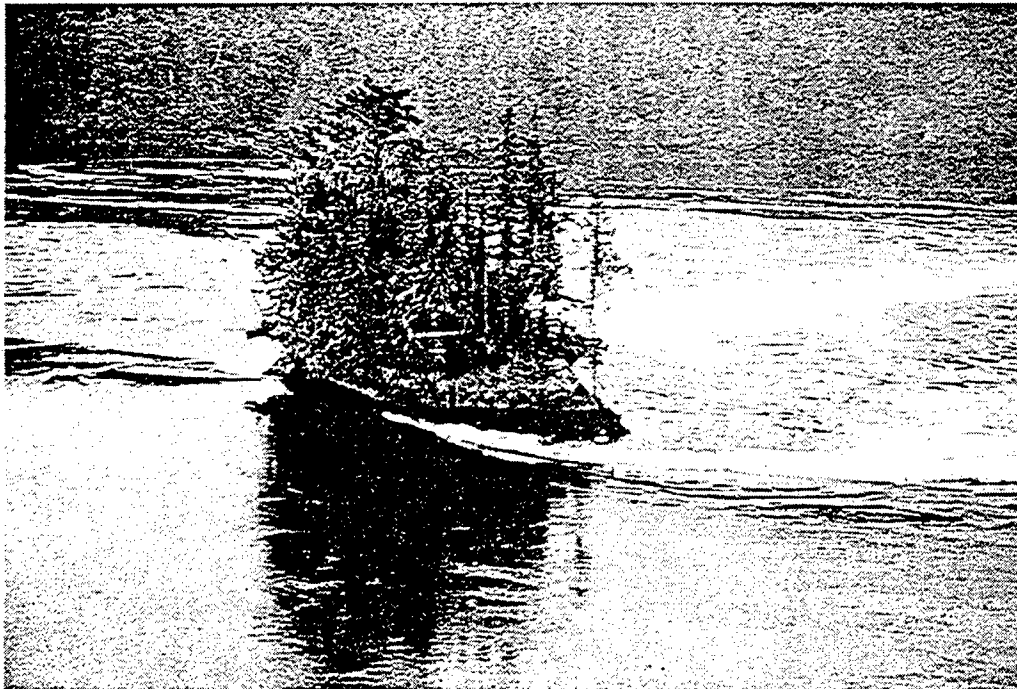

Villefranche,
15th-19th April 2002

Cover picture. Flow past Turret Rock, an island in Nakwatka Rapids, a strait connecting a complex of fjords on the British Columbia coast with the Pacific Ocean. See the article by Farmer for further details.

REPORT DOCUMENTATION PAGE

Form Approved OMB No. 0704-0188

1. AGENCY USE ONLY (Leave blank)	2. REPORT DATE 2002	3. REPORT TYPE AND DATES COVERED 15-19 April 2002 Final

4. TITLE AND SUBTITLE	5. FUNDING NUMBERS
2nd Meeting on the Physical Oceanography of Sea Straits. Held in Villefanche-sur-Mer, France on 15-19 April 2002.	N00014-02-1-1028

6. AUTHOR(S)

7. PERFORMING ORGANIZATION NAME(S) AND ADDRESS(ES) National Oceanography Centre, Southampton, University of Southampton Waterfront Campus, European Way, Southampton, SO14 3ZH, UK	8. PERFORMING ORGANIZATION REPORT NUMBER

9. SPONSORING/MONITORING AGENCY NAME(S) AND ADDRESS(ES) Office of Naval Research, European Office PSC 802 Box 39 FPO AE 09499-0039	10. SPONSORING/MONITORING AGENCY REPORT NUMBER

11. SUPPLEMENTARY NOTES
This work relates to Department of the Navy Grant N00014-02-1-1028 issued by the Office of Naval Research International Field Office-Europe. The United States has a royalty-free license throughout the world in all copyrightable material contained herein.

12a. DISTRIBUTION/AVAILABILITY STATEMENT Approved for Public Release; Distribution Unlimited. (1)	12b. DISTRIBUTION CODE A

12. ABSTRACT (Maximum 200 words)

13. SUBJECT TERMS ONRIFO, Foreign Reports, Conferences	15. NUMBER OF PAGES
	16. PRICE CODE

17. SECURITY CLASSIFICATION OF REPORT UNCLASSIFIED	18. SECURITY CLASSIFICATION OF THIS PAGE UNCLASSIFIED	19. SECURITY CLASSIFICATION OF ABSTRACT UNCLASSIFIED	20. LIMITATION OF ABSTRACT UL

NSN 7540-01-280-5500

Standard Form 298 (Rev. 2-89)
Prescribed by ANSI Std. 239-18
298-102

The 2nd Meeting on the Physical Oceanography of Sea Straits, Villefranche, 15th-19th April 2002

Acknowledgements

Copyright

The 2nd Meeting on the Physical Oceanography of Sea Straits,
Villefranche, 15th-19th April 2002

Part I: Review talks

Part II: Poster presentations

SEA STRAITS MEETING SUMMARY

During April 15-19, 2002, a meeting was held in Villefranche-sur-Mer, France, to discuss the physical oceanography of sea straits. The meeting was attended by 50 or so participants and was a follow-on to a similar workshop held in Les Arcs, France, in 1989. Half-day sessions were devoted to overviews of recent field programs, advances in instrumentation, and development of new theories and models over the past decade. Each session consisted of an overview talk, a poster session, and a group discussion. Extended abstracts describing the talks and posters can be downloaded from the following sites:

> http://www.soc.soton.ac.uk/JRD/PROC/STRAIT/talks.zip
> http://www.soc.soton.ac.uk/JRD/PROC/STRAIT/posters.zip

The following is a summary of the major topics of discussion that took place as reported by the session rapporteurs. The unedited session reports appear at the end of this report.

One of the main topics that occupied discussion over the week was 'mixing'. Early talk centered on the growing evidence of the importance of Helmholtz vs. Homboe (vs. Kelvin-Helmholtz) instability in hydraulically-driven two-layer systems. This was followed by an exchange, somewhat semantic in nature, concerning the use of the terms 'entrainment' and 'detrainment'. A related and more important point concerned the applicability of entraining shallow-water layer models such as streamtube models. How well do they reproduce the physics of hydraulically driven turbulent flows with continuous stratification and what is their range of applicability? This topic is important in the modeling of mixing in the immediate lee of a sill or over larger scales in outflow plumes. Plume modelers wondered whether there is a universal (parameterizable) behavior of the entrainment processes. One difficulty with developing such a parameterization is the presence of multiple physical processes (bottom boundary layer turbulence, interfacial instability, etc.).

One of the central methods of visualizing mixing is through acoustic backscatter. However, this subject still excites a variety of opinions regarding what is actually seen in acoustic images. The signal depends on the biological content (plankton and other organisms) and on the presence of bubbles, turbulent patches, and other physical properties. Hence, it is best to interpret the images in the presence of concurrent biological or physical data.

The bottom boundary layer is also responsible for drag and for the establishment of secondary circulations. There is a need for improvements in BBL closure schemes. Bottom and interfacial Ekman layers are thought to be responsible for lateral circulation cells observed in experiments. Such cells may give rise to the 'pinching' of isotherms observed in the Faroe-Bank and Vema Channels. It is extremely difficult to incorporate Ekman layers into models of finite Rossby number flows, at least in a deductive way. Little progress has been made on this subject for 30 years. There is also a lack of adequate measurements of bottom or interfacial stresses in straits, though ADCPs offer an emerging capability in this area.

Hydraulic control was a central topic throughout the week. Much discussion centered on ways of thinking about control and how classical ideas based on conservative models apply in the presence of mixing and dissipation. Some people prefer to think of control in terms of information transmission (wave propagation) throughout the flow, others ground their intuition on maximization (or minimization) volume flow rate, energy, and so on, while still others think in terms of asymmetries caused by hydraulic transitions. The pitfalls in the latter interpretation were pointed out by those who recognize that asymmetries also develop due to friction and entrainment. More specific discussions covered topics such as the location of control point(s) in presence of entrainment and friction. There was also considerable interest in cases where these processes are so strong that traditional features such as control sections are completely expunged. It is thought that some cases (e.g. the Bab el Mandeb) may lie in this regime. The important discussion of hydraulic control in continuously stratified systems received some attention. The models that allow such behavior are still largely (though not entirely) limited to those that do not allow upstream influence. The audience also heard about advancements that have occurred over the past decade in the elucidation of hydraulic effects in the presence of non-uniform cross-sections and continuous stratification. In the area of rotating hydraulics, advancements include exploration of more general upstream conditions, potential vorticities, and layer stratification.

A discussion of hydraulic control naturally leads to a consideration of hydraulic jumps. It is well known that jumps, or some form thereof, occur in straits where rotational effects are minimal. Examples include the Bosphoros, the Strait of Gibraltar, and the Romanch Fracture Zone. It was also generally acknowledged that jumps have not been observed in locations such as the Denmark Strait and Faroe-Bank Channel, where rotation is quite important. Numerical and laboratory experiments have shown that jumps can exist in the presence of rotation, often in the form of a transverse expansion in the width of the flow. It could be that observations that would reveal the presence of such a feature have not been made. It is also possible that jumps are subsumed by the instability, mixing, and entrainment that are observed downstream of the sills in the locations mentioned.

Time-dependence is the topic that was identified at the 1989 Les Arcs workshop as being one of central importance, yet just a few studies have been made since then of cases involving true (non-parametric) time variation. We do not know the extent to which hydraulic control is relevant in time-dependent flows. Some results have been established concerning the increase or decrease in volume flux due to time-periodicity, but these are limited to specific cases. It is not known why seasonal time-dependence fails to show up in the Nordic overflows.

A subject of growing importance to investigators is the large-scale effects of straits and implications for climate and climate monitoring. Meridional fluxes of physical properties tend to be concentrated by and funneled through straits such as the Faroe-Bank Channel, making these sites ideal for climate monitoring. Traditional hydraulic theory has suggested ways in which monitoring of volume flux can be carried out using remote measurements of free surface or isopycnal level in hypothetical upstream reservoirs. A recent attempt to apply this thinking using an empirical 'weir' relation for the Norwegian Sea/Faroe-Bank system excited a discussion concerning the dynamical consistency of such an approach. Is it possible to uniquely determine

the volume flux across the Faroe-Bank sill on the basis of a single measurement in the Norwegian Sea? The answer seems to be 'no'. A related discussion focused on the general problem of upstream effects of sills in numerical simulations and how these effects might be parameterized. Of more fundamental interest is the question of how deep straits and sills might serve as dynamical choke points that regulate the thermohaline circulation in some way. For example, how would the strength of the meridional overturning cell change if deep sills were removed from the bottom topography?

Throughout the week, there were frequent exchanges concerning what to do next in the way of field programs. A strong temptation exists to explore straits for which relatively few observations exist. Two examples mentioned are the Makassar Strait (which contains the bulk of the Indonesian throughflow) and the Bering Strait. Both cases may involve unique dynamical regimes and physical processes. The Makassar Strait marks the site of equator crossing of the Indonesian throughflow. Because the Bering Strait lies between two continents, a version of the Island Rule can be used to predict the transport. This prediction apparently leads to a value nearly an order of magnitude greater than the observed value. Why?

Some in attendance were of the opinion that resources for new fieldwork should be aimed at places that have already been the subject of major field programs. One example is the Bab-el-Mandeb, where hydraulic models seem to work well in portraying the seasonal fluctuation between two- and three-layer regimes, but where direct measurements have failed to confirm the presence of critical or supercritical flow. A careful sampling of the along-axis structure of the flow using towed instruments might clarify greatly the situation. Some locations such as Knight Inslet are small enough to be thought of as a 'laboratory model', allowing highly resolved observations of mixing and other physical processes.

Verbatim Reports from Session Rapporteurs

Monday a.m.   Process-Orientated Field Studies
Speaker: David Farmer
Chair: David Smeed

Summary by Bill Johns, Rapporteur:

The discussion on field oriented process studies was wide-ranging and continued throughout the week. A number of posters that pertained to this topic were scattered through the week and therefore this summary is intended to incorporate aspects of these poster results, the discussions, and the introductory talk given by David Farmer.

A key point related to field studies that was stressed by Dr. Farmer is the growth of new technology that is now available for application to studies of sea straits. These include a wide variety of tools such as shipboard and moored ADCPs, acoustic imaging techniques, XCPs and XCTDs, acoustic transmission techniques (time of flight and scintillation), radar/SAR and photography, and HF radar for surface current mapping.

A few main themes dominated most of the discussion on field oriented process studies and in the related posters. These themes were:

1. Hydraulics and Application to Observed Flows
2. Time-dependence of Strait Exchanges
3. Entrainment in Overflow Plumes and Mixing in Straits, and
4. Monitoring Techniques

The state of knowledge on hydraulic control in several important straits was reviewed and discussed. The control mechanisms in Gibraltar Strait are considered to be well established but there remains a debate on whether and how often a maximal exchange occurs. Bab-el-Mandeb has been the subject of intensive recent field work and new model studies; these have focused on the possibility of both 2 and 3-layer controlled flows during the winter and summer regimes, and on properly accounting for topography and strait cross sectional geometry in the estimation of wave speeds and criticality conditions. Evidence of hydraulic control in the Bosphorus exchange and in the Faroe Bank overflow channel was also presented. A recurring point of discussion in the workshop was the applicability of various control theories to exchange flows. For example: Can we identify "asymmetric" flows that are not clearly hydraulically controlled? Or does friction/mixing always tend to drive flows toward criticality?

Time dependence in strait flows was a major topic of the posters and discussion. Evidence for strong low-frequency (subtidal) exchange variability caused by atmospheric forcing was presented or was already known for several straits (Gibraltar, Bab-el-Mandeb, Bosphorus, Korea, and for a Chilean coastal channel). In some cases (e.g., Gibraltar and Bab-el-Mandeb), simple models of forced exchange, including Helmholtz dynamics, have been shown to account for a significant part of the transport and exchange variance. Tidal forcing, including the structure and dynamics of internal tides and bores, and the role of tidal forcing in the enhancement of property transports relative to steady hydraulic solutions, was acknowledged as a problem that especially needs attention. A key question is: How do these time-dependent processes interact dynamically with the hydraulics?

Recent observations were presented in several overflow plumes, including the Denmark Strait, Faroe Bank Channel, Sicily Strait, Red Sea Overflow, and Romanche Fracture Zone. Several of these programs have attempted to estimate the entrainment or mixing rate of ambient waters into the plumes by either direct (turbulence) or indirect (bulk transport) methods. The entrainment in these plumes is recognized as a key process to be properly represented in GCMs and climate models. Important questions are: Is there a universal (parameterizable) behavior of the mixing processes in these plumes? What is the next step forward from streamtube models? Another topic of discussion was the lack of adequate measurements of bottom or interfacial stresses in straits, and the demonstration of an emerging capability in this area using ADCPs.

Finally, developing efforts in long-term monitoring of important straits (e.g., Gibraltar, Korea) and overflows (e.g., Faroe Bank Channel) were presented and some discussion followed. Optimization of methods including direct and indirect techniques (e.g., sea level difference or

internal hydraulic head monitoring) for efficient monitoring of important exchanges, especially climatically relevant ones, was acknowledged as an important area for future research.

Monday p.m.   Small-scale Effects
                    Speaker: Mike Gregg
                    Chair: Harvey Seim

Summary by Tom Sanford, Rapporteur:

The purposes and goals for the measurement and study of small-scale processes include 1) understanding the physics and local consequences and 2) providing guidance for the subgridscale parameterization for numerical models. The presentation and discussion covered field and laboratory experiments and analytical and numerical modeling. Experiments are becoming more complex and sophisticated but remain under-sampled. Numerical modeling is replacing analytical studies.

Improvements are needed in our concepts and methodologies to deal with the 3-D aspects of most flows, effects of mixing and complex influences of multiple controls. Clearly, many flows have significant temporal and spatial variability that is difficult to include in steady and 1- and 2-D formulations. Mixing is a confounding effect that jeopardizes the application of simple hydraulic theory. Outlet water properties change, entrainment stresses occur, and control points move. Mixing effects increase with L/D, channel complexity (e.g., bends) and bottom stress and are difficult to quantify and predict adequately. Non-steady flows, such as solibores, contribute to dissipation and may be responsible for thickening some interfaces. Most channels have topographic features leading to possible multiple control locations and difficulty in applying hydraulic theory. Experimentalists need guidance in the application of theory to experimental sites.

Future work should focus on 1) the causes of acoustic backscatter (to understand and interpret this method better), 2) real-time and direct measurement of bottom stress (necessary to understand role of bottom friction), 3) improvements to BBL closure schemes, and 4) understand solibores (especially in terms of causing mixing). These activities and "hard thinking" should provide the guidance in interpreting observations, improving numerical simulations and evaluating mixing parameterizations in straits.

Tuesday a.m.   Frictional Processes
                    Speaker: Chris Garrett
                    Chair: Steve Murray

Summary by Anders Enqvist, Rapporteur:

1. Bottom friction exerted on a subcritical layer will accelerate it (Pratt, 1986).

2. Entrainment may thicken an accelerating subcritical ($F<0.5$) layer (Gerdes, 2002).

3. Skewedly distributed mean-layer properties such as velocity compared to a homogeneous layer with the same property average, leads to contradictory results concerning the criticality of the layer ensemble (Gerdes). Mean flow energy consideration indicates F<1, while internal wave derivation suggests F>1. This seemingly paradoxical result was, however, resolved by the lecturer by introducing a stream function-based functional. The ensuing debate suggested the following resolutions to deal with frictional flow: "Vorticity equations should be more adequate to describe the flow than Bernoulli equations. Since the vorticity fields are solely advected, this presents a complication that can be overcome. In rotating flows, vorticity formulation is the key" (Chris Garrett). "Continuous vertical distribution of fluid properties implies an infinite number of solutions" (Larry Pratt). "This leads to an eigenvalue type of problems" (Peter Baines). "Solutions should include viscosity" (Andy Hogg). "The control definition for continuously stratified layers was suggested to be that infinitely short long waves should not pass through the control" (Chris Garrett). "Frictional effects do not amount to much. A control by any other name is still constituted by an asymmetric flow connecting two reservoirs, blocking information of changes therein from passing through the constriction" (Larry Armi). "Are there not points in the flow where the derivatives cannot be established? What is meant by a long wave?" (Peter Killworth). "Long waves by definition should be non-dispersive" (Larry Pratt). "Can deploying 3D-models cast light on frictional effects? Science must relate to engineering results to have an impact on societal decisions" (Peter Baines). "The common understanding seemed to be that even though the capacity of 3D-models develops rapidly (e.g. grid insertion), it will always heavily depend on subgrid parameterization and boundary condition formulation. At the least, they should be non-hydrostatic so that vertical acceleration terms may be included. Most likely one would see progress made in engineering literature than by field experiments" (Chris Garrett). "Fundamental limitations still prevail, e.g. in treatment of soliton dynamics with mixing, breaking and overturning" (David Farmer). The possibility to find overriding principles for flow regimes including frictional effects was left as an open question.

Wednesday a.m. Topographic and Boundary Effects
              Speaker: Gregory Lane-Serff
              Chair: Peter Baines

Summary by Bruno Ferron, Rapporteur:

The discussion focused on the question, "Should we observe new passages to quantify their impact for the global circulation or go back to already measured straits in order to get a better understanding of what is going on?" Two straits that have already been investigated were mentioned: Knight Inlet appears to be a real lab for studying fluid dynamics, except for rotational effects, since we can observe a large variety of responses that involve lots of parameters. It is especially interesting for those who want to study time-dependent phenomena. The inlet is forced by tides that give rise to bore generations. This is the right place to go for studying dissipation associated with bores, propagation of information from the control point, set-up of a hydraulically controlled state. . . The time-dependent aspect of exchange flows has been a recurrent subject of the meeting. Concerning the Bab-El-Mandab strait, the variability of its transport on seasonal time-scales is reasonably understood and reproduced (poster by Siddall et al.). However, the hydraulic character of the flow is still questionable since local

measurements do not show criticality with respect to the Froude number, neither at the main sill nor at the main narrow. The flow is critical at the sill only during short periods. Further observations are needed to locate the hydraulic control point. It might be close to the sill since the Froude numbers are larger than at the main narrow. The bathymetry composed of multiple channels near the bottom and the thin bottom layer (possibly controlled), which requires measurements close to the bottom does not help in finding the hydraulic control point. The role of bottom friction could also be of primary importance especially at the exit of the strait and a need for studying the bottom boundary layer appears to quantify the friction.

For those who are not afraid of complexity, biology is strongly coupled to the hydraulic character of exchange flows. For instance, plankton develops where fronts are, where hydraulic jumps occurs (e.g. Gibraltar). Studies that link physics of straits and biology are an interesting challenge.

Lastly, acoustic backscatter images were discussed. The signal obtained from such measurements depends on the biological content (plankton, organisms), on the presence of bubbles, and on the occurrence of turbulent patches. Hence, to be useful, these images should be taken with concurrent measurements in order to understand the nature of backscatter images.

Wednesday p.m. Rotational Effects
       Speaker: Larry Pratt
       Chair: Doron Nof

Summary by Peter Lundberg, Rapporteur:

Summary of Discussion Concerning Rotating Hydraulics. The overall discussion progressed on the basis of a number of questions concerning the role and nature deep-water flows posed by the main lecturer, D. L. Pratt:

1. Regulation of the thermohaline circulation?

2. Can the geometry and dynamics of deep straits be exploited for climate monitoring?

3. Possible role of traditional hydraulics in view of the time-dependence characterizing many deep-water flows in nature?

4. Can the upstream influence and mixing associated with deep-water flows be parameterized in numerical models of the general ocean circulation?

5. Why no observations of rotating hydraulic jumps?

Initially the discussion focused on the previous question above and two main reasons for the absence of field observations of rotating hydraulic jumps, i.e., mixing and the fact that channels in nature tend to be of a non-ideal character. It was, however, pointed out that mixing does not "kill" non-rotating hydraulic jumps and, furthermore, it was emphasized that precise bottom-

stress measurements are becoming available. Questions 1 and 2 were not explicitly discussed, but the deafening silence implied consent with regard to the speaker's viewpoint that recent attempts at climatological hind casts from Faroe-Bank Channel are not entirely uncomplicated. Question 3 was not explicitly dealt with during the session, but was partly covered Thursday morning in connection with the discussion concerning "matrix" and "functional" formulations of hydraulic theory. Similarly, Question 4 regarding parameterizations in OGCMs and climate models was instead dealt with during the Friday morning session. The question, "Where do we go from here?" emerged spontaneously from the audience and was interpreted in a very literal sense, since the answers mainly were of a geographical nature. The possible global importance of the Bering Strait was discussed, a theme which was further expanded in a very nice presentation by Doron Nof during the Friday morning session. The moot question whether hydraulic or geostrophic control is exerted here was raised. The Indonesian throughflow was also brought up, with special emphasis on the Lombok and Timor passages, and it was pointed out that the Malacca Straits are exceedingly important from a commercial/navigational standpoint. This overall discussion was somewhat inconclusive but showed the necessity of continued field observation programs. This was underlined in a very nice way by Rolf Käse who concluded the session by showing a happy marriage between "field" and "theoretical" activities from the Denmark Strait. Here optimal measuring-device locations had been determined on the basis of model studies, thus underlining the fundamental unity between observational and theoretical approaches to the problem of deep-water flow.

Thursday a.m.   Exchange Control Mechanisms
                      Speaker: Larry Armi
                      Chair: Emin Ozsoy

Summary by Karl Helfrich, Rapporteur:

In his plenary talk Larry Armi began by reviewing the theory for two-layer hydraulically controlled exchange flows and used this problem to point out several generic features of hydraulically controlled flows. The main messages from this part of the talk were "embrace nonlinearity", "look for asymmetry", and "be lazy". The first of these might translate to "hydraulics is fundamentally nonlinear, so accept it", or "nonlinearity has got us by the neck, so get used to it". The second points out that because of the nonlinearity, hydraulically controlled solutions are asymmetric, so the focus of our search should be for asymmetric solutions (though it was noted by Larry Pratt that friction can give asymmetric flows which are not controlled). The last tells us to start by looking for the steady solutions to the governing equations, a much easier task than solving the complete initial value problem leading to a hydraulically controlled flow. Next, advantages of the differential, or matrix approach to hydraulics, in comparison to the functional (i.e., Gill) approach, were discussed using the two-layer exchange flow solutions as a case in point (e.g., it is easy to identify the nature of the multiple control points with the differential approach). This generated much discussion and it was agreed that the two approaches must, in the end, give the same answer. The use of one approach over the other would seem to come down to issues of easy of use or interpretation. However, Chris Garrett gave an example, hydraulic control of a barotropic fluid with vertical shear, in which the functional approach appears to be the only method of solution (at this time).

At the previous Straits meeting in Les Arcs in 1989, the problem of hydraulics of continuously stratified was identified as an area in which progress needed to be made. Larry Armi discussed his work in this area and several interesting point of discussion emerged. First, to construct these solutions the assumption of self-similarity of the flow must be made. Though these appear to be the only solutions to have been found one is always left with the uncomfortable feeling that other solutions are available but not found. However, these self-similar solutions do compare well with the few available laboratory experiments. As an example of the failure of self-similar solutions Chris Garrett showed that for the problem of barotropic flow with shear mentioned above an assumption of self-similarity of the flow implies that frictional effects must be important. Secondly, these self-similar solutions involve regions in continuously stratified flows, or one or more layers in the N-layer approximation to continuously stratified flows, in which the flow is stagnant and the density uniform. That these layers are required to obtain solutions immediately brings up the question of how these layers are established and their (likely) connection to mixing processes. Mathematically, these stagnant zones decouple regions of the flow. Andrew Hogg noted that stagnant layers produced by mixing would in fact imply a dynamical coupling of the layers. This is true at least initially as the layers are formed since the mixing processes (e.g., Richardson number) involve flow above and below the stagnant zones (in the exchange flow case). Thus it seems that we cannot avoid the question of time-dependence. How are the exchange flow and the stagnant well mixed zones generated in an initial value problem? For example, consider the problem of a dam at a contraction separating two basins each filled with stagnant, linearly stratified fluid, but with the lightest fluid in one basin heavier than the densest fluid in the other basin. An exchange flow will develop after removal of the barrier. Initially there are no stagnant well-mixed zones. As the flow approaches a steady state does it evolve to one of the self-similar solutions (Engqvist, 1996, JFM 328, 49-67)? If so, how is the thickness and density of the required stagnant layer determined? It is a free parameter in the theory. Is the requirement of the stagnant regions (and the dissipation required to generate them) equivalent to Garrett's finding that his self-similar solution requires friction?

Lastly, there was some discussion about the fact that strait flows are coupled to basins, which are never infinite in extent. Also the reservoir levels, their stratification, the potential vorticity of the fluid approaching the strait, are given parameters in the local hydraulic flow problem. However, a complete picture of the role of hydraulic control must consider coupling of the overflow to the basins. This, too, will require investigation of time-dependent effects. Though any available steady (i.e., lazy) solutions are always a good place to start.

Thursday p.m.   Stratification Issues
                    Speaker: Greg Ivey
                    Chair: Kraig Winters

Summary by Andy Hogg, Rapporteur:

This session focused on the effects of stratification in exchange flows. The review talk was presented by Greg Ivey and included results from laboratory, field and numerical studies.

The review talk used three primary examples of stratified exchange flow in straits. Firstly, in a semi-enclosed basin, which is connected to the sea by a strait, the exchange through the strait and the mixing in the basin interacted to govern the evolution of the system. Secondly, the effect of internal mixing in exchange flows was investigated demonstrating that when mixing is significant, the hydraulic solution may not be the best way of estimating flux through a strait. Thirdly, results from an experiment into time-varying exchange flows were presented, showing that tides could act to either increase or decrease flux through a strait. The talk demonstrated the need to move away from depending on the hydraulic solution to describe exchange flows, and to incorporate the effects of mixing and unsteadiness into our models of flow through straits.

The discussion after the talk was lead by Kraig Winters, and started on the topic of whether a regular taxpayer would be content with the approach taken to sea strait research, and whether sufficient progress is being made. This sparked a wide-ranging debate in which many tried to clarify the purpose of current research. Notable points included the goal of advancing basic science and knowledge of underlying processes, budgets for ocean transport, and public education. The spectrum of opinions ranged from those who consider the purpose of their research to be to produce information or answers to questions for use by other scientists; to those who work on problems for their own enjoyment in the belief that this is the most productive way to work.

Friday a.m.   Large-Scale Consequences of Straits
                  Speaker: Jim Price
                  Chair: Peter Killworth

Summary by Ettori Salusti, Rapporteur:

Effect of Water Exchanges in Sea Straits on the Oceans. Water exchanges through marine straits and their effects on oceanic circulation can be seen as a difficult problem. Indeed, let us consider the general scheme described by J. Price, namely: shelves, marginal sea, strait, ocean. It is clear how water exchanges, currents, downflows etc., are ruled by some small-space or small-time scales fundamental "mechanisms" as dense water outflows, hydraulic-geostrophic-PV control of flows through straits. These "mechanisms" are rather difficult to be schematized in an effective manner: so the results of numerical investigations have to be analyzed critically also considering the results of simple intuitive models.

Let me add first that also the scheme of Price can be generalized: as an example in the Ross sea (Antarctica) a complex set of banks and canyons plays a role similar to that of a marginal sea. Of interest is also that Budillon has observed there that some CTD casts reveal in the deepest layer a homogeneous concomitant jump of salinity, potential temperature and light adsorption. This strongly suggests that entrainment of bottom particulate can play an active role on bottom water dynamics.

Second, the densest water evolution, as discussed by Bryden and Nurser, can somehow be intuitively controlled, despite complications due to entrainment and frictional effects. For the more superficial layers an interesting "tracer" can be the PV, and its evolution as well.

In addition, time-variations of flows through straits give origin to a complex system of Kelvin waves, propagating along the coasts and the Equator. Once they arrive on the eastern coasts, a westward propagating Rossby wave can be observed, on time scales of about 20 years. The reconstruction of this westward propagation off, say, the strait of Gibraltar is rather impressive.

To finish, a totally different approach of Doron Nof allows one to gain a penetrating insight into these problems. Nof uses suitable integral relations to infer particular aspects of the strait-ocean circulation; his technique is elegant and powerful but that requires a noticeable creativity to master the choice of the path of various integrals.

Friday p.m.   Summary by Rapporteurs

Overflows and the large-scale circulation: A review

James F. Price

Woods Hole Oceanographic Institution, Woods Hole, Massachusetts, USA

Abstract. Overflows from marginal seas have a variety of important effects upon the thermohline circulation of the oceans, including in the upper ocean. A well known effect of marginal seas is that they serve as concentration basins that produce water types that can be considerably denser (colder or saltier) than would result from the same air-sea flux applied over a comparable open ocean region. Thus many abyssal water masses have the T/S stamp of marginal sea and overflow processes. Modelling studies have suggested that the potential vorticity (PV) flux associated with an overflow may be a major component of the PV budget of an abyssal layer. The steady circulation that is in steady PV balance with this flux can be quite different from the PV balance associated with a free convection process, for example. The entrainment of mid or upper ocean water is now recognized to be a significant process for the upper ocean circulation, at least in the vicinity of a major overflows (e.g., the Mediterranean overflow). Entrainment represents a significant diapycnal mass flux out of the upper (or mid) ocean and into the overflow current. This can induce a large scale, upper ocean circulation akin to a beta-plume.

Introduction

The geography and physics of marginal sea overflows and strait flows are a key element of many regional oceanographic problems and phenomenon. Overflows (and here we emphasize the major marginal sea overflows from the Nordic Seas and the Mediterranean Sea) are also now widely appreciated to be a major element of the large scale ocean circulation. Because the high latitude overflows produce some of the densest water types that enter the world ocean, they have a significant impact upon the abyssal circulation and the global thermohaline circulation. Overflows are thus a central problem for ocean general circulation modelling. The challenge that overflows present is that they are relatively small scale features, typically 100 - 300 m in thickness and with a horizontal scale set at first by the strait width, 10 to 50 km, and later by geostrophic adjustment and frictional processes (Figure 1). Overflow currents are also typically much more energetic and much more dissipative than are most other bottom currents. Thus, realistic overflows do not arise spontaneously in the present generation of OGCMS, even those with the highest resolution [*Willebrand et al.*, 2001] [*Boning and Semtner*, 2001].

This note reviews some of the recent efforts to include or in one way or another to represent overflows in large scale ocean models. There are two aspects of this - the first is to understand what the consequences of the overflows are, and thus to understand the motivation for their inclusion in
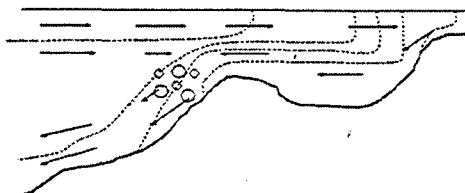
Figure 1. Schematic of a descending, entraining overflow. Since the upper and lower layer flows are shown to nearly balance, this is closest to the Mediterranean overflow through the Strait of Gibraltar.
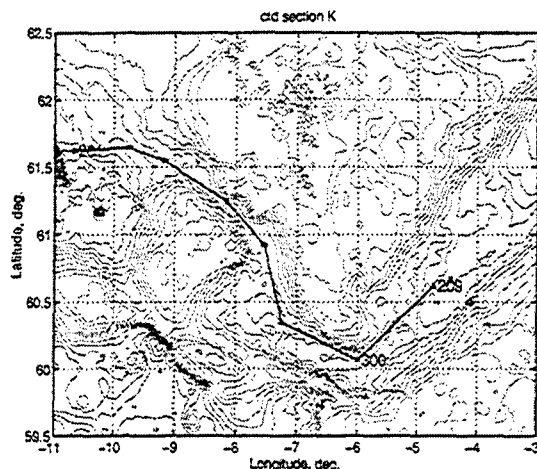
Figure 2. CTD stations strung together to make a section near the axis of the Faroe Bank Channel overflow.

Figure 3. A section of potential temperature constructed from CTD stations made near the axis of the Faroe Bank Channel overflow. The station-to-station horizontal variability evident near the sill is not synoptic. From *Price et al.* [2001]

OGCMs, and the second is to define the physical processes that should be represented. In all of this we take the perspective that the marginal sea conditions (hydrography at minimum) are given, and then consider the effects of a marginal sea overflow upon the open ocean. It goes almost without saying that the dynamics of the marginal sea itself are crucial in setting these conditions, and are in no way simpler or less interesting than the is the dynamics of the open ocean that is the topic here.

A schematic view of an overflow [*Price and Baringer*, 1994] is that they are bottom-intensified density currents. As they descend over steep topography (shelf-slope break) they may accelerate up to critical Froude number, and vigorously entrain water from the overlying oceanic water. This entrainment process is a distinguishing feature of overflows compared with other bottom currents. The entrainment is sufficient to cause the transport to more or less double, typically, while causing significant changes in T/S and density within the overflow (Figures 2 and 3). A compilation of the mixing endpoints for six of the larger overflows after *Bower et al.* [2000]) shows that the change in T/S of overflow water typically extends at least half way from the source water (the pure marginal sea water) toward the ocean water T/S end point (Fig. 4.

A North Atlantic basin-averaged view of this water mass transformation process is provided by the analysis of *Lumpkin and Speer* [2002]. They have used a density coordinate inverse model of the North Atlantic WOCE data set to determine where (with high resolution in density but only roughly in latitude) water mass transformations occur. Aside from the surface-effected layers, the most prominent transformation is found to be in the region of the Nordic Sea overflows. Water at the density of Labrador Sea water (neutral density 27.9 - 28.0, roughly) is made denser, evidently by entrainment into the densest Nordic Sea overflow water, which in
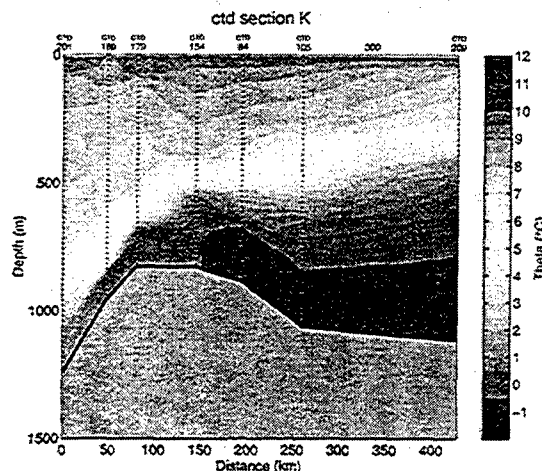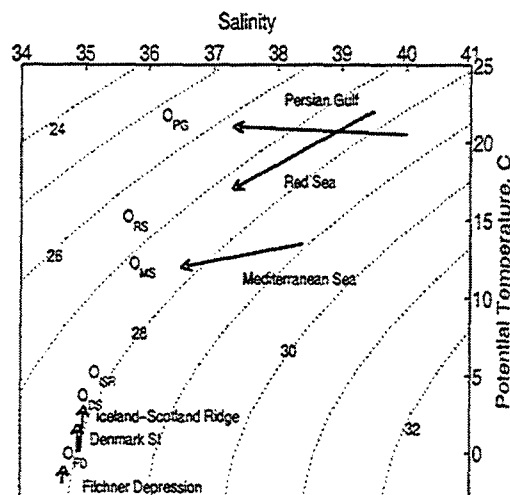
Figure 4. A T/S diagram constructed from ocean observations to show the source, oceanic and product water gross properties of some major marginal sea overflows [*Bower et al.*, 2000]. The arrows start on the source water T/S, and terminate on the product water (where the overflow floats away from the bottom or reaches geostrophy on the bottom). The small circles are the approximate T/S of the oceanic water through which the overflows descend.

turn is made somewhat less dense. In density space, trajectories denoting water mass volume appear to converge onto the density that characterizes the product water of the Nordic Sea overflows. *Lumpkin and Speer* [2002] conclude that this water mass transformation is a fundamental element of the North Atlantic meridional overturning circulation.

Abyssal and thermohaline circulation

Mechanisms of deep water production. The pioneering models of a dynamic thermohaline circulation *Bryan* [1987] *Maier-Reimer et al.* [1993] necessarily used highly idealized models of the ocean bathymetry that did not include realistic passages to the Nordic Seas. A consequence of this was that the formation of North Atlantic deep water occured by an open ocean convection process in regions south of the Scotland-Iceland-Greenland Ridge. Given plausible fields of the air-sea fluxes these models yielded quite reasonable estimates of the amplitude of the North Atlantic thermohaline circulation. These models then also indicated a substantial sensitivity of the thermohaline circulation to the air-sea exchange in the regions south of the Ridge. *Redler and Boning* [1997] examined this aspect of ocean climate modelling by using a high resolution, regional OGCM that could be configured to include or omit the Nordic Sea overflows while maintaining a nominal air-sea flux over the North Atlantic. They found that the sensitivity of the meridional circulation amplitude to surface forcing was minimal in cases where the overflows were prescribed at nominal values (or stronger). On the other hand, if the Nordic Sea overflows were weakened, then their model began to exhibit the kind of significant sensitivity to air-sea fluxes found earlier in the early models that omitted the overflows altogether. Thus, they concluded that the primary sensitivity of the North Atlantic meridional circulation (and assuming present, nominal values for the density of the overflows and open ocean convection regions) was to the Nordic Sea overflows rather than to the open ocean convection process that is driven directly by air-sea fluxes over the Northern North Atlantic.

A more recent study of high resolution North Atlantic OGCMs was reported by the DYNAMO Group [*Willebrand et al.*, 2001] who compared a suite of highly resolved numerical models that differed mainly in their vertical discretization. The models included at least partial representation of the Nordic Sea overflows by means of a relaxation of the model hydrography toward a high resolution ocean climatology imposed along their northern boundary (within the Nordic Seas). Although driven by nearly identical boundary conditions, the models each developed a unique deep and general circulation, that depended a great deal upon the way that the models treated or produced a deep western boundary current as a consequence of the Nordic Sea overflows. The models differed in the way that they represented topography, and thus in the way that they handled the overflows (bottom-trapped density currents) over the topography. To quote "Of fundamental importance is the conclusion that the large-scale thermohaline circulation is strongly

influenced by rather localized processes; in particular by the overflow crossing the Greenland-Scotland region, their water mass properties, and the details of mixing within a few hundred kilometers south of the sills." For the short term (decadal) simulations reported by DYNAMO, the differences attributed to this overflow mixing process included significant differences in the meridional heat transport, and if run much longer (centuries), the differences in overflow properties would ultimately affect the T/S climate of the global abyssal ocean.

Boning and Semtner [2001] studied the effects of the meridional circulation upon the model-computed heat transport within the North Atlantic basin at mid-latitudes. The meridional heat transport is determined largely by the meridional overturning circulation (rather than the upper ocean wind-driven circulation), and is thus very sensitive to the depth-dependence and the amplitude of the meridional overturning circulation. The differences between high resolution models, each driven by very similar boundary conditions, was found to exceed the difference in heat transport found upon occupying ocean sections over successive decades. The differences from model-to-model are due mainly to the differences in the way they treat the mixing and cross-isobath flow near the source of the Nordic Sea overflows. Level models (of the late 90's generation) tend to mix too much and thus produce an insufficiently dense Deep Western Boundary Current, while isopycnic models may not mix enough. Either way the meridional circulation and heat transport are directly effected, with the result that any individual model solution can be difficult to interpret with the extant observations. In models that have prescribed air-sea fluxes (not interacting with an atmosphere) the result is that the meridional heat transport, H in pettawatts, is given fairly closely by $H = 0.2 + M/20$, with M the transport at 25 N in Sverdrups (Fig.2.2.11 of *Boning and Semtner* [2001] and references therein). The small offset, 0.2 Pw, is roughly the contribution from the wind-driven circulation with the much larger linear term attributed to the thermohaline circulation. Thus the model-simulated heat transport is extremely sensitive to changes in the thermohaline circulation.

Steady circulation and PV balances. The circulation of an abyssal layer that is drained or supplied by a deep water source has been studied by *Pratt* [1997], *Yang and Price* [2000] and Helfrich and Pratt (in this volume). The PV balance of the steady basin-wide circulation is between the torque exerted by bottom friction and the PV flux supplied by the deep water source. If the deep water source is associated with a downwelling in the open ocean, as might occur in mid-gyre convection, then the PV source vanishes, as must the basin-wide bottom torque. In that case, the major boundary currents are likely to have a rather complex pattern that may include a very strong recirculation near the downwelling source. If the deep water source is the horizontal boundary flux associated with an overflow from a marginal sea, then the source brings a significant PV flux that must balanced by the frictional torque of the basin wide bound-

ary currents. In that case the boundary currents tend to have a simpler basin-wide pattern, usually without strong recirculation and consisting of a monotonic flow away from the overflow. In either case, the PV balance is an important aspect of the abyssal circulation, and strongly effected by the form of the deep water source.

Aspects of the observed PV distribution of the abyssal world ocean have been described by *O'Dwyer and Williams* [1997]. The observed PV distributions in some basins (some regions) show a correlation with the deep water source. One intriguing pattern is that basins ventilated from a single source (horizontal inflow to the basin) coming in at a low latitude tend to have a large region of nearly uniform PV and values of PV that are low in amplitude. In general, though, the observed PV distribution of the abyssal ocean is a good deal more complex and richer in structure than the very simple models noted above. There are large regions where PV follows latitude lines, other regions that have PV contours inclined to latitude, and still other regions that have nearly uniform PV. This may mirror the complex way in which water masses are formed by air-sea interaction; *Mauritzen* [1996] and *Spall and Pickert* [2001] have argued that convection occurs mainly near ocean boundaries, and thus the sharp distinction between downwelling and overflow as a PV source is blurred from the beginning.

Time scales of the transient response. The transient response to a change in the deep water formation process has been examined recently by *Huang et al.* [2000] and in greater detail and over much longer durations by *Goodman* [2001]. A principal finding is that there are two distinct time scales over which the ocean adjusts to a change in deep water formation (say in the North Atlantic). Over a period of several decades, the signal is propagated basin-to-basin by Kelvin waves that travel at the speed of fast, nondispersive (baroclinic) gravity waves, up to 3 m s^{-1}. These Kelvin waves propagate along coastal and equatorial wave guides; when the wave signal propagating along the equator reaches an eastern ocean boundary, the wave bifurcates, with Kelvin waves continuing poleward. As the Kelvin waves propagate along eastern ocean boundaries they spawn a westward propagating Rossby wave, whose arrival in the open ocean marks the final stage of the wave adjustment process. All of this happens comparatively quickly; with the wave adjustment well underway throughout the world ocean (excepting the Southern Ocean) within only about 20 years. A decrease in deepwater formation in the North Atlantic causes a downward motion of the main thermocline globally, and small changes in the SST. For a (large) change of 10 Sv, the equilibrium change in the thermocline depth was found to be about 100 m in the Atlantic, and about 50 m in the Pacific Ocean. Within the North Atlantic, a decrease in the deep water formation rate causes a decrease in SST, while over the rest of world ocean the result is a slightly deeper main thermocline and slightly warmer SST. Thus the North Atlantic and global ocean SST were found to vary out of phase

(though with small amplitude) with changes in the deepwater formation rate.

Goodman (2001) has extended these calculations to much longer times and in a model with much greater vertical and topographic resolution. The wave adjustment in this more complex model is qualitatively like that of the much simpler *Huang et al.* [2000] model, being almost complete in less than about 50 years. This is thus the time scale over which the currents respond to change in deepwater formation in the North Atlantic. The time to flush out and replace the abyssal ocean is a much longer advection time, that is often associated with a changing abyssal ocean. This is more like the 1000 year time scale that we know characterizes the age of North Pacific intermediate waters, for example.

Spreading of Mediterranean water

Once the mixed Mediterranean water descends to a depth of around 1 km it approaches neutral buoyancy but retains a large salinity anomaly compared with other North Atlantic waters near the same density. Much of the mixed Mediterranean water lifts away from the bottom in the western Gulf of Cadiz and ceases to be a bottom-trapped density current (a significant fraction stays in contact with the bottom and flows northward along the Iberian coast). The large scale distribution of salinity in the North Atlantic thermocline is marked by a saline tongue of Mediterranean water that extends across most of the North Atlantic basin. The salinity contributed to the thermocline by the Mediterranean clearly has a significant impact on the T/S properties of the North Atlantic thermocline, and though the details are controversial, may contribute to the global thermohaline circulation by raising the salinity (and the temperature) of the intermediate waters that contribute to the Nordic Sea inflow [*Candela*, 2001].

The westward spreading of the mixed Mediterranean water has been the object of many studies, including recently by *Gerdes et al.* [1999] who considered a wide range of mechanisms that could be represented in a coarse-resolution OGCM (one that does not support submesoscale eddies, Meddies). They found that the most effective and least *ad hoc* process was that associated with the source/sink flow of the overflow itself. That is, the modeled salt tongue was most realistic when the model boundary condition included not just the T/S properties of the Gulf of Cadiz, but also the zonal mass flux that makes up the exchange. With that boundary condition present, their model produced a jet-like westward mean flow that was just slightly south of the Mediterranean overflow and gave a very realistic looking salt tongue (and assuming plausible horizontal diffusion). Other process, including double diffusion and cabelling, gave much less realistic salt distributions and much weaker salt fluxes, generally.

In the ocean or in models having very high resolution, the westward salt flux is carried in part by submesoscale coherent vortices, or Meddies. These features occur also in outflows from the Red Sea [*Bower et al.*, 2000]. The ori-

gin of submesoscale is probably varied, but dependent upon the structure (horizontal and vertical) of an overflow current. *Morel and McWilliams* [2001] examined the effects of diapycnal mixing upon the PV structure of the Mediterranean overflow. They used the integral constraint of Haynes and McIntyre to infer that a layer that loses volume on account of mixing will acquire a positive PV anomaly, and conversely a layer that gains volume will acquire a negative PV anomaly. Thus, diapycnal mixing can alter the PV distribution of an otherwise stable current so that the Charney-Stern criterion for baroclinic instability may then be satisfied. Baroclinic instability in turn produces baroclinic dipoles, or hetons, that detach from the main current, and then transporting the overflow anomaly in a way that the mean current could not. The observed PV distributions in the western Gulf of Cadiz is not inconsistent with this scenario. Some more direct evidence of this kind of Meddy generation comes from float experiments that show the development of anticyclonic looping characteristic of Meddies and overlying a deeper cyclonic looping characteristic of baroclinic dipoles. Thus mixing effects may alter the stability of overflow currents, and thus their subsequent stability and the long term evolution of their tracers.

Upper ocean circulation

The effects of a marginal sea overflow extend into the upper ocean, as well. The surface inflow is an obvious manifestation, and is of course an important feature regionally in the Mediterranean and Nordic Seas. There is another aspect of the upper ocean circulation that has only recently been appreciated [*Jia*, 2000; *Ozgokmen et al.*, 2001], and that follows from the effect of entrainment by a descending overflow. Entrainment represents a substantial volume sink for the upper ocean that must be supplied by a convergent flow within the upper layer (upper ocean). In turn, entrainment is a significant volume source to the lower layer (the overflow layer). This kind of source/sink flow has the potential to produce a large secondary circulation by the beta-plume mechanism. Jia (2000) and Ozgokmen et al. (2001) have shown that the upper ocean circulation induced by the descending Mediterranean overflow (or the equivalent water mass transformation) includes a mean eastward flowing upper ocean current that is much like the actual Azores Current, and which is nearly absent in models without some representation of the water mass transformation associated with an entraining overflow. In the quasi-geostrophic model of Ozgokmen et al. (2001) there is a nearly equal countercurrent to the south of the modelled Azores Current and that may be an equivalent to the Azores Countercurrent.

Summary and remarks

Overflows from marginal seas have been found to be a crucial element of the general circulation of the oceans. The strong imprint of overflow T/S properties has been evident for some time; what is comparatively recent is the appre-

ciation that water mass transformation (mixing and entrainment) that occur as overflows descend into the open ocean is also of first importance. This mixing strongly effects the transport and the depth of the Deep Western Boundary Current (and thus of the meridional heat flux predicted by ocean models). The upper ocean sink associated with entrainment appears to be responsible (in some OGCMs) for the Azores Current. Important questions and issues related to this new understanding include the following:

- How much (and where) entrainment occurs in overflows? This is a question that can only be addressed by process-oriented field observations.

- What external variables control or set the entrainment rate? This requires field observations to define the entrainment rate and the local setting (Froude numbers, etc.). Inferences of entrainment laws can be tested in laboratory and perhaps high resolution numerical experiments.

- How can the entrainment process be represented in large scale models? This is a classic parameterization problem; the goal is to achieve the right outcome (the right entrainment rate) in models that can not be expected to resolve fully the small spatial scales of overflows. Thus, the task will be to tailor parameterizations that are appropriate to a given OGCM.

References

Boning, C. W., and A. J. Semtner, High-resolution modelling of the thermohaline and wind-driven circulation, *Ocean Circulation and Climate*, pp. 59–77, 2001.

Bower, A. S., H. D. Hunt, and J. F. Price, The character and dynamics of the Red Sea and Persian Gulf outflows, *J. Geophys. Res.*, *105*, 6387–6414, 2000.

Bryan, F., Parameter sensitivity of primitive equation ocean general circulation models, *J. Phys. Oceanogr.*, *17*, 970–985, 1987.

Candela, J., Mediterranean water and global circulation, *Ocean Circulation and Climate*, pp. 419–429, 2001.

Gerdes, R., C. Koberle, A. Beckmann, P. Herrmann, and J. Willebrand, Mechanisms for spreading of Mediterranean water in coarse-resolution numerical models, *J. Phys. Oceanogr.*, *29*, 1682–1700, 1999.

Goodman, P., Theromhaline adjustment and advection in an OGCM, *J. Phys. Oceanogr.*, *31*, 1477–1497, 2001.

Huang, R. X., M. A. Cane, N. Naik, and P. Goodman, Global adjustment of the thermocline in response to deepwater formation, *Geophys. Res. Lett.*, *27*, 759–762, 2000.

Jia, Y., Formation of an Azores Current due to Mediterranean overflow in a modeling study of the north atlantic, *J. Phys. Oceanogr.*, *30*, 2342–2358, 2000.

Lumpkin, R., and K. Speer, Meridional overturning in the North Atlantic, *International WOCE Newsletter*, pp. 3–5, 2002.

Maier-Reimer, E., U. Mikolajewicz, and K. Hasselman, Mean circulation of the Hamburg OGCM and its sensitivity to the thermohaline forcing, *J. Phys. Oceanogr.*, *23*, 731–757, 1993.

Mauritzen, C., Production of dense overflow waters feeding the North Atlantic across the Greenland-Scotland Ridge, *Deep-Sea Res.*, *43*, 769–835, 1996.

Morel, Y., and J. C. McWilliams, Effects of diapycnal mixing on the stability of oceanic currents, *J. Phys. Oceanogr.*, *31*, 2280–2296, 2001.

O'Dwyer, J., and R. G. Williams, The climatological distribution of potential vorticity over the abyssal ocean, *J. Phys. Oceanogr.*, *27*, 2488–2506, 1997.

Ozgokmen, T. M., E. P. Chassignet, and C. G. H. Rooth, On the connection between the Mediterranean outflow and the Azores Current, *J. Phys. Oceanogr.*, *31*, 461–480, 2001.

Pratt, L. J., Hydraulically drained flows in rotating basins. part ii: Steady flow, *J. Phys. Oceanogr.*, *27*, 2522–2535, 1997.

Price, J. F., and M. O. Baringer, Outflows and deep water production by marginal seas, *Progr. Oceanogr.*, *33*, 161–200, 1994.

Price, J. F., C. Mauritzen, T. B. Sanford. and M. . Prater, A report of XCP and CTD data taken during the June 2000 RRS Discovery cruise 247b. a process study of the Faroe Bank Channel overflow, 2001.

Redler, R., and C. W. Boning, Effect of the overflows on the circulation in the subpolar North Atlantic: A regional model study, *J. Geophys. Res.*, *102*, 18,529–18,552, 1997.

Spall, M. A., and R. S. Pickert, Where does dense water sink? a subpolar gyre example, *J. Phys. Oceanogr.*, *31*, 810–826, 2001.

Willebrand, J., B. Barnier, C. Boning, C. Dietrich, P. D. Killworth, C. L. Provost, Y. Jia, J. Molines, and A. L. New, Circulation characteristics in three eddy-permitting models of the North Atlantic, *Progr. Oceanogr.*, *48*, 123–161, 2001.

Yang, J., and J. F. Price, Water-mass formation and potential vorticity balance in an abyssal ocean circulation, *J. Mar. Res.*, *58*, 789–808, 2000.

James F. Price, Dept. of Physical Oceanography, MS 29, Woods Hole Oceanographic Institution, Woods Hole, MA, USA, 02543. email: jprice@whoi.edu

web: http://www.whoi.edu/science/PO/people/jprice

Overview of process oriented field studies

David M. Farmer

Graduate School of Oceanography, University of Rhode Island, Rhode Island, USA

Abstract. Process oriented observations in straits have been concerned with the overall structure of the flow and the factors that control the exchange or modify water properties of the exchanging layers. These include the existence and location of exchange controls, the formation and behavior of distinct layers, time dependent effects associated with tidal and meteorological forcing, boundary layer separation in both a lateral and a vertical sense, entrainment and mixing between layers and the radiation of internal bores or solitary waves.

Introduction

Observations of the circulation in straits have a long history with notable contributions stimulated by the challenge of explaining flow in the Straits of Bosphorus and Gibraltar (Deacon 1985). Early observations made use of drogue studies, which revealed the bi-directional character of the exchange in these straits, but the advent of modern instrumentation has stimulated rapid advances in our understanding. These developments in turn are stimulating parallel theoretical and modeling efforts.

The focus of field measurements has evolved from observations designed to acquire a basic description of the oceanography, towards systematic attempts to test hypotheses, such as the presence or absence of maximal exchange conditions, or the mechanisms by which internal bores are generated. In addition to the overall measurement of exchange rates, field studies have started to address the smaller scale processes that have usually been neglected in models. Detailed measurements of shear flow instability and its contribution to mixing, of boundary layer separation effects, 3-dimensional circulation and the radiation of internal bores are now identified as significant components of many strait flows, posing new challenges for theoretical analysis and explanation. This brief discussion summarizes some of the measurement techniques and the recent observations. The focus is on straits that are not wide relative to the deformation radius. A primary interest is in the factors that influence control over the exchange.

Observational approaches

Measurement technology has evolved rapidly and is transforming the way in which we can observe both small scale and time dependent phenomena, presenting new challenges and opportunities for modeling and analysis. The observational challenges come from the range of scales involved. If the circulation is time varying, it is obviously desirable to acquire measurements throughout the area of interest over a period short relative to the time scale of the forcing, especially in straits subject to meteorological rather than predictable tidal forcing.

Many of the most significant contributions to our understanding have come from measurements using a combination of different *in situ* and remote sensing techniques from ships. Acoustic Doppler Current Profilers (ACDP) have played a key role here, as the structure of the current field is fundamental to identifying exchange flows. By combining repeated CTD profiles with the Doppler data it is possible to estimate Froude numbers directly as a function of position and time. Such measurements are fundamental to the determination of flow control, as well as to the calculation of layer transports, shear stability and other characteristics.

In situ measurement of shear microstructure has been used to infer dissipation, providing additional insight on the time and location of turbulent energy losses. For example Wesson & Gregg (1994) acquired direct measurements of dissipation both in the vicinity of the sill and within the internal bore in the Strait of Gibraltar. The measured values appear fully consistent with expectations based on the

energy loss calculated from internal hydraulic considerations (Farmer & Armi, 1988).

A novel measurement approach that has proven effective in tracking transports in the vicinity of sills is the Lagrangian float (D'Asaro et al. 1996), a technique that has also been used to explore the transition between turbulence and buoyancy dominated flow (D'Asaro & Lien, 2000).

Acoustic imaging of the back-scatter field has proven particularly helpful to the identification of small scale structure. Quite often a shear or density interface will be associated with enhanced acoustic target strength, allowing acoustic imaging to map the interface structure, even when a ship is traveling rapidly. The combination of ADCP mapping of
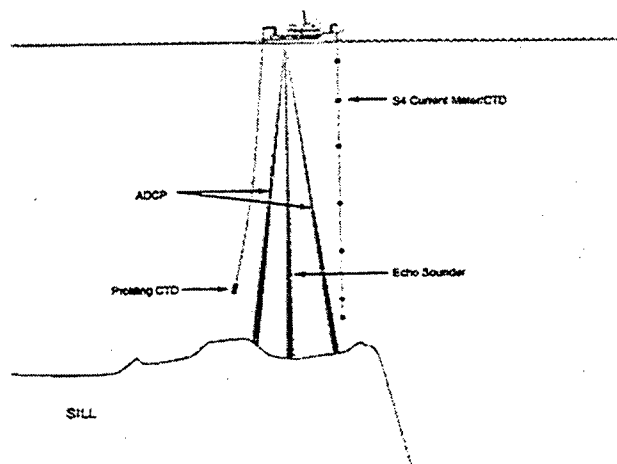
Figure 1 Sketch showing a typical ship based application of profiling and remote acoustic measurements, along with towed sensors at fixed depths. When combined with simultaneous aerial or satellite observations the larger scale features can be interpreted in conjunction with detailed subsurface measurements.

the velocity field with high resolution imaging (Fig. 1) provides a powerful technique for resolving the flow over large areas in a relatively short time. Continuous CTD profiling is not possible except at low speed, but the acoustic methods provide an effective means of interpolating the density structure between more widely spaced CTD stations.

Internal hydraulic controls are often associated with rapidly varying interface depths, shear instability and jumps. Acoustic imaging may provide the only technique for highly resolved measurement of these processes, since it may be impractical to profile with sufficient density using *in situ* sensors. Accurate positioning of the vessel is essential for

generating accurate data maps. This task has been transformed by the availability of GPS.
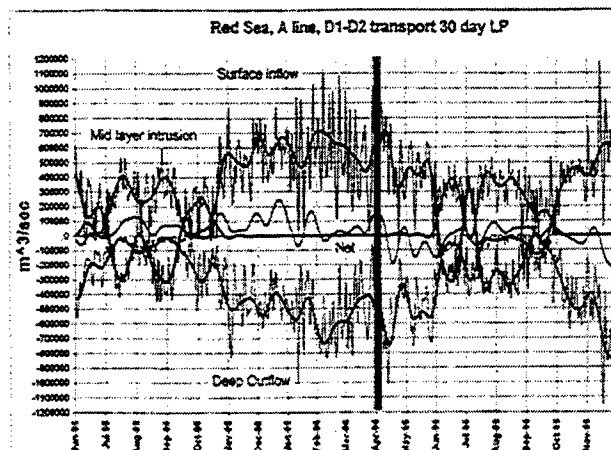
Figure 2 Time series measurements of flow in Bab el Mandeb acquired with a moored ADCP, showing the seasonal transition from two-layer to three-layer flow (Murray & Johns, 1997).

Although recording in situ current meters are a well established tools for acquiring longer time series than is possible from a ship, the moored ADCP has proven useful because of its high vertical resolution (Fig. 2), especially when combined with a dense vertical array of recording temperature/salinity sensors. The passage of internal bores is easily recognized with almost any recording sensor, but the depth change or amplitude measurement typically requires a higher resolution than is usually practical with in situ current meters. Highly resolved back scatter imaging is also useful for identifying density interfaces and even the ADCP back scatter intensity output which tends to have lower resolution than a dedicated imaging sonar, has proven helpful in monitoring the internal response to changing tide and meteorological conditions.

Well resolved pressure measurements also have an important role to play. Modern quartz pressure sensors can resolve pressure fluctuations which may be interpreted in terms of energy losses, associated, for example, with tidal effects. Extensive studies of sub-tidal fluctuations in sea surface slope using tide gauges at either end of a strait suggest the potential of this approach, especially for monitoring seasonal and longer term effects (i.e. Freeland & Farmer, 1980).

Integral methods of measurement that average over large volumes or over the total transport through a strait have obvious potential for monitoring flows in

Straits. Motionally induced electric fields (the Geomagnetic ElectroKinetograph or GEK method and its derivatives) can be measured and interpreted in terms of transport, once the subtle aspects of calibration have been resolved, a technique that is being actively explored at a number of sites.

Time-of-flight acoustic propagation provides another approach for integral measurement. The difficulty in this case is that the integration is along a path that will depend on the variable sound speed structure of the channel. Nethertheless, this approach does seem to offer interesting possibilities and has been demonstrated in the Strait of Gibraltar (Fig. 3).
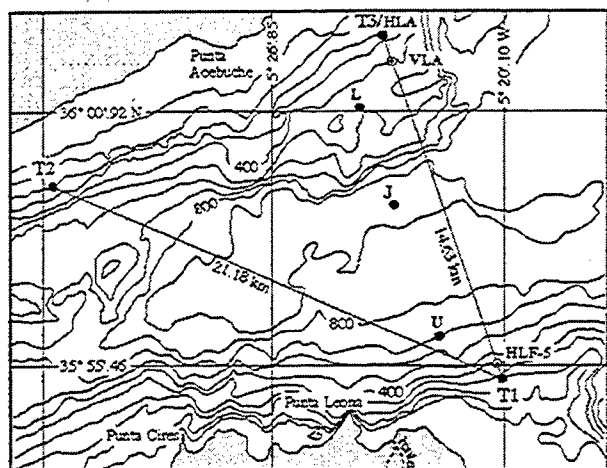
Figure 3 Reciprocal acoustic transmission paths used by Send et al. (2002) to monitor fluctuations associated with the passage of internal bores.

Yet another integral method is space-time acoustic scintillation, which relies on measurement of the translation of fine scale structure in the forward scattered acoustical field as it is advected by the current. This technique has been demonstrated in several coastal channels including the Bosphorus (Di Iorio & Yuce, 1999). The distinction between the time of flight measurement and the space-time scintillation analysis is that the former resolves the current along the path whereas the latter resolves the flow perpendicular to the path. The fine scale acoustical structure is related to the fine scale oceanographic features and inversion techniques allow derivation of integral properties of the scattering medium. For example Di Iorio and Farmer (1998) were able to separate temperature and velocity fluctuations and calculate the path averaged turbulence dissipation.

Remote sensing adds the power of large scale imaging. A particularly striking contribution of both

visual and radar imaging of straits has been the identification of internal wave radiation. Radar systems (Watson & Robinson, 1989) or cameras mounted on mountains (Pawlowicz, 2002) overlooking a strait also have potential here.

Finally, both radar measurement (especially synthetic aperture) and aerial photography can be used to detect smaller scale surface structure which contains many clues to the subsurface properties. Aircraft measurements in particular provide a flexibility in deployment timing and location that may not be available with measurements from space. In the case of observation from a light aircraft or helicopter, the aircraft can fly along particular features, such as a front or internal wave, using GPS to provide a precise spatial measurement.

Internal hydraulic response

The concept of hydraulic control is of particular importance in straits, as it exercises direct influence on the exchange. Maximal exchange is a special case in which two controls act to determine the maximum rate at which a two-layer flow can exchange. In its simplest form, a control occurs when the sum of the layer Froude numbers is unity (see, for example, Armi, 1986):

$$G^2 = F_1^2 + F_2^2 = 1$$

where the subscript defines the layer *1,2* and

$$F_i^2 = \frac{U_i^2}{g'h_i}$$

where U_i is the layer speed, g' is the reduced gravity and h is the layer depth. This definition is suitable for discrete layers, which are often characteristic of flow in straits. However, a layer may be density stratified and sheared, in which case an equivalent definition may be stated in terms of the relative propagation speed of long internal waves. A control occurs where a long internal wave is arrested. As discussed by Pratt (1986) and others, friction acts to drive the flow towards criticality. In longer straits for which friction is expected to be important (c.f. Pratt's 1986 criterion), there are good reasons to look for the implications of frictional effects.

In straits for which the internal Froude number approaches unity, rapid adjustments in velocity and density structure can occur over short distances. This is particularly true in straits such as Gibraltar where one of the controls occurs over a steep sided sill.

Most recent observations in straits have addressed the presence of layered structure and internal controls. Murray & Johns (1997) used moored ADCP measurements to find a seasonally varying two- and three-layered structure in Bab el Mandeb (see Fig. 2), raising interesting questions about the role of controls in limiting the heat flux. Gregg, Ozsoy & Latif (1999) and Gregg & Ozsoy (2002) and others searched for an internal control using ADCP measurements at the Southern end of the Bosphorus, to check whether or not a maximal exchange condition applied; the control at the northern end is readily identifiable. This measurement is particularly challenging in the southern Bosphorus, because the surface layer becomes extremely shallow at this location and the measurements are limited by instrument depth and other factors. Farmer & Armi (1988), Armi & Farmer (1988) found two controls in the Strait of Gibraltar in April 1986, supporting the concept of maximal exchange. Their measurements were also acquired with an ADCP, supported by XBT/XSSV profiles which could be acquired with the vessel traveling at speed.
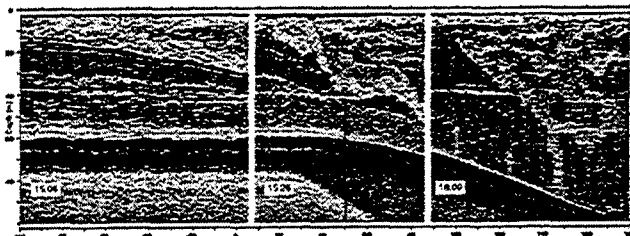

Figure 4 Three successive traverses over the Knight Inlet sill illustrating the transition between controlled and uncontrolled flow as the Froude number increases.

A single control acting on a lower layer as it passes over a sill is relatively common and has been measured, for example, using an ADCP in Knight Inlet by Farmer & Armi, 2000. Rapid traverses allow the structure of the control to be tracked as it changes under the varying tidal current, providing insights on the time dependent response. Figure 4 shows three such sections as the flow makes the transition between the controlled and uncontrolled state.

Entrainment

The advent of highly resolved density measurements acquired in conjunction with ADCP and acoustic imaging has revealed features of the internal response that can only be explained by mass transfer between different moving layers. For example, the repeated acoustic and CTD sections shown in Figure 4 illustrate a special case of the consequences of entrainment from the lower to the intermediate layer. Even though the tidal current was decreasing during these measurements, the Froude number was increasing, due to the reduced density difference at the interface, allowing the intermediate layer to be pushed downstream over the sill as control at the crest is effectively lost (Armi & Farmer, 2002).

On a larger scale, measurements in the Bosphorus make it clear that Black Sea water moving in the upper layer becomes progressively more saline as it travels south and a smaller but still measurable decrease in salinity occurs in the lower layer as it moves north.

Gerdes, Garrett & Farmer (2002) showed that in all but one unidirectional case, where the upper layer flow is larger than the lower layer by a certain Froude number dependent margin, entrainment acts to force the flow towards criticality in the same way as friction. A general result describing the interface slope as a function of Froude number F^2 and entrainment speed u_e is:

$$\frac{dh}{dx} = \frac{F^2}{1-F^2} \left[\begin{array}{l} -2\frac{u_e}{u}\left(1-\frac{1}{4}F^2-\frac{1}{2}\frac{v}{u}\right) \\ +\frac{h}{W}\frac{dW}{dx}-F^{-2}\frac{dH}{dx}-Cd \end{array} \right]$$

where v is the upper and u is the lower layer speed, H is the elevation of the sea floor, W is the channel width and Cd is the drag coefficient. This result provides a framework for interpreting the evolution of an exchange flow in straits such as the Bosphorus where both friction and entrainment are of comparable importance and an interpretation in terms of discrete layers is justified. It also accounts for the overall shape of the interface, especially in the southern narrow section where both entrainment and friction play a significant role in determining the exchange process.

Although there are numerous laboratory estimates of entrainment rates, the applicability of these to natural environments is at best uncertain. This motivates the use of acoustic imaging and other techniques to reveal the underlying mechanisms of entrainment. Acoustic images of sheared flow often reveal the presence of shear instabilities at the interface between the layers. These can be seen on a massive scale in sill flows and have been examined

in a laboratory setting (Pawlak & Armi, 1998), revealing the way in which additional vorticity is provided by the sloping interface. Both laboratory and field observations show whisps of denser fluid rising from the cusps of the instability.

Analysis of the detailed mechanisms associated with entrainment inevitably demand highly resolved measurements of the velocity field within the instabilities. These are hard to achieve by conventional means and push the limit of the stand ADCP. For example Fig. 5 shows instabilities above the lee face of the sill in Knight Inlet. ADCP measurements (not shown here) delineate the overall structure of the flow in these features, but push the limits of robust Doppler interpretation. The JANUS configuration Doppler current profiler is limited in resolution by the spreading beams, which must be combined to generate a current vector. The combination of data from the different beams is based on assumption that the flow is similar in all three beams.

Figure 5. Instabilities in dense flow over a sill illustrating whisps of lower layer fluid leaving the instability cusps as they are entrained into the upper layer. Red vectors indicate magnitude and orientation of the flow.

In certain cases, entrainment can be measured in a rather direct way by mapping the transport between discrete layers, where the layers are identified for example by density steps or well defined scattering layers. The rate at which these layers are transported through a sheared interface then defines the entrainment rate (Farmer & Armi, 1999).

Ultimately the success of predictive modeling will depend on our ability to parameterize the sub-grid scale processes. Laboratory models provide insight, but are generally limited by their ability to represent high Reynolds number flow. This provides

motivation for using observations in real environments to explore the small scale structure, thus motivating models of these process that will lead to reliable parameterizations for incorporation in strait models.

Time dependent processes

Temporal variability in straits presents one of the greatest challenges to accurate description. Most ocean straits are subject to tidal forcing. An important practical consideration is whether or not the flow can be considered quasi-steady. For example, in the case of maximal exchange flows, the relavant time scale for internal adjustment is the time taken for a long wave to propagate from one control to the other. In the Strait of Gibraltar this condition is met approximately. For longer period seasonal or atmospheric forcing, quasi-steady assumptions are almost certainly justified.

A striking consequence of the inherent nonlinearity in controlled flows is the transformation of tidal into higher frequency energy. The most prominent expression of this is the formation of internal bores. Fig. 6 shows a synthetic aperture radar image of an undular bore radiating from the Strait of Gibraltar into the Alboran Sea and is typical of many similar radar and is similar to many other optical and radar images. The waves tend to be rank ordered, spread radially from the source and are accompanied by a net deepening of the shallow surface stratification, consistent with the properties of an internal undular bore.

The generation mechanisms associated with radiating wave patterns have been the subject of fairly active research in recent years. Several studies have pointed to the relaxation of an internal hydraulic jump during the slackening tidal current as a source of the waves. This appears to be the case, for example in the Strait of Gibraltar and has been observed in great detail in a particular example for flow over the sill in Knight Inlet when the stratification was weak (Farmer & Smith 1980). In the latter case the downstream jump in the lee of the sill was undular – the signature might also be interpreted as constituting a set of finite amplitude lee waves – and successive wave troughs passed back over the sill as the tidal current slackened to form a sequence of waves propagating upstream with the character of an internal undular bore.
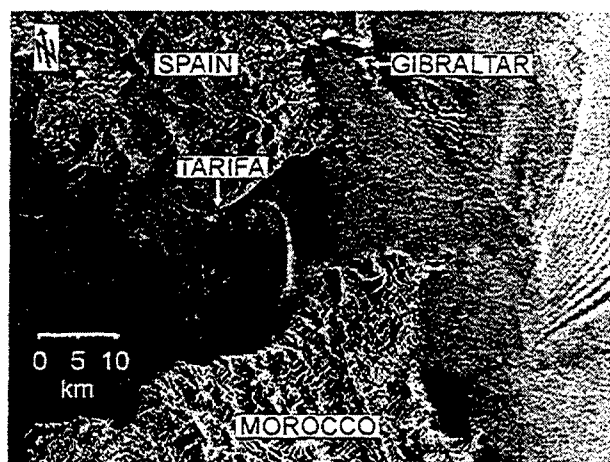
Figure 6 Internal undular bores radiating from the Strait of Gibraltar into the Alboran Sea, One set of waves is leaving the figure to the right, while a second set is forming within the strait. (Alpers et al., 1996)

This mechanism completely fails to explain all cases, however. Recent studies by Cummins et al. (2002) seek to explain observations of waves generated upstream of a sill when the flow is controlled. These waves do not pass over the sill crest, but represent the evolution of upstream influence. The observations show that tidal interaction with the sill produces a deformation of the interface propagating upstream; the interface has positive slope in the direction of propagation and therefore steepens due to nonlinearity, eventually forming a 'shock front' that radiates internal solitary waves.

Propagation of the internal bore in the Strait of Gibraltar produces a strong signal on the acoustic propagation measurements discussed above. Figure 7 shows a superposition of travel time measurements from several tidal cycles, illustrating both the overall tidal modulation of the signal and the sharp jump when the bore passes through. Full advantage of these novel measurements requires a combined application of acoustic propagation theory and a model for the bore behavior.

In straits that are subject to only weak tidal influence, meteorological effects may dominate the time dependent response. Gerdes (*personal communication*) observed an Orkuz event in the Bosphorus, in which the barotropic pressure gradient resulting from a passing storm, completely arrested the lower layer, transporting the brackish surface waters back towards the Black Sea (Fig 8). Observation of such infrequent phenomena depends on the availability of time series measurements from

moored instruments, in this case an ADCP mounted on the sea floor.
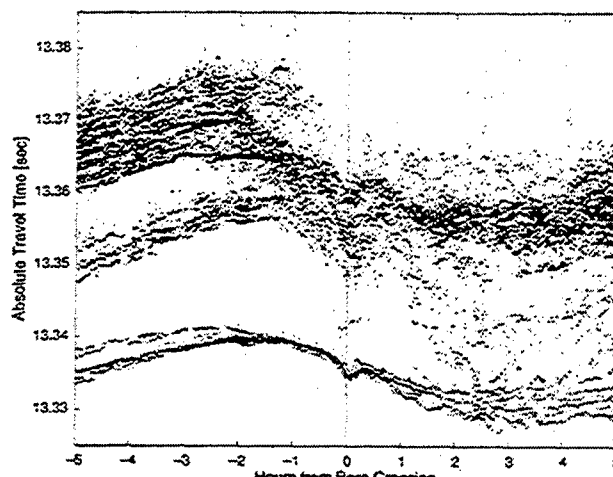
Figure 7 Time series of acoustic propagation across the Strait of Gibraltar (see Send et al., 2002 and references therein). Acoustic travel times for the paths shown in Figure 2 over a tidal cycle, superimposed for a seven day period. The overall modulation of the tide is apparent; the internal bore passes through at the time indicated by the red line.
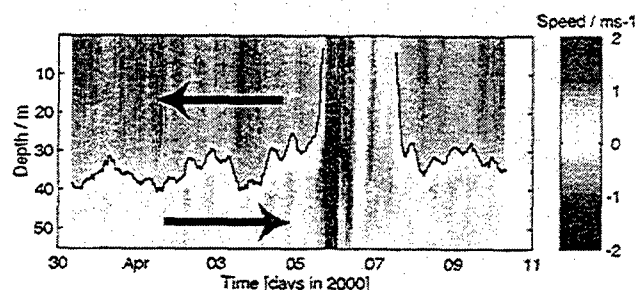
Figure 8 Doppler velocity time series in the Bosphorus (Frank Gerdes, *personal communication*) showing reversal of surface flow during an 'Orkuz' event. The water remained stratified, even though the the two layers moved northwards together, with little shear between them.

Boundary layer separation

Straits often exhibit abrupt changes in topography in the form of coastal headlands along the shores, or sills and other subsurface features. As the flow encounters such topographic features an adverse pressure gradient may arise, sufficient to cause the flow to separate. This occurs in a striking way in the Bosphorus, for example, where there is complete separation of the flow around one particularly sharp bend.

Separation can also occur over sills and has stimulated lively discussion in the literature. This topic is important, because separation can effectively inhibit transition of stratified flow over topography to the high drag state. Failure to properly include separation in model calculations has led to a misinterpretation of results. Boundary layer effects are not generally included in strait models, but may have to be considered for a comprehensive description where abrupt topography is present.

Fig. 9 shows an example of flow forming a separated jet downstream of the Knight Inlet sill. Later in the tidal cycle, as the intermediate layer fills in, separation is suppressed and the jet descends, reverting to the fully established state.
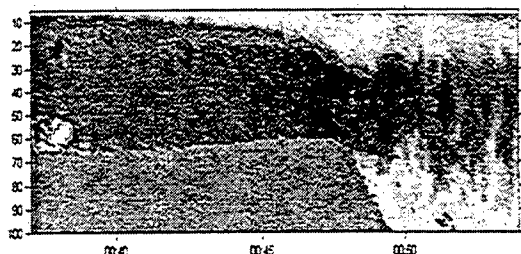
Figure 9 Flow over a sill illustrating boundary layer separation from the crest. Red corresponds to flow from left to right.
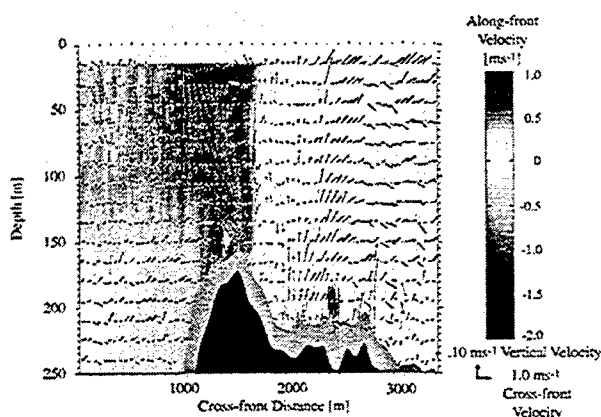
Figure 10a Doppler flow speed measured across a separation zone where a tidal current has separated from a headland in Haro Strait. Blue represents flow toward the observer, yellow is away. Arrows indicate transverse and vertical components.

It has been common to interpret exchange flow problems in terms of two-dimensional representation. This may be justified in many cases, but care is required, especially in the presence of rapidly varying topography. Particularly interesting situations arise when flow separates from a headland, leading to a

vertical shear zone dividing separate water masses with distinct and different density structure. An example of this process in Haro Strait is shown in Figures 10a,b. Figure 10a illustrates the separation zone immediately after it has left the headland. The shear zone is essentially vertical. Figure 10b shows the same front approximately 20 minutes later. This time delay is too short for rotational effects to play a significant role and the tilting of the interface appears to result from a horizontal density difference across the shear zone, leading to tilting. This tilting also stretches the vortex lines associated with the shear leading to intense turbulence and mixing (Farmer et al. 2002).
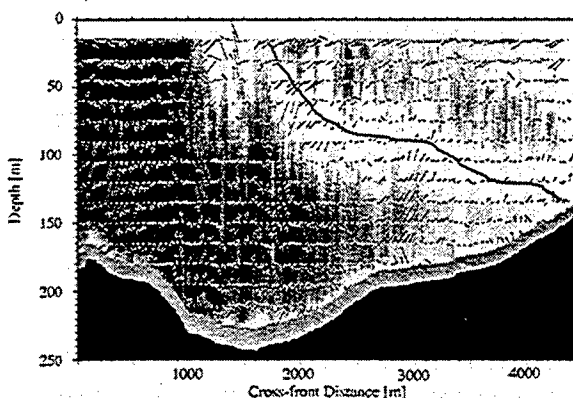
Figure 10b As for Fig 10a, but a few km downstream by which time density differences across the front have led to tilting of the interface.

Single layer controlled flow in straits

The discussion thus far has focused on stratified flow and it is true that most oceanographic flows in straits are indeed stratified and the stratification plays an important role in the circulation. Nevertheless, it is worth commenting that in coastal regions subject to strong tides, straits may exist in which the current is strong enough to drive the flow through a control with respect to the surface mode. In this case, even though the water may be stratified, the buoyancy effects are negligible relative to the inertial effects. One of many such examples on Canada's west coast is Nakwatka Rapids, a short strait connecting a large inland complex of fjords with the Pacific Ocean.
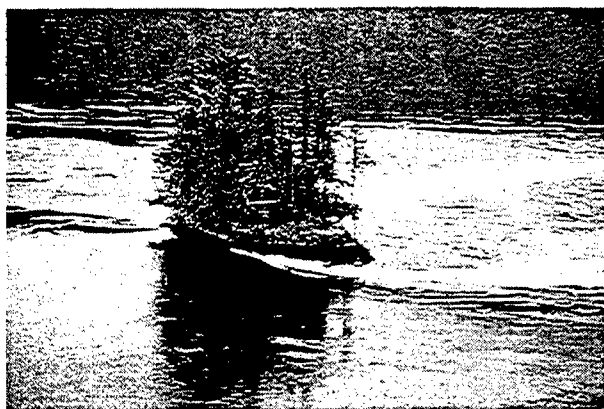
Figure 11 Flow past Turret Rock, an island in Nakwatka Rapids, a strait connecting a complex of fjords on the British Columbia coast with the Pacific Ocean. The flow is supercritical and drops 2.5m in a few hundred meters. The slope of the water surface is clearly visible in the figure.

Currents exceed 12knots and the surface visibly descends over 2.5m over the course of a few hundred meters (Fig.11). All stratification is destroyed as the water passes through the channel and the transition from controlled to supercritical flow, back to subcritical flow via a surface hydraulic jump, which has been examined for the internal controls discussed above, now becomes visible to the naked eye, providing a striking example of hydraulic response in a strait where the surface Froude number exceeds unity.

Conclusions

This necessarily cursory survey of observations in straits makes no attempt to be comprehensive, but is intended to provide a representative sample of the techniques now being used and the phenomena being studied. Straits will continue to be important for many reasons and the oceanography of straits has rightly attracted attention. Apart from their significance to the surrounding oceanography and their sensitive location for monitoring climatic and other changes, straits also serve as excellent laboratories for the study of geophysical fluid dynamics.

References

Alpers, W., P. Brandt, A. Rubino, and J. O. Backhaus, Recent contributions of remote sensing to the study of internal waves in the straits of Gibraltar and Messina, in *Dynamics of mediterranean straits and channels*, Briand F. ed., CIESM Science Series n°2, *Bulletin de l'Institut océanographique, Monaco*, 17, 21-40, 1996.

Armi, L., 1986, The hydraulics of two flowing layers with different densities. *J. Fluid Mech.*, 163, 27-58.

Armi, Laurence & David Farmer, 2002, Stratified flow over topography: Bifurcation fronts and the transition to the uncontrolled state. *{roc. Roy. Soc. A*, 458, 513-538.

Briand, F. (ed.), 1996, Dynamics of Mediterranean straits and channels, Bulletin de l'Institut océanographicque, numéro spécial 17 Musee océanographique, Monaco.

Cummins, P., S. Vagle, L. Armi & D. Farmer, 2002, Stratified flow over topography: upstream influence and generation of nonlinear internal waves, submitted to *Proc. Roy. Soc. A.*

D'Asaro, E, D. Farmer, J. Osse & G. Dairiki, 1996 A Lagrangian float, *J. Atmos. & Ocean. Tech.*, 13, 1230-1246.

D'Asaro, E. & R.-C. Lien, 2000, Lagrangian measurements of waves and turbulence in stratified flows, *J. Phys. Oceanogr.*, 30, 641-655.

Deacon, M., 1985, An early theory of ocean circulation: J.S. Von Waitz and his explanation of the currents in the Strait of Gibraltar, *Progr. In Phys. Oceanogr.* 14, 89-101.

Di Iorio, D. and D.M. Farmer, (1998). "Separation of current and sound speed in the effective refractive index for a turbulent environment using reciprocal acoustic transmission", *J. Acoust. Soc. Am.* 103:321-329.

Di Iorio, D. and H. Yuce, 1999. "Observations of Mediterranean flow into the Black Sea", *J. Geophys. Res.* 102:3091-3108

Farmer, David M., and Laurence Armi, 1988, The Flow of Mediterranean Water Through the Strait of Gibraltar, and Armi, Laurence and David M. Farmer, 1988, The Flow of Atlantic Water Through the Strait of Gibraltar, *Progress in Oceanography*, 21, 1-105.

Farmer, D. & L. Armi, 1999, Stratified flow over topography: the role of small scale entrainment and mixing in flow establishment, *Proc. Roy. Soc. A*, 455, 3221-3258.

Farmer D. & J. Dungan Smith, 1980, Tidal interaction of stratified flow with a sill in Knight Inlet, *Deep Sea Research*, 27a, 239-254.

Farmer, D., R. Pawlowicz & R Jiang, 2002, Tilting separation flows: a mechanism for intense vertical mixing in the coastal ocean, To appear, *Dynamics of Atmospheres and Oceans*.

Freeland, H.J., and D. M. Farmer, 1980, Circulation and energetics of a deep, strongly stratified inlet, *Canadian Journal of Fisheries and Aquatic Sciences*, 37 (9).

Murray, S.P. & W Johns, 1997, Direct observations of seasonal exchange throught he Bab el Mandeb strait, *Geophys. Res. Let.*, **24**, 2557-2560.

Gerdes, F., C Garrett & D. M. Farmer, 2002, A note on internal hydraulics with entrainment, *to appear, J. Phys. Oceanogr.*

Gregg, M.C. & E. Ozsoy, 2002, Flow, water mass changes and hydraulics in the Bosphorus, *J. Geophys. Res.*, i9n press.

Gregg, M.C., E. Ozsoy & M.A. Latif, 1999, Quasi-steady exchange flow in the Bosphorus, *Geophys. Res. Lett.*, **26**, 83-86.

Murray, S. & W.E. Johns, 1997, Direct observations of seasonal exchange through the Bab el Mandeb strait, *Geophys. Res. Let/*, **24**, 2557-2560.

Pawlak, G. & L.Armi, 1998, Vortex dynamics in a spatially accelerating shear layer, *J. Fluid Mech.*, **376**, 1-35.

Pawlowicz, R 2002, Website: http://www2.ocgy.ubc.ca/~rich/research.html#Flow visualization using Time-Lapse Photography

Pratt, L.J. 1986, Hydraulic control of sill flow with bottom friction. *J. Phys. Oceanogr.*, **16**, 1970-1980.

Ross, T., C. Garrett, and P.-Y. Le Traon. 2000. Western Mediterranean sea level rise: Changing exchange flow through the Strait of Gibraltar. *Geophys. Res. Lett.*, **27**, 2949-2952.

Send, U., P. F. Worcester, B. D. Cornuelle, C. O. Tiemann, and B. Baschek, "Integral measurements of mass transport and heat content in the Strait of Gibraltar from acoustic transmissions," Deep-Sea Res. (in press, 2002).

Watson, G. & I S Robinson, 1989, A study of internal wave propagation in the strait of Gibraltar using shore based radar, *J. Phys. Oceanogr.*, **20**, 374-395.

Wesson, J. C., and M. C. Gregg, 1994: Mixing at Camarinal Sill in the Strait of Gibraltar. *J. Geophys. Res.*, **99**, 9847-9878.

Frictional processes in straits

Chris Garrett

Department of Physics and Astronomy, University of Victoria, Victoria, British Columbia, Canada

Abstract. Within the context of layered models, friction and entrainment tend to drive a flow towards hydraulic criticality and to shift control points downstream. However, friction and entrainment also induce vertical gradients in velocity and density, rendering layered models dubious. In such situations, the nature of hydraulic control is uncertain: even for a homogeneous fluid there is an apparent contradiction between control conditions based on an energy argument on the one hand and on the speed of long waves on the other. The parameterization of bottom friction seems to be reasonably well-established, but the nature and quantification of lateral and internal frictional processes are uncertain. In a rotating system, secondary cross-strait flows are expected to be driven by the vertical gradient of the vertical Reynolds stress and can be diagnostic for bottom and internal friction.

1. Introduction

For a physicist, the study of physical oceanography seems to be curious occupation. After all, the governing equations have been established for well over a century, and surely modern computing power permits the numerical solution of these equations for any situation of interest?

A physical oceanographer's reply to this view is twofold. Firstly, we argue that resolving all the scales of motion that occur is far beyond modern, or foreseeable, computing capability, even for comparatively simple situations, and that there is thus a need to continue basic studies of the unresolved processes so that we can parameterize their effects in terms of those processes that are resolved in numerical models. This is a strong argument, though there are certainly situations where the behaviour of the ocean is rather insensitive to the effects of small-scale processes, and low resolution models provide reliable results independently of uncertainty about the parameterization of unresolved processes. For flow through straits, the effects of unresolved processes, such as those giving rise to friction and mixing, may indeed be of secondary importance in some circumstances, though in others they may exert a first order influence on the flow. One purpose of this short paper will be to review studies that help us decide on the importance of the small-scale processes.

A second part of the physical oceanographer's reply is that even if a numerical model does capture all the essential physics, it is still important to develop an intuitive understanding of the output, thus, for example, thinking of the existence of the Gulf Stream in terms of vorticity arguments for western intensification rather than merely as a solution of the Navier-Stokes equations. This philosophy seems to be particularly appropriate for strait flows, where concepts such as hydraulic control and maximal exchange are powerful aids to understanding and, hence, prediction.

In Section 2 of this paper I will review the general influence of friction on layered flows through straits, starting with one layer and then extending the discussion to two layers. Brief mention will also be made of the effects of rotation. In Section 3 I add the effects of entrainment, focussing on a one-layer reduced gravity flow.

While idealised studies involving the approximation of a flow by separate homogeneous layers are valuable, observations clearly show that the effects of friction and entrainment lead to gradual rather than abrupt transitions between water masses, so Section 4 will include a discussion of the extent to which layer concepts can be easily extended to include more complicated flows.

To this point the paper will not have been specific about the precise form for the parameterization of unresolved frictional and mixing processes, so this will be discussed briefly in Section 5, along with an account of some observations of Reynolds stresses. It will be clear that there are significant gaps in our ability to provide reliable parameterizations. Some open questions will be summarised in Section 6.

The subject area is vast, and the reader of this preliminary review is urged to recognise that omissions are a consequence of ignorance rather than malice! Please provide me with information on what I have got wrong and what I have left out, and also read the complementary review in this volume by Mike Gregg.

2. The effect of friction

A simple problem to start with is that of homogeneous shallow water flow down a channel of rectangular cross-
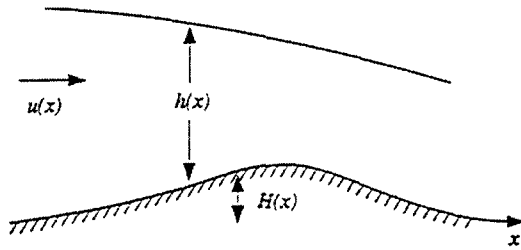
Figure 1. Definition sketch for a single layer flow.

section, width $W(x)$ and bottom height $H(x)$ (Figure 1). If the layer thickness is $h(x)$ and the current is $u(x)$, the governing equation for momentum is

$$u\frac{du}{dx} + g\frac{d}{dx}(h + H) = -C_d\frac{u^2}{h} \qquad (1)$$

assuming quadratic bottom friction with drag coefficient C_d. This may be combined with the continuity equation

$$\frac{d}{dx}(uhW) = 0 \qquad (2)$$

which integrates to give $uhW = Q$, the constant volume flux.

A key parameter is the Froude number F, where $F^2 = u^2/(gh)$ and (1) may be rearranged to give

$$\frac{d\beta}{dx} = \frac{2}{3}\frac{\beta}{W}\frac{dW}{dx} - \left(\frac{gW^2}{Q^2}\right)^{1/3}\left(\frac{dH}{dx} + C_dF^2\right) \qquad (3)$$

where β is the usual hydraulic function $\frac{1}{2}F^{4/3} + F^{-2/3}$. This has a minimum of 3/2 where $F = 1$ and $d\beta/dx = 0$, corresponding to a control point where the flow can switch from subcritical with $F < 1$ to supercritical with $F > 1$.

We see that the effect of friction is the same as that of decreasing width or increasing bottom height in pushing the flow towards criticality and that a control point is shifted downstream of where it would be without friction. In particular, the control point occurs where the bottom slope $dH/dx = -C_d$ if the width W is constant (Pratt 1986) or at a location where $dW/dx = C_d(W/h)$ if the bottom is flat, as is effectively the case for a reduced-gravity surface flow.

The latter result comes from (3) using the simple identity $(gW^2/Q^2)^{1/3} = h^{-1}F^{-2/3}$. In fact, for this simple problem it is only necessary to follow one dependent variable since h and u are connected by volume flux conservation $uhW = Q$ and the Froude number may be written as $F = (h_0/h)^{3/2}$, where $h_0 = [Q^2/(gW_0^2)]^{1/3}$ is the layer depth at the control section where $W = W_0$.

One interesting problem is flow through a channel with a flat bottom and constant width. The control will be at the exit where the channel deepens or widens abruptly. Taking this to be at $x = 0$ and defining $x = (h_0/C_d)x'$ and $h' = h/h_0$, the equation for the surface slope is

$$dh'/dx' = -(h'^3 - 1)^{-1} \qquad (4)$$
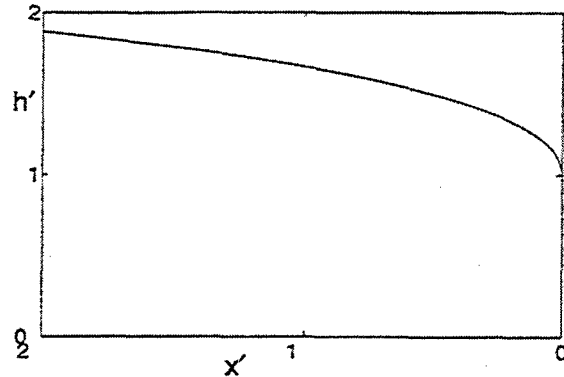
Figure 2. The scaled free surface for a single-layer frictional flow through a uniform channel with exit control at $x' = 0$.

with the simple integral

$$x' = h' - h'^4/4 - 3/4 \qquad (5)$$

as illustrated in Figure 2. The surface is parabolic near the exit control at $x = 0$ and acquires an infinite negative slope near there (thus violating the shallow water assumption; a problem that would disappear with more realistic topography), but the main point to make is that the horizontal scale for significant changes in layer depth is h_0/C_d. This result is easily established, of course, by scale analysis of the inertial and friction terms in equation (1). It provides a guide to the circumstances under which friction will be important, namely if the channel is long compared with h_0/C_d. For a reduced gravity flow with $h_0 = 100\,\mathrm{m}$ and an interfacial friction coefficient of, say, 5×10^{-4} (one quarter of a drag coefficient of 2×10^{-3} using the velocity difference to the centre of the interface between the active and stagnant layers), this distance is 200 km. Pratt (1986) tabulates an equivalent parameter for a number of straits and suggests that the Strait of Gibraltar is the only one on his list for which frictional effects are small.

Two layers

The one-layer situation provides a good guide to the effect of interfacial friction on a two-layer exchange flow through a channel of finite length, as discussed by Assaf and Hecht (1974). Submaximal exchange, controlled only at one exit, will have a small Froude number in the layer that is not controlled, so that the active layer may be treated to a reasonable approximation as a reduced gravity flow, with applicability of the one-layer model. Maximal exchange through a channel of constant width and with a flat bottom will have exit controls at each end and subcritical flow in between. If friction is important, there will be a significant change in the thickness of each layer along the channel so that at each end the active layer will be much thinner than the other layer. In the neighbourhood of the exit controls the flow will thus again resemble that of a reduced gravity flow.
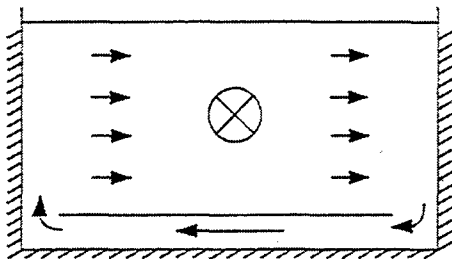
Figure 3. Bottom friction in a rotating channel flow acts via a bottom Ekman layer and a returning cross-channel flow in the interior.

One assumption that might well be questioned for both one-layer and two-layer flows is that of the uniformity of flow in the layers; one would expect bottom friction to induce a turbulent shear flow. I will return to this issue of shear later, but turn first to the role of rotation.

Rotation

If the time taken for a single-layer flow through a channel is longer than the inertial period, a bottom Ekman layer will be established. The effect of friction on the interior flow is due to the Coriolis force acting on the secondary flow across the channel driven by the returning Ekman flux (Figure 3), rather than by the vertical transfer of frictional stresses by turbulence. It is thus possible for the main flow, above the bottom Ekman layer, to remain laminar and slab-like while experiencing the effect of bottom friction.

The effect of friction in a two-layer exchange flow has been examined in a laboratory experiment by Johnson and Ohlsen (1994). Their schematic of the flow (Figure 4) shows the cross-channel interfacial tilt expected even for inviscid flows and also shows the presence of bottom and interfacial Ekman layers. The behaviour of the latter in the laboratory experiment was rather more complicated than expected, in that the interfacial Ekman layer just below the interface did not extend all the way to the side boundary, but seemed to meet an outflow from converging bottom boundary layers.

3. Entrainment

Internal friction in stratified shear flows is most likely to be accompanied by vertical mixing of density. Within a framework that treats the flow in terms of layers, this exchange of mass may be represented as entrainment. In particular, Csanady (1990) shows that if the vertical mixing is parameterized by an eddy coefficient $K_v(z)$, then the upward entrainment speed across the isopycnal located at the density inflection point, where $d^2\rho/dz^2 = 0$, is given by dK_v/dz evaluated at that depth.

As for friction alone, considerable insight into the effects of entrainment may be obtained from consideration of the flow of a single active layer. Gerdes et al. (2002) have discussed a reduced gravity single-layer flow beneath (Figure
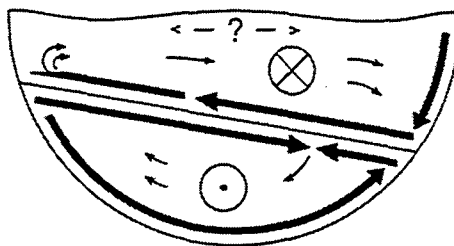
Figure 4. The secondary cross-channel flows induced by bottom and interfacial friction in a two-layer exchange flow (Johnson and Ohlsen 1994). The Ekman layer flows (thick lines) are as for the northern hemisphere. The return flows in the layer interiors are illustrated by the thin lines.
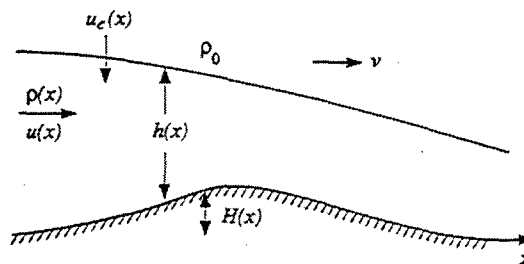
Figure 5. A single-layer reduced gravity with an entrainment rate u_e from an inactive layer of density ρ_0 and speed v. (After Gerdes et al. 2002.)

5) or above a deep inactive layer with constant speed v. For simplicity I will take $v = 0$ in this review.

The volume conservation equation giving changes in $Q = uhW$ is now $dQ/dx = u_e W$ and mass conservation requires $d(\rho Q)/dx = \rho_0 u_e W$. Together these imply that $g'Q =$ constant, where $g' = g(\rho - \rho_0)/\rho_0$ is the reduced gravity. Consideration of momentum conservation in a control volume leads to relationships for the evolution of flow properties. The governing equations are simplified if one makes the Boussinesq approximation of ignoring the difference between ρ and ρ_0 unless it is multiplied by g.

Unlike the non-entraining case in which it was sufficient to have an evolution equation for just one dependent variable, we now need two. Choosing these to be the Froude number F, where $F^2 = u^2/g'h$, and the layer depth h, Gerdes et al. (2002) show that

$$\frac{dF^2}{dx} = \frac{-3F^2}{h(1 - F^2)} \times$$
$$\left[\frac{(2 + F^2)}{3} \frac{h}{W} \frac{dW}{dx} - \frac{dH}{dx} - F^2 C_d - \left(\frac{1}{2} + F^2 \right) \frac{u_e}{u} \right]. \quad (6)$$

It is clear that entrainment acts in qualitatively the same way as friction in driving the flow towards criticality. The equa-

tion for layer depth h is

$$\frac{dh}{dx} = \frac{1}{(1-F^2)} \times$$

$$\left[F^2 \frac{h}{W} \frac{dW}{dx} - \frac{dH}{dx} - F^2 C_d + \left(\frac{1}{2} - 2F^2 \right) \frac{u_e}{u} \right]. \quad (7)$$

This is interesting because it shows that entrainment may *thicken* a subcritical flow with $F < 1/2$ even though the Froude number is increasing and friction thins the layer.

Reduced gravity flow over a sill, through a channel of constant width and with a stagnant upper layer, will now have a control shifted downstream to a location where $dH/dx = -C_d - (3/2)u_e/u$. The second term may be comparable with the first if, as Gerdes et al. (2002) discuss, $u_e/u = 0.002F^2$ from the entrainment law proposed by Christodoulou (1986). Similarly, the entrainment and friction terms may be of comparable importance in (6) and (7) at other locations, or, if u_e is increased by the action of things like breaking solibores (e.g. Wesson and Gregg 1994), entrainment could dominate.

One final interesting consequence of adding entrainment to a reduced gravity flow occurs for the sea surface elevation ζ in a reduced gravity flow at the surface (such as occurs, for example, with the Atlantic water inflow into the Mediterranean Sea at the eastern end of the Strait of Gibraltar). It is simple to derive

$$\frac{d\zeta}{dx} = \frac{g'}{g} \left(\frac{dh}{dx} - \frac{u_e}{u} \right) \quad (8)$$

$$= \frac{g'}{g(1-F^2)} \left[F^2 \frac{h}{W} \frac{dW}{dx} - F^2 C_d - \left(\frac{1}{2} + F^2 \right) \frac{u_e}{u} \right] \quad (9)$$

where there is now no term in H since the lower layer is passive. Entrainment may lead to a *decrease* in ζ for subcritical flow, even when widening would cause an increase. Moreover, the different coefficients in the u_e/u term in (7) and (9) show that entrainment can cause the sea surface to slope down at the same time as it is acting to increase the thickness of the upper layer. This seems contrary to the expectation of opposing surface and interface slopes if the lower layer is stagnant; it is a consequence of the downstream increase in density of the upper layer caused by entrainment.

This result may, in fact, help to resolve a long-standing mystery in connection with the nature of the exchange flow through the Strait of Gibraltar. Many pieces of evidence pointed to a seasonal switch between maximal and submaximal exchange (Garrett et al. 1990, although see Ross et al. (2000) for a discussion of major interannual changes), but the ratio of the fluctuations of sea level differences across and along the eastern end of the Strait seemed to agree year round with the expectations for maximal flow (Bormans and Garrett 1989). This was mainly because of an expectation of increasing sea level along the eastern end of the Strait for submaximal flow; we see now that entrainment can reverse that gradient.
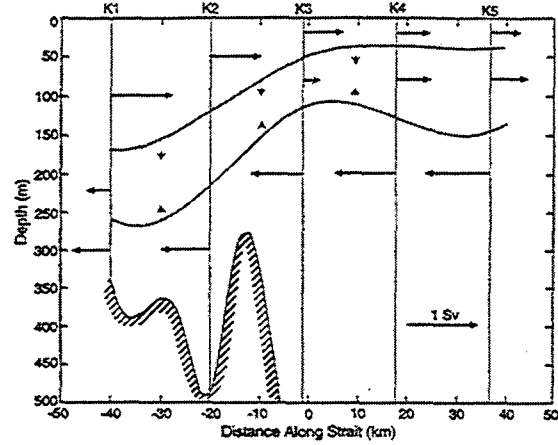
Figure 6. Transports at the eastern end of the Strait of Gibraltar. The dotted lines show the interfaces between the interface layer and the basic layers of inflowing Atlantic water and outflowing Mediterranean water. (From Bray et al. 1995.)

4. Beyond layers

One does not have to look far in data or in the output of numerical models to realise that the assumption of discrete, slab-like, layers is dubious. Vertical profiles of density and horizontal velocity often, maybe usually, show significant gradients. These gradients may, of course, be a consequence of friction and entrainment.

The inflow of Atlantic water through the Strait of Gibraltar provides one clear example from nature. At the eastern end of the Strait the inflowing water clearly entrains significant amounts of Mediterranean water that was otherwise heading out towards the Atlantic. This is discussed by Bray et al. (1995) who analyse the situation by introducing an interface layer that has an increasing transport as it flows into the Mediterranean, having acquired it from the basic layers above and below it. Their summary of the along-strait and inter-layer transports is shown here in Figure 6. The data suggest an upward entrainment from the lower layer in the eastern part of the strait with $u_e/u \simeq 10^{-3}$, taking u as the average inflow in the surface and intermediate layers. This entrainment rate is perhaps larger than the Christodoulou (1986) formula $u_e/u = 0.002F^2$ if one bases an estimate of F^2 on a layer depth to the middle of the interface layer, giving $F^2 \simeq 0.1$.

Interface layers are also generated in the numerical simulation by Winters and Seim (2000) of the exchange through a constriction of two different water masses. Hogg et al. (2001a) examine the problem further, finding that as the vertical mixing of mass and momentum is increased the exchange flow evolves from one resembling the two-layer hydraulic exchange to one in which the turbulence plays a dominant role. For a contraction of length L and height H, with a vertical eddy viscosity ν, they find that the key dimensionless parameter is $Gr_T A^2$, where Gr_T is the tur-

bulent Grashof number, given by $g'H^3/\nu^2$, with g' based on the density difference between the two reservoirs, and $A = H/L$. The hydraulic limit occurs for large values of this parameter. We note that, taking $U = (g'H)^{1/2}$ as a velocity scale, $(Gr_T A^2)^{-1/2}$ may be written as the ratio of viscous forces of order $\nu U/H^2$ to an inertial term of order U^2/L, in much the same way that this comparison is represented by $C_d L/H$ for one-layer flow.

The overall physics found in observations and numerical models is not surprising, with the main challenge appearing to be the determination of correct parameterizations of the vertical exchange of mass and momentum. I will return to this later, but first remark that another challenge is to understand the criteria for hydraulic control in models with continuous profiles of density and velocity. This was discussed by Hogg et al. (2001b) who examined the propagation of waves through a stratified shear flow established by "lock exchange" through a constricted channel. They do find an extension of the usual concept of control, in that the various waves that exist do not seem to be able to carry information about the interface depth upstream through the constriction, but the situation is complicated.

I will next address the much simpler situation in which there is no density stratification and one seeks merely to extend the simple hydraulic theory for a homogeneous fluid with a free surface. This will raise an apparent paradox.

Control conditions in a sheared flow

Chow (1959) and Henderson (1966) have suggested that the usual hydraulic conditions for a single layer are readily modified to allow for shear by incorporation of so-called "Coriolis coefficients" derived by integrating relevant quantities over the cross-section of the flow. Consider, for example, the horizontal momentum equation for the flow of a homogeneous fluid with velocity $P(z)\bar{u}$, where $P(z)$ is a profile shape factor with a vertical average of 1 and $\bar{u}$ is the vertical average of u. The inertial term $u\,\partial u/\partial x$ then has a vertical average of $\alpha\bar{u}\,d\bar{u}/dx$ where

$$\alpha = h^{-1} \int_0^h P^2 dz \geq 1. \tag{10}$$

The continuity equation is the same as for an unsheared fluid, but now using $\bar{u}$ in place of u. Thus critical conditions are apparently reached when the Froude number $\bar{u}/(gh)^{1/2} = \alpha^{-1/2}$ which is less than 1.

This condition may be compared with the expectation based on the speed of long waves. To derive this we start with the linearised momentum equation for a uniform channel of constant mean depth h. This is

$$\frac{\partial u'}{\partial t} + u\frac{\partial u'}{\partial x} + w'\frac{du}{dz} + g\frac{\partial\zeta}{\partial x} = 0 \tag{11}$$

where a perturbation velocity (u', w') is superimposed on the basic sheared flow $u(z)$ and the surface elevation perturbation is ζ.

Seeking a wavelike solution with the perturbation variables proportional to $\exp[ik(x-ct)]$ and using the continuity equation $\partial u'/\partial x + \partial w'/\partial z = 0$ leads to

$$(c - u)\frac{\partial w'}{\partial z} + w'\frac{du}{dz} + gik\zeta = 0. \tag{12}$$

After dividing this $(c - u)^2$, the left hand side may be written as a differential. Integrating the resulting equation vertically and using the free surface kinematic boundary condition $w' = \partial\zeta/\partial t + u\partial\zeta/\partial x$ at $z = h$ we obtain

$$g\int_0^h (c - u)^{-2} dz = 1. \tag{13}$$

This result is well-established (e.g. Freeman and Johnson 1970) but has been derived here to illustrate the simplicity of the derivation. It clearly gives $c^2 = gh$ if $u = 0$, and $(c - \bar{u})^2 = gh$ if u is independent of depth. For a small departure from depth-uniform flow, and taking $\bar{u} = 0$ for convenience, we take $u = (gh)^{1/2}\epsilon(z)$ with $|\epsilon| \ll 1$ and $\int_0^h \epsilon\,dz = 0$. Expansion of the integrand in (13) then gives

$$c^2 = gh\left(1 + 3h^{-1}\int_0^h \epsilon^2 dz\right) \tag{14}$$

as given on page 54 of Baines (1995). Thus the magnitude of the speed of long waves is greater than $(gh)^{1/2}$ and is clearly sufficient to carry information upstream through an alleged control point at which the mean flow is, as shown earlier, less than $(gh)^{1/2}$.

This easily demonstrated paradox was drawn to my attention by Frank Gerdes (personal communication 2002). I hope that there is a simple resolution in the literature. Possibilities include allowing, in the wave equation, for internal frictional processes that must be present to preserve the basic sheared flow. These will cause wave damping to first order, but will also lead to a second order correction to the wave speed which could make it less than $(gh)^{1/2}$ rather than greater. The effect of friction certainly seems to be to reduce the wave speed as well as to damp the waves, as shown by Wajsowicz (1993) for a single slab-like layer with bottom friction. The question is whether, with a shear flow, this reduction is as big as the difference between the wave speed given by (13) and the critical speed implied using the Coriolis coefficient of (10).

It is clearly necessary to resolve this paradox in order that one may continue to determine the presence or absence of control through evaluation of long wave speeds in continuous profiles of density and velocity, as carried out, for example, for Bab al Mandab by Pratt et al. (2000).

5. Parameterizations

This brief review has so far focussed on general considerations of the effect of friction and entrainment on hydraulic flows in straits. There will certainly be situations, as with

short or deep straits, where inertial effects are dominant, though even then, as shown by Bray et al. (1995) for the Strait of Gibraltar, significant interface thickening can occur. In situations where unresolved small-scale processes are important we need to learn how to parameterize them.

Bottom friction

The parameterization of bottom friction is perhaps the best established with the formula $C_d u^2$ being generally accepted. The extensive literature on appropriate values for C_d will not be discussed here; C_d is generally larger if u is the current speed above some bottom boundary layer, smaller if u is the current speed averaged over the layer depth. I have used 2×10^{-3} as a representative value for the latter case.

Most straits, of course, have sloping lateral boundaries rather than the flat bottoms and vertical sidewalls of the simplest models. With sloping boundaries and in the presence of stratification and rotation it is possible that the bottom Ekman layer will be "arrested" as discussed by MacCready and Rhines (1991) and Trowbridge and Lentz (1991). In this situation, a near-bottom thermal wind brings the bottom velocity to zero and the flow becomes essentially frictionless. The time for arrest to occur is approximately $(C_d N/f)^{-1/2}(f/N)^2 s^{-2} f^{-1}$ if the flow is upwelling-favourable (and longer if it is downwelling-favourable), where N is the buoyancy frequency and s is the bottom slope (e.g. Garrett et al. 1993). This time may be compared with the transit time for flow through a strait. Using $C_d = 2 \times 10^{-3}$, $N = 10^{-2} s^{-1}$, $f = 10^{-4} s^{-1}$, $s = 10^{-2}$ the arrest time is only 6 hours which is likely to be less than a transit time, but is sensitive to the parameter values, particularly the bottom slope. One weakness of this simple model is, of course, the neglect of small-scale bottom features.

Lateral friction

A topic which seems to have been somewhat ignored is that of lateral mixing. For a homogeneous fluid the small slope of the bottom means that the fluid interior is more likely to be affected by turbulence originating at the sea floor beneath it than farther away laterally. In the presence of stratification, however, the vertical transfer of stress may be greatly inhibited, allowing the influence of lateral eddy momentum transfer from side boundaries. This is likely to be particularly significant if the lateral boundary has significant protuberances.

These considerations apply in a situation where rotation is not important. In a rotating system, as discussed earlier and illustrated in Figure 3, bottom friction can act via the secondary cross-channel flow driven by the bottom Ekman layer. If the channel depth varies laterally, the deceleration will be more pronounced near the shore, giving lateral gradients of the along-channel flow on which lateral mixing can act.

While discussing the role of lateral boundaries, it should also be stressed that even channel curvature can lead to major secondary flows and cause overturning with considerable mixing (Seim and Gregg 1997).

Internal friction

There are numerous parameterizations in the literature of the vertical transfer of mass and momentum in a stratified shear flow (e.g. Bowden 1984). Most assume fluxes proportional to the local gradients, with the eddy viscosity and eddy diffusivity being described in terms of local properties, such as the tidal current which is assumed to be a source of turbulence. Recent models (e.g. Masson and Cummins 1999) tend to rely on closure schemes such as those of Mellor and Yamada (1982), with justification of the closure relying on the circumstantial evidence that model predictions of mean flows agree adequately with observations.

Along-strait sea level gradients can sometimes provide clues to the average internal friction required, at least in situations where the inertial terms are not dominant. For example, in Juan de Fuca Strait, Ott and Garrett (1998) used seasonal differences in sea level gradient (thus bypassing the levelling problem, given the weak flow in winter) to estimate an interfacial eddy viscosity of up to $0.02 \, m^2 s^{-1}$. This value is twice as large as implied by the traditional formula of Bowden and Hamilton (1975) that is based on the r.m.s. (mainly tidal) current with a reduction related to the stratification.

There is a dearth of direct observations of the eddy fluxes of mass and momentum. For mass, a variety of microstructure techniques (e.g. Wesson and Gregg 1994) have provided reasonably direct estimates for the eddy diffusivity, but measurements of the eddy viscosity in a stratified shear flow are rare.

Ideally, one would like direct measurements of the vertical eddy momentum fluxes $\overline{u'w'}$ and $\overline{v'w'}$. Acoustic Doppler current profilers (ADCPs) can be used to good effect if the eddies are large enough to be resolved by the bin size and if the eddy statistics are spatially homogeneous so that the beam variance technique can be used (e.g. Lohrmann et al. 1990; Lu and Lueck 1999). These papers describe Reynolds stress measurement in homogeneous flows with the turbulence generated at the sea floor, whereas we also need data from the stratified shear flows of estuaries and straits. Ott et al. (2001) have been able to determine the Reynolds stresses in Juan de Fuca Strait at various depths below the surface, in water 130 m deep, using a 300 kHz bottom-mounted ADCP sampling with 2 m bins (Figure 7). The occurrence of significant Reynolds stresses at neap tides coincided with an increase in the mean shear, and decrease in gradient Richardson number, associated with the relaxation of tidal mixing at a constriction upstream of the Strait, thus releasing brackish water from the Strait of Georgia.

Ott et al. (2001) found no simple relationship between the Reynolds stress and the local mean shear, but they did observe secondary flows across the Strait that were similar in some respects to those shown in Figure 4 and expected
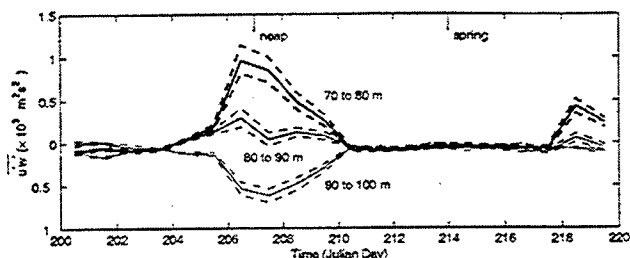
Figure 7. The daily-averaged Reynolds stress $\overline{u'w'}$ at various depths in the stratified shear flow in Juan de Fuca Strait in 1996. From Ott et al. (2001).

dynamically. The simplest situation would be a steady response with ageostrophic cross-strait flow v_a given by

$$v_a = f^{-1} \frac{d}{dz} \left(\overline{u'w'} \right). \tag{15}$$

This balance was not well satisfied, possibly because advective terms were important, but further efforts to determine the Reynolds stresses and the associated ageostrophic secondary flows would seem to be justified. Even without direct Reynolds stress measurements, secondary flows can provide a strong suggestion of internal friction, as in the St. Lawrence estuary (Mertz and Gratton 1995) or the deep Faroe Channel (Johnson and Sanford 1992).

6. Conclusions

Much has been learnt about the effect of friction on flows through straits, but fundamental problems remain. On the theoretical side, a key issue is the nature and diagnosis of hydraulic control for flows which have continuous, rather than layered, vertical profiles of density and velocity by virtue of the action of mixing and friction. On the observational side, we need more direct measurements of vertical and lateral Reynolds stresses for comparison with parameterization formulae used, rather than arguing that the plausible output of a numerical model justifies the choice of all its ingredients. Observational programs are complicated, of course, by the inhomogeneity on multiple scales of the topography of most real straits; choosing "representative" locations for observational programs is a major challenge.

References

Assaf, G. and A. Hecht, Sea straits: a dynamic model. *Deep-Sea Res., 21,* 947–958, 1974.

Baines, P. G., *Topographic Effects in Stratified Flows.* Cambridge University Press, 1995.

Bormans, M. and C. Garrett, The effects of nonrectangular cross section, friction and barotropic fluctuations on the exchange through the Strait of Gibraltar. *J. Phys. Oceanogr., 19,* 1543–1557, 1989.

Bowden, K. F., *The Physical Oceanography of Coastal Waters.* Ellis Horwood, 1984.

Bowden, K. F. and P. Hamilton, Some experiments with a numerical model of circulation and mixing in a tidal estuary. *Est. Mar. Coastal Sci., 3,* 281–301, 1975.

Bray, N. A., J. Ochoa, and T. H. Kinder, The role of the interface layer in exchange through the Strait of Gibraltar. *J. Geophys. Res., 100,* 10,755–10,776, 1995.

Chow, V.T., *Open Channel Hydraulics.* McGraw Hill, 1959.

Christodoulou, G. C., Interfacial mixing in stratified flows. *J. Hydraul. Res., 24,* 77–92, 1986.

Csanady, G. T., Mixing in coastal regions. *The Sea, 9A,* 593–629, 1990.

Freeman, N. C. and R. S. Johnson, Shallow water waves on shear flows. *J. Fluid Mech., 42,* 401–401, 1970.

Garrett, C., P. MacCready, and P. B. Rhines, Boundary mixing and arrested Ekman layers: rotating stratified flow near a sloping boundary. *Ann. Rev. Fluid Mech., 25,* 291–323, 1993.

Garrett, C., M. Bormans, and K. Thompson, Is the exchange through the Strait of Gibraltar maximal or submaximal? *The Physical Oceanography of Sea Straits,* ed. L. J. Pratt, Kluwer, 271–294, 1990.

Gerdes, F., C. Garrett, and D. Farmer, On internal hydraulics with entrainment. *J. Phys. Oceanogr., 32,* 1106–1111, 2002.

Henderson, F. M., *Open Channel Flow.* MacMillan, 1966.

Hogg, A. M., G. N. Ivey, and K. B. Winters, Hydraulics and mixing in controlled exchange flows. *J. Geophys. Res., 106,* 959–972, 2001a.

Hogg, A. M., K. B. Winters, and G. N. Ivey, Linear internal waves and the control of stratified exchange flows. *J. Fluid Mech., 447,* 357–375, 2001b.

Johnson, G. C. and D. R. Ohlsen, Frictionally modified rotating hydraulic channel exchange and ocean outflows. *J. Phys. Oceanogr., 24,* 66–78, 1994.

Johnson, G. C. and T. B. Sanford, Secondary circulation in the Faroe Bank channel outflow. *J. Phys. Oceanogr., 22,* 927–933, 1992.

Lohrmann, A., B. Hackett, and L. P. Roed, High resolution measurements of turbulence, velocity and stress using a pulse-to-pulse coherent sonar. *J. Atmos. Oceanic Technol., 7,* 19–37, 1990.

Lu, Y. and R. G. Lueck, Using a broadband ADCP in a tidal channel. Part II: Turbulence. *J. Atmos. Oceanic Technol., 16,* 1568–1579, 1999.

MacCready, P. and P. B. Rhines, Buoyant inhibition of Ekman transport on a slope and its effect on stratified spin-up. *J. Fluid Mech., 223,* 631–661, 1991.

Masson, D. and P. Cummins, Numerical simulations of a buoyancy-driven coastal countercurrent off Vancouver Island. *J. Phys. Oceanogr., 29,* 418–435, 1999.

Mellor, G. L. and T. Yamada, Development of a turbulent closure model for geophysical fluid problems. *Rev. Geophys. Space Phys., 20,* 851–875, 1982.

Mertz, G. and Y. Gratton, The generation of transverse flows by internal friction in the St. Lawrence estuary. *Continental Shelf Res., 15,* 789–801, 1995.

Ott, M. and C. Garrett, Frictional estuarine flow in Juan de Fuca Strait, with implications for secondary circulation. *J. Geophys.*

Res., 103, 15,657–15,666, 1998.

Ott, M., R. Dewey, and C. Garrett, Reynolds stresses and secondary circulation in a stratified rotating shear flow. *J. Phys. Oceanogr.*, submitted, 2001.

Pratt, L. J., Hydraulic control of sill flow with bottom friction. *J. Phys. Oceanogr., 16*, 1970–1980, 1986.

Pratt, L. J., H. E. Deese, S. P. Murray, and W. Johns, Continuous dynamical modes in straits having arbitrary cross sections, with applications to the Bab al Mandab. *J. Phys. Oceanogr., 30*, 2525–2534, 2000.

Ross, T., C. Garrett, and P.-Y. Le Traon, Western Mediterranean sea level rise: changing exchange flow through the Strait of Gibraltar. *Geophys. Res. Lett., 27*, 2949–2952, 2000.

Seim, H. E. and M. C. Gregg, The importance of aspiration and channel curvature in producing strong vertical mixing over a sill. *J. Geophys. Res., 102*, 3451–3472, 1997.

Trowbridge, J. H. and S. J. Lentz, Asymmetric behavior of and oceanic boundary layer above a sloping bottom. *J. Phys. Oceanogr., 21*, 1171–1185, 1991.

Wajsowicz, R. C., Dissipative effects on inertial flows over a sill. *Dyn. Atmos. Ocean, 17*, 257–301, 1993.

Wesson, J. and M. Gregg, Mixing at Camarinal Sill in the Strait of Gibraltar, *J. Geophys. Res., 99*, 9847–9878, 1994.

Winters, K. B. and H. E. Seim, The role of dissipation and mixing in exchange flow through a contracting channel. *J. Fluid Mech., 407*, 265–290, 2000.

Chris Garrett, Department of Physics and Astronomy, University of Victoria, Victoria, B. C. V8W 3P6, Canada. email: garrett@phys.uvic.ca

Overview of topographic and boundary effects

G.F. Lane-Serff

Manchester Centre for Civil and Construction Engineering, UMIST, PO Box 88, Manchester M60 1QD, UK.

Abstract. An overview of topographic and boundary effects in flows through straits is presented. The emphasis is on the various types of interaction of uniform and stratified flow with the topography of straits, especially the interaction with sills. The interaction of a single-layer flow in a channel with a sill (obstacle) depends on the Froude number of the flow and the relative height of the sill. Two classification schemes (one steady and one pseudo-steady) are given. For single layer flow in straits where the effects of rotation are important a further parameter, the ratio of the channel width to a Rossby radius, is needed and a similar classification scheme as for the non-rotating flows can be obtained. Unsteady flows often result in bores (for single layer flows) and internal bores (in stratified flows) and the behaviour of these is discussed. The flow of stratified flow past sills may generate lee waves, while the increased flow speeds at the sill may allow deep water to be drawn up and over the sill (aspiration). Features of the strait topography away from the sill, including slopes at the side of the channel and also downstream of the sill, channel curvature and channel widening have important effects on the character of the flow and on mixing.

Introduction

Because of the restrictions in width or depth, flows through straits are generally more rapid than flows in the deep ocean. Straits also often mark natural boundaries in the ocean system, so that water masses of very different properties (and thus densities) are brought together. The interaction of fast-flowing, stratified fluid with the topography of the strait results in a range of important flow phenomena. In this paper we will focus on viewing the strait as topography interacting with flow rather than looking in detail at how the sill controls the flow (see the paper by Armi in this volume for details of hydraulic control in straits).

Unsteady effects, such as surface and internal waves and bores; are considered, as is flow separation in both vertical and horizontal planes (on downstream slopes, and due to rotation and 3D effects). Effects of sloping boundaries will be considered briefly, but general overviews of frictional processes and of small-scale processes are given in other papers in this volume (by Garrett and by Gregg).

While we are considering sea straits here, it is important to note that much relevant work has been done outside oceanography. For example, problems in hydraulic engineering have motivated the study of open channel flows, flow over weirs, hydraulic jumps and selective withdrawal; while work on lee waves, and on internal wave generation and propagation is found in the meteorological literature.

In this paper we will begin with flows having a single active layer, first non-rotating flows and then including some effects of rotation (there are more details on the effects of rotation in the paper by Nof in this volume). Next stratified uni-directional flow is considered, where the flow is driven in one direction through the strait (e.g. by tidal forcing), including lee wave formation and selective withdrawal. Then cases with flow in both directions are considered (stratified shear flows), including exchange flows and internal bores. This is followed by a section on some of the effects of slopes, including the effect of sloping lateral boundaries on shear flows and the flow of dense water down slopes beyond the sill (overflows). Next some 3D effects are described, such as recirculation and the effects of curvature. We finish with a summary of important results and some conclusions.

Single (and 1_) layer flows: non-rotating

First we consider the flow of a single layer of fluid in an open channel having a simple obstacle. The flows and features found in this case correspond to those found in more complex flows, so it is worth examining this flow in some detail. It is assumed that the flow can be described at any along-channel position, x, by the depth of the fluid $d(x)$ and (uniform) velocity $u(x)$, with the topography described by $h(x)$.
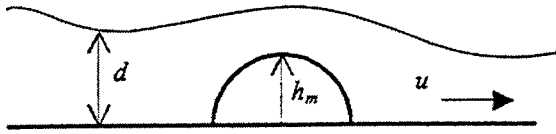

Figure 1. Single layer flow over an obstacle of maximum height $h = h_m$.

The flow of a dense fluid beneath a deep and stationary layer of slightly less dense fluid is found to behave in a very similar way, if we replace the gravitational acceleration g, with a "reduced gravity" g_-, given by

$$g' = g \frac{\Delta \rho}{\rho} \qquad (1)$$

where $\Delta \rho$ is the density difference between the fluid layers (assumed small) and ρ is the density of the lower layer. Representing the flow in this way is known as a 1_-layer or reduced gravity model.

These (and many other) flows are reviewed in detail by Baines (1987 and 1995). The most useful parameter in describing single-layer flows is the Froude number, defined as

$$F = u / \sqrt{gd} , \qquad (2)$$

which is the ratio of the flow speed to long, small amplitude linear surface waves. If the upstream depth of the flow is d_0 (with Froude number F_0) and the non-dimensional height of the obstacle is given by $H_m = h_m/d_0$, then the flow can be classified according to the two parameters F_0 and H_m.

For small obstacles, the flow will remain similar to the upstream condition: i.e. subcritical ($F<1$, marked I on figure 2) or supercritical ($F>1$, marked III on figure 2), with small deflections in the surface where the flow passes over the obstacle. In other cases the flow is controlled at the obstacle with hydraulic

jumps or bores upstream and/or downstream of the obstacle.
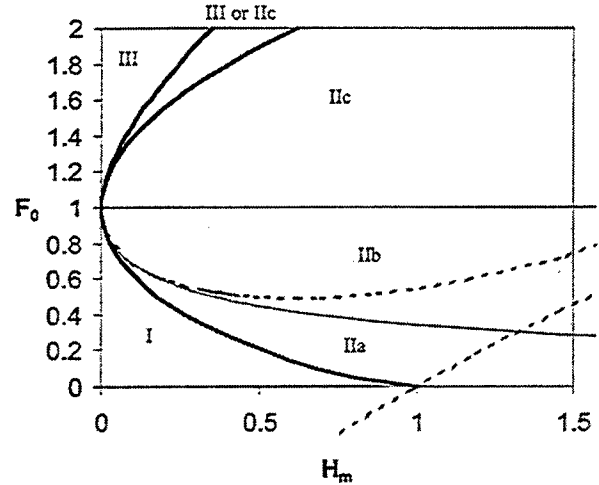
Figure 2. Two classification schemes for single-layer flow with Froude number F_0, over an obstacle of non-dimensional height H_m. The bold lines appear in both schemes. The solid lines and the roman numerals denote the classification according to Lawrence (1987), while the dotted lines appear in the classification given in Baines (1987) and earlier.

The precise nature of the flow depends to some extent on the way the flow is set up, leading to different ways of classifying the regimes between simple subcritical and supercritical flow. Many laboratory experiments have used a stationary fluid and towed the obstacle to simulate the flow. These give pseudo-steady flows with bores propagating upstream and are classified (for example) in Baines (1987). Under this scheme, the region on figure 2 in the bottom right hand corner has completely blocked flows; the region between the two dotted lines has a bore moving upstream and a jump on the lee side of the obstacle, while the region above the top dotted line has an upstream propagating bore and no jump.

Lawrence (1987) uses a fixed obstacle to perform strictly steady experiments. Flows controlled at the obstacle are then classified slightly differently, there are no propagating bores but there is a fixed hydraulic jump located: on the lee of the obstacle (region IIa), downstream of the obstacle (IIb) and upstream of the obstacle (IIc). Both classification schemes have an overlap region (marked "IIc or III" on figure 2) where two flow states are possible depending on the history of the flow (and hysteresis is possible).

Bores (and internal bores) are observed in straits, and, while they cannot occur in strictly steady flows,

they can be observed in the pseudo-steady flows mentioned above. Bores mark a sudden change in the layer depth from shallow to deep, with a corresponding change in the flow from supercritical to subcritical flow (when observed in a frame of reference moving with the bore). It is normally assumed that there is no change in "flow force" (i.e. rate of change of momentum is equal to the applied forces) or of flow rate across the jump, but energy is dissipated either locally in the form of a continuously breaking wave or carried away by surface waves in an "undular bore."

The observed behaviour of bores depends on the ratio of the depths either side of the jump (d_d/d_u), which is in turn related to the local Froude number upstream of the jump (F_u). For undular bores an interesting feature is the amplitude of the first wave compared to the wavelength, α/λ.
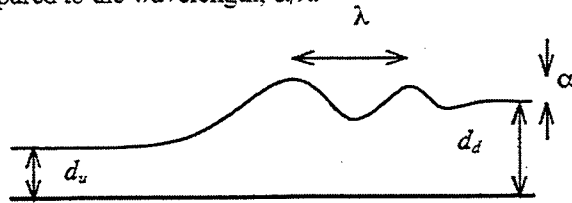

Figure 3. Sketch of an undular bore.

a) $d_d/d_u < 1.4$ ($F_u < 1.3$) undular bore, α/λ reaches 0.025 as d_d/d_u approaches 1.4. Waves decrease in amplitude away from the jump possibly due to nonlinear effects (cnoidal waves) or dissipation.

b) $1.4 < d_d/d_u < 1.75$ ($1.3 < F_u < 1.55$) first wave breaks but there are still clear waves, α/λ decreases.

c) $d_d/d_u > 1.75$ ($F_u > 1.55$) fully turbulent bore, no waves (though some irregularity) behind the bore.

In analysing the flow, the details of the jump can often be ignored, simply treating the jump as a discontinuity. A detailed mathematical analysis of the form of the jump requires consideration of non-hydrostatic terms. This analysis suggests that the bore could be a source of solitons (Pergrine 1966), though consideration of the energetics (Baines 1995) show that the form of the bore is likely to depend on the nature of energy dissipation and in practice we find undular and turbulent bores of the type described above.

Effects of rotation

For single layer flow along a channel with (northern hemisphere) rotation, we expect the fluid to slope up against the right-hand wall (looking downstream). Pratt et al. (2000) considered a rotating flow similar to the non-rotating towed obstacle flows described above. If the flow is assumed to come from a wide (initially stagnant) reservoir of depth D_∞, we can define a Rossby radius based on this depth: $L_d = \sqrt{gD_\infty}/f$. The importance of rotation can be characterized in terms of the ratio of the channel width at the sill to the Rossby radius: $w = W/L_d$. We can again define a Froude number, F_d, but now depending on wave speeds in the rotating system. These approach long gravity waves in the non-rotating (narrow channel) limit and Kelvin waves in the strongly rotating (wide channel) limit.

For each value of w, semigeostrophic theory gives a regime diagram somewhat similar to Figure 2, with subcritical flows (fluid deflected to the right over the sill), supercritical flows (fluid deflected to the left) and a region where we expect upstream influence, jumps and bores.

It is possible for the flow to separate from the left side-wall, and for recirculating regions to form. For flows with uniform potential vorticity (PV - set in the scenario above by the reservoir depth D_∞), the recirculation cannot extend over the sill (since the flow must be unidirectional at a control for uniform PV), see Borenäs & Whiehead (1998), for example. However, real flows have dissipation and this must also be allowed for at jumps and bores (even if it is negligible elsewhere), so that fluid need not retain its PV. Examples of flows with non-uniform PV and recirculating regions extending over a sill are given in Pratt et al. (2000).

Stratified flows: unidirectional flows

Next we consider a stratified flow through a channel with a sill (or obstacle). In principle the upper free surface may vary in height but for many flows (including most flows through straits) the external Froude number is small so that a "rigid-lid" approximation is valid (treating the upper surface as horizontal).

The simplest case is a two-layer flow in a channel of depth D, with the same (upstream) velocity (U) in both layers and with upstream lower layer depth rD and upper layer depth $(1-r)D$. The flow types can be

expressed in terms of the obstacle height (relative to the lower layer) and a Froude number defined in terms of the linear wave speed,

$$F_o^2 = \frac{U^2}{r(1-r)g'D} \qquad (1)$$

where $g\_$ is the reduced gravity. Regime diagrams similar to figure 2 are obtained, with a different diagram for each value of r. In laboratory experiments the flows are often produced by towed obstacles resulting in a similar range of behaviours to the single layer flows, including the generation and propagating of internal bores (see e.g. Baines 1995). Again a strictly steady classification scheme is possible (Lawrence 1993 - this paper also considers non-hydrostatic effects and flow separation on the downstream side of the sill).
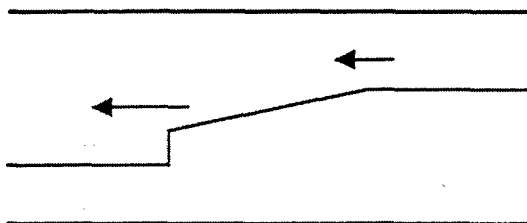

Figure 4. Sketch of a bore (hydraulic jump) followed by a rarefaction in two-layer flow. The arrows indicate the movement of the bore and the top of the rarefaction, not the fluid (which could be flowing to the right throughout both layers).

An important difference between single and two-layer flows is in the behaviour of bores. For the single layer flows an increased interface height gives a faster speed so that the even a gradual jump inevitably steepens. However, this is not the case for two-layer flows where the speed of disturbances has a maximum at a finite amplitude and then decreases. This can result in a bore followed by a rarefaction (see figure 4). Details about the analysis of internal bores are given in the next section.

In some cases it may be more appropriate to think of a stratified flow being pulled (rather than pushed) past an obstacle. This is then related to the engineering problem of selective withdrawal of water from a stratified reservoir. For flow out of a reservoir through a channel, fluid much deeper than the sill depth may be drawn up and over the sill (figure 5). This process is known as "aspiration" (e.g. Seim & Gregg 1997, Kinder & Parrilla 1987).
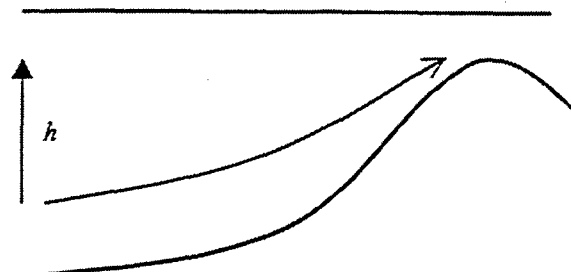
Figure 5. Fluid from a depth h below the sill depth drawn up and over the sill.

If the speed of the flow over the sill is U, then the interface in a two-layer fluid can be raised by a height h, given by,

$$h \sim \frac{U^2}{2g'},$$

and in a continuously stratified fluid with buoyancy frequency N,

$$h \sim \frac{U}{N},$$

with Seim & Gregg (1997) giving an empirical estimate of $h = (2$ to $4)$ U/N.

The presence of an obstacle in a stratified flow can be thought of as a perturbation to the flow resulting in wave formation. If the phase speed of the waves is stationary relative to the obstacle (i.e. the phase speed relative to the fluid matches the flow speed) then lee waves can be formed downstream of the obstacle. While the phase speed is stationary, the group velocity (and energy) propagates away from the obstacle. In continuously stratified flows the propagation may be at an angle to the horizontal, so that lee waves provide a mechanism that can result in momentum transport and mixing in fluid well above the topography.

Lee waves are observed in flows over sills and also in atmospheric flows over hills and mountains (the latter are reviewed by Wurtele et al. 1996). The effects of shear on internal wave generation over sills are considered by Hibiya (1990).

Stratified flows: exchange flows and bores

Many straits separate waters of different density, so that the flow in the strait consists of an exchange flow with a dense lower layer moving in one direction and a lighter upper layer moving in the opposite direction. The exchange flow is often

"controlled" where it flows over a sill in the strait (see the paper by Armi in this volume for details about hydraulic control).

Exchange flows are often modulated, especially by tidal forcing, though the changes are usually sufficiently slow that analyzing the flow at any instant as if it were steady is a valid approximation. The adjustment of the flow to changing forcing may involve mixing (e.g. Farmer & Armi 1999b) and will often involve the generation of internal bores (figure 6).

time (mins)

Figure 6. Interface between Mediterranean and Atlantic water in the Strait of Gibraltar showing the passage of an undular bore as the interface deepens from 50 m to 125 m.

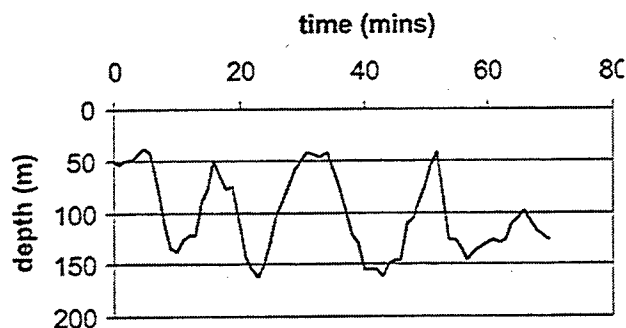To analyze an internal bore it is convenient to switch to a frame of reference moving with the bore, so that the bore can now be considered as a stationary hydraulic jump. In this frame, the flux of fluid in each layer is conserved while the change in momentum flux is equal to the pressure forces (generally assumed hydrostatic) applied either side of the jump. Energy is dissipated at the jump and different treatments of the energy dissipation give different analytical results.
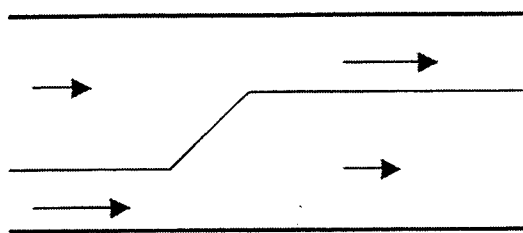
Figure 7. In a frame of reference moving with the bore, the jump appears stationary and the flux in each layer is constant (note the flow in the upper layer may be in the opposite direction).

Yih & Guha (1955) do not consider energy directly but assume the pressure changes smoothly through the hydraulic jump. This approach has been widely used but for some flows it predicts a gain (rather than dissipation) of energy, which is clearly unphysical. An alternative simple approach is to assume the energy dissipation is confined to one of the layers. The flow in the other layer then has no dissipation so that we can use a Bernoulli Equation there to close the problem.

Usually the energy is assumed to be dissipated in the expanding layer (e.g. Wood & Simpson 1984, Lane-Serff et al. 1995). However, if the real flow has a stationary thin layer with a bore advancing over it (in the limit as the thin layer vanishes this tends towards a simple gravity current) it may be more appropriate to assume the energy dissipation occurs in the other layer (e.g. Lane-Serff & Woodward 2001 - dealing with the generation of internal bores in exchange flows over sills).

While two (or more) layers are a good approximation to many strait flows, in reality the stratification is more complex than this. An example of a numerical model of a more realistic system compared with observations at Knight Inlet is given by Cummins (2000). The flows can also generate non-hydrostatic phenomena such as internal solitons (e.g. Farmer & Armi 1999a), with non-linearities perhaps becoming more pronounced as waves propagate into regions where a layer-depth becomes small. Rotation also has an effect on internal bores, confining them to one side of a channel.

Slopes

The side walls of straits are generally sloping and this will affect the development of shear instabilities near the boundaries. The orientation of the classic Kelvin-Helmholtz billows is distorted, leading to more connections between neighbouring billows and possibly enhanced mixing (Thorpe & Holt 1995). (Overviews of mixing and boundary friction are given in the papers by Gregg and by Garrett in this volume.) In many straits relatively dense water flows through the strait and then down a slope into fluid that is relatively lighter (the dense flow is referred to as an overflow). For flows where rotation is not important the dense flow descends straight down the slope, entraining ambient fluid as it descends. If the ambient fluid is stratified then a more complex flow is found, with both entrainment and detrainment at the boundary between the overflow and the ambient fluid and a largely unmixed dense core next to the slope (Baines 2001).

In larger overflows the effects of rotation are important and the overflow turns and flows predominantly along the slope. Bottom friction results in some downslope flow which is usually confined to a thin Ekman layer. There is evidence that deep sea canyons and other topographic features on the continental slope are important in steering dense fluid down into the deep ocean. In overflows beneath shallow overlying fluid or into strongly stratified water the overflow tends to break up into a series of dense domes with strongly cyclonic eddies in the overlying ambient fluid (Lane-Serff & Baines 1998 and 2000, Spall & Price 1998, Etling et al. 2000).

Three-dimensional effects

Flow of a homogeneous fluid along a curved channel generally results in secondary circulation, with fluid at the surface moving to the outside of the bend and a return flow at depth. This will tend to mix the fluid. For a stratified flow, density surfaces tilt as the fluid flows around a bend and this stops the secondary circulation (and mixing) unless the flow or curvature is strong enough. Seim & Gregg (1997) estimate that the condition for overturning the stratification in a curved channel is,

$$u^2 > \left(\frac{1}{\alpha}\right)\left(\frac{R}{W}\right)\frac{\Delta\rho g h}{\rho},$$

where u is the mean along-channel speed, R the radius of curvature, W the channel width, h the channel depth, $\Delta\rho$ the top to bottom density contrast and α a measure of the vertical shear (e.g. they find $\alpha \sim 0.55$ for an observed flow).

We have seen how rotation can result in recirculating flows even in a 2D channel. Where flows leave a narrow strait there are often regions of recirculation (e.g. Klymak & Gregg 2001). In estimating flows through straits measurements must be taken carefully to avoid misleading results from partial surveys of recirculating regions in the flow.

Summary and conclusions

In analysing flow over through channels and over sills, the Froude number is still perhaps the most useful parameter in defining the flow. Defined first for single-layer flows, the concept can be extended to stratified and rotating flows. This ratio of a flow

speed to a wave speed, combined with parameters describing the topography (and rotation, if important) allow us to characterise flows in an organised way. Critical values of the Froude number are also important in determining how flows are controlled by the topography (hydraulic control).

The mathematical models used to analyse the flows generally use a simplified version of the flow (layered or uniformly stratified fluid and a simplified topography) and an approximate version of the physics (e.g. hydrostatic). This approach is very valuable in helping us to understand observations and in constructing simple process models (for use within larger models and other applications). However, all real flows are three-dimensional, non-hydrostatic, unsteady, non-linear, viscous and usually turbulent. Thus, while the flow types derived from simple models are useful in interpretating observations, it is unwise to try to force every observation into classification schemes derived from approximate and simplified models. Two important areas for current and future research are (i) the unsteady development of a flow towards one of the classically defined regimes (often involving mixing and wave generation) and (ii) the more complete and realistic description of flows where effects not included in the simpler models are significant.

References

Baines, P.G., Upstream blocking and airflow over mountains, *Ann. Rev. Fluid Mech., 19*, 75-97, 1987.

Baines, P.G., *Topographic effects in stratified flows,* Cambridge University Press, 1995.

Baines, P.G., Mixing in flows down gentle slopes into stratified environments, *J. Fluid Mech., 443*, 237-270, 2001.

Baines, P.G., and D.L. Murray, Topographic influence on the pattern of flow through Bass Strait, *Mar. Freshwater Res., 46*, 763-767, 1995.

Borenäs, K.M., and J.A. Whitehead, Upstream separation in a rotating channel flow, *J. Geophys. Res., 103(C2),* 7567-7578, 1998.

Cummins, P.F., Stratified flow over topography: time-dependent comparisons between model solutions and observations, *Dyn. Atmos. Oceans, 33,* 43-72, 2000.

Etling, D., F. Gelhardt, U. Schrader, F. Brennecke, G. Kühn, G. Chabert d'Hieres and H. Didelle, Experiments with density currents on a sloping bottom in a rotating fluid, *Dyn. Atmos. Oceans, 31,* 139-164, 2000.

Farmer, D. and L. Armi, The generation and trapping of solitary waves over topography, *Science, 283,* 188-190, 1999a.

Farmer, D. and L. Armi, Stratified flow over topography: the role of small-scale entrainment and mixing in flow establishment, *Proc. Roy. Soc. Lond. A 455,* 3221-3258, 1999b.

Hibiya, T., Generation mechanism of internal waves by a vertically sheared tidal flow over a sill, *J. Geophys. Res., 95(C2),* 1757-1764, 1990.

Kasê, R.H., and A. Oschlies, Flow through Denmark Strait, *J. Geophys. Res., 105(C12),* 28257-28546, 2000.

Kinder, T.H., and G. Parrilla, Yes, some of the Mediterranean outflow does come from great depth, *J. Geophys. Res., 92,* 2901-2906, 1987.

Klymak, J.M., and Gregg, M.C., Three-dimensional nature of flow near a sill, *J. Geophys. Res., 106(C10),* 22295-22311, 2001.

Lane-Serff, G.F., and P.G. Baines, Eddy formation by dense flows on slopes in a rotating fluid, *J. Fluid Mech., 363,* 229-252, 1998.

Lane-Serff, G.F., and P.G. Baines, Eddy formation by overflows in stratified water, *J. Phys. Oceanogr., 30,* 327-337, 2000.

Lane-Serff, G.F., L.M. Beal and T.D. Hadfield, Gravity current flow over obstacles, *J. Fluid Mech., 292,* 39-53, 1995.

Lane-Serff, G.F., and M.D. Woodward, Internal bores in two-layer exchange flows over sills, *Deep-Sea Res. I, 48,* 63-78, 2001.

Lawrence, G.A., Steady flow over an obstacle, *J. Hydaul. Eng. – ASCE, 113(8),* 981-991, 1987.

Lawrence, G.A., Steady two-layer flow over a fixed obstacle, *J. Fluid Mech., 254,* 605-633, 1993.

Lawrence, G.A., The stability of a sheared interface, *Phys. Fluids A., 3(10),* 2360-2370, 1999.

Onken, R., and J. Sellschopp, Seasonal variability of flow instabilities in the Strait of Sicily, *J. Geophys. Res., 103(C11),* 24799-24820, 1998.

Pratt, L.J., K.R. Helfrich and E.P. Chassignet, Hydraulic adjustment to an obstacle in a rotating channel, *J. Fluid Mech., 404,* 117-149, 2000.

Seim, H.E., and M.C. Gregg, The importance of aspiration channel curvature in producing strong vertical mixing over a sill, *J. Geophys. Res., 102(C2),* 3451-3472, 1997.

Spall, M.A., and J.F. Price, Mesoscale variability in Denmark Strait: The PV outflow hypothesis, *J. Phys. Oceanogr., 28,* 1598-1623, 1998.

Thorpe, S.A., and J.T. Holt, The effects of laterally sloping upper and lower boundaries on waves and instabilities in stratified shear flows, *J. Fluid Mech., 286,* 49-65, 1995.

Wood, I.R., and J.E. Simpson, Jumps in layered miscible fluids, *J. Fluid Mech., 140,* 329-342, 1984.

Wurtele, M.G., R.D. Sharman and A. Dutta, Atmospheric lee waves, *Ann. Rev. Fluid Mech., 28,* 429-476, 1996.

Yih, C.S., and C.R. Guha, Hydraulic jump in a fluid system of two layers, *Tellus, 7,* 358-366, 1955

Recent progress on understanding the effects of rotation in sea straits

L. J. Pratt

Woods Hole Oceanographic Institution, Woods Hole, MA, USA

Abstract This paper reviews progress in understanding the effects of rotation in sea straits during the last decade. First the governing equation for single-layer reduced gravity flows through traits are reviewed. Then the question of upsteam influence is considered. The application of theory, including the determination of bounds on transportm to a number of specific straits is examined. Finally hydraulic jumps and potential vorticity hydraulics are discussed.

Introduction

This brief review of recent progress in understanding the effects of rotation in sea straits will concentrate on work carried out during the past decade. Reviews of prior work can be found in *The Physical Oceanography of Sea Straits* (the volume of proceedings from the 1989 Les Arcs meeting, published by Kluwer) and in Pratt and Lundberg (1991). In addition, there are several important topics which involve rotation but will be covered by other review speakers and poster presenters at the conference. Chris Garrett will talk about Ekman layers and related frictional effects. A number of investigators (Price, Lundberg, Astraldi, Gasparini, Salusti, Girton, Laanearu and the Nordic WOCE investigators) have carried out exciting work in places like the Denmark Strait, the Faroe-Bank Channel, the Baltic, the Strait of Sicily. I will defer to them. Finally, I will not attempt to review the dynamics of 'outflows'; that is, the descending, entraining portion of an overflow that occurs well downstream of a sill. Jim Price is an expert on this subject and he will have something to say about it in his review.

Among the broad scientific questions that theories and models of rotating strait flow hope to address are the following: To what extend do deep straits and sills regulate the thermohaline circulation in the Ocean? How much water mass modification can be accounted for by local processes occurring in straits? How can the special geometry and dynamics of deep straits be exploited for the purposes of climate monitoring?

More specific questions address the physical processes involved in mixing, upstream influence, and the way in which signals are routed from basin to basin. What waves are most important in regulating the upstream flow? How far does this influence extend? Where does the bulk of the mixing occur? What does a rotating hydraulic jump look like and why has one never been observed? What is the importance of recirculations and flow reversals common in models? To what extent do traditional hydraulics principles hold in the presence of time dependence? Can upstream influence and mixing be parameterized in numerical models of the general circulation?

Governing equations

With the exception of the models of Dalziel (1988, 1990) and Pratt and Armi (1989) analytical models of inviscid, hydraulically-driven flows in rotating straits have been confined to single-layer (reduced gravity) systems. The benchmark steady models are those of Whitehead et al. (1974), hereafter WLK, and Gill (1977). The strait or channel is aligned in the y-direction and the bottom elevation $h(x,y)$ and flow properties are assumed to vary gradually with y. Under these conditions a simple scaling argument suggest that the along-channel velocity v is geostrophic:

$$fv = g' \frac{\partial d}{\partial x} + g' \frac{\partial h}{\partial x}. \tag{1}$$

Here d is the layer depth, g' the reduced gravity, and f the Coriolis parameter. The shallow-water potential vorticity in the gradually-varying flow can be approximated by

$$q = \frac{1 + \frac{\partial v}{\partial x}}{d}. \tag{2}$$

Eliminating v between (1) and (2) yields a second order equation governing the cross sectional structure of the flow:

$$\frac{\partial^2 d}{\partial y^2} - \frac{fq}{g'}d = -\frac{f^2}{g'} - \frac{\partial^2 h}{\partial y^2}. \tag{3}$$

Although v is geostrophic, the cross channel velocity u is not and thus the momentum balance in the y-direction is unapproximated:

$$\frac{\partial v}{\partial t} + u\frac{\partial v}{\partial x} + v\frac{\partial v}{\partial y} + fu = -g'\frac{\partial d}{\partial y} \tag{4}$$

If the flow is steady, the potential vorticity is a function of the transport stream function ψ and is related to the Bernoulli function

$$B(\psi) = \frac{v^2}{2} + g'd + g'h \tag{5}$$

by the relation

$$\frac{dB}{d\psi} = q. \tag{6}$$

The most common procedure used to obtain solutions (analytical or numerical) is to solve (3) for the cross-channel structure of the flow. The y-dependence of the solutions is contained in the two constants of integration and is determined from (4) or a derived relation. The early models of rotating flow are based on solutions to (3) with $q=0$ (used by WLK) and $q=const.>0$ (used by Gill, 1977).

A difficulty arising in the application of reduced-gravity models to deep straits and sills lies in the identification of the active layer. For example, the overflows in the Denmark Strait and Faroe-Bank Channel are composed of various deep and intermediate water masses with different origins and it can be argued whether all of these or some subset comprises the 'active' layer of a reduced gravity system.

Flow criticality

Given a strait with a certain geometry and the general features of the flow in the upstream basin it is possible to identify among the family of possible solutions certain ones that are subject to critical control. Such solutions are 'choked', meaning that the volume transport and other upstream properties are influenced by the geometry of the strait itself, usually the characteristics of the sill. Hydraulically controlled solutions pass through a subcritical-to-supercritical transition at a 'control' section and typically have the maximum transport of all members of the family. The upstream-downstream asymmetry associated with the hydraulic transition is manifested by the overflow itself; the pouring and descent of water across

the sill (or through a narrows). It is this feature that has led investigators to believe that the overflows of the Denmark Strait, Faroe-Bank Channel, Vema Channel, and others are hydraulically controlled.

It is notable, however, that in none of these cases has the criticality of the sill flow been verified by direct measurement. 'Nonrotating' applications such as Gibraltar can be assessed by calculating a composite Froude number (Armi, 1986) which is $<0,=0,$ or >0 for subcritical, critical, and supercritical conditions. Unfortunately the assessment of the criticality of a rotating channel flow is more difficult. If the channel has a rectangular cross section, it can be shown (Stern 1974) that critical flow requires

$$\int_0^w \frac{1}{dv^2}\left(1 - \frac{v^2}{g'd}\right)\partial x = 0. \tag{8}$$

The local Froude number at a critical section must range above and below unity. Since the potential vorticity can be nonuniform, it is possible that the flow might become critical with respect to a Rossby wave. It is surprising that such a state should depend on the behavior of the local Froude number, however it is possible that the requirement of unidirectional flow might be restrictive. I have extended (8) to include bands of reverse flow and the result for the case of a single velocity reversal (at $x=x_m$) is much more complicated:

$$\frac{1}{2}[1 - q(\psi_m)d_m]\int_0^{x_1} \frac{1}{v^2 d}\left(1 - \frac{v_+^2}{g'd}\right)\partial x \tag{9}$$

$$= \frac{q(\psi_m)(d_w - d_m) + 1}{v_w d_w}$$

$$+ \int_{x_1}^{x_m} \frac{q(\psi)q(\psi_m)(d_m - d) + q(\psi_m) - q(\psi)}{v^2}\partial x$$

Here x_1 and x_m denote the locations of the maximum interior values of ψ and the zero crossing of v. Evaluation of (8) or (9) using data is severely limited by the assumption of rectangular geometry.

The presence of topographic variations in the cross section make the problem much more difficult. Critical states for uniform potential vorticity have been found for specific nonrectangular sections by Borenäs and Lundberg (1986, 1988) and Borenäs and Nikolopoulos (2000), however the results must be obtained numerically. It is a pity that there is no simple formula allowing the assessment of the criticality of a rotating flow past a nonuniform cross section, even when the potential vorticity is zero.

Upstream influence

In classical hydraulics, the upstream influence of a sill (or width contraction) is typically contained in a relation between the volume transport and the elevation Δz of the water surface in the upstream basin above the sill. If the sill is raised, as is possible in engineering applications, the transport and upstream surface elevation are altered. This alteration is caused by a blocking wave that is generated at the sill and moves upstream. For a fixed sill, upstream influence occurs as a response at the sill section to information generated upstream. Changes in the upstream basin are communicated to the sill in the form of incident waves and the choking effect is transmitted back into the basin by reflected waves. In principle, this process could be used as the basis for parameterization of upstream influence in numerical models unable to resolve straits. The strait and sill system is replaced by a partially reflecting boundary which allows fluid to pass through. The reflection coefficient for an incident wave is calculated using hydraulic relation (such as 11 below). Pratt and Chechelnitsky (1997) present some examples of this procedure.

All simple models of rotational effects in straits employ idealize upstream conditions. The simplest situation, originally suggested by WLK, involves an infinitely deep upstream basin containing quiescent fluid. To pass over a shallow sill a fluid column must be severely squashed and thus the potential vorticity near the sill is small in that

$$q = D_{sill} / D_\infty << 1 \qquad (10)$$

where D_∞ is the reservoir depth and D_{sill} is a scale for the depth at the sill. In this 'zero potential vorticity' limit, the transport over a sill with a rectangular cross-section is given, in the WLK model, by

$$Q = \begin{cases} \left(\frac{2}{3}\right)^{3/2} w_s (g')^{1/2} \left[\Delta z - (w_s^2 f^2 / 8g')\right]^{3/2} & \text{(Non-sep.)} \\ (g'/2f)(\Delta z)^2 & \text{(Separated)} \end{cases} \qquad (11)$$

where Δz is the elevation of the reservoir interface above the sill. This expression reduces to the nonrotating formula

$$Q = \left(\frac{2}{3}\right)^{3/2} w_s (g')^{1/2} (\Delta z)^{3/2} \qquad (12)$$

in the limit $w_s^2 f^2 / (g' \Delta z) << 1$. This last parameter provides a measure of the importance or rotation at the sill section.

It should be pointed out that the assumption of quiescent flow in the infinitely deep basin cannot

be verified using the zero potential vorticity model, since the approximation (10) fails there. However, Borenäs and Pratt (1994) have verified the hypothetical upstream state can exist by integrating the equations for finite (but still uniform) potential vorticity.

A more sophisticated view of the upstream basin (Gill, 1977) is that it is infinitely wide but not necessarily deep. The potential vorticity is assumed uniform and this filters Rossby waves from the system, leaving just Kelvin waves to provide communication. The basin flow is confined to boundary layers with thickness $L_d = (g'D_\infty)/f$, where D_∞ is depth in the quiescent interior of the basin. In addition to Δz, which is now interpreted as the elevation of the interface in the basin interior above the sill, the transport of a critically controlled state depends on an additional parameter. Gill chose the later to be a measure of how the transport is partitioned between the boundary currents on the two side walls of the basin. The resulting transport relations involve solutions to higher order polynomials and cannot be expressed as simply as (11). The transports are generally smaller than what would be predicted by WLK for flow from an infinitely deep basin.

Killworth (1992) presents an alternative view of the flow in a wide upstream basin in which boundary layers are not present. The transport is contained in a weak flow that is smoothly distributed across the whole basin width. The basin bottom is assumed horizontal (with $h=0$) and therefore the basin Bernoulli function is approximated by $g'd$. In addition, the transport streamfunction and depth are related by $\psi = (g'/2f)(d^2 + const)^{1/2}$, which follows from (1). The basin Bernoulli function is therefore given by $B(\psi) = \left[(2f\psi/g') - const\right]^{1/2}$ and the potential vorticity $dB/d\psi$ is clearly nonuniform. In addition to the total transport, the upstream flow is completely specified by the constant, which can be related to the depth along one of the side walls. The basin flow therefore has one fewer degree of freedom than in the Gill model. The transport relation for a critically controlled solution must be obtained numerically the fluxes are generally smaller than what is predicted by (11).

Among the many approximations that one might call in to question is the conservative nature of the upstream flow. In the WLK model, fluid is expected to rise from the bottom of a rapidly rotating, deep reservoir and pass over a shallow sill, all without the benefit of forcing or dissipation. The spatial scales of the motion in the basin are typically an order of magnitude or

more greater than the length of the strait, further suggesting the importance of forcing and dissipation. Pratt and Llewellyn Smith (1997) and Pratt (1997) attempted to come to grips with this problem by matching an inviscid model for hydraulically controlled flow in a strait to a basin containing a nearly geostrophic flow with distributed sources of mass and with bottom friction. The basin topography is bowl-shaped with closed f/H contours (accept for those contours leading into the strait) and f=const. Fluid introduced into the basin through the side walls is fed directly into the strait through frictional boundary layers whose dynamics are equivalent to that of an arrested topographic wave. When fluid is fed into the interior of the basin from above, an anticyclonic circulation is set up causing the fluid columns to move in a widening spiral which eventually reaches the basin edge. From there, the fluid is channel into boundary layers that feed into the strait.

How can these four visions of the upstream flow be used to understand the effects of deep sills on the thermohaline circulation? One way to pose the question is to ask how the upstream state reacts to a small change in the elevation of the sill. In the WLK case, the interface level of the upstream basin would tend to rise and the transport would be reduced by some small amount. In the Gill model, the change in sill level would be transmitted by a Kelvin wave that would move into the basin along the northern hemisphere left wall (facing downstream). (If the basin was closed, this wave might circle the basin and interact again with the sill, resulting in the generation of a secondary upstream wave.) It is not clear if or how interface level in the quiescent interior of the basin could be influenced by these changes, and this begs the question of how that interior level is established in the first place. In the Killworth (1992) model, the potential vorticity is nonuniform and signals would presumably be carried upstream by Rossby and Kelvin waves. In contrast to the Gill model, it is clear how information would propagate into the interior of the basin. However, it is not clear that the sluggish conditions envisioned by Killworth (with no boundary layers) would be maintained in the presence of Kelvin wave influence. Finally, the model proposed by Pratt (1997) involves an upstream basin who's flow is completely determined by linear dynamics. Thus the circulation pattern is remains independent of the magnitude of the flux across the sill. If the sill height is altered, the mean elevation of the interface in the basin rises but the streamline patters remains fixed.

As suggested by these last remarks, the necessity of tractability has resulted in the development of idealized models which are somewhat disjoint. Attempts to relate the hypothetical upstream states to the ocean have been frustrated by a lack of upstream observations. For example, it is difficult to trace the various deep and intermediate water masses that compose the Denmark Strait and Faroe Bank Channel to specific upstream current systems or source regions.

Models with conservative upstream states are helpful in developing intuition but may be unrealistic. For example, the presence of deep western boundary layers in upstream basins suggests that friction cannot be ignored. In understanding an upstream circulation subject to forcing and dissipation a helpful constraint can be developed in the form of a circulation theorem. If the tangential component of the shallow-water momentum equation is integrated about the basin edge, and across the entrances of any straits leading into and out of the basin, if follows that:

$$\frac{d}{dt}\oint_C \mathbf{u}\cdot\mathbf{t}\,ds = -\oint_C (f+\varsigma)\mathbf{u}\cdot\mathbf{n}\,ds - r\oint_C \mathbf{u}\cdot\mathbf{t}\,ds \quad (13)$$

where ς is the relative vorticity, $\mathbf{n}$ and $\mathbf{t}$ are unit normal and tangent vectors to the boundary, and r is a linear drag coefficient. Equation (13) tells us that the rate of change of circulation about the basin edge (zero for steady flow) equals the flux of absolute vorticity across the basin edge due to inflows and outflows, plus the dissipation due to contact with the bottom. In Pratt's (1999) steady model, f is constant and $>>\varsigma$, so that

$$\oint_C f\mathbf{u}\cdot\mathbf{n}\,ds = r\oint_C \mathbf{u}\cdot\mathbf{t}\,ds.$$

If fluid is fed into the interior of the basin and drains out through the strait, the flux of total vorticity $\oint_C f\mathbf{u}\cdot\mathbf{n}\,ds$ into the strait is >0 and thus the rim circulation must be generally cyclonic $r\oint_C \mathbf{u}\cdot\mathbf{t}\,ds > 0$ as observed. On the other hand, if fluid is fed into the basin entirely through a second strait (such as the Jan Mayan fracture zone in the Norwegian Sea) and if the inflows and outflows have the same velocity, then $\oint_C f\mathbf{u}\cdot\mathbf{n}\,ds=0$ and thus $\oint_C \mathbf{u}\cdot\mathbf{t}\,ds = 0$. In this case the inflow splits into two boundary currents that move around the edge of the basin. If the inflows and outflows have similar velocity but the value of f is significantly higher at the entrance to the inflow, then $\oint_C \mathbf{u}\cdot\mathbf{t}\,ds > 0$, implying an intensification of the rim current on the western

side of the basin. Further applications of this constraint are illustrated in Yang and Price (2000) and Helfrich and Pratt (2002, in this volume).

The interaction between the sill and the upstream basin is important from the standpoint of climate monitoring. In a recent study, Hansen et al. (2001) attempted to establish a relation between the directly measured transport Q of the Faroe-Bank Channel overflow and the upstream hydrography. They empirically fitted a six-month record of transport to $\gamma(\Delta z)^n$ ($n=1$ or $3/2$), where Δz is the elevation above the Faroe-Bank sill of the upstream 'interface' or bounding isopycnal, here the $\sigma_j=28.0$ surface. The upstream elevation of this surface has been monitored for over five decades at a station in the eastern Norwegian Sea by a weather ship. After estimating the constant γ based on the six-month transport record they applied the resulting model to the five-decade record of Δz and found a 20% decrease in transport from the mid 1990's to the present time.

Is this a reasonable thing to do? The $n=3/2$ law agrees only with the nonrotating limit of (12) of the flux relation. The $n=1$ law does not agree with any hydraulic relation, but is claimed by the authors to correspond to a frictionally dominated overflow. A more important question is whether the time-dependence of a single upstream station tells us anything about the time-dependence of the overflow. This is exactly the type of problem that models of upstream influence should be able to address. Interestingly, the Gill model tells requires *two* independent upstream parameters to predict Q. In addition, the upstream station in the case in point lies close to the Norwegian-Atlantic Current and therefore dynamics of the upper layer may be relevant.

There is an even more basic question that one might ask about upstream effects. How shallow must a sill be in order to influence fluxes associated with the abyssal circulation. This question was first addressed by Long (1953), who was able to predict how large an obstacle must be to alter the upstream state of a moving stream. His calculations and laboratory experiments have served as a model for understanding upstream effects of obstacles in stratified flows. P. Baines is responsible for much of this work and the interested reader should consult his text. Recently, this approach has been extended to flows in rotating straits by Pratt et al. (2000) who used the Gill model to predict how large an obstacle height is required in order to establish hydraulic control over an initially steady, geostrophically balanced stream. The predictions were in fairly good agreement with numerical

simulations of the adjustment process itself. The idealizations present make it difficult to extrapolate the results to the ocean, but the general approach might prove helpful when used with regional numerical models. For example, one might take a model of the Nordic seas, calculate thermohaline circulation that would exist if the bottom was horizontal, then gradually grow topography into the model and observe the point at which overflows appear. If the sill heights are increased past that point, what is the effect on the overflow transports and other meridional fluxes?

These issues will be discussed further at the meeting.

Application of simple models to specific straits.

The application of simple models of rotating, hydraulically driven flow to deep straits is largely limited to transport comparisons based on formulas such as (11) and to comparisons between observed outflow characteristics and plume models. The second subject is reviewed by Jim Price in this volume. Comparison between the flow upstream of the sill section and that predicted by models has been limited by the lack of upstream observations. However, an intriguing controversy that has recently been brought to light involves the apparent approach of overflow water in the Denmark Strait along the eastern (Iceland) side of the channel (Jonsson, 1999, Nikolopoulos et. al. 2002). Where would a boundary current of this type originate? Does it involve a crossing of boundary flow along the Greenland coast to the Iceland coast? Such crossing seems to be feature of the solutions found by Pratt (1999) and also occurs in the numerical solutions of Helfrich and Pratt (2002, this volume). The crossing is due to the shoaling bottom topography that the approaching flow seas as it moves into the strait and towards the sill. The sloping bottom creates a topographic beta effect in which the Iceland coast becomes the dynamical western boundary. A current that flows southwards along the Greenland coast and is deep enough to feel the shoaling topography would tend to cross the strait and collect in a 'western' boundary layer along the Iceland coast.

Returning to the subject of transport comparisons, Whitehead (1989) has applied (11) to a number of well-known deep sills and found that the transport Q is overestimated by 160% to 400%. A number of complications including time-dependence, non-zero potential vorticity, interactions with upper layers, and the non-

rectangular geometry of the cross-section, and perhaps the outright lack of hydraulic control at the sill section might contribute to the error. For example, the work of Borenäs and Lundberg (1986,1988, and 1990) suggests that non-uniform cross sections tend to reduce the transport below that of a rectangular geometry. Killworth (1992) furthers this point in the

context of a dynamically wide sill. Using the actual geometry of the Jungfern Passage, Borenäs and Nikolopoulos (2000) present a estimate of the deep transport that is quite close to the observed value. Some of the results of these calculations are presented in the following table:

Table 1.
Overflow transport Q (Sv), observed and estimated from hydraulic theory. All values are taken from Killworth (1992) unless otherwise indicated.

	Denmak Strait	Faroe=Bank Channel	Ceara Rise	Vema Channel	Jungfern Passage
Observed	2.5	1.4	1.1-2.1	4.0	0.072 - 0.092**
Rectangular sill, zero pv***	3.8	3.6	4.6	16.0	
Parabolic sill, Killworth '92	0.6	0.53	2.1	4.5	
Parabolic sill, zero pv	0.5	0.5	1.4	2.9	
Actual sill geometry, zero pv					0.079*
Actual sill geometry, zero pv, band of reverse flow excised.					0.085*

*   Borenäs and Nikolopoulos (2000)
**   Frantantoni et. al. (1997)
***   For the first four straits, all of which are dynamically wide, the Killworth 1992 model and WLK (zero potential vorticity model) produce the same Q in this case. The values quoted are therefore the same as those appearing in Whitehead, 1989.

A striking feature of the results is the extent to which Q is reduced when the sill geometry is changed from rectangular to parabolic. In the cases of the Ceara Rise and Vema Channel, the reduction brings the estimate into better agreement with the observations. For the Denmark Strait and Faroe-Bank Channel, the reduction lowers the predicted Q below that observed values.

A predicted feature of hydraulically controlled flows is that rounded cross-sections, particularly wide ones, tend to produce flow reversals. A common situation is that the predicted sill flow has a band of reverse flow along the Northern Hemisphere right wall (e.g. Borenäs and Lundberg 1986 and Killworth 1992). Such reversals are sometimes regarded as violations of the assumptions underlying a theory based on specification of upstream conditions. Perhaps a more significant point is that flow reversals at sill sections are not generally observed in the ocean, in laboratory models (Borenäs and Whitehead 1998), or in numerical models of overflows (see the Helfrich and Pratt poster). For example, the Denmark Strait overflow is bounded on the right (facing downstream) by a region of sluggish motion and level isopycnals. It is in this region that inviscid hydraulic theory tends to predict flow reversals. Because of this behavior, it has

been suggested that regions of reverse flow arising in models should be replaced by stagnant regions in the estimation of Q. No firm dynamical explanation for this behavior as yet been offered.

Transport bounds

Given the difficulty of establishing transport relations, one might at least try to formulate bounds. Killworth and McDonald (1993) and Killworth (1994) have done so, using conservation of mass, energy (and therefore potential vorticity), and the geostrophic relation as a foundation. As an example of the procedure and reasoning they use, consider the reduced gravity flow at a section of channel with arbitrary geometry. If η denotes the elevation of the interface, the transport is given by

$$Q = \frac{g'}{f} \int_{x_o}^{x_1} (\eta - h)\frac{\partial \eta}{\partial x}dx = \frac{g'}{f}\left\{ \tfrac{1}{2}(\eta_1^2 - \eta_o^2) - \int_{x_o}^{x_1} h\frac{\partial \eta}{\partial x}dx \right\}$$

where x_o and x_1 are the positions of the left and right edges of the current, where d goes to zero.

An upper bound on Q can be formulated by modifying the profile in a way that only adds to the flux and then calculating the transport of the modified state. This procedure involves

chopping off regions of negative velocity at the end points of the profile and replacing them with regions of positive flow in which the depth is smoothly brought to zero. A slightly more involved procedure is used to replace certain interior regions with negative flux by stagnant regions. The bound that results can be written as

$$Q \leq \frac{g'}{2f}\left(\eta_1 - h_{min}\right)^2$$

The last expression (which follows from $h_{min} = \eta_o$) is exactly the geostrophic transport associated with a current in a rectangular channel if the flow is separated from the left wall (facing downstream) and if the depth along the right wall is $\eta_1 - h_{min}$. More generally, we not that $g\eta_1$ cannot be greater than the maximum value of the Bernoulli function over the cross-section. If the latter is conserved following streamlines leading from the upstream basin into the channel, than $g\eta_1$ is bounded by the maximum value E of the Bernoulli function in the basin, at least for those streamlines that connect with the channel section in question. Thus

$$Q \leq \frac{g'}{2f}\left(\frac{E}{g'} - h_{min}\right)^2 . \tag{14}$$

where E is the maximum value of the Bernoulli function along streamlines that connect to the upstream basin and h_{min} is the minimum value of the topographic height at the sill.

In the WLK ('zero potential vorticity') model the upstream basin is assumed to be quiescent and therefore $E = g'(h_{min} + \Delta z)$. Substitution into the above bound yields the WLK expression for 'zero potential vorticity' flux for the case in which the flow is separated from the left wall of the rectangular channel. The connection between the bound and 'zero-potential' vorticity flow lies in the fact that $B(\psi)$ is uniform when $q=0$. Given an arbitrary flow with variable $B(\psi)$ one could pick out the maximum E of B and ask what the transport would be if each streamline had $B=E$ (zero potential vorticity) , if the elevation of the channel bottom had the uniform value h_{min}, and if the flow depth went to zero at the left edge of the stream. This flux is exactly that given by (14).

It is not known whether the above bound holds in the presence of time dependence. Indeed, it is not understood whether time-dependence reduces or increases the transport relative to mean values.

Hydraulic jumps

Although hydraulic jumps have been detected in Gibraltar, Knight Inlet, (apparently) the Romanch Fracture Zone, and in other ocean straits, they only tend to be observed where rotation is weak. One of the most interesting aspects of rotationally-dominated overflows is that no direct observations of hydraulic jumps have been made. The strongest indirect evidence for a jump involves data from the Vema Channel (Hogg, 1983) suggesting a sharp decrease in the Bernoulli function over a short distance interval downstream of the sill.

Can hydraulic jumps exist in strongly rotating flows and what would they look like? Different possibilities have been suggested by Pratt (1983, 1987), Nof (1984,1986), and Pratt et al. (2000), all of which assume rectangular cross-sections. The most robust version seems to be a transverse jump that occurs when the supercritical flow downstream of a sill becomes separated from one of the side walls. The jump consists of an abrupt widening and reattachment of the current. The abrupt depth change characteristic of a nonrotating jump is suppressed. No strong evidence of such a feature has been found in the Denmark Strait outflow, which hugs the right-hand boundary (e.g. Girton and Sanford, 2002). It is conceivable that something like transverse jumps could be integral to the eddies that occur regularly in the strongly time-dependent plume. Or, the jump may be sublimated by friction and entrainment processes. The fact that rotating jumps have not been identified in other overflows could, of course, be due to a lack of observations in the right places.

Potential vorticiy hydraulics

The past 15 years has seen the development of a number of models of Rossby-wave critical flow. Most of the applications involve jets and fronts and are beyond the scope of this meeting. However there have been a few studies of channel flow, including Pratt and Armi (1987), Haynes, et. al. (1993), and Johnson and Clark (1999). It is questionable whether a flow that is strong enough to arrest Kelvin waves (i.e. $u/(g'd)^{1/2}=O(1)$ could become critical with respect to the slower Rossby waves, and therefore the major deep overflows do not seem to be strong candidates for Rossby wave control. However, a larger scale strait such as the Drake Passage might be a candidate

References

The following is a general reference list that contains papers relevant to the observation and dynamics of flows rotating straits.

Armi, L. 1986. The hydraulics of two flowing layers of different densities. *J. Fluid Mech.*, 163, 27-58.

Astraldi, M., G.P. Gasparini, L. Gervasio, and E. Salusti 200? . Dense water dynamics along the strait of sicily (Mediterranean Sea). *J. Phys. Oceanogr.* , in press.

Baines, P. G. 1987 Upstream blocking and airflow over mountains. *Ann. Rev. Fluid Mech.* 19, 75-97.

Baines, P. G. 1995 *Topographic Effects in Stratified Flows*. Cambridge University Press, 482 pp.

Borenäs, K. M., Lundberg, P. A. 1986 Rotating hydraulics of flow in a parabolic channel. *J. Fluid Mech.* 167, 309-26.

Borenäs, K. M., Lundberg, P. A. 1988 On the deep-water flow through the Faroe Bank Channel. *J. Geophys. Res.* 93(C2), 1281-92.

Borenäs, K. M., Lundberg, P. A. 1990 Some questions arising from the application of hydraulic theory to the Faroe Bank Channel deep-water flow. *Pure Appl. Geophys.*, 133, 574-585.

Borenäs, K. M. and L. J. Pratt 1994 On the use of Rotating Hydraulic Models. *J. Phys. Oceanor.* 24, 108-123.

Borenäs, K. M. and J. A. Whitehead (1998) Upstream separation in a rotating channel flow. *J. Geophys. Res.* 103, C4, 7567-7578

Borenäs, K. M. and A. Nikolopoulos (2000) Theoretical calculations based on real topography of the maximum deep-water flow through the Jungfern Passage. *J. Marine Res.* 58, 709-719.

Bennett, J. R. 1973 A Theory of Large-Amplitude Kelvin Waves. *J. Phys. Oceanogr.* 3, 57-60.

Bormans, M. and C. Garrett 1989. A simple criterion for gyre formation by the surface outflow from a strait, with applications to the Alboran Sea. *J. Geophys. Res.* 94, 12,637-12,644.

Bryden, H. L. and T. H. Kinder 1991. Steady two-layer exchange through the Strait of Gibraltar. *Deep-Sea Res.*, 38 (Suppl. 1), S445-S463.

Bryden, H. L. and H. M. Stommel (1984) Limiting processes that determine basic features of the circulation in the Mediterranean Sea. *Oceanologica Acta*, 7, 289-296.

Crease, J. 1965 The flow of Norwegian Sea water through the Faroe Channel. *Deep-Sea Res.* 12, 143-50.

Dalziel, S. B. 1988 *Two-layer hydraulics: maximal exchange flows*, PhD thesis. Univ. Cambridge, Engl.

Dalziel, S. B. 1990 Rotating two-layer sill flows. In *The Physical Oceanography of Sea Straits. NATO-ASI Ser.*, ed. L. J. Pratt. Dordrecht: Kluwer. 587 pp.

Dalziel, S.B. 1991 Two-layer hydraulics: a functional approach. *J. Fluid Mech.* 223, 135-163.

Dalziel, S. B. 1992 Maximal Exchange in Channels with Nonrectangular Cross Sections. *J. Phys. Oceanogr.* 22, 1188-1206

Fratantoni, D. M., R. J. Zantopp, W. E. Johns, and J. L. Miller 1997. Updated bathymetry of the Anegada-Jungfern Passage complex and implications for Atlantic inflow to the abyssal Caribbean Sea. *J. Marine Res.* 55, 847-860.

Gerdes, F., C. Garrett, and D. Farmer 200? A note on internal hydraulics with entrainment. *J. Phys. Oceanogr.* accepted.

Gill, A. E. 1976 Adjustment under gravity in a rotating channel. *J. Fluid Mech.* 77, 603-621.

Gill, A. E. 1977 The hydraulics of rotating-channel flow. *J. Fluid Mech.* 80, 641-71.

Girton, J. B. and T. B. Sanford (2002) Descent and modification of the overflow plume in the Denmark Strait. *J. Phys. Oceanograph.* (submitted).

Grimshaw, R. H. J. and N. Smyth 1986. Resonant flow of a stratified fluid over topography. *J. Fluid Mech.* 169, 429-464.

Haines, P., Johnson, E. and R. Hurst, 1993: A simple model of Rossby-wave hydraulics behavior. *J. Fluid Mech.*, 253, 359-384.

Hansen, B., W. R. Turrell, and S. Osterhus, 2001. Decreasing overflow from the Nordic seas into the Atlantic Ocean through the Faroe Bank channel since 1950. *Nature,* 411, 927-930.

Helfrich, K. R., A. C. Kuo and L. J. Pratt 1999 Nonlinear Rossby adjustment in a channel. *J. Fluid Mech.* 390, 177-222.

Herman, A.J., P.B. Rhines and E.R. Johnson 1989. Nonlinear Rossby adjustment in a channel: beyond Kelvin waves. *J. Fluid Mech.* 205, 469-502.

Hogg, N. G. 1983 Hydraulic control and flow separation in a multi-layered fluid with application to the Vema Channel. *J. Phys. Oceanogr.* 13, 695-708.

Hogg, N. J. 1989 Finite-amplitude effects on deep planetary circulation over topography. *J. Phys. Oceanogr.* 19, 1697-1706.

Hogg, N. G., Biscaye, P., Gardner, W., Schmitz, W. J. 1982 On the transport and modification of Antarctic Bottom Water in the Vema Channel. *J. Mar. Res. (Supp.)* 40, 231-63.

Houghton, D. D. 1969 Effect of rotation on the formation of hydraulic jumps. *J. Geophys. Res.* 74, 1351-60.

Hughes, R. L. 1985a. On inertial currents over a sloping continental shelf. *Dyn. Atmos. Oceans* 9, 49-73.

Hughes, R. L. 1985b. Multiple criticalities in coastal flows. *Dyn. Atmos. Oceans* 9, 321-340.

Hughes, R. L. 1986a. On the role of criticality in coastal flows over irregular bottom topography. *Dyn. Atmos. Oceans* 10, 129-147.

Hughes, R. L. 1986b. On the conjugate behaviour of weak along-shore flows. *Tellus* 38A, 277-284.

Hughes, R. L. 1987 The role of the higher shelf modes in coastal hydraulics. *J. Mar. Res.* **45**, 33-58.

Hughes, R. L. 1989 The hydraulics of local separation in a coastal current, with application to the Kuriosho meander. *J. Phys. Oceanogr.* **19**, 1809-1820.

Johnson, E. R. and S.R. Clark, 1999: Dispersive effects in Rossby-wave hydraulics. *J. Fluid Mech.* **401**, 27-54.

Johnson, G. C. and T. B. Sanford 1992: Secondary circulation in the Faroe Bank Channel Outflow. *J. Phys. Oceanogr.* **22**, 927-933.

Johnson, G. C. and Ohlsen D. R. 1994 Frictionally Modified Rotating Hydraulic Channel Exchange and Ocean Outflows. *J. Phys. Oceanogr.* **24**, 66-78.

Jonsson, S. 1999. The circulation in the northern part of the Denmark Strait and its variability. *Int. Counc. for the Explor. of the Sea,* **L:6.**

Killworth, P. D. 1992 Flow properties in rotating, stratified hydraulics. *J. Phys. Oceanogr.* **22**, 997-1017.

Killworth, P. D. 1994 On Reduced-Gravity Flow Through Sills. *Geophys. Astrophys. Fluid Dynamics* **75**, 91-106.

Killworth, P. D. and N. R. McDonald 1993 Maximal Reduced-Gravity Flux in Rotating Hydraulics. *Geophys. Astrophys. Fluid Dynamics* **70**, 31-40.

Kubokawa A. and K. Hanawa 1984 A theory of semigeostrophic gravity waves and its application to the intrusion of a density current along a coast. Part 1. Semigeostrophic gravity waves. *J. Oceanographical Society of Japan,* **40**, 247-259.

Kubokawa A. and K. Hanawa 1984 A theory of semigeostrophic gravity waves and its application to the intrusion of a density current along a coast. Part 2. Intrusion of a density current along a coast of a rotating fluid. *J. Oceanographical Society of Japan,* **40**, 260-270.

Laanearu, J. 2001. Topographically constrained deep-water flows in channels (rotating-channel flow modelling, Baltic straits overflows.) Ph. D. Dissertation, University of Tartu, 59pp.

Nielson, J. N. 1912. Hydrography of the Mediterranean and adjacent waters. *Report on the Danish Oceanographical Expeditions* 1908-1910, **1**, 77-191.

Nikolopoulos, A., K. Borenäs, R. Hietala, and P. Lundberg 2002. Hydraulic Estimates of the Denmark Strait Overflow. *J. Geophys. Res.* (submitted).

Nof, D. 1984 Shock waves in currents and outflows. *J. Phys. Oceanogr.* **14**, 1683-1702.

Nof, D. 1986 Geostrophic shock waves. *J. Phys. Oceanogr.* **16**, 886-901.

Phillips, O. M. 1966 On turbulent convection currents and the circulation of the Red Sea. *Deep-Sea Res.* **13**, 1147-1160.

Pratt, L. J. 1983 On inertial flow over topography. Part 1. Semigeostrophic adjustment to an obstacle. *J. Fluid Mech.* **131**, 195-218.

Pratt, L. J. 1984a. On inertial flow over topography. Part 2. Rotating channel flow near the critical speed. *J. Fluid Mech.* **145**, 95-110

Pratt, L. J. 1984b. A time-dependent aspect of hydraulic control in straits. *J. Phys. Oceanogr.* **14**, 1414-18.

Pratt, L. J. 1986 Hydraulic control of sill flow with bottom friction. *J. Phys. Oceanogr.* **16**, 1970-80.

Pratt, L. J. 1987 Rotating shocks in a separated laboratory channel flow. *J. Phys. Oceanogr.* **17**, 483-91.

Pratt, L. J. 1989 Critical control of zonal jets by bottom topography. *J. Mar. Res.* **47**, 111-130.

Pratt, L.J. 1991: Geostrophic Versus Critical Control in Straits. *J. Phys. Oceanogr.* **21**, 728-732.

Pratt, L. J. 1997a Hydraulically Drained Flows in Rotating Basins. Part I: Method. *J. Phys. Oceanogr.* **27**, 2509-2521.

Pratt, L. J. 1997a Hydraulically Drained Flows in Rotating Basins. Part I: Steady Flows. *J. Phys. Oceanogr.* **27**, 2522-2535.

Pratt, L. J., Armi, L. 1987 Hydraulic control of flows with nonuniform potential vorticity. *J. Phys. Oceanogr.* **17**, 2016-29.

Pratt, L. J., Armi, L. 1990 Two-layer rotating hydraulics: strangulation, remote and virtual controls. *Pure Appl. Geophys.* **133**(4), 587-617.

Pratt, L. J., Chechelnitsky M. 1997 Principles for capturing the upstream effects of deep sills in low resolution ocean models. *Dynamics of Atmospheres and Oceans* **26**, 1-25.

Pratt, L. J., K. R. Helfrich, and E. P. Chassignet (2000) Hydraulic adjustment to an obstacle in a rotating channel. *J. Fluid Mech.* **404**, 117-149.

Pratt, L. J., Lundberg, P. A. 1991 Hydraulics of rotating strait and sill flow. *Ann. Rev. Fluid Mech.* **23**, 81-106.

Ried, L. P. 1980 Curvature effects on hydraulically driven inertial boundary currents. *J. Fluid Mech.* **96**, 395-412.

Rydberg, L. 1980 Rotating hydraulics in deep-water channel flow. *Tellus,* **32**, 77-89.

Sambuco, E., Whitehead J. A. 1976 Hydraulic control by a wide weir in a rotating fluid. *J. Fluid Mech.* **73**, 521-28.

Saunders, P. M. 1987. Flow through Discovery Gap. *J. Phys. Oceanogr.*, **17**, 631-643.

Saunders, P. M. 1990 Cold outflow from the Faroe Bank Channel. *J. Phys. Oceanogr.* **20**, 29-43.

Schär, L. and R. B. Smith (1993) Shallow-Water Flow past Isolated Topogrophy. Part I: Vorticity Production and Wake Formation. *J. Atmos. Sci.* **50**, 1373-1400.

Shen, C. Y. 1981 The rotating hydraulics of open-channel flow between two basins. *J. Fluid Mech.* **112**, 161-88.

Smith, T. 1684 A conjecture about an under-current at the Streights mouth. *Phil. Trans.*, **14**, 30-31.

Stalcup, M. C., Metcalf, W. G., Johnson, R. G. 1975 Deep Caribbean inflow through the Anegada-Jungfern Passage. *J. Mar. Res.* 33, 15-35.

Stern, M. E. 1972 Hydraulically critical rotating flow. *Phys. Fluids* 15, 2062-2064.

Stern M. E. 1974 Comment on rotating hydraulics. *Geophys. Fluid Dyn.* 6, 127-130.

Stern, M. E. 1980 Geostrophic fronts, bores, breaking and blocking waves. *J. Fluid Mech.* 99, 687-703.

Stoker, J. J. 1957 *Water Waves*. New York: Interscience. 567 pp.

Sturges, W. 1975 Mixing of renewal water flowing into the Caribbean Sea. *J. Mar. Res.* 33, 117-30 (Suppl.).

Swift, J. H. 1984 The circulation of the Denmark Strait and Iceland-Scotland overflow waters in the North Atlantic. *Deep-Sea Res.* 28, 1107-29.

Swift, J. H., Aagaard, K., Malmberg, S.-A. 1981 The contribution of the Denmark Strait overflow to the deep North Atlantic. *Deep-Sea Res.* 27, 29-42.

Tomasson G. G. and W. K. Melville 1992. Geostrophic adjustment in a channel: nonlinear and dispersive effects. *J. Fluid Mech.* 241, 23-57.

Toulany, B. and C.J.R. Garrett, 1984: Geostrophic control of fluctuating flow through straits. *J.Phys. Oceanogr.*, 14, 649-655.

Whitehead, J. A. 1986 Flow of a homogeneous rotating fluid through straits. *Geophys. Astrophys. Fluid Dyn.* 36, 187-205.

Whitehead, J. A. 1989a Surges of Antarctic Bottom Water into the North Atlantic. *J. Phys. Oceanogr.* 19, 853-61.

Whitehead, J. A. 1989b Internal hydraulic control in rotating fluids—applications to oceans. *Geophys. Astrophys. Fluid Dyn.* 48, 169-92.

Whitehead, J. A., Leetma, A., Knox, R. A. 1974 Rotating hydraulics of strait and sill flows. *Geophys. Fluid Dyn.* 6, 101-25.

Whitehead, J. A., Worthington, L. V. 1982 The flux and mixing rates of Antarctic Bottom Water within the North Atlantic. *J. Geophys. Res.* 87(C10), 7903-24.

Williams, R. T., Hori, A. M. 1970 Formation of hydraulic jumps in a rotating system. *J. Geophys. Res.* 75, 2813-21.

Woods, A. W. 1993 The topographic control of planetary-scale flow. *J. Fluid Mech.* 247, 603-621.

Yang, J. and J. F. Price 2000 Water mass formation and potential vorticity balance in an abyssal ocean circulation model. *J. Marine Res.*, 58, 789-808.

Yih, C. S., Gascoigne, H. E., Debler, W. R. 1964 Hydraulic jump in a rotating fluid. *Phys. Fluids* 7, 638-42.

Zenk, W. 1981. Detection of Overflow Events in the Shag Rocks Passage, Scotia Ridge. *Science,* 213, 1113-1114.

Zenk, W., G. Seidler, B. Lenz, and N. G. Hogg 1999. Antarctic Bottom Water Flow through the Hunter Channel. *J. Phys. Oceanogr.*, 29, 2769-2784.

Overview of exchange control mechanisms

L. Armi

Institute of Geophysics and Planetary Physics, Scripps Inst. of Oceanography, La Jolla, California 92093-0225

Abstract. Most of the essential aspects of hydraulic control are illustrated with layered systems. Here these essentials are discussed and generalized to exchange flows. Controlled flows are always asymmetric in some sense. For a single layer this asymmetry links a subcritical with a supercritical flow. For exchange flows through a strait one side may be subcritical in which case the exchange flow is not maximal. If on both ends of the strait, the flow is supercritical, the flow is a maximal exchange.

Single layer hydraulics

Among an infinite number of nonunique possible steady flows with a given flow rate and upstream reservoir height, hydraulics searches out the one that is asymmetric. The existence of a unique steady asymetric solution is an empirical fact. For example, we talk about flows *over* a sill or *through* a strait. The flow searched for among the infinite possible flows must be asymmetric in the sense that it must connect two reservoirs with different fluid depths. For a single layer only one such possible flow exists and this asymmetric flow is called 'controlled' because certain distinct regularity conditions must be satisfied for its existence. For an isolated sill the Froude number must be unity at the sill crest and in order to satisfy this criticality relationship at the crest, no longer can both the flow rate and upstream reservoir depth be specified independently of each other. This is why the flow is called 'controlled' with the crest acting as the control since it is here that the critical condition must be satisfied.

The only thing needed to procede in the search for this unique controlled solution is the requirement that the flow be asymmetric in some sense. (No mumbo jumbo about maximizing flow rate or minimizing energy found in standard hydraulics texts is needed or desired as we move on to more layers, although in the case of a single layer these concepts are correct.) We need not even specify the location of the 'control' as this will be seen to be located through satisfying the asymmetry requirement and the associated regularity condition. The asymmetry is needed in all flows in which the role of friction is weak since the only mechanism that can dissipate energy and allow a flow to connect two different reservoir depths is the hydraulic jump. For a hydraulic jump to exist, supercritical flow is a prerequisite condition. Hence asymmetry is equivalent to a search for a solution that transitions from a subcritical reservoir to supercritical flow downstream of the control, followed by a hydraulic jump to new lower energy than in the upstream reservoir.

Two layers – one interface

The first important new effect that occurs for flows through a strait with a single interface, and with two layers of comparable depths and flow rates, is that two unique controlled asymmetric flows are possible. The single interface still admits only one internal wave speed although the speed of this wave is a function of both layer speeds and depths. One controlled asymmetric solution has the lower layer as the active layer and looks like the familiar single layer flow. The other unique solution has the upper layer as the active layer and looks identical to the first, only inverted.

Which one of the two asymmetric flows, 'up' or 'down' is actually realized depends on which asymmetric solution is needed to match the different reservoir conditions. Another way of saying this is that by being lazy and only searching the solution space of steady solutions we need to input a little more information to decide among the two possible unique solutions. That information comes from knowing if the interface is higher on one side of the straight or the other. Another way of thinking about this is that the standing long wave at the control can have either of two possible forms favoring either acceleration of the upper or lower layer.

Virtual control

This concept, first introduced by Wood (1968), is that control need not occur at a topographically obvious location, such as the narrowest section. For unidirectional flows (exchange flows are a little more subtle) the interfacial mode controlled at the virtual control vanishes. So as the flow rates for a two layer single interface flow increase, there may no longer be the possibility of the two unique asymmetric 'up' and 'down' solutions. They in fact merge and the control moves further and further upstream as a virtual control always able to satisfy a composite critical condition at the wider section upstream. For a virtual control in a two layer unidirectional flow the control imposes no shear associated with vanishing of the interfacial mode. For exchange flows the virtual control imposes equal and opposite velocities.

Exchange flows

Flows of two fluids in opposite directions are in general controlled unless they are through a very long straight in which frictional effects dominate. If on one side of the strait, the flow is everywhere subcritical and on the other side of the strait the flow has some region which is supercritical followed by an internal hydraulic jump, this type of flow has been called a submaximal exchange. Of course for any given exchange rate the side of the straight on which the hydraulic jump occurs must be specified to decide among the two possible solutions is achieved. These are the 'up' or 'down' solution discussed earlier depending on which of the two layers is active. The active layer will dominate the hydraulic jump.

If there is supercritical flow on both sides of the strait then both layers are active and the flow is called maximal. Since the flow is supercritical on both sides of the strait, neither reservoir condition enters into determining the flow anymore. The exchange is only determined by the density difference, the geometry of the strait and any uniform additional barotropic component. The essence of this idea was introduced by Stommel and Farmer (1953) in their seminal study of 'overmixing'.

The fundamental requirement for maximal exchange is that the flow be supercritical on both sides of the controlling region. This fundamental requirement is quite general and not limited to inviscid, quasisteady flows. Whenever this requirement is met, the flow will be maximal in the

sense that for a given density difference and specified barotropic component, the exchange is fully determined by the processes in the controlling region and the greatest that can occur. If the maximal exchange conditions are not met, for example if supercritical flow only occurs on one end of the strait, the exchange can never be greater than the maximal rate and in general will be less.

Conclusion

In the talk, I will attempt to demonstrate these generalizations with figures, photographs and very few equations. These concepts will be extended to three layer and continuously stratified flows as well.

References

Stommel, H. and H. G. Farmer 1953. Control of salinity in an estuary by a transition. *J. Mar. Res.* ,*12*, 13-20.

Wood, I. R. 1968. Selective withdrawal from a stably stratified fluid. *J. Fluid Mech.*, *32*, 209-223.

Stratification and mixing in exchange flows in sea straits

G. N. Ivey

Present address: Shimizu Visiting Professor, Department of Civil and Environmental Engineering, Stanford University, Palo Alto, CA 94305. USA.
Permanent address: Centre for Water Research, The University of Western Australia, Western Australia, 6009. Australia

Abstract. Quantifying the transport through relatively narrow straits connecting basins with differing fluid properties is an important issue both at large and small scale. Prediction of lateral exchange rates, both dynamically and historically, can be thought of as a progression from hydraulics to mixing. This progression and the roles of mixing, stratification and the effects of flow unsteadiness are discussed in this work.

Introduction

Predicting the bi-directional exchange rate in sea straits connecting two basins with differences in density is a classical and important problem in physical oceanography. The exchange rate, combined with the basin volumes, determines the flushing and residence time in the basins which, in turn, lies at the heart of issues relating to water mass properties and water quality in both freshwater and marine environments. Well known examples include the Red Sea (*Pratt et al*, 1999), the Black Sea (*Gregg et al* (1999), the Mediterranean Sea (*Wesson and Gregg*, 1994), and Shark Bay in Western Australia (*Burling et al.*, 1999) which are connected to ocean basins by relatively narrow passages. Freshwater input, evaporation, freezing and differential heating and cooling all act to create lateral density differences. Once bi-directional flows have passed through the strait, they can travel great distances and influence large areas, as in the case of density-driven abyssal flows in the ocean passing through narrow gaps in the mid-ocean ridges (e.g. *Whitehead*, 1998) separating the major ocean basins.

The strength of the exchange flow will be dependent on the nature of the topographic constriction between the basins. In particular, the width of the strait, the local water depth and the length can all be important. Topographic control has long been recognized as playing an important role in the overall dynamics and has been the subject of numerous investigations (e.g. *Armi and Farmer*, 1998; *Garrett et al*, 1990; *Bray et al*, 1995; *Murray and Johns*, 1997; *Smeed*, 1997). Similarly, the strength of the density contrast between the basins is a driving force for the motion and this, in turn, implies a connection to basin scale processes, which determine the density of water in the basins. *Stommel and Farmer* (1953) first addressed this issue in the context of an estuarine application. They argued that the level of mixing within an estuary would affect the density of estuarine water, in turn affecting the rate of exchange through the mouth of the estuary into the open ocean. In other words, there can be a coupling between basin scale dynamics and the local exchange flow in the strait.

Within the strait itself, internal mixing can also be important. For example, field observations (e.g. *Wesson and Gregg*, 1994; *Bray et al*, 1995; *Gregg et al*, 1999) show the presence of two counterflowing layers separated by a finite thickness layer of intermediate density. This suggests active internal mixing and indeed in some cases the vertical mixing can be so active that there is little, if any, vertical density gradient (e.g. *Burling et al*, 1999). How then does internal mixing influence the density stratification, and how does this influence the flow through the strait? What are the implications for the role of topography and the concept of hydraulically controlled flow in straits? And finally, how can the effects of unsteadiness of the flow field be accounted for in the strait flow in such situations?

Internal hydraulics and basin dynamics

Internal hydraulic theory has provided a powerful tool to examine this problem and models of exchange flow in the case of flow over a sill and flow through a contraction are shown in Figures 1 and 2, respectively. The relatively narrow constriction in Figure 1 connects two infinite reservoirs of fluid with different densities, and the density difference drives a bi-directional exchange flow as shown. Internal hydraulic theory provides a

useful model for this flow providing there is no internal mixing of either momentum or mass and the individual layers have constant density and velocity, as shown. This approach has been utilized by a number of authors (*Armi*, 1986; *Armi and Farmer*, 1986; *Lawrence*, 1990; *Dalziel*, 1991; *Baines*, 1995; *Pratt et al*, 1999) to predict the layer thickness and velocities under the assumption of a steady state balance between inertia and buoyancy forces.
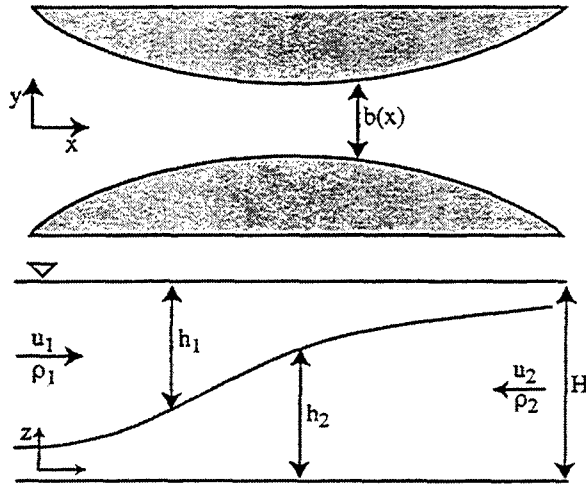

Figure 1. Schematic of the exchange flow through a contraction.
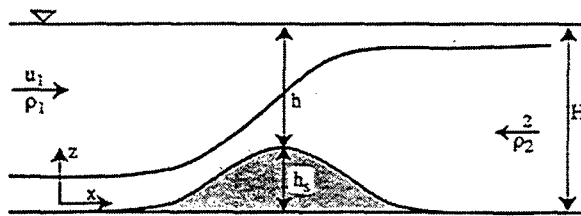
Figure 2. Schematic of the exchange over a sill

If the horizontal variations in channel width and depth are small and the pressure remains hydrostatic, then using conservation of mass in each layer and applying Bernoulli's equation along the surface streamline and at the interface between the two flowing layers, the rate of change of layer depth can be written as (*Armi*, 1986)

$$\frac{\partial h_1}{\partial x} = \frac{h_1}{b}\frac{\partial b}{\partial x}\left(\frac{G^2 - (1+h_2/h_1)Fr_2^2}{1-G^2}\right) - \frac{\partial h_s}{\partial x}\left(\frac{-Fr_2^2}{1-G^2}\right) \quad (1)$$

$$\frac{\partial h_2}{\partial x} = \frac{h_2}{b}\frac{\partial b}{\partial x}\left(\frac{G^2 - (1+rh_1/h_2)Fr_2^2}{1-G^2}\right) - \frac{\partial h_s}{\partial x}\left(\frac{1-Fr_1^2}{1-G^2}\right) \quad (2)$$

where the density ratio is $r = \rho_1/\rho_2$, the internal Froude numbers are $Fr_i^2 = u_i^2/g'h_i$ and the

parameter G is the composite Froude number defined as (*Armi*, 1986)

$$G^2 = Fr_1^2 + Fr_2^2 - (1-r)Fr_1^2 Fr_2^2 \quad (3)$$

Consider first the case of a pure contraction in Figure 1. At the minimum width of the contraction (i.e. $\partial b/\partial x = 0$) equations (1) and (2) imply either that both layers are flat ($\partial h_i/\partial x = 0$) or from the denominator terms

$$G^2 = 1 \quad (4)$$

Similarly for the case of a pure sill in Figure 2, at the crest of the sill (i.e. $\partial h_s/\partial x = 0$) equations (1) and (2) imply either that both layers are flat ($\partial h_i/\partial x = 0$) or again $G^2 = 1$.

At any point in the flow where (4) holds, the flow is said to be controlled as the relationship between the flow variables is constrained, and in these cases it represents a topographic control point (*Lawrence*, 1990). At any other point in the domain where the terms in the numerator of (1) and (2) are zero and again $G^2 = 1$, the point is termed a virtual control (*Wood*, 1970). If the flow has both topographic and virtual control points, then the flow rates are said to be maximal (*Armi and Farmer*, 1987).

Dalziel (1991) showed

$$G^2 = 1 + \frac{C_1 C_2}{h_1 h_2} \quad (5)$$

where C_1 and C_2 are the phase speeds of the long internal waves (non-dimensionalised by $1/2(g'H)^{1/2}$). Clearly at control points where $G^2 = 1$, either C_1 or C_2 must be zero, implying that information can only propagate in one direction only. For supercritical flows where $G^2 > 1$, C_1 and C_2 must both be non-zero and of the same sign.

This approach can be generalized to multi-layer systems (e.g. *Smeed*, 2000), but the arguments above illustrate the power of the hydraulic approach and the importance of locating control points (e.g. *Pratt et al*, 2000). For example, for the case of a two-layer contraction flow shown in Figure 1, *Armi and Farmer* (1986) introduced the flow rate ratio $q_r = Q_1/Q_2$ and in the case of steady flow between two infinite reservoirs with no other driving forces, such as tide or wind, then $q_r = 1$. In this case, at the narrowest point of a contraction where $b = B$ the two layers are of equal thickness (i.e. $h_1 = h_2$) and the volume flux Q and mass flux M in each layer is simply given by (*Armi and Farmer*, 1986; *Lawrence*, 1990; *Hogg et al*, 2001)

$$Q_i = (1/4)g'^{1/2}BH^{3/2}, \quad M = (1/4)\Delta\rho Bg'^{1/2}H^{3/2} \quad (6a,b)$$

Provided that the underlying assumptions of the theory are met, the channel can be described in terms of a characteristic width and depth and a control point is known to exist in the domain, then exchange rates can be directly determined from (6) given the easily measured external length scales and the density contrast between layers – assumed equal to the density contrast between the basins at each end of the strait.

This imposed density difference is determined by the density in the respective basins and thus must be influenced by the dynamics in these basins themselves (e.g. *Stommel and Farmer*, 1953; *Tragou and Garrett*, 1997). Finnigan et al (1999, 2000, 2001) examined this connection by considering the model shown in Figure 3 where flow over a sill is connected to an enclosed basin with buoyancy forcing at the surface of the basin. Explicitly addressing the question of how the driving density contrast $\Delta\rho$ is established, they considered the case where the semi-enclosed basin has a net surface buoyancy flux B_0 due to net cooling and/or evaporation.
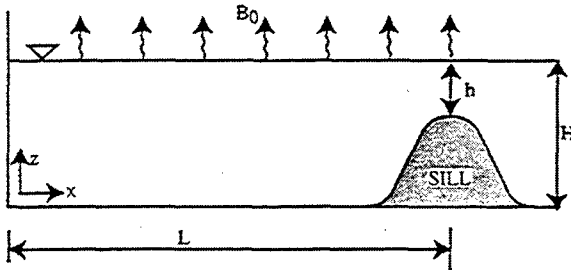
Figure 3. Schematic of convectively driven exchange in a sill-enclosed basin.

At the crest of the sill the flow rates are the same in both layers and a single control point exists in the flow. Using the fact the density ratio $r \approx 1$ in most practical applications, (4) can be re-arranged (*Finnigan and Ivey*, 1999; 2000) to yield

$$Q = B\left[g'\left(\frac{1}{h_1^3} + \frac{1}{(h-h_1)^3}\right)^{-1}\right]^{1/2} \tag{7}$$

If the system is at steady state, then conservation of buoyancy for the whole basin requires that

$$Qg' = B_0 LB \tag{8}$$

Hence from (7) and (8)

$$Q = B\left[B_0 L\left(\frac{1}{h_1^3} + \frac{1}{(h-h_1)^3}\right)^{-1}\right]^{1/3} \tag{9}$$

Equation (9) expresses the coupling between the local hydrodynamic balance at the sill crest and the global or basin scale forcing, quantified by the surface buoyancy flux B_0, the length L and width B of the semi-enclosed basin. Providing that the depth of the upper layer h_1 is known at the crest of the sill, the problem is closed as g' and Q can be determined from (8) and (9).

The depth of the upper layer h_1 at the sill crest is generally not know, but it has been argued that for a particular density contrast g', there is a maximum possible flow rate (*Stommel and Farmer*, 1953; *Garrett et al*, 1990). *Farmer and Armi* (1986) argued that in the case of a sill the maximum possible flow rate was achieved when $h_1 \approx 0.625h$, implying from (9) that the maximal possible flow rate is

$$Q_m \approx 0.35B(B_0 L)^{1/3}h \tag{10}$$

The force balance in the basin has been examined in several studies (*Phillips*, 1966; *Tragou and Garrett*, 1997; *Grimm and Maxworthy*, 1999; *Finnigan and Ivey*, 2000). *Finnigan and Ivey* (2000) conducted a laboratory experiment and made measurements of the mean and turbulent velocity fields in the basin. The experiments demonstrated that inertia, buoyancy and friction, associated with the turbulent convection from the free surface, each contribute to the basin scale force balance. The density of the lower layer at the sill reflects the cumulative effect of the mixing processes in the basin. As the surface buoyancy flux B_0 increases in intensity, entrainment and recirculation between the upper and lower flowing layers in the basin increases, and accordingly there is a decrease below the maximal limit predicted in (10). In longer basins (L/H>>10), entrainment appears to be less important, as in the study of *Grimm and Maxworthy* (1999), for example. The transition between these two limiting cases is not yet resolved. In all cases the flow rates appear to be less than maximal rates yet always characterized by a coupling between basin mixing processes and hydraulic control at the sill.

Internal mixing in straits

The arguments above rely on the effect of turbulent mixing of both momentum and mass to be confined to the basin. Crucially, in the strait region itself these effects can be neglected and theories based on internal hydraulics such as the ones leading to (6) and (10), for example, may apply. But what if there is mixing in the contraction itself? While hydraulic theory can be modified to account

for non-hydrostatic effects (e.g. *Zhu and Lawrence*, 1998) it cannot be corrected for the effect of mixing between layers. It is well known that instabilities can occur at the interface between the two counterflowing layers (e.g. *Pawlak and Armi*, 1998; *Zhu and Lawrence*, 2001), but the resulting mixing and how it should be incorporated in exchange flow estimates is not well understood.

In nature the sources of turbulence responsible for mixing in straits can include (e.g. *Hill*, 1995) cooling or evaporation from the free surface leading to a de-stabilizing buoyancy flux, wind stress on the free surface, shear stress on the bottom as well as the internal shear in the stratified fluid passing through the strait. All these mechanisms can provide sources of turbulent kinetic energy, which acts to work against the stabilizing effects of the potential energy in the water column induced by the horizontal flux of buoyancy through the strait from the end basins. When there is significant vertical transport of mass and momentum, the basic premises of the hydraulic theories above are no longer valid, and yet field examples of this limit abound (e.g. Figure 4).
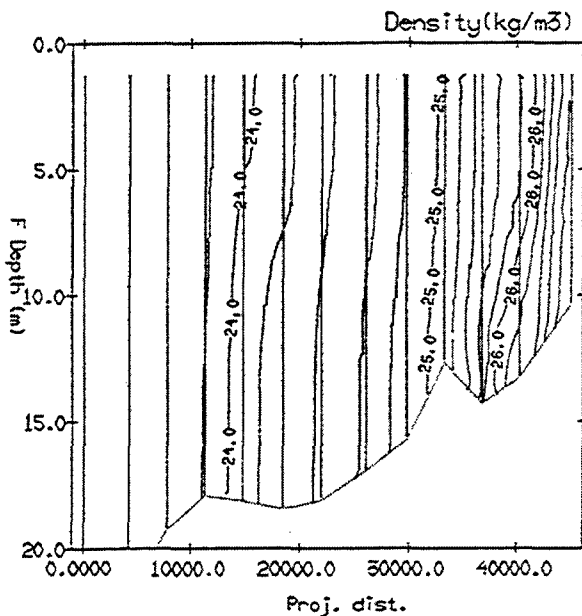
Figure 4. Field data from Shark Bay, Western Australia from *Nahas* (2002).

The problem of specifying horizontal flux when there is significant vertical mixing has historically been examined in two contexts: heat transfer in cavities (e.g. *Cormack et al, 1974; Bejan, 1995*) and in estuarine circulation (*Officer*, 1976). Under the assumption that the aspect ratio $A = H/L$ is small, *Cormack et al.* (1974) were the first to derive a formal asymptotic solution to the problem defined in Figure 5. In this limit, the flow is only

weakly stratified in the vertical but is still forced by a horizontal density contrast maintained at the ends of the strait, as suggested by the field data in Figure 4. While the flow is hydrostatic in the vertical, the steady state force balance is between buoyancy and vertical turbulent diffusive terms, and at leading order reduces to

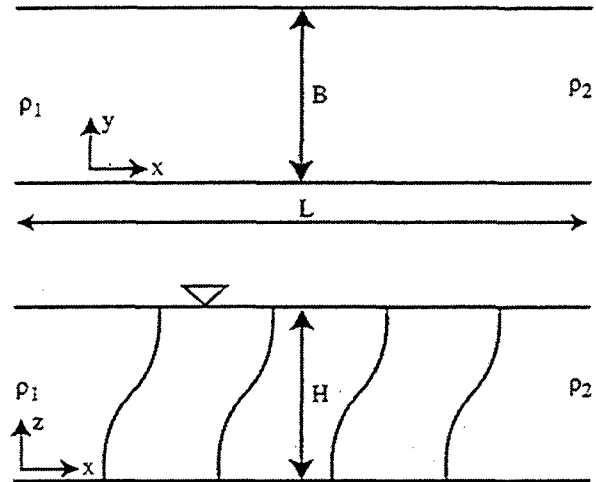$$g\frac{\partial\rho}{\partial x} = \rho_0 K_v \frac{\partial^3 u}{\partial z^3} \qquad (11)$$

Figure 5. Schematic of density field in viscous-diffusive limit.

At this leading order the density gradient is linear in the horizontal and the volume and mass fluxes can be written as (*Hogg et al*, 2001)

$$Q = \frac{5}{384} Gr_T ABK_v \qquad (12)$$

$$M = K_\rho AB\Delta\rho + \alpha Gr_T^2 A^3 BK_v\Delta\rho \qquad (13)$$

where K_ρ and K_v are the eddy diffusivities for the stratifying species and momentum, respectively, and the Grashof number $Gr_T = g'H^3/K_v^2$. The mass flux in (13) demonstrates that the horizontal flux is due to both a diffusive component and a convective component, as confirmed by the laboratory experiments of *Imberger* (1974).

The results in (6) and (12) represent the two limiting conditions, one the hydraulic limit, and the other the diffusive limit. Note that the predictions in (12) or (13) can be non-dimensionalised by their hydraulic limit counterparts in (6a,b). For example, dividing (12) by (6a) yields the non-dimensional flow rate in the viscous diffusive limit

$$q_v = \frac{5\left(Gr_T A^2\right)^{1/2}}{96} \qquad (14)$$

As (14) demonstrates, the naturally occurring parameter that defines the transition between the diffusive and hydraulic limits is the non-dimensional grouping $Gr_T A^2$.

Between these two theoretical limits, there will be a whole range of possibilities and *Hogg et al* (2001) explored these in a numerical simulation. The philosophy in the numerical modeling was to use the turbulent diffusivity as an independent free parameter – generated by an unspecified source - to determine the influence of mixing on the exchange rate. In all simulations it was assumed $K_\rho = K_\nu$. The results are shown in Figure 6. As the figure demonstrates, the hydraulic limit represents the maximal flow rate and as the intensity of vertical mixing increases (i.e. as Gr_T decreases) the horizontal mass flux decreases. This effect was demonstrated in a laboratory experiment (*Linden and Simpson*, 1986; *Linden and Simpson*, 1988) with air bubbles passed through the base of a tank to simulate the influence of turbulence in the environment on horizontal exchange flows. *Winters and Seim* (2000) showed how entrainment between the counterflowing layers leads to a recirculation, hence reducing the horizontal flux through the strait.

From *Hogg et al.* (2001) the non-dimensional exchange flow rate q is given by

$$Gr_T A^2 < 40 \qquad q = 0.052\left(Gr_T A^2\right)^{1/2}$$

$$40 < Gr_T A^2 < 10^6 \qquad q = 1 - 1.7\left(Gr_T A^2\right)^{-1/4} \qquad (15)$$

$$Gr_T A^2 > 10^6 \qquad q = 1$$

What is of interest is where in this parameter range typical field cases lie and some examples are shown in Figure 6 for the non-dimensional mass flux m. Not included is the Shark Bay example in Figure 4, which lies in the diffusive limit around $Gr_T A^2 = 10^{-1}$. Clearly many examples lie in the transitional regime $40 < Gr_T A^2 < 10^6$ where the flux is neither in the hydraulic limit or the diffusive limit.

This approach, as summarized in figure 6, thus provides a simple direct estimate of horizontal flux based on the dimensional grouping $Gr_T A^2$. This does not circumvent the requirement that an estimate must be made for the vertical diffusivity. *Hogg et al* (2001) reasoned that the value of this diffusivity would, in turn, determine the vertical thickness of the intermediate layer δ and found that
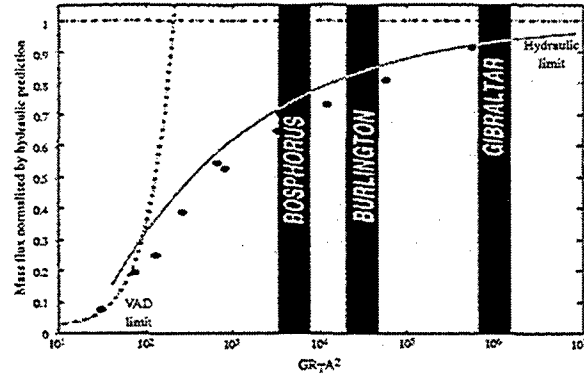

Figure 6. Non-dimensional mass flux m vs GrA² and comparison with field sites.

$$\frac{\delta}{H} = 3.4\left(Gr_T A^2\right)^{-1/4} \qquad (16)$$

As the thickness of the density interface δ can thus be determined from mean property measurements, (16) can be used to infer $Gr_T A^2$ and hence determine the flux from (15). Clearly this method breaks down if $\delta > H$, so in general this requires an independent estimate of the diffusivity K_ρ, which is not easy to make and still the subject of ongoing debate (e.g. *Barry et al*, 2001).

Not only do turbulent effects retard the buoyancy-driven horizontal exchange as shown in Figure 6, but they can also affect the speed of propagation of waves which control the flow near the hydraulic limit. The concept of control must therefore be generalized to continuously stratified fluids where momentum and species are allowed to diffuse. Classical strait flows such as the Bab al Mandab do not have a distinct layer character and yet the ability of signals to propagate from the open Gulf of Aden into the Red Sea is an important issue (*Pratt et al*, 2000).

Hogg et al. (2001) examined the propagation of the gravest vertical mode internal wave within a contracting channel with a generalized density stratification with a finite thickness intermediate layer with continuously variable density stratification. Two approaches were used. First, waves were mechanically excited at discrete locations within a bi-directional exchange flow. The waves were then tracked in time and space to determine propagation characteristics, under the assumption of linear internal wave dynamics. While useful, it is difficult to extract individual modes, so a second technique based on linear stability theory was employed. In particular, viscous and diffusive terms were retained, leading to a 6th order generalized version of the Taylor-Goldstein equations (*Kopel*, 1964) describing the stability of the flow. This was solved under the

assumption that for control we are interested in only the long internal wave limit (i.e. small wavenumber).

Both approaches show that as, as in two-layer flows, control may be thought of in terms of information propagation. A single mode, centered on the maximum density gradient, appears to conform to the behavior for the interfacial mode in two-layer theory. When the phase speed is zero, this location is the point of control. Two other important modes also were found to exist but skewed from the density interface with the maximum in the eigenvector located at the point of maximum vorticity gradient, hence the term vorticity modes.

The fundamental difference from hydraulic theory is that, rather than a point; there now exists a region over which control gradually takes effect. The overall effect is, however, maintained: end reservoir conditions can change without altering the flow. This has important implications for geophysical flows. In particular, if this allows the determination of whether a channel is super or sub-critical, then flux variations can be determined from changes in external conditions. The study of *Hogg et al.* (2001) considered the case of a steady mean flow and, as *Pratt et al* (2000) point out, the issue of critical flow and control points in a highly time-dependent mean flow remains unexplored.

Time-dependent effects

The results discussed to this point rely on the idea that the exchange flow is steady. In many oceanographic applications, unsteadiness is a major issue and it can take two forms. Firstly via the time dependency of the boundary conditions or forcing conditions in the basin, and secondly that superimposed on the baroclinic exchange forced by density differences there can be an independent barotropic flow which can be time dependent – i.e. the tide. This must influence not only the issue of control, but can also influence mixing and exchange as outlined below.

Finnigan et al. (2001) used a numerical model to investigate the flow field associated with the configuration shown in Figure 3 where the surface forcing condition was allowed to be time dependent, that is $B_0 = B_0(t)$. Various forcing conditions were examined, including both step changes and sinusoidal forcing – reflecting the seasonal variation of forcing that occurs in such systems as the Red Sea, for example. Using an energetics analysis, *Finnigan et al.* (2001) developed a general description of the flow

response at the sill. In particular, the system can be characterized by a response timescale defined as

$$T_r = 0.3 L^{2/3} \Delta B_0^{-1/3} (H/h) \qquad (17)$$

where ΔB_0 is the magnitude of the buoyancy flux variation. When the forcing frequency ω is low (i.e. $\omega \ll (1/T_r)$), the system is well described by steady state theories and the response at the sill is in phase with the forcing. As the forcing frequency increases, the magnitude of the response decreases at the sill and there is an increasing phase lag. At high frequencies (i.e. $\omega \gg (1/T_r)$), the oscillation of the forcing is completely damped within the system and the flow at the sill is steady at the mean value of the forcing. In terms of application to the Red Sea (*Murray and Johns*, 1997; *Smeed*, 1997), for example, this predicts that the flow over the sill always lags behind the seasonal forcing by about 2 months, and flows at the sill never reach more than 90% of the values predicted by steady state theories (*Finnigan et al*, 2001). Their model is still only preliminary and its application of field sites should still be treated with some caution and warrants considerable more attention.

A second form of unsteadiness that can be important is when there is a barotropic flow due to a tide for example superimposed on the baroclinic flow. When a barotropic flow is superimposed on the exchange, the layer flow rate ratio $q_r \neq 1$ and the position of the virtual control in a simple contracting channel no longer coincides with the topographic control point. More fundamentally, if the barotropic flow is time dependent, the exchange process can be fundamentally altered. This effect has been examined in some novel laboratory experiments (*Stigebrandt*, 1977, *Helfrich*, 1995, *Phu*, 2001). *Phu*'s experiments are shown schematically in Figure 7. At the start of the experiment, fluid of different densities are placed in each reservoir and separated by the gate. The experiment starts by simultaneously withdrawing the gate and initiating the rocking of the tank where the rocking of the tank is a convenient way to simulate the tidal action.

The mechanism of exchange is shown in Figure 8. For the basin shown, on the flood phase (Figure 8a) there is a strong jet-like flow entering the basin, while on the ebb flow (Figure 8b) there is a radial draining towards the narrow contraction. The same fluid mass is not transferred in and out of the basin on each half cycle, the difference being a net mass transfer between basins. This is similar to the mechanism proposed many years ago by *Stommel and Farmer* (1953). This experimental configuration enables the estimation of flux, not by
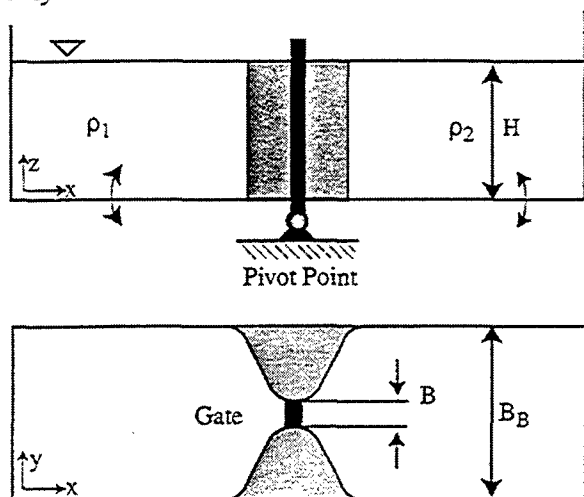
Figure 7. Schematic of unsteady exchange experiment.

direct measurement in the strait, but rather by observing the change in reservoir conditions. By opening the dividing barrier at time t=0, and then closing the barrier at time t later after a number of cycles, the fluid in each now closed reservoir is then homogenized and the mean density determined by measurement using a digital densitometer. Since the volume of each reservoir is known, the mass flux can thus be inferred by measuring the increase in mean density in one reservoir and the corresponding decrease in density of the opposing reservoir over the time interval.

The barotropic component has amplitude a and period T. The tidal flux will be given by

$$Q_T = \frac{a}{T} L B_B. \tag{18}$$

Non-dimensionalising the baroclinic flux in (6a) above by (18) yields a tidal exchange parameter defined as

$$E_T = \frac{g'^{1/2} H^{3/2} B_B T}{a L B} \tag{19}$$

where we have ignored the constant. Measured exchanged flows non-dimensionalised by either (6) or (18) are shown in Figure 9 as a function of this non-dimensional parameter.

There are two limiting conditions for the flux. For $E_t > 5$, the baroclinic flux dominates and the predicted flow rate from (6) is valid. For $E_t < 0.5$ the tidal forcing dominates and the exchange flux is $Q_T = 0.4(a/T)LB$. For the intermediate range where $0.5 < E_t < 5$, both the baroclinic and the unsteady tidal components contribute to the total flux.

The experiments and the results in figure 9 implicitly assume that the baroclinic flux is best described by the flow rate in the hydraulic limit – from (15) when $Gr_T A^2 > 10^6$. If this is not the case, then the definition of E_T in (19) will be different

and this regime remains unexplored although it is clearly relevant in applications like Shark Bay.

Conclusions

As can be seen, the combination of theory and experiment has yielded considerable insight into the nature of exchange flows in ocean straits. Recent work has allowed us to go beyond the predictive capabilities of hydraulic theory by including the effects of turbulence and mixing, not only within the strait where exchange is occurring, but also in the basins, which maintain the supply of fluid of differing densities that are driving the motion. In cases where the flow can be modeled as
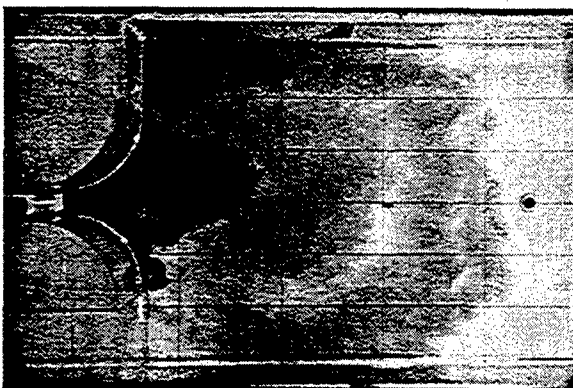

Figure 8(a). Plan view of exchange flow on flood tide.

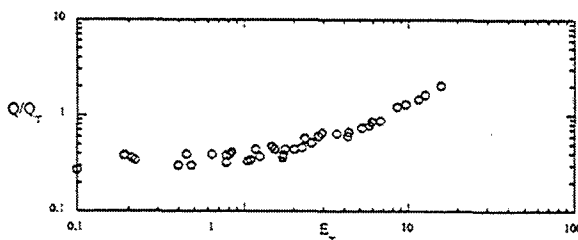

Figure 8(b). Plan view of exchange flow on ebb tide.

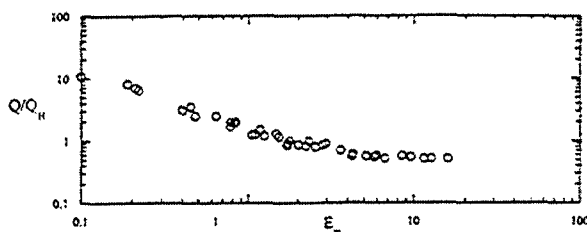Figure 9(a). Flow rate as a function of tidal exchange parameter (18).

Figure 9(b). Flow rate as a function of tidal exchange parameter from (*Phu,* 2001).

layered flow, flows can be predicted provided that control points can be identified in the domain. In the strong mixing case where the vertical stratification is weak or even absent, the concept of hydraulic control is no longer relevant, and rates of exchange are then determined by the magnitude of the parameter $Gr_T A^2$. This requires an estimate of the effective vertical diffusivity and specifying this quantity in a density stratified fluid is a subject of active research in itself (e.g. *Barry et al.,* 2001). Despite its importance, our understanding of the issues of control and exchange in flows, which are unsteady remains poorly, understood and there appears to be a number of issues to be examined in this class of flows. Finally, the effects of rotation have only been explored in the hydraulic limit (e.g. *Whitehead,* 1998) and identifying the transition to these large-scale rotationally controlled flow problems remain a challenge for the future.

References

Armi, L., The hydraulics of two-layer flows with different densities. *J. Fluid Mech.,* **163**, 1986, 27-58.

Armi, L. and Farmer, D.M. Maximal two-layer exchange through a contraction with barotropic net flow. *J. Fluid Mech.,* **164**, 1986, 27-51.

Armi, L. and Farmer, D.M. A generalization of the concept of maximal exchange in a strait. *J. Geophys. Research,* **92**, 1987, 14,679-10,680.

Armi, L. and Farmer, D.M. The flow of the Mediterranean through the Strait of Gibralter.. *Prog. in Oceanogr.,* **21**, 1988, 1-105.

Baines, P.G. Topographic effects in stratified flows. *Cambridge Univ. Press.,* 1995.

Barry, M.E., Ivey, G.N., Winters, K.B. & Imberger, J., Measurements of diapycnal diffusivities in stratified fluids. *J. Fluid Mech.,* **442**, 2001, 267-291.

Bejan, A., *Convection Heat Transfer,* John Wiley, 1995.

Bray, N., Ochoa, W.J. and Kinder, T. The role of the interface in exchange through the Strait of Gibralter. *J. Geophys. Research,* **100**, 1995, 10,755-10,776.

Burling, M.C., Ivey, G.N. and Pattiaratchi, C.B. Convectively driven exchange in a shallow coastal embayment. *Cont. Shelf Res.,***19**, 1999, 1599-1616.

Cormack, D.E., Leal, L.G. & Imberger, J., Natural convection in a shallow cavity with differentially heated endwalls. Part 1. Asymptotic theory. *J. Fluid Mech.,* **65**, 1974, 209-229.

Dalziel, S.B., Two layer hydraulics: a functional approach. *J. Fluid Mech.,* **223**, 1991, 135-163

Farmer, D.M. & Armi, L., Maximal two-layer exchange flow over a sill and through a combination of a sill and contraction with barotropic flow. *J. Fluid Mech.,* **164**, 1986, 53-76.

Finnigan, T.D. & Ivey, G.N., Submaximal exchange between a convectively forced basin and a large reservoir. *J. Fluid Mech.,* **378**, 1999, 357-378.

Finnigan, T.D. & Ivey, G.N., Convectively driven exchange in a stratified sill-enclosed basin. *J. Fluid Mech.,* **418**, 2000, 313-338.

Finnigan, T.D., Winters, K.B. & Ivey, G.N. (2001) Response characteristics of a buoyancy-driven sea. *J. Phys. Oceanogr.,* **31**, 2001, 2721-2736.

Garrett, C., Bormans, M. & Thompson, K. (1990) Is the exchange through the Straits of Gibralter maiximal or submaximal? In the Physical Oceanography of Sea Straits (ed. L.J. Pratt) pp. 271-294. NATO ASI Series, Kluwer.

Gregg, M.C., Ozsoy, E. & Latif, M.A., Quasi-steady exchange flows in the Bosphorus. *Geophys. Res. Let.,* **26**, 1999, 83-86.

Grimm, Th. & Maxworthy, T., Buoyancy-driven meanflow in a long channel with a hydraulically-constrained exit condition. *J. Fluid Mech.,* **398**, 1999, 155-180.

Helfrich, K., Time-dependent two-layer hydraulics exchange flow. *J. Phys. Oceanogr.,* **25**, 1995, 67-113

Hill, A.E., Buoyancy Effects in Coastal and Shelf Seas, in *The Global and Coastal Ocean, The Sea,* Vol 10, editors K.H. Brink and A.R. Robinson, John Wiley, 1998.

Hogg, A., Ivey, G.N. & Winters, K. B., Hydraulics and mixing in controlled exchange flows. *J. Geophys. Research,* **106**, 2001, 959-971.

Hogg, A.McC., Winters, K.B. & Ivey, G.N., Linear internal waves and the control of stratified exchange flows. *J. Fluid Mech.,* 2001, in press

Imberger, J., Natural convection in a shallow cavity with differentially heated endwalls. Part 3. Experimental Results. *J. Fluid Mech.* **65**, 1974, 247-260.

Kopel, D., On the instability of a thermally stratified fluid under the action of gravity. *J. Meth. Phys.,* **5**, 1964, 963-982.

Lawrence, G.A., On the hydraulics of Boussinesq and non-Boussinesq two-layer flows. *J. Fluid Mech.,* **215**, 1990, 457-480.

Linden. P.F. and Simpson, J.E. Gravity-driven flows in a turbulent fluid. *J. Fluid Mech.,* **172**, 1986, 481-497.

Linden. P.F. and Simpson, J.E. Modulated mixing and frontogenesis in shallow seas and estuaries. *Cont. Shelf Res.,* **8**, 1988, 1107-1127.

Murray, S.P. & Johns, W. Direct observations of seasonal exchange through the Bab al Mandab Strait. *Geophys. Res. Lett.*, 24, 1997, 2557-2560.

Nahas, B. Dynamics of Shark Bay. *M.Eng Sc. Thesis, Univ. of W.A.*, 2002, in preparation.

Officer, C. B., *Physical Oceanography of Estuaries*. John Wiley and Sons, 1976.

Pawlak, G. & Armi, L. Vortex dynamics in a spatially accelerating shear layer. *J. Fluid Mech.*, 376, 1998, 1-35.

Phillips, O.M., On turbulent convection currents and the circulation of the Red Sea. *Deep Sea Res.*, 13, 1966, 1149-1160.

Phu, A. Tidally driven exchange flows. *Honours thesis, Dept. Environmental Eng., Univ. of W.A.*, 2001.

Pratt, L. J., Johns, W., Murray, S.P. & Katsumatra, K., Hydraulic interpretation of direct velocity measurements in the Bab al Mandab. *J. Phys. Oceanogr.*, 29, 1999, 2769-2784.

Pratt. L.J., Deese, H.E., Murray, S.P. & Katsumata, K.,. Continuous dynamical modes in straits having arbitrary cross-sections, with applications to the Bab al Mandab *J. Phys. Oceanogr.*, 30, 2000, 2515-2534.

Smeed, D. Seasonal variation of the flow in the strait of Bab al Mandab. *Oceanol. Acta*, 20, 1997, 773-781.

Smeed, D. Hydraulic control in three-layer exchange flows: application to the Bab al Mandab. *J. Phys. Oceanogr.*, 30, 2000, 2574-2588.

Stommel, H. & Farmer, H.G., Control of salinity in an estuary by a transition. *J. Mar. Res.*, 12, 1953, 13-20.

Stigebrandt, A. On the effect of barotropic current fluctuations on the two-layer transport capacity of a constriction. *J. Phys. Oceanogr.*, 7, 1977, 118-122.

Tragou, A. and Garrett, C., The shallow thermohaline circulation of the Red Sea. *Deep Sea Res.*, 444, 1997, 1355-1376.

Wesson, J.C. & Gregg, M.C., Mixing at Carmarinal Sill in the Strait of Gibraltar *J. Geophys. Research*, 99, 1994, 9847-9878.

Whitehead, J.A., Topographic control of oceanic flows in deep passages and straits. *Reviews of Geophys.*, 36, 1998, 423-440.

Winters, K.B. & Seim, H.E., The role of dissipation and mixing in exchange flows through a contracting channel. *J. Fluid Mech.*, 407, 2000, 265-290.

Winters, K.B., Seim, H.E. and Finnigan, T.D. Simulations of non-hydrostatic, density-stratified flow in irregular domains. Int. *J. Num. Meth. Fluids.*, 32, 2000, 263-284.

Wood, I.R., A lock exchange flow. *J. Fluid Mech.*, 42, 1970, 671-687

Zhu, Z. & Lawrence, G.A., Non-hydrostatic effects in layered shallow water flows. *J. Fluid Mech.*, 355, 1998, 1-16.

Zhu, Z. & Lawrence, G.A., Holmboe's instability in exchange flows. *J. Fluid Mech.*, 429, 2001, 391-409.

54

Small-scale processes in straits

M. C. Gregg

College of Ocean and Fishery Sciences, University of Washington, Seattle

Abstract. Small-scale studies in straits are revealing much about the internal dynamics and complexity of straits. Highlights of some recent work are described to provide an overview of the rapid progress being made in understanding the details of small-scale dynamics in straits.

1. Roles of Small-Scale Processes in Straits

Straits provide several attractions for studies of small-scale processes. Many straits are excellent natural laboratories for observing specific phenomena, because, unlike the unpredictable open ocean, swift tidal currents and restricted topography regularly produce strong interactions at specific locations. Vessels can be scheduled with confidence that the targeted events will occur, and the studies have a realism not available in artifical channels or numerical simulations. Moreover, the net changes resulting from mixing can often be observed directly, rather than being small effects that are difficult to pin down, such as potential energy increases produced by internal waves breaking in the open ocean. Finally, the net effects of mixing seem to be important factors in the dynamics of some straits, giving an immediate, local feedback to the large-scale flow driving the small scale processes.

Frasetto [1964] reported one of the earliest studies of small-scale processes in a strait. an examination of strong internal waves at Gibraltar with a thermistor chain. In 1991 he told me that this was occasioned by an impending visit of a admiral to SACLANT to determine if the laboratory was doing anything useful. Frasette recalled stories of WWII submarines using the waves to surf quietly into the Mediterranean and thought studying them would appeal to NATO navies.

Two decades later. David Farmer's acoustic images began revealed fascinating details of sill flows and the mixing they produced, e.g. *Farmer and Denton* [1985]. Using calibrated acoustic backscatter and simultaneous microstructure profiles through a 15-m billows in a tidal channel, *Seim et al.* [1995] demonstrated that returns came from strong microstructure produced the acoustic images they observed in 15-m billows in an inland strait. *Seim* [1999] extended the analysis to backscatter from salinity microstructure, expected to dominate signals in some straits, e.g. the Bosphorus.

The primary reasons for including small-scale studies in experimental programs focused on straits are: 1) to estimate how much friction retards the flow and to parameterize it in ways useful to numerical models, 2) to determine the rates of density change from mixing and also paramterize it, and

3) to understand how solibores are generated and propagate. In addition to being important components of mixing within straits, solibores often generate strong flows affecting surface and subsurface navigation within straitss and beyond. In short, the importance of small-scale processes to strait dynamics increases the more the flow departs from the hydraulic assumptions.

In the following we will review some of the findings and issues about small-scale processes. After considering theoretical and laboratory results, aspects of some recent field programs are discussed. Finally, different aspects of studies about solibores are described. *Henyey and Hoering* [1997] coined the term 'solibores' to recognize the dual nature of the internal bores/soliton packets released from hydraulic controls.

2. Theoretical and laboratory results

2.1. Analytical modelling of friction and entrainment

Examining the effect of bottom friction on sill control, *Pratt* [1986] assumed that the flow was controlled by the bottom layer. The ratio of friction to the inertial term is $(C_d u^2/h_2)/(u^2/l) = C_d l/h_2$, where l is the along-channel distance over which h_2 and u change significantly. This simple expression condfies intuition: bottom friction should be important in long, shallow straits but not in short, deep ones. Accordingly, Pratt estimated $C_d l/h_2 = 1$ in the Bosphorus and 0.1 in Gibraltar. In his analysis bottom friction did not change the basic ideas of hydraulic control, but it did move the control point down the lee side of the sill (relative to the barotropic flow) to where $db/dx|_{cr} = -C_d$, with b as the bottom elevation. If the drag coefficient is too large to satisfy this relation, the flow cannot be hydraulically controlled and will be limited by friction. Friction also produces asymmetries in the interface profiles.

Bormans and Garrett [1986] used $\epsilon \approx 10^{-6}$ W kg^{-1}, measured in the eastern end of Gibraltar by *Wesson and Gregg* [1988], to infer an interfacial drag coefficient of $C_i \approx 10^{-4}$. They considered this as evidence of nearly inviscid flow, and hence concluded that interfacial friction is of little importance. They also pointed out that using realistic

cross-sections, i.e. tapered in toward the bottom, requires a thicker bottom layer for a given transport. Froude numbers will therefore be smaller than those estimated with standar hydraulic analyis based on rectangular cross-sections. Bottom friction on the sloping sides also affects interface height.

Examining the stability of two-layer flows with barotropic components, *Lawrence* [1990a, b] noted that in addition to considering the composite Froude number,

$$G^2 \equiv \frac{u_1^2}{g'h_1} + \frac{u_2^2}{g'h_2} - \frac{\rho_2 - \rho_1}{\rho_2} \frac{u_1^2}{g'h_1} \frac{u_2^2}{g'h_2} , \qquad (1)$$

where ρ_1, u_i, and h_i are the density, velocity, and thickness of the upper, $i = 1$, and lower, $i = 2$, layers, it is also necessary to evaluate the stability Froude number

$$F_\Delta^2 \equiv \frac{(u_2 - u_1)^2}{g'(h_1 + h_2)} . \qquad (2)$$

before understanding two-layer flows fully. When F_Δ^2 exceeds a critical value, depending on g' and $4h_1h_2/h^2$, long internal waves become unstable and hydraulic analysis produces imaginary phase speeds. Lawrence also pointed out that the interface is unstable to short-wave instabilities even when F_Δ^2 is far below critical and that mixing from these instabilities will produce an interface with finite thickness, violating the hydraulic assumptions.

Gerdes et al. [2002] examined the effects of entrainment by adding it to the reduced gravity equations describing a single dense layer crossing a sill beneath a thick passive upper layer. Entraining fluid from the upper layer caused the lower layer to thin and accelerate, driving it toward criticality as does including friction [*Pratt*, 1986; *Bormans and Garrett*, 1986]. This, however, is a consequence of requiring the layer to maintain the same transport. In reality, entraining slow fluid and adding friction will move the layer farther from criticality, as seen below when numerical models are discussed.

2.2. Numerical models of mixing in exchange flows

Using an orthogonal curvilinear coordinate system to represent accurately flow through a contraction, *Winters and Seim* [2000] numerically investigated the effects of interfacial and bottom friction on an exchange flow through a contraction. They used a Smagorinsky-type closure scheme based on a local balance of turbulent kinetic energy in which dissipation and the buoyancy flux balance shear production. Adding interfacial friction produced shear instabilities, resolved by the fine grid, and produced large amounts of mixed water. The exchange remained symmetric about the throat. Hydraulic controls were similar to the inviscid case, and the flow remained maximal. However: 1) positions of the controls did not coalesce in the absence of a barotropic component to the flow, contrary to the hydraulic solution, 2) Froude numbers were generally smaller, owing to thicker active layers and slower speeds, and 3) positions of the controls differed substantially. In addition to moving the topographic

control downstream, interfacial friction shifted the virtual control upstream, further shortening the supercritical interval.

When *Winters and Seim* [2000] added bottom friction the average eddy viscosity did not increase, but the exchange changed from maximal to submaximal. When the bottom boundary layer was an appreciable fraction of the lower layer the increased drag decreased the composite Froude number to be much less than one nearly everywhere. Hydraulic control, i.e. $G^2 = 1$, occured over such a short distance that the authors doubt that the control could be found in a field experiment. The exchange also became very asymmetric. The interface was flat on the light side of the contraction and rose steeply and thickened rapidly on the dense side as the light water accelerated and mixed. Most of the transport leaving the contraction toward the dense basin was in the interface.

Analyzing the numerical results in terms of three layers rather than two showed net entrainment into the interface from the faster of the bounding layers. Considering them in terms of only two layers gave the opposite view, i.e., net entrainment was into the faster layer from the slower. The interface was not well-mixed and the density classes within it moved at different speeds, and always carried mixed water away from the contraction. Bounding layers that were supercritical anywhere lost about half of their fluid to the interface.

Using the same numerical code as Winters and Seim, *Hogg et al.* [2001a] found that changing the level of turbulence produced a continuous shift from flow satisfying the hydraulic assumptions to one dominated by viscosity. Their results are consistent with analytic solutions for both limits. Fluxes and volume fluxes depend on three dimensionless parameters: D/L, the aspect ratio, $Gr_T \equiv g'D^3/K_\nu^3$, the turbulent Grashof number, and $Pr_T \equiv K_\nu/K_\rho$, the turbulent Prandtl number. K_ν and K_ρ are the eddy coefficients for momentum and mass. Hogg et al. used $Pr_T = 1$, and the mass flux depended on $Gr_T(D/L)^2$. By comparing reported values of interface thickness with their calculations, they estimated $Gr_T(D/L)^2 = 10^4$ for the Strait of Gibraltar and 5×10^{-3} for the Bosphorus. Calculated flows matched the hydraulic limit when $Gr_T(D/L)^2 \approx 10^7$ and the viscous-advective-diffusive limit when $Gr_T(D/L)^2 \approx 10^2$. Hence, the Bosphorus is nearer the later, and Gibraltar is close to the former, as found analytically by *Pratt* [1986].

Hogg et al. [2001b] considered hydraulic control in continuously stratified fluids by studying the propagation of linear internal waves in the flow fields of their previous study. One approach was to track waves generated mechanically where the stratification was greatest and then evolving with linear dynamics. The other approach used eigenvalue solutions from sixth-order stability theory of parallel shear flows to interpret the evolution of the test waves. They identified two types of mode-1 solutions capable of transmitting information about baroclinic changes in the basins along the entire channel: density modes, appearing only when viscosity is not zero and having eigenfunction maxima centered on the

peak stratification, and vorticity modes, with maxima close above and below the stratification peak. Sites where mode-1 density waves have a phase velocity of zero seem analogous to topographic controls of hydraulic theory and were found at the contraction throat. Likewise, their zero-crossings seem analogous to virtual controls of hydraulic theory, shifting upstream with increasing barotropic flow and carrying information out from the zero-crossing. Vorticity modes evolve gradually along the channel as their maxima shift vertically and cross the stratification maximum. These transition zones appear to be sites of controls present in viscous flows having continuous stratification. Hence, there are no analogs in inviscid two-layer flows.

2.3. Examinations of mixing mechanisms

To understand better the shear instabilities generating interfacial friction, *Zhu and Lawrence* [1996] analytically extended hydraulic theory by including the dynamic pressure produced by curved streamlines over sills. In addition, they introduced a friction slope similar to that used for one-layer flows. The friction slope included a coefficient for interfacial friction and another for friction at the bottom and side walls. The stability of the flow depended on

$$Ri_B \equiv \frac{g'\delta}{(\Delta u)^2}, \quad a \equiv \frac{2\pi\delta}{\lambda} \text{ and } \frac{d}{\delta} \qquad (3)$$

where δ is the thickness of the shear layer, λ is wavelength, and d is the offset between the centers of the density and velocity interfaces. The density interface is much thinner than the velocity interface. For $d = 0$, no offset, they predicted that Kelvin-Helmholtz instabilities would develop when $Ri_B < 0.07$ and Holmboe instabilities would appear at larger Richardson numbers. Laboratory experiments confirmed their predictions, including detection of Holmboe waves traveling in both directions. *Zhu and Lawrence* [2001] followed by by using a laboratory sill flow to verify predictions about the initiation of Holmboe instabilities.

Also examining the stability of two-layer flows to small disturbances, *Pawlak and Armi* [1996] did a linear analysis of inviscid flow having tanh velocity and density profiles with different relative thickness and with boundaries at varying distances. Because shear increases downstream when there is a barotropic component of the flow, Ri_B is lowest downstream, Kelvin-Helmholtz instabilities were found downstream in their laboratory experiments. Holmboe instabilities were found upstream, where Ri_B was larger.

A strong barotropic component to a two-layer exchange can arrest the upper layer to form a stationary wedge (Fig. 1). *Pawlak and Armi* [1998] studied the development of modified Kelvin-Helmholtz instabilities in the spatially accelerating shear layer beneath an arrested wedge. They found a new finite-amplitude mechanism in which the core of the growing vortex progressively rises above the shear layer that created it(Fig. 2). Pawlak and Armi suggest that this mechanism transfers vorticity and mass into the wedge from the swift flow below it.
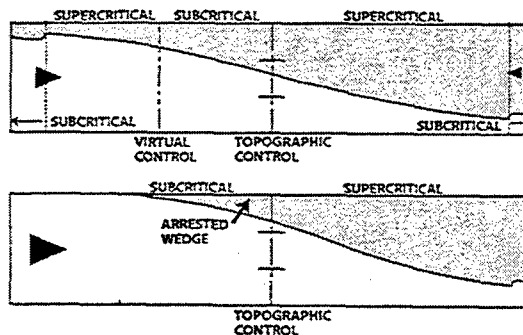

Figure 1. Schematic of two-layer flow with a barotropic component to the right, adapted from *Pawlak and Armi* [1998]. In the lower panel the increased barotropic flow arrested the upper layer, forming a stationary wedge above the plunging interface.
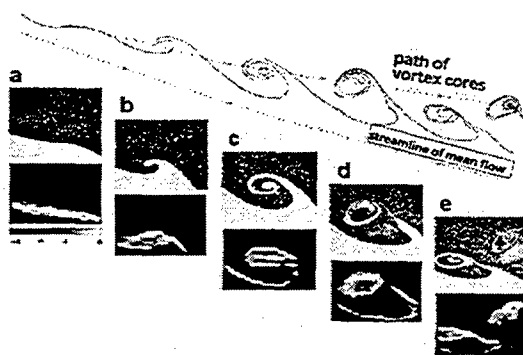

Figure 2. Schematic of the formation of vortex cores in a spatially accelerating shear layer between the plunging flow and the stationary wedge and images of the structure and vorticity (lower), adapted from *Pawlak and Armi* [1998].

Smythe and Winters [2002] used Direct Numerical Simulation to compare the evolution of Kelvin-Helmholtz and Holmboe instabilities. As had been found previously, both instabilities generated highly efficient mixing prior to their transitions to turbulence. The Holmboe instabilities, however, had slower growth rates but sustained efficient mixing longer than the Kelvin-Hemlholtz instabilities. Consequently, the net mixing was comparable in both, leading to the conclusion that Holmboe instabilities may be important sources of mixing in natural flows.

3. Field Observations

3.1. The Gibraltar Experiment, 1985-86

The Gibraltar Experiment, 1985-86, was probably the first large experiment in a strait, and included the first microstructure observations reported from any strait. Although Gibraltar is one of the straits in which friction is believed to be relatively unimportant, abundant discrepancies from the hydraulic assumptions were found. In particular:

- The interface was thick and carried about half the transport leaving the strait [Bray et al., 1995].

- Flow separated from the north shore [Farmer and Armi, 1988].

- Turbulence was intense throughout the strait [Wesson and Gregg, 1988]. It peaked over and immediately west of Camarinal sill (Tbl. 1), the result of interface instabilities that grew into 25-75 m billows (Fig. 3). A somewhat smaller peak occured south of Tarifa, where solibore mixing was strongest.

- Evolution of the θS relation in the region of strong mixing just west of Camarinal showed that the flow was not two-dimensional [Wesson and Gregg, 1994].

Table 1. Average diapycnal diffusivities, in $m^2\ s^{-1}$ over and near Camarinal Sill in the Strait of Gibraltar [Wesson and Gregg, 1994]. The density classes correspond the the incoming Atlantic water, the interface, and the Mediterranean water. Deepest profiles went to 250 m. Only one profile penetrated the descending plume of Mediterranean water west of the sill.

Density Range	West of Sill	Over Sill	East of Sill
$\sigma_\theta < 27$	1.7×10^{-3}	2.1×10^{-3}	2.7×10^{-3}
$27 < \sigma_\theta < 29$	2.3×10^{-1}	1.2×10^{-2}	6.2×10^{-4}
$29 < \sigma_\theta$	2.9×10^{-1}	9.2×10^{-3}	2.2×10^{-2}
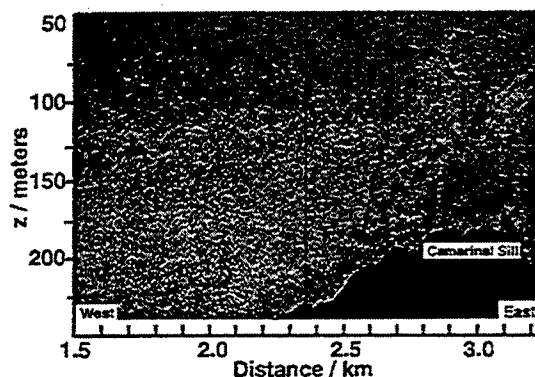
Figure 3. Huge billows over the lee side of Camarinal sill in the Strait of Gibraltar during ebb tide [Wesson and Gregg, 1994].

3.2. Knight Inlet Experiment, 1995

Farmer and Armi [1999a] and *Farmer and Armi* [1999b] used acoustic images, ADCP profiles, and closely-spaced CTD tow-yos to examine the formation of a stagnant wedge over the seaward face of the sill during ebb tide (Fig. 4). The
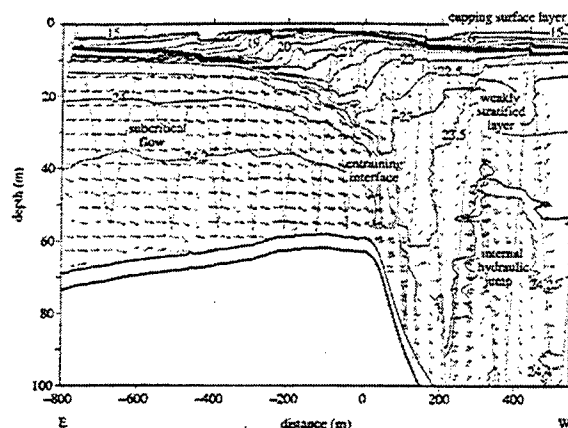
Figure 4. Plunging flow over the Knight Inlet sill during ebb tide [Farmer and Armi, 1999b]. Isopycnals are thin solid lines and flow vectors are arrows. The sawtooth is the CTD path.

images show small instabilities developing on the interface as the ebb flow accelerates, similar to those found at Gibraltar They identify this with the vortex formation mechanism discovered by *Pawlak and Armi* [1998] and argue that this mixing entrains water out of the fast flow into a steadily growing, weakly-stratified, stagnant wedge. Owing to its increasing density, the wedge eventually descends to suppress the flow separating at the sill crest, thereby initiating a strong down-slope flow. Farmer and Armi argue that the down-slope flow on the seaward side of the Knight Inlet sill is dynamically similar to severe down-slope winds occasionally experienced on mountain lee sides.

Subsurface Lagrangian floats tracked by *D'Asaro and Lien* [2000] provided a novel way of observing sill flow. Capable of being ballasted to 1 gram, the floats can track vertical water velocities to $\pm 0.01\ m\ s^{-1}$ [D'Asaro et al., 1996]. All floats passing over the sill during flood tide were deflected south (Fig. 5), consistent with the velocities in the previous figure, and some of them responded to hydraulic jumps.

When examined in a Lagrangian framework, float motions sort naturally into internal waves, $\omega < N$, and turbulence, $\omega > N$. The Lagrangian forms for internal wave velocity spectra are $\propto \omega^{-2}$ for u and v and ω^0 for w. All cut off sharply at $\omega = N$. Taking ω_0 as the overturning frequency of energy-containing scales of turbulence, Lagrangian spectra for homogenous isotropic turbulence are flat for $\omega < \omega_0$ and $\propto \omega^{-2}$ in the inertial subrange, which corresponds to $\omega > 2\omega_0$. In stratified fluids Buoyancy, or Ozmidov, scaling gives $\omega_0 \approx N$.

For $\omega < N$ observed spectra are consistent with internal wave dynamics. For example, in Figure 6 compare W, the average observed vertical spectrum for $\omega < N$, with W_{iw}, calculated from the average u and v spectra and the linear internal wave equations.
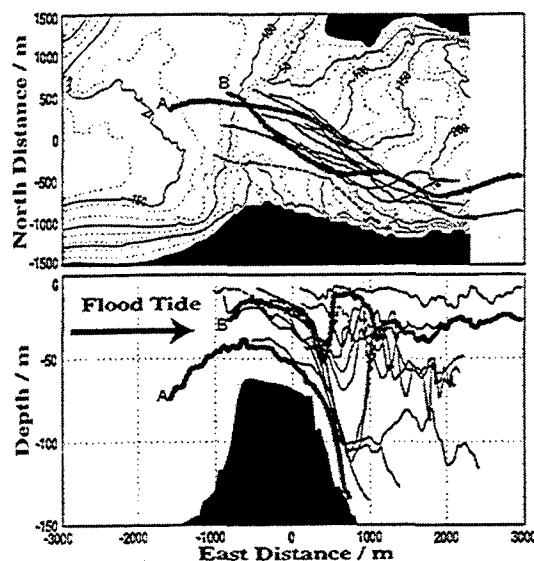
Figure 5. Tracks of Lagrangian floats released upstream of the Knight Inlet sill during flood tide [*D'Asaro and Lien*, 2000].
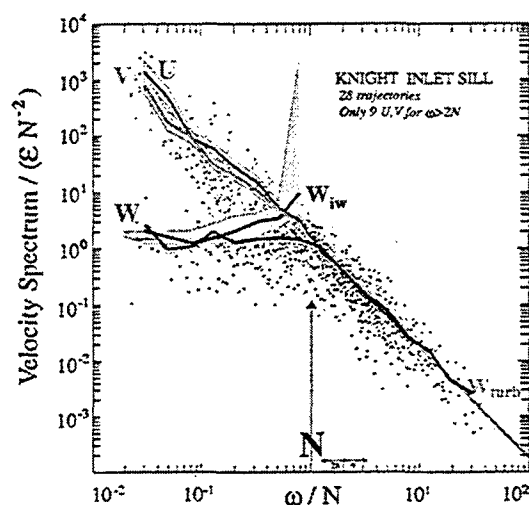

Figure 6. Spectra of float velocity plotted as individual points [*D'Asaro and Lien*, 2000]. Shading shows 95% confidence limits.

When turbulence is to weak to to produce overturns larger than 1 m, the height of the float, all spectra cut off sharply at $\omega = N$. This was found in low-energy regions of Knight Inlet. However, when overturns exceed 1 m all spectra extend past $\omega = N$ and follow the Lagrangian turbulent form. Their magnitude gives estimates of ϵ. This was found in high-energy regions of Knight Inlet, e.g. just landward of the sill during strong flood.

In response to the evidence for three-dimensional flow on the lee side of Camarinal sill, *Klymak and Gregg* [2001a] ran

a box survey across the Knight Inlet sill crest and landward slope during flood tide. Using a depth-cycling towed CTD, SWIMS, provided tightly spaced density profiles to complement the resoluton of a broadband ADCP. Although the flow was nearly barotropic over the sill crest, downstream the up-inlet flow bifrucated into a shallow surface jet and a density current that was channeled toward the south wall by the bathymetry (Fig. 7). At mid-depth only a narrow column
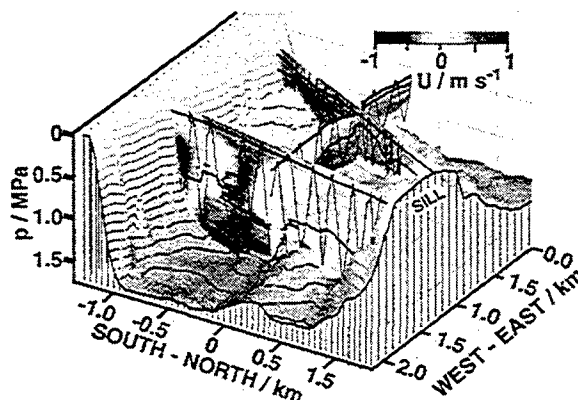
Figure 7. Flood tide over the Knight Inlet sill [*Klymak and Gregg*, 2001a]. Flood tide over the Knight Inlet sill [*Klymak and Gregg*, 2001a] showing strong recirculation cells on the lee side.

flowed up-inlet, connecting the two jets. On either side were two large, rapidly recirculating dipole vortices. Their transport was 25% of the tidal flux. Klymak and Gregg inferred that the eddies were generated by flow separating from headlands at the sill crest. Because Knight Inlet has been used as an example of two-dimensional flow, the overall conclusion is that three-dimensionality should be assumed until proven otherwise.

Based on SWIMS runs along the Knight Inlet channel, *Klymak and Gregg* [2001b] examined the large-scale response of flow over the sill to the half-daily tidal cycle and used the two-dimensional *Hallberg* [2000] isopycnal model to examine the importance of dynamical elements affecting the flow. Both flood and ebb tides form large lee waves, but the lee wave forms early during flood and late during ebb. They found that upstream influence, the mean density contrast across the sill, and the pool of salty water trapped on the seaward side are crucial to the dynamics. They concluded that the density contrast and pool of trapped seawater delay formation of the lee wave during ebb tide. In particular, the trapped pool acts as a 'virtual bottom' for the tidal flow, much as the cap of very light brackish water acts of a 'virtual surface' in the fjord. General consequences are 1) studying a small part of the sill regime before understanding these large-scale factors can lead to misleading or incorrect conclusions, and 2) the classification scheme for sill flows based on Nh/u [*Baines*, 1995] is incomplete because it does not include mean gradients across the sill.

3.3. Other straits

The roster of important straits is not confined to those at the surface. *Polzin et al.* [1996] found intense mixing in a rise within the Romanche fracture zone, at depths of 4500 m (Fig. 8). Spread over a distance of 100 km, the complicated bathymetry includes the principal sill followed by a constriction and two smaller sills. In some profiles dissipation rates are elevated above background over 500 m in the vertical and rise to 10^{-6} W kg^{-1}, extraordinary levels for those depths, producing an average diapycnal diffusivity of $K_\rho = 1.5 \times 10^{-2}$ m^2 s^{-1}. The pattern and K_ρ resemble Gibraltar; ϵ is 4-5 decades smaller, but the stratification is much weaker. This mixing plays a very important role in large-scale dynamics because 1.0×10^6 m^3 s^{-1} of Antarctic Bottom water pass through the fracture zone.
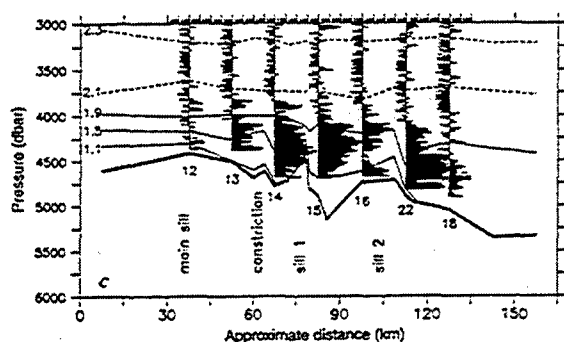
Figure 8. Dissipation rates, plotted as $\log_{10}(\epsilon/\text{W kg}^{-1})$, through the Romanche fracture zone [*Polzin et al.*, 1996]. Flow was left to right, and the vertical reference lines for $\log_{10} \epsilon$ are -10. Peak dissipation rates are 10^{-6} W kg^{-1}.

Tacoma Narrows is a strait connecting the main and southern basins of Puget Sound. Currents exceed 1.5 m s^{-1} through the channel, which is 10 km long and 40 m deep. During flood and ebb strongly stratified flows entering the Narrows are homogenized before leaving. Initially assuming that the homogenization was produced by upward growth of the bottom boundary layer, *Seim and Gregg* [1997] noticed that the boundary layer did not thicken rapidly enough to do this. Moreover, during both tides the homogenization occured rapidly downstream of a 50° near the longitudinal midpoint. They concluded that the strong cross-channel circulation resulting from rounding the bends was overturning the water column.

Providing the only link between the Black Sea and the ocean, the Bosphorus is 30 km long, 34-100 m deep and 0.75-3 km wide. The narrowest place, known as the Contraction, ends in a 60° bend. Currents often exceed 1.5 m s^{-1}. The dense outflow leaves the Bosphorus into the pre-Bosphorus channel, a narrow grove cut into the Black Sea shelf [*Di Iorio and Yüce*, 1999].

Taking acoustic images and tightly-spaced density and ADCP profiles when the flow was quasi-steady, *Gregg et al.*

[1999] and *Gregg and Özsoy* [2002] verified hydraulic control of the dense outflow over the crest of the pre-Bosphorus channel and found probable controls over the shallowest part of the strait, near its southern entrance. They, however, failed to locate a hydraulic control in or south of the Contraction, which had been considered the principal control of the exchange flow. They concluded that friction is most likely the primary regulator of the flow, perhaps aided by overturning at the bend south of the Contraction. This is consistent with conclusions of *Hogg et al.* [2001a] based on their numerical analysis of generalized exchange flows through contractions.

Examining details of flow in the Bosphorus illustrates how much some regimes depart from the hydraulic assumptions [*Gregg and Özsoy*, 2002]. Specifically, 1) Owing to the channel shape, the lower layer transits in about half the time taken by the upper layer; 2) Many bends and points along the channel cause the flow to separate from the sides. 3) Much of the exchange flow crosses the southern sill on opposite sides of the channel, the upper layer flowing along the Asian coast and the lower layer along the European side. This is a consequence of 60° bends north and south of the sill. 4) The lower layer was strongly stratified as it enters the strait. During our measurements the upper layer entered as a homogenous surface mixed layer and its strongly stratified base. Both contained entrained some of the opposing outflows. In a similar vein, *Özsoy et al.* [2001] examine details of the Bosphorus outflow through the pre-Bosphorus channel and down the shelf and compare the results with a reduced-gravity model. Owing to the thinness of the outflow, its path and mixing are responsive to details in the bathymetry.

Working in the Strait of Juan de Fuca, *Stanisfield et al.* [2001] examined Thorpe's technique for estimating overturns by comparing shipboard CTD data with dissipation measurements from a microstructure profiler. Although it is primarily an investigation of the technique, it illustrates a useful means for estimating mixing in straits where swell is small or moderate and CTDs fall with less heaving than in the open ocean. Average rms overturning lengths were 0.77 m in February and 0.45 m in August of 1998. The former corresponded to $K_\rho = 5 \times 10^{-4}$ m^2 s^{-1} and the latter to $K_\rho = 2 \times 10^{-4}$ m^2 s^{-1}. These are markedly smaller than estimates of $K_\nu \approx 2 \times 10^{-2}$ m^2 s^{-1} estimated for the vertical viscosity by *Ott and Garrett* [1998], who assumed that internal friction balances the along-strait pressure gradient.

4. Solibores

During the Gibraltar Experiment extensive efforts were made to track the wave trains, or solibores, that were released at the sill as the outflow slackened and then propagated eastward through the strait and out into the Mediterranean. Operating an airborne synthetic aperture radar (SAR) *Richez* [1994] flew repeated passes along the strait, while *Watson and Robinson* [1990] used an x-band radar sited on the Rock to follow waves through the eastern end of the strait. The waves arrived at Gibraltar 4 to 9 hours after high water, de-

pending on the current in the upper layer. Their phase speeds depended on direction and water depth, causing the wave fronts to diverge (Fig. 9).

Watson and Robinson approximated the dispersion relation as $c_p = U_1 \cdot \hat{k} + (g'h_1)^{1/2}$ to obtain $c_{p1} = U_1 k + (g'h_1)^{1/2}$, the phase speed in the direction of the current, and $c_{p2} = (g'h_1)^{1/2}$, the phase speed perpendicular to the current. Then they evaluated the hydraulic state with

$$F_1^2 = \frac{u_1}{g'h_1} = \left(\frac{c_{p1} - c_{p2}}{c_{p2}} \right)^2 . \qquad (4)$$

Using their best estimates of $c_{p1} = 1.85$ m s^{-1} and $c_{p2} = 0.5$ m s^{-1} yields $F_1^2 = 7.3$, indicating strongly supercritical flow in the east end. They caution, however, that c_{p2} may be an underestimate, but $c_{p2} > 0.95$ would be needed for subcritical flow.
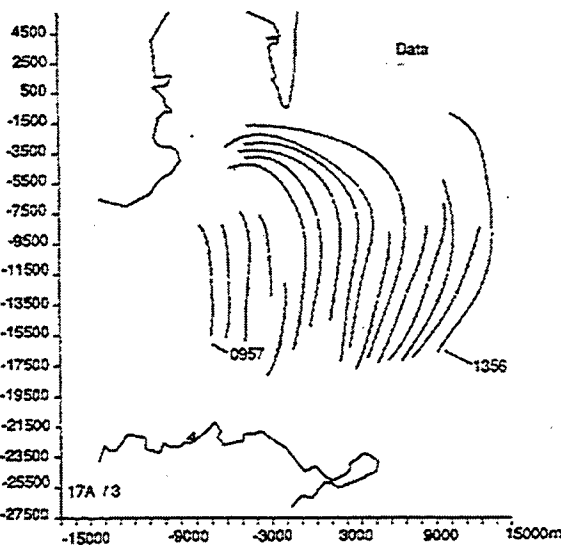
Figure 9. Sequence of positions, at 15 minute intervals, for the second wave in a packet passing Gibraltar [*Watson and Robinson*, 1990]. *Watson and Robinson* [1990]

Watson and Robinson [1990] also observed faint images of waves traveling obliquely across the strait toward the north. Similar to features noted by *Farmer and Armi* [1988], these were attributed to waves formed by the shallow supercritical flow interacting with several headlands on the Morrocan coast. They are believed to have formed as stationary shock waves oriented at $\theta = \pm \arcsin(c_g/U)$ to the flow and been released to propagate as the flow relaxed.

Watson and Robinson [1991] compared the radar observations with a numerical model of wave propagation, and *Watson* [1994] used Farmer and Armi's shipboard ADCP and echo sounder records to determine wave amplitudes. This enabled them to solve the Taylor-Goldstein equation numerically. The calculated phase speeds agreed within observational accuracy with the radar observations, but the uncer-

tainity was large enough that nonlinear behavior of the waves could not be verified, in spite of their large amplitude.

Brandt et al. [1996] simulated the generation, release, and propagation of the Gibraltar solibore using a two-dimensional model using nonlinear primitive Boussinesq equations for two layers which include horizontal diffusion and vertical shear stresses at the interface and bottom. Changing the value of a parameter allowed runs with both the hydrostatic and the weakly non-hydrostatic approximations. The model's seafloor was taken from the realistic bathymetry along the axis of the strait. When initialized with realistic densities and interface heights, the model was tested against the exchange-flow model of *Helfrich* [1995].
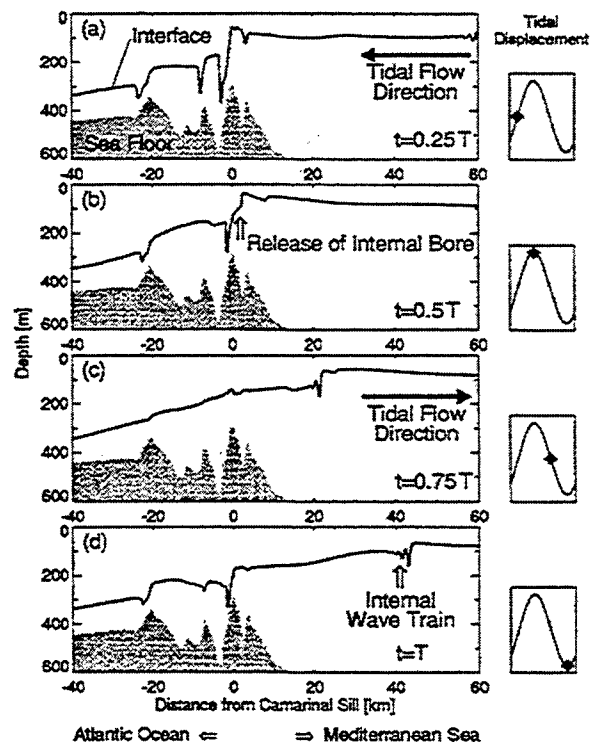

Figure 10. Sequence of calculated interface positions showing formation, release, and propagation of the Gibraltar solibore *Brandt et al.* [1996].

Hydrostatic model runs showed the hydraulic jump forming at the sill and the subsequent release of the solibore, but only the weakly non-hydrostatic simulations contained the disintegration of solibore into a soliton train (Fig. 10). Calculations of surface convergence agreed well with roughnesses obtained from ERS 1. The model also showed weak solibores propagating westward into the Atlantic, a result verified by finding three SAR images showing faint westward waves. Brandt et al. believe that these waves propagate on the summer thermocline rather than on the much stronger and deeper halocline.

Bogucki and Garrett [1993] estimate the rate solibores lose energy by treating them as waves decaying at rates

matching the dissipation they produce. They assume two homogenous layers separated by a thin interface, and interface displacements, d, that are less than h_1. Continuity in the upper and lower layers is used to derive Ri_B as a function of d. Ri_B falls below 1/4 when $d > 2(h_i h_1)^{1/2}$. Adding stratification in the upper layer changes the critical displacement to $0.82h_1$. After the critical displacement has been exceeded, mixing is assumed to thicken the interface until Ri_B becomes subcritical, allowing for hysteresis. The rate of energy lost via the mixing gives the solibore decay rate.

Henyey and Hoering [1997] modeled solibore energetics by assuming they are similar to those of surface bores, i.e. the solibore feeds off of the net decrease in upper layer (usually) thickness accompanying its passage. They estimate the dissipation rate by assuming it equals the rate of energy is supplied to the solibore by the decrease in upper layer thickness. Comparisons with data from Gibraltar and Knight Inlet could not distinguish between the two models of solibore energetics, probably owing to poor statistics of ϵ. *Cummins and Li* [1998] note that other assumptions about the 'jump relation' exist in the literature, but the differences are too small to alter the conclusions of *Henyey and Hoering* [1997].

5. Afterward

Even this cursory and selective review reveals astonishing progress in the last few decades. Hard thinking, new observational techniques, and increasingly sophisticated models offer the prospect of changing strait work from exploration to hypothesis-driven studies. The need for hard thinking will not go away, but the guiding models are changing from analytic to numerical. Once the small-scale phenomenology is mostly discovered, model sensitivity studies will be needed to determine their importance to strait dynamics and to define how accurately mixing must be parameterized.

References

Baines, P., *Topographic effects in stratified flows*, 1 ed., Cambridge, Cambridge, U.K., 1995.

Bogucki, D., and C. Garrett, A simple model for the shear-induced decay of an internal solitary wave, *J. Phys. Oceanogr.*, *23*, 1767–1776, 1993.

Bormans, M., and C. Garrett, The effects of nonrectangular cross section, friction, and barotropic fluctuations on the exchange through the Strait of Gibraltar, *J. Phys. Oceanogr.*, *19*, 1535–1542, 1986.

Brandt, P., W. Alpers, and J. Backhaus, Study of the generation and propagation of internal waves in the Strait of Gibraltar using a numerical model and synthetic aperture radar images of the european ERS1 satellite, *J. Geophys. Res.*, *101*, 14,237–14,242, 1996.

Brandt, P., A. Rubino, W. Alpers, and J. Backhaus, Internal waves in the Strait of Messina studied by a numerical model and syn-

thetic aperature radar images from the ERS 1/2 satellites, *J. Phys. Oceanogr.*, *27*, 648–663, 1997.

Bray, N., J. Ochoa, and T. Kinder, The role of the interface in exchange through the Strait of Gibraltar, *J. Geophys. Res.*, *100*, 10,755–10,776, 1995.

Cummins, P., and M. Li, Comment on 'energetics of borelike internal waves' by Frank S. Henyey and Antje Hoering, *J. Geophys. Res.*, *103*, 3339–3341, 1998.

D'Asaro, E., and R.-C. Lien, Lagrangian measurements of waves and turbulence in stratified flows, *J. Phys. Oceanogr.*, *30*, 641–655, 2000.

D'Asaro, E., D. Farmer, J. Osse, and G. Dairiki, A Lagrangian float, *J. Atmos. Ocean. Tech.*, *13*, 1230–1246, 1996.

Di Iorio, D., and H. Yüce, Observations of Mediterranean flow into the Black Sea, *J. Geophys. Res.*, *104*, 3091–3108, 1999.

Farmer, D., and L. Armi, The generation and trapping of solitary waves over topography, *Nature*, *283*, 188–190, 1999a.

Farmer, D., and L. Armi, Stratified flow over topography: The role of small scale entrainment and mixing in flow establishment, *Proc. Roy. Soc. Lond. A*, *455*, 3221–3258, 1999b.

Farmer, D. M., and L. Armi, The flow of Atlantic water through the Strait of Gibraltar, in *Progress in Oceanography*, edited by M. V. Angel and R. L. Smith, pp. 1–105, Pergamon Press, Oxford, 1988.

Farmer, D. M., and R. A. Denton, Hydraulic control of flow over the sill in Observatory Inlet, *J. Geophys. Res.*, pp. 9051–9068, 1985.

Frasetto, R., A preliminary survey of vertical displacements of the upper layer of the Strait of Gibraltar, *Deep-Sea Res.*, *7*, 152–162, 1964.

Gerdes, F., C. Garrett, and D. Farmer, On internal hydraulics with entrainment, *J. Phys. Oceanogr.*, *32*, 1106–1111, 2002.

Gregg, M. C., and E. Özsoy, Flow, water mass changes and hydraulics in the Bosphorus, *J. Geophys. Res.*, in press, 2002.

Gregg, M. C., E. Özsoy, and M. A. Latif, Quasi-steady exchange flow in the Bosphorus, *Geophys. Res. Lett.*, *26*, 83–86, 1999.

Hallberg, R., Time integration of diapycnal diffusion and Richardson number dependent mixing in isopycnal coordinate ocean models, *Mon. Wea. Rev.*, *10?*, 1402–1419, 2000.

Helfrich, K. R., Time-dependent two-layer hydraulic exchange flows, *J. Phys. Oceanogr.*, *25*, 359–373, 1995.

Henyey, F. S., and A. Hoering, Energetics of borelike internal waves, *J. Geophys. Res.*, *102*, 3323–3330, 1997.

Hogg, A., G. Ivey, and K. Winters, Hydraulics and mixing in controlled exchange flows, *J. Geophys. Res.*, *103*, 30,696–30,711, 2001a.

Hogg, A., K. Winters, and G. Ivey, Linear internal waves and the control of stratified exchange flows, *J. Fluid Mech.*, submitted, 2001b.

Klymak, J., and M. Gregg, The three-dimensional nature of flow near a sill, *J. Geophys. Res.*, *106*, 22,295–22,311, 2001a.

Klymak, J. M., and M. C. Gregg, The role of upstream waves and a downstream density-pool in the growth of lee-waves: Stratified flow over the Knight Inlet sill, *J. Phys. Oceanogr.*, submitted, 2001b.

Lawrence, G., Can mixing in exchange flows be predicted using internal hydraulics?, in *The Physical Oceanography of Sea Straits*, edited by L. Pratt, pp. 519–536, Kluwer Acad. Pub., Dordrecht, The Netherlands, 1990a.

Lawrence, G. A., On the hydraulics of Boussinesq and non-Boussinesq two-layer flows, *J. Fluid Mech.*, *215*, 457–480, 1990b.

Ott, M., and C. Garrett, Frictional estuarine flow in Juan de Fuca Strait, with implications for secondary circulation, *J. Geophys. Res.*, *103*, 15,657–16,666, 1998.

Özsoy, E., D. D. Iorio, M. Gregg, and J. Backhaus, Mixing in the Bosphorus Strait and the Black Sea continental shelf: Observations and a model of the dense water outflow, *J. Mar. Syst.*, *31*, 99–135, 2001.

Pawlak, G., and L. Armi, Stability and mixing of a two layer exchange flow, *Dyn. Atmos. Oceans*, *24*, 139–151, 1996.

Pawlak, G., and L. Armi, Vortex dynamics in a spatially accelerating shear layer, *J. Fluid Mech.*, *376*, 1–35s, 1998.

Polzin, K. L., K. G. Speer, J. M. Toole, and R. W. Schmitt, Intense mixing of Antarctic Bottom Water in the equatorial Atlantic Ocean, *Nature*, *380*, 54–57, 1996.

Pratt, L., Hydraulic control of sill flow with bottom friction, *J. Phys. Oceanogr.*, *16*, 1970–1980, 1986.

Richez, C., Airborne synthetic aperture radar tracking of internal waves in the Strait of Gibraltar, *Prog. Oceanogr.*, *33*, 93–159, 1994.

Seim, H., Acoustic backscatter from salinity microstructure, *J. Atmos. Ocean. Tech.*, *16*, 1491–1498, 1999.

Seim, H. E., and M. C. Gregg, The importance of aspiration and channel curvature in producing strong vertical mixing over a sill, *J. Geophys. Res.*, *102*, 3451–3472, 1997.

Seim, H. E., M. C. Gregg, and R. Miyamoto, Acoustic backscatter from turbulent microstructure, *J. Atmos. Ocean. Tech.*, *12*, 367–380, 1995.

Smythe, W., and K. Winters, Turbulence and mixing in Holmboe waves, *J. Phys. Oceanogr.*, *Submitted*, 2002.

Stanisfield, K., C. Garrett, and R. Dewey, The probability distribution of the Thorpe displacement within overturns in Juan de Fuca strait, *J. Phys. Oceanogr.*, *31*, 3421–3434, 2001.

Watson, G., Internal waves in a stratified shear flow: The Strait of Gibraltar, *J. Phys. Oceanogr.*, *24*, 509–517, 1994.

Watson, G., and L. Robinson, A study of internal wave propagation in the Strait of Gibraltar using shore-based marine radar images, *J. Phys. Oceanogr.*, *20*, 374–395, 1990.

Watson, G., and L. Robinson, A numerical study of internal wave refraction in the Strait of Gibraltar, *J. Phys. Oceanogr.*, *21*, 185–204, 1991.

Wesson, J., and M. Gregg, Turbulent dissipation in the Strait of Gibraltar and associated mixing, in *Small-Scale Turbulence and Mixing in the Ocean, Proceedings of the 19th International Liege Colloquium on Ocean Hydrodynamics*, edited by J. Nihoul and B. Jamart, pp. 201–212, Elsevier, Amsterdam, 1988.

Wesson, J., and M. Gregg, Mixing at Camarinal Sill in the Strait of Gibraltar, *J. Geophys. Res.*, *99*, 9847–9878, 1994.

Winters, K. B., and H. E. Seim, The role of dissipation and mixing in exchange flow through a contracting channel, *J. Fluid Mech.*, *407*, 265–290, 2000.

Zhu, D., and G. Lawrence, Holmboe's instability exchange flows, *J. Fluid Mech.*, *429*, 409, 2001.

Zhu, Z., and G. Lawrence, Exchange flow through a channel with an underwater sill, *J. Fluid Mech.*, *24*, 153–161, 1996.

M. C. Gregg. Applied Physics Lab., 1013 NE 40th St., Seattle, WA 98105-6698, email: greggapl.washington.edu

Part II:
Poster presentations

Dynamics of a dense water vein along the Strait of Sicily

M. Astraldi, G. P. Gasparini and E. Salusti

[1] C.N.R. - Istituto per lo Studio dell'Oceanografia Fisica, Forte Santa Teresa, 19036 Pozzuolo di Lerici, La Spezia, Italy
[2] I.N.F.N. - Dip.to di Fisica, Università "La Sapienza" Piazzale A.Moro 2, 00185 Roma, Italy

Abstract. Hydrographic and current meter data, gathered in different periods in the Strait of Sicily and in the southern Tyrrhenian Sea, allow the outflow characteristics from the eastern towards the western Mediterranean Basin to be analyzed. The evolution through the Strait of a deep vein of dense water from the Eastern Mediterranean is described, together with the dynamic interaction with overlying MAW and LIW layers. Taking into account the dynamic influence of the two overlying currents, and in particular their friction and mixing, this model explain the path of this deep flow and enables estimates of entrainment and bottom friction to be made.

Introduction

The Strait of Sicily (Figure 1) connects the eastern and the western Mediterranean basins. It has a minimum width of about 150 km and a length of about 600 km. At its western boundary is the rather irregular Sicilian shelf, while eastward there is the Tunisian plateaux and the Malta bank. Two sill systems delimit the Strait: in the western part two passages, deep respectively 430 and 365 m, connect the Strait with the western Mediterranean Basin; in the eastern side the connection with the Ionian sea is south of Malta Bank, across a sill 560 m deep. The central region, the real deep part of the Strait, is 50-100 km wide and 700-900 m deep with some trenches even reaching 1800 m.
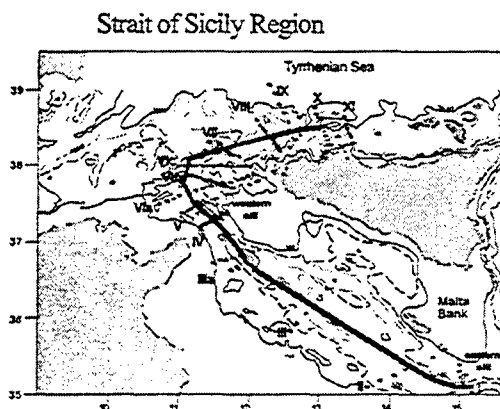
Figure 1. General map of Strait of Sicily. Dots represent the locations of the hydrographic stations (sections indicated by roman numerals).

The water masses present in the region are characterized by a surface eastward flow of Modified Atlantic Water (MAW) in the upper 200 m, over which a westward flow of Levantine Intermediate Water (LIW) crosses the Strait before entering the Tyrrhenian Sea. Recently, a vein with a slightly different characteristics has been observed (Sparnocchia et al., 1999). This water, less salty and colder than LIW, is a mixing between LIW and Eastern Mediterranean Deep Water (EMDW).

The observations

The observations made during the 1990's (Astraldi et al., 2002) indicate the presence of a quasi-steady current flowing westward directly over the bottom of the Strait. It consists of a dense vein of EMDW, which is able to cross the Malta sill, flows along the deep region of the Strait and finally outflows westward into the western basin. The bold line of Figure 1 clearly indicates how the vein moves through the Strait along the Sicilian shelf break towards the Tyrrhenian Sea.

At section I (Figure 2) the vein is characterised by a $\sigma_\theta \sim 29.16$ and, at its lowest depth (section V), reaches a density of ~ 29.14. A subsequent decrease is found in section VII with $\sigma_\theta \sim 29.11$. Due to its high density, when it reaches the Western Mediterranean Basin it sinks, finding its neutral buoyancy at a depth of about 1500-1800 m (Section X of Figure 1). In each of the observational periods, which covered different year and seasons, the geometric properties of the current (*height (h), width*

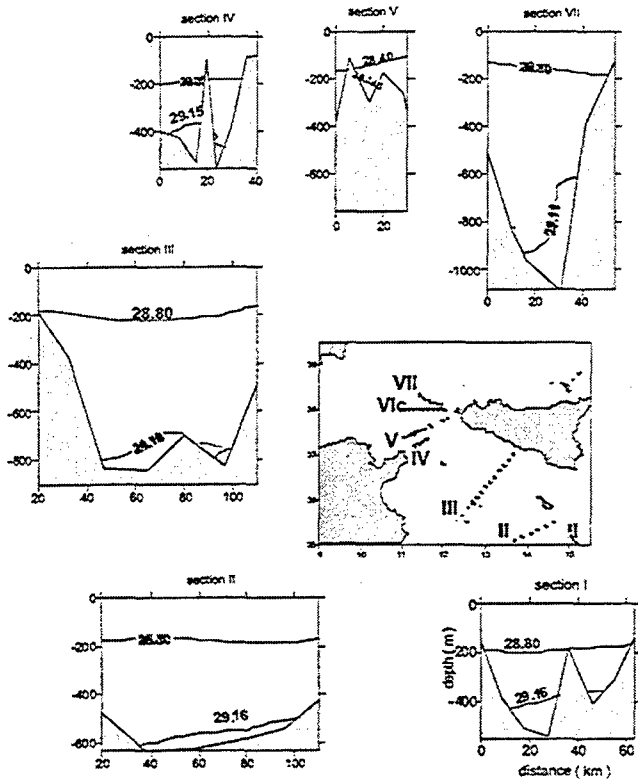(*W*), *section area* (*A*), *path*) showed only minor variations (Astraldi *et al.*, 2002).

(section V) as the site where the most noticeable changes in the vein properties and the most significant dynamics effects take place.

The stream-tube model

The classical streamtube model (Smith 1975), was generalized by taking into account the effects of moving upper layers, LIW and MAW, to evaluate the importance of Bernoulli suction (Baringer and Price 1997; Lane-Serff *et al.*, 2000), and, more specifically,

MATER 2 cruise (January 1997)

Figure 2. Isopycnal cross-sections. In each section interfaces between surface (MAW), intermediate (LIW), and deep (EMDW) layers are indicated.
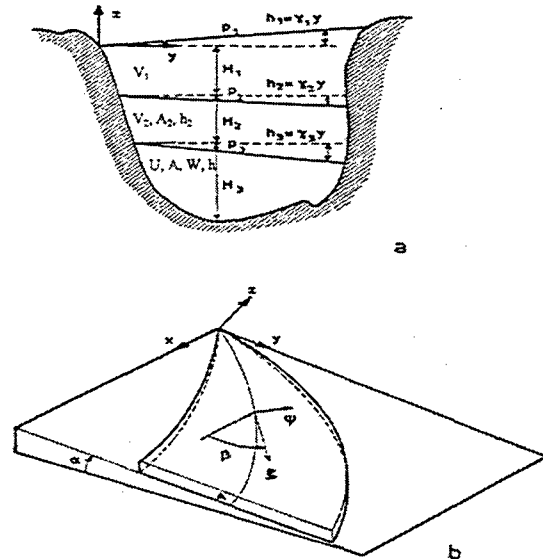
Figure 3. (a) Schematic representation of layers. (b) Coordinate system of the streamtube model.

The stable behaviour of the vein allows us to identify the main mechanisms responsible for its evolution and point to the westward sill region

of the influence of MAW-LIW entrainment stress on the along channel pressure gradients, that finally push the deep vein through the western sill:

MASS CONSERVATION EQUATION :
$$\frac{\partial}{\partial \xi}(AU) = E^+ |U - V_2| W$$

CROSS-STREAM MOMENTUM EQUATION :
$$f(U - V_2) + g' \frac{\partial}{\partial y}[h + b] = 0$$

ALONGSTREAM MOMENTUM EQUATION :
$$\frac{\partial}{\partial \xi}(U^2 A + g'A[h/2 + b]) - \frac{\partial}{\partial \xi}\frac{1}{2}V_2^2 A + \frac{A}{A_2}E^+W(V_2 - V_1) - \frac{A_2 + A}{A_2}E^+W(U - V_2) + KWU^2 = 0$$

Kinetic energy   Potential energy   Bernoulli suction   MAW-LIW entrainment stress   LIW-EMDW entrainment stress   bottom stress

where U and $V_{1,2}$ are the along-stream velocity components, E', E^* entrainment parameters and K drag coefficient. b is the bottom depth, while A, W and h are the geometric characteristics of the vein (Figure 3).

The diagnostic analysis of the alongstream momentum equation shows (Figure 4) that the kinetic energy reaches a maximum at the western sill (section V). Taking this western sill as a reference, the potential energy has negative values both east and west of the sill.
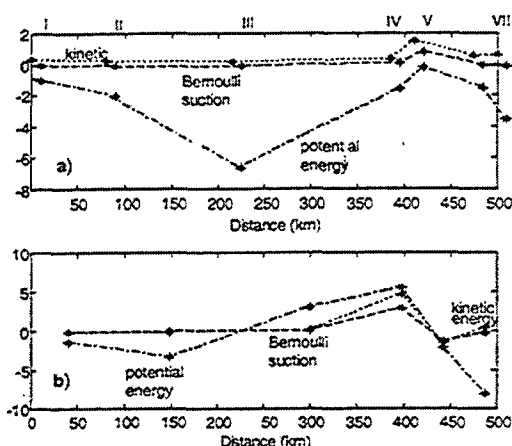
Figure 4. Alongstream momentum balance: (a) available energy; (b) alongstream derivative of the previous terms.

Further east (Sec. I - IV) the elementary mechanism moving the vein towards the sill consists of the upper layer pressure gradients, that are able to raise the vein from 800 to 300 m depth, thus increasing both the potential energy and the kinetic energy to their highest values. Subsequently, we observe that a decrease of potential energy does not correspond to any kinetic energy increase (Sec. VI - VII). This underlines the important role played by stresses downstream of the western sill towards the Tyrrhenian Sea.

While the entrainment stress between LIW and EMDW has a relatively negligible dynamical effect (Figure 5a), the MAW-LIW stress (dotted line) has the same importance as bottom stress (dashed line), deeply influencing the resulting total stress and allowing a considerable uplift of EMDW in the sill region.

The satisfactory balance between alongstream momentum gradients and total stresses, as estimated from the experiments data, is clearly evident in Figure 5b.
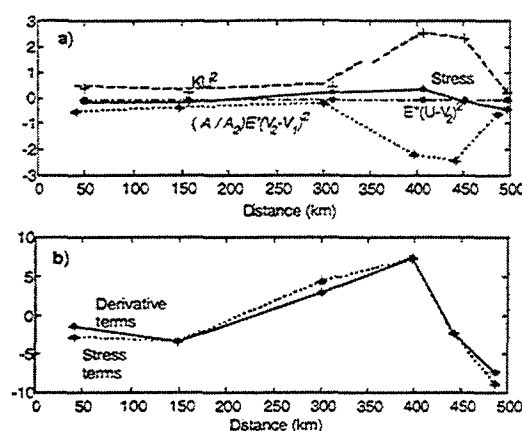
Figure 5. (a) Stress components; (b) alongstream derivative terms (continuous line) and their resultant, namely the stress terms (dotted line).

Conclusions

The observations made in the Strait of Sicily evidence the presence of a quasi-steady current flowing westward directly over the bottom of the strait. We focused our attention especially on the peculiarities of the interface slope of the vein immediately upstream of the sill, and on evaluating the relative importance of stresses (bottom and entrainment), alongflow pressure gradients and Bernoulli aspiration. The results, obtained by applying the previous generalisation of the Smith streamtube model, allows to state that in the presence of a multi-layer system and when there is a considerable velocity difference between the two layers immediately over the vein, the dynamics of these layers can have a very important effect on the vein and therefore it has to be taken into account.

References

Astraldi M., G.P. Gasparini, L. Gervasio and E. Salusti (2002): Dense Water Dynamics along the Strait of Sicily. *J. Phys. Ocean.*, in press.

Baringer M. and J. Price (1997): Momentum and energy balance of the Mediterranean outflow. *J. Phys. Ocean.*, 27, 1678-1692.

Lane-Serff G.F., D.A. Smeed and C.R. Postlethwaite (2000): Multi-layer hydraulic exchange flows. *J. Fluid Mech.*, 416, 269-296.

Smith P. (1975): A streamtube model for bottom boundary currents in the ocean. *Deep Sea Res.*, 22, 853-873.

Analysis of in-situ observations in the Strait of Gibraltar

Tom Avsic[1], Uwe Send[1], and Burkard Baschek[2]

[1]Institut für Meereskunde, Physikalische Ozeanographie II, Kiel, Germany
[2]Institute of Ocean Sciences, Sidney, BC, Canada

Abstract. During the EU-project CANIGO intensive ship-board observations were carried out in April 1996 and October 1997 in order to observe the spatial and temporal variability of the flow, of the internal bore and of the water mass structure in the Strait of Gibraltar. An inverse model for the current and interface-fluctuations was developed to remove tidal currents from the measurement and to calculate the volume transport for the in and outflow seperately. In addition traveltime measurements across the strait have been analysed to test the suitability of acoustical instruments for a longterm monitoring of the exchange through the strait.

Introduction

The Strait of Gibraltar is the choke point for the water mass exchange between the Atlantic Ocean and the Mediterreanean Sea. Accurate observations of the mass, salt, and heat transports in the strait provide important integral information about the processes in the interior of the Mediterranean basin. Also the outflow of Mediterranean Water has significant influence on the water mass properties and the circulation of the North Atlantic.

The Strait of Gibraltar is a complicated environment with strong tidal currents, large horizontal and vertical shears, internal bores, and hydraulically controlled flow which contribute to the difficulty in studying this area.

Figure 1. Topography of the Strait of Gibraltar, showing the position of the acoustical instruments T1, T2 and the raypath between them (dashed line). ADCP sections are shown as solid lines and CTD stations at the eastern entrance as dots.

The mean flow can be approximately described with a system of three layers. The upper one is formed by the inflowing fresh Atlantic Water and the lower one by the outflowing salty Mediterranean Water. In between is a region of high shear in flow, temperature, and salinity. However, it is quite common to describe the flow through the Strait of Gibraltar with a two-layer model, where the strong shear zone (intermediate layer) is neglected.

Measurements

During CANIGO, intensive oceanographic measurements were carried out focusing on the monitoring of the currents and the depth of the interface between Atlantic and Mediterranean water. The scientific goal of these measurements was to determine the volume transport through the Strait of Gibraltar (*Baschek et al.*, 2001), to obtain a better understanding of the dynamics and temporal changes of the exchange processes between the Atlantic and Mediterranean Sea, and to design future observing systems (*Send and Baschek*, 2001).

The eastern entrance of the strait (Algeciras-Ceuta section) was intensively observed during two cruises in April 1996 and September 1997. Here, the interface fluctuations are much smaller than at the Camarinal Sill, therefore contributing significantly less to the volume transport.

Figure 2 shows a mean of the quasi-synoptic ADCP sections at the eastern entrnce, over the depth range covered by the vmADCP. The typical currents here ($+20\,\mathrm{cm\,s^{-1}}$ to $+100\,\mathrm{cm\,s^{-1}}$, and $-80\,\mathrm{cm\,s^{-1}}$ to $+40\,\mathrm{cm\,s^{-1}}$ for upper/lower layers) are not as extreme as at the sill, but the resolved shears are comparable (up to $0.034\,\mathrm{s^{-1}}$ in the vertical and $9.3\,10^{-4}\,\mathrm{s^{-1}}$ in the horizontal). One sequence of vmADCP sections over a tidal cycle is available from spring and one from fall. Although there are some differences be-
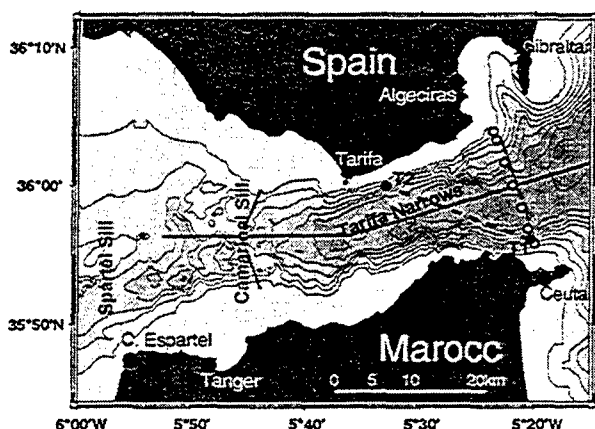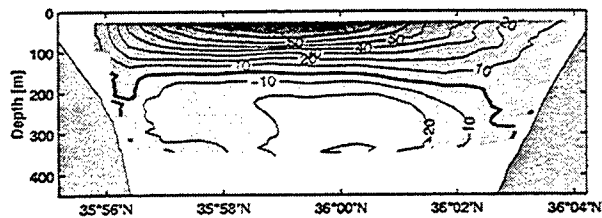
Figure 2. Approximate tidal-mean along-strait current [$cm\,s^{-1}$] through the eastern entrance of the Strait of Gibraltar from vmADCP sections.
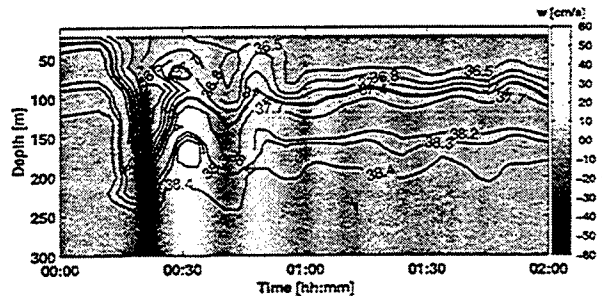

Figure 3. Obsevation of an internal bore (April 1996) near Camarinal Sill. The given time is relative to high water in Tarifa. *Shaded:* Vertical current [$cm\,s^{-1}$] (vmADCP). *Lines:* Isohalines (CTD). Bold line is the 37.4-isohaline.

tween these two tidal averages, we only show the total average from both seasons.

Another set of intensive observations was dedicated to the internal bore, which is released at the Camarinal Sill when the outflowing tide weakens and the water is pushed from the Atlantic back into the Strait of Gibraltar. The measurements of the internal bore at various locations in the strait with rapid CTD yoyos and vmADCP data allowed us to observe the evolution of the bore while it propagates towards the east into the Mediterranean Sea. It is a dominant but very short-lived feature, and it is not clear whether it is of importance for processes of larger scale. Figure 3 shows an observation of the bore at the Camarinal Sill. Before the bore reaches the location of measurement, the current has nearly no vertical shear. Vertical velocities are neglegible and the 37.4-isohaline, which roughly represents the location of the interface between Atlantic and Mediterranean water at the sill, lies in about 30 m depth. The arrival of the bore is indicated by a sudden lowering of the interface by about 150 m. This is accompanied by a strong increase of the vertical shear (values up to $0.035\,s^{-1}$ were observed) with currents in the upper layer of up to $150\,cm\,s^{-1}$ and in the lower layer of up to $-80\,cm\,s^{-1}$. All this happens within minutes and is associated with extreme vertical currents reaching values of $\pm 50\,cm\,s^{-1}$.

It is still not clear whether the flow through the Strait of Gibraltar is hydraulically controlled or not, or if it may flip from one state to the other (*C. Garrett et al.*, 1990). In
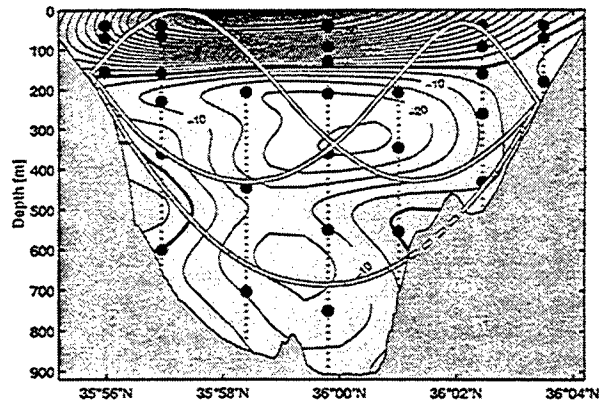
Figure 4. Measured mean along-strait current [$cm\,s^{-1}$] at the eastern section. Tides were removed by the inverse model. The dots represent moored rotor-current-meters and some ray paths of the acoustic transmission are shown.

the theory these two possible states are related to maximal and submaximal exchange (*L. Armi and D. Farmer*, 1986, *D. Farmer and L. Armi*, 1986). Timeseries of the composite Froude number were estimated from simultaneous vmADCP and CTD measurements at the eastern entrance of the Strait in spring (spring and neap tides) and in fall.

These estimates, as well as the observed qualitative tilt of the interface in along-strait direction, are consistent with hydraulically controlled flow and maximal exchange in April 1996. Corresponding conditions were not observed in October 1997, the interface being lower and with typical surface flows of smaller amplitudes.

Inverse model

Inverse modeling provides a tool to combine long timeseries from moorings with ship-board observations providing high spatial resolution, which allows it to extract the temporal as well as the spatial information from the measurements. This means that also the locations with an insufficient temporal sampling (where averages would normally be aliased by tides) can be taken into account and complemented with information from adjacent locations.

All data, which were measured at the eastern entrance of the Strait, were sorted into a grid of 16 horizontal and 29 vertical boxes. The distance between the boxes is approximately 1 km in the horizontal and 20-50 m in the vertical. To reduce the amount of data, 2-hour mean values were taken before they were sorted into the boxes, yielding a total of approximately 135,000 data.

To calculate the mean flow (Figure 4), the model was used to remove the tidal currents from the measurements. The mean currents of the residuals was calculated for every model box. The spatial gaps due to empty boxes were filled by using an objective analysis.

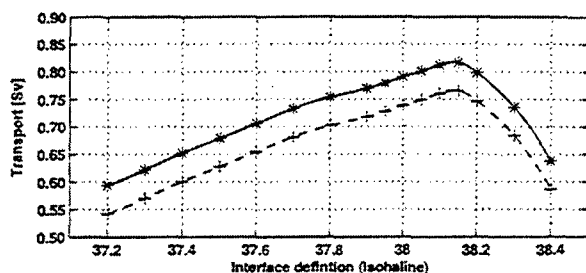A similar model has been used for the movement of the

Figure 5. Relation between the interface definition (isohaline) and the calculated volume transport of the upper layer (solid) and lower layer (dashed).

interface at the eastern entrance. , which was used in combination with the inverse model for the current speed to calculate the volume transports in both layers. The estimate of the upper and lower layer volume transports depends on the choice of the separating isohaline. When for example the chosen isohaline lies somewhere in the upper layer, the area of the cross section used for the upper-layer calculations is smaller than it should be and hence also the estimated upper-layer transport is too small. The relationship between the separating isohaline and the volume transport for both layers is shown in Figure 5. The isohaline for which the transport is maximal ($S = 38.1$) is taken as interface definition yielding a volume transport of $0.81 \pm 0.07Sv$ for the upper layer and $-0.76 \pm 0.07Sv$ for the lower layer.

Acoustic measurement

In the Strait of Gibraltar tomographic transceivers were deployed at locations T1, T2 (Figure 1) measuring the two-way traveltime of sound for the acoustic path in between the instruments.

The difference in traveltime ($t_{T1T2} - t_{T2T1}$) is a direct measure of the flow along and parallel to the raypath while the traveltime sum ($t_{T1T2} + t_{T2T1}$) is a measure for the soundspeed, which mostly depends on temperature.

Assuming that the current across the strait is negligable, lower layer current can be calculated using the traveltime differences of the deepest ray (Figure 4), which is sampling only the layer of Mediterranean Water. The lower layer current is shown in Figure 6 together with the model current integrated along the raypath. Since the inverse model cannot describe longterm variability, it has been calculated from the current meter moorings and added to the model current. It was found, that 98% of the lower layer tidal transport variance was resolved by the acoustic measurement (*Send et al.*, 2001).

The small differences between the measured and the modelled currents are mainly of tidal effects, which can be a consequence of different phases and amplitudes between the T1-T2 section and the eastern entrance (*Candela et al.*, 1990) where the model was calculated.
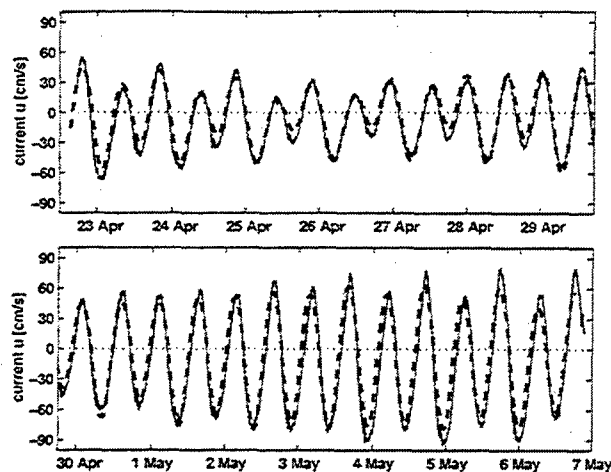

Figure 6. Longstrait current measured with the T1-T2 transceivers (solid line) compared with the sum of the model current and the longterm fluctuations from mooring data (dashed line).
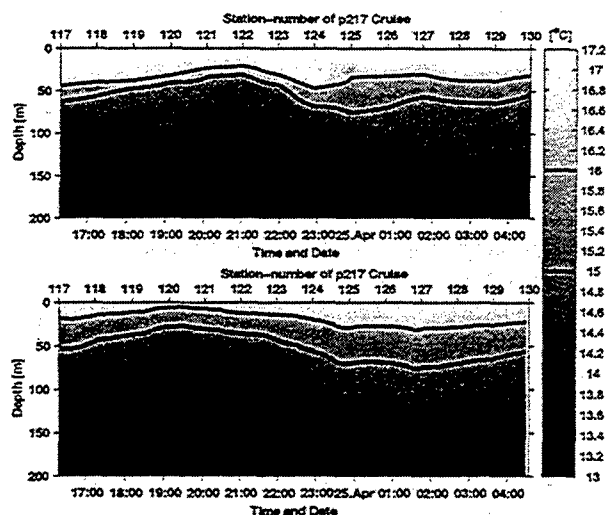

Figure 7. Temperature at the center of the eastern entrance. Upper panel: CTD masurement. Lower panel: Calculation from the traveltime sum.

From the traveltime sums temperature and salinity sections were estimated. Nonlinear effects on the raypath of the ± 2 rays (Figure 4) had to be taken into account to obtain meaningful results. An comparison with 14 repeated CTD casts at the center of the eastern entrance is shown in Figure 7. For this also the slope of the interface along the strait (which was calculated from the acoustic data) and the different amplitudes of the M2 tide between the eastern entrance and the T1-T2 section had to be considered.

Figure 8 shows the 38.1-isohaline depth at the center of the T1-T2 section for the whole period of the acoustic measurements. It shows variations of ± 50 m at a semidiurnal period and remarkably strong longterm variations of about
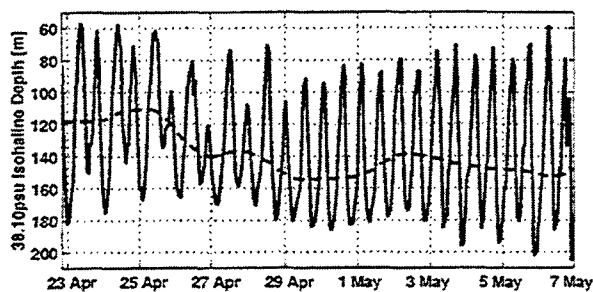
Figure 8. Depth of the interface at the center of the T1-T2 section (solid line). The dashed line shows the 2 day lowpass filtered data.

$\pm 20\ m$. With this method the interface depth can be determined within 10 to 20% (depending on the interface definition). Most of the error is due to small scale variations seen in the CTD profiles, whereas the tomography is an integral technique measuring integrated properties of the water. Therefor the error in the longterm variability is expected to be less than 20%.

The work on the acoustic data was motivated to test the feasibility of installing a quasi-permanent, real-time, shore-based observing system. The results show that tomography is a suitable tool for observing fluctuations in the Strait of Gibraltar.

Summary

Intensive ship-board observations from two cruises in the Strait of Gibraltar were carried out and were complemented with moorings in that region, yielding to new views of the joint spatio-temporal structures of the flow and stratification fields. All these data were combined with an inverse model to describe the flow and the depth of the interface as a function of space and time. Additionally a test with acoustical transceiver was carried out to determine their suitability of monitoring the Strait of Gibraltar, showing the important results of measuring the lower layer flow and interface depth.

References

Armi L., and D.M. Farmer, Maximal two-layer exchange through a contraction with barotropic net flow, *J. Fluid Mech., 164*, 27–51, 1986.

Baschek, B., U. Send, J.G. Lafuente, and J. Candela, Transport estimates in the Strait of Gibraltar with a tidal inverse model, *J. Geophys. Res., 106 (C12)*, 31,033–31,044, 2001.

Candela, J., C. Winant, and A. Ruiz, Tides in the Strait of Gibraltar, *J. Geophys. Res., 95 (C5)*, 7,313–7,335, 1990.

Farmer D. M., and L. Armi, Maximal two-layer exchange over a sill and through a combination of a sill and a contraction with barotropic flow. *J. Fluid Mech. 164*, 53–76, 1986.

Garrett, C., M. Bormans, and K. Thompson, Is the exchange through the Strait of Gibraltar maximal or submaximal?, in *The physical oceanography of sea straits*, edited by L.J. Pratt, pp. 271-294, Kluwer Academic Publishers, Dordrecht, 1990.

Send, U., B. Baschek, Intensive ship-board observations of the flow through the Strait of Gibraltar, *J. Geophys. Res., 106 (C12)*, 31,017–31,032, 2001.

Send, U., P. Worcester, B. D. Cornuelle, C. O. Tiemann and B. Baschek, Integral measurements of mass transport and heat content in the strait of Gibraltar from acoustic transmission, submitted to *Deep-Sea Research*, 2001.

Tom Avsic, Uwe Send, Institut für Meereskunde, Düsternbrooker Weg 20, 24105 Kiel, Germany. (e-mail: tavsic@ifm.uni-kiel.de, usend@ifm.uni-kiel.de)

Burkard Baschek, Institute of Ocean Sciences, P.O. Box 6000, Sidney, BC, V8L 4B2 Canada. (e-mail: burkard@uvic.ca)

The hydraulics of downslope flows in rotating stratified environments

Peter G. Baines

CSIRO Atmospheric Research, Aspendale, VIC3195 - Australia

Abstract. This paper explores the dynamics of two-dimensional gravity currents flowing down slopes in a rotating stratified environment, in a manner representative of dense flows exiting from oceanic straits. Hydraulic-type equations for downflows with entrainment and detrainment are given, and solution regimes are described for ranges of the relevant parameters: slope angle θ, drag coefficient C_D, and the frequency ratio parameter $\hat{R} = N^2 \tan\theta / f^2$, where N and f are the buoyancy and Coriolis frequencies respectively. In general, for initially supercritical downslope flows into stratified environments, the effect of rotation tends to make the flow subcritical, and under certain conditions a transition across the critical state may require a hydraulic jump. Entrainment into the downflow may cause similar effects.

Introduction

Flows of dense fluid exiting from straits are controlling factors in deep circulations in many ocean basins. These flows are driven down slopes by buoyancy and have the character of deep gravity currents, influenced by bottom topography and drag, mixing and entrainment, and the Coriolis force. In some situations the flow emanating from the strait is supercritical (in the hydraulic sense), in that events downstream do not influence conditions at the strait, as at Gibraltar. In other locations the flow is subcritical, and the nature of the downflow affects the strait.

Recent experiments on downslope flows in non-rotating stratified environments (Baines 2001a,b, 2002) show that for steep slopes the flows have the character of plumes, but over slopes of less than about 20° the flows have the character of gravity currents rather than plumes. Further, over gentle slopes the current detrains fluid to the environment as well as entraining some environmental fluid into the current. Since the associated mixing processes are small-scale, they should have the same effects in flows in rotating systems. This implies that a gravity current model with these mixing processes would give a more accurate description of some features of the physics of oceanic downflows than the often-used entraining plume-type model (e.g. Price and Baringer 1994). The question then arises, how would such a model describe the behaviour of the observed flows, including the disparate mixing properties of various observed oceanic downflows? This paper describes initial steps to address this question, by extending the model described in Baines (2001) to rotating systems.

This model is necessarily simplistic, and is intended to illuminate important processes affecting such flows as the Mediterranean outflow

Model Equations

We consider a plane slope at angle _ to the horizontal, with coordinates s downslope, r normal to it, y alongslope and z vertically upward. The model discussed here employs equations for steady downslope flow with no y-dependence of a layer of thickness d, downslope velocity U, alongslope velocity V and buoyancy $G=g\_/\_0$ in a rotating stratified environment with Coriolis frequency f and buoyancy frequency N. Here __ is the difference in density between the dense layer and the local environment, and $\_0$ is an overall mean density. We also define $Q = Ud$, and D is the vertical distance below the initial level ($s = z = 0$) of the source of dense fluid where the density of the environment equals the density of the dense fluid at the source. With initial values of U_0, Q_0 and G_0 for U, Q and G respectively, the mean buoyancy frequency N_0 is then given by $N_0^2 = G_0/D$. N is assumed to be uniform here. The flow is assumed to be sufficiently turbulent for the bottom drag (represented by a drag coefficient) to act on the whole layer.

For present purposes, the best way of defining dimensionless variables is in terms of Q_0 and f. Accordingly, we have $\hat{Q} = Q/Q_0$, and define

$$S = s\left(\frac{f\cos\theta}{Q_0}\right)^{1/2}, \quad \hat{d} = d\left(\frac{f\cos\theta}{Q_0}\right)^{1/2},$$

$$\hat{G} = \frac{G\cos\theta}{\left(Q_0 f^3 \cos^3\theta\right)^{1/2}}, \quad \hat{V} = \frac{V}{\left(fQ_0\cos\theta\right)^{1/2}},$$

$$\hat{R} = \frac{N^2\tan\theta}{f^2}, \text{ and } F^2 = \frac{Q^2}{Gd^3\cos\theta} = \frac{1}{\hat{d}^3\hat{G}},$$

where F is the downslope Froude number. The hydrostatic single layer equations for mass, momentum and buoyancy for steady flow yield for $\hat{Q}, \hat{G}, \hat{V}$ and $\hat{d}$

$$\frac{\partial\hat{Q}}{\partial S} = \left(E_e - E_d\right)\frac{\hat{Q}}{\hat{d}}\left(1 + \hat{V}^2\hat{d}^2\right)^{1/2}, \tag{2}$$

$$\frac{\partial\hat{G}}{\partial S} = -\hat{R} - E_e\frac{\hat{G}}{\hat{d}}\left(1 + \hat{V}^2\hat{d}^2\right)^{1/2}, \tag{3}$$

$$\frac{\partial\hat{V}}{\partial S} = -1 - \left(E_e + C_D\right)\frac{\hat{V}}{\hat{d}}\left(1 + \hat{V}^2\hat{d}^2\right)^{1/2}, \tag{4}$$

$$\left(1 - F^2\right)\frac{\partial\hat{d}}{\partial S} = \left(\tan\theta + \frac{\hat{V}}{\hat{G}} + \frac{\hat{R}\hat{d}}{2\hat{G}} + \left(1 + \hat{V}^2\hat{d}^2\right)^{1/2}T_1\right) \tag{5}$$

where

$$T_1 = \frac{1}{2}E_e - \left(C_D + 2E_e - E_d\right)F^2. \tag{6}$$

The local Richardson number is given by

$$R_i = \frac{Gd\cos\theta}{U^2 + V^2} = \frac{1}{F^2\left(1 + \hat{V}^2\hat{d}^2\right)}. \tag{7}$$

C_D is a constant drag coefficient with a typical ocean value of 0.006, and E_e, E_d are entrainment and detrainment coefficients respectively. Expressions for these depend on the model assumed. For the "plume" model of Ellison and Turner (1959), $E_d = 0$, and E_e is a function of R_i, whereas both E_e and E_d are non-zero in the "gravity current" model of Baines (2001a), where E_d depends on the ambient stratification in the environment. E_e and E_d are

numerically small and cause gradual, secular changes to the flow as it proceeds downslope. Although these changes may be important, and they are in the ocean, they are omitted here to obtain a "zeroth order" picture of the properties of the equations.

Equation (5) has the customary hydraulic singularity at $F = 1$, and the only external dimensionless parameters affecting the solutions are θ, C_D and $\hat{R}$. These equations describe steady flow with no variation in the y-direction. This may appear to be an unrealistic approximation to describe three-dimensional downslope currents. However, for broad currents (where width is much greater than depth), if the three-dimensional equations are integrated across the current, similar equations to (2-5) are obtained but with additional profile factors, as shown for the plume model by Price and Baringer (1994). In the stratified environment, the usefulness of the equations terminates when the dense fluid reaches its level of neutral buoyancy at a finite value of S, and the solutions may become unrealistic as this limit is approached. Downslope variations in topography may be included by allowing θ to vary with S (but not with the scaling used in (1)). Also, it should be noted that, for application to the ocean, this model only describes the motion of the bottommost layer. Fluid detrained into the environment will engender buoyancy-driven motion there also, which may be modelled by one or more additional layers, not considered here.

Steady Solutions

For the remainder of this discussion we consider solutions to (2-5) where $E_e = E_d = 0$, with the initial conditions

$$\hat{Q}(0) = 1, \quad \hat{G}(0) = \hat{G}_0, \quad \hat{V}(0) = 0, \quad \hat{d}(0) = \hat{d}_0. \tag{8}$$

The effects of including entrainment and/or detrainment may be inferred later. The solutions for $\hat{Q}$ and $\hat{G}$ are then

$$\hat{Q} = 1, \quad \hat{G} = \hat{G}_0 - \hat{R}S, \tag{9}$$

and $\hat{d}$ and $\hat{V}$ are now determined by (4) and (5). These equations have "equilibrium" solutions $\hat{V}_e, \hat{d}_e$ when the right hand sides of both equations vanish, given by

$$\hat{V}_e = -\frac{1}{2^{1/2}\hat{d}_e}\left[\left(1 + \frac{4\hat{d}_e^4}{C_D^2}\right)^{1/2} - 1\right]^{1/2}, \tag{10}$$

$$\hat{G}\tan\theta = -\frac{\hat{R}\hat{d}_e}{2} - \hat{V}_e + C_D\frac{\left(1 + \hat{V}_e^2\hat{d}_e^2\right)^{1/2}}{\hat{d}_e^2}. \quad (11)$$

Curves for $\hat{d}_e$ as a function of $\hat{G}\tan\_$ for various values of C_D are shown in Figure 1 for $\hat{R} = 0$, and in Figure 2 for $\hat{R} = 100$. Any point on these diagrams represents a possible initial flow state (8). We now discuss these cases separately in detail.

Homogeneous Environment - $\hat{R} = 0$

Each point on a C_D-curve in Figure 1 represents a downslope equilibrium flow solution for $\hat{d}_e$, with no variation with S, as a function of $\hat{G}\tan\_$. There is a lower cut-off for $\hat{G}$ for these curves, denoted $\hat{G}_{emin}$,
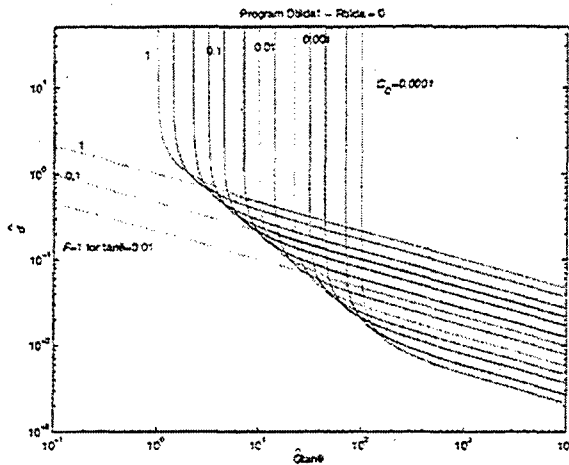
Figure 1. Each point on a solid curve represents an equilibrium solution for $\hat{d}_e$ in terms of $\hat{G}$ for that value of C_D, for downslope flow into a homogeneous environment ($\hat{R}=0$). C_D values are: 1, 0.5, 0.2, 0.1, 0.05 etc.. The lightly dashed straight lines denote conditions for critical flow, for three slopes (0.01, 0.1 and 1).

where the curves become vertical, given by

$$\hat{G}_{emin} = 1/(\tan\_\sqrt{C_D}). \quad (12)$$

For $\hat{G}$ values less than this, solutions independent of S are not possible. The dashed lines in Figure 1 denote lines where the Froude number $F = 1$ for three slopes: 0.01, 0.1 and 1. When a solution curve crosses the appropriate critical line for the given slope, the flow changes from supercritical ($F>1$) below to subcritical ($F<1$) above this line. The crossing point is a *control point*, in the conventional terminology of hydraulics. An analysis of the stability of these flows shows that solutions of

equation (4) always converge to $\hat{V}_e$, and the solutions $\hat{d}_e$ are stable for $F>1$, in the sense that flow states near this curve will converge towards it as S increases. However, the solution $\hat{d}_e$ is unstable when $F < 1$, implying that neigbouring flow states will diverge away from the curve as S increases. If flows become subcritical at the downstream end the flow may be determined by conditions at large S, and a boundary condition at this end is needed to fully specify the problem once steady state has been assumed. For values of $\hat{G}$ below $\hat{G}_{emin}$, numerical solutions and simple analysis of (4) and (5) shows that the flow (i.e. $\hat{d}$, $\hat{V}$) converges toward the critical state $F = 1$ from both above and below. $\hat{d}$ then oscillates violently about this state as the fluid descends further. In physical terms, one expects this to result in quasi-periodic oscillations and waves in the downflow for larger S.
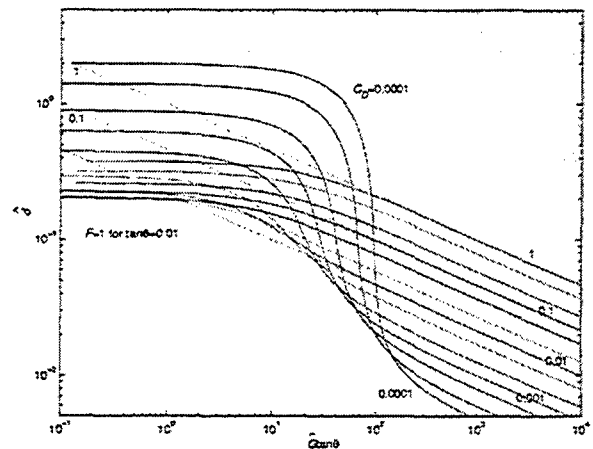

Figure 2. Same as for Figure 1 but for stratified environments with $\hat{R} = 100$. For smaller values of $\hat{R}$, the patterns of the equilibrium curves generally have similar form to those here, but level out at larger values of $\hat{d}$.

Stratified environment - $\hat{R} > 0$.

The equilibrium solution curves for $\hat{d}_e$ for $\hat{R}=100$ are shown in Figure 2. In these flows, $\hat{G}$ is not constant but decreases linearly with downstream distance to zero at $S = \hat{G}_o/\hat{R}$. Hence, we interpret the curves in Figure 2 as solutions evolving with increasing S in a quasi-static sense, $\hat{d}_e$ increasing as $\hat{G}$ decreases with downstream distance. A stability

analysis based on equations (4) and (5) again shows that flow states close to $\hat{d}_e$ converge to it with increasing S if $F > 1$, but diverge from it if $F < 1$. Hence, if the initial conditions are supercritical, as they often are in real oceanic situations, flow states will tend to converge to the solution $\hat{d}_e$ while F remains greater than unity.

Examination of (4-5) shows that as $S \rightarrow S_{max} = \hat{G}_0 / \hat{R}$ in the subcritical regime $F<1$, $\hat{d}$ increases to infinity as

$$\hat{d} \sim \frac{1}{(S - S_{max})^{1/2}} \,. \tag{13}$$

Flow states that are initially subcritical may approach this limit directly. Flow states that are initially supercritical may take one of four possible forms, as follows. (i) The flow may approach and join the equilibrium curve, and with it cross the line $F=1$ to subcritical states, and thence approach (13). (ii) Solutions with smaller $\hat{G}_0$ may approach $F = 1$ from below, and then oscillate about it as $\hat{G}$ decreases, until it again intersects the equilbrium curve, which it then follows as $\hat{G} \rightarrow 0$. (iii) As a possible alternative to (ii), the flow may avoid the singularity at $F=1$ by a hydraulic jump, with its subcritical downstream state located just above the equilibrium curve $\hat{d} = \hat{d}_e$. For a single layer, the hydraulic jump condition linking the upstream and downstream d-values d_u and d_d is (Baines 1995, section 2.3)

$$\frac{\cos\theta}{\hat{d}_u^2} = \frac{\hat{G}\hat{d}_d}{2}\left(1 + \frac{\hat{d}_d}{\hat{d}_u}\right). \tag{14}$$

Equating $\hat{d}_d$ with $\hat{d}_e$ then determines $\hat{d}_u$ and hence the jump's amplitude and location. Which of these two possibilities ((ii) or (iii)) actually happens may be best resolved by experiments. (iv) For sufficiently small $\hat{G}$ the equilibrium curve flattens and again passes below the critical line $F = 1$, and becomes stable. Accordingly, initially supercritical flows with similarly small $\hat{G}_0$ will converge to this curve, and give the finite value $\hat{d} = \hat{d}_e$ as $S \rightarrow S_{max}$, as for (ii). For all these cases, the corresponding value for $\hat{V}$ will be given approximately by (10), with $\hat{V}, \hat{d}$ replacing $\hat{V}_e, \hat{d}_e$.

Entrainment into a flow tends to increase Q and decrease G, implying that $\hat{G}$ becomes smaller. If E_e is comparable with C_D or smaller, the equilibrium curves will only be changed slightly, and hence d will increase as in Figure 2. R_i values are approximately uniform on the supercritical section of the equilibrium curves.

References

Baines, P.G., *Topographic Effects in Stratified Flows.* Cambridge University Press, 482 pp, 1995.

Baines, P.G., Mixing in flows down gentle slopes into stratified environments. *J. Fluid Mech.*, 443, 237-270, 2001a.

Baines, P.G., Regimes for flows down slopes into stratified environments. *Proc. 3rd Int'l Symposium on Environmental Hydraulics*, Arizona State Univ., Tempe AZ, USA, 6 pp., 2001b.

Baines, P.G., Two-dimensional plumes in stratified environments. *J. Fluid Mech.*, submitted, 2002.

Ellison, T.H. and Turner, J.S. Turbulent entrainment in stratified flows. *J. Fluid Mech.* 6, 423-488, 1959.

Price, J.F. and Baringer, M. O. Outflows and deep water production by marginal seas. *Prog. Oceanog.* 33, 161-200, 1994.

Seasonal transport variability through Gibraltar, Sicily and Corsica Straits

K. Béranger[1,2], L. Mortier[1,2] and M. Crépon[2]

[1] ENSTA, Unité d'Enseignement et de recherche en Mécanique, Chemin de la Hunière, 91761 Palaiseau, France
[2] LODYC, Université P. et M. Curie , BC 100, 4 place Jussieu, 75252 Paris cedex 05, France

Abstract. We have investigated the transport variability through three major straits of the Mediterranean Sea (Gibraltar, Sicily and Corsica) with a very high resolution model of the Mediterranean Sea. It is found that the Gibraltar and Sicily strait transports present a weak seasonal variability whilst that of the Corsica Strait is high. Results are compared to recent estimates from in-situ observations. Good agreements are obtained and illustrate the advantage in improving the resolution in numerical models to correctly simulate some circulation patterns.

Introduction

Straits and passages of the Mediterranean Sea play an important role in controlling the circulation through mass transport exchanges. The Mediterranean Sea is a thermodynamic system which transforms the incoming Atlantic Water (AW) into denser water masses through processes dependent on interaction with the atmosphere. The difference of density between the Mediterranean Sea and the Atlantic Ocean drives the mean mass transport through the Strait of Gibraltar. This transport contributes to the forcing of the cyclonic circulation of modified Atlantic Water in both the western and eastern Mediterranean seas (Herbaut et al., 1998; Millot, 1999).

In the present paper, we investigate with a high resolution numerical model, the volume transport seasonal variability through three major straits of the Mediterranean Sea, i.e. the Gibraltar, Sicily and Corsica straits.

The numerical model

The model is an extended version of the primitive equation numerical model OPA with a rigid lid. We used a 1/16° horizontal grid mesh, and 43 levels on the vertical. The horizontal grid was stretched at Gibraltar in order to better fit the coast line. Owing to the small size of the horizontal grid, we used a no slip condition at the coast. The initial hydrological conditions were provided by the Mediterranean climatology. The model has been run for eleven years. It was forced using a repeated annual cycle of daily sea surface fluxes from ECMWF analysis (0.5°*0.5° real grid scale) for the period March 1998 to February 1999.

The physical problems

The mass transport through the Gibraltar Strait is forced by the density difference between the Atlantic Ocean and the Mediterranean Sea (Bryden and Stommel, 1984; Bryden and Kinder, 1991; Garret, 1996; Lafuente et al., 2001). Light (warm and fresh) AW penetrates the Mediterranean Sea while dense (cold and salty) Mediterranean Outflow Water (MOW) flows into the Atlantic Ocean. Observations from current meters give an AW volume transport around 0.8 Sv (Bryden et al., 1994; Lafuente et al., 2001) and a MOW volume transport of about 0.7 Sv. The difference compensates the Mediterranean Sea evaporation which is of the order of 0.7 m/ yr. No strong seasonal variability is found in these transports.

The volume transport through the Sicily Strait is still controversial with estimates ranging from 1 up to 2 Sv. Recent observations reported by Astraldi et al. (1999) estimate this transport at about 1.1 +/-0.58 Sv. The major forcing component is the transport of AW coming from the Atlantic Ocean (as suggested by Herbaut et al., 1998), rather than the density gradient between the western and the eastern Mediterranean seas, which is very weak at the level of the AW.

The northward volume transport through the Corsica Strait is about 1 Sv and presents a strong seasonal variation with a minimum in summer and a

maximum in late winter (Astraldi and Gasparini, 1992).

The model results

Strait of Gibraltar

The mean eastward transport in the Gibraltar Strait is 0.53 Sv (Figure 1) which is somewhat lower than that reported above. This low value can be explained as a consequence of the no slip boundary parameterization used at the coast. The transport seems hydraulically controlled according to a vertical zonal section of salinity done through the strait (Figure 2). We denote a weak seasonal transport variation (Figure 1). A large AW inflow (and MOW outflow) maximum occurs in Spring, as in Bryden and Kinder (1991), and an AW inflow minimum is in Summer in agreement with Astraldi *et al.* (1999). We could notice a semi-annual signal, with a second short AW inflow maximum in October and a second AW inflow minimum at the end of December. This is probably linked to local wind forcing, as suggested by Astraldi *et al.* (1999) and Lafuente *et al.* (2001), and so interpreted as barotropic variability.

Figure 2. Salinity vertical section along the Gibraltar Strait in February (year 8 of the simulation).

Strait of Sicily

The mean AW south-eastward transport through the Sicily Strait is 0.95 Sv (Figure 3) with a maximum of 1.5 Sv in November-December and an AW inflow minimum of 0.7 Sv in March–April, in agreement with the seasonal variations reported in Astraldi *et al.* (1999).

Figure 1. Eastward transport of AW through the Gibraltar Strait for years 4 to 8 of the simulation. Opposite values are obtained for the MOW path.
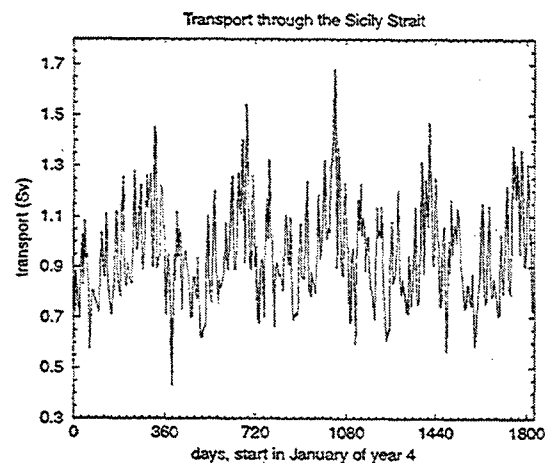
Figure 3. South-eastward transport of AW through the Sicily strait during the years 4 to 8. Opposite values are obtained for the EOW transport.

exp: MED16-05, date: February, year 8, champ: Speed, profondeur 44 m

Champ en couleur ( ): Min= 0.00, Max= 0.42, Int= 0.02
Norme vecteur ( ): Min= 0.00, Max= 0.41

exp: MED16-05, date: February, year 8, champ: Speed, profondeur: 208 m

Champ en couleur ( ): Min= 0.00, Max= 0.43, Int= 0.02
Norme vecteur ( ): Min= 0.00, Max= 0.41
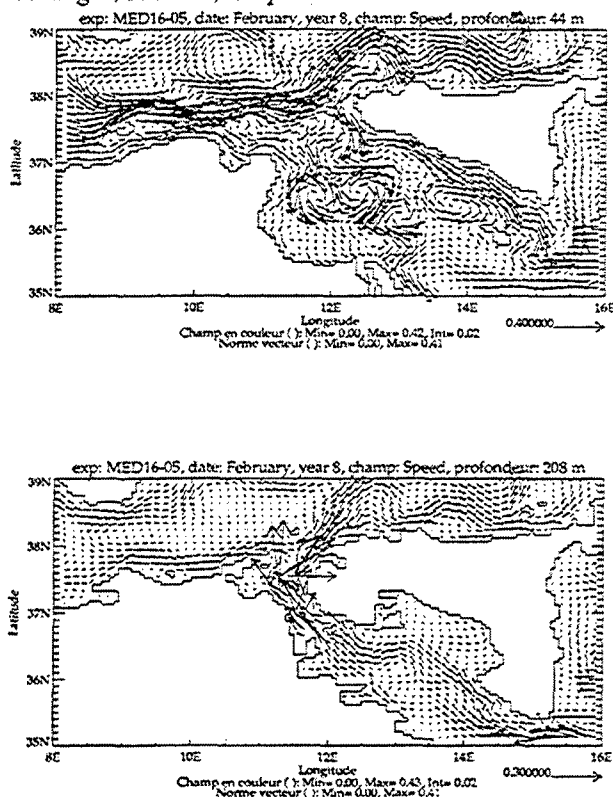
Figure 4. Circulation in the Sicily Strait in February (year 8 of the simulation) at 44m (AW, top) and at 208m (EOW, bottom).

The fact that the Sicily Strait transport is larger than that of the Gibraltar Strait is due to a recirculations. The summer surface current pattern is in agreement with the measurements (Robinson *et al.*, 1999; Lermussiau and Robinson, 2001). In winter (Figure 4), we note the splitting of the surface current into two branches at the entrance of the Sicily Strait and the EOW progression into the Tyrrhenian Sea veering to the North Sicily coast as it exits the strait. These patterns are in agreement with the theoretical studies of Herbaut *et al.* (1998) and Gervasio (this issue). The high resolution of the model allows us to correctly represents the two deep and narrow channels through which the EOW inflows into the Tyrrhenian Sea.

Strait of Corsica

The mean northward transport is 0.78 Sv (Figure 5). It is maximum in March (1.3 Sv) and minimum in September (0.3 Sv) in agreement with measurements (Astraldi *et al.*, 1999). In contrast to the Gibraltar and Sicily strait transports which are strongly baroclinic, the Corsica Strait transport

presents a strong barotropic component. This behavior is associated with the wind stress curl variability as shown by Astraldi and Gasparini (1992) and demonstrated by Herbaut (1994).
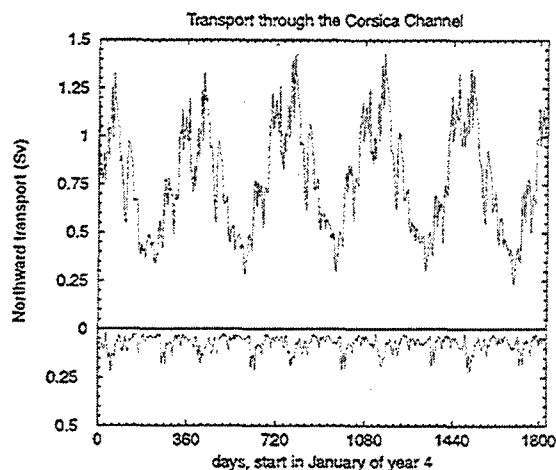
Figure 5. AW northward (top) and EOW southward (bottom) transports through the Corsica Channel during the year 4 to 8 of the simulation.

Conclusions

Flows through three major straits of the Mediterranean Sea simulated by a high resolution primitive equation model have been analysed. The seasonal variability of the transport is in good agreement with the observations reported in Astraldi *et al.* (1999) and Lafuente *et al.* (2001).

References

Astraldi M., and Gasparini G.P. (1992): The seasonal characteristics of the circulation in the North Mediterranean Basin and their relationship with the atmospheric-climatic conditions, *J. Geophys. Res.*, 97, 9531-9540.

Astraldi M., Balopoulos S., Candela J., Font J., Gacic M., Gasparini G.P., Manca B., Theocharis A., Tintoré J. (1999): The role of straits and channels in understanding the characteristics of Mediterranean circulation, *Progr. Oceanog.*, 44, 65-108.

Bryden H.L., Candela J., and Kinder T.H. (1994): Exchange through the Strait of Gibraltar, *Progr. Oceanog.*, 33, 201-248.

Bryden H.L., and Kinder T.H. (1991): Recent progresses in strait dynamics, *review of Geophysics* (Suppl.), 617-631.

Bryden H.L., and Stommel H. (1984): Limiting processes that determine basic features of the circulation in the Mediterranean, *Oceanologica Acta*, 7, 289-296.

Drillet Y., Béranger K, Bremond M., Gaillard F., Le Provost C., Siefridt L., Theetten S. (2000) : Rapport de projet MERCATOR, Expérimentation PAM, CERFACS, Toulouse, France.

Garett C. (1996): The role of the Strait of Gibraltar in the evolution of the Mediterranean water properties and circulation. In F. Briand Dynamics of Mediterranean straits and channels, CIESM Science series.

Herbaut C., Codron F., and Crépon M. (1998): Separation of a coastal current at a strait level: Case of the Sicily Strait, *J. Phys. Oceanog.*, 28,1346-1362.

Herbaut C. (1994) :PhD University Curie, Paris VI.

Lafuente J.C., Vargas J.M., Delgado J., Sarhan T., Plaza F., Vargas M. (2001): Seasonal variability of the exchange through the Strait of Gibraltar and the Mediterranean mean sea level, *36° CIESM Congress*, Monaco.

Lermussiaux P.F.J., and Robinson A.R. (2001): Features of dominant mesoscale variability, circulation patterns and dynamics in the Strait of Sicily. *Deep Sea Res,*. I 48, 1953-1997.

Millot (1999): Circulation in the western Mediterranean Sea, *J. Mar. Sys.*, 20, 423-442.

Robinson A.R., Sellschopp J., Warn-Varnas A., Leslie W.G., Lozano C.J., Haley P.J.Jr, Anderson L.A., Lermusiaux P.F.J (1999): The Atlantic Ionian Stream, *J. Mar. Sys.*, 20, 129-156.

Some recent results on the Faroe-Bank Channel overflow

K. Borenäs[1], I. Lake[2] and P. Lundberg[2]

[1] Swedish Meteorological and Hydrological Institute, Göteborg, Sweden
[2] Department of Meteorology/Physical Oceanography, Stockholm University, Stockholm, Sweden

Abstract. On the basis of field programmes conducted in the Faroe-Bank Channel during the last decade, some results concerning the water-mass and potential-vorticity characteristics of the overflow are discussed.

Introduction

The Faroe-Bank Channel, with a threshold depth of around 850 metres, is the deepest passage through the Greenland-Scotland Ridge. It is hence of considerable importance as a conduit for deeper waters from the Norwegian Sea in their motion towards the North Atlantic.
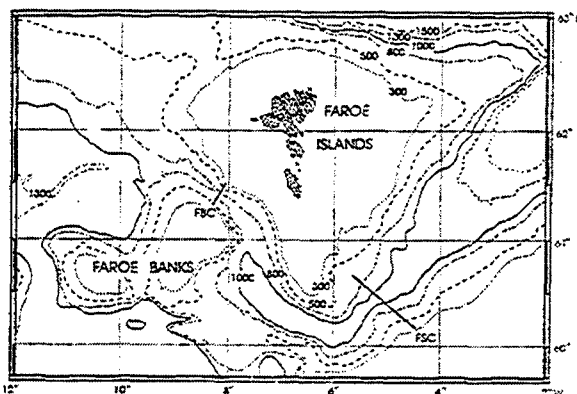
Figure 1. Map of the Faroe region with transects across the Faroe-Shetland and Faroe-Bank channels.

The first study to take into account its possible effects on the hydrography of the North Atlantic proper was carried out by Cooper (1955). During the following two decades ICES on two occasions organized large multi-ship programmes, during which considerable efforts were devoted to the Faroe-Bank Channel. These joint efforts resulted in a number of important studies, e.g. Crease (1965), Dooley and Meincke (1973), both of which concluded that the transport of deep water with temperatures below 3°C was on the order of 1-2 Sv. In the 1980s work in the passage was carried out on a

more limited scale, cf. Van Aken (1988), Borenäs and Lundberg (1988), Saunders (1990).

During the last decade, however, the deep-water overflow through the Faroe-Bank Channel has, once again, become the object of well-earned interest. This time the field activities have been carried through within the framework of WOCE and the European Union VEINS programme, and the aim here is to try to summarize some of these more recent results, with focus not on the climatological implications (which have been dealt with elsewhere, cf. Hansen et al. (2001)), but rather on some features of possible dynamical interest.

Field activities

The Nordic-WOCE programme as well as the VEINS project were aimed at obtaining an overview of the deep- and surface-water transports in the Faroe region. For this purpose a number ADCP arrays were deployed, and furthermore regular hydrographic surveys were conducted along sections extending northwards from the Faroes, across the Faroe-Shetland Channel, and across the Faroe-Bank Channel, at the approximate threshold of which a bottom-mounted ADCP was deployed for the purpose of monitoring the long-term behaviour of the deep-water transport.

We shall here focus on the observations from the Faroe-Bank Channel. This data set is of special interest from the standpoint of dynamical analysis, since during a three-month period three ADCPs were deployed over the same cross-section. A comprehensive set of hydrographic data from the passage was furthermore used for examining the water-mass properties of the overflow. The results from this analysis will next be discussed.

TS-characteristics of the overflow

The deeper parts of the Norwegian Sea are characterized by very stable water-mass properties. This water, of temperature -0.5°C and salinity 34.92, does not discharge in its pure form through the Faroe-Bank Channel, but rather as an admixture with other water masses.

The main slope of the isotherms across the Faroe-Bank Channel clearly indicates that the overflow is in geostrophic balance. However, a closer inspection of data reveals that this overall state assumes two guises, one where the isotherms are more-or-less parallell across the passage, the other where they show a pronounced pinching towards the southwestern edge of the channel. This is illustrated in the hydrographic sections of Figure 2, taken along the FBC transect shown in the map of Figure 1.
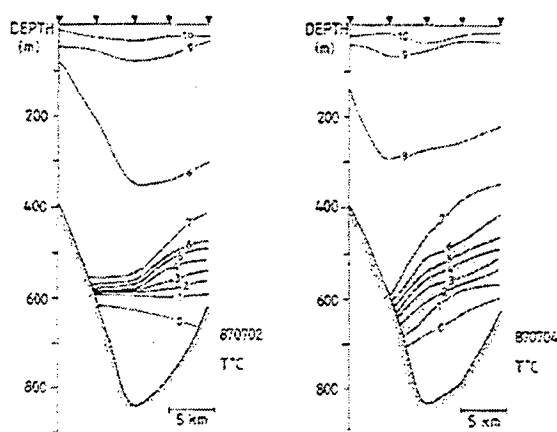
Figure 2. Hydrographic sections across the Faroe-Bank Channel, one with pinching, the other with almost parallel isotherms.

From a considerable number of hydrographic sections taken at the sill region of the channel, Borenäs *et al.* (2001) could demonstrate that the pinching phenomenon most likely can be associated with the presence of a distinct intermediate water mass. This was borne out by the water-mass characteristics, since composite TS-diagrams from a hydrographic station located on the Faroe side of the passage tend to show a bimodal structure as seen from Figure 3. An almost straight TS-curve between the NSDW and the North Atlantic surface water predominates when the cross-channel isotherm distribution is parallell, whereas the slightly convex relationship between temperature and salinity is found in conjunction with isotherm pinching. This

curvature is induced by the presence of a third water mass, which must be somewhat warmer and more saline than the NSDW. It was shown that this third water mass most likely is North Icelandic/Arctic Intermediate water (NI/AI), which arises at the polar front northeast of Iceland from wintertime convection.

This seasonality in the generation of the intermediate water mass is consonant with the period of its predominance in the Faroe-Bank Channel. Borenäs *et al.* (2001) showed that the intermediate water almost always is present in the channel from June to September, whereas it during the rest of the year may or may not be found on the threshold section. The basis for this assertion is that the pinching phenomenon primarily was encountered during summer, a season characterized by the fact that no single instance of a "linear TS-curve" was found in the entire 20-year hydrographic record from June to September.

On the basis of the available data it was, however, not possible to unambiguously settle the vexing question of whether the pinching is frictionally determined or if it is an inviscid effect. Johnson and Sanford (1992) argued that it arises within the framework of a two-layer situation, where the cross-channel bottom and interface Ekman transports are the causative agents. The analysis due to Hogg (1983) of a similar phenomenon rather suggests that the pinching can be explained in inviscid terms using hydraulic three-layer theory, which leads to the interior layer assuming the characteristic wedge-shape seen in Figure 2.
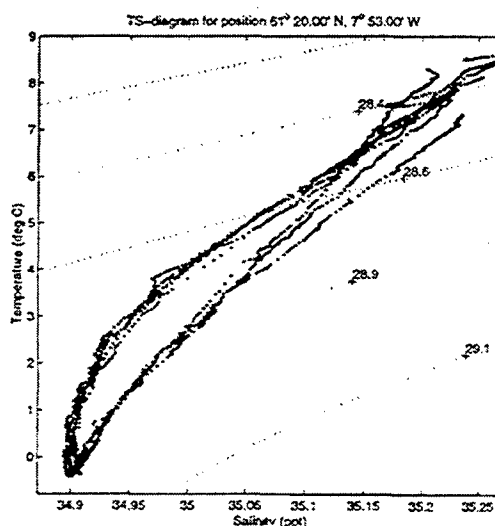

Figure 3. Composite TS-diagram from the Faroe-Bank Channel.

From the discussio above it is fairly evident that Borenäs *et al.* (2 1) favoured the inviscid hypothesis advanced by Hogg (1983). These investigators, nevertheless, also underlined that almost synoptic hydrography from the Faroe-Bank Channel and the Faroe-Shetland Channel (at the section denoted FSC in the map of Figure 1) showed that the intermediate water mass was much more distinct at the latter section. This weakening of its characteristics along the path to the threshold cannot be accomplished without pronounced mixing. Thus Borenäs *et al.* (2001) concluded their study by noting that possibly both processes may play a role for establishing the isotherm pinching.

PV-characteristics of the overflow

During the summer months of 1998 three ADCPs were deployed across the FBC section shown in the map of Figure 1. Detailed hydrographic surveys were also undertaken when the current-meters were launched and retrieved. These records are not only of interest for the long-term monitoring, but are also useful for examining the cross-channel potential-vorticity (PV) distribution of the overflow, a crucial quantity for hydraulic analyses.

In Figure 4 vertical profiles of observations from the three ADCP sites are shown, comprising acoustically derived information (back-scatter intensity as well as along-channel velocity) and the temperature structure as obtained from the CTD casts. It is recognized that the level of maximum shear corresponds fairly well to the pycnocline as given by its temperature proxy. It thus appears feasible to discuss the dynamics of the kinematically defined overflow in terms of a two-layer situation, where the interface is identified with the maximum-shear zone. From the vertical location of this quantity at the three sites in Figure 4, the geostrophically balanced character of the overflow is clearly in evidence.
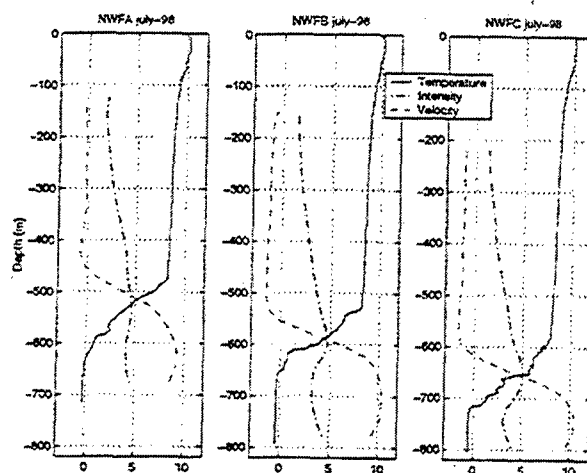
Figure 4. Vertical profiles at the three ADCP sites.

Estimates of the potential vorticity on the two sides of the passage may thus be obtained from the three ADCP records. The results from the 70-day intensive-study period are shown in Figure 5. The overall magnitude of the potential-vorticity estimates is consonant with the average upstream-basin depth and the local value of Coriolis parameter. It is furthermore seen that the calculated potential vorticities differ significantly across the passage. Their behaviour nevertheless shows a high degree of coherence, excepting a week-long period in August when an anomalous water mass passed the north-eastern ADCP site.
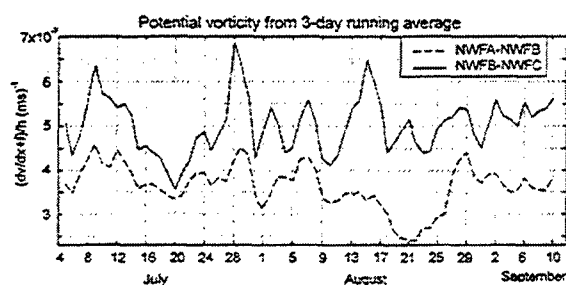

Figure 5. Calculated PV on the two sides of the passage.

This characteristic of the deep-water flow through the Faroe-Bank Channel is of theoretical interest, since previous hydraulic estimates of the transports have been based on the assumption of a constant PV of the overflow. In order to investigate how a non-constant PV distribution might affect the outcome of a hydraulic analysis, a series of diagnostic calculations has been undertaken. These were based on the assumption of a linearly varying PV distribution across the passage, its precise characteristics being given by the average values determined from Figure 5. A 1-layer model was thus applied. Under the auxiliary assumption of an upstream-reservoir transport confined to the eastern boundary of the Norwegian-Sea deep basin, solutions could be calculated. With this formulation of the problem, the diagnostic quantity was the interface level in the interior of the upstream reservoir. For the consistent solution, with a deep-water transport equal to that directly determined from the ADCP records, this calculated quantity turned out to be reasonably close to the level known from the climatology of the Norwegian Sea.

Outlook

In addition to already having contributed to the analyses briefly outlined above the hydrographic and current-meter data set from the Faroe-Bank Channel obtained during Nordic-WOCE and VEINS is of considerable interest for future studies. Hence, it will for instance be used for examining nonstationary processes as well as hydraulic two-layer flow with an active upper layer, the latter being possible since the range of the bottom mounted ADCPs extended well into the upper layer.

References

van Aken, H.M., Transports of water masses through the Faroese Channels determined by an inverse method. *Deep-Sea Res.*, 35, 595-617, 1988.

Borenäs, K., I. Lake, and P. Lundberg, On the Intermediate Water Masses of the Faroe-Bank Channel Overflow, *J. Phys. Oceanogr.*, 20, 29-43, 2001.

Borenäs, K., and P. Lundberg, On the deep-water flow through the Faroe Bank Channel, *J. Geophys. Res.*, 93C, 1281-1292, 1988.

Cooper, L.H.N., Deep water movements in the North Atlantic as a link between climatic changes around Iceland and biological productivity of the English Channel and the Celtic Sea, *J. Mar. Res.*, 14, 347-362, 1955.

Crease, J., The flow of Norwegian Sea water through the Faroe Bank Channel. *Deep-Sea Res.*, 12, 143-150, 1965.

Dooley, H. and J. Meincke, Circulation and water masses in the Faroese Channels during Overflow-73, *Dtsch. Hydr. Z.*, 34, 41-55, 1981.

Hansen, B., W.R. Turrell and S. Østerhus, Decreasing overflow from the Nordic seas into the Atlantic Ocean through the Faroe Bank Channel since 1950, *Nature*, 411, 927-929, 2001.

Hogg, N.G., Hydraulic control and flow separation in a multi-layered fluid with application to the Vema Channel. *J. Phys. Oceanogr.*, 13, 695-708, 1983.

Johnson, G.C., and T.B. Sanford, Secondary circulation in the Faroe Bank Channel outflow. *J. Phys. Oceanogr.*, 22, 927-933, 1992.

Saunders, P. M. , Cold outflow from the Faroe Bank Channel, J. Phys. Oceanogr., 20, 29-43, 1990.

Density structures and intermittency associated with breaking internal gravity waves

P. Bouruet-Aubertot[1], J. Sommeria[2] and C. R. Koudella[3]

[1] LODYC/U. Pierre et Marie Curie/UMR 7617, Paris, France
[2] LEGI, Grenoble, France
[3] DAMTP, Cambridge, UK

Abstract. Nonlinear interactions of internal gravity waves lead to intermittent breaking events with density overturning and vertical turbulent mixing. We analyze the statistics of density and velocity fluctuations in this process, using direct numerical simulations. We characterize the density and velocity gradients at different scales along the vertical and horizontal directions. The velocity gradients behave in a very similar way to usual turbulence, while the density gradients are very intermittent. This can be attributed to the formation of sheets with strong stable density gradients. Unstable density gradients are rare and form intermittent patches of different scales for which we have analysed the statistics. We discuss the link with mixing properties of the internal wave field and compare with observations in the ocean and the atmosphere.

Introduction

Internal wave breaking is an important source of turbulence in stably stratified fluids. Because wave breaking occurs intermittently in space and time it is important regarding the interpretation of microstructure measurements (for instance the estimate of mixing) to have a "good" knowledge of the statistical properties at small scales. To this aim process-oriented studies performed with the use of numerical simulations constitute an efficient approach. We start with a simple initial condition (a large scale internal gravity wave), so that turbulence is produced by an intrinsic sequence of instabilities, without external noise, and our calculations can be exactly reproduced and checked. We performed two-dimensional direct numerical simulations which allow better resolution. It is representative of three dimensional cases, as shown by Bouruet-Aubertot *et al.* (2001), Carnevale *et al.* (2001). We also analyse three-dimensional numerical simulations (but with a lower resolution).

The purpose of this paper is to analyze statistical properties of the turbulence induced by the breaking of a large scale primary wave and characterize rare events responsible for the intermittency.

Moments and exponants

We computed the moments of the horizontal and vertical velocity, u and v, and of the density fluctuations, ρ' versus the separation Δz. We obtained power laws versus Δz over one decade approximately.

We then looked at the behaviour of the exponants ζ_n of the moments of u, v and ρ'. The ratios ζ_n/ζ_2 for the velocity components and the density are displayed versus n in Figure 1. The behaviour of a system with no intermittency and the same ζ_2 exponant as our system is represented for comparison (see the dotted line in Figure 1).
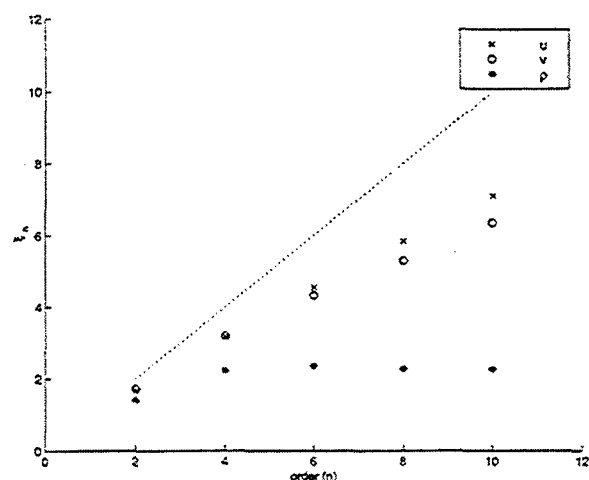
Figure 1. Scaling exponents ζ_n of the order n structure functions (along z direction) for u, v and ρ.

All points are below the dotted line showing that indeed both velocity components and density are intermittent. Interestingly scaling exponants for u and v are very closed suggesting that physical events responsible for the intermittency of the flow occur at very small scales where the anisotropy introduced by the stratification does not come into play.

In contrast density fluctuations are more intermittent than velocity components. This point is very similar to ordinary turbulence in which the passive scalar has a more intermittent behaviour than velocity.

We then compared the scaling exponents for the density fluctuations with those obtained in ordinary three-dimensional turbulence. Density fluctuations are found to be more intermittent than passive scalar in three-dimensional turbulence. This suggests that the dynamical coupling between buoyancy and inertial forces is a crucial process for the intermittency of density fluctuations.

Probability density functions of density fluctuations and of velocity components

We analyzed the probability density functions (pdfs) of density fluctuations. Our main purpose was to investigate whether the shape of the pdfs could be related to the dynamical regime. To this aim we first filtered the primary wave to focus on the "large

scale" resonantly interacting waves. A close to Gaussian pdf was obtained (Figure 2a). Consistently values of the skewness and kurtosis are closed to those of a normal distribution: the skewness is almost zero and the kurtosis is equal to 3.3.

We then filtered the largest scales in order to characterize the wavebreaking dynamical regime. The shape of the pdfs strongly differed from that of the weakly nonlinear waves with close to exponential tails (Figure 2b)
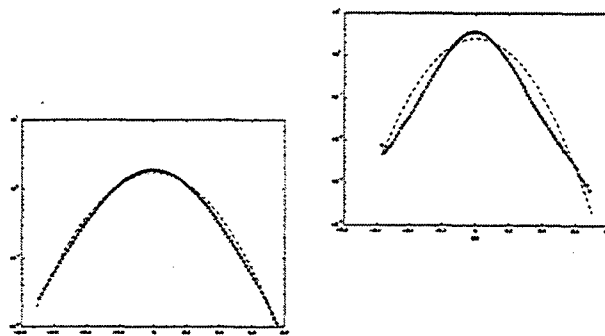
Figure 2. Probability density functions of the density fluctuations, ρ': (a) with filtering the primary wave, (b) in the wave breaking spectral range (kz^{-3} spectra, see text). The associated Gaussian distribution is shown for comparison (dotted line).

Pdfs of the density gradients at differents vertical scales

We next characterized the density and velocity gradients at different scales along the vertical and horizontal directions. The velocity gradients behave in a very similar way to usual turbulence, while the density gradients at small scales are very intermittent More precisely pdfs of the density gradients at small scales are highly skewed. The pdf decreases more strongly toward unstable density gradients while the decrease is less steep toward stable stratification until the pdfs reaches almost a plateau for the highest values.
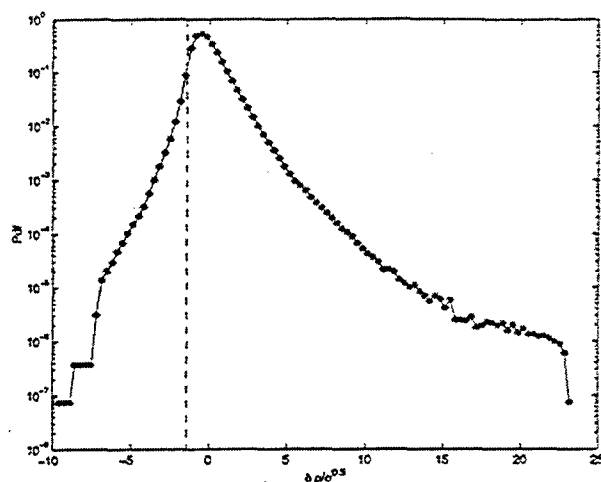
Figure 3. Probability density function of density differences at vertical scale $\Delta z=4\ \delta z$ (where δz is the vertical resolution of the model): $Pdf([\rho(z)-\rho(z+\Delta z)]$. The dotted line shows the value for neutral stratification.

We identified the physical events responsible for this density structure. These strongly stratified regions are correlated with breaking events. Indeed density overturnings can lead in some cases to a convergence of fluid which results in a local increase of the vertical density gradient (Figure 4). The resulting density structure is made of a succession of sheets with strong stable density gradients and turbulent regions of greater vertical extent.
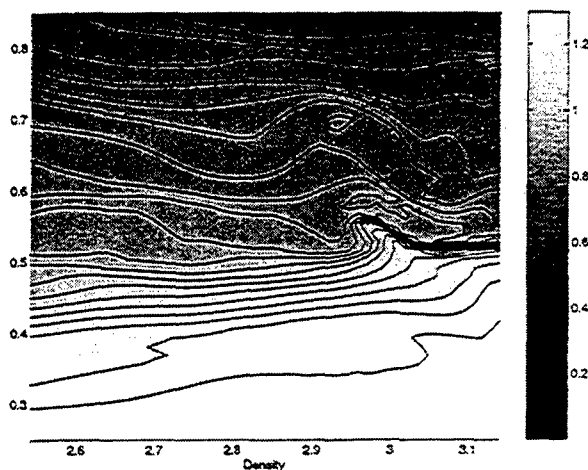
Figure 4. Density field in a vertical plane: Zoom over the rare events. The strongly stratified region is located around z~0.52.

Discussion

We found that an internal wave field consisting of resonantly interacting modes is Gaussian. This is an interesting result which confirms to some extent the hypothesis of Gaussianity of the internal wave field which is usually assumed in weakly nonlinear theories (e.g. Olbers, (1976)). Also, these results give a new light on the interpretation of oceanic measurements. Indeed the fact that contradictory results have been reported in the literature might result from the fact that the large scales contributing to most of the pdfs differed dynamically. For instance the same range of scales can correspond either to a weakly nonlinear regime or to breaking internal gravity waves, depending on the value of the Ozmidov length scale. As a consequence different pdfs were obtained.

Regarding the strongly nonlinear regime of breaking waves we have compared our results with those obtained by Alisse and Sidi (2000) in their so called "calm regions" of the stably stratified atmosphere. Note that they discriminated between calm regions characterized by energy spectra following a kz^{-3} law and turbulent regions for which Kolmogorov energy spectra were obtained. Their "calm regions" thus correspond to our wavebreaking dynamical regime. They obtained pdfs with exponential tails for the temperature fluctuations which is consistent with our results.

Histograms of the temperature gradient at different vertical scales in the ocean have shown that the vertical fine structure of the temperature field becomes highly skewed as the vertical scale decreases (e.g. Hayes et al. (1975), Desaubies and Gregg (1981)). Presumabely two processes might be responsible for this shape, either the strain produced by internal gravity waves or mixing events. These two alternatives were addressed in theoretical models proposed by these authors. It appeared that both models can describe the skewness of the pdfs though the wave model would be more adequate at the intermediate scales and the sheets and layers model at the smallest scales. However there is no objective criterion to predict the scale of this transition and it is more than likely that both processes come into play. To address these questions we tested the validity of the two models against our numerical data. We found that the Hayes et al.'s model fits quite well with the pdfs provided that the vertical scale is of the same order as the Ozmidov length scale whereas the model based upon internal wave straining (Desaubies and Gregg) is valid for larger scales typically about 6

times the Ozmidov length scale in our numerical data.

It is clear that both internal waves and mixing processes contribute to the observed temperature gradient skewness. Nevertheless it appears that at the smallest scales mixing processes dominates and therefore one could try to infer an eddy diffusion coefficient, Kd, from these pdfs. We have used results from simple kinematics models which lead to the following expression for Kd (see Gregg (1989), eq.(24)) :$Kd = \gamma_{mix} H^2 / 12 T_{event}$ where γ_{mix} is the mixing efficiency, H the typical scale of the overturning regions and T_{event} the time interval between instabilities. We assumed $\gamma_{mix}=0.5$ (according to Figure 10 from Bouruet-Aubertot *et al.* (2001)), and estimated H and T_{event}. We thus obtained a value for the ratio between the eddy diffusivity and the "molecular" diffusivity (the diffusivity put into the model) of 11. This value is very close to the maximum value obtained with a direct method (Figure 7 from Bouruet-Aubertot *et al.* (2001)).

References

Alisse, J.R., and Sidi, C., Experimental probability density functions of small-scale fluctuations in the stably stratified atmosphere, *J. Fluid Mech., 402*, 137-162, 2000.

Bouruet-Aubertot, P., Koudella, C.R., Staquet, C. and Winters, K.B., Particle dispersion and mixing by breaking internal gravity waves , *Dyn. Atmos Oceans, 33*, 95-134, 2001.

Carnevale, G.F., Briscolini, M. and Orlandi, P., Buoyancy to inertial range transition in forced stratified turbulence, *J. Fluid Mech., 427*, 205-239, 2001.

Desaubies, Y. and Gregg, M.C., Reversible and irreversible finestructure, *J. Phys. Oceanogr., 11*, 541-556, 1975.

Gregg, M.C., Diapycnal mixing in the thermocline. *J. Geophys. Res., 92, C5*, 5249-5286, 1989.

Hayes, S.P., Joyce, T.M. and Millard, JR., Measurements of vertical fine structure in the Sargasso Sea. *J. Geophys. Res., 80, no.3,* 314-319, 1975.

Olbers, D.J., Non-linear energy transfers and the energy balance of the internal wave field in the deep ocean, *J. Fluid Mech., 74*, 375-399, 1976.

Effects of strait mixing on ocean stratification

Harry L. Bryden and George Nurser

Southampton Oceanography Centre, Southampton, United Kingdom

Abstract. The density distribution in the abyssal Atlantic Ocean suggests that mixing associated with overflows across deep sills may account for substantial amounts of deep mixing. Estimates of the strait mixing are made from published estimates of the overflows and the difference between Antarctic Bottom Water densities across the Vema Channel and the Romanche Fracture Zone to demonstrate that the strait mixing is an order of magnitude larger than the abyssal mixing estimated for a standard diffusivity of 1 x 10^{-4} m^2 s^{-1}.

Introduction

Recent discussions on the size of deep ocean mixing and whether it is done by boundary mixing over rough topography or by slow vertical diffusion appear to have neglected mixing in strait and sill regions and associated descending outflow plumes. Measurements of turbulent mixing in the ocean indicate mixing coefficients of order 0.1 x 10^{-4} m^2 s^{-1} in interior regions away from topography, 10 x 10^{-4} m^2 s^{-1} above rough bottom topography and 1000 x 10^{-4} m^2 s^{-1} in straits (Polzin *et al.* 1996, 1997). The widely accepted global average diffusivity of 1 x 10^{-4} m^2 s^{-1} (Munk and Wunsch, 1998) is then thought to be due to boundary mixing over 10% of the ocean underlain by rough topography. This work asks whether the global mixing might actually be accomplished by intense mixing over 0.1% of the ocean representing straits and sill and descending outflows.

Model

We consider here an ocean consisting of a series of deep basins separated by sills. The basins have smooth bottom topography and the entire ocean is initially filled with water of a single density, ρ. We begin to fill the ocean with a cold, dense deep water from the south perhaps being formed in the Antarctic at a rate Q_1, with a density ρ_1. For simplicity we assume initially that there is no interior mixing (Figure 1). The dense water fills up the basin behind the first sill until it reaches the crest of the sill when it begins to spill into the next basin. We expect that the height of the ρ_1 reservoir above sill depth will achieve a level sufficient that the flux Q_1 can flow over the sill in some kind of hydraulically controlled process and then there is "strait" mixing as the dense water plunges down into the next basin so that the dense water filling the next basin has density ρ_2, less dense than ρ_1 but more dense than ρ. The amount of water filling this second basin is proportionally larger than the original source of dense water, Q_1, by a factor of $(\rho_1 - \rho)/(\rho_2 - \rho)$ because of the mixing in of less dense water.

The second basin fills with dense water until the ρ_2 reservoir height reaches the height of the second sill and ρ_2 water begins to spill into the third basin, mixing as it descends as a density current to fill the third basin with slightly lesser density ρ_3 waters. When the reservoir in the third basin fills to the height of the third sill, water begins to spill over the sill and mix as it fills the fourth basin with again slightly less dense ρ_4 waters. Now we imagine the fourth basin represents the northern end of the ocean basin so it fills higher and higher with ρ_4 waters which then begin to flow back southward displacing the original low density waters up to the height of the shallowest sill. In this evolutionary process, the sill mixing and resulting basin densities would then be modified because the background density for the strait mixing would have changed. But if we consider this to be a steady state process the only change to the mixing is that we change the reservoir density from ρ to ρ_4. At the end of the process we have stratification that varies from basin to basin depending on the configuration of the sills; narrower sills would have stronger currents and more mixing in the descending outflow.

The motivation for this model comes from the observed distribution of density in the deep waters of the Atlantic Ocean (Figure 2). At the southern end of

the A16 section, Antarctic Bottom Water (AABW) piles up in the Argentine Basin behind the sill in Vema Channel at about 31°S. There is then a discontinuity in bottom water density between the Argentine Basin and the Brazil Basin as the AABW flowing through Vema Channel mixes as it descends and fills the Brazil Basin (Hogg *et al.* 1982). Similarly, at the equator, the modified AABW in the Brazil Basin piles up behind the sill in the Romanche Fracture Zone and then mixes as it flows over the sill and down into the eastern North Atlantic (Mercier and Speer, 1998). As a result, there is again a discontinuity in bottom water density between the Brazil Basin and the eastern North Atlantic. Finally, there appears to be a small discontinuity in bottom water density at 37.5°N where there is a sill at Discovery Gap (Saunders, 1987).

Amount of strait mixing

If Q is the flow over the sill, and $\Delta\rho$ the difference in density between the overflow (ρ_1) and the deep water filling the next basin (ρ_2), then the overall amount of mixing in the strait, sill and descending outflow regions, or, more precisely, the turbulent density flux across the ρ_2 isopycnal, can be estimated as $Q\Delta\rho$. A turbulent density flux across the ρ_2 isopycnal of strength $Q\Delta\rho$ is needed if the flow Q is to increase its density by $\Delta\rho$ (see the discussion of entrainment fluxes at the base of the surface mixed layer in Nurser *et al.* (1999)).

In the case of the Vema Channel, we can estimate $\Delta\rho$ to be 0.05 kg m^{-3} from Figure 4 in Tsuchiya *et al.* (1994) and Q to be 6.9 Sv from Hogg (2001). Thus, the amount of mixing in the Vema Channel overflow amounts to about 3 x 10^5 kg s^{-1}. For comparison, interior mixing using an average diffusivity of 1 x 10^{-4} m^2 s^{-1} over the abyssal Brazil Basin with an area of 3 x 10^6 km^2 where the vertical density gradient in the bottom water is 0.3 to 1 x 10^{-4} kg m^{-4} amounts to only 1 to 3 x 10^4 kg s^{-1}, an order of magnitude less than our estimate for the Vema Channel mixing.

For the flow through the Romanche Fracture Zone, we can estimate $\Delta\rho$ to be 0.12 kg m^{-3} from Figure 4 in Tsuchiya *et al.* (1992) and Q to be 1.22 Sv from Hogg (2001) so the amount of mixing, $Q\Delta\rho$, associated with the flow of AABW from the Brazil Basin to the eastern North Atlantic over the sill in the Romanche Fracture Zone is about 1.5 x 10^5 kg s^{-1}. The vertical density gradient in the abyssal eastern North Atlantic is 2 to 5 x 10^{-5} kg m^{-4}, so for a surface area of 8 x 10^6 km^2 from the equator to 30°N and a

standard diffusivity of 1 x 10^{-4} m^2 s^{-1}, the interior mixing in the abyssal eastern North Atlantic would amount to 1.6 to 4 x 10^4 kg s^{-1}, again an order of magnitude less than the mixing in the Romanche Fracture Zone overflow.

Discussion

Strait mixing can be considered to be a form of mixing over rough topography, but where the velocity is enhanced due to constriction by the strait.

Mixing may also be substantial for shallower straits such as the Strait of Gibraltar or Bab al Mandab. For the Strait of Gibraltar outflow of 0.7 Sv and a density difference between the "Mediterranean Waters" in the Mediterranean and in the North Atlantic of about 1.8 kg m^{-3}, the overall strait mixing can be estimated to be 1.3 x 10^5 kg s^{-1}, which again represents a substantial amount of mixing in the thermocline of the North Atlantic Ocean.

References

Hogg, N. G., 2001: Quantification of the deep circulation. In *Ocean Circulation and Climate*, G. Siedler, J. church and J. Gould eds., Academic Press, 259-270

Hogg, N.G., P. Biscaye, W. Gardner, and W.J. Schmitz Jr., 1982: On the transport and modification of Antarctic Bottom Water in the Vema Channel. *J. Mar. Res.,* 40(suppl.), 231-263.

Mercier, H., and K.G. Speer, 1998: Transport of bottom water in the Romanche Fracture Zone and the Chain Fracture Zone. *J. Phys. Oceanogr.,* 28, 779-790.

Munk, W., and C. Wunsch, 1998: Abyssal recipes II: energetics of tidal and wind mixing. *Deep-Sea Res.,* 45, 1977-2010.

Nurser, A.J.G., R. Marsh and R.G. Williams, 1999: Diagnosing water mass formation from air-sea fluxes and surface mixing. *J. Phys. Oceanogr.* 29(7): 1468-1487.

Polzin, K.L., K.G. Speer, J.M. Toole, and R.W. Schmitt, 1996: Intense mixing of Antarctic Bottom Water in the equatorial Atlantic Ocean. *Nature,* 380, 54-57.

Polzin, K.L., J.M. Toole, J.R., Ledwell, and R.W. Schmitt, 1997: Spatial variability of turbulent mixing in the Abyssal Ocean. *Science,* 276, 93-96.

Saunders, P.M., 1987: Flow through Discovery Gap. *J. Phys. Oceanogr.*, 17, 631-643.

Tsuchiya, M., L.D. Talley, and M.S. McCartney, 1992: An eastern Atlantic section from Iceland southward across the equator. *Deep-Sea Res.*, 45, 1977-2010.

Tsuchiya, M., L.D. Talley, and M.S. McCartney, 1994: Water mass distributions in the western Atlantic: a section from South Georgia Island (54°S) northward across the equator. *J. Mar. Res.*, 52, 55-81.
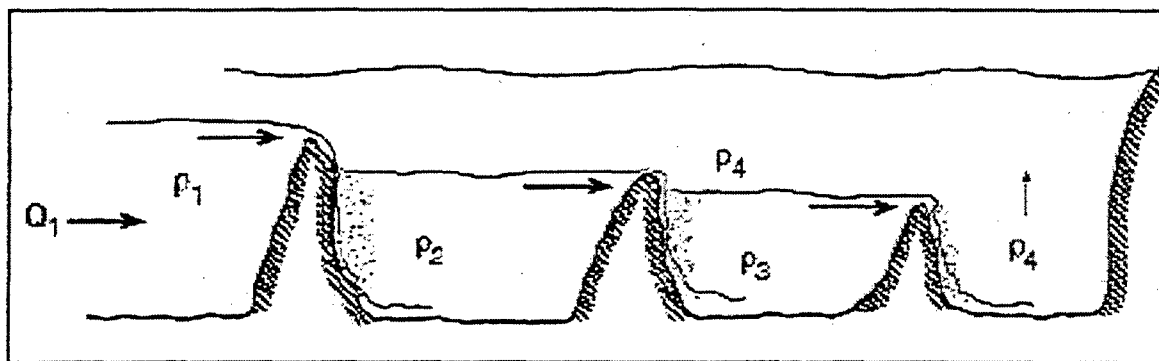
Figure 1 Schematic model for the effects of strait mixing on the properties of bottom water.
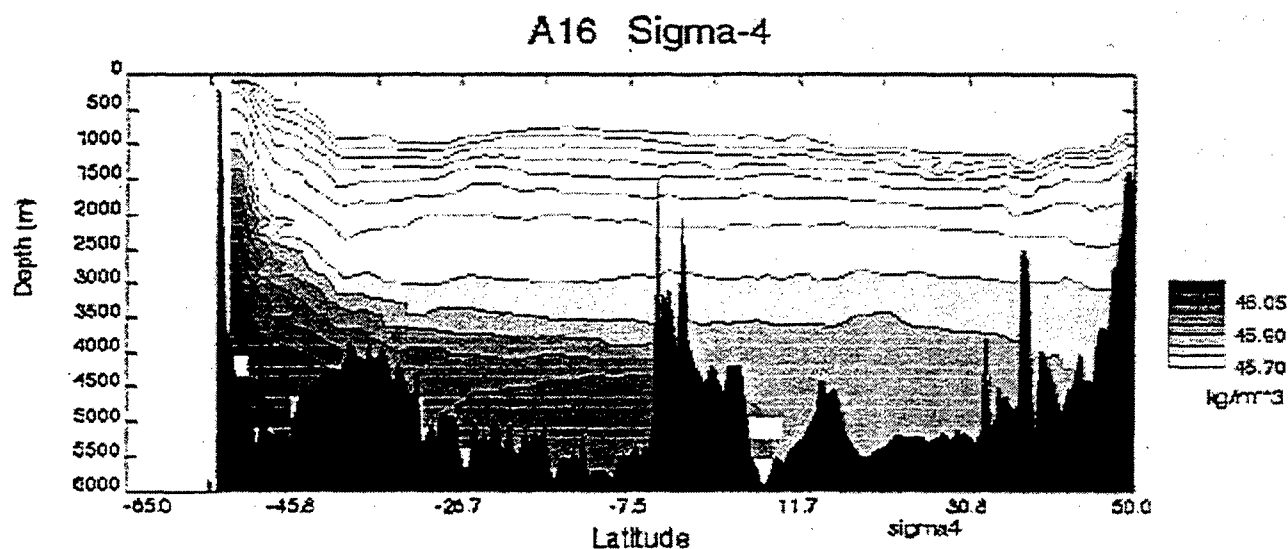
Figure 2. Meridional density distribution in the Atlantic Ocean

92

Friction and mixing in the Faroe Bank Channel outflow

L. M. Duncan, H. L. Bryden and S. A. Cunningham

Southampton Oceanography Centre, Southampton, UK

Abstract. Hydrographic sections made during *DISCOVERY* cruise 242, in September 1999, are used to study friction and mixing in the Faroe Bank Channel overflow. From bottom Ekman spirals we estimate bottom stress and relate it to overflow velocity with a drag coefficient of 0.5×10^{-3} and relate the height of the bottom Ekman layer to the bottom stress with a 'von Karman' constant of 0.75. In the region downstream of the sill, entrainment is initially maximum near the 0°C isotherm just above the cold dense outflow and turbulent diffusivities reach as high as $500 \text{cm}^2\text{s}^{-1}$. At 50km downstream of the sill the depth of maximum entrainment has moved upwards to the 2°C isotherm and turbulent diffusivity has decreased to $50 \text{cm}^2\text{s}^{-1}$.

Introduction

The Faroe Bank Channel is the deepest channel by which cold, dense Norwegian Sea water overflows into the Iceland Basin, eventually going on to form part of the North Atlantic Deep Water. With a maximum depth of 840m it has been estimated that 2 Sv of water overflows the Faroe Bank Channel sill with temperatures below three degrees (Saunders, 1990). Although the amount of overflow through the Faroe Bank Channel sill is well established, there are still questions regarding the amount of friction and entrainment taking place downstream from the sill. Understanding the physics of such descending outflow plumes is fundamental for improving the parameterisation of these processes in current numerical models. As part of the Atlantic-Norwegian Exchanges (ANE) cruise, in September 1999, a study was carried out on the outflow from the Faroe Bank Channel.

Figure 1. Bathymetry near the Faroe Bank Channel with hydrographic sections made during cruise RRS Discovery 242 (dots give station locations). Bathymetry is from the satellite derived bathymetry of Sandwell and Smith (1997).

Data

The ANE cruise took place, from 07 September 1999 to 06 October 1999, on board RRS *Discovery* as part of cruise D242. Five LADCP/CTD sections were made perpendicular to the bathymetry of the Faroe Bank Channel, in and downstream from the sill at horizontal separations between 15 and 40 km. These sections, completed within five days of each other, are shown in Figure 1.
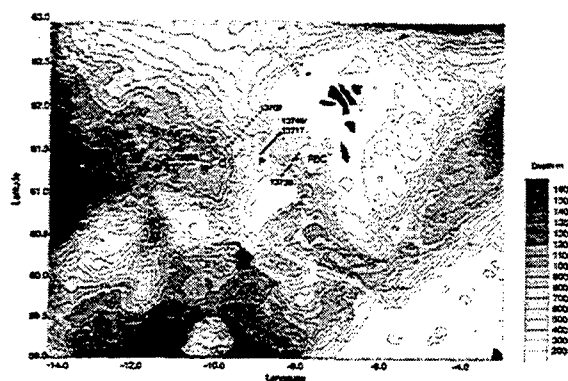
One section is a repeat of section P, the first section downstream from the sill. All the hydrographic stations used a Neil Brown Mark III CTD (Conductivity, Temperature and Depth). Water samples were collected using a 24 bottle rosette for calibration of the CTD conductivity and to enable chemistry observations. The Lowered Acoustic Doppler Current Profiler (LADCP) provided full depth direct velocity measurements. Current measurements were also made with an onboard

ADCP, which could measure currents to a depth of approximately 400 m.

We consider the three hydrographic sections; FBC, the second P section and section Q. Due to a beam failure on the LADCP during the first half of section P and all the Faroe Bank sill section, most of the current measurements were lost in these sections. In total 14 stations were occupied along section Q and 11 stations on the sections FBC and P. However only 10 stations make up our section P, as the LADCP data for the first shallowest station in this section are unretrievable.

Overflow characteristics

The LADCP measurements recorded profiles for the up and down casts. In the post cruise processing these profiles were averaged into five metre bins which were then combined together to produce one velocity-depth profile for each cast. These profiles were merged onto CTD depth, temperature, salinity and potential temperature and rotated into along track and across track velocities. The rotations were 136°, 144° and 137° for section Q, FBC and P respectively. Velocity and potential temperature contours are shown in Figure 2. Positive velocities indicate north westward flow.

Within the Faroe Bank Channel section the core is seen at a depth of 550 to 800 m. The outflow, water colder than 3°C, at this point is confined by the channel bathymetry which keeps the core width at approximately ten kilometres. Most of the outflow has a temperature below 0°C, with maximum velocities up to 70 cms^{-1}. The overflow has salinities less than 34.95 and densities greater than 28.1kgm^{-3}. Further downstream at section P, the core is seen banked up on the northern slope as expected for geostrophic flow, but the overflow has deepened by 50 metres to depths of 600 to 850 metres. Overflow water is still confined within the channel, allowing the width to increase only slightly. Between the Faroe Bank Channel section and section P, the quantity of water with temperatures below 0°C has dropped by almost half indicating mixing and entrainment have taken place with the warmer, saltier water above. The maximum velocities in section P are faster by 10 cms^{-1}, at 80 cms^{-1}, than in the channel. Finally, reaching section Q, the outflow core has increased its maximum speed to 90 cms^{-1} and increased its depth to 650 to 950 metres. The width of the outflow has also doubled to 30

kilometers since section P. This increase follows from the unbounded bathymetry of section Q. The core is still seen banked up on the northern slope in this final section. Transport of waters colder than 0°C in section Q is less than section P.
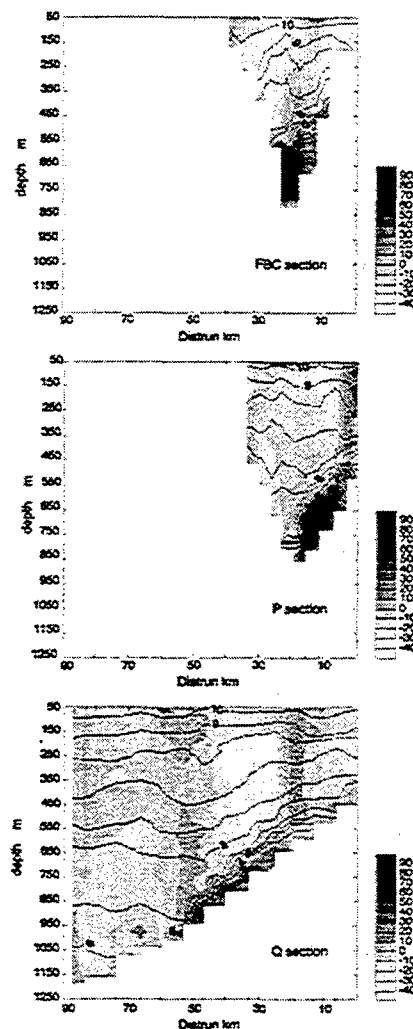

Figure 2. Velocity (cm/s) and Temperature (°C) contours of CTD/LADCP sections FBC, P and Q.

Friction

An important process on an outflow plume is the amount of bottom friction. In the bottom layer, the outflow is acted on by bottom stresses which create an Ekman layer and associated cross channel flow. To determine the amount of bottom stress in the

bottom Ekman layer, our velocity profiles were first extended to reach as close to the bottom as possible.

In the usual LADCP processing, velocity profiles are clipped near the bottom due to the possibility of contaminated signals from bottom echos. The amount of clipping depends on the angle of the LADCP beam. In our processing we do not clip the velocity data so as to extend our profiles as deep as possible.

The bottom Ekman layer appears in velocity profiles as a spiral, like that shown in Figure 3, for station 13707 from section Q. In order to determine the amount of bottom friction, the near bottom LADCP measurements for stations across FBC, P and Q were used. Spirals, like Figure 3, are only seen in fast velocity stations, but estimates of bottom friction were made for all stations in each section. Before using the newly extended velocity profiles for stress calculations, the profiles in strong currents were first carefully compared with VMADCP and bottom tracking from LADCP profiles to choose a single barotropic velocity adjustment for each profile.
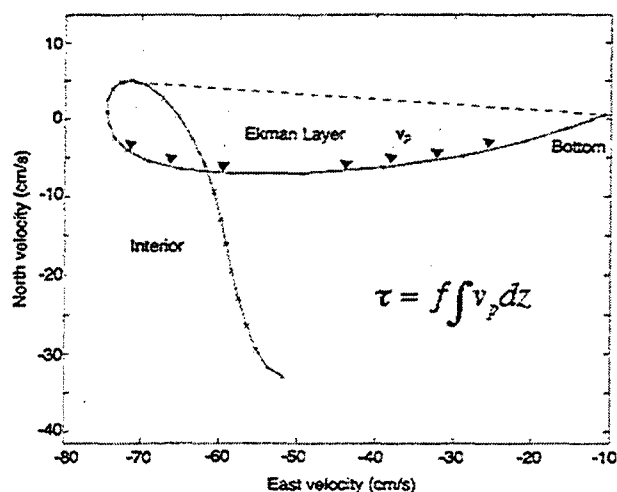
Figure 3. An Ekman spiral seen from LADCP data on station 707 in section Q.

The bottom Ekman layer is a region of non constant stress. Determination of bottom friction in this non constant stress region can be made by estimating the flow perpendicular to the principal orientation of the plume velocity. (The principal orientation of the flow is the direction the flow would have if there was no bottom friction effects). The

dashed line in Figure 3 shows the principal orientation of the flow for station 13707 and the light arrows indicate the perpendicular flow, v_p. Vertical integration of this perpendicular velocity, v_p, provides estimates of bottom stress, τ.

In calculating bottom friction, we determined the principal plume direction from hodographs of northward and eastward velocity. The direction of the principal plume was taken as the direction between the bottom most velocity point and the point of maximum speed. Maximum speed occurs at the end of the spiral and hence the top of the Ekman layer.
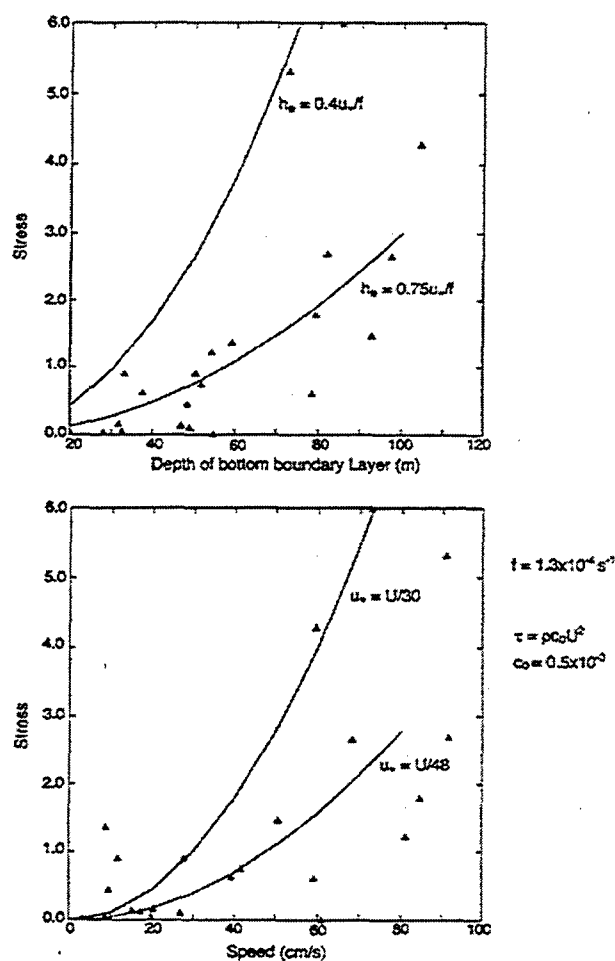

Figure 4. Relationship between properties in the bottom Ekman Layer.

Relationships in the bottom Ekman layer

A discussion of bottom boundary layers in Armi (1977) utilises theories of a turbulent Ekman layer on a flat bottom to determine Ekman layer height. We use the relations given in Armi to see how well our results compare with standard predictions (Figure 4).

Armi's paper relates the properties, friction velocity, u_*, Coriolis parameter, f, maximum speed, U and height of the turbulent Ekman layer, h_e, as given in Figure 4. Using the estimates of these properties from all our LADCP sections where the frictional stress is positive and taking f to be 1.3×10^{-4} sec^{-1} our results agree reasonably well with Armi. In particular, we examine the relations between the height of the Ekman layer and the bottom stress: $h_e = ku^*/f$ where $u^* = (\tau/\rho)^{1/2}$ and k is von Karman constant, and between the stress and the speed of the outflow: $\tau = \rho c_D U^2$ where c_D is the drag coefficient.

Higher stress values are related both to higher Ekman speeds and deeper Ekman layers. Plotting stress versus Ekman layer height (Figure 4a) we find the best fit is for a k of 0.75 compared with a standard value of 0.4. Plotting stress versus outflow speed (Figure 4b) we find the best fit is for a c_D of 0.47×10^{-3} compared with a standard value of 2.5×10^{-3}.

Mixing

The amount of mixing taking place along the path of the Faroe Bank Channel overflow can be considered through the changes in transport for different temperature classes. To obtain transport estimates for a particular section, the five meter bin averaged LADCP velocities at each station are multiplied by half the distance to the adjacent stations, each side, at the same depth. For the two outer most stations at the end of each section, only half the distance to its only adjoining station is used. Near the bottom some stations extend deeper than their neighbouring stations. To account for this, linear interpolation between the bottom depth of neighbouring stations is used to calculate areas in this region. Matching the LADCP depth with the CTD depth, we use the CTD potential temperature to divide transports into temperature classes. These are shown in Figure 5 for temperature classes below 0°C, 1°C, to below 5°C.

Figure 5 shows the amount of transport below each temperature class decreasing as the distance downstream from the sill increases. Transport below the three degree isotherm declines from 1.60 Sv to 1.24 Sv between the FBC section and Q section. Following a transport of 1.60 Sv from the FBC section downstream we find that by section Q this same transport accounts for all water below 5 °C.

Turbulent diffusion rates

The amount of mixing occurring along the Faroe Bank Channel outflow path can be seen by estimating the turbulent diffusion rates across isotherms between each of our sections. Initially we determine the height of each isotherm, from 0°C to 5°C, by averaging the height of individual isotherms on all stations making up each section. Combining these to give an average height for the section, the downward slope of each isotherm could be seen along the outflow path (Figure 5). The isotherm slope does not approach zero until we reach the 8°C isotherm. Using these estimates and the overflow transport between each isotherm, we build a picture of changes in transport (Figure 5). A certain amount of cold Norwegian sea water crosses the Faroe Bank Channel, but due to a lesser amount of this same temperature water crossing at section P or Q, means some water has crossed the isotherm above. Each of these amounts is indicated in Figure 5 by the light upward arrow. From these changes in transport below a given isotherm, turbulent diffusion rates can be determined using

$$Q_{in}T_{in} + Q_{out}T_{out} + \left(Q_{in} - Q_{out}\right)N°C + K\frac{\partial T}{\partial z} \times \Delta x \Delta y = 0$$

where the vertical temperature gradient is calculated at the N degree isotherm and $\Delta x \Delta y$ is the area between the sections. The temperature gradient is determined by taking the temperature difference between the neighbouring isotherms divided by the difference in height between them. For the zero degree isotherm, the difference between the -0.15°C and one degree isotherm is used while all others are based on a difference over two degrees. The distance downstream between sections is determined using
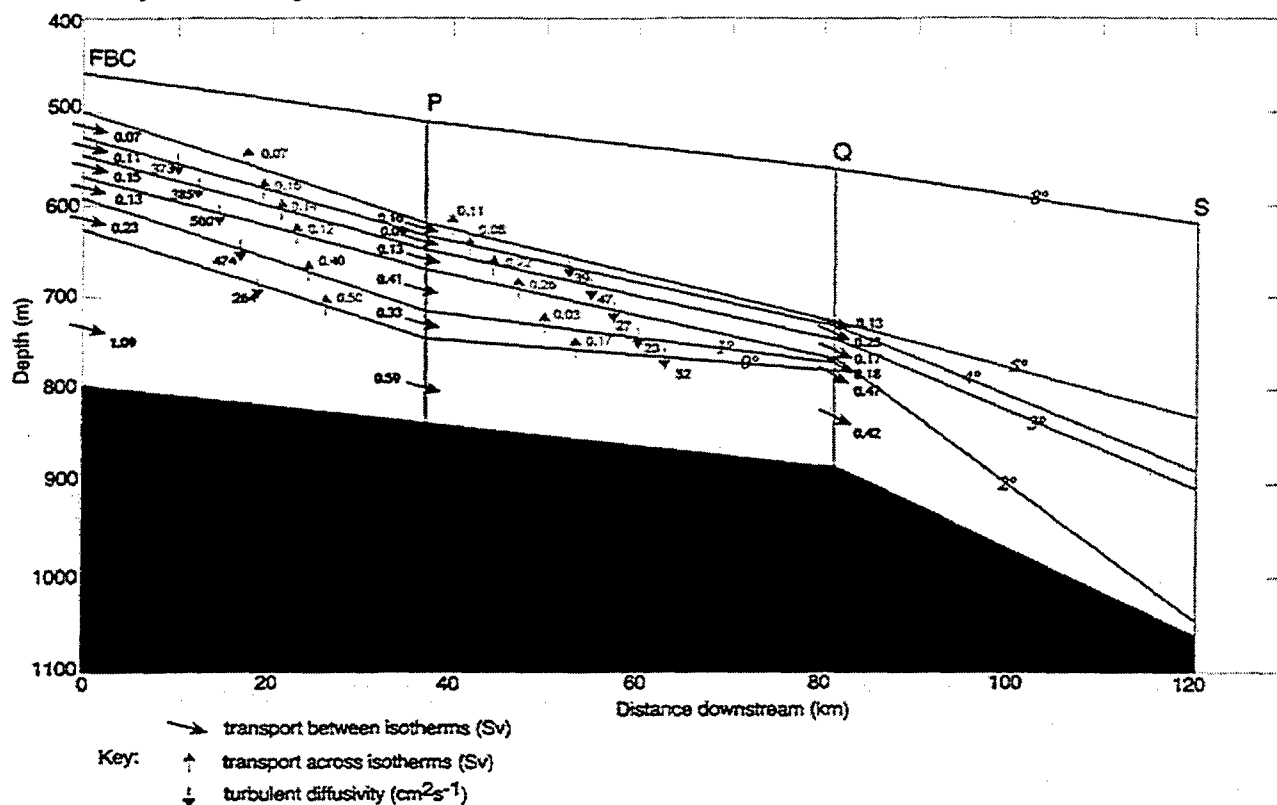
Figure 5. Schematic of entrainment in the Faroe Bank Channel outflow.

station positions where the average zero degree isotherm height most closely matches the station. The resulting estimates of K are indicated by the darker downward arrows in Figure 5.

According to our calculations, most mixing takes place between sections FBC and P with diffusion rates as high as 500 cm^2s^{-1}. Further downstream between sections P and Q, rates decrease to about $30cm^2s^{-1}$.

Conclusions

Results indicate high friction and entrainment in the Faroe Bank Channel. Work is still in progress and we hope to use our findings to improve numerical models in this region.

References

Armi, L, The dynamics of the bottom boundary layer of the deep ocean, *Proc. Of the 8th Int. Liège Colloq. On Ocean Hydrodynamics*, 1977.

Baringer, M. O., and J. Price, Mixing and Spreading of the Mediterranean Outflow, *J. Phys. Oceanogr.*, 27, 1654-1677, 1997.

Cunningham, S. A., Atlantic-Norwegian Exchanges, RRS *Discovery* 242. SOC Cruise Report No. 28, 2000.

Killworth, P. D., On the rate of descent of overflows, submitted to *J. Fluid Mech.*, 2000.

Sandwell, D. T., and W. H. F. Smith, Marine gravity anomalies from Geosat and ERS 1 satellite altimeters, *J. Geophys. Res.*, 102(B5), 10039-10054, 1997.

Saunders, P. M., Cold Outflow from the Faroe Bank Channel, *J. Phys. Oceanogr.*, 20, 29-43, 1990.

Saunders, P. M., The Dense northern overflows In: Ocean Circulation and Climate: Observing and Modelling the Global Ocean, 401-417, 2001.

Subinertial and seasonal variability in the Strait of Gibraltar from CANIGO observations

J. García Lafuente, J. M. Vargas, J. Delgado and F. Criado

Departamento de Física Aplicada, Universidad de Málaga, Málaga, Spain

Abstract. Observations taken at the eastern exit of the Strait of Gibraltar during CANIGO project have been processed to estimate variable inflow, outflow and net flow. A summary of the results concerning subinertial and seasonal variability is presented in this work. Observed flows confirm that atmospheric forcing and seasonal heating-cooling of surface waters, respectively, are the driving forces for flow variability in those frequency bands. The analysis of inflow, outflow and interface depth time series provides insights into the internal dynamics of the Strait.

Introduction

The Strait of Gibraltar, connecting the Atlantic Ocean with the Mediterranean Sea through a rather complicated system of sills and narrows, is the scenario of a well-studied baroclinic exchange driven by the net evaporative losses in the Mediterranean Sea. A long term averaged net flow of the order of Q_0^- =0.05 Sv is necessary to compensate for the evaporation in the Mediterranean. This averaged net flow is the difference of two quantities Q_1^- and Q_2^-, the inflow and outflow, respectively, which are one order of magnitude greater.

This baroclinic exchange has been often compared with the predictions of the two-layer hydraulic theory (Farmer and Armi, 1986). Many works based on this theory have been published since, focussing mainly on Camarinal sill cross section. However, Bormans and Garrett (1989) showed that the eastern section of the Strait of Gibraltar is equally interesting to investigate the exchange (to elucidate the question of whether or not the exchange is maximal) and the interface oscillations at this section a potential tool to do it.

Flow variability has been properly classified into tidal, subinertial, seasonal and long term or interannual. Tidal signal is typically three to four times greater than the mean exchange Q_1^- and Q_2^-, causing flow reversals in some places of the Strait at certain periods of the tidal cycle (Bryden et al., 1994; Garcia Lafuente et al., 2000). The interface of null along-strait velocity makes no sense in this case. On

the contrary, subinertial velocities only reverse in exceptional situations of extreme meteorological forcing which may last 3 or 4 days at most. In these rare cases the problem of the interface definition is
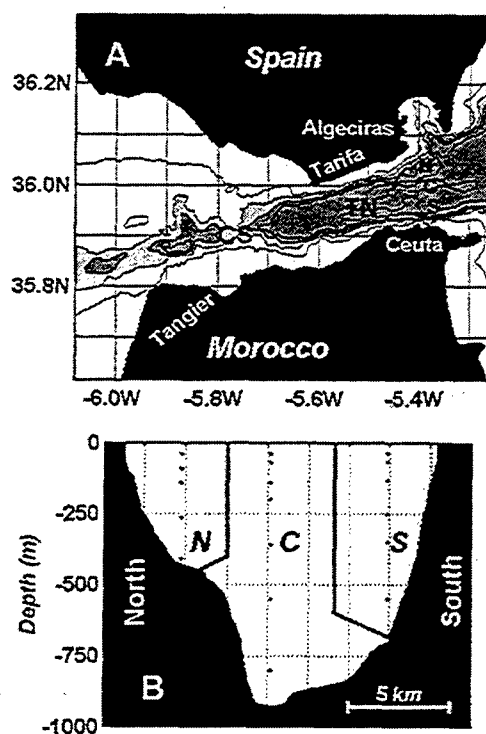

Figure 1. Map of the Strait of Gibraltar showing the main topographic features of Camarinal Sill (CS) and Tarifa Narrows (TN) as well as the location of the mooring lines. Lower panel shows the depths of sampling at the three mooring sites.

faced again, though these unusual events could be considered as brief events of arrested inflow or outflow. Seasonal and interannual fluctuations are always too weak to reverse flows and the interface of null velocity is well-defined (Garcia Lafuente *et al.* 2002a). Thus, this interface is appropriate to carry out the analysis of the two-way exchange at subinertial frequencies and will be used in this paper. Next two Sections show results concerning seasonal and subinertial variability, respectively. Most of this work focus on the response of the interface depth to the barotropic fluctuations, which are compared with the predictions of a simple two layer model based on the aforementioned work of Bormans and Garrett (1989), which has been further explored in Delgado *et al.* (2001).

Figure 1 shows the map of the Strait and the depths of sampling in the eastern section. A description of the data set, data processing and flows computation can be found in Garcia Lafuente *et al.*, (2002a,b) for low frequency (seasonal) and atmospherically forced (subinertial) fluctuations and is not presented here.
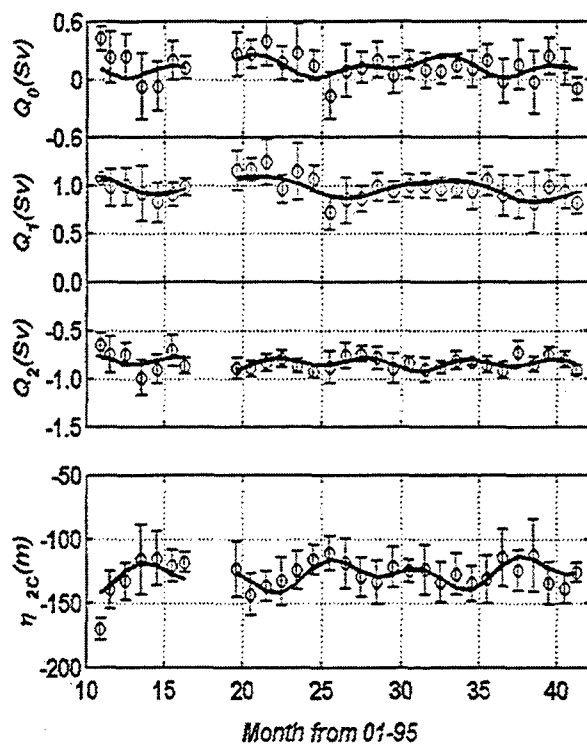
Figure 2. From top to bottom: Net flow (dots) and standard deviation of the fifteen-days mean (bars). Solid line is the mean square fit of the data to a model that includes annual and semiannual signals. The following three panels show the same information for inflow, outflow and the interface depth.

Seasonal variability

The data set used to analyze the seasonal variability covers the period from October 1995 to May 1998. The procedure to estimate the flows is explained in Garcia Lafuente *et al.* (2002a). Fifteen-days average of daily data has been carried out in order to remove meteorologically forced variability, which is dealt with in next Section. Figure 2 shows that the annual signal prevails in the inflow while semiannual contribution is important in the outflow and interface depth. The net flow annual signal would be a consequence of the important annual cycle of the inflow, whose phase, in turns, strongly suggest a close relationship to the annual cycle of solar heating.

Net flow signal is compatible with the observed sea level seasonal cycle in the Mediterranean Sea after removing the steric effect (Garcia Lafuente *et al.* 2002a). More intriguing is the clear semiannual signals of the outflow and interface depth that are linked to each other. It might be related to the presence/absence of the Western Alboran gyre, whose size and depth changes throughout the year, if the exchange through the Strait were submaximal. To this respect, we present in Figure 3 the relationship between net flow and interface depth fluctuations. We will discuss this Figure later.
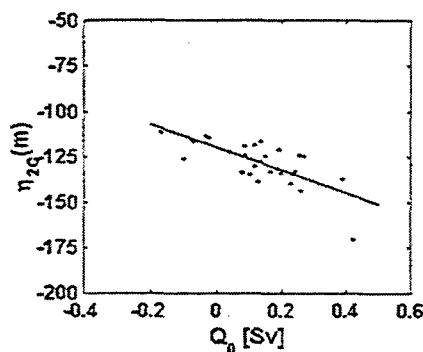

Figure 3. Scattering plot of interface depth against net flow. The solid line (slope = -62 ±11 m/Sv) is the mean square fit of the data (r=-0.72).

Subinertial variability

Figures 4 and 5 show similar information as Figures 2 and 3 for the meteorologically induced subinertial flow. The period of observations in this analysis spans from October 1997 to May 1998 and the data come from the central mooring ("C" in

Figure 1). Details of data processing can be seen in Garcia Lafuente *et al.* (2002b).

The net barotropic flow has been compared with the hindcast provided by the barotropic model NIVMAR (Álvarez Fanjul *et al.*, 2001) used by Puertos del Estado, Spain to forecast sea level around Spain. The model domain covers the Mediterranean Sea and a large part of the Atlantic Ocean and is forced by the diagnosed wind and atmospheric pressure fields provided by HIRLAM application run by Instituto Meteorologico Nacional (Spain). The correlation between observed and hindcast flow (top panel of Figure 4) is above 0.8, and improves by more than 20% the prediction of the widely used analytical model of Candela *et al.* (1989). As in the case of seasonal variability, inflow contributes more than outflow to the fluctuations of the net barotropic flow. Both contributions have the same sign (middle panels of Figure 4), meaning that positive fluctuations of the net flow are achieved by inflow increase and simultaneous outflow decrease.
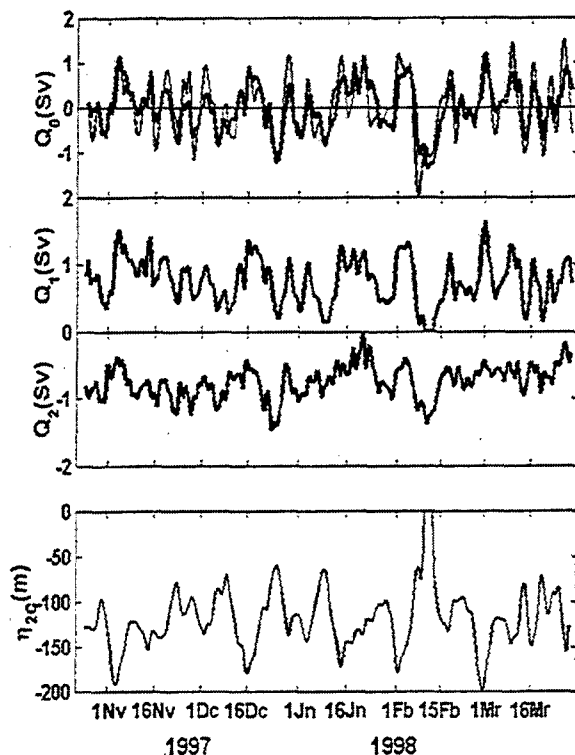
Figure 5 shows the scatter diagram of the depth of the interface against the net barotropic fluctuation, in the same manner as Figure 3 does for seasonal signals. Points are well aligned along the straight line, which is the least-square fit of the data points.
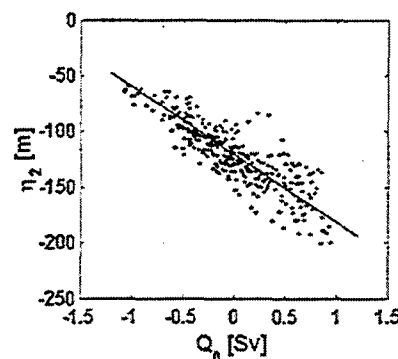

Figure 5. Plot of interface depth against net flow for subinertial fluctuations. Solid line is the mean square fit of the data. Numerical values of the slope (-60 ± 2 m/Sv) and the regression coefficient ($r=-0.85$) are similar to those of seasonal flow.

A simple numerical model

Two layer theory states that under maximal exchange and moderate barotropic fluctuations in the sense defined by Farmer and Armi (1986), inflow and outflow contribute very approximately the same to the net barotropic fluctuation. Figures 2 and 4 indicate that inflow fluctuations are more important than outflow fluctuations. The simple 1-D model put forward by Bormans and Garrett (1989) makes theoretical predictions of interface oscillations, assuming hydraulic control in Camarinal Sill (see Figure 1). The validity of this assumption is supported by the fact that Mediterranean outflow is much less buoyant than Atlantic water at the same depth and therefore it cascades down to around one thousand meters depth in the Atlantic Ocean. The second control in Tarifa Narrows may or may not exist, giving rise to maximal exchange with supercritical flow downstream the contraction or submaximal exchange with subcritical flow downstream, respectively. Both solutions bifurcates in the so-called marginally submaximal exchange that provides the same exchanged flows as the maximal solution but differs from it in the way the interface downstream of the contraction behaves. Thus,

Figure 4. From top to bottom: Net flow computed from the data (thick line) and flow predicted by the barotropic model (thin line). Middle panels are inflow and outflow fluctuations, respectively, and bottom panel is the interface oscillation.

interface oscillations at the eastern section of the Strait provide information about the state of the exchange.

Bormans and Garrett (1989) only considered maximal and marginally submaximal situations. In both cases the control section at Tarifa Narrows is present and the exchanged flows are fully determined, providing that Strait's geometry and flows density are known. The predicted response of the interface at the eastern section (where observations were taken) to the barotropic fluctuations computed in Delgado *et al.* (2001) is shown in Figure 6.
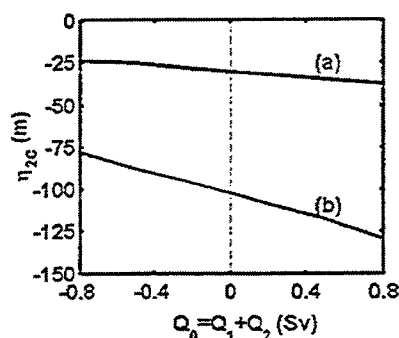
Figure 6. Predicted response of the interface to barotropic flow fluctuations. Case (a) is for maximal exchange (slope −9 m/Sv) and case (b) is for marginally submaximal (slope −32 m/Sv).

Strictly submaximal exchange has also been explored in Delgado *et al.* (2001), extending Bormans and Garrett's (1989) model. The problem has a new degree of freedom (no control in Tarifa Narrows) and cannot be solved unless an additional condition is prescribed. This agrees with the well-known fact that there is a unique maximal solution but infinite submaximal solutions. With control in Camarinal Sill, interface oscillations are closely bound to outflow fluctuations (Delgado *et al.* 2001, Garcia Lafuente *et al.* 2002a) and are even larger than what Figure 6 shows for the marginally submaximal case. Regarding interface oscillations, which are good references for the state of the exchange in the two-layer inviscid models, CANIGO observations suggest submaximal exchange. The mean depth of the interface shown in Figures 3 and 5 is also much higher than the predicted depth in case of maximal exchange (see Figure 6-a), supporting the submaximal exchange solution as well.

References

Álvarez Fanjul, E., B. Pérez, and I. Rodríguez Sánchez-Arévalo, NIVMAR: A storm-surge forecasting system for Spanish waters. *Scientia Marina,* 60, 145-154, 2001.

Bormans, M. and C. Garrett, The effects of non-rectangular cross-section, friction and barotropic fluctuations on the exchange through the Strait of Gibraltar. *J. Phys. Oceanogr.*, 19, 1543-1557, 1989.

Bryden, H.L., J. Candela, and T.H. Kinder, Exchange through the Strait of Gibraltar, *Prog. Oceanogr.*, 33, 201-248, 1994.

Candela, J., C.D. Winant, and H.L. Bryden, Meteorologically forced subinertial flows through the Strait of Gibraltar, *J. Geophys. Res.*, 94, 12667-12674, 1989.

Delgado, J., J. Garcia Lafuente, and J.M. Vargas, A model for submaximal exchange through the Strait of Gibraltar, *Scientia Marina,* 65, 313-322, 2001.

Farmer, D. M., and L. Armi, Maximal two-layer exchange over a sill and through the combination of a sill and contraction with barotropic flow, *J. Fluid Mech.*, 164, 53-76, 1986.

Garcia Lafuente, J., J.M. Vargas, J. Candela, B. Bascheck, F. Plaza and T. Sarhan, The tide at the eastern section of the Strait of Gibraltar, *J. Geophys. Res.*, 105, C6, 14197-14213, 2000.

Garcia Lafuente, J., J. Delgado, J.M. Vargas, M. Vargas, F. Plaza and T. Sarhan, Low frequency variability of the exchanged flows through the Strait of Gibraltar during CANIGO, *Deep Sea Res.* (in press), 2002a.

Garcia Lafuente, J., E. Alvarez, J.M. Vargas, Subinertial variability in the flow through the Strait of Gibraltar, *J. Geophys. Res.* (submitted), 2002b.

The Sicily Strait dynamics: A sensitivity study with a high resolution numerical model

L. Gervasio, L. Mortier and M. Crépon

LODYC, University P. et M. Curie, BC 100, 4 place Jussieu, 75252 Paris cedex 05, France

Abstract. Using a primitive equation numerical model we show, in agreement with a previous theoretical study, that topographic constraint is the essential mechanism explaining the separation of the Algerian current at the Sicily Strait.

Introduction

In situ and satellite observations show that the Algerian current separates into two branches at the Sicily Strait: one is flowing into the Eastern Mediterranean, the other into the Tyrrhenian Sea (Lermussiaux and Robinson, 2001, Astraldi *et al.*, 1999, Herbaut *et al.*, 1998). A sensitivity study was performed with a high-resolution primitive equation model (3.7 km x 4 km, 31 levels in the vertical) of the Sicily Strait region to understand the mechanisms governing the surface and deep circulation in the Strait of Sicily. This resolution allows us to model the two deep (450 m for the south channel and 625 m for the north channel) and narrow (20 km) channels whose correct representation is essential for the transport of the deep LIW flow. The present study can be considered as complementary to the study of Herbaut *et al.* (1998) who investigated the response to the density gradient forcing through the Straits of Gibraltar and Sicily using simplified theoretical and numerical models.

The experiments

The numerical simulations were performed with the LODYC finite difference primitive equation model as in Speich *et al.* (1996). The modeled domain covers the central part of the Mediterranean, encompassing the Strait of Sicily. The Algerian current is generated by the dam breaking procedure as in Speich *et al.* (1996) and Herbaut *et al.* (1998).

Analysis of the experiments

We first ran three experiments denoted S1, S2 and S3 with different topography where the density is constant and equal to 1029 except in the MAW. The MAW density is 1028. At the Tunisian coast, the MAW depth is about 150 m, its surface offshore extension is 50 km and its transport is 2 Sv.

- Flat bottom experiment (S1).

In the S1 experiment, the bottom is flat and the depth constant (1000 m) everywhere. As soon as the gate of the basin filled with MAW is removed, one notices the formation of a baroclinic Kelvin front propagating along the Algerian coast at a speed of about 0.5 ms-1. This front is linked to the advection of MAW. When arriving at the Sicily strait level, the Kelvin wave front passes through the strait and continues to propagate along the African coast forming a baroclinic coastal jet. After one month, the circulation is stabilized (Figure 1a). One notes that no MAW crosses the Sicily strait and flows along the Northern coast of Sicily. The surface current then becomes unstable generating large anticyclonic eddies which drift westwards which can be interpreted as generated by the conservation of momentum according to the theory of Pichevin and Nof (1997).

PARAMETERS	EXPERIMENTS					
	S1	S2	S3	S4	S5	S6
flat bottom, no sill	Y					
flat bottom + step like sill		Y				
Realistic topography			Y	Y	Y	Y
Homogeneous stratification	Y	Y	Y			
Realistic Stratification				Y	Y	Y
Wind					Y	
Ionian Water						Y

Table 1. Characteristic of the six experiments.

— Step like sill experiment (S2).

In the S2 experiment, the Tyrrhenian Sea is flat; its depth is of 1000 m. The Sicily strait sill is modeled by a step whose upper level is at 200 m below the sea surface. The depth of the Ionian basin is set at 200 m. When arriving at the Sicily strait level, the current advecting the MAW separates into two branches; one passes through the strait and flows along the Tunisian coast advecting part of the MAW into the Eastern basin, the other crosses the strait and flows along the Northern coast of Sicily, advecting part of MAW into the Tyrrhenian Sea (Figure 1b). This experiment is in agreement with the results of Herbaut *et al.* (1998) showing that the topography of the sill controls the surface circulation in the strait.

— Realistic bottom topography experiment (S3).

In the S3 experiment, we use a real topography obtained from IBMC (International Bathymetric Chart of the Mediterranean). The fine grid mesh allows us to correctly represent the two deep channels which are in the middle of the Sicily strait. As the topography is realistic, the Algerian current is trapped by the shelf topography rather than by the coast as in S2. Its pattern is quite different from this of the above experiments (Figure 1c). At the Sicily strait level, the current divides into two branches, one passing through the strait, the other one crossing it and flowing along the Northern coast of Sicily. We clearly see the advection of MAW flowing as a coastal jet along the Northern Sicily coast. The branch passing through the strait is trapped by the Tunisian shelf topography, meanders in the middle of the strait and enters the Eastern Mediterranean without flowing along the Southern Sicily coast.

— Realistic stratification experiment (S4).

We also ran an experiment S4 with the real topography used in S3 but with realistic stratification for the Tyrrhenian Sea, the western part of the Eastern Mediterranean (Ionian Sea) and the MAW. The stratification was obtained by averaging MODB data (Brasseur *et al.*, 1996).

The coastal current is forced as in the previous experiments by now filling the adjacent basin with waters having a MAW profile. By looking at the spin up phase, we notice that the currents at surface, and at depth, are negligible in the strait before the arrival of MAW. The surface circulation (Figure 2a, left) is very similar to this observed in experiment S3. The arrival of the MAW at the strait level generates deep

LIW currents flowing into the Tyrrhenian Sea through the two deep channels (Figure 2a, right). LIW is advected in form of a baroclinic coastal current trapped at the coast and progressing along the Northern coast of Sicily.

We have also investigated two potential mechanisms for explaining the presence of an eastwards current flowing along the Southern Sicily coast and penetrating into the Eastern Mediterranean.

— Effect of wind (S5).

We ran an experiment identical to S4 during 48 days and then we added a constant 10 ms^{-1} wind blowing from North-West. After 12 days (day 60 of the experiment) we observe a noticeable current flowing eastwards along the Southern Sicily coast (Figure 2b, left). Its transport is about 0.15 Sv. A strong upwelling is generated along the Southern Sicily coast.

It is concluded that the wind is a potential candidate for explaining the presence of a current flowing eastwards along the Southern Sicily coast and the presence of the Southern Sicily coast upwelling as often observed (Lermussiaux and Robinson, 2001).

The LIW transport is now 1.3 Sv. This value is higher than that found during S4 can be interpreted by the fact that the wind generates a slight Eastward transport through the strait in addition to this due the MAW advection. The increase of LIW transport compensates the mass transport due the wind.

— Ionian water effect (S6).

The water of the Ionian basin is somewhat denser than this of the Malta basin and may have an impact on the circulation of the strait. In order to investigate this effect we ran an experiment similar to S4 where we added a source of Ionian water in the North-East region of Sicily. This reservoir is open at initial time. After 10 days we notice the presence of a strong eastward coastal current flowing along the Southern coast of Sicily (Figure 2c, left). The responsible mechanism is similar to this described in Herbaut *et al.* (1998) and explaining the separation of the MAW in the Sicily strait but in a mirror situation.

The transport associated to this current flowing along the south Sicily coast is of the order of 0.3 Sv. It may drive some MAW penetrating in the Eastern Mediterranean. It is associated to upward isopycnal slopes which are less intense than in experiment S5.

Discussion and conclusion

The above experiments allow us to clarify our understanding of the functioning of the Sicily strait. The major outcomes of our study are the following:

- We found that the topography controls the circulation at the strait level. The shallower the sill depth, the more intense the separation. When comparing experiments S2 and S3 it is found that the real topography enhances the separation of the Algerian current; this is probably due to the large variety of topographic waves occurring in the case of real topography and helping the current to follow the sill and consequently to cross the strait. Besides, the current crossing the strait does not feel the small scale features of the topography like the two deep channels: it is only sensitive to large scale topographic features of the order of the width of the strait which are shallow in the present case.

- The LIW flows into the Tyrrhenian through the two deep channels located in the middle of the strait and then turns right following the Northern coast of Sicily (Figure 2, left). At 350 m in the two deep channels of the strait, we observe a velocity between 10 and 15 cms-1. This supports the description of Millot *et al.* (1999) and Astraldi *et al.* (1999).

- When looking at the spin-up phase of S4, we see that the currents at the strait level are negligible until the arrival of the MAW. The small density gradient between the Tyrrhenian Sea and the Malta basin is unable to generate a noticeable current at depth or at surface. When the MAW penetrates the strait, the continuity equation implies an outflow of LIW at depth. We can thus state that the Sicily strait circulation is mainly controlled by the density gradient between the Atlantic and the Mediterranean rather than the along Sicily strait density gradient.

- In the S4 experiment, the ratio of the surface transport passing through the strait versus that crossing it is close to the observed value.

- Two mechanisms were investigated for explaining the current along the Southern Sicily coast. First we showed that a north-west wind (S5) is able to generate such a current and the associated upwelling observed on infra red satellite images (Astraldi *et al.*, 1996). Second the presence of an Ionian water denser than that of the Malta basin is also a good candidate for driving such a current (S6). The latter current is more stable than the former. The transport of the S6 current is twice this of S5 experiment, but the S5 upwelling is more intense than that due to the upwards slope of the isopycnes associated with the S6 current. In fact both processes may contribute to generate the South Sicily current. When looking at hydrographic sections perpendicular to the coast both in in-situ observations (Astraldi *et al.*, 1999) and in the numerical experiments, it does not seem that this coastal current advects a significant quantity of MAW.

References

Astraldi M., Balopoulos S., Candela J., Font J., Gacic M., Gasparini G. P., Manca B., Theocharis A., and Tintoré J., (1999): The role of straits and Channels in Understanding the characteristics of the Mediterranean circulation. *Progress on Oceano.*, 44 (1-3), 65-108.

Herbaut C., Codron F., and Crepon M., (1998): Separation of a Coastal Current at a Strait Level: Case of the Strait of Sicily. *J. Phys. Oceanogr.*, 28,.1346-1362.

Lermussiaux P. F. J., and Robinson A. R., (2001): Features of dominant mesoscale variability, circulation patterns and dynamics in the Strait of Sicily. *Deep Sea Res.*, I 48, 1953-1997

Millot C., (1999): Circulation in the Western Mediterranean Sea. *J. Mar. Systems*, 20, 1-4, 423-442.

Speich S, Madec G., and Crepon M., (1996): A process study on a strait outflow circulation: The case of the Alboran Sea. *J.Physc.Oceanogr.*, 26, 3, 320-340.

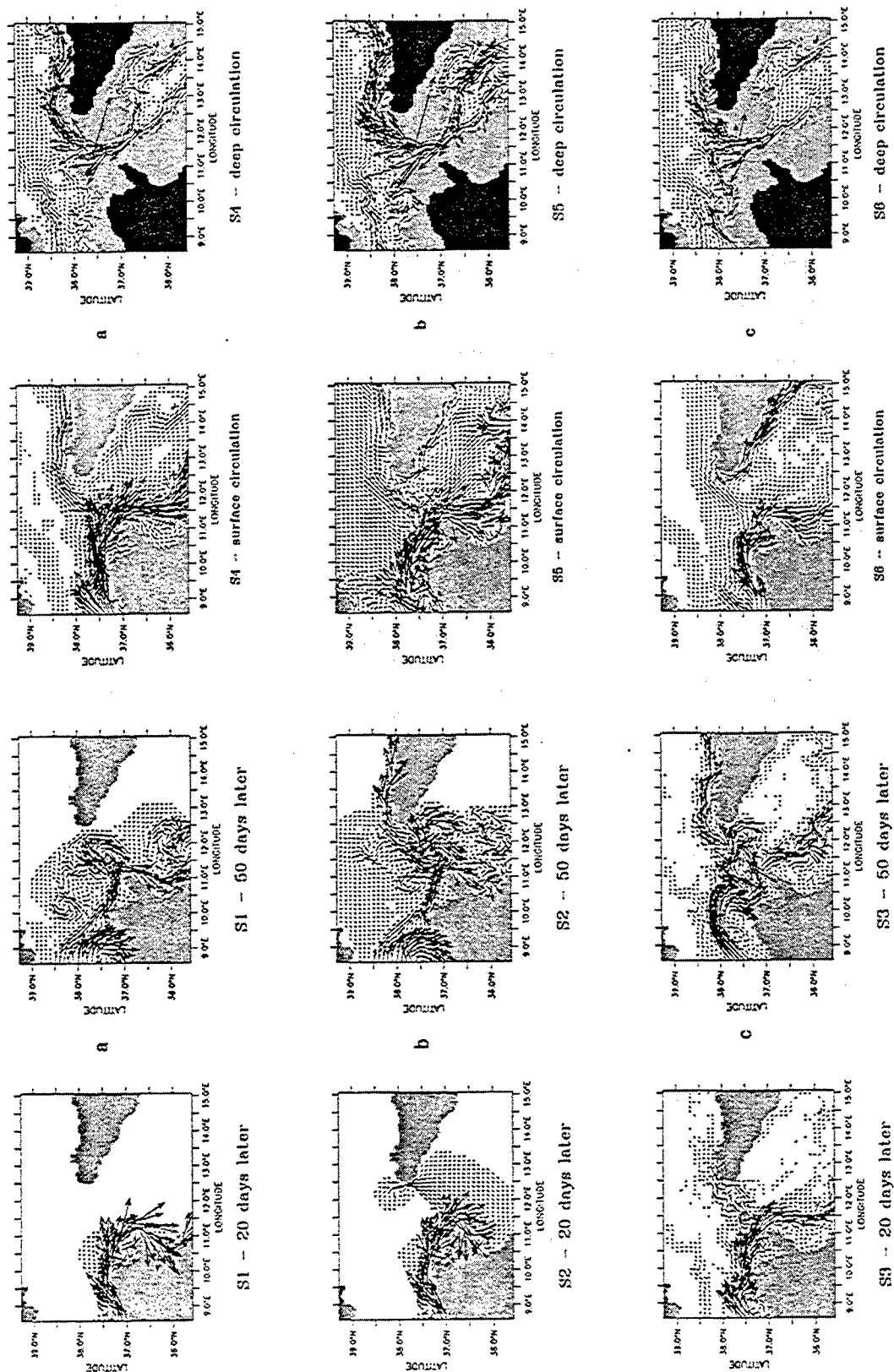Pichevin T., and Nof D., (1997): The momentum imbalance paradox. *Tellus.* 49A, 298-319.

Fig.2 Surface (left) and 350 m(right) currents at 60 days for experiments: a) S4, b) S5, c) S6

Fig.1 The surface currents for the three first experiments, a) S1, b) S2, c) S3

A process study of the Denmark Strait Overflow

James B. Girton [1] and Thomas B. Sanford [2]

[1] Woods Hole Oceanographic Institution. Woods Hole. Massachusetts. USA

[2] Applied Physics Laboratory. University of Washington. Seattle. Washington, USA

Abstract. Two recent surveys of velocity, temperature and salinity in the Denmark Strait are used to characterize the flow structure, transport and dynamics of the dense overflow from the Nordic Seas. The mean transport of dense water found at the sill is indistinguishable from measurements made in 1973 (to within 20%), and the statistics of variability are similarly identical. Estimates of entrainment rate from watermass dilution in the descending plume are consistent with the near-doubling of transport deduced from previous current meter arrays. In addition, the rate of descent of the dense plume agrees with that of a streamtube retarded by bottom stress.

Introduction

The Denmark Strait has long been one of the more difficult of the large ocean straits in which to carry out a program of measurements. Inhospitable weather and the frequent presence of ice makes ship operations difficult, and heavy fishing and strong currents pose a constant threat to moored instrumentation. Interpretation of results has been complicated by many factors, including energetic mesoscale variability, thin near-bottom currents over steep topography and a complex watermass and flow structure. Nevertheless, considerable interest has remained focused on the Denmark Strait due to its importance as a choke point in the thermohaline overturning circulation and source of North Atlantic deep water. Dense water formed in the Nordic Seas passes between Greenland and Iceland and cascades down the continental slope, forming the Denmark Strait Overflow (DSO) and eventually the deep western boundary current of the North Atlantic. Surface currents and ice passing through the Strait also play an important role in the freshwater budget of the Nordic and Arctic seas.

In a departure from the traditional types of measurements heretofore employed in the Denmark Strait, we undertook a study of the DSO using expendable instruments deployed in a rapid survey pattern designed to resolve and characterize the strong variability of the flow. Our results show the value of direct high-resolution velocity measurements in process studies of this kind and reinforce the need for synoptic sampling in regions of significant temporal and spatial variability.

Measurement techniques

The primary tools used in the rapid survey were expendable profilers measuring velocity (XCP) and temperature and salinity (XCTD). In most cases, the two types of profilers were deployed simultaneously, although there were instances in which XCPs were used in conjunction with the ship-lowered CTD, providing more accurate T and S information but resulting in a slower survey speed.

The XCP (eXpendable Current Profiler) measures ocean velocity through the method of geomagnetic induction [*Sanford et al.*, 1978] and so yields a profile relative to an unknown constant offset. By combining the instantaneous velocity profiles from the XCP with near-surface currents continuously measured by the shipboard ADCP we were able to obtain full water-column absolute velocity to an accuracy approaching $0.01 \, \mathrm{m \, s^{-1}}$. This method proved quite successful and has great potential for future measurement programs in oceanic straits.

A further advantage of the XCP is that its small probe size (30 cm long) allows detailed resolution of velocity shear even into the turbulent bottom boundary layer. By fitting a logarithmic profile to the velocity data in the bottom 15 m of the water column we have estimated the direction and magnitude of the shear stress (τ) exerted on the fluid by the boundary. In aggregate, a comparison of these estimates to the velocity 50 m above the bottom (still within the fast-flowing density current) gives an estimated quadratic drag coefficient (C_D) of 3×10^{-3}, in good agreement with other studies of oceanic flows. This log profile technique has been used previously [*Johnson et al.*, 1994] in a study of the Mediterranean outflow and is a valuable asset for evaluating the influence of friction on near-bottom flows.

Field study

In August 1997 we occupied 3 sections from the R/V *Aranda* as part of the EC VEINS program. Our more extensive survey took place on a cruise with Rolf Käse of IfM Kiel on the R/V *Poseidon* in September 1998. The main goals of
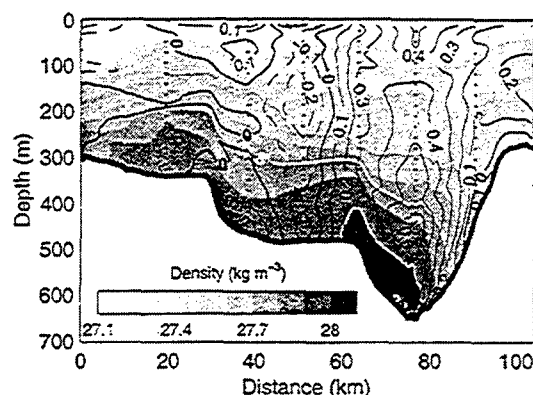
Figure 1. Velocity and density section across the sill from one of 7 near-sill sections in the *Poseidon* survey. Greenland is to the left and Iceland to the right. The positions of XCP/XCTD drops are marked by vertical dotted lines. Positive through-section velocity (solid lines) is southwestward, *i. e.*, towards the viewer.

Figure 2. CPDF for O73 current meter transports (solid), array-sampled $\theta < 2°C$ transports from the 7 near-sill *Poseidon* sections (dashed), and numerical model transports from *Käse and Oschlies* [2000] (dotted). "Array-sampled" sections attempt to estimate the transport that the O73 array would have measured at the time of the survey by projecting to the instrument positions.

the survey were to: 1) estimate the transport through several sections, 2) map the dynamical properties of the overflow plume, including Froude number and bottom stress, 3) determine the upstream condition for hydraulic considerations and 4) characterize the velocity and watermass structure of one or more surface eddies. As it turned out, the CTD survey was not as extensive as hoped, while the expendable survey underwent substantial modification. Fortunately, even when the winds and sea state made cable-lowered CTD operations impossible, we were often still able to launch the expendable probes from the O1 level and continue our survey, albeit at a slower pace due to the difficulty of maintaining headway.

Near-sill structure and transport

Our observations have revealed the structure of the overflow velocity and density in a new light, showing the presence of a barotropic jet above the dense deep layer as well as strong lateral shear and a nearly vertical front separating the outflow from the Atlantic water on the south-eastern side of the strait (Fig. 1).

We have used our 7 sections closest to the sill to estimate the transport of water denser than $\sigma_\theta = 27.8$ at 2.7 ± 0.6 Sv [*Girton et al.*, 2001]. A comparison of the statistics of transport determined by our sections with those from the current meters deployed during the OVERFLOW '73 (O73) project [*Ross*, 1984] has shown no detectable change over the period 1973–1998. We have calculated the transport that the O73 array would have measured in 1998, given the velocity and temperature structure in our 7 sections, and arrived at a mean of 2.9 Sv, identical to the 1973 measurement. We have also calculated the range of mean, median, std. dev., max and min values expected from a random sampling of 7 points from the O73 transport timeseries and found that our values lie within the $\pm 1\sigma$ (67%) confidence range for each of these statistics. Finally, a Kolmogorov-Smirnov test compar-
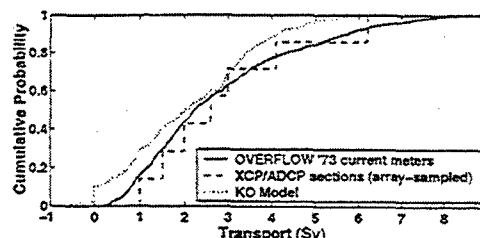
ing the cumulative probability distribution function (CPDF, Fig. 2) of transport from both sets of measurements finds the distributions to be indistinguishable to the 99% confidence level.

Descending plume

Further from the sill the barotropic character of the overflow becomes less pronounced and a bottom-intensified current develops in the descending dense layer. In most of our sections a southwestward-flowing barotropic current is still present near the Greenland shelf-break, but very little, if any, of the dense water remains in this current. It appears that the bottom and surface flows have become more-or-less decoupled by a distance of 100 km from the sill.

Under the "streamtube" description of bottom density currents [*Smith*, 1975; *Price and Baringer*, 1994] the DSO can be thought of as a slab of dense water under the influences of gravity, friction and Coriolis acceleration sliding down the continental slope through a stratified background. The resulting force balance produces an angled path, with the flow's downward angle decreasing as slope and density anomaly decrease through entrainment or flow into denser background water or less-steep topography.

The observed path of the dense water (Figure 3) is, in fact, quite consistent with this description, despite all of the variability present. The dots in the lower inset to Figure 3 show the depth of the center of the plume mass anomaly at each section, plotted *vs.* distance from the sill (located at approximately 66.1°N, 27.1°W). The descent is relatively slow at first (during the first 50 km) and then reaches a more-or-less constant rate of 6 m km^{-1}. The angled bars in the inset show the rate of descent expected from the average bottom stress (τ) estimated over each section using logarithmic velocity fits in the bottom boundary layer. Integrating these slopes (thin black line) gives a very close match to the total observed descent of the dense water (thin gray line, derived from a smoothing of the center-of-mass dots), indicating that bottom stress is, in fact, the dominant mechanism allowing
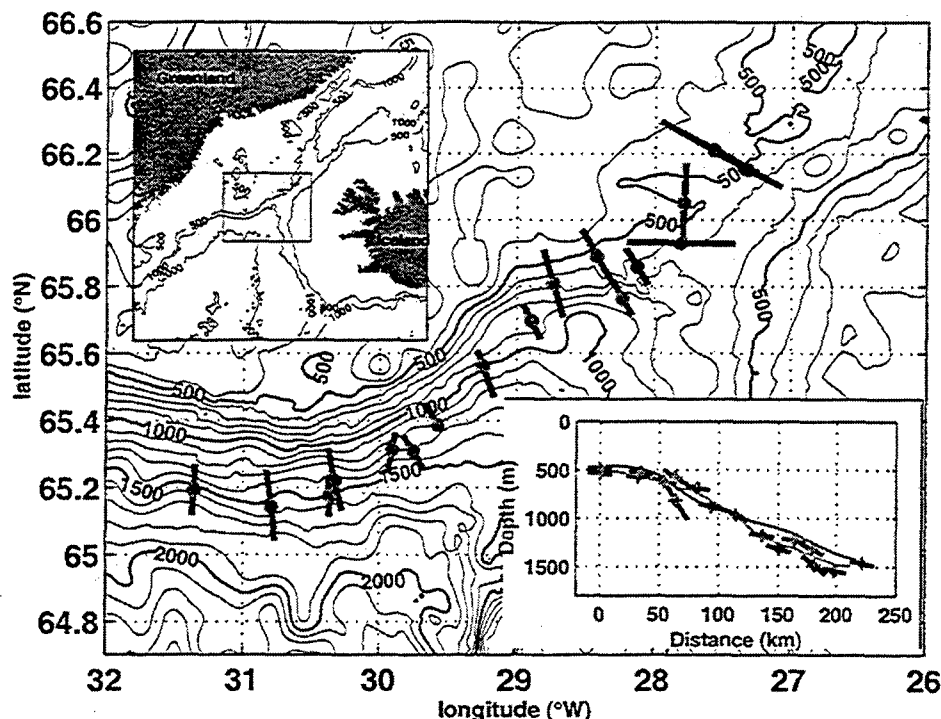
Figure 3. Position of overflow center of mass (dots) and half-width (bars) on each of 18 cross-sections. Apart from some variability at the sill and early in the descent, the flow follows a well-defined path with remarkably little cross-stream scatter. The two insets show the geographical location in a larger context (upper left) and the descent of the dense water plume with distance from the sill (lower right). See text for additional details.

the descent of the dense water.

Entrainment and energy budget

During the descent, the average density of the plume $(\overline{\sigma_\theta})$ decreases due to the entrainment of ambient fluid. This decrease appears to become steeper beyond ~125 km from the sill (Fig. 4). Using the slopes $(\frac{d\overline{\sigma_\theta}}{d\xi})$ before and after 125 km along with mean plume velocity $(\overline{V})$, thickness (H) and density anomaly $(\overline{\rho'})$ over each region, the entrainment rate,

$$w_e = \frac{\overline{V}H}{\overline{\rho'}}\frac{d\overline{\sigma_\theta}}{d\xi}, \tag{1}$$

is estimated to increase by an order of magnitude from $6 \times 10^{-5}\,\mathrm{m\,s^{-1}}$ to $8 \times 10^{-4}\,\mathrm{m\,s^{-1}}$.

In addition to its consequences for overflow mean density, w_e should have a profound effect on transport changes resulting from the inclusion of new water. Figure 5 shows the through-section transport of $\sigma_\theta > 27.8\,\mathrm{kg\,m^{-3}}$ water on all sections, demonstrating that the effect of entrainment may be particularly difficult to pick out of the short-term variability present in the measurements. Perhaps this is due to the fact that the constituent measurements of velocity and cross-sectional area are themselves highly variable. In fact, a substantial fraction of total transport may be due to the co-
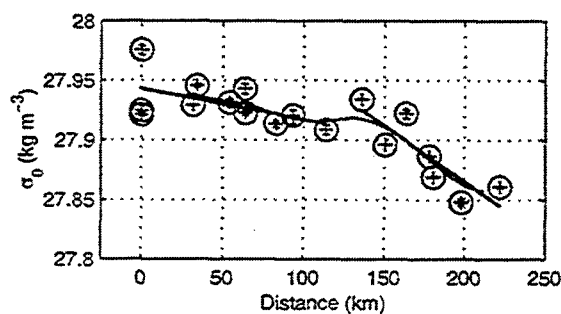

Figure 4. Evolution of plume density $(\overline{\sigma_\theta})$ with distance from the sill. The thin solid line is from a smoothing of the points with a 20 km Gaussian window. The two thick straight lines are from linear fits to the regions before and after 125 km, and seem to show a significant change in slope.
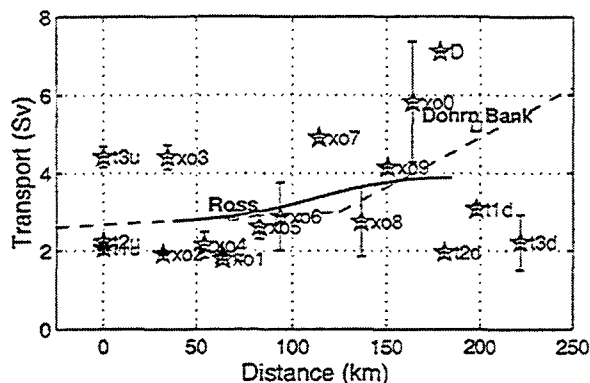
Figure 5. Dense water transport *vs.* distance from the sill, as measured by all 18 sections with XCPs (including two from the *Aranda*) as well as two current meter arrays (labeled as "Ross" and "Dohrn Bank") [*Ross*, 1984; *Dickson and Brown*, 1994, respectively]. The dashed lines show rates of transport increase expected from the two w_e values estimated from Eq. 1 and Fig. 4. The solid curve is a smoothing of the transport values using a 75 km Gaussian window.

variability of these quantities, casting further doubt on the simplified streamtube model.

Energy *vs.* energy flux

Given a certain success in interpretation using a streamtube framework, we are tempted to examine the energetics of the overflow in the same light. The energy source for the overflow is the potential energy (PE) of the density anomaly due to its thickness (internal potential energy—iPE) and height on the slope (external potential energy—ePE). Previous studies of oceanic outflows—particularly from the Mediterranean [*Johnson et al.*, 1994]—have suggested that the loss of potential energy is primarily accounted for by frictional stresses at the ocean bottom and plume interface. In terms of their contribution to the along-stream momentum budget, frictional forces applied over the surface of the plume should produce changes in total energy with downstream distance. In fact this only appears to be the case in the region far enough from the sill that the plume does, in fact, appear as a bottom-trapped density current. The near-sill sections contain much higher ePE and iPE which does not carry over into the downstream sections. Evidently, the sill sections do not release all of their APE into the downslope overflow.

The situation is partially clarified by considering the *flux* of energy in the overflow plume. This approach has the advantage that the total flux should not depend very strongly on the angle of the section to the flow. A major disadvantage to interpreting energy flux is the additional variability produced by an extra factor of velocity included in most of the terms. In fact, flux estimates do show large section-to-section variability, even suggesting that the amplitude of the variability increases in the downstream direction (not unlike

the transport variability of Fig. 5). The continuity from the near-sill sections to the downstream region does appear to be improved over the available energy description above.

Conclusions

Knowledge of the structure of the velocity through the Denmark Strait has been, until now, fairly minimal. The full water column sections described here illustrate the persistence of a barotropic jet in the near-sill flow, often including a recirculation on the Greenland shelf in addition to the counter-flow on the Iceland slope. The mechanism underlying this barotropic flow in a situation in which the primary forcing is by internal density gradients has still to be explained.

After a careful comparison between the different geographical coverages and temporal distributions of the current meter measurements from OVERFLOW '73 and the velocity profiles from the *Poseidon* cruise, it appears that not only was the *mean* overflow transport during the two periods statistically identical (to an accuracy of about 0.6 Sv), but also the *distribution* of variability was indistinguishable. In fact the measured mean transport values only differed by 0.2 Sv, suggesting that a relatively brief survey, as long as it spans the lateral extent of the outflowing waters and resolves the banded velocity structures at the sill, is sufficient to quantify the overflow flux with equivalent accuracy to a current meter array of substantially longer duration.

Once the agreement between the 1973 and 1998 observations is established, it becomes more plausible that significant features observed in the new surveys can be considered universal characteristics of the DSO. In particular, the changes to the plume-averaged properties in the region studied are the first major step in the modification of the overflow into North Atlantic Deep Water. Some of the important points resulting from the bulk overflow (streamtube) analysis include:

- The path of the dense water as it descends the Greenland continental slope has surprisingly little variability, following a path of essentially constant rate of descent over topography. This rate is consistent with a balance between buoyancy, Coriolis acceleration and bottom stress.

- The rate of change of plume-averaged density with distance increases at just over 100 km from the sill, indicating an increase in entrainment velocity (w_e) from 6×10^{-5} m s^{-1} to 8×10^{-4} m s^{-1}. This increase in entrainment rate could provide the increases in transport observed by previous current meter moorings along the overflow path [*Dickson and Brown*, 1994].

- Also at close to 100 km from the sill, both the plume-averaged velocity and the propagation speed of eddies identified in the survey reach a maximum of approximately 0.9 m s^{-1}. This is the location that the surface manifestations of these eddies appear as cyclonic

spirals of cold East Greenland Current water in satellite infrared images, as previously reported by *Bruce* [1995].

The reasons for the various changes occurring at around 100 km from the sill are not entirely clear. One possibility is a steepening of the Greenland slope beneath the overflow path, increasing approximately linearly from zero at the sill to almost 0.03 at about 125 km and remaining roughly constant between 125 and 225 km from the sill (essentially to the end of our survey region). The increased slope clearly prevents the plume from spreading too rapidly in this region (see Fig. 3) but may also lead to increased entrainment. The maximum in plume velocity at the start of the steep region does not entirely agree with this picture, however. Another candidate is the fact that the plume encounters a reduction in background stratification at approximately 1000 m depth (a depth reached at about 125 km from the sill, as shown in the inset to Fig. 3). It is possible that this change in background stratification has an effect on the entrainment process, although an alternate possibility is simply that the reduction in plume density anomaly through entrainment and increased background density allows for greater mixing. Bulk Richardson numbers are highly variable and do not provide conclusive evidence one way or the other.

The dramatic watermass modification and eddy formation processes occurring in the Denmark Strait remain complex phenomena and will continue to be a subject of interest as future trends in climate forcing result in increasing changes to the source regions in the Nordic Seas. While it is clear that questions remain, we are encouraged that our approach of synoptic velocity surveying was able to illuminate new features of the DSO and go a long way toward solidifying the understanding of the dynamics of the descending plume. We also hope that similar techniques will be considered for the study of other mesoscale oceanic processes involving strong velocities and energetic bottom boundary layers.

References

Bruce. J. G., Eddies southwest of the Denmark Strait, *Deep-Sea Res.*, *42*, 13–29, 1995.

Dickson, R. R., and J. Brown, The production of North Atlantic Deep Water: Sources, rates, and pathways, *J. Geophys. Res.*, *99*, 12,319–12,341, 1994.

Girton, J. B., T. B. Sanford, and R. H. Käse, Synoptic sections of the Denmark Strait overflow, *Geophys. Res. Lett.*, *28*, 1619–1622, 2001.

Johnson, G. C., T. B. Sanford, and M. O. Baringer, Stress on the Mediterranean outflow plume I: Velocity and water property measurements, *J. Phys. Oceanogr.*, *24*, 2072–2083, 1994.

Käse, R. H., and A. Oschlies, Flow through Denmark Strait, *J. Geophys. Res.*, *105*, 28,527–28,546, 2000.

Price, J. F., and M. O. Baringer, Outflows and deep water production by marginal seas, *Progr. Oceanogr.*, *33*, 161–200, 1994.

Ross, C. K., Temperature–salinity characteristics of the "overflow" water in Denmark Strait during "OVERFLOW '73", *Rapp. P.-v. Réun. Cons. int. Explor. Mer.*, *185*, 111–119, 1984.

Sanford, T. B., R. G. Drever, and J. H. Dunlap, A velocity profiler based on the principles of geomagnetic induction, *Deep-Sea Res.*, *25*, 183–210, 1978.

Smith, P. C., A streamtube model for bottom boundary currents in the ocean, *Deep-Sea Res.*, *22*, 853–873, 1975.

On the effect of friction and entrainment on potential vorticity in the shallow water approximation

Silvia Gremes Cordero[1] and Ettore Salusti[2]

[1]Dept. of Physics, University of Rome "La Sapienza"
[2]I.N.F.N. - Dept. of Physics, University of Rome "La Sapienza"

Abstract. We analyse potential vorticity conservation for systems in shallow water, when friction and mixing play a role as in the Strait of Gibraltar dense water outflow into the Atlantic Ocean.

The problem

Potential vorticity Π and its dynamics have been studied by numerous authors, such as Gill (1982), Pedlosky (1987), Haynes and McIntyre (1987 and 1990), Kurgansky (1991), Müller (1995) among many others, and has proved useful in oceanographic and meteorological fluid-dynamics analyses. In addition, Salusti and Serravall (1999) recently analysed the evolution of Π for a fluid in the presence of mild friction or rotational forcings, a study of some interest for realistic oceanographic analyses.

In many cases the "shallow water" version of Π is of some utility as for shelf phenomena or currents in thin marine layers, where friction certainly plays an important role. In many oceanographic problems a fundamental role is also played by entrainment. This idealization was first introduced in fluid dynamics by Taylor (Turner 1986) that proposed that $\varepsilon = E^* U$, where ε is the lateral velocity across the edge of a turbulent flow with mean velocity U. The coefficient E^* is generally determined by the specific system geometry, the environmental fluid stratification etc., but for oceanographic cases it can be considered as a small constant $\sim 10^{-3} - 10^{-4}$.

So, now we discuss a classical shallow water problem for a layer of homogeneous water bounded by the sea bottom $b(x, y)$ and the surface $h(x, y, t)$. In formulae the horizontal momentum equations are

$$\frac{\partial u}{\partial t} + u\frac{\partial u}{\partial x} + v\frac{\partial u}{\partial y} - fv = -g^*\frac{\partial h}{\partial x} + \frac{F^{(x)}}{\rho}$$

$$\frac{\partial v}{\partial t} + u\frac{\partial v}{\partial x} + v\frac{\partial v}{\partial y} + fu = -g^*\frac{\partial h}{\partial y} + \frac{F^{(y)}}{\rho} \quad (1)$$

where $\vec{u} = (u, v)$ is the horizontal velocity, ρ the density, f the Coriolis parameter, t the time, x and y the horizontal space coordinates. $g^* = g\Delta\rho/\rho$.

In $\vec{F} \equiv (F^{(x)}, F^{(y)})$ we will analyse friction: $\vec{F} = \rho\bar{\nu}\vec{u}$. where $\bar{\nu}$ is a still undetermined operator. In the open sea one usually has $\vec{F} = \rho\nu''\nabla^2\vec{u}$ while, for the case representing bottom friction, a popular approach is also $\vec{F} = -\rho\nu'\vec{u}$. where $\nu'' \sim 10^{-3} - 10^{-4}\mathrm{m}^2\mathrm{s}^{-1}$ and $\nu' \sim 10^{-6} - 10^{-8}\mathrm{s}^{-1}$

are positive constants (Smith 1975; Pedlosky 1987). In any case, for the sake of simplicity we assume in the following that $\bar{\nu}$ is linear.

For such $\vec{F}$, by cross differentiation of (1) one obtains the vorticity equation (Gill 1982) for viscous fluids

$$\frac{d}{dt}(\zeta + f) + (\zeta + f)(\frac{\partial u}{\partial x} + \frac{\partial v}{\partial y}) = \bar{\nu}\zeta$$

$$\text{with } \zeta \equiv \frac{\partial v}{\partial x} - \frac{\partial u}{\partial y}. \quad (2)$$

where $\frac{d}{dt}$ is the material time-derivative.

In the full 3-dimensional case, depth-integrating the mass conservation equation $\frac{\partial u}{\partial x} + \frac{\partial v}{\partial y} + \frac{\partial w}{\partial z} = 0$ for a homogeneous, or incompressible, fluid between the sea bottom b and h, considering the effect of entrainment, gives

$$\frac{d}{dt}(h - b) + (h - b)(\frac{\partial u}{\partial x} + \frac{\partial v}{\partial y}) =$$

$$E^*\sqrt{u^2 + v^2}. \quad (3)$$

All this brings us to realistic problems where both friction and entrainment must be considered. By combining (2) and (3) we obtain

$$\frac{d}{dt}(\frac{\zeta + f}{h - b}) + (\frac{\zeta + f}{h - b})\frac{E^*\sqrt{u^2 + v^2}}{h - b} \equiv$$

$$(\frac{d}{dt} + \Gamma)\frac{\zeta + f}{h - b} = (\frac{d}{dt} + \Gamma)\Pi = \frac{\bar{\nu}\zeta}{h - b} \quad (4)$$

In realistic cases, as for mild entrainment and friction, we have the possiblity of approximating (4). Salusti and Serravall (1999) discuss some purely viscous cases. For general problems, if we know from other sources that $\sqrt{u^2 + v^2}$ and $h - b$ are slowly varying quantities, we may tentatively assume $\Gamma = E^*\frac{\sqrt{u^2+v^2}}{h-b} \sim const \sim 10^{-6} - 10^{-8}\mathrm{s}^{-1}$, and solve (4).

Density currents

These considerations clearly hold also for density currents, namely dense water veins flowing geostrophically along bottom isobaths, as studied by Smith (1975), and recently by Emms (1997), Baringer and Price (1997). Note that, since the current flows over the sea-floor, its path and speed are particularly affected by the entrainment of ambient fluid and by bottom friction, usually schematized as $\vec{F} = \bar{\nu}\rho\vec{u} \simeq -\frac{\bar{\nu}\rho}{h-b}\vec{u}$.
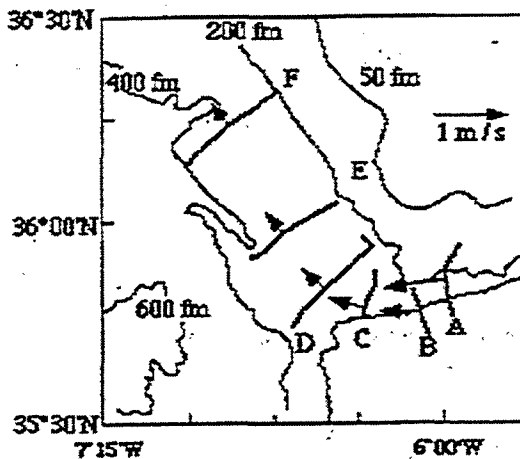

Figure 1. Geographical positions of the hydrologic Sections off Gibraltar (Baringer and Price 1997), with a sketch of the average velocities at the center of the Section.

As scale estimates we have velocities $u \approx 0.1-0.5\,\mathrm{ms}^{-1}$, bottom current thicknesses $h - b \approx 10-100$ m, the length $L \approx 100-1000$ km, a width $W \approx 10$ km, all giving a small Rossby number ~ 0.1. Moreover, these quantities do not vary substantially along the flow even if their variability cannot be totally disregarded.

For such systems equation (4) gives

$$\frac{d}{dt}\frac{\zeta+f}{h-b} + \Gamma\frac{\zeta+f}{h-b} = -\frac{\bar{\nu}\zeta}{(h-b)^2} \tag{5}$$

We applied these ideas to the flow off Gibraltar of dense salty water of Mediterranean origin (Fig 1) as observed by Baringer and Price (1997). Their transect A is near the sill, in B one has $u \sim 0.6\,\mathrm{ms}^{-1}$, $h - b \sim 96$ m and $\Pi \sim 8.3 \times 10^{-7}$ m^{-1}s^{-1}. It is of interest that near the sill the motion is not rectilinear but turns geostrophically towards north, with an apparent curvature radius of ~ 30 km. Consequently one can estimate $\zeta \sim -2\times10^{-5}$ s^{-1}, also having clear that at the current boundaries some local variations of ζ are certainly present. After ~ 11 km, in transect C these values change into $\zeta = -10^{-5}$s^{-1}, $\bar{u} \sim 0,34$ ms^{-1}, $\Pi \sim 1.03 \times 10^{-7}$ m^{-1}s^{-1} and $h - b \sim 87$ m. This Π increase with time is

an effect of considerable interest. For the other D, E and F transects, respectively at 11, 18 and 34 km, the behaviour of $h - b, and\bar{u}$, is more regular (Fig 2).
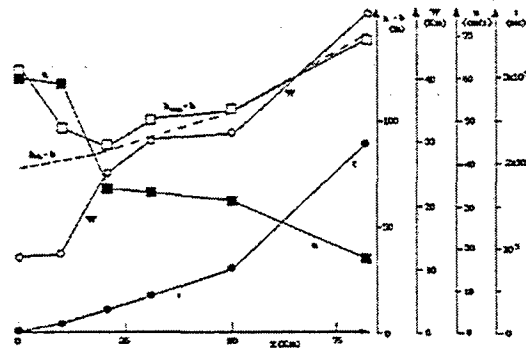

Figure 2. Evolution of velocity u and thickness $h - b$ for the bottom current off Gibraltar.

Since a detailed estimate of entrainment of these data has been obtained by Baringer and Price, corresponding to $E^* \sim 1 - 3 \times 10^{-3}$, we use these values to compute $\Gamma\Pi$, a positive quantity. To balance these quantities, the viscous term is $\frac{\bar{\nu}\zeta}{h-b} = -\frac{\bar{\nu}\zeta}{(h-b)^2}$ for $\bar{\nu} \sim 8 \times 10^{-2}$ ms^{-1}. It is of interest to note that whilst entrainment is proportional to Π and consequently it can only decrease potential vorticity, if ζ is negative the effect of friction can also give an alongflow increase of Π. This indeed happens for the vigorous geostrophic bottom flow immediately off Gibraltar, turning northward in transect B and C.

References

Baringer M. and Price J., 1997: Momentum and energy balance of the Mediterranean outflow. *J. Phys. Oceanography,* 27,1678-1692.

Emms P.W., 1997: Streamtube models of gravity currents in the ocean. *Deep-Sea Research,* 44, 1575-1610.

Gill A.E., 1982: Atmosphere-Ocean Dynamics. Academic Press, pp. 662.

Griffiths R.W., 1986: Gravity currents in rotation systems. *Ann. Rev. Fluid Mech.,* 18, 59-89.

Haynes P.H. and McIntyre M.E., 1987: On the evolution of vorticity and potential vorticity in the presence of diabatic heating and frictional or other forces. *J. Atmos. Sci.,* 44, 828-841.

Haynes P.H., McIntyre M.E., 1990: On the Conservation and Impermeability theorems for potential vorticity. *J. Atmos. Sci.,* 47-16, 2021-2031.

Kurgansky, M.V., 1991: The atmospheric vorticity charge. *Izv. Atmospher. Ocean. Phys.,* 27, 510-516.

Müller P., 1995: Ertel's potential vorticity Theorem in Physical Oceanography. *Rev. Geophysics,* 33, 1, 67-97.

Pediosky J., 1987: Geophysical Fluid Dynamics. Springer, pp 710.

Salusti E., R. Serravall 1999: On the Ertel and Impermeability theorems for oceanographic problems. *Geophy. Astr. Fluid Dyn.*, **90**, 247-264.

Smith P.C., 1975: A streamtube model for bottom currents in the ocean. *Deep-Sea Res.*, **22**, 853-873.

Turner J.S., 1986: Turbulent entrainment: the development of the entrainment assumption, and its application to geophysical flows. *J. Fluid Mech.*, **173**, 431-471.

Rotating Hydraulics and Upstream Basin Circulation

K. R. Helfrich and L. J. Pratt

Woods Hole Oceanographic Institution, Woods Hole, MA, USA

Abstract. The flow in a finite source fed f-plane basin drained through a strait is explored using a single-layer (reduced gravity) shallow water numerical model that resolves the hydraulic flow within the strait. The steady upstream basin circulation is found to be sensitive to the nature of the mass source (e.g., uniform or localized downwelling, boundary inflow). In contrast, the hydraulically controlled flow in the strait is nearly independent of the basin circulation and agrees very well with the Gill (1977) solution obtained using the numerically determined average potential vorticity in the strait entrance region. The coupled basin-strait system selects an average overflow potential vorticity that corresponds to the Gill solution with maximum fluid depth on the strait boundaries. This result is robust to changes in the basin and strait geometries, variations in the dissipation parameter (linear drag), and the net mass flux. The non-unique relation between basin conditions and overflow transport is significant with regard to deep overflow transport monitoring.

Introduction

Any effort to understand the effects of deep sills on abyssal circulation must address the issue of flow in the upstream basin. These effects may involve substantial feedback between the basin and the sill flows. For example, characteristics of the overflowing water (such as potential vorticity) are determined forcing and dissipation of the circulation in the upstream basin. This circulation may also be affected by the hydraulic control at the sill (such as setting the mean upstream fluid depth) which, in turn, depends on the potential vorticity of the overflowing water.

In the classic Gill (1977) theory for rotating hydraulic sill flow the ratio of the transports in the boundary layers on the left and right-hand walls (looking toward the sill), the (uniform) potential vorticity of the overflow fluid, and the sill geometry are needed to solve for the overflow transport. One possible upstream state comes from a flow established by breaking a dam at the sill. A Kelvin wave propagates back into the basin along the left wall to establish the flow towards the sill. The right wall remains unaffected for an infinite upstream basin. However, the assumption of an infinite basin is rarely realistic. For example, the deepest outflow through the Faroe-bank Channel is bounded upstream by the Norwegian and Lofoten Basins, which are closed at depth except for the Jan Mayen Fracture Zone. Other factors such as friction, topography and the beta-effect can also be expected to introduce departures from the idealized Gill (1977) picture of upstream flow. Lastly, there is no reason to expect uniform potential vorticity in the water approaching the sill.

The result is a potentially significant coupling between the geostrophic and dissipative basin circulation and the in-ertial sill flow that we examine using a numerical model of coupled basin-strait flow that resolves the rotating hydraulic flow within the strait.

Potential Vorticity Budget

A useful tool for investigating this coupling is the basin potential vorticity budget obtained by integrating the tangential component of the steady single-layer reduced gravity shallow-water momentum equations (see (2) below) along a closed contour C (Figure 1) that bounds the basin (Pratt and Llewellyn Smith, 1997; Pratt, 1997; Yang and Price, 2000). The result is

$$\oint_C qh u \cdot n \, ds = \oint_C (D + M) \cdot t \, ds, \qquad (1)$$

where $u = (u, v)$ is the horizontal velocity vector, D is the dissipation operator, and M is the interlayer momentum flux (defined in the next section), which is typically small. The potential vorticity $q = (f + \zeta)/h$, where ζ is the vertical relative vorticity, f is the Coriolis parameter and h is the layer thickness. Here t and n are, respectively, the unit tangent and outward normal vectors to C and ds is the incremental arc length along C. Thus for steady flows the net potential vorticity flux through the basin boundary must be balanced by the net dissipation around the basin boundary.

Fluid can be fed into the closed basin either through a distributed downwelling or through a boundary inflow. The constraint (1) then implies two quite different basin circulations. Consider a bowl-shaped f-plane basin and $D = -ru$. Downwelling involves no potential vorticity flux through C and so the strait outflow is the only contributor to the left
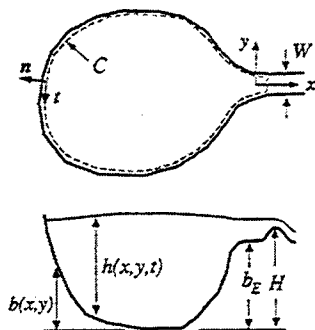
Figure 1. Sketch of a basin and strait system.

hand side of (1), which as a consequence will be positive for nonzero q. Equation (1) then implies a circulation that on average flows anticyclonically around the basin boundary as illustrated in Figure 2a. The flow approaches the strait on the left wall and may flow away from the strait on the right wall. When the inflow is through the boundary the left hand side of (1) will generally be small (identically zero if the potential vorticity of the inflow and outflow are equal). One solution is for the inflow to split into two boundary currents that round the basin to rejoin at the entrance to the strait where they flow out of the basin (Figure 2b).

Flows of these two types were found by Pratt (1997) in an analytical study of coupled basin-strait circulation. However, one crucial limitation, necessary for analytical progress, was matching of the linear geostrophic basin circulation to a limited subset of hydraulic models of the strait flow (e.g., zero potential vorticity outflow).
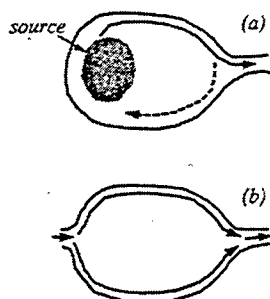
Figure 2. Examples of expected basin circulation for (a) interior downwelling and (b) boundary inflow.

Numerical Model

The coupled basin-strait flow (Figure 1) is studied through numerical solutions of the non-dimensional single-layer reduced gravity shallow-water momentum,

$$\frac{\partial u}{\partial t} + u \cdot \nabla u + k \times u = -\nabla(h + b) + D + M, \quad (2)$$

and continuity,

$$\frac{\partial h}{\partial t} + \nabla \cdot (uh) = -w, \quad (3)$$

equations. The equations are non-dimensionalized using $\sqrt{g'H}$ for the horizontal velocity $u = (u, v)$, the deformation radius $\sqrt{g'H}/f$ for the lateral dimensions (x, y), f^{-1} for time t, and H for the layer depth h and the bottom topography $b(x, y)$. Here g' is the reduced gravity and k is the vertical unit vector. The vertical downwelling velocity $w(x, y) \, (< 0)$ is scaled by Hf and $M = -\frac{w}{h}u\Theta(-w)$ is the momentum flux due to downwelling. The Heaviside function $\Theta(x) = 1$ for $x > 0$ and 0 otherwise. In all cases the dissipation is a linear bottom drag $D = -ru$ with coefficient r.

The model solves (2), in flux form, and (3) on a general quadrilateral grid using a finite-volume method designed to handle flow complexities of rotating hydraulics (e.g., flow grounding, hydraulic jumps). Details of the model and testing are given in Helfrich et al. (1999). The model domain consists of a finite upstream basin drained by a rectangular strait with width W (Figures 1 and 3). The strait bottom elevation is b_E at the strait entrance ($x = 0$) and $b = 1$ at the sill crest ($x = 6$). The flow is forced by either a downwelling distribution or uniform inflow through a segment of the basin boundary. The imposed mass flux is Q. The flow exits the domain downstream of the sill through an open (supercritical) boundary.
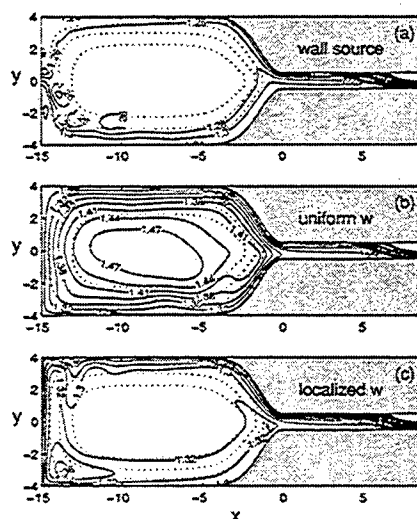
Results

Figure 3. Examples of basin circulation for (a) boundary inflow, (b) uniform downwelling and (c) localized downwelling in a bowl-shaped basin. The solid lines are contours of free surface height and the dotted lines indicate the basin topography. In all cases $W = 1$, $b_E = 0.8$, $Q = 0.05$, and $r = 0.01$.

An example of the numerical solutions for several mass

source types and a bowl-shaped basin is shown in Figure 3. In all cases the basin and strait geometry are the same ($W = 1$ and $b_E = 0.8$), $Q = 0.05$, and $r = 0.01$. In these examples the solutions are steady. Unsteady solutions do arise for decreasing r, but we will focus on the steady solutions. For boundary inflow ($-1/2 \leq y \leq 1/2$) the flow splits into two boundary currents that flow around the periphery of the basin (Figure 3a). With uniform downwelling (for $x < 0$) the basin circulation is anticyclonic with a small fraction of the flow that is drained off into the strait (Figure 3b). For localized downwelling (a thin strip from $-4 \leq y \leq 4$ and $-15 \leq x < -13$) the flow approaches the strait along the left boundary and nearly all of this boundary layer transport enters the strait to flow flow over the sill (Figure 3c). These circulations are qualitatively similar to the flows anticipated from basin potential vorticity budget analysis (c.f., Figure 2).

Although it is difficult to see in Figure 3, the flow in the strait is nearly identical in all three cases. The similarity is evident in both the h and q fields. Indeed, the average values of q in the strait entrance region $\bar{q}_E$ (= q averaged over $1 \leq x \leq 2$ and $-W/2 \leq y \leq W/2$) are $\bar{q}_E = 1.78, 1.79$ and 1.68 for Figures 3a,b and c, respectively. The strait flow is insensitive to the characteristics of the basin circulation. For example, the interface level at $(x, y) = (-2, 0)$ above the sill height is not a unique indicator of the of the overflow transport (c.f., Whitehead, 1998; Hansen *et al.*, 2001). This also suggests the difficulty of extending the Gill model of strait flow back into the basin since all three cases above have different boundary layer flux splittings.
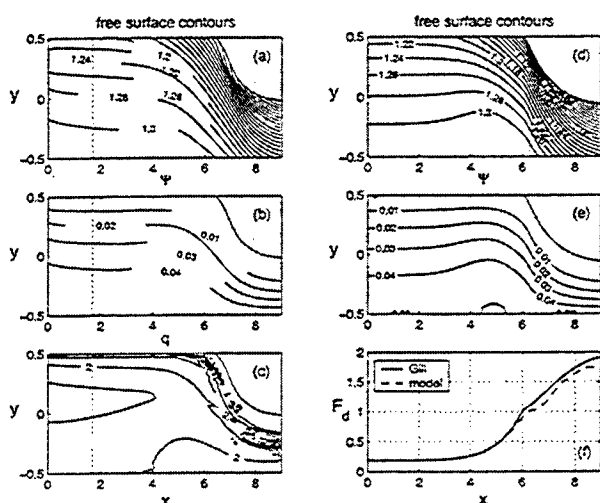
streamfunction Ψ and q, respectively, from the numerical model. The corresponding solution to the Gill (1977) model using $q = \bar{q}_E = 1.78$ and $Q = 0.05$ for $h + b$ and Ψ (Figures 4c and d agrees quite well with the numerical solution despite the non-uniform q in the numerical solution. There is also good agreement between the semi-geostrophic Froude number F_d from the Gill solution and that computed from the numerical solution h field and $\bar{q}_E = 1.78$ (Figure 4e). However, the Gill solution gives a boundary layer flux splitting that disagrees with all three numerical examples.

The value of $\bar{q}_E$ depends on strait geometry, but is relatively insensitive to r (Figure 5). (The circulation in the flat basin cases mimics those observed in Figure 3.) Differences due to mass source type arise for decreasing r and are associated with the emergence of time-dependence in the solutions.

It is surprising that these different basin flows deliver fluid of essentially the same potential vorticity to the strait. This suggests that the strait is controlling the overflow q by setting the upstream basin level at the strait entrance and for flows with small relative vorticity $q \approx 1/h$. Still, the Gill model permits an infinite choice of overflow q for a given Q and strait geometry so there is no *a priori* reason that the overflow q should be independent of the basin circulation.
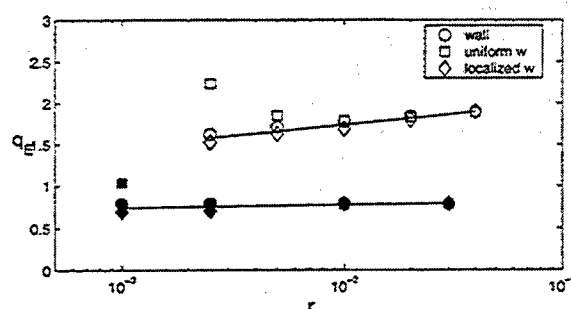
Figure 5. $\bar{q}_E$ versus r for a bowl-shaped basin ($W = 1$, $b_E = 0.8$), open symbols, and a flat basin ($W = 1$, $b_E = 0.8$), solid symbols. The different symbols indicate mass source type (see inset). In all cases $Q = 0.05$.

The selection of $\bar{q}_E$ is clarified some by considering the possible Gill theory solutions for the fluid depth against the left wall, h_L, in the strait entrance region ($b = b_E$) as a function of q and Q for a given strait geometry. Contours of allowable h_L are shown in Figure 6 for a strait with $W = 1$ and $b_E = 0.8$. For a fixed Q there is a $q = q_{max}(Q)$ that maximizes h_L (thick solid line). The symbols are numerical results for $\bar{q}_E$ for two basin geometries and two mass source types. The numerical results all fall approximately along the curve $q_{max}(Q)$. The thick dashed line shows the q that minimizes the ratio of kinetic energy flux to total energy flux for a given Q in the Gill solutions.

The result $\bar{q}_E \approx q_{max}(Q)$ is robust to changes in basin and strait geometries (Figure 7). Note that the relation $q_{max}(Q)$ changes with the strait geometry (e.g., W or b_E)
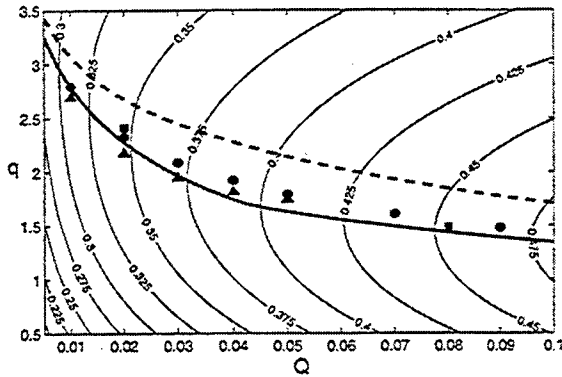
Figure 4. Details of the flow in the strait from Figure 3a. (a) $h + b$. (b) Ψ, and (c) q fields from the numerical solution. Solutions of the Gill (1977) theory using $Q = 0.05$ and $\bar{q}_E = 1.78$ are shown in (d) $h + b$ and (e) Ψ. (f) theoretical and model semi-geostrophic Froude number F_d.

Details of the flow in the strait from Figure 3a are shown in Figure 4. Figures 4a,b and c show $h + b$, the transport

Figure 6. Solution for h_L from the Gill (1977) theory for a strait with $W = 1$ and $b_E = 0.8$ as a function of q and Q. The thin solid lines are contours of h_L. The thick solid line is $q_{max}(Q)$, the locus of maximum h_L and the thick dashed line is the locus of the minimum of the ratio of kinetic energy flux to total energy flux. The symbols are $\bar{q}_E$ from the numerical solutions for a bowl basin with uniform downwelling (circles), boundary inflow (triangles) and a bowl basin with a uniform slope just before the strait entrance and uniform downwelling (squares). For all numerical runs $r = 0.01$.
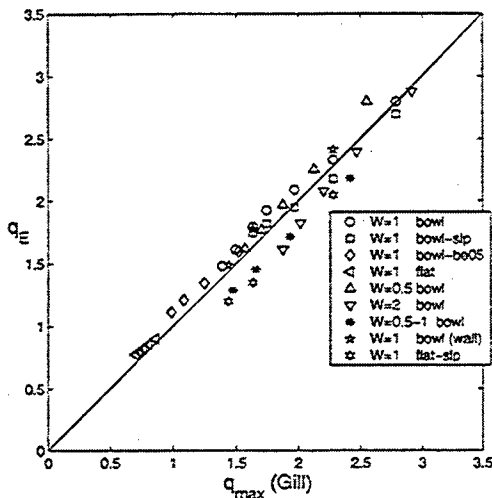
Figure 7. $\bar{q}_E$ versus q_{max} from the Gill theory for a variety of strait and basin geometries indicated in the inset.

but is independent of the basin geometry. The selected $\bar{q}_E$ is the one that maximizes the upstream fluid depth along the basin boundary. In the basin, where the kinetic energy is insignificant, this corresponds to maximizing the available potential energy. The presence of a hydraulically controlled strait exerts a strong influence on the basin circulation by controlling the upstream stratification (h) and also by selecting the overflow potential vorticity flux, which is a crucial component of the basin potential vorticity budget (1).

Discussion

The failure in connecting the Gill (1977) model to the basin flow is perhaps not too surprising given the very different dynamical regimes in the basin (geostrophic and dissipative) and in the strait (inertial and essentially inviscid). The Gill model does, however, agree with the computed flow in the strait given $\bar{q}_E$. Surprisingly, the coupled system acts to select the (average) overflow potential vorticity that maximizes the water level along the strait, and consequently the basin, boundaries. The dynamical reason for this selection principal has not been resolved, but it does seem reasonable that a solution that maximizes available potential energy and reduces mechanical dissipation within the basin should be obtained.

The dynamical disconnect between the strait and basin flows does pose a serious impediment to the use of the hydraulic theories to predict or monitor the flux over the sill from measurements of sill geometry and the upstream conditions. Just where should these measurements of upstream state be made and do they result in unique predictions for the flux? In the examples in Figure 3 the overflow transport is the same yet the mean upstream levels, or the levels just outside the strait, say at $(x, y) = (-2, 0)$, are different.

This non-uniqueness may help explain the roughly factor of 2 discrepancy between predicted and observed transport that Whitehead (1998) found when applying simple rotating hydraulic formulae to several deep overflows. Hansen *et al.* (2001) recently applied an empirical formula $Q \sim \Delta h^n$, where Δh is the height difference of an upstream isopycnal above the Faroe Bank Channel sill crest and $n = 1$ or $3/2$, to deduce a systematic reduction of overflow flux over the last 50 years. But given the results above, it is clear that the predicted transport may be far from the actual transport. The upstream height difference could change due to changing source conditions (e.g., different contributions of interior deep convection and boundary inflow through the Jan Mayen Fracture Zone) yet the net Faroe Bank Channel overflow transport could remain constant.

Further complicating the picture, Mauritzen (1996) has suggested a new schematic for the production of Denmark Strait and Faroe Bank Channel dense overflow waters wherein the cooling of Atlantic inflow water along the Norwegian coast plays the primary role. The cooling corresponds roughly to a downwelling along the boundary, and as seen above, the basin and near strait circulations depend critically on the mass source type and location. The nature of how these deep overflows are fed is still not settled.

Our results indicate that a better monitoring variable is h_L which, through $q_{max}(Q)$ for the particular strait geometry, can be used to uniquely determine the overflow transport. However, we have focused on simplified basin and strait geometries and single-layer flow with a specific form of dissipation. Many questions remain on the dynamics of coupled basin and strait flows.

References

Gill, A. E., 1977. The hydraulics of rotating-channel flow. *J. Fluid Mech.*, **80**, 641-671.

Hansen, B., W. R. Turrell and S. Østerhus, 2001. Decreasing overflow from the Nordic seas into the Atlantic Ocean through the Faroe Bank channel since 1950. *Nature*, **411**, 927-930.

Helfrich, K. R., A. C. Kuo and L. J. Pratt, 1999. Nonlinear Rossby adjustment in a channel. *J. Fluid Mech.*, **390**, 187-222.

Mauritzen, C., 1996. Production of dense overflow waters feeding the North Atlantic across the Greenland-Scotland Ridge. Part 1: Evidence for a revised circulation scheme. *Deep-Sea Res.*, **43**, 769-806.

Pratt, L. J. and S. G. Llewellyn Smith, 1997. Hydraulically drained flows in rotating basins. Part I: Method. *J. Phys. Oceano.*, **27**, 2509-2521.

Pratt, L. J., 1997. Hydraulically drained flows in rotating basins. Part II: Steady Flow. *J. Phys. Oceano.*, **27**, 2522-2535.

Whitehead, J. A., 1998. Topographic control of oceanic flows in deep passages and straits. *Rev. Geophys.*, **36**, 423-440.

Yang, J. and J. F. Price, 2000. Water mass formation and potential vorticity balance in an abyssal ocean circulation model. *J. Mar. Res.*, **58**, 789-808.

K. R. Helfrich and L. J. Pratt, Department of Physical Oceanography, WHOI, MS-21, Woods Hole, MA, 02543, USA. (e-mail: khelfrich@whoi.edu; lpratt@whoi.edu)

Hydraulic control of stratified exchange flows

A. McC. Hogg[1], K. B. Winters[2] and G. N. Ivey[3]

[1] Southampton Oceanography Centre, Southampton, United Kingdom.
[2] Applied Physics Laboratory, Seattle, USA.
[3] Centre for Water Research, Perth, Australia.

Abstract. Continuously stratified exchange flows occur in channels connecting stratified reservoirs and between homogeneous basins when interfacial mixing is significant. Hydraulic control is difficult to evaluate under these conditions. Solutions of the sixth order stability equation applied to data from a numerical simulation are used to demonstrate that internal waves cannot carry interfacial information from one end of the channel to the other. It is argued from this that the sixth order stability equation may be useful as a diagnostic for determining the hydraulic state of a stratified exchange flow.

Introduction

Internal hydraulic theory [see *Wood*, 1970; *Armi*, 1986] can be used to describe density driven flows in which fluid motion is determined by a buoyancy and inertia force balance. Inviscid flow through constricted channels is the major application of hydraulic theory. If mixing and friction are negligible, the hydraulic solution can be used to calculate fluid velocity in distinct layers which interact in only a limited way. We consider exchange flow through a laterally contracting channel separating two infinite basins filled initially with homogeneous fluid of different densities. For channels with slowly varying width, the solution in the inviscid, non-diffusive limit can be obtained using two-layer hydraulic theory as described in *Armi* [1986] and *Lawrence* [1990].

The key to understanding hydraulic flows lies in the existence of control points. Points of control occur when the composite Froude number,

$$G^2 \equiv \frac{u_1^2}{h_1} + \frac{u_2^2}{h_2} - \frac{(1-r)u_1^2 u_2^2}{h_1 h_2} = 1, \qquad (1)$$

where h_i is the dimensionless depth of each layer (non-dimensionalised by H), and u_i the dimensionless velocity (normalised by the inviscid wavespeed $(g'H)^{1/2}$). The ratio of layer densities is $r \equiv \rho_1/\rho_2$, and $g' = g(1-r)$ is the reduced gravity. It can be shown [*Dalziel*, 1991] that for a two-layer flow the hydraulic control condition can be written,

$$G^2 = 1 + \frac{c_1 c_2}{h_1 h_2}, \qquad (2)$$

where c_1 and c_2 are the phase speeds of the two interfacial waves non-dimensionalised by $(g'H)^{1/2}$. In a quiescent fluid, we expect c_1 and c_2 to be of opposite sign: one travelling to the right, and one to the left. When flow is critical

($G^2 = 1$) one wave has zero phase speed, and in supercritical flow ($G^2 > 1$) both waves propagate in the same direction. For the case we consider here, with flux in each direction being equal, there are two critical points near the contraction. Interfacial waves can thus travel in either direction from the centre of the channel, but cannot travel towards the centre of the contraction. Therefore changes can occur in the reservoirs without altering flow in the channel.

It is often difficult to determine whether an exchange flow between two basins is hydraulically controlled. Observed flows are continuously sheared and stratified, and interfaces may be displaced vertically from one another, making an approximate decomposition into layers difficult and subjective. Unfortunately, using the results of hydraulic theory to determine whether such flows are controlled depends sensitively on how one defines the layers [see, for example, *Gregg and Özsoy*, 2000; *Pratt et al.*, 1999].

Our objective here is to extend the notion of hydraulic control to continuously stratified flows in such a way that determining whether a flow is controlled and locating the position of control points can be done in an objective manner. We use the numerically simulated flow field shown in figure 1 which is similar to the hydraulic solution of flow through a channel except that there is considerable mixing. See *Hogg et al.* [2001a, b] for details of the simulations. Under the assumption that this flow is the viscous equivalent of a two-layer hydraulically controlled flow, we look for the propagation of linear internal waves in this flow field.

Calculation of eigenmodes

The propagation of waves in inviscid continuously stratified fluids is described by the Taylor-Goldstein equation [see, for example, *Banks et al.*, 1976]. However, in exchange flows where strong shear is present, the Taylor-Goldstein
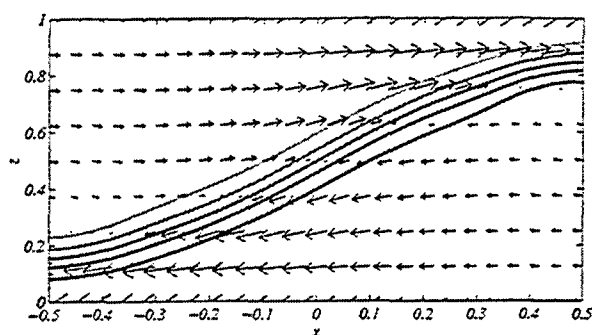
Figure 1. Numerical simulation of exchange flow with finite viscosity and diffusion. Isopycnals and velocity vectors are shown in elevation view.

equation becomes singular at some points [see *Pratt et al.*, 2000, for a more complete description of this problem]. Such levels are called critical layers [see, for example, *Drazin and Reid*, 1981] where viscosity and diffusivity, which are neglected by the Taylor-Goldstein equation, play a greater role [*Drazin and Reid*, 1981]. In the exchange flow shown in figure 1, viscosity and diffusivity play a significant role in determining the flow. This requires the use of a more generalised wave equation originally derived by *Koppel* [1964]. This is the sixth order viscous stability equation, which can be derived in the same way as the Taylor-Goldstein equation. The stability equation is written as follows:

$$- c^2[\partial^2 - k^2]\hat{\psi} + c[2iK_c(\partial^2 - k^2)^2$$
$$+ 2\bar{u}(\partial^2 - k^2) - \bar{u}_{zz}]\hat{\psi} + [K_c^2(\partial^2 - k^2)^3$$
$$- 2i\bar{u}K_c(\partial^2 - k^2)^2 - 2i\bar{u}_z K_c\partial(\partial^2 - k^2) - \bar{u}^2(\partial^2 - k^2)$$
$$+ 2i\bar{u}_{zz}K_c\partial + \bar{u}\bar{u}_{zz} + i\bar{u}_{zzz}K_c - N^2]\hat{\psi} = 0, \quad (3)$$

where ∂ and z subscripts are used to represent the derivative with respect to z. $N^2 = -g/\rho_0(\partial\bar{\rho}/\partial z)$ is the buoyancy frequency, the perturbation streamfunction ψ is based on the perturbation velocities in the standard way, and waves are assumed to be of the form $\psi(x, z, t) = \mathrm{Re}[\hat{\psi}(z)e^{ik(x-ct)}]$. Therefore k is the horizontal wavenumber and c the horizontal phase speed. K_c is defined as the ratio of viscosity K to wavenumber, $K_c = K/k$ where we have assumed a turbulent Prandtl number of unity in all of these calculations. The sixth order stability equation reduces to the Taylor-Goldstein equation if one removes the effect of viscosity and diffusion by setting $K_c = 0$. We can make an immediate simplification to (3) by assuming that we are interested in long waves (small wavenumber), so that $k^2\hat{\psi}$ will be small compared to $\partial^2\hat{\psi}$. Therefore we eliminate those terms, simplifying (3) to,

$$- c^2[\partial^2]\hat{\psi} + c[2iK_c\partial^4 + 2\bar{u}\partial^2 - \bar{u}_{zz}]\hat{\psi} + [K_c^2\partial^6$$
$$- 2i\bar{u}K_c\partial^4 - 2i\bar{u}_z K_c\partial^3 - \bar{u}^2\partial^2 + 2i\bar{u}_{zzz}K_c\partial$$
$$+ \bar{u}\bar{u}_{zz} + i\bar{u}_{zzz}K_c - N^2]\hat{\psi} = 0. \quad (4)$$

This problem is reduced to a linear matrix eigenvalue equation, following the procedure of *Winters and Riley* [1992] and solved numerically using the complex analogue of the QZ algorithm [*Golub and van Loan*, 1983; *Moler and Stewart*, 1973]. The equation is solved with free-slip rigid surfaces at top and bottom.

Numerical solutions to (4) require vertical profiles of $\bar{u}$ and N^2, and a constant value for K_c. The vertical profiles are taken from the numerically simulated steady flow shown in figure 1. K_c is determined from the value of turbulent eddy viscosity in the simulations, with wavenumber such that wavelengths are 1/8th of the channel length, resulting in a value of $K_c = 0.003$. The solution to (4) will then give information about the modes which can exist, and the phase speed (the real part of c) and rates of growth or decay (the imaginary part of c) of those modes. The structure and phase speed of vertical mode 1 waves as a function of position in the channel is of primary concern, and will be used to characterise the behaviour of waves in the flow.

Results

The numerical solution of (4) produces a large number of modes. The lowest modes (those with a simple eigenvector structure) will be the most important from the point of view of communicating information. Figure 2 shows density (a) and velocity profiles (b) at $x = 0$, with eigenvectors of the lowest mode waves (defined to be those modes with only one turning point). The modes shown here are typical of the modes observed at any point in the channel. In panels (c), (e) and (f) we see modes which are trapped in either one of the two layers, and are propagating in the same direction as the layer velocity. These modes are not of interest to the concept of hydraulic control, as the information which they communicate is by and large related to the portion of the domain which is homogeneous in density and thus irrelevant to the baroclinic flow. Modes shown in (d), (g) and (h) are of greater interest as they are centred on the interfacial region, and thus have the potential to carry information about any possible variation in the main baroclinic state of either reservoir.

The effect of strong shear on the low modes can be seen in figure 2 (g) and (h). Without shear or viscosity, one would find two mode 1 waves travelling in opposite directions, and the eigenfunction would have a maximum value on the density interface. By incrementally increasing the magnitude of the velocity field, it can be demonstrated that shear distorts these modes so that the mode travelling to the left (2g) is skewed upwards, and conversely the mode travelling to the right (2h) is skewed vertically downwards. For the purposes of this paper we will call these two modes the *vorticity* modes. The peak of each of the two vorticity modes are coincident with one edge of the interfacial region (the region of maximum curvature in the velocity profile), rather than with the region of maximum density gradient. Mathematically, this result is due to the relative importance of the $\bar{u}_{zz}$ terms
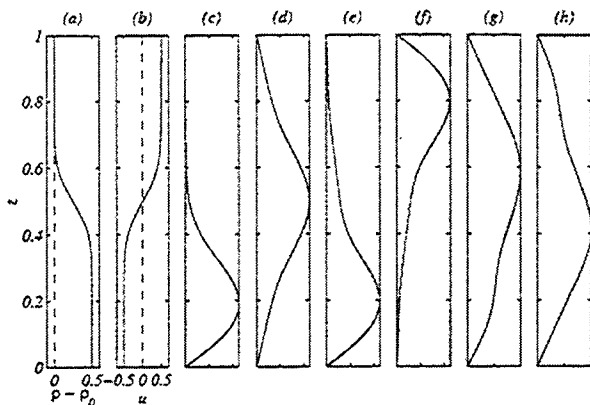
Figure 2. Modal structure of selected eigenvectors at $x = 0$ as determined by the numerical solution of (4). (a) Input density profile; (b) input velocity profile; (c) eigenvector for mode with phase speed $c = -0.61$; (d) $c = 0.0013$ (density mode); (e) $c = -0.27$; (f) $c = 0.28$; (g) $c = -0.51$ (vorticity mode); (h) $c = 0.51$ (vorticity mode).

(representing the largest vorticity gradients) in (4).

There is also a single mode which propagates on the density interface (figure 2d) and we therefore refer to this mode as the *density* mode. The density mode is only present when viscosity is finite, and while it is a persistent feature at all points of the channel, it appears to be unaffected by the shear. Instead, the speed of propagation of this mode is best approximated by the velocity of fluid at the mid-isopycnal (see the centre contour in figure 1).

It is possible to track the density mode, as well as the two vorticity modes along the whole channel. On the assumption that these three are the most important mode 1 waves from the point of view of communication of information about stratification, we show the variation of phase speed and modal structure with x in figure 3. Here the dots show the phase speed, while the curved lines show the hydraulic prediction of wave speeds. At every second gridpoint a panel shows the modal structure of each of the three modes. For the vorticity modes (upper and lower rows of panels) we plot two lines showing the two curvature extrema, and for the density mode (central row of panels) one horizontal line is shown at the maximum of N^2.

Figure 3 shows that modes exist which propagate rightwards at all points in the channel. Upon examination of the top row of panels in figure 3 one sees that the rightward travelling vorticity mode undergoes a change on the left hand side of the domain. As we travel from the centre to the left, a second peak in the eigenvector materialises at $x \approx -0.08$, and at $x \approx -0.12$ the second peak dominates the eigenvector profile. The transition from a vorticity mode to a mode which is trapped in the upper layer is complete at $x \approx -0.20$. The same argument can be applied to the leftward travelling vorticity mode on the right hand side of the domain.

We now consider the implications of the modal structure for hydraulic control. The data of interest in figure 3 pertains to the physical communication of information in the channel which would usually be carried by the baroclinic mode 1 wave. The two vorticity modes are capable of carrying interfacial information, however there is a progressive transformation in the eigenfunction. A transition occurs at $x \approx -0.1$ for the right travelling mode, and $x \approx 0.1$ for the left travelling mode. The end result is that these modes are capable of carrying interfacial information away from the contraction, but are not effective carriers of interfacial information from the reservoirs towards the contraction. Unlike the two layer case which has definable critical points, their inability to carry information the length of the channel relies upon the gradual evolution of eigenvector shape. However, the vorticity modes do illustrate that interfacial variations in either reservoir will not be able to propagate into the channel.

Interfacial information is also likely to be carried by the density mode, since the maximum of the eigenfunction of this mode is coincident with the interface. The phase speed of the density mode varies along the length of the channel, and is positive on the right hand side, negative on the left hand side, and intersects with $c = 0$ at the centre of the contraction. Therefore, this mode is carrying information away from the centre of the contraction. For the density mode, we can specify the critical point to be close to the minimum of the contraction.

Conclusion

The solution of the sixth order stability equation is used to find both the phase speed and modal structure of linear internal waves in the flow shown in figure 1. The results show that, as in two layer flows, control may be thought of in terms of information propagation. More precisely, it is the propagation of information regarding the vertical location of the maximum density gradient that is important. A single mode, centred on the maximum density gradient, appears to conform to the behaviour of the interfacial mode in two layer theory. It is the intersection of the phase speed with zero which indicates the position of a control in the flow.

There are two vorticity modes, which each have a maximum near the interface. While neither of these modes have zero phase speed, they undergo a transition so that upstream of the transition (relative to the direction of travel of the wave) the eigenfunction peak is not in the interfacial region. This is a different concept from hydraulic control, as the transition occurs gradually and thus instead of a critical point at which wavespeeds are zero we find a critical region over which control gradually takes effect. Nonetheless, the vorticity modes cannot carry information towards the contraction, and hence may represent an analogue of hydraulic control in stratified exchange flows.
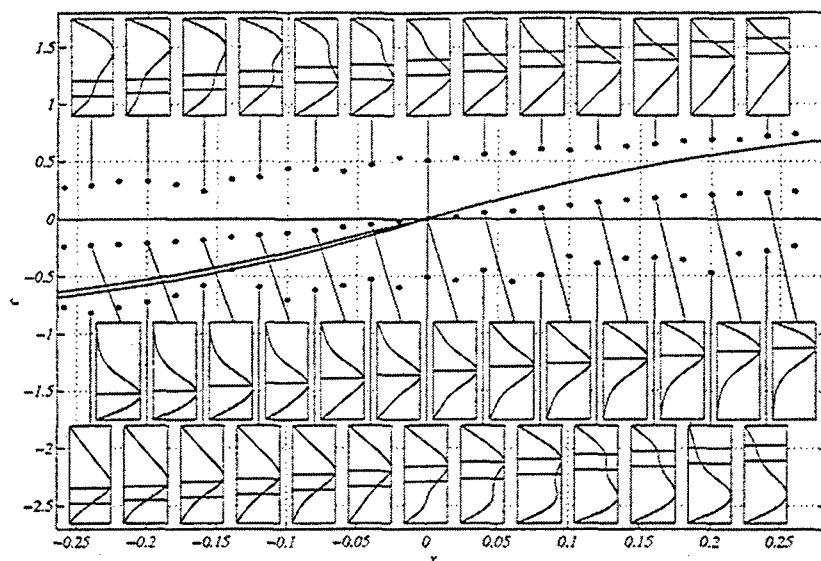
Figure 3. Horizontal phase speeds (dots) from the numerical solution of (4) are plotted against position with hydraulic prediction of wavespeeds (solid curves). Panels show details of modal structure for selected waves, with a line joining each panel to the associated wavespeed. Within the panel, either $\bar{u}_{zz}$ extrema is shown by two horizontal lines (top and bottom row of panels), or N^2 maxima is shown by a single horizontal line (central row of panels).

References

Armi, L., The hydraulics of two flowing layers with different densities, *J. Fluid Mech.*, *163*, 27–58, 1986.

Banks, W. H. H., P. G. Drazin, and M. B. Zaturska, On the normal modes of parallel flow of an inviscid stratified fluid, *J. Fluid Mech.*, *75*, 149–171, 1976.

Dalziel, S. B., Two layer hydraulics: a functional approach, *J. Fluid Mech.*, *223*, 135–163, 1991.

Drazin, P. G., and W. H. Reid, *Hydrodynamic stability*, Cambridge University Press, Cambridge, UK, 1981.

Golub, G. H., and C. F. van Loan, *Matrix Computations*, John Hopkins University Press, Baltimore, 1983.

Gregg, M. C., and E. Özsoy, Flow, water mass changes, and hydraulics in the Bosphorus, *J. Geophys. Res.*, 2000, submitted for review.

Hogg, A. M., G. N. Ivey, and K. B. Winters, Hydraulics and mixing in controlled exchange flows, *J. Geophys. Res.*, *106*, 30,695–30,711, 2001a.

Hogg, A. M., K. B. Winters, and G. N. Ivey, Linear internal waves and the control of stratified exchange flows, *J. Fluid Mech.*, *447*, 357–375, 2001b.

Koppel, D., On the stability of a thermally stratified fluid under the action of gravity, *J. Meth. Phys.*, *5*, 963–982, 1964.

Lawrence, G. A., On the hydraulics of Boussinesq and non-Boussinesq two-layer flows, *J. Fluid Mech.*, *215*, 457–480, 1990.

Moler, C. B., and G. W. Stewart, An algorithm for generalized matrix eigenvalue problems, *SIAM J. Numer. Anal.*, *10*, 241–256, 1973.

Pratt, L. J., W. Johns, S. P. Murray, and K. Katsumata, Hydraulic interpretation of direct velocity measurements in the Bab al Mandab, *J. Phys. Oceanogr.*, *29*, 2769–2784, 1999.

Pratt, L. J., H. E. Deese, S. P. Murray, and W. Johns, Continuous dynamical moddes in straits having arbitrary cross sections with applications to the Bab al Mandab, *J. Phys. Oceanogr.*, *30*, 2515–2534, 2000.

Winters, K. B., and J. J. Riley, Instability of internal waves near a critical level, *Dynamics of Atmospheres and Oceans*, *16*, 249–278, 1992.

Wood, I. R., A lock exchange flow, *J. Fluid Mech.*, *42*, 671–687, 1970.

A. McC. Hogg, James Rennell Division, Southampton Oceanography Centre, Empress Dock, Southampton SO14 3ZH, United Kingdom.

K. B. Winters, Applied Physics Laboratory, 1013 NE 40th St, Seattle, Washington, 98105-6698, USA.

G. N. Ivey, Centre for Water Research, University of Western Australia, 35 Stirling Highway, Crawley 6009, Australia.

Local wind forcing of Korea/Tsushima Strait transport

G. A. Jacobs, D. S. Ko, H. Ngodock, R. H. Preller and S. K. Riedlinger

Naval Research Laboratory, Stennis Space Center, MS, USA

Abstract. The wind forcing and transport response in the synoptic frequency band (2-20 days) is examined through the Korea/Tsushima Strait. The lagged correlation of transport to wind stress indicates southerly wind stress across the both the Yellow Sea and Japan/East Sea is related increased transport. A linear barotropic adjoint model indicates more directly where and at what time lag the wind stress is most important in determining the strait transport. Results indicate that the southerly wind stress across the Japan/East Sea off the Korea coast is most important in forcing the transport through the strait. The wind stress across the Yellow Sea is not dynamically linked to the strait transport. The wind stress information is carried through Kelvin waves that propagate to the strait from the Japan/East Sea, but away from the strait in the Yellow Sea.

Introduction

The mechanism through which the wind stress is connected to the transport through the Korea/Tsushima strait depends on the time period of interest. The mean and seasonally varying transport are expected to be driven by the sea level drop across the strait. The large scale gyre circulation in the Pacific Ocean determines sea level at the entrance to the strait, and the Japan/East Sea (JES) determines the sea level at the exit. The transport through the Korea/Tsushima Strait has been observed through sea level variations across the strait (Yi, 1966), hydrography (Isobe, 1994), ship-board acoustic Doppler current profiler (ADCP) (Katoh, 1993), and moored instruments (Jacobs et al., 2001), and these measurements are all in rough agreement on the mean and seasonal transport. However, the short time period variations and the connection to wind stress are not well known.

Mizuno et al. (1986) examine the correlation of one current meter mooring deployed between Tsushima Island and Japan to the simultaneous wind stress near the same point. Only a small portion of the current variability appear to be correlated to the wind stress at the same point. The wind stress across the Yellow and East China Seas forces large sea level changes (Hsueh, 1988, Jacobs et al., 1998), and it would be expected that the sea level variations would force transport changes through the strait. Correlation of transport to wind stress indicates this mechanism as a possibility. However, a more detailed examination of the ocean physics through numerical models indicates that it is the wind stress across the JES off the Korea coast that is more important.

Numerical model

The numerical model employed is sigma coordinate model similar to the Princeton Ocean Model (POM) [Blumberg and Mellor, 1987]. The main difference between the present model and POM is that the time stepping of the external mode is provided through an implicit scheme. The external mode numerical stability is maintained even with much large time steps [Martin, 2000]. The model contains the Mellor-Yamada level 2.5 turbulence closure scheme [Mellor and Yamada, 1974]. The East Asian Seas (EAS) model covers the South China Sea through the JES at 1/8° horizontal resolution (Figure 1) so that boundary conditions do not exist at straits connecting the Asian marginal seas. Open boundary conditions are provided by a _° horizontal resolution model covering the Pacific north of 20°S with 26 sigma levels. Subsurface temperature and salinity are initialized from the Modular Ocean Data Assimilation System (MODAS) climatology. Both models are forced by wind stress and heat flux from the Navy Operational Global Atmospheric Prediction System (NOGAPS).
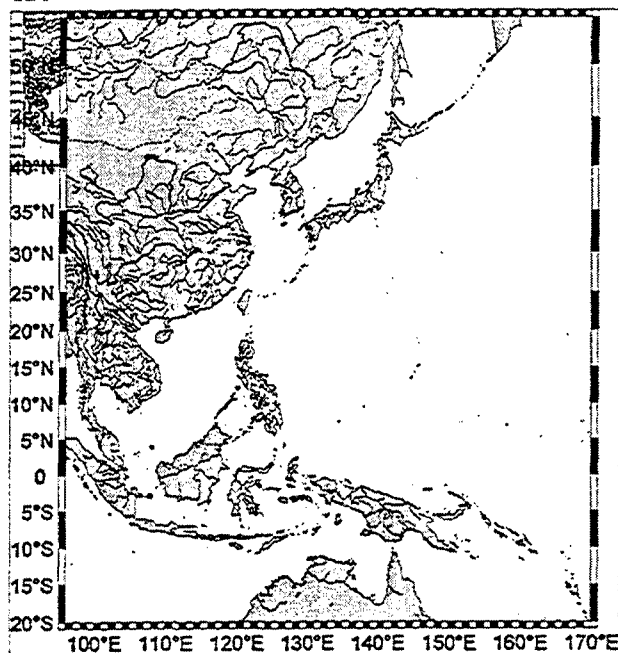
Figure 1. The numerical model is run at 1/8 degree resolution and forced by NOGAPS analysis wind stress.

The transport through the Korea Strait is computed from the model velocity and band-pass filtered using two Bartlett filters with first 0 power points at 2 days and 20 days (Figure 2). A time series of observed transport over the same time period is provided from acoustic Doppler current profilers (ADCPs) moored along a line spanning the strait southwest of Tsushima Island (Jacobs *et al.*, 2001). The transport time series has been filtered by the same method as the model transport.
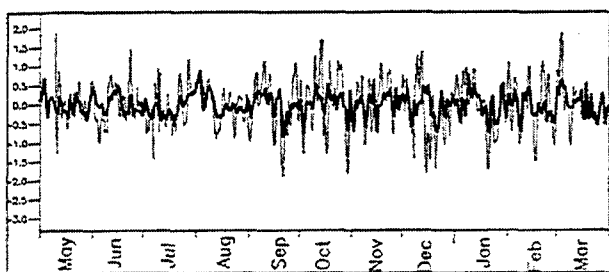
Figure 2. Transports filtered to the synoptic band (2-20 days) during 1999-2000 produced by the numerical model (thick line) and observed by current meters (thin line).

Correlation to wind stress

A first examination of possible mechanisms through which wind stress forces the strait transport is conducted by correlating wind stress to the transport. In this analysis the time-lagged covariance

is computed between the transport times series and the time series of the wind stress components at each point in space. The covariance to the x wind stress and the covariance to the y wind stress may be plotted as a vector at each point (Figure 3).

A significance test is performed on each lagged cross-covariance by first computing the variance of the estimated cross covariance. The square root of this variance is used in Figure 3 to denote the significance. Cross covariance values less than the square root of the expected variance are not plotted, values less than 2 times the expected variance are plotted with thin lines, values less than 3 times the expected variance are plotted with medium lines, and values greater than 3 times the expected variance are plotted with thick lines.

The results indicate significant covariance of transport to wind stress in the Yellow Sea and the Japan/East Sea. The area over which the largest covariance occurs propagates southward with increasing time (from -2 day lag to 0 day lag). This is due to the typical atmospheric events that move through the region. These are frontal systems that create northerly wind bursts mainly during winter.

The difficulty in making definitive conclusions from the covariance analysis is the large scale nature of the atmospheric events. The spatial scales of features in the atmosphere are hundreds to thousands of kilometers. The wind stress at one point may be very influential to the strait transport, and the covariance is large at this point. However, second nearby point may not be influential to the transport, but the wind stress at this second may be very similar to the first point. The result will be that the covariance to the second point will be large even though the wind stress at the second point is not dynamically connected to the transport through the strait.

This effect is evident in the covariance analysis as wind stress over the Asian continent is significantly related to the transport through the strait. We would be hard pressed to define a physical mechanism through which the wind stress acting on the Asian land mass would force transport through the strait on synoptic time scales.
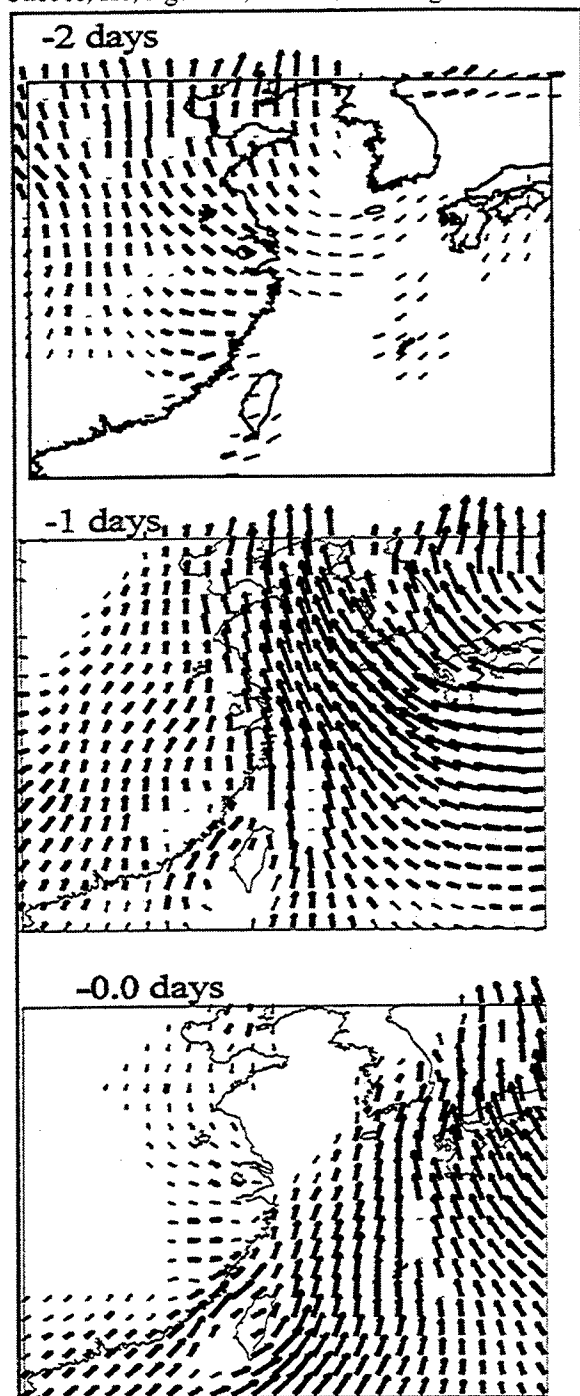
Figure 3. The model transport and wind stress cross covariance at several time lags (negative lag indicates that wind stress leads the transport). Thickness of the vectors indicates significance. The covariance indicates that the winds across either the Yellow Sea or the Japan/East Sea force the transport through the strait.

Adjoint analysis

The model could be used to determine the areas at which wind stress is most influential. By providing a small perturbation to the wind stress at a single point, the effect on transport could be gauged. However, this would require running the model once for every point at which wind stress is applied. This would be computationally unfeasible. Another method to derive the same information is through an adjoint model. The adjoint model provides a method to derive the derivative of a quantity that depends on the model with respect to the model inputs such as wind stress. The quantity of interest here is the transport through the strait, which is a linear functional of the model state.

A single adjoint run provides the sensitivity of strait transport to wind stress for all time lags and for all points in space. The adjoint model used here contains linear barotropic dynamics, which are greatly simplified relative to the forward model. However, the adjoint model indicates that the wind stress over the Yellow Sea is not greatly influential (Figure 4).
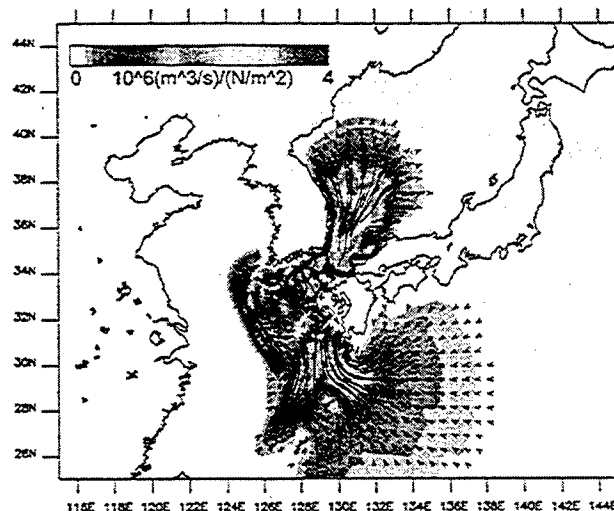
Figure 4. The results from the adjoint model experiment provide the derivative of the strait transport with respect to the wind stress over all time and space. The color shading indicates the amplitude of the derivative, and the vectors indicate the direction. This is at a time lag of -3 hours.

The wind stress across the Japan/East Sea off the coast of Korea is the most influential forcing for the strait transport. Wind stress south of the strait also contributes to the transport.
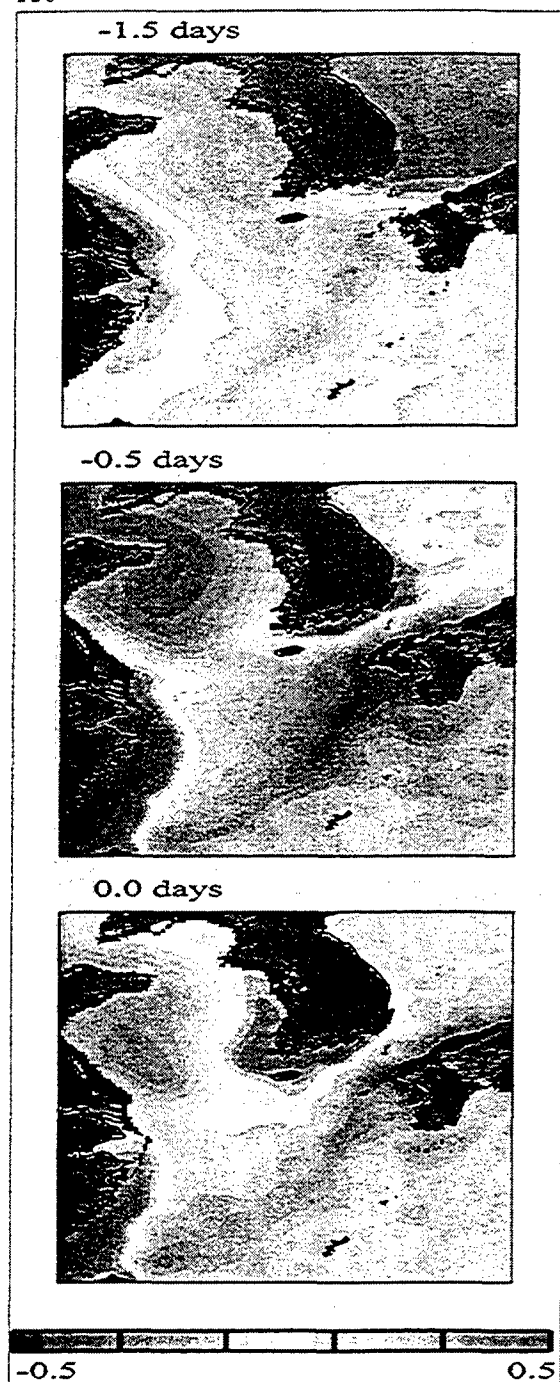
-1.5 days

-0.5 days

0.0 days

-0.5   0.5

Figure 5. Correlation of the sea level to the transport in the East Asian Seas model indicates that a sea level setdown in the Japan/East Sea propagates through the strait. The cross-strait pressure gradient produces a geostrophic transport anomaly.

The reason that wind stress across the Japan/East Sea is much more influential than wind stress across the Yellow Sea is due to the propagation of Kelvin waves. A southerly wind stress produces a setdown

along the eastern Korea coast and a setup along the western Korea coast. These sea level anomalies propagate as Kelvin waves. The Japan/East Sea setdown propagates to the strait while the Yellow Sea setup propagates away from the strait (Figure 5).

Conclusions

On time scales of 2-20 days the transport through the Korea/Tsushima Strait is forced by wind stress predominantly over the Japan/East Sea off the coast of Korea. A southerly wind stress initially causes a sea level setdown that propagates to the strait and produces a transport anomaly through the strait in near geostrophic balance.

References

Blumberg, A., and G. Mellor, A description of a three-dimensional coastal ocean circulation model, in Three-Dimensional Coastal Ocean Models, *Coastal Estuarine Sci., vol. 4,* edited by N.S. Heaps, pp. 1-16, AGU, Washington, D.C., 1987.

Hsueh, Y., Recent current observations in the eastern Yellow Sea, *J. Geophys. Res., 93,* 6875-6884, 1988.

Isobe, A., Seasonal variability of the barotropic and baroclinic motion in the Tsushima-Korea Strait, *J. Oceanogr., 50,* 223-238, 1994.

Jacobs, G. A., H. T. Perkins, W. J. Teague, and P. J. Hogan, Summer transport through the Tsushima-Korea Strait, J. Geophys. Res., 106, 6917-6930, 2001.

Jacobs, G. A., W. J. Teague, S. K. Riedlinger, R. H. Preller, and J. P. Blaha, Sea surface height variations in the Yellow and East China Seas, 2, SSH variability in the weekly and semiweekly bands, *J. Geophys. Res., 103,* 18,479-18,496, 1998.

Katoh, O., Detailed current structures in the eastern channel of the Tsushima Strait in summer, *J. Oceanogr., 49,* 17-30, 1993.

Martin, P. J., Description of the Navy Coastal Ocean Model Version 1.0, *Naval Research Laboratory report NRL/FR/7322—00-9962,* 42 pp.

Mellor, G. L., and T. Yamada, A hierarchy of turbulence closure models for planetary boundary layers, *J. Atmos. Sci., 31,* 1791-1806, 1974.

Yi, S. U., Seasonal and secular variations of the water volume transport across the Korea Strait, *J. Oceanogr. Soc. Korea, 12,* 7-13, 1966.

Tides in the Bab el Mandab Strait

E. Jarosz[1] and S. P. Murray[2]

[1] Coastal Studies Institute, Louisiana State University, Baton Rouge, Louisiana, USA
[2] Office of Naval Research, Arlington, Virginia, USA

Abstract. Tidal motion in the Bab el Mandab Strait is examined by means of analyzing measurements collected in the Strait between May of 1995 and July of 1997 azs well as by numerical modeling. Tidal elevations and currents were numerically simulated with a two-dimensional finite element model (ADCIRC-2DDI).

Introduction

The Bab el Mandab Strait is located in the southern part of the Red Sea and is its major link with the Gulf of Aden and Indian Ocean (Figure 1). This Strait is a region where the transition occurs between two noticeably different tidal regimes: the Gulf of Aden, where tidal fluctuations are mixed and have a range in excess of 2 m, and the Red Sea, where the tides are principally semidiurnal and their range is less than 1 m.
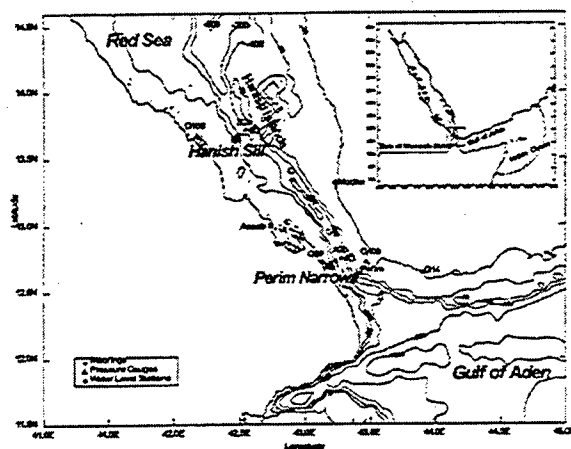
Figure 1. Map of the Bab el Mandab Strait (depth contours are in meters); locations of the subsurface pressure gauges, current meter moorings and water level stations are also shown.

A few analytical analyses were done to determine tides in the Bab el Mandab Strait, and they were used to explain tidal dynamics in the entire Red Sea. Results from these analyses (Defant, 1961) showed that tides in the Red Sea should be considered as a superposition of a tide co-oscillating with those observed in the Gulf of Aden and an independent tide. Historical observations of tides, especially tidal currents, are also very limited and restricted to the southern end of the Strait. Based on short time series of current, salinity and temperature measurements, Vercelli (1925, 1927) and Siedler (1969) characterized the tidal currents in this part of the Strait as exceptionally strong with clear diurnal and semidiurnal oscillations. Both researchers also indicated the presence of internal tides in the Bab el Mandab.

Recent measurements (current, subsurface pressure, salinity and temperature), which were collected in the Strait between May of 1995 and July of 1997 for a project entitled "Observation and Modeling – an Integrated Study of the Transport through the Strait of Bab el Mandab" (the BAM project), as well as results from a two-dimensional finite element hydrodynamic model named ADvanced Two-Dimensional Depth-Integrated CIRCulation Model for Shelves, Coasts and Estuaries

(ADCIRC-2DDI) developed by Luettich et al., (1992) and Westerink et al. (1994) allowed us to examine in more details variability of tidal elevation and currents in the entire Strait.

Surface tide in the Strait

Within the Bab el Mandab Strait, subsurface pressure and water level observations (see Figure 1 for locations of tidal gauges) indicate that the tidal fluctuations have a larger range (~ 2 m) in the southern part than in the northern part where their range is below 1 m. The largest amplitudes among diurnal components are observed for the K_1, while among semidiurnal constituents, the M_2 is a dominant component. The major changes in amplitudes and

phases of these constituents are observed along the Strait. For the K_1 component, the along-strait variability is generally associated with amplitudes, which decrease from maximum values observed at the southern end (~ 35 cm) to their minimum values present at the northern end (~ 6 cm). For the M_2 component, both tidal constants display large changes within the Strait. Amplitudes show a minimum (~ 7 cm) in the nodal zone (Defant, 1961) located approximately in the middle of the Strait and larger values at Perim Narrows (~ 37 cm) in the south and the Hanish Sill in the north (~ 24 cm), while the phase distribution implies nearly an 180° difference between these two locations. The different variability of the amplitudes and phases of the semidiurnal and diurnal surface tides generates three different tidal regimes within the Strait: (1) mixed, predominantly semidiurnal in the south, (2) mixed, predominantly diurnal in the middle, and (3) semidiurnal in the northern part.

Tidal currents

Observations indicate that the tidal currents in the Bab el Mandab Strait are nearly rectilinear and generally aligned with the along-strait axis. They are the most energetic near Perim Narrows. Farther north, the tidal currents fluctuations are still very distinct but their range is smaller. Variance estimated from the observations indicate that the tidal currents are of the mixed type even near the Hanish Sill where the surface tide regime is semidiurnal (Figure 2).
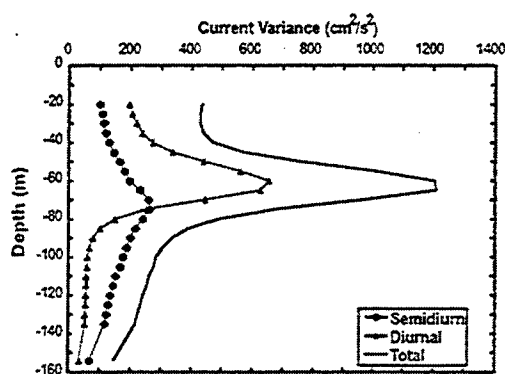
have the largest values in the southern part of the Strait and show smaller values farther north. The vertical structure of these constituents is complicated, differs between semidiurnal and diurnal components, and depends on the location and stratification type (there are two different types of stratification in the Strait: (1) winter stratification, which is associated with the two-layer subtidal circulation and is usually present between October and May, and (2) more variable summer stratification, which is generally observed between June and September when the three-layer subtidal circulation develops in the Strait).

All parameters (semimajor axis, semiminor axis, inclination angle, phase) of the tidal current ellipse are influenced by the change in stratification regime; however, the most evident changes are observed in the vertical profiles of the semimajor axis. When the profiles are compared at three different moorings located in a deep channel (A2b, C, and B2b moorings; see Figure 1 for moorings locations) the changes are more distinct for the K_1 constituent than those for the M_2 constituent. A noticeable maximum in the pycnocline layer is observed for the K_1 component during the winter stratification period (Figure 3a), whereas for summer stratification (Figure 3b), this maximum is not observed at Perim Narrows and in the middle of the Strait (C mooring), and it is smaller and present only in the lower pycnocline (~ 100 m) at the Hanish Sill. At the same time, larger amplitudes of the M_2 semimajor axis in the pycnocline layer for both stratification regimes are only observed near the Hanish Sill.
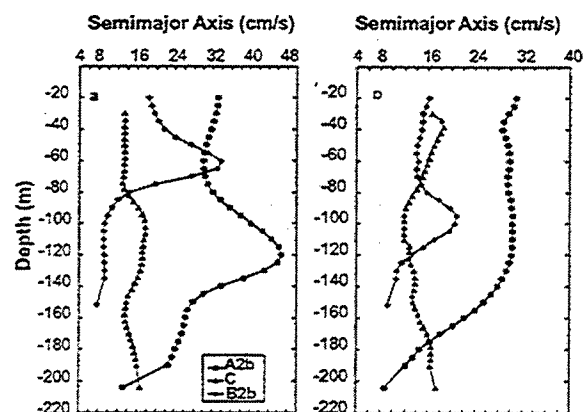

Figure 2. Vertical distributions of the total current variance and variance associated with the semidiurnal and diurnal frequency bands for the winter stratification near the Hanish Sill.

Similar to fluctuations of the surface tide, the most energetic tidal currents are generated by the K_1 and M_2 constituents. Amplitudes of these constituents

Figure 3. Vertical distributions of the K_1 semimajor axes at Perim Narrows (A2b mooring), C mooring, and near the Hanish Sill for (a) winter and (b) summer stratifications.

Non-uniform vertical distributions of the current amplitudes clearly indicate that tidal currents in the Bab el Mandab Strait are not strictly barotropic but

they are superposition of barotropic and baroclinic components. The baroclinic component is primarily of diurnal period, and the strongest baroclinic signal is observed in the pycnocline layer. Additionally, this baroclinic signal is more pronounced for the winter stratification period, and it is very distinct at Perim Narrows and the Hanish Sill. Results from dynamic mode decomposition (Figure 4) as well as results from EOF analysis suggest that for the winter stratification period, the baroclinic velocities seem to contain strong contributions from the second and third baroclinc modes at Perim Narrow, and from the first and second modes at the Hanish Sill.
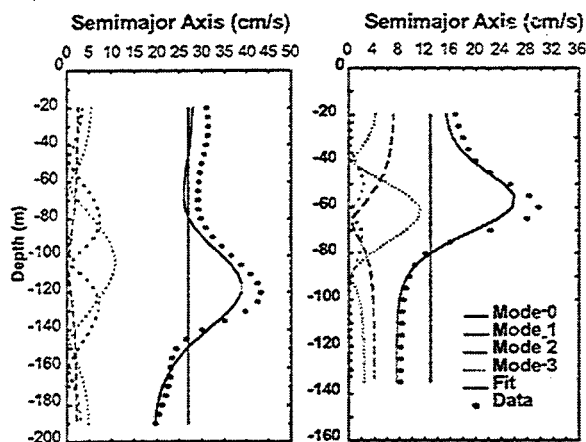
Figure 4. Amplitudes of the semimajor axes of barotropic (mode 0), first baroclinic (mode 1), second baroclinic (mode 2), and third baroclinic (mode 3) modes of the diurnal tidal currents for the winter stratification at (a) Perim Narrows (A2b mooring), and (b) the Hanish Sill (B2b mooring); amplitudes of the semimajor axis computed from the current data are denoted by pluses and amplitudes obtained from fitting first four modes (modes 0 through 3) are shown as a thick continuous line.

Results from dynamic mode decomposition also clearly show that the diurnal tidal currents (Figure 4) as well as the semidiurnal tidal currents are dominated by the barotropic signal. The structure of the barotropic currents in the deep channel and surface tides near Perim Narrows is fairly well explained by simple momentum balance. To first order, a balance exists in the along-strait direction between local acceleration and the elevation gradient, while in the cross-strait direction, a balance between local acceleration, Coriolis term, and elevation gradient is observed.

Residual circulation, energy flux and dissipation

The barotropic tides, their energy fluxes, dissipation, and residual circulation generated by them were examined in more details using results from the high-resolution two-dimensional finite element model (ADCIRC-2DDI). The model was forced at open boundaries by elevations generated by four diurnal (K_1, O_1, P_1, Q_1) and four semidiurnal (M_2, S_2, N_2, K_2) tidal constituents. In addition, an effective tidal potential within the domain was applied for the same eight constituents.

The model simulates well diurnal tidal elevations (an rms varies between 0.9 cm and 2.2 cm). However, its performance for the semidiurnal tidal elevations (an rms varies between 3.0 cm and 9.4 cm) is less satisfactory due to the errors between observed and computed phases in the region where there is a nodal line for these tides in the Strait. The comparison between observed and computed currents is satisfactory for both semidiurnal and diurnal constituents because differences between observed and computed current ellipse parameters are small and, for instance, the computed amplitudes of the semimajor axis are only 20% or less smaller than those estimated from the data and the phase difference is always less than 1 h.

Residual circulation generated by the tidal currents is rather weak in the major part of the Strait and consists of mean (time-averaged) and fluctuating (deviation from the mean) components. The velocities of the mean component averaged over the entire area of the Strait are ~ 1 cm/s so in general, the residual flow contributes little to the overall circulation. In addition, the fluctuating component is dominated by fortnightly oscillations, which are generated by the interactions of the K_1 and O_1 constituents as well as the interaction between the M_2 and S_2 components.

Examination of the momentum balance terms indicates that in the deep parts of the Strait, the tidal dynamics is linear, i.e., the momentum balances are dominated by the linear terms. The elevation gradient, Coriolis term and local acceleration are the dominant terms for the cross-strait balance, while for the along-strait balance, the local acceleration and elevation gradient are the most important ones.

However, in shallow waters, the nonlinear terms, such as friction and advection, become as important as the linear terms. Therefore, to capture the variability of the barotropic tides in the entire Bab el Mandab Strait, one needs to employ a fully nonlinear hydrodynamic set of the momentum equations.

Mean energy fluxes of the K_1 and M_2 constituents are small, mainly due to nearly $\sim 90°$ phase difference between tidal velocity and elevation, which is observed in the major part of the Strait. They are directed from the Gulf of Aden for the K_1 and from the Red Sea proper and Gulf of Aden for the M_2. Very small energy fluxes from the Strait to the adjacent basins indicate that almost all tidal energy is dissipated within the Strait. The distribution of the rate of energy dissipation due to bottom friction implies that the major area of dissipation is located between Perim Narrows and the Assab-Mocha line (see Figure 1 for locations). The energy dissipation, which was estimated from a difference between the output and input fluxes through two transects located at the southern and northern ends of the Strait, is 0.226 GW and 0.199 GW for the K_1 and M_2 constituents, respectively. These estimates are comparable to other estimates of the energy dissipation, which were obtained from the integration of the dissipation rate over the area of the Strait, and they are 0.16 GW and 0.12 GW for the K_1 and M_2 constituents, respectively.

Conclusions

The Bab el Mandab Strait is where the transition occurs between two noticeably different tidal regimes: the Gulf of Aden, where tidal fluctuations are mixed and have a range in excess of 2 m, and the Red Sea, where the tides are principally semidiurnal and their range is less than 1 m. Within the Strait, observations collected between May of 1995 and July of 1997 indicate that tidal currents are a mixed type and dominant constituents are the K_1 and M_2. The vertical structure of the tidal currents is complicated, differs between semidiurnal and diurnal constituents, and depends on the location and stratification. In addition, the stratification impacts more the vertical distribution of the diurnal tidal currents. The major part of this signal is barotropic but energetic baroclinic currents are observed near Perim Narrows and the Hanish Sill during the winter stratification. Results of the EOF analysis and internal velocity modes estimated from observed density profiles indicate that the baroclinic currents of diurnal frequency have vertical structure, which is a combination of the second and third baroclinic modes near Perim Narrows and of the first and second modes near the Hanish Sill.

To examine in more details the barotropic tides in the Strait, a two-dimensional finite element model (ADCIRC-2DDI) was implemented. Results from the model imply that residual circulation induced by the barotropic tides is generally weak in the Strait and consists of mean and fluctuating components. Average barotropic energy fluxes over a tidal period are small and their direction depends on the constituent. The K_1 component has one source of energy, which is the flux from the Gulf of Aden, while there are two sources of energy for the M_2: one from the Gulf of Aden and another from the Red Sea. In addition, these results show that the major part of the tidal energy for both constituents is dissipated within the Strait itself.

References

Defant, A., Physical Oceanography, Vol. 2. Pergamon Press, 598 pp, 1961.

Luettich, R.A., J.J. Westerink, and N.W. Scheffner, ADCIRC: An Advanced Three-Dimensional Circulation Model for Shelves, Coasts and Estuaries, Report 1: Theory and Methodology of ADCIRC-2DDI and ADCIRC-3DL. Dredging Research Program Technical Report DRP-92-6, U.S. Army Engineers Waterways Experiment Station, Vicksburg, MS, 137 pp, 1992.

Siedler, G., On the fine structure of density and current distribution and its short-time scale in different areas, *Prog. Oceanog.*, 5, 81-94, 1969.

Vercelli, F., Richerche di oceanografia fisica eseguite della R. N. AMMIRAGILIO MAGNAGHI (1923-24), Part I, Correnti e maree, *Annali Idrografici*, 11, 1-188, 1925.

Vercelli, F., Richerche di oceanografia fisica eseguite della R. N. AMMIRAGILIO MAGNAGHI (1923-24), Part IV, La temperatura e la salinita, *Annali Idrografici*, 11, 1-66. 1927.

Westerink, J.J., C.A. Blain, R.A. Luettich, and N.W. Scheffner, ADCIRC: An Advanced Three-Dimensional Circulation Model for Shelves, Coasts and Estuaries; Report 2: Users Manual for ADCIRC-2DDI. Dredging Research Program Technical Report, U.S. Army Engineers Waterways Experiment Station, Vicksburg, MS., 156 pp, 1994.

Atmospherically-Forced Exchange through the Bab el Mandeb

W. E. Johns[1] and S. S. Sofianos[2]

[1] Rosenstiel School of Marine and Atmospheric Science, University of Miami
[2] Division of Applied Physics, University of Athens

Abstract. The exchange between the Red Sea and the Gulf of Aden on synoptic
time scales (days to weeks) is investigated using moored time series data collected
in the strait of Bab el Mandeb from June 1995 to November 1996. Transport
variations through the strait on these time scales can reach amplitudes of up to
0.6 Sv, or nearly twice as large as the mean rate of exchange through the strait
driven by annual evaporation over the Red Sea. The synoptic transport variability
appears to be driven by two primary forcing mechanisms: wind stress variability
over the strait, and variation in the large-scale barometric pressure over the Red
Sea. Simple linear models of the forced response are developed and are shown to
reproduce the essential features of the observations. The response to barometric
pressure forcing over the Red Sea is isostatic (inverted barometer) at the lowest
frequencies, with inflow through the Strait lagging high atmospheric pressure (low
sea level) in the Red Sea. However, at frequencies higher than the Helmholtz
resonance frequency for the Red Sea, which occurs at a period of about 5 days,
the response changes to a co-oscillating mode between sea level and atmospheric
pressure with inflow through the strait leading high atmospheric pressure. The
transition between these regimes is well reproduced by a linear barotropic model
incorporating a reasonable value of friction. The wind forced response is described
by a 2-layer model driven by the alongstrait wind stress and a barotropic alongstrait
pressure gradient. A key feature of this model is the role of the wind-generated
transport through the strait in setting up an adverse pressure gradient that modifies
the response. At low frequencies this results in the upper and lower layer transports
being nearly out of phase with each other, but tending toward an in-phase variation
at frequencies above the Helmholtz frequency. The linear 2-layer model, again
with reasonable friction, reproduces the basic features of this response, including
an elevated response amplitude near the Helmholtz resonance period. Combined,
the barometric pressure and alongstrait wind forcing appear to account for about
70

Introduction

The exchange between the Red Sea and the Indian Ocean
is driven by the extensive rate of evaporation over the Red
Sea and influenced by the wind field of the Indian Monsoon
system in the southern part of the basin. The basic pattern
of the exchange at Bab el Mandeb (connecting the Red Sea
and the Gulf of Aden) is of the inverse estuarine type, inter-
rupted during summer (June to September) by a three layer
exchange pattern. The strength of the annual mean exchange
is of the order of 0.3 Sv. Superimposed on the mean ex-
change and its annual cycle, fluctuations of higher frequency
are observed that can reach amplitudes several times as large
as the mean exchange. Here we investigate the exchange at

Bab el Mandeb at synoptic time scales (from a few days to
several weeks) using moored time series data collected from
June 1995 to November 1996 (Murray and Johns, 1997), and
relate it to local and regional atmospheric forcing. A simple
2-layer model of the forced exchange is developed which is
shown to explain a large fraction of the transport variance on
these time scales.

Data and Model

Detailed observations of the exchange through the Bab el
Mandeb were obtained by Murray and Johns (1997) using
moored current meter arrays at two locations in the strait.
In addition to quantifying the annual cycle of the exchange,

these measurements revealed large fluctuations in transport through the strait on relatively short (subtidal) time scales, of order 0.6 Sv (Fig. 1).

The synoptic transport variability appears to be driven by two primary forcing mechanisms: variations of the large scale barometric pressure over the Red Sea and local wind stress variability. Fig. 1 presents the time series of sea level pressure over the Red Sea and the along channel local wind stress for the period of the transport measurements. The former was obtained from the National Climatic Data Center (NCDC) and calculated using weighted meteorological station data around the coast of the Red Sea. The latter was recorded during the same project (Murray and Johns, 1997) at a meteorological station that was installed in the strait. The transport fluctuations are found to be significantly coherent with the basin-averaged atmospheric pressure fluctuations in a period band from about 3-10 days and coherent with the local along-strait wind fluctuations from 3-20 days.

In order to explain this variability, a simple, linear model of the response of the strait to the local wind and changes of the atmospheric pressure over the Red Sea is developed. The basic variables and constants used are shown in the schematic of Fig. 2. Several assumptions and simplifications are used in the basic equations describing the model. The present approach is two-dimensional, so that the rotational effect is neglected and no geostrophic control is implied. The neglect of rotation is not unreasonable in this case since the width of the strait at its narrowest point is less than the internal deformation radius of $O(35\ km)$.

The sea level inside the basin is taken to be uniform, under the assumption that long gravity waves will equilibrate the sea surface in the basin on time scales much faster than synoptic time scales of interest. Outside the basin the sea surface is assumed to respond isostatically to the atmospheric pressure forcing, since it is openly connected to the Indian Ocean.

An important difference of this model with previous approaches is not only the introduction of the local winds but also the assumption that the effect of the wind is distributed only in an upper layer of thickness H_1, which is here taken to be 70 m, the depth of the zero crossing of the most energetic EOF of the transport profile (not shown). This layer does not necessarily coincide with surface layer of the inverse estuarine exchange. In order to simplify the solution forms, density differences will be not taken into account and a average density (ρ_0) will be used in the equations.

Under these assumptions the governing equations are

$$\frac{\partial Q_1}{\partial t} = -\frac{A_{S_1}}{\rho_0}\frac{\partial P}{\partial x} + \frac{A_{S_1}\tau_x}{H_1\rho_0} - \lambda_1 Q_1 \qquad (1)$$

$$\frac{\partial Q_2}{\partial t} = -\frac{A_{S_2}}{\rho_0}\frac{\partial P}{\partial x} - \lambda_2 Q_2 \qquad (2)$$

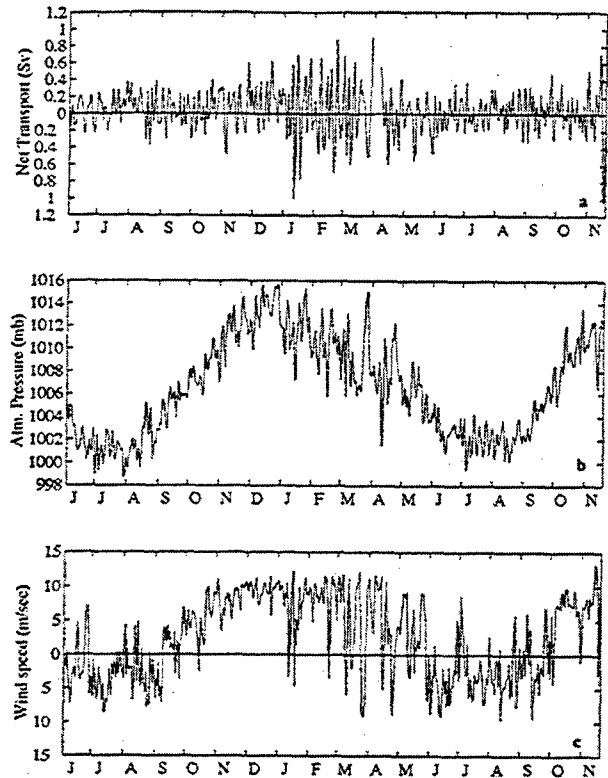$$\frac{\partial \eta}{\partial t} = \frac{Q_1 + Q_2}{A_{RS}} \qquad (3)$$

Figure 1. ime series of the net transport at the strait of Bab el Mandeb (a), the atm. pressure over the Red Sea (b), and the along-axis wind field at the Hanish Sill (c), for the period June, 1995 to November, 1996.).

$$P = P_a + g\,\rho_0\,\eta \qquad (4)$$

where A_{S_1} and A_{S_2} are the cross-sectional areas of the two layers and they sum to the cross-sectional area of the strait ($A_{S_1} + A_{S_2} = A_S$) taken as the average value somewhere in the middle of the channel. Q_1 and Q_2 represent the transport at the surface and lower layer, respectively. A_{RS} is the surface area of the Red Sea and η the sea level in the basin. The friction is represented by the linear forms $\lambda_1 Q_1$ and $\lambda_2 Q_2$, following Candela et al. (1989) and Middleton and Viera (1991). In general $\lambda_1 \neq \lambda_2$ and friction at the lower layer is expected to be larger than that in the surface layer. In the solutions presented here and the comparison of the results with the observations a single value ($\lambda_1 = \lambda_2 = \lambda$) is used in order to reduce the number of parameters involved.

The frequency response functions (gain and phase) of the net transport response to the wind stress and atmospheric pressure is plotted in Fig. 3 for three different frictional parameters ($\lambda = 0.25 \times 10^{-5}$, $\lambda = 0.5 \times 10^{-5}sec^{-1}$, and $\lambda = 1.25 \times 10^{-5}sec^{-1}$) chosen as the most appropriate values according to similar models (Candela et al., 1989) and the observations, and compared with the observed data. To a first order approximation the system behaves as a forced
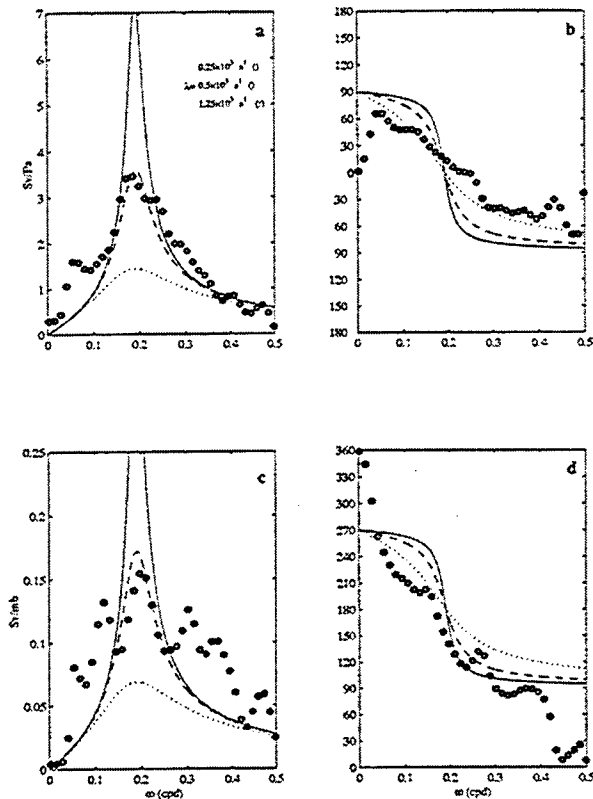
Figure 3. Frequency response function (gain on the left and phase on the right) comparison between observation (circles) and model (three frictional parameters) results for the net transport forced by the winds (a and b) and the atmospheric pressure over the Red Sea (c and d).)
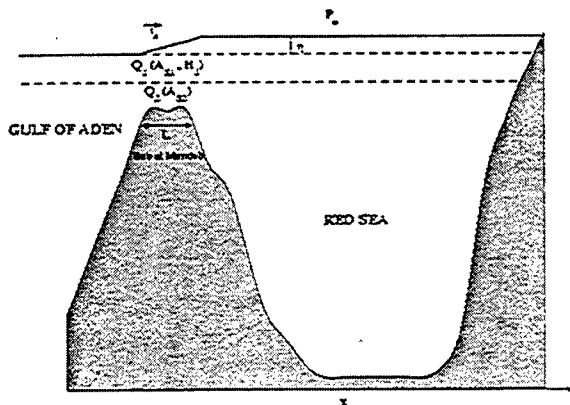

Figure 2. Sketch of the configuration used in the model, presenting the basic constants and variables used.).

oscillator subject to some friction, with the Helmholtz resonance frequency

$$\omega_0 = \sqrt{\frac{g A_S}{A_{RS} L_S}} \qquad (5)$$

occurring at a period of about 5 days.

Discussion

Although it is simple, the model can reproduce the basic response of Bab el Mandeb to local meteorological forcing and the atmospheric pressure variability inside the Red Sea. It can explain 70% of the observed variance and if we consider only the winter season (October to May) when the synoptic atmospheric forcing is the strongest this value amounts to almost 80%. The wind seems to be more important in the case of Bab el Mandeb and the correlation between the observed transport fluctuations and model wind-driven solutions is highest. This can be attributed to the strength of the fluctuations and the orographic effect in combination with the small width of the channel. The key feature of this model is the role of the wind generated transport through the strait in setting up an adverse pressure gradient that modifies the response. At low frequencies this results in the upper and lower layer being nearly out of phase but tending toward an in phase variation at frequencies around and above the Helmholtz frequency. The actual exchange driven by the winds reaches a maximum at the lower frequencies (20 days), with the upper and lower layers being accelerated in opposite directions but with little net transport change, while the net transport itself peaks near the Helmholtz resonance period.

More elaborate models can investigate the influence of parameters neglected in the model described here, like the rotation effect when layers of different density are allowed and the internal deformation radius becomes critically close to the width of the strait. The choice of a constant λ can simplify our derivations but the investigation of other forms of friction may improve the performance of similar models. Furthermore, the role of the different forms of remote forcing that can influence the variability in the strait should be investigated. Future numerical models incorporating synoptic meteorological forcing can produced a more detailed picture and improve our understanding of the dynamics governing the region.

References

Candela, J., C. D. Winant, and H. L. Bryden, 1989, Meteorologicaly forced subinertial flows through the Strait of Gibraltar, *J. Geophys. Res.*, , *94*, 12667-12679.

Middleton, J. F., and F. Viera, 1991, The forcing of low frequency motions within Bass Strait, *J. Phys. Oceanogr.*, , *21*, 695-708.

Murray, S. P., and W. Johns, 1997, Direct observations of seasonal exchange through the Bab el Mandeb strait, *Geophys. Res. Lett.*, , *24*, 2557-2560.

W. E. Johns, Rosenstiel School of Marine and Atmospheric Science, University of Miami, 4600 Rickenbacker Causeway, FL 33149, USA

S. S. Sofianos, Department of Physics, Division of Applied Physics, University of Athens, University Campus Builds Phys-5, Athens 15784, Greece

Intensive direct current measurements at the Bussol Strait

Katsurou Katsumata, Kay I. Ohshima[1], Tokihiro Kono[2], Motoyo Itoh[1], Ichiro Yasuda[3], and Masaaki Wakatsuchi[1]

[1]Institute of Low Temperature Science, Hokkaido University, Sapporo, Japan.
[2]Department of Marine Sciences and Technology, Hokkaido Tokai University, Sapporo, Japan.
[3]Department of Earth and Planetary Science, University of Tokyo, Tokyo, Japan

Abstract. Direct current measurements were made at the largest strait (depth about 2400m) in the Kuril Islands that separate the Sea of Okhotsk and the North Pacific. The narrowest part (roughly 80 km wide) of the strait is covered by 13 stations and more than 140 casts of an lowered acoustic Doppler current profiler and a CTD were performed. The tidal flow is mostly less than 0.3 m/s, but a strong peak trapped near the bottom below 1000m of more than 1 m/s is found. The spatial structure of the tidal flow is complex. The steady exchange between the Sea of Okhotsk and the North Pacific takes place mainly in the southwest valley where the strong tidal activity is found. The net transport is roughly 2.5 Sv from the Okhotsk to the Pacific.

Introduction

The Sea of Okhotsk is a marginal sea of the North Pacific (Figure 1), known the southmost seasonal ice zone. Production of sea-ice occurs mainly at the northwestern shelf and the Okhotsk circulation is affected by vertical convection driven by the brine rejection. Its impact is not limited within the Sea of Okhotsk. Recent analysis [*e.g. Yasuda*, 1997] reveals that the Sea of Okhotsk plays a crucial role in the formation of North Pacific Intermediate Water — water mass found widely in the Pacific subtropical gyre and characterized by the salinity minimum around $\sigma_\theta = 26.8$ [*Sverdrup et al.*, 1942]. In fact, the Sea of Okhotsk is believed to be the only strong thermohaline source in the Pacific circulation, and the isopycnal $\sigma_\theta = 26.8$ can be ventilated only in the Sea of Okhotsk to form the salinity minimum. Its potential in absorbing and transporting anthropogenic CO_2 has also attracted attention of chemical oceanographers [*e.g. Andreev et al.*, 2001].

Despite the recent realization of the importance of the Sea of Okhotsk in the Pacific circulation system, the water exchange between the Sea of Okhotsk and the adjacent North Pacific gyre is hardly known. These basins are separated by the Kuril Islands with numerous straits. In situ observations at these straits have been difficult because of the severe winter conditions and the political issues. Another difficulty is the strong tide around the islands; the tide is so strong that the geostrophic transport calculation based on snapshot hydrographic observations yields unrealistic estimates.

Katsumata et al. [2001] made direct current measurements at the second largest strait in the Kuril Islands, where they employed an LADCP (lowered acoustic Doppler cur-
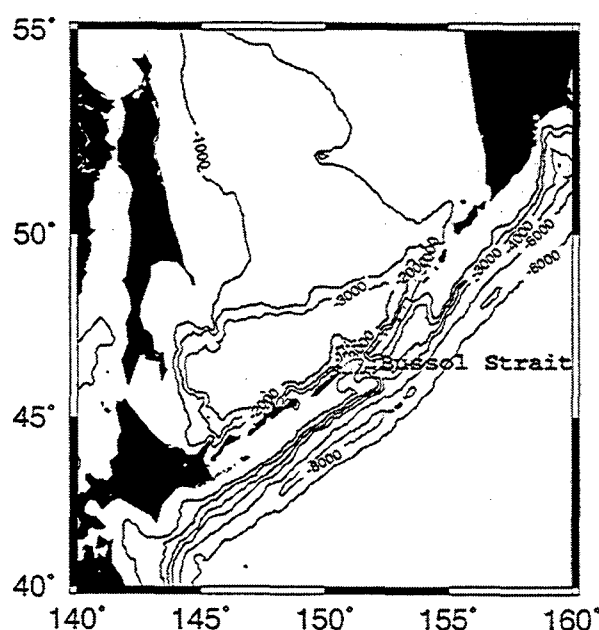

Figure 1. The Sea of Okhotsk. The contours show depth in meters.
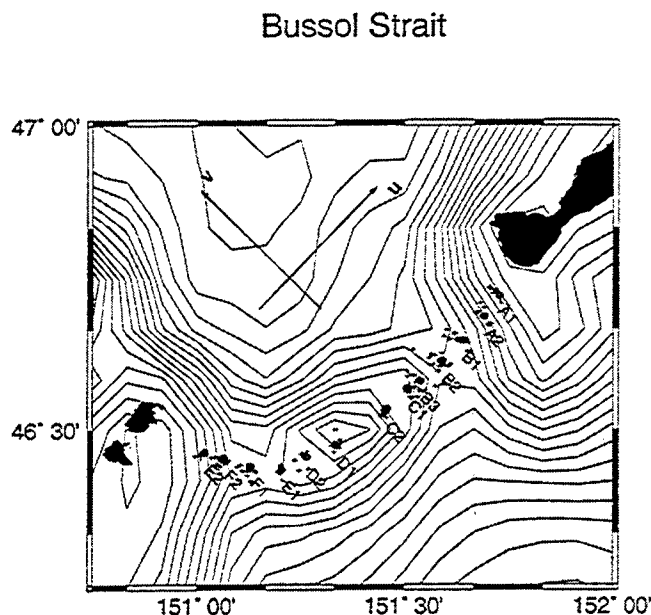
Bussol Strait

Figure 2. Observation stations. The circle shows the position where a cast was started; the cross shows where the cast was finished. First letter of the station name indicates its group. Rotated coordinate (u, v) is also shown.
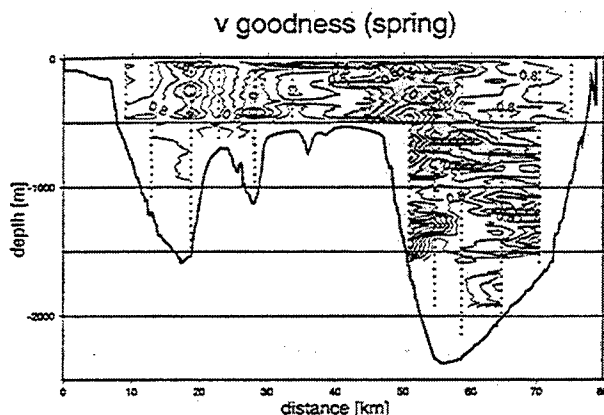
v goodness (spring)

Figure 3. Goodness of fit for v at the spring tide. Area with less than 70 % goodness is shaded. Contour interval is 0.1. The cross section is taken along the line connecting the stations shown in Figure 2. Bathymetry is derived from underway echo sounding obtained during the cruise.

rent profiler) to obtain the velocity profile independent of the geostrophic calculation. They made consecutive casts at two stations in the strait and separated the tidal and residual components from the measured velocities. In summer of 2001, similar but more intensive measurements were made at the largest strait in the Kuril Islands, namely the Bussol Strait. Priority of the observation was given to the spatial resolution, since better temporal resolution and coverage should be expected from a mooring observation. Preliminary result of this observation is described here.

Observation

LADCP

In order to measure absolute velocities, an LADCP was employed. It is an ADCP mounted on a CTD (conductivity, temperature, depth profiler) frame along with a CTD. Every second, it measures the velocity relative to the CTD as it goes down and up during a CTD cast. The velocity ensembles are statistically processed to yield the relative velocity profile at all depth. The bottom track velocity is then used to convert the relative velocity to the absolute velocity. For the detail of the data processing, readers are referred to *Fischer and Visbeck* [1993].

Observation

Thirteen observation stations are placed across the Bussol Strait (Figure 2). These stations consist of 6 groups. Casts were repeated at one station after another in one group. In order to filter out the diurnal tide, the casts were repeated for at least 25 hours at one station, which gives 5 to 7 casts at one station. Since timescale of the tidal dynamics is of the order of an hour, data obtained during upcast and downcast are considered as different, which means 10 to 14 data are obtained at one depth at one station except for the bottom of the cast. The groups B and F occupy two deep part of the Strait (see Figure 2) and observations in these groups were repeated at the spring tide and at the neap tide. Observations in other groups were made only once.

Data process

The velocities were rotated such that u means the along-strait component and v means the across-strait component (see Figure 2). The timeseries thus obtained consists of various signals. Following components are separated by the least square fitting.

- Diurnal tide (M2 tide with period 12.42 hour)
- Semi diurnal tide (K1 tide with period 23.93 hour)
- Linear trend
- Steady component

It is necessary to fix two variables for one tidal component (i.e. magnitude and phase), and the fitting fixes six variables out of 10 to 14 data. The goodness of fit is defined as the ratio of the variance explained by the fitted components to the total variance. It is seen from Figure 3 that the fitting is
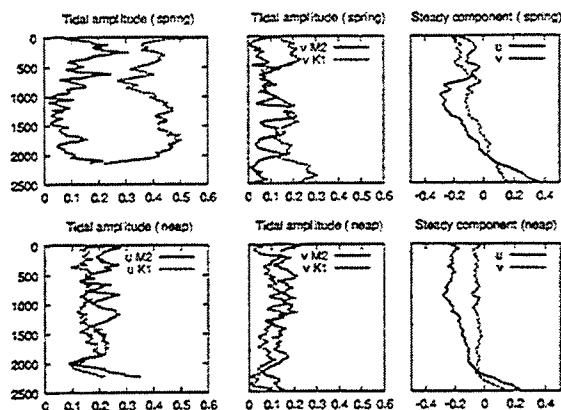
Figure 4. Fitted components at the station B2. The ordinate shows depth in meters. The abscissa shows the velocity in m/s.

Figure 5. Fitted v component of the K1 amplitude. Velocity more than 0.7 m/s is shaded. Contour interval is 0.2 m/s.

worse near the sloping bottom ($x \sim 50, 70$km). This misfit is caused by disturbances of shorter time scale, possibly such nonlinear phenomena as breaking. On the other hand, fitting is successful on the flat bottom.

Result

Spring and neap tides

As mentioned above, observations at groups B and F were made at the spring tide and neap tide. Figure 4 shows the fitted components at the spring and neap tides. It is seen that the K1 components are sensitive to the difference between the spring and neap, while the M2 components do not change much. The steady components are stronger at the spring tide.

Observations at other groups were made at tidal phases which are not the spring nor the neap. Therefore, cross sections shown henceforth do not represent exact snapshots, but we expect that the data at other groups represent some state between the spring and the neap. A cross section 'at the spring' means a cross section composed of data with groups B and F measured at the spring tide. Same for 'at the neap'.

Tidal components

As suggested by the numerical tidal model [*Kowalik and Polyakov*, 1998] the K1 amplitude is larger than the M2 amplitude at this strait. The phase suggests the tide is barotropic in the deep valley, while it shows two to three layer structure on the shallow sill or on the steep bottom. There is no clear node of the phase and the structure of the tidal flow is complex. Figure 5 shows the fitted v component of the K1 amplitude. It should be noted that the tidal amplitude in the valley near $x \sim 18$km becomes more than 1 m/s, although this strong tide is confined below 1000m. It is not clear from Figure 5, but similar bottom-trapped peak of nearly 0.5 m/s can be found in the valley near $x \sim 27$km. These strong tidal flows are also found for u component although the depth of
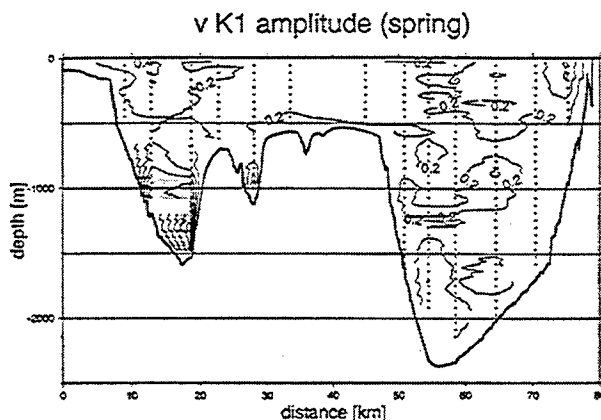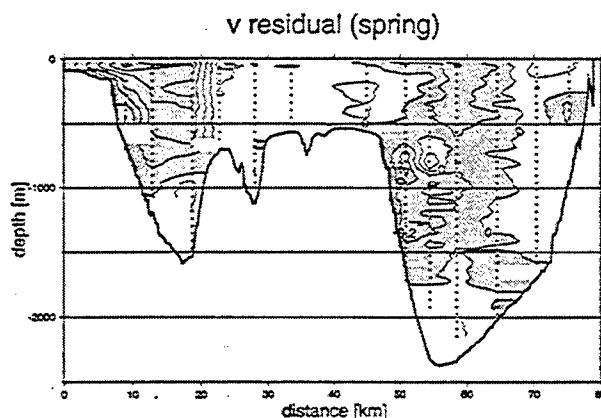

Figure 6. Steady component of v at the spring tide. Contour interval is 0.1 m/s. Negative flow (towards the Pacific) is shaded.

the peak is slightly different.

Steady components

Figure 6 shows the steady v component. In the deep valley, the flow shows a two-layer structure, where the upper layer flows out of the Okhotsk and the lower layer in the opposite direction. The outflow is stronger in the southwestern valley than the northeastern valley although the area of the latter is much larger. These features are also found for the neap tide. It is possible to determine the total transport from the cross section. The net transport is -2.5 Sv for both spring-tide cross section and neap-tide cross section.

References

Andreev, A., M. Honda, Y. Kuramoto, M. Kusakabe, and A. Murata, Excess CO_2 and pHexcess in the intermediate water layer of the northwestern Pacific, *J. Oceanogr.*, *57*, 177–188, 2001.

Fischer, J. and M. Visbeck, Deep Velocity Profiling with Self-contained ADCPs, *J. Atmos. Oceanic Tech.*, *10*, 764–773, 1993

Katsumata, K., I. Yasuda, and Y. Kawasaki, Direct current measurements at Kruzenshterna Strait in summer, *Geophys. Res. Lett.*, , *28*, 319–322, 2001

Kowalik, Z. and I. Polyakov, Tides in the Sea of Okhotsk, *J. Phys. Oceanogr.*, , *28*, 1389–1409

Sverdrup, H., M. W. Johnson and R.H.Fleming, *The Oceans, Their Physics, Chemistry, and Biology*, Prentice-Hall, 1087pp, 1942

Yasuda, I., The origin of the North Pacific Intermediate Water, *J. Geophys. Res.*, , *102*, 893–909, 1997

K. Katsumata, K. I. Ohshima, M. Itoh, M. Wakatsuchi, Institute of Low Temperature Science, Hokkaido University, Nishi 8, Kita 19, Kitaku, Sapporo, 060-0819, Japan

T. Kono, Department of Marine Sciences and Technology, Hokkaido Tokai University, 1-1-1 Minamizawagojo, Minamiku, Sapporo, 005-8601, Japan

I. Yasuda, Department of Earth and Planetary Science, University of Tokyo, 7-3-1 Hongo, Bunkyoku, Tokyo, 113-0033, Japan

On tracers and potential vorticities in ocean dynamics

M. V. Kurgansky[1,2] and E. Salusti[3]

1. Department of Atmospheric and Oceanic Physics, Faculty of Physics and Mathematics, University of Concepcion, Chile
2. A.M. Obukhov Institute of Atmospheric Physics, Russian Academy of Sciences, 109017 Moscow, Russia
3. INFN - Phys Dept University of Rome "La Sapienza", Rome, Italy

Abstract. Ertel's potential vorticity theorem for stratified viscous fluids in a rotating system is analyzed. A set of "tracers", i.e. materially conserved scalar quantities, and the corresponding Ertel's potential vorticities, are applied to diagnose the absolute velocity field in non-horizontal (inclined) marine currents. In particular, two Ertel's potential vorticities, those of potential temperature and salinity, are analyzed to infer quasi-steady properties of the Mediterranean Sea water outflow through the Gibraltar Strait.

Introduction

In modern oceanography *in situ* field measurements of the salinity S and temperature T (via CTD) are still far more frequent and available than those of the current velocity **u**. Velocity **u** is usually computed diagnostically based on the known information on S and T. In these circumstances, the baroclinic component of **u** is most easily estimated. The determination of the barotropic flow component, which includes the well-known problem of specifying the level of no-motion, still provides serious difficulties.

Therefore, any alternative method of current velocity determination, free from the above mentioned complications, is of practical importance. As a potential tool for the operational analysis of individual *T-S* casts to obtain information on **u**, such methods would compare favorably with much more rare and expensive current meter data. In this contribution a variant of such a method is proposed, which enables one to estimate the absolute velocity vector **u** from *T-S* measurements by means of a general vectorial analysis under the assumption of the steadiness of the flow.

Fluid tubes

Let us recall Vilhelm Bjerknes' classical idea (Godske *et al.*, 1957). Surfaces $\alpha(\mathbf{x}, t)$=const and

$\beta(\mathbf{x}, t)$=const of two conserved tracers α and β, such that $D\alpha/Dt=D\beta/Dt=0$, divide a fluid into (α, β)-solenoids along which the fluid parcels flow. In a steady case the mass continuity equation and tracer equations give

$$\nabla \cdot (\rho\mathbf{u}) = 0, \mathbf{u} \cdot \nabla\alpha = 0, \mathbf{u} \cdot \nabla\beta = 0. \quad (1)$$

One can moreover show (Wunsch 1996) that (1) imply

$$\rho\mathbf{u} = \varphi(\alpha, \beta)\nabla\alpha\times\nabla\beta, \quad (2)$$

where φ is an arbitrary single-valued function: indeed the vector **u** is normal to both $\nabla\alpha$ and $\nabla\beta$, whilst $\rho\mathbf{u}$ is divergence-free (Ertel and Kühler 1949). Here we discuss a choice of some utility when a supplementary third scalar field is known: assume that we have some information about a non-conservative quantity $\gamma(\mathbf{x}, t)$, such that $D\gamma/Dt=\Gamma(\mathbf{x}, t)$ where $\Gamma\neq0$. In a steady case, when

$$\mathbf{u} \cdot \nabla\gamma = \Gamma, \quad (3)$$

equations (2) and (3) give

$$\mathbf{u} = \frac{\Gamma(\mathbf{x})}{(\nabla\alpha \times \nabla\beta) \cdot \nabla\gamma(\mathbf{x})}\nabla\alpha \times \nabla\beta, \quad (4)$$

allowing one to obtain **u** from the knowledge of α, β, γ and Γ.

143

Applications to potential temperature and salinity

Ertel's (1942) vorticity theorem

$$\frac{D}{Dt}\Pi_\chi = \frac{D}{Dt}\left(\frac{\bar{\omega}_a \cdot \nabla\chi}{\rho}\right) = \frac{\nabla\chi \cdot \nabla\rho \times \nabla p}{\rho^3} + \frac{\nabla\chi}{\rho} \cdot \nabla \times \frac{F}{\rho}$$

where ϖ_a is the vorticity and F is taken for any tracer χ, provides a very convenient choice $\gamma = \Pi_\chi$ because the Γ-value is fixed by the right hand side.

In more detail, we can consider a current velocity

$$
\mathbf{u} = -\frac{g\rho^{-2}(\partial\rho/\partial\theta)\nabla S \cdot \nabla\theta \times \mathbf{k}}{\nabla\Pi_S \cdot \nabla\theta \times \nabla S}\left(\nabla\theta \times \nabla S\right)
$$
$$
+ \frac{\rho^{-1}\nabla S \cdot \nabla \times (F/\rho)}{\nabla\Pi_S \cdot \nabla\theta \times \nabla S}\left(\nabla\theta \times \nabla S\right)
\tag{5}
$$

assuming that salinity and potential temperature are materially conserved.

The two different absolute velocity determinations, namely for $\{\theta, S, \Pi_\theta\}$ like (5) and $\{\theta, S, \Pi_s\}$ as below

$$
\mathbf{u} = -\frac{g\rho^{-2}(\partial\rho/\partial S)\nabla\theta \cdot \nabla S \times \mathbf{k}}{\nabla\Pi_\theta \cdot \nabla\theta \times \nabla S}\left(\nabla\theta \times \nabla S\right)
$$
$$
+ \frac{\rho^{-1}\nabla\theta \cdot \nabla \times (F/\rho)}{\nabla\Pi_\theta \cdot \nabla\theta \times \nabla S}\left(\nabla\theta \times \nabla S\right)
\tag{6}
$$

must result in the same vector $\mathbf{u}$ for every dynamically possible case of θ and S. Indeed, subtraction of equation (6) from (5) for steady currents of incompressible inviscid fluids ($c^2 = \partial p/\partial\rho \to \infty$) illustrates that these two formulations are equivalent.

Mediterranean water outflow

To get some idea of the practical applicability of these relations we now discuss a classical density current, that of salty dense Mediterranean water which crosses the deepest part of the Gibraltar Strait flowing towards the Atlantic Ocean (Baringer and Price 1997 a, b), see Figure 1.

Downstream from Gibraltar, a density current flows along the local topography into the Atlantic Ocean (Baringer and Price 1997 a, b): between their hydrologic Sections B and D the current turns

northward with a curvature radius $R \sim 40$ km. Outside these Sections the flow is essentially rectilinear. From Sections A to F, over an irregular sea bottom, the current thickness h and the width W are found to increase whilst the velocity $\mathbf{u}$ and density difference $\Delta\rho$ with the surrounding water masses decrease as the current moves away from Gibraltar. From equations (5) and (6) one can see that the velocity is along the θ=const and S=const surfaces, and this occurs even if friction F is considered. The velocity intensity is ruled by the gradients of θ, S, as well as by the frictional effects. The Baringer and Price data set relative to their transects A, C and F downstream the strait of Gibraltar, are now discussed in more detail. In the Table we estimate values of the main physical quantities of this outflow, denoting as the "central region" the one characterized by the highest velocities, and $S > 36.4$ ppt, as computed by Baringer and Price (1997 a, b). We use (5) since S is better defined than θ and this implies smaller uncertainties.
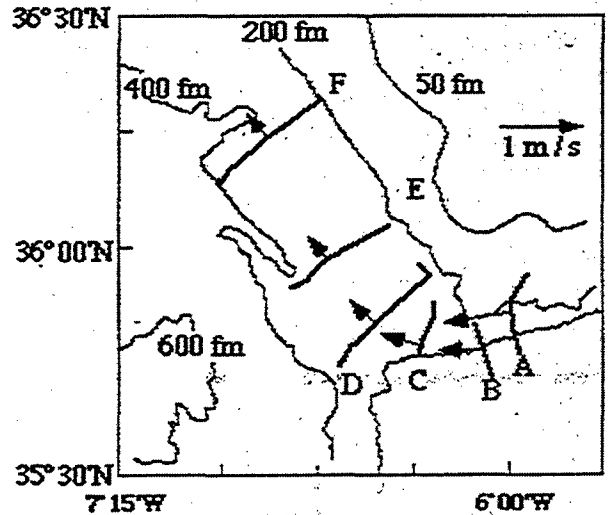

Figure 1. Map of the field measurements of the dense water outflow off Gibraltar (Baringer and Price 1997 a, b).

Simple parameterization is used in (5) for F/ρ, which we estimate as $(\tau_B + \tau_I)h^{-1}\rho^{-1}$ using the Baringer and Price (1997) notations, τ_B and τ_I being viscous stresses on the sea bottom and deep current upper interface, respectively.

Table 1. Values relative to the bottom current flowing off Gibraltar, estimated from the Baringer and Price (1997 a,b) data set.

Quantity (MKS units)	Transect A	Transect C	Transect F
Δx, distance from transect A (km)	0	21	84
Bottom current thickness h (m)	125	90	140
Current radius of curvature R (km)	300	50 ± 10	200
$w/|u| = \Delta z/\Delta x$	$(40\pm4)\times10^{-4}$		$(40\pm4)\times10^{-4}$
Average bottom current velocity (ms^{-1})	0.6 ± 0.1	0.34 ± 0.1	0.18 ± 0.1
$|\nabla S|$ in the bottom current (ppt m^{-1})	$(16\pm1)\times10^{-3}$	$(16\pm1)\times10^{-3}$	$(11\pm1)\times10^{-3}$
$|\nabla\theta|$ in the bottom current (°C m^{-1})	$(4\pm1)\times10^{-3}$	$(6\pm1)\times10^{-3}$	$(5\pm2)\times10^{-3}$
Angle between $\nabla\theta$ and ∇S	$(9\pm2)\times10^{-3}$	$(2\pm1)\times10^{-3}$	$(2\pm2)\times10^{3}$
$\dfrac{f+\omega_z}{\rho}\dfrac{\partial}{\partial z}S \cong \dfrac{f-|u|/R}{\rho}\dfrac{\partial S}{\partial z}$ (ppt m^3/s kg m)	$-(16\pm1)\times10^{-10}$	$-(14\pm1)\times10^{-10}$	$-(11\pm1)\times10^{-10}$
$|\nabla\theta\times\nabla S|$ (°C ppt/m^2)	$(58\pm10)\times10^{-8}$	$(19\pm10)\times10^{-8}$	$(11\pm11)\times10^{-8}$
$F/\rho = c_D u^2/h = 0.02\, u^2/h$ (N/kg)	$(7\pm2)\times10^{-5}$	$(4\pm1)\times10^{-5}$	$(5\pm1)\times10^{-5}$
estimated inviscid velocity (m s^{-1}) using (5)	0.5 ± 0.1	0.3 ± 0.2	0.2 ± 0.2
estimated viscous correction (m s^{-1}) using (5)	0.1	0.05	0.03

In this table the first part comes from direct estimates taken from Baringer and Price (1997 ab), often without errors also if one can reasonably assume uncertainties of ~10%. The values of $\nabla\theta$ and ∇S are computed from the values of θ and S in the center of the current minus the value along the $S = 36.4$ ppt surface. In the same way we have tentatively estimated the angles. Finally C_D is usually taken as 5×10^{-3} (MKS units), but the total stress (bottom and interfacial) from Baringer and Price (1997 a,b) is about twice the bottom stress (in their Figure 6a), given by $C_D = 2\text{-}12\times10^{-3}$ in their estimates, so we assumed $C_D =0.02$ (MKS units).

The *curl* of frictional force is approximated here by $\nabla\times(F/\rho)\approx h^{-1}k\times(F/\rho)$ and is directed in a nearly horizontal cross-stream direction. All this finally gives that the inviscid part of the velocity is 0.2-0.5 m s^{-1} and the viscous component is $-(0.05\text{-}0.10)$ m s^{-1} with errors of 20-100%, largely due to angle uncertainties; all of this is in agreement with the experimental data set. Minus sign for the viscous correction means that we probably overestimate the current velocity when using the "inviscid" formula.

References

Baringer M. O., and Price J. F., (1997a): Mixing and spreading of the Mediterranean outflow. *Journ. Phys. Oceanogr.*, 27, 1654-1677.2

Baringer M. O., and Price J. F., (1997b): Momentum and energy balance of the Mediterranean outflow. *Journ. Phys. Oceanogr.*, 27, 1678-1992.

Ertel H., (1942): Ein neuer hydrodynamischer Wirbelsatz. *Meteorol. Z.*, 59, 277-281.

Ertel H., and Kühler H., (1949): Ein Theorem über die stationäre Wirbelbewegung kompressibler Fluessigkeiten. *Z. angew. Math. Mech.*, 29(4), 109-113.

Godske C. L., Bergeron T., Bjerknes J., and Bundgaard R. C., (1957): *Dynamic Meteorology and Weather Forecasting*. AMS - Boston, Ms - Carnegie Inst. Washington, 800 pp.

Wunsch C., (1996): *The Ocean Circulation Inverse Problem*. Cambridge Univ. Press, 442 pp.

146

Use of the rotating hydraulics for description of overflows through the Baltic Straits

J. Laanearu

Department of Mechanics, Tallinn Technical University, Ehitajate tee 5, 19086 Tallinn, Estonia

Abstract. The deep-water renewal of the Baltic sub-basins is a consequence of gravity-driven currents and it is thus important to know the flow rates through connecting passages. The earth's rotation is a leading-order effect that modifies the deep-water dynamics in the Baltic Sea, since the internal Rossby radius of deformation is smaller than the width scale of the straits. The methodology of 1_-layer rotating-channel flow is used for the description of the strong deep-water flows through the Bornholm Channel and the Irbe Strait. The analysis deals with how to specify the gross geometrical features of the straits and how the associated critical-flow problem can be resolved on the basis of functional-theoretical formalism. The usefulness of rotating-hydraulic theory is demonstrated for a channel of parabolic cross-section, since the non-standard Froude number formulation and a perturbative solution to the uniform, non-zero potential-vorticity flow model are derived.

Summary

The Baltic deep-water motion is topographically constrained since the bathymetry of the seabed induces the heavier fluid to move through passages connecting adjacent basins. The Baltic straits are wide compared to the internal Rossby radius of deformation, which varies from 2 to 10 kilometers (Lehmann and Hinrichsen, 2000). The effects of the earth's rotation are consequently important, and give rise to geostrophically balanced baroclinic coastal- and strait-currents. The theory of rotating hydraulics is useful when elucidating the dynamics of topographically constrained currents, and it can be employed to make predictions of maximal volume-flux. To apply the 1_-layer rotating-channel flow model (the deep-water flow with less-dense quiescent upper water) in the Baltic Sea it is necessary to include specific assumptions such as a finite upstream-basin depth and a non-rectangular cross-section of the channel. The Baltic sub-basins are comparatively shallow and wide, and it thus does not appear likely that currents in the straits can be described in terms of the deep upstream-basin approach, based on the zero potential vorticity proxy (Whitehead et al., 1974; Borenäs and Lundberg, 1988). These specific approximations, however, do not alter the branch-point character of the hydraulic-problem solution, well-known from the inviscid hydraulics for subcritical, critical and supercritical flows (cf. Pratt, 1986), but rather help to improve agreement between hydraulic theory and nature. The rotating hydraulics of flow, emanating from a wide and shallow basin into a channel, deal with a more general problem, since specification of the circulation in the upstream-basin is required (Gill, 1977; Borenäs and Lundberg, 1986).

An important restriction that complicates application of the 1_-layer rotating-channel flow model in the Baltic Sea is that the straits do not have a well-defined bathymetry, i.e. one with an *a priori* given topographic control (where the location of the maximum sill height coincides with that of the most pronounced horizontal constriction of the passage, cf. Whitehead, 1998). This situation necessitates the use of theoretical principles of hydraulics that assume the existence of a flow-dependent control section between the topographically extremal sections of the channel (cf. Armi, 1986). However, the general critical-flow solutions can occur at a topographic constriction or expansion (cf. Gill, 1977). A "splitting effect" of the critical-section location was found when the functional-theoretical approach to the hydraulically driven flow problem was applied in the case of the Bornholm Channel by Laanearu and Lundberg (2000). It yielded three possible locations

for the control section, where two critical sections were located adjacent to the geometrical constrictions of the channel, separated by a spurious section associated with a local maximum of the flow cross-sectional area. This situation is of great importance, since in the shallow-water approximation only one transition between the subcritical and supercritical flow states can be stable, this due to long-wave arguments (cf. Pratt, 1984). However, a more important aspect is the unidirectional critical flow, which fits with the classical concept of hydraulic control, since downstream conditions in this case cannot exert any influence upstream of the critical section, neither through advection proper nor through long-wave signals. When modeling hydraulically driven flows, problems may arise regarding a flow discontinuity at some location in the channel (Laanearu *et al.*, 2000). The 1_-layer continuous flow that changes steadily from the subcritical to the supercritical solution branch requires a definition of the control-section in the channel that yields a maximum of the potential depth scaled by the volume flux. (Following Borenäs and Pratt, 1994, the potential depth is the fluid column depth where the relative vorticity vanishes.)

The Baltic Sea deep-passages investigated by Laanearu (2001b) gave no serious problems when the parabolic cross-sectional geometry was used, but the modelling was complicated since the along-channel width and depth variations of the passage were of great importance. The method introduced by Laanearu and Lundberg (2000) was based on the use of sparse discretization of the strait topography. A dense equidistant discretization did not prove to be particularly useful, since the roughness of the strait topography gave rise to a multitude of spurious critical-flow sections using general theory of hydraulics (cf. Gill, 1977). Hence, it was possible to describe the topographic characteristics of the passages using a minimal number of cross-sections by adjusting the overall features of the channel.

The main differences in the outcome of the hydraulic modelling of the deep-water flows through the Baltic straits were caused by the unique topographic situations. In order to solve the hydraulic problem for dense-water flow through straits using the 1_-layer rotating-channel flow model, it is necessary to carry out a two-layer approximation, to specify the conditions in the upstream basin, and to define the topographic characteristics of the passage. In what follows deal with the concrete examples of the strong deep-water

flows through the Bornholm Channel and the Irbe Strait, see boxes in Figure 1.
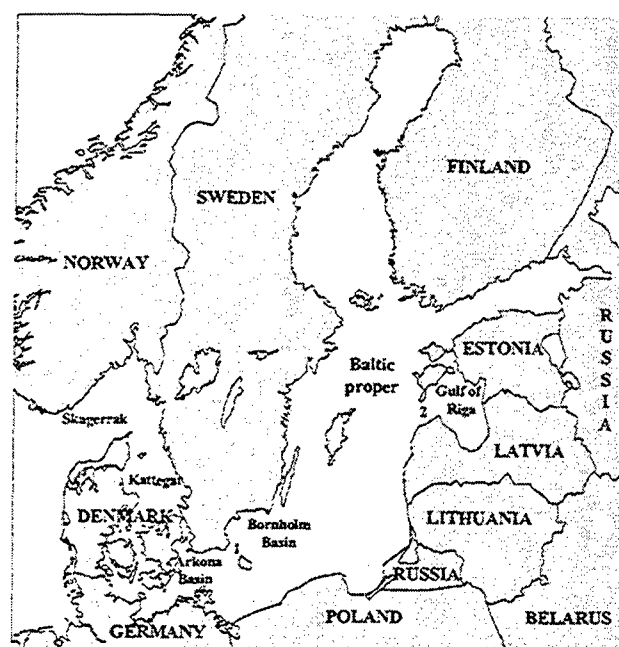

Figure 2. Map of the Baltic Sea. 1 - Bornholm Channel, 2 - Irbe Strait.

Bornholm Channel flow

The Arkona Basin, which is the first Baltic sub-basin to be filled by "oceanic" water originating from the Kattegat, only has a low sill obstructing the deep-water flow through the Bornholm Channel, and thus the horizontal constriction of this passage constitutes the main topographic restriction experienced by the deep-water (cf. Gidhagen and Håkansson, 1994). Due to geological evolution the most shallow part of the Arkona Basin exit area between the Swedish mainland and the Danish island of Bornholm is located considerably to the west of the greatest horizontal constriction. The "water-fall" like topographic conditions at the exit of the Bornholm Channel suggest that the flow is determined by mechanisms similar to those governing reservoir flow over a dam. The deep-water motion in the Bornholm Channel takes place in a quasi-continuous fashion and intensifies during strong dense-water inflow events from the Kattegat (cf. Mattheus and Frank, 1992). The observations by Liljebladh and Stigebrandt (1996), undertaken during the winter of

1993, clearly showed a well-defined pool of deep water in the Arkona Basin. They furthermore did justice to the section between Skåne peninsula and Bornholm Island where the deep-water discharge into the Bornholm Basin took place. From the observations a geostrophic boundary current along the northern rim of the Arkona Basin became evident, which made it possible to specify the upstream conditions for the 1_-layer rotating-channel model. On the basis of the constant (non-zero) potential vorticity model, the control section with unidirectional flow was found to be located between the topographically extremal sections of the Bornholm Channel, adjacent to the point where the deep-passage cross-sectional area has its minimum below the 30-meter isobath (Laanearu and Lundberg, 2000). The predicted controlled transport was 143000 m^3s^{-1}, which represents an overestimate of the measured baroclinic flux 100000 m^3s^{-1} (where the latter quantity is an average of the Liljebladh and Stigebrandt, 1996, cross-sectional baroclinic volume fluxes observed from the central parts of the Arkona Basin to the Bornholm Channel).

Irbe Strait flow

The Irbe Strait, which constitutes the largest gap between the Gulf of Riga and the Baltic proper, has a comparatively high sill, which blocks intrusions of the Baltic deep-water (cf. Kõuts and Omstedt, 1993), and thus only water originating from above the main halocline of the Baltic proper at a depth of 60-70 meters can penetrate into the gulf. The upstream-basin conditions affecting the Irbe Strait flow are rather complicated to use in the 1_-layer rotating-channel model, since the upstream basin is comparatively large. The control section with unidirectional flow, determined using the functional-theoretical approach to the hydraulically driven flow, was found in close proximity to the location where the deep passage, below 10-meter isobath, had its most pronounced horizontal constriction. This is consistent with the general requirement that in practise the most extreme section of the channel exerts topographic control on the flow. From Laanearu *et al.* (2000) it was found that the constant (non-zero) and zero potential vorticity flow model controlled transport predictions were 7200 m^3s^{-1} and 8000 m^3s^{-1}, respectively. These were in close agreement, but overestimated the observational average result for the baroclinic flux of 5200 m^3s^{-1}

(Lilover *et al.*, 1998). The low-frequency current observed in the Irbe Strait during the spring of 1995 was related to the increased density differences between the waters of the Gulf of Riga and the Baltic proper associated with the freshwater fluxes from the gulf rivers. The baroclinic flow was favoured also by the calm weather conditions prevailing during spring and the existence of a seasonal thermocline.

Non-standard Froude number

The theory of rotating hydraulics can be applied in channels with non-rectangular cross-sections where the Froude number is not readily defined. The subcritical, critical and supercritical flow states in the rotating channel are related to the long-wave speeds. The general Kelvin-wave speed, based on the constant potential vorticity proxy (cf. Pratt *et al.*, 2000), and geostrophy of the along-channel flow permits the derivation of a formula for the non-standard Froude number: $F = \overline{v}/(\overline{v} - c_{\_})$, where the average along-channel velocity is given by $\overline{v}$ and the long-wave speed is $c_{\_}$ (cf. Gill, 1977). The non-standard Froude number is consonant with the standard solutions of inviscid hydraulics where critical flow corresponds to $F = 1$, subcritical and supercritical flows correspond to $F < 1$ and $F > 1$, respectively.

Perturbative solution

The perturbation method permits taking model dynamical effects into consideration to desired order. The solution, based on a small parameter corresponding to the reciprocal of the scaled potential depth, can remove an analytic gap between the zero and constant potential vorticity model branch-point solutions, Laanearu (2001a). The perturbative solution employs the deep upstream-basin case as the lowest-order result. The higher-order corrections of the general model power-series solution are singular at the lowest-order solution branch-point, and incorporate the effects of the upstream-basin circulation. (Borenäs and Lundberg, 1986, showed that a perturbative scheme based on a small parameter expansion of the channel-width measure yields the lowest-order result of the constant potential vorticity model, which represents the classical solution for hydraulic flow through a non-rotating channel.)

Concluding remarks

When modelling the topographically constrained deep-water flows through the Baltic straits it proved feasible to predict the baroclinic part of the deep-water fluxes, neglecting, however, the possible dynamical effects associated with the upper-layer motion. These currents took place predominantly through one passage, but the surface-water moved through several passages, see Figure 1. The Baltic sub-basins are comparatively small, and strong inflows can change the sea level in the basins. For a complete treatment of the water-exchange problem, it would be necessary to let the hydraulic analysis include the sea-level difference between the neighbouring basins, which would give rise to a two-layer hydraulics problem (cf. Pratt and Armi, 1990; Dalziel, 1991).

The coastal- and strait-currents are important elements of the Baltic Sea general circulation. The non-standard Froude number can be useful when characterizing the "criticality" of these currents.

A perturbative solution of the constant (non-zero) potential vorticity flow model, which has been obtained, is useful analysing a branch-point character of the hydraulic problem. This solution underlies the mathematical method permitting determination of the analytical relationships between the different hydraulic models and their simpler approximants.

References

Armi, L., The hydraulics of two flowing layers with different densities. *J. Fluid Mech.*, 163, 27–58, 1986.

Borenäs, K., Lundberg, P., Rotating hydraulics of flow in a parabolic channel. *J. Fluid Mech.*, 167, 309–326, 1986.

Borenäs, K., Lundberg, P., On the deep–water flow through the Faroe–Bank Channel. *J. Geophys. Res.*, 93C, 1281–1292, 1988.

Borenäs, K.M., Pratt, L.J., On the use of rotating hydraulic models. *J. Phys. Oceanogr.*, 24, 108–123, 1994.

Dalziel, S.B., Two–layer hydraulics: a functional approach. J. Fluid Mech., 223, 135–163, 1991.

Gidhagen, L., Håkansson, B., A model of the deep water flow into the Baltic Sea. *Tellus*, 44, 414–424, 1992.

Gill, A.E., The hydraulics of rotating–channel flow. *J. Fluid Mech.*, 80, 641–671, 1977.

Kõuts, T., Omstedt, A., Deep water exchange in the Baltic Proper. *Tellus*, 45, 311–324, 1993.

Laanearu, J., Lips, U., Lundberg, P., On the application of the hydraulic theory to the deep–water flow through the Irbe Strait. *J. Marine Syst.*, 25, 323–332, 2000.

Laanearu, J., Lundberg, P., Topographic control of rotating deep–water flow through the combination of a sill and a horizontal constriction. *J. Geophys. Res.*, 105, 28663–28669, 2000.

Laanearu, J., Perturbative analysis of a sill–flow problem within rotating–channel hydraulics. *International Meteorological Institute in Stockholm*, Report DM–86, 1–28, 2001a.

Laanearu, J., Topographically constrained deep–water flows in channels (Rotating–channel flow modeling. Baltic straits overflows). *Dissertationes Geophysicales Universitatis Tartuensis*, 13, 1-143, 2001b.

Lilover, M.J., Lips, U., Laanearu, J., Liljebladh, B., Flow regime in the Irbe Strait. *Aquat. Sci.*, 60, 253–265, 1998.

Liljebladh, B., Stigebrandt, A., Observations of the deepwater flow into the Baltic Sea. *J. Geophys. Res.*, 101, 8895–8911, 1996.

Lehmann, A., Hinrichen, H.H., On the thermohaline variability of the Baltic Sea. *J. Mar. Syst.* 25, 333–357, 2000.

Matthäus, W., Franck, H., Characteristics of major Baltic inflows – a statistical analysis. *Cont. Shelf Res.*, 12, 1375–1400, 1992.

Pratt, L.J., On nonlinear flow with multiple obstructions. *J. Atmos. Sci.*, 41, 1214–1225, 1984.

Pratt, L.J., Hydraulic control of sill flow with bottom friction. *J. Phys. Oceanogr.*, 16, 1970–1980, 1986.

Pratt, L., Armi, L., Two-layer rotating hydraulics: strangulation, remote and virtual controls. *Pageoph.*, 133, 587–617, 1990.

Pratt, L.J., Helfrich, K.R., Chassignet, E.P., Hydraulic adjustment to an obstacle in a rotating channel. *J Fluid Mech.*, 404, 117–149, 2000.

Whitehead, J.A., Leetmaa, A., Knox, R.A., Rotating hydraulics of strait and sill flows. *Geophysical Fluid Dynamics*, 6, 101–125, 1974.

Whitehead, J. A., Topographic control of oceanic flows in deep passages and straits. *Annu. Rev. Geophys.*, 36, 423–440, 1998.

Laboratory experiments of internal bores in non-rotating and rotating exchange flows over sills

G. F. Lane-Serff, D. R. Munday* and M. D. Woodward

Manchester Centre for Civil and Construction Engineering, UMIST, PO Box 88, Manchester M60 1QD, UK
*Department of Meteorology, University of Reading, Earley Gate, PO Box 243, Reading, RG6 6BB, UK.

Abstract. Results from laboratory experiments illustrating internal bore formation are presented. The bores are formed in two-layer exchange flows in straight-sided rectangular channels containing a sill. Both non-rotating and rotating examples are given. In a natural flow the sill is at the bottom of the channel and the bore marks an increase in thickness of the upper layer. In the laboratory experiments an inverted configuration is used, with the sill being modelled by a partially raised barrier and the bore marking a jump in the thickness of the lower layer. In many cases the internal bore has an undular form, with a growing group of internal waves behind the bore carrying and dissipating energy. In strongly rotating flows the internal bore occupies one side of the channel, with a width somewhat less than the Rossby radius and a form that slopes across the channel. Some of the rotating bores also have a head region and possibly an undular form, though the wave crests are now tilted both in plan and side view, giving a complicated flow.

Introduction

Unsteady flows, often due to tidal forcing, interacting with topography can generate internal bore (moving hydraulic jumps). These jumps mark sudden changes in the depth of an interface between waters of different density and can be accompanied by turbulent mixing and/or internal waves. Here we concentrate on internal bores in a two-layer fluid flowing through a straight-sided channel containing a sill. The flow in the channel is assumed to be predominately an exchange flow, with dense fluid flowing one way and lighter fluid flowing the other. If the exchange flow is modulated by a net tidal flow then it is possible to generate internal bores (see Figure 1). If there is a net flow out of the denser reservoir then there will be a deep layer of dense fluid flowing over the sill and a relatively shallow and slow layer of light fluid flowing in the opposite direction. As the tide slackens the flow in the two layers will become similar and the depth of the interface will deepen. Depending on the rate of change of the forcing and the geometry of the channel, the change in depth of the interface may take

the form of a sudden jump (internal bore). For larger scale flows the effects of the earth's rotation are important.
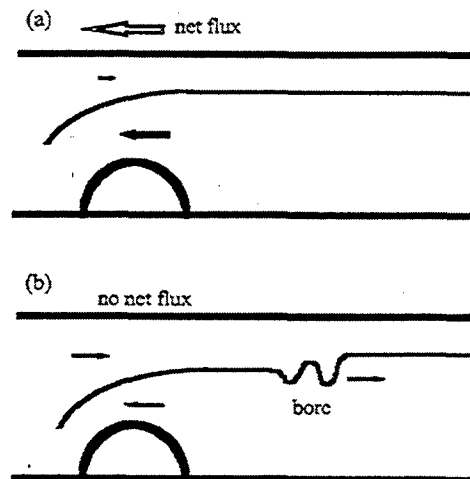

Figure 1. Internal bore generation in a two-layer exchange flow. A net flux out of the dense reservoir sets up a shallow upper layer. As the net flux reduces the flow and depth of the upper layer increases, with the change in layer depth taking the form of a moving hydraulic jump.

In the next section we briefly review the theory and identify the important parameters. We then present laboratory experiments investigating both non-rotating and rotating flows with internal bores.

Theory

We assume simple two-layer flow in a channel, with an upper, light layer moving to the right and a dense lower layer moving to the left (see Figure 2). Far to the right of the sill the upper layer has depth D_{U0}, assumed to have been set by earlier flow conditions. The flow is adjusting to new conditions (which may still have a steady net flux Q in either direction) with an upper layer depth at the sill of D_{U2} and an increasing region to the right of the sill where the upper layer depth is D_{U1} (greater than D_{U0}). The jump in layer depths between D_{U0} and D_{U1} is achieved through an internal bore moving at speed U.
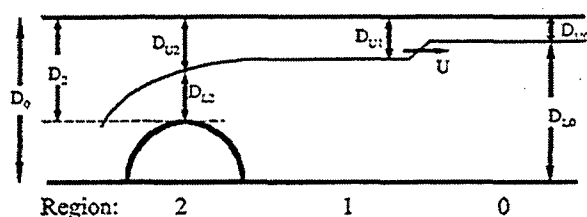
Figure 2. Definition sketch for the theoretical analysis of internal bores in two-layer exchange flows.

It is convenient to scale depths with the channel depth at the sill, D_2, velocities with $\sqrt{(g\_D_2)}$ (where $g\_$ is the reduced gravity) and thus fluxes (per unit width) with $D_2\sqrt{(g'D_2)}$. The parameters that define the problem are then the net flux,

$$q = \frac{Q}{D_2\sqrt{g'D_2}},$$

and the channel depth and the initial upper layer depth,

$$d_0 = \frac{D_0}{D_2} \quad \text{and} \quad d_{U0} = \frac{D_{U0}}{D_2}.$$

An analysis of this flow using the shallow water equations is given in Lane-Serff and Woodward (2001). For cases with no net flow ($q = 0$) the theory suggests the bore speed varies very little with the geometric parameters, with $U = (0.6 \pm 0.1)\sqrt{(g\_D_2)}$ for a wide range of cases.

For rotating flows a further parameter is needed. Here we use the ratio of the width of the channel, W, to a Rossby radius, R,

$$\frac{W}{R} = \frac{Wf}{\sqrt{g'D_2}},$$

where f is the Coriolis parameter. This ratio is effectively an inverse Rossby number, with large values of W/R corresponding to strong rotation. By analogy with rotating gravity currents in channels (e.g. Griffiths 1986, Martin 1999) we would expect that after an initial adjustment phase the bore would be confined to one side of the channel (right-hand side in the northern hemisphere).

Experiments

The laboratory experiments were performed using clear-sided rectangular tanks in an inverted configuration compared to the natural flow (Figure 3). Two reservoirs were separated by a simple barrier with one reservoir full of dense fluid while the other reservoir contains mostly light fluid with a shallow layer of dense fluid. This shallow layer corresponds to the upper layer of depth D_{U0} in the natural flow.
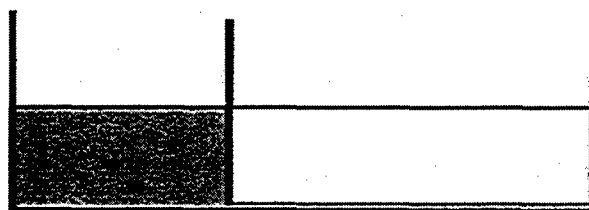

Figure 3. Side view of the experimental apparatus with the dense fluid (shaded) occupying the left-hand reservoir and a shallow layer in the right-hand reservoir.

The barrier is partially raised and an exchange flow is quickly established underneath the barrier. Dense fluid moves to the right in a deeper layer forming a bore (Figure 4). Note that the speed of the fluid in the lower layer is lower than the bore speed. For rotating flows the tank was placed on a rotating table and allowed to adjust to solid-body rotation before the start of the experiment. The fluid was marked by dyes or particles and recorded and analysed using video and image processing.

All of the experiments had no net flow ($q = 0$) but a wide range of the other parameters: $0 \le d_{U0} < 1$, $1 \le d_0 < 7$ and (for rotating flows) $0 \le W/R < 4$.

Results

Non-rotating flows

An example of the flow is shown in Figure 4. In many cases an undular bore was formed, with the number of waves increasing with time. Undular bores consist of waves whose phase speed matches the bore speed, so that the wave appears stationary in a frame of reference moving with the bore (similar to lee waves). The wave group velocity is slower than the bore speed, so viewed in the bore's frame of reference the waves carry energy away from the bore.
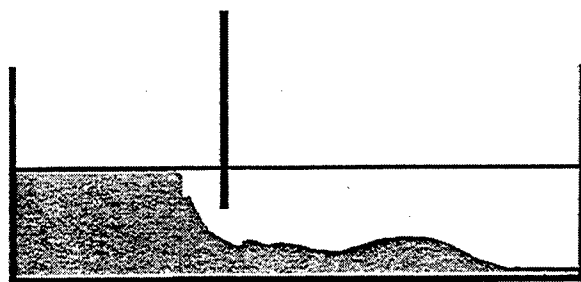

Figure 4. Side view showing an undular bore propagating to the right. The sketch is traced from a laboratory flow image with $d_0 = 1.8$ and $d_{U0} = 0.16$.

The amplitude of the first wave (with respect to its wavelength) is shown in Figure 5. The amplitude increases with the size of the jump (i.e. D_{U1}/D_{U0}). There is also some indication that the amplitude is reduced in shallow channels, presumably because of the effects of flow in the upper layer (which are stronger when this layer is shallower).
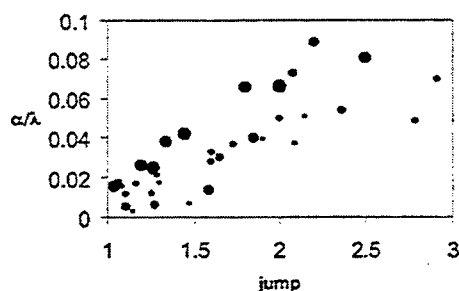
Figure 5. Amplitude of the first wave of an undular internal bore as a function of the relative height of the jump (D_{U1}/D_{U0}). The larger dots have larger values of the total channel depth $d_0 = D_0/D_2$.

A shallow upper layer also has an effect on bore propagation, with the counter flow slowing the bore. Further results for the non-rotating flows can be found in Lane-Serff & Woodward 2001).

Rotating flows

Initially the flow moves out approximately one Rossby radius before forming a bore concentrated towards one side. Considering the results for experiments with a range of parameters we see that the width of the bore scales on the Rossby radius defined above, perhaps increasing with increasing rotation rate (Figure 6). A typical bore speed is again approximately $0.6\sqrt{(g'D_2)}$.
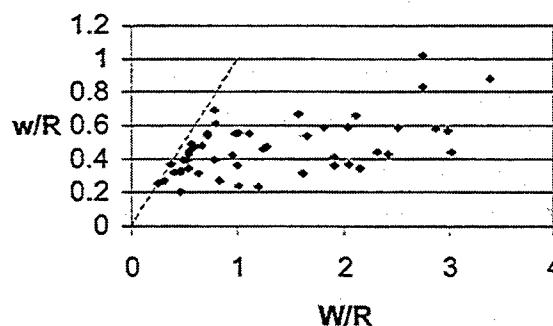

Figure 6. Width of the internal bore (non-dimensionalised by the Rossby radius, R) as a function of the rotation rate (expressed as W/R). Bores cannot be wider than the channel, marked by the dashed line.
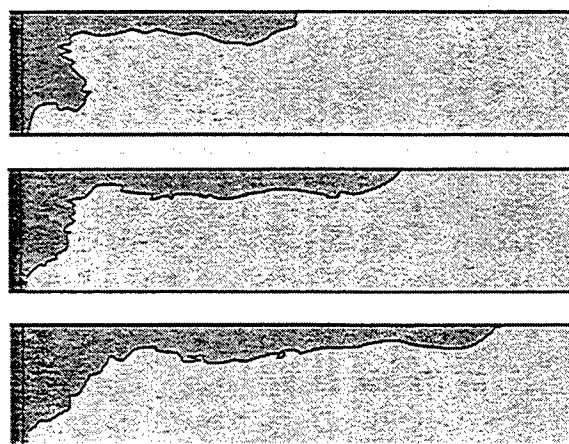

Figure 7. Plan view of a bore in a strongly rotating flow with $W/R = 3.39$ (sequence from a single experiment). As the bore passes, the layer depth increases giving a darker image (as the layer is dyed). For these images a particular intensity contour has been identified as marking the bore boundary. The straight line marks the position of the barrier.

For strongly rotating flows the bore looks very similar to a rotating gravity current (Figure 7 - where the view is via a mirror so the flow appears to be

along the left-hand wall). While the initial shallow layer is uniform across the width of the tank, the bore slopes across the channel so that it is deepest against the sidewall.

At slower rotation rates the behaviour is similar but there is evidence of a raised head (possibly the start of an undular bore) in some cases (Figure 8). The crest is at an angle to the channel wall and the bore as a whole is deeper near one sidewall, giving a more complicated image. Picking a darker intensity as marking the boundary of the bore gives a "hook" effect at the front of the flow.

Figure 8. Plan view of a bore with $W/R = 0.8$, some distance downstream of the barrier. In this case two intensity contours have been identified, showing the curved crest of the raised head at the front of the bore.

Clearly the interface is complicated, with even a simple description having slopes in two directions. Various instabilities and mixing phenomena were noted, including waves on the leading edge, rolls/billows formed on the interface (especially just behind the head) and vortices penetrating into the other layer and carrying fluid away from the bore. Similar features are observed in rotating gravity currents (e.g. see Griffiths 1986).

Conclusions

Internal bores have been modelled in the laboratory using simplified forcing and geometry. The results for non-rotating flows compare well with theoretical shallow water analysis (and also fit oceanographic observations, see Lane-Serff & Woodward 2001). In many cases undular bores are formed, with a series of waves forming behind the bore. In the two-dimensional cases studied here no non-linear effects were apparent, though if the bore propagated into a wider channel or region where the layer depths changed then we might expect to see more non-linear features.

For flows where rotation is important the bores are restricted to a width that scales with the Rossby radius and the interface slopes across and down the channel. The experiments indicate that bores may

result in complicated flow and mixing patterns. There is no existing theory for rotating bores corresponding to the non-rotating theory, though in principle an approach combining the non-rotating bore analysis with the analysis used in rotating gravity currents in channels might be possible. However, the analysis of rotating gravity currents is already very complicated (Martin 2000), so extending this to bores would certainly be a challenging task.

The flows examined here have effectively a steady forcing (constant net flux) so a full comparison with strait flows would require some consideration of unsteady effects (this could also be included in future laboratory experiments). An extension to more complicated topography (e.g. a channel of varying width) and more detailed examination of the mixing accompanying these flows would also be valuable.

References

Griffiths, R.W., Gravity currents in rotating systems, *Ann. Rev. Fluid Mech., 18,* 59-89, 1986.

Lane-Serff, G.F., and M.D. Woodward, Internal bores in two-layer exchange flows over sills, *Deep-Sea Res. I, 48,* 63-78, 2001.

Martin, J.M., *Rotating gravity current and channel flows,* PhD thesis, University of Southampton, 1999.

Transport estimation from the sea level difference across the Korea Strait

Sang Jin Lyu and Kuh Kim

OCEAN Laboratory, School of Earth and Environmental Sciences, Seoul National University, Seoul, Korea

Abstract. Comparison of the sea level difference (SLD) between Hakata, Japan and Pusan, Korea with the transport through the Korea Strait reveals a good linear relationship between them after removing the steric expansion part, which does not contribute to the net transport but is as large as 50% of the real transport in August. The conversion factor from SLD to the transport is estimated as $\Lambda_0 = (13.0 \pm 0.7) \times 10^6$ m^2 s^{-1} with a reference value of SLD, $\Delta\eta_0 = 82 \pm 5$ cm. Therefore, SLD provides a means to investigate a long-term variation of transport through the Korea Strait and its relation to changes in the Pacific Ocean, such as El Nino and decadal climate variations.

Introduction

The Tsushima Current flows into the East (Japan) Sea through the Korea (Tsushima) Strait carrying heat and salt from the Western Pacific Ocean (Figure 1) and forms the major surface currents; the East Korean Warm Current along the east Korean coast and the Nearshore Branch along the Japanese coast (Uda, 1934; Lee et al., 2000; Cho and Kim, 2000). Recently it has become possible to obtain a reliable estimate of the transport through the Korea Strait by the implementation of the vessel-mounted ADCP (Takikawa et al., 1999) and the bottom-mounted, trawl-resistant ADCP (Teague et al., 2001). Moreover, the motion-induced voltage has been measured using the abandoned submarine cable between Pusan in Korea and Hamada in Japan (Figure 1) since March 1998 (Kim et al., 2002, in preparation). The voltage has a good linear relationship with the above two observed transports. However, these transport observations are still too short to resolve long-term changes in the transport through the Korea Strait.

Since the flow through a strait is gestrophically balanced at subinertial frequency (Toulany and Garrett, 1984), the sea level difference (SLD) across the strait can be used to estimate the volume transport. As the sea level data have been measured on both sides of the Korea Strait since 1960, they can be used for long-term analysis of the transport. Mizuno et al. (1989) applied this concept to the east channel of the Korea Strait using the current meter data and SLD across the east channel in winter, when the flow is predominantly barotropic. However, they
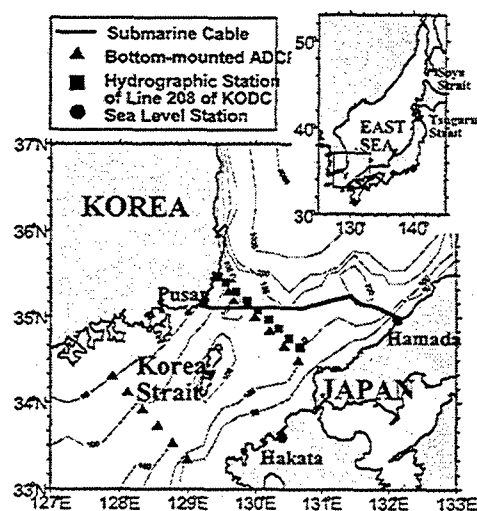

Figure 1. Arrangement of the submarine cable between Pusan, Korea and Hamada, Japan, bottom-mounted ADCP mooring stations, hydrographic stations of line 208 of KODC, and sea level stations. Light lines are depths in meters.

used current data measured at only one mooring station and did not compare SLD with the total volume transport through the Korea Strait. Isobe (1994) investigated the seasonal variability of barotropic and baroclinic motion in the Korea Strait using SLD and the hydrographic data across the strait. He defined SLD associated with the baroclinic motion as the depth-averaged geostrophic current, which does not contribute to the net transport, and concluded that SLD across the Korea Strait has a

large baroclinic part. However, he could not obtain the absolute value of the volume transport from SLD because there was no corresponding transport observation. Moreover, the baroclinic part of SLD, i.e. the depth-averaged geostrophic current by his definition, actually contributes to the net volume transport.

In this study we'll estimate SLD, which is related to only the steric expansion. After removing this part from the observed SLD, the linear relationship between SLD and the absolute volume transport will be found. Finally the discussion is provided for the limitation as well as the possibility of this method in investigating long-term transport changes in the Korea Strait.

Data

The sea level data at Pusan and Hakata are selected because the line connecting them is nearly perpendicular to the main axis of the Korea Strait (Figure 1). Since the currents in the Korea Strait are horizontally non-divergent at subinertial frequency (Kim *et al.*, 2002), there is little difference of the transport in terms of magnitude and phase along the strait. So SLD between Hakata and Pusan ($\Delta\eta_{obs}$) can be compared with the voltage-derived transport (T_V) between Hamada and Pusan to obtain the linear relationship between SLD and the transport.

The Korea Oceanographic Data Center (KODC) and the Japan Oceanographic Data Center (JODC) provided the hourly sea level data for a period from 1998 to 2000. Since the width of the Korea Strait is much shorter than the synoptic length scale of the atmospheric pressure fluctuation, the inverse barometric correction is not necessary for SLD between Hakata and Pusan. The hydrographic data across the Korea Strait have been observed bimonthly along the line 208 of KODC (Figure 1). The steric expansion in the observed SLD is estimated from the hydrographic data from 1970 to 1998. The voltage-derived transport (T_V) is converted from the voltage using the linear relationship with the observed transport from March 1998 to June 2000. Its standard error is estimated as $0.6 \times 10^6 \, \text{m}^3\text{s}^{-1}$ for a transport of $3 \times 10^6 \, \text{m}^3\text{s}^{-1}$ (Kim *et al.*, 2001). T_V and SLD between Hakata and Pusan are sub-sampled every day after a low-pass filtering with a half-power period of 4.57 day.

Estimation of SLD related to the steric expansion

The along-strait flow is assumed to be geostrohpically balanced in the Korea Strait at subinertial frequency. We split the along-strait flow ($v(x,z)$) into barotropic ($v_T(x)$) and baroclinic ($v_C(x,z)$) part, i.e. the former is the velocity at the reference depth ($v_T(x)=v(x,z=-H)$) and the latter is the difference between $v(x,z)$ and $v_T(x)$ (Figure 2). $v_C(x,z)$ can be calculated from the density structure (Fofonoff, 1962).

$$v_c(x,z) = \frac{1}{f}\frac{\partial D(x,z)}{\partial x}, \qquad (1)$$

$$D(x,z) = -\int_{P_o}^{P(z)} \frac{1}{\rho} dP, \qquad (2)$$

where D is geopotential height, P_0 is pressure at the reference depth ($P_0 = P(z = -H)$), ρ is water density, and f is the Coriolis parameter.
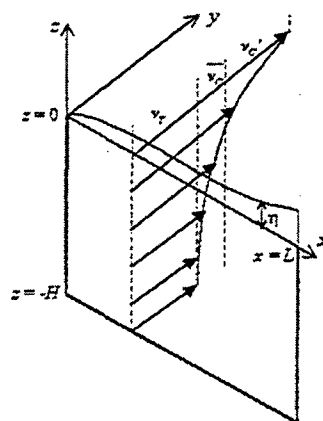

Figure 2. Schematic diagram of the along-strait flow, which is split into barotropic (v_T) and baroclinic (v_c) parts. v_c consists of depth-averaged ($\overline{v_c}$) and depth-dependent (v_c') parts. η is the sea surface elevation, H is the mean depth, and L is the width of the strait.

And $v_C(x,z)$ can be divided into a depth-averaged ($\overline{v_c}$) and a depth-dependent (v_c') part as

$$\overline{v_c}(x,z) = \frac{1}{H}\int_{-H}^{\zeta} v_c(x,z)dz = \frac{1}{f}\frac{\partial \overline{D}(x,z)}{\partial x}, \qquad (3)$$

$$v_c'(x,z) = v_c(x,z) - \overline{v_c}(x,z), \qquad (4)$$

where $\overline{D}$ is depth-averaged geopotential height. $\overline{v_c}$ also contributes to the net transport as the barotropic part (v_T). The cross-strait sea level gradient is related to the surface flow ($v(x,0)$) by the geostrophic balance.

$$v(x,0) = v_T(x) + \overline{v_c}(x,0) + v_c{}'(x,0) = \frac{g}{f}\frac{\partial \eta}{\partial x}\bigg|_{x=0}, \quad (5)$$

where g is gravity and η is sea surface elevation. If the water depth is assumed to be constant as the mean depth of $H = 100$ m between Pusan and Hakata (Figure 1), the net transport can be simply related to the observed SLD between Hakata and Pusan ($\Delta\eta_{obs}$) by integrating $v_T + \overline{v_c}$ over the cross section of the strait.

$$H\int_0^L \left[v_T(x) + \overline{v_c}(x,0) \right] dx = H\int_0^L \left[\frac{g}{f}\frac{\partial \eta}{\partial x} - v_c{}'(x,0) \right] dx \quad (6)$$

$$= H\left\{ \frac{g}{f}(\Delta\eta_{obs} - \Delta\eta_0) - \frac{1}{f}\left[D'(L,0) - D'(0,0) \right] \right\}, \quad (6a)$$

where L is the width of the strait (180 km), $\Delta\eta_0$ is the reference value of $\Delta\eta_{obs}$ which will be determined later by comparing $\Delta\eta_{obs}$ with the transport, and $D' = D - \overline{D}$. $\Delta\eta_{obs}$ contains SLD ($\Delta\eta_c{}'$) related to $v_c{}'$, which originates from the steric expansion without contribution to the net transport and has to be removed from $\Delta\eta_{obs}$ to obtain a linear relationship between SLD ($\Delta\eta_T$) and transport.

$$\Delta\eta_c{}' = \frac{1}{g}\left[D'(L,0) - D'(0,0) \right], \quad (7)$$

$$\Delta\eta_T = \Delta\eta_{obs} - \Delta\eta_c{}' \quad (8)$$

The bimonthly hydrographic data of the line 208 of KODC from 1970 to 1998 are used to obtain $\Delta\eta_c{}'$ across the Korea Strait, where the reference depth is set to be 125 m. Since the depth at station 1 is shallow (Figure 1 and 3), the hydrographic data deeper than 50 m at station 1 are filled with them at station 2 to obtain $D'(0,0)$. There is no hydrographic station near the Japanese coast in the line 208 of KODC. However, $\Delta\eta_c{}'$ between station 9 and the Japanese coast may not be large because the mean of $\Delta\eta_c{}'$ between station 8 and 9 is only 0.5 cm (Figure 4). Besides the baroclinicity of the flow is dominant in the west channel of the Korea Strait due to the occurrence of the Korea Strait Bottom Cold Water (KSBCW) (Cho and Kim, 1998; Isobe, 1994), which is defined as the water less than 10°C (Figure 3).

Therefore the data at station 9 are used to calculate $D'(L,0)$.

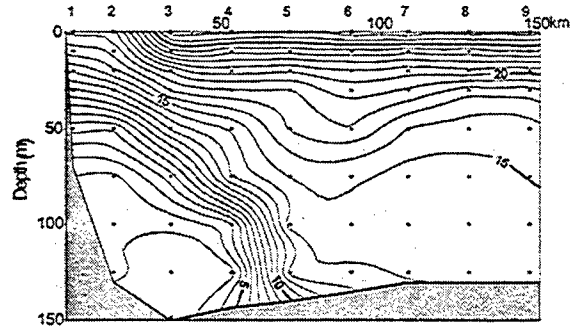The mean $\Delta\eta_c{}'$ in each month is calculated and it is

Figure 3. The vertical section of temperature along the line 208 of KODC in August 1996. Observation depths are denoted by dots and the horizontal distance from the west Korean coast and the station number appear together in x axis.

interpolated to a daily value by cubic spline method (Figure 4). The mean $\Delta\eta_c{}'$ has a maximum of 12.6 cm in August and a minimum of 1.0 cm in March. Most of $\Delta\eta_c{}'$ in summer is caused by the extension of the KSBCW along the west channel of the Korea Strait (Cho and Kim, 1998). Since the barotropic structure is dominant in late winter and early spring, $\Delta\eta_c{}'$ is small in those seasons (Figure 4). The standard error in $\Delta\eta_T$ is estimated as 7 cm considering the variation of $\Delta\eta_c{}'$.
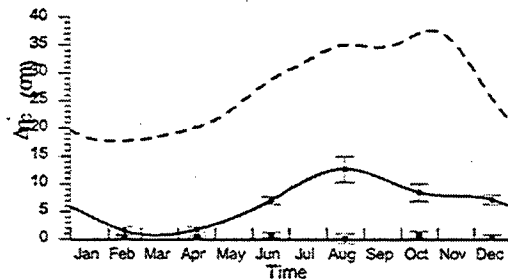

Figure 4. Solid line is time-series of the sea level difference (SLD) related to the steric expansion without contribution to the net transport ($\Delta\eta_c{}'$), which is calculated from the bimonthly hydrographic data at station 1 and 9 of the line 208 of KODC from 1970 to 1998 and is interpolated to a daily value by cubic spline method. Monthly mean values of $\Delta\eta_c{}'$ between station 8 and 9 are designated by square. The vertical bar denotes one

standard deviation of each monthly mean $\Delta\eta_C'$ is. Dashed line is time-series of $\Delta\eta_{obs}'$ ($= \Delta\eta_{obs} - \Delta\eta_0$) in 1999, where $\Delta\eta_0$ is the reference SLD between Hakata and Pusan determined by the comparison of SLD with the transport through the Korea Strait

Linear relationship between SLD and transport

The maximum likelihood method (Macdonald and Thompson, 1992) is used to get the linear relationship between $\Delta\eta_T$ and the voltage-derived transport (T_V). Standard errors of each coefficient of the linear regression are obtained using each estimated errors, i.e. 7 cm for $\Delta\eta_T$ and 0.6×10^6 m^3 s^{-1} for T_V. The conversion factor from SLD to transport is estimated as $\Lambda = (13.0 \pm 0.7) \times 10^6$ m^2 s^{-1}, and the reference value of SLD as $\Delta\eta_0 = 82 \pm 6$ cm with their correlation coefficient of 0.79 (Figure 5). The standard error in Λ is $\pm 5.4\%$, which corresponds to a transport error of $\pm 0.16 \times 10^6$ m^3 s^{-1} for a transport of 3×10^6 m^3 s^{-1}. Considering the error in the estimated $\Delta\eta_0$, the total standard error becomes $\pm 0.8 \times 10^6$ m^3 s^{-1} for a transport of 3×10^6 m^3 s^{-1}.
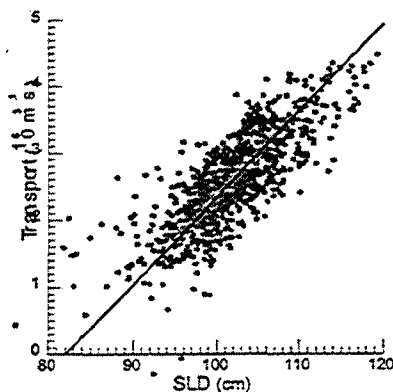
Figure 5. Linear regression between transport and SLD between Hakata and Pusan ($\Delta\eta_T$), which results from the subtraction of $\Delta\eta_C'$ from the observed SLD ($\Delta\eta_{obs}$), after low-pass filtering with a half-power period of 4.57 days.

Since the reference value, $\Delta\eta_0$ as well as the conversion factor, Λ of SLD between Hakata and Pusan are obtained, the absolute transport (T_{SLD}) can be estimated from SLD. T_{SLD} is compared with T_V and the observed transport (T_{obs}) from bottom-mounted ADCPs by the US NRL across the Korea Strait (Figure 1) from May 1999 to March 2000 (Teague *et al.*, 2001, accepted in JPO) in Figure 6.

The correlation coefficient is 0.82 between T_{SLD} and T_V and 0.76 between T_{SLD} and T_{obs}. Their rms misfits are 0.42×10^6 m^3 s^{-1} and 0.48×10^6 m^3 s^{-1}, respectively. Most of the differences between T_{SLD} and T_V are less than the estimated standard error, 0.8×10^6 m^3 s^{-1}.
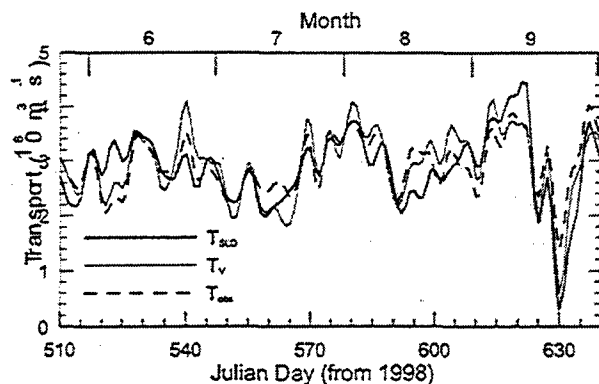
Figure 6. Time-series of SLD-derived transport, T_{SLD} (dark line), voltage-derived transport T_V (light line), and observed transport T_{obs} (dashed line) from bottom-mounted ADCPs by the US NRL across the Korea Strait (Teague *et al.*, 2001).

To compare them at low frequency, T_{SLD} and T_V are low-pass filtered with a half-power period of 90 days (Figure 7). T_{SLD} has a mean of 2.6×10^6 m^3 s^{-1} with a maximum of 3.8×10^6 m^3 s^{-1} in October 1999 and a minimum of 1.8×10^6 m^3 s^{-1} in January 1999. T_V has the same mean as T_{SLD} and a maximum of 3.4×10^6 m^3 s^{-1} in October 1999 and a minimum of 1.6×10^6 m^3 s^{-1} in January 2000. T_{SLD} has similar variations with T_V within 95% confidence intervals of T_{SLD}. T_{SLD} is also compared with the monthly mean observed transport (T_{obs}) in Figure 7, where the transport from the vessel-mounted ADCP between Pusan and Hakata (Takikawa *et al.*, 1999) is supplemented. T_{SLD} agrees well also with the observed transports within 95% confidence intervals.
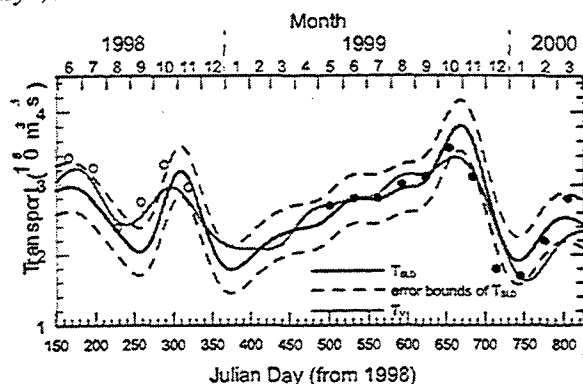
Month

1998   1999   2000

Julian Day (from 1998)

Figure 7. Low-frequency variations of T_{SLD} (dark line) and T_V (light line) after low-pass filtering with a half-power period of 90 days with 95% confidence intervals of T_{SLD} (dashed lines). Monthly mean transports observed by the vessel-mounted ADCP (Takikawa *et al.*, 1999) and the bottom-mounted ADCP (Teague *et al.*, 2001) are denoted by open and closed circles, respectively.

Discussion and Conclusions

If the along-strait flow is geostrophically balanced and the water depth is assumed to be constant as H across the strait, the conversion factor from SLD to transport (Λ) can be simply estimated as $\Lambda_0 = Hg/f$ from Eq. (6a). Λ_0 is estimated to be about 12×10^6 m^2 s^{-1} when H is assumed to be 100 m as the mean depth between Pusan and Hakata. The difference between Λ_0 and Λ obtained from the comparison of SLD with the transport may be caused by the ageostrophic motion and the variable bottom topography in the Korea Strait. However, the difference is not large and Λ_0 is within the 95% confidence range of the estimated Λ. This result implies that the along-strait flow is geostrophically balanced well in the Korea Strait.

To quantify the steric expansion effect on $\Delta\eta_{obs}$, the estimated reference SLD, $\Delta\eta_0$, is subtracted from $\Delta\eta_{obs}$ in 1999 ($\Delta\eta_{obs}' = \Delta\eta_{obs} - \Delta\eta_0$) and then $\Delta\eta_{obs}'$ is low-pass filtered with a half-power period of 90 days (dashed line in Figure 4). $\Delta\eta_C'$ is more than 30% of $\Delta\eta_{obs}'$ in August 1999. Therefore, $\Delta\eta_C'$ should be removed in estimating the transport from SLD across the Korea Strait especially in summer and autumn, when the baroclinicity of the flow is dominant. If $\Delta\eta_C'$ is not removed from $\Delta\eta_{obs}$, T_{SLD} will be overestimated up to 1.6×10^6 m^3 s^{-1} in August, which amounts to about 50% of the real net transport through the Korea Strait in August. However, it should be remembered that $\Delta\eta_C'$ has large

interannual variations especially in summer depending on the occurrence and strength of the KSBCW. One standard deviation of the estimated mean $\Delta\eta_C'$ in summer is as large as about 2.3 cm (Figure 4).

A good correlation between SLD and the transport in the Korea Strait is obtained after removing $\Delta\eta_C'$, which does not contribute to the net transport. SLD between Hakata and Pusan can provide good estimates of transport through the Korea Strait continuously. Since the sea level data have been measured at Pusan and Hakata for a long time, it is possible to investigate long-term transport variations in the Korea Strait, which affect the circulation in the East Sea decisively and may be related to the changes in the Pacific Ocean, such as El Nino and decadal climate variations.

References

Cho, Y. K., and K. Kim, Branching Mechanism of the Tsushima Current in the Korea Strait. *J. Phys. Ocean.*, 30, 2788-2797, 2000.

Cho, Y. K., and K. Kim, Structure of the Korea Strait Bottom Cold Water and its seasonal variation in 1991. *Contin. Shelf Res.*, 18, 791-804, 1998.

Fofonoff, N. P., Dynamics of Ocean Currents, *The Sea*, Vol. 1, M. N. Hill, Ed., Wiley & Sons, 323-395, 1962.

Isobe, A, Seasonal variability of the barotropic and baroclinic motion in the Tsushima-Korea Strait. *J. Ocean.*, 50, 223-238, 1994.

Kim, K., S. J. Lyu, Y.-G. Kim, B. H. Choi, K. Taira, H. T. Perkins, W. J. Teague, and J, W. Book, Monitoring Volume Transport in the Korea Strait through Measurement of Cable Voltage between Pusan and Hamada, *in preparation*, 2002.

Lee, D.-K., P. P. Niiler, S.-R. Lee, K. Kim, and H.-J. Lie, Energetics of the surface circulation of the Japan/East Sea, *J. Geophys. Res., 105*, 19,561-19,573, 2000.

Macdonald, J. R., and W. J. Thompson, Least-squares fitting when both variables contain errors: Pitfalls and possibilities. *Am. J. Phys.*, 60, 66-73, 1992.

Mizuno, S., K. Kawatate, T. Nagahama, and T. Miita, Measurements of East Tsushima current in winter and estimation of its seasonal variability. *J. Oceanogr. Soc. Japan*, 45, 375-384, 1989.

Takikawa, T., J.-H.Yoon, H. Hase, and K.-D. Cho, Monitoring of the Tsushima Current at the Tsushima/Korea Straits. in *Proceedings of the 3rd CREAMS International Symposium*, Fukuoka, Japan, 15-18, 1999.

Teague, W. J., G. A. Jacobs, H. T. Perkins, J. W. Book, K.-I. Chang, and M.-S. Suk, Low frequency current

observations in the Korea Strait. *J. Phys. Ocean.*, accepted, 2001.

Toulany, B., C. Garrett, Geostrophic Control of Fluctuating Barotropic Flow through Straits. *J. Phys. Ocean.*, 14, 649-655, 1984.

Uda, M., The results of simultaneous oceanographical investigations in the Japan Sea and its adjacent waters in May and June, 1932. *J. Imp. Fish. Exp. St.*, 5, 57-190, 1934.

Froude angle control at a highly stratified estuarine front

D. G. MacDonald and W. R. Geyer

Massachusetts Institute of Technology/Woods Hole Oceanographic Institution Joint Program, Woods Hole, MA, USA

Abstract. Observations at the mouth of the Fraser River (British Columbia, Canada) indicate an abrupt frontal zone between unstratified river outflow and a highly stratified river plume. The internal Froude number at the front significantly exceeds one, based on velocities in the along-flow direction. However, the front is oriented obliquely to the outflow. If a coordinate system is selected that is normal to the front, then the critical Froude number of one is obtained. This indicates that a Froude angle, similar in application to a Mach angle for trans-sonic flows, can be used to determine critical conditions when the front is oblique to the principal flow direction.

Introduction

Estuarine fronts can vary from weakly stratified to highly stratified, as a function of river discharge and tidal forcing at the river mouth. The highly stratified limit can be effectively modeled as a two-layer system, and the dynamics of these fronts have been examined analytically by Armi and Farmer (1986), and Farmer and Armi (1986) [these two papers are collectively referred to hereafter as A&F]. Two-layer exchange flows can be described with respect to an internal Froude number, G, defined as:

$$G^2 = F_1^2 + F_2^2 \qquad (1)$$

where, $F_j^2 = \dfrac{u_j^2}{g'h_j}$, and $g' = g\dfrac{\Delta\rho}{\rho_o}$.

Here u_j represents the mean velocity of layer j, h_j the thickness of each layer, and ρ the fluid density. At an idealized estuarine front, the lower layer is arrested, with no velocity, so that the internal Froude number is equal to the upper layer component. With flow conditions uniform in the cross-channel direction, as in the cases studied by A&F, the Froude number is exactly one at the front, with supercritical values ($G=F_1>1$) seaward of the front, where two distinct layers are present. In supercritical regions, information carried by long internal waves can only be transmitted in one direction, in this case, away from the front, preventing further landward intrusion of the front and maintaining a stable frontal position.

Garvine (1982) introduced the concept of a Froude angle, analogous to the Mach angle from supersonic flow theory, and defined as:

$$\phi = \sin^{-1}\left(G^{-1}\right) \qquad (2)$$

This angle defines an envelope of wave influence in two dimensions, as shown in Figure 1, expanding the typical one-dimensional concept of the Froude number. Garvine (1982) used the concept of the Froude angle within an estuarine plume model to define the characteristic lines from points within the flow field based on the local Froude number. The model also assumed that the local Froude number at the front, defined using the velocity component perpendicular to the front, was equal to 1.
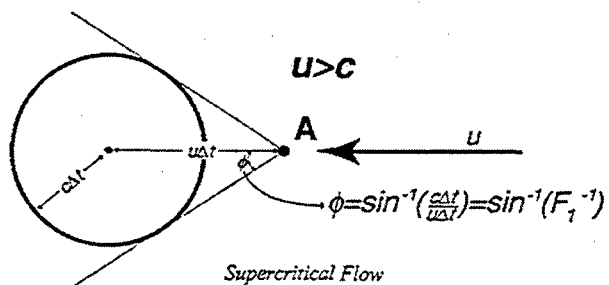

Figure 1. Propagation of wave front for supercritical flow. A flow with velocity u flows from right to left, and an instantaneous disturbance is initiated at point A. The angle ϕ represents the envelope of the resulting disturbance, as shown.

At the mouths of real estuaries, cross channel homogeneity, as assumed in A&F, is rare. Local bathymetry, the angle of the estuarine channel with respect to the shoreline, and ambient currents (tidal and otherwise) in the receiving waters can all contribute to transverse heterogeneities, which may require a 2-dimensional treatment of the frontal dynamics, similar to Garvine (1982). This paper presents an investigation of the Froude number dynamics associated with the highly stratified front near the mouth of the Fraser River (British Columbia, Canada), in which the geometry of the front does not permit the one-dimensional analysis of A&F.

Figure 2. Location of the Fraser River Estuary. Estuary mouth is outlined in black.

The Fraser River

The Fraser River Estuary is located in the southwest corner of British Columbia, approximately 20 km south of the city of Vancouver (Figure 2). River discharge peaks during early summer, with flow rates on the order of 10,000 m^3s^{-1}. This discharge, combined with tidal amplitudes on the order of 2.5 to 4 meters, sets up highly stratified conditions in the estuarine channel, and an oscillating salt wedge that can intrude some 20 km landward from the mouth on each tidal cycle. This study focuses on several hours during the late ebb, when the salt wedge has been forced back to the river mouth (Geyer and Farmer, 1989), and remains in a quasi-steady state position slightly seaward of the mouth. Data was collected from shipboard instrumentation, including two ship mounted acoustic Doppler current profilers (ADCPs) and a towed conductivity-temperature-depth (CTD) unit.

At the mouth of the Fraser, a jetty extends along the northern side of the channel, terminating at the Sand Heads lighthouse (Figure 3). The southern boundary of the channel is defined by an intertidal bank, which extends approximately 1.5 km seaward of Sand Heads. Bathymetry outside the mouth is transected by a steep bathymetric break that runs at an angle of approximately 45° to the channel boundary. Across the break, depths increase rapidly from approximately 10 m to greater than 50 m. These and other characteristics of the mouth contribute to cross-channel heterogeneity and the development of flow with significant 2-dimensional structure in the horizontal plane.
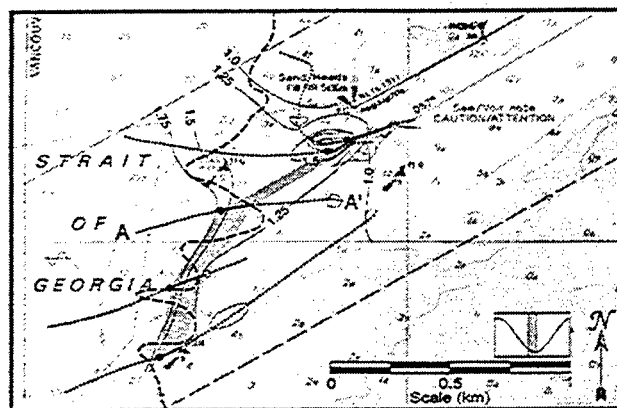

Figure 3. Geometry of the frontal zone at the mouth, showing the oblique orientation of the front relative to the channel. Contours indicate the value of the upper layer Froude number across the lift-off zone during the late ebb on June 30, 2000. The 14 psu front is defined by the open and closed circles, and the shaded region. Upper layer Froude numbers across the region are estimated using a representative value of *g'*. Dotted lines represent ship tracks, and the dashed line represents the 12 m isobath and the bathymetric break.

Structure of the front

Figure 3 shows the location of the front, as identified from five roughly parallel passes through the region. The frontal location is identified as the shaded area, and is based on the first detection of water with salinity exceeding 14 psu. A region of uncertainty is provided by the open (bottom water less than 14 psu) and closed (first CTD observation of 14 psu water) circles, based on the path of the tow-yoed CTD unit. It is clear that the front is not normal to the channel, but instead roughly follows the bathymetric break, as identified by the 12 m isobath (highlighted). Contours of the upper layer Froude number, F_l, are also shown on Figure 3. These

values, calculated using mean streamwise velocities, with a layer interface defined coincident with the 14-psu isohaline, are substantially supercritical across almost the entire frontal region. Froude numbers shown in Figure 3 for regions where only one layer is present were generated using a representative value of g' from the stratified region.
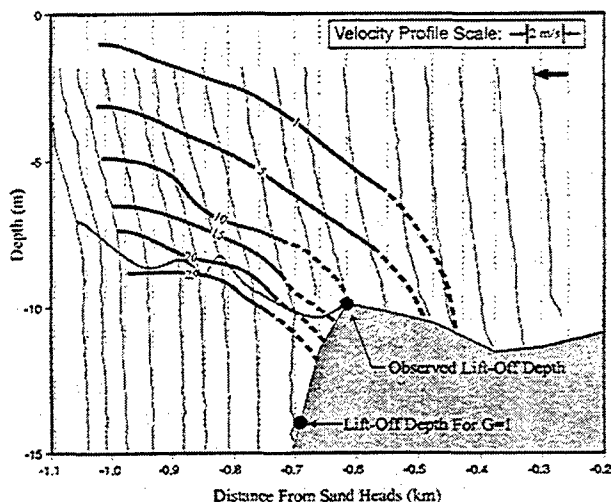

Figure 4. Cross section A-A' from Figure 3, showing salinity contours (black), and streamwise velocity profiles. The bold gray line represents the interface boundary as defined by a visual assessment of the point of the most abrupt change in the slope of the velocity profiles. At locations where robust velocity data does not extend deep enough, a lowest case estimate has been made by extrapolating the observable slope to $u=0$ (dotted lines). The front location, or lift-off point, observed from this method is also compared to the theoretical lift-off point corresponding to a critical internal Froude number.

The front itself is highly stratified, as shown in cross section in Figure 4 (transect line A-A' in Figure 3). A salinity difference on the order of 25 psu is observed in approximately 5 meters in the vertical, and less than 300 meters in the horizontal. Profiles of streamwise velocity are also shown on Figure 4, with the bold line delineating an interface boundary defined by a visual assessment of the most abrupt change in slope of the velocity profiles. This method of interface delineation would indicate a front location coincident with an intermediate value of salinity (10-15 psu), as shown. Also shown is the front location that would be required to meet the condition of an internal Froude number equal to one, using a mean velocity across the upper layer. This

point is located down slope considerably from the region of the steepest salinity gradient. It is clear that velocities are too large in the upper layer to support a Froude number of unity, even allowing for some uncertainty in the depth of the lift-off point.

Significant mixing occurs across the halocline in this region, with production rates of turbulent kinetic energy on the order of 10^{-3} m^{2}s^{-3} (MacDonald and Geyer I, in preparation). Within this turbulent zone, saline water is entrained upward into the outflowing river plume. Analysis of the velocity structure indicates that the entrained salt water does not originate from a landward-directed undercurrent, as it would in a simple estuarine channel. Rather it is supplied by a southward-directed flow (with velocities on the order of 20 to 50 cm/s), with its primary component normal to the direction of the river outflow (MacDonald and Geyer II, in preparation). This southward flow is associated with the ambient tidal flow within the Strait of Georgia during the ebbing tide (Crean *et al.*, 1988), and contributes to the cross-channel heterogeneity at the river mouth.

Froude angle dynamics at the front

The significant deviation of the observed Froude number at the front from the prediction of the theory of A&F suggests that the angle of the front relative to the outflow should be addressed. A critical Froude number value of unity is sufficient for the one-dimensional problem, or if the front is normal to the oncoming flow. For oblique fronts, at an angle α to the oncoming flow, the Froude angle (Garvine 1982) must be considered, and the critical condition becomes $\phi = \alpha$. The one-dimensional case is then the special case where $\alpha = 90°$. The general condition implies that the front lies along one of the outbound characteristics, so that information can travel along the front, but no information can be transmitted landward of the front, which meets the general requirements for a critical condition.

Figure 5 shows a plan view of the mouth. The open and closed circles show the limits of the frontal region as in Figure 3. The Froude angle at each of these locations, based on the local streamwise Froude number, is delineated by the bold black lines. A front can then be drawn (gray line) which meets both of these constraints. The mouth of the Fraser exhibits significant cross-channel heterogeneity in bathymetry and ambient flow conditions, resulting in a front that traverses the channel at varying angles to the channel

axis. Figures 4 and 5 together demonstrate that a one-dimensional view of Froude number dynamics is not sufficient to adequately predict the location of the front, but that the more general Froude angle condition provides a good fit with observations.
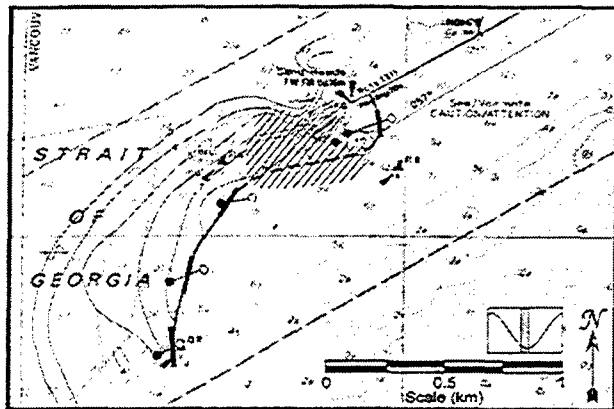

Figure 5. Froude angle estimates for the frontal region, calculated from the Froude numbers shown in Figure 3. Bold black segments represent the Froude angles within the identified front locations. The gray line is drawn to represent the front, and meets the constraints of both the observed front location and the Froude angle at all points. The hatched area, and dashed portion of the front, represent a region where the front is not well constrained by the available data. Contours represent the depth of the 14 psu isohaline surface.

Bottom attached fronts with an oblique orientation have been predicted analytically and observed in laboratory experiments (Adams and Stolzenbach, 1977) for buoyant jets discharged over a uniformly sloping bottom. The bottom-attached region in these cases consisted of a long and narrow triangular region, with the bottom front emanating into the jet region at an angle from the end of both channel boundaries. The basic geometry of this solution is the same as that which would be expected based on the Froude angle theory.

A similar example of Froude angle criticality has been seen within the confines of the estuarine channel in the Hudson River (New York), where angled fronts have been observed at supercritical streamwise Froude numbers (Geyer et al., 1998). This observation suggests that transverse bathymetric heterogeneity alone is capable of sustaining an oblique front, and an ambient cross channel flow, such as that present at the mouth of the Fraser, is not required. A cross channel circulation is essential, but

develops independently of any ambient current, following the outward going characteristics that run parallel to the sustained front.

Conclusions

The concept of Froude angle criticality has been shown to be a robust predictor of front location in a highly stratified estuary, providing an important extension of the A&F theory for two-layer fronts in channels with transverse bathymetric homogeneity.

References

Adams E. E. and K. D. Stolzenbach, 1977: Analysis of a buoyant surface discharge over a shallow sloping bottom. *Proceedings of the XVII International Association of Hydraulic Research (IAHR) Congress,* Baden Baden, 363-370.

Armi, L. and D. M. Farmer, 1986: Maximal two-layer exchange through a contraction with barotropic net flow. *J. Fluid Mechanics,* vol. 164, 27-51.

Crean, P. B., T. S. Murty and J. A. Stronach, 1988: *Mathematical Modeling of Tides and Estuarine Circulation.* Springer-Verlag, Berlin, 30.

Farmer, D. M. and L. Armi, 1986: Maximal two-layer exchange over a sill and through the combination of a sill and contraction with barotropic flow. *J. Fluid Mechanics,* vol. 164, 53-76.

Garvine, R. W., 1982: A steady state model for buoyant surface plume hydrodynamics in coastal waters. *Tellus,* vol. 34, 293-306.

Geyer, W. R., R. P. Signell and G. C. Kineke, 1998: Lateral trapping of sediment in a partially mixed estuary. *8th International Biennial Conference on Physics of Estuaries and Coastal Seas, 1996,* Dronkers and Scheffers (eds), Balkema, Rotterdam, pp 115-124.

Geyer, W. R., and D. M. Farmer, 1989: Tide-induced variation of the dynamics of a salt wedge estuary. *J. Physical Oceanography.* vol. 19, 1060-1072.

MacDonald, D. G., W. R. Geyer (I), in preparation: Turbulent kinetic energy production and mixing at a highly stratified estuarine front.

MacDonald, D. G., W. R. Geyer (II), in preparation: The three-dimensional structure of a highly stratified estuarine front.

Sustained measurements of the Denmark Strait Overflow

A. Macrander[1], R. H. Käse[1], U. Send[1], H. Valdimarsson[2] and S. Jónsson[2]

[1]Institut für Meereskunde an der Universität Kiel 24105 Kiel, Germany
[2]Hafrannsóknastofnunin Reykjavík 101 Reykjavík, Iceland

Abstract. Analysis of a high resolution Denmark Strait Overflow model is used to determine optimal positions of a small number of bottom mounted acoustical devices. The instruments allow a determination of i) the upper boundary of dense overflow water, ii) the current velocity with the bottom layer and iii) instantaneous difference of SSH between the instrument locations. A field experiment was implemented in the Denmark Strait and the results from 14 months long timeseries are presented.

Transport estimates

Transport estimates of dense overflows are needed to judge the importance of changes in water mass production for climate fluctuations.

There are indications [Pratt, 1986], that hydraulic restraints limit the flow across sills. This has been shown for the Denmark Strait by *Käse and Oschlies* [2000]. *Girton et al.* [2001] have established a transport estimate that is not different from the 1973 value by *Ross* [1984], thus suggesting a long term stability of the throughflow in spite of the vigorous fluctuations on timescales of a few days.

Since 1999 IfM Kiel has cooperated with Hafrannsóknastofnunin in Reykjavík to enhance their existing long term current meter site in the deepest part of the sill by additional instruments upslope on the Greenland shelf. We report on an optimized array of acoustic Doppler current profilers (ADCP) and inverted echo sounders with bottom pressure sensors (PIES) that allows for the first time to establish a long term estimate of dense water transport via the combined registration of dense layer thickness and velocity. The interface determination by PIES improves the estimates that are possible from the maximum shear in the velocity profiles.

The geographical locations of instruments are determined by an analysis of a process model that was able to reproduce the physical processes observed in several field experiments [Käse et al., 2002]. Figure 1 shows an instantaneous snapshot of the density structure on a section across the Denmark Strait and the instrument positions.

The first step was to validate the overall performance of acoustic measurements by implementing moorings at every grid point of the model. In this case, the "observed" transport showed no significant differences to the actual "real" DSOW transport in the model.

In a second step, the correlation of "observed" and "real" DSOW transport was determined for different numbers and locations of simulated moorings.

The implementation of the array in the process model suggested

- accuracy of the transport estimates (not surprisingly) increases with increasing instrument density. Correlation between "real" and "observed" transport is 0.58 for one ADCP, 0.68 for two, 0.9 for three and 0.93 for four ADCPs.

- for three instruments, best locations are one instrument directly at the deepest part, the second 11 km and the third 25.8 km northwest of the sill at the Greenland slope.

- the presently deployed array with 2 ADCPs systematically underestimates the transport by 0.5 Sv, a third instrument (not recovered yet) would still miss 0.23 Sv that is contributed from the shelf flow.

- the combined measurements of bottom pressure and interface depth allow us to estimate the sea surface displacement and to judge the suitability for transport determination via remote sensing.

Figure 2 reveals the energetic transport fluctuations present on short time scales. Typically, the dominating fluctuations have periods of 2 to 7 days, variations on timescales longer than one month are not significant.

The first two sets of moorings have covered the periods from October 1999 to February 2000 and August 2000 to May 2001 and yielded a DSOW transport time series of more than 14 months. A 20 day running mean time series of SSH, interface depth and transport are shown in figure 3; the standard deviation (shaded) is mainly due to the dominating 2 to 7 days variations. The upper panel reveals an almost perfect correlation between interface depth and sea surface height differences (as observed between the two PIES positions), which are plotted with a scale factor of -1/1000, i.e. 1 cm
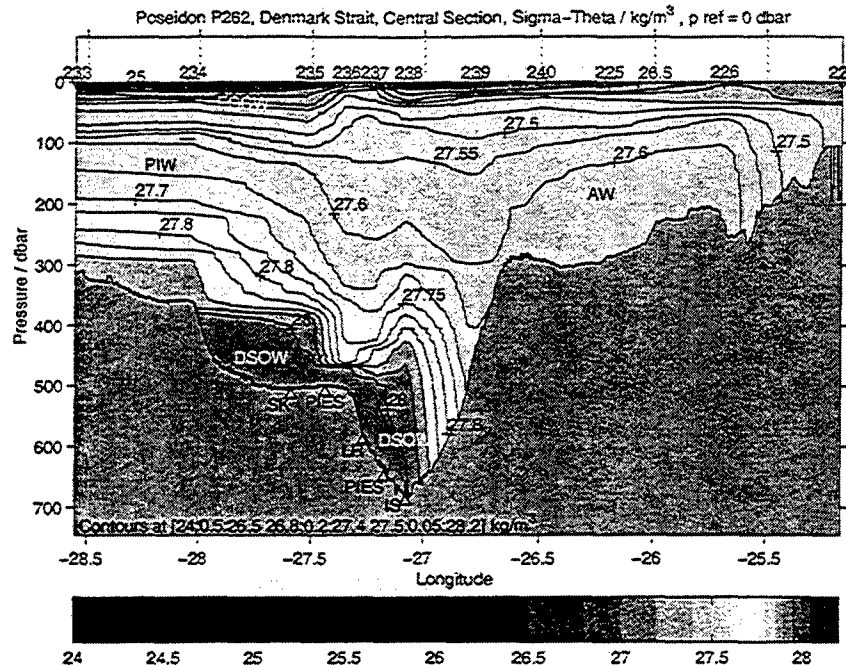
Figure 1. *Section of potential density across the Denmark Strait. DSOW denotes the dense Overflow water mass with* $\sigma_\Theta \geq 27.8\,\mathrm{kg/m^3}$. *EGCW and PIW indicates positions of East Greenland Current Water and Polar Intermediate Water, respectively; Atlantic Water ist marked as AW. SK, LR, IS are the presently deployed ADCPs. Inverted echo sounders with bottom pressure sensors are indicated by PIES.*

sea surface depression corresponds to 10 m interface elevation. The lower panel shows the DSOW transport time series calculated from ADCP current measurements and interface depth, determined from the depth of maximum current shear.

A thermistor chain, deployed upstream from October 1999 to February 2000, monitored the reservoir height of the dense water. We found a significant correlation between changes in this quantity (thin line "TK" in figure 3, lower panel) and the throughflow, suggesting a hydraulic relation as predicted by *Whitehead* [1998] and *Käse and Oschlies* [2000].

This opens a new perspective to monitor transport changes via reservoir height measurements upstream and interface gradient of the overflow layer by two bottom pressure sensors and inverted echo sounders. The recovered data are not yet sufficient to support this possibility. An extended data set will probably be available in summer 2002.

References

Girton, J. B., Dynamics of transport and variability in the denmark strait overflow, Ph.D. thesis, University of Washington, Seattle, WA, 2001.

Girton, J. B., T. B. Sanford, and R. H. Käse, Synoptic sections of the denmark strait overflow, *Geophys. Res. Lett.*, 28, 1619–1622, 2001.

Käse, R. H., and A. Oschlies, Flow through denmark strait, *Journal of Geophysical Research*, 105, 28,527–28,546, 2000.

Käse, R. H., J. B. Girton, and T. B. Sanford, Structure and variability of the denmark strait overflow: Model and observations, 2002, to be submitted.

Pratt, L. J., Hydraulic control of sill flow with bottom topography, *JPO*, 27, 1970–1980, 1986.

Ross, C., Temperature-salinity characteristics of the "overflow" water in denmark strait during "overflow '73", *Rapp. P.-v. Réun. Cons. int. Explor. Mer.*, 185, 111–119, 1984.

Whitehead, J. A., Topographic control of oceanic flows in deep passages and straits, *Reviews of Geophysics*, 36, 423–440, 1998.
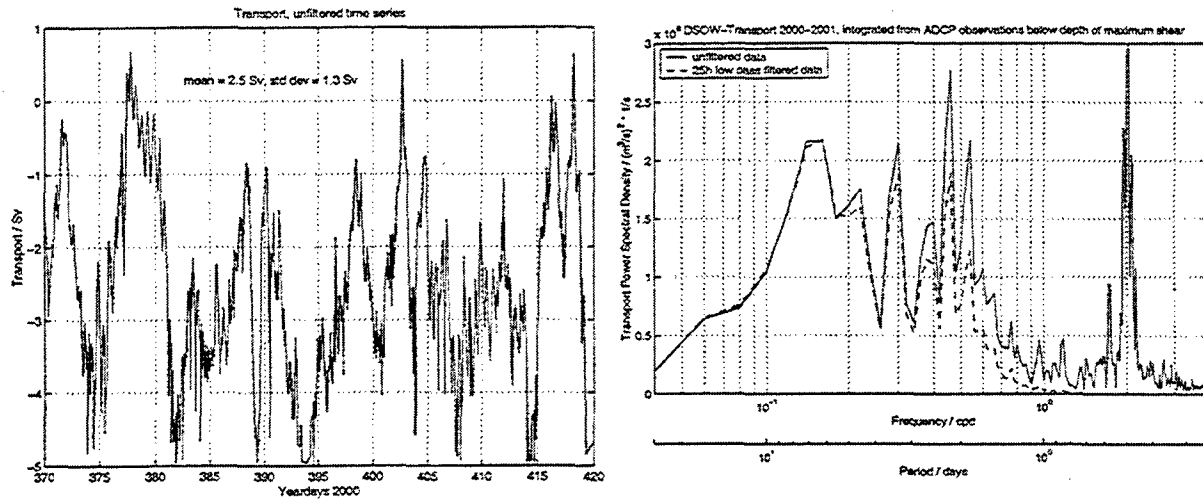
Figure 2. *Left panel: Typical 50 day section of uncorrected and unfiltered transport time series, showing tidal and the dominating 2 to 7 days fluctuations. Right panel: Energy spectrum of DSOW transport, calculated from six 50 day sections.*
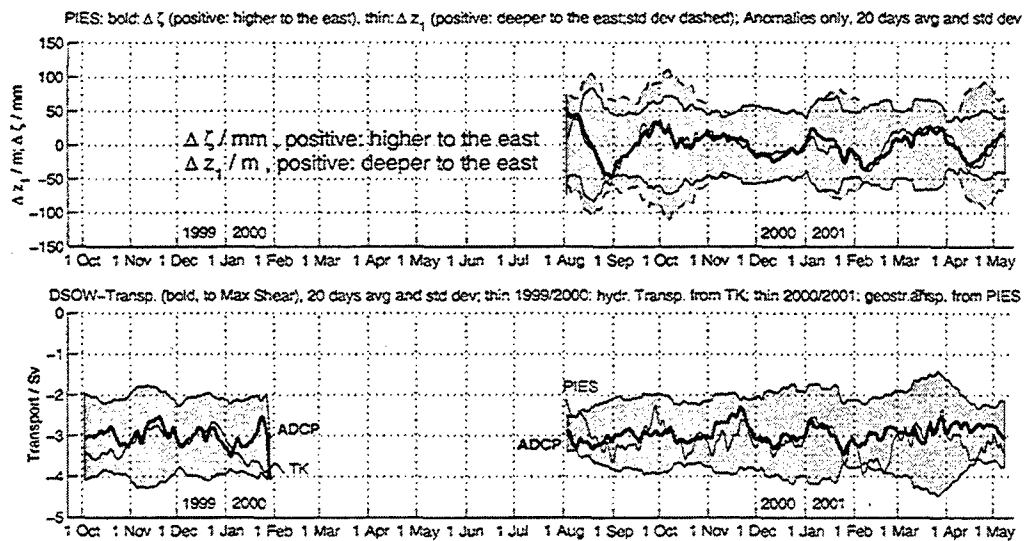

Figure 3. *Upper panel: Total time series of surface height (bold line) and interface depth (thin line) differences between the two PIES. Lower panel: ADCP DSOW transport, corrected for the 0.5 Sv underestimate (bold lines), additionally transport estimated from upstream reservoir height (TK) and from geostrophic calculations (PIES). 20 days running means, standard deviations shaded.*

A box model study of the feedback between basin and strait processes in the Mediterranean Sea

Stephan Matthiesen[1] and Keith Haines[2]

[1]Institute for Meteorology, The University of Edinburgh, United Kingdom
[2]Environmental Systems Science Centre, Reading University, Reading, United Kingdom

Abstract. The Strait of Gibraltar limits the exchange with the Atlantic and therefore influences the water properties in the Mediterranean, but is also influenced by the conditions in the basin. To investigate this feedback, a 3-box model of the Mediterranean with a hydraulically controlled strait was programmed. The model is used in an explorative study to find new dynamical aspects of the system. Firstly, changing air-sea fluxes induce a nonlinear response with a transitional state for several decades which can be very different from both the initial and the final steady state. Secondly, the effect of rising sea level since the Late Pleistocene is modelled, and we find that the stratification inside the Mediterranean can increase significantly at times of rapid sea level change due to a reservoir effect. Finally, we investigate the impact of mixing between in- and outflowing water on the transient and the steady state of the coupled system.

Model description

We programmed a hydraulically controlled box model (HYCOBOX) which consists of a 3-box model of the Mediterranean basin, coupled to a hydraulically controlled strait model, thus reflecting the fundamental feedbacks between basin and strait processes (fig. 1). The strait submodel is based on the time-independent fluid dynamical hydraulic control theory for a two layer exchange (e.g. *Dalziel* [1991]). It takes the water densities, the interface depth and the sea levels in both reservoirs as boundary conditions and calculates the strait transport. Both maximal and submaximal situations are modelled depending on the boundary conditions. The strait is assumed to have separate sill and narrows, and the cross-section at the sill can be chosen freely (for this study only triangular cross-sections are used).

The basin submodel consists of three boxes, whose volumes can change freely. Inflowing Atlantic water enters the upper layer U and is mixed into the surface layer F. Air-sea fluxes only affect the surface layer F, leading to the formation of denser water, which sinks and is mixed into the lower layer L. This process is parameterised by the water formation rate c_{FL}. A simple but realistic parameterisation depends on the density difference between the newly formed water and the lower layer

$$c_{FL} = \mu(\rho_F - \rho_L)h_U,$$ (1)

Other parameterisations have also been used for experiments not shown here. There is also some mixing and diffusion between the upper and the lower layer.

Only the air-sea fluxes and the Atlantic water properties are imposed as boundary conditions on the model, all other model variables evolve freely. In particular, the model does not assume a priori a balanced water, heat or salt budget. However, in the steady state all budgets are balanced. Three timescales are relevant: The sea level reacts to imbalances in the water budget on timescales of the order of a few days; the interface depth between upper and lower layer reacts on timescales of the order of 5 years; while salinity and temperature adjustments involve the bulk of the lower layer and have timescales of centuries.
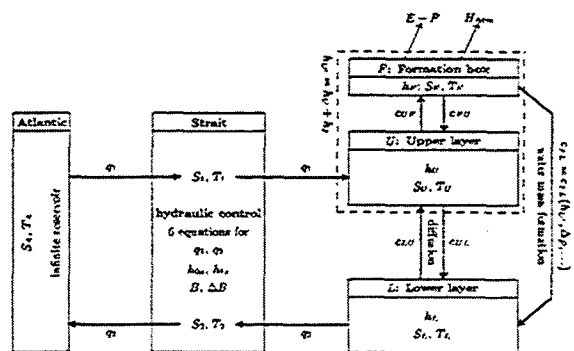

Figure 1. HYCOBOX, the hydraulically controlled box model.

Response to changing air-sea-fluxes

In a set of 24 experiments, the heat loss or evaporation was changed suddenly when the system was in a steady state. From fundamental budget constraints, one can show that the salinity and the strait transport for the steady state are related to the change in net evaporation by the following equation (see *Matthiesen* [2001] for details):

$$\left(\frac{\Delta S_{new}}{\Delta S_{old}}\right)^{(1+x)} = \left(\frac{q_{new}}{q_{old}}\right)^{(1+1/x)} = \frac{(E-P)_{new}}{(E-P)_{old}} \quad (2)$$

$$\text{with} \quad x = \frac{1}{2} \cdot \frac{1}{1-\frac{\alpha \Delta T}{\beta \Delta S}} \quad (\approx 1/3 \quad \text{for Gibraltar}) \quad (3)$$

where ΔS, ΔT are the salinity and temperature difference between in- and outflow in the strait, q is the strait transport, and $E - P$ the excess evaporation.

The set of experiments confirm that (2) is true for the initial and final steady state. However, the interaction of different timescales and processes leads to transitional states which are not predicted by the steady state considerations. As an example, figures 2-4 show an experiment in which the evaporation was reduced by 20% from year 500 onwards, after the system reached a steady state based on present day air-sea fluxes.

The interface depth (fig. 2) is an indicator of how close the system is to maximal strait transport. Although initial and final state are not too different, there is a significant deviation during the transition, and the interface moves to greater depths, leading to a submaximal strait regime for approximately a century. This behaviour is a result of the interaction of processes with different timescales. The salinity (fig. 3) needs a century to adjust to the new steady state given by the SQE equation (2). Therefore initially the stratification in the basin is too high, which reduces the water formation, leading to a lowering of the interface within a few years. The water formation rate and the interface then recover slowly as the lower layer freshens.

Although the heat loss remains constant, the temperature (fig. 4) also changes as a secondary effect, because the decreasing salinity difference reduces the strait transport and therefore the heat influx through the strait. For a 20% change in evaporation with constant heat loss, the salinity changes by 0.3 psu and the temperature by 0.2°C. Similarly, for a change in heat loss by 20% with constant evaporation, the temperature changes by 0.6°C and the salinity by 0.04 psu. These results suggest that the observed increase of 0.05 psu and 0.07°C between 1955 and 1989 (*Rohling and Bryden* [1992]) cannot be explained by one factor – either reduced river runoff or atmospheric warming – alone.

The deglaciation experiments

During the last 18000 years, sea level has risen by $\approx$ 120 m, with two meltwater peaks centred around 12000 yr BP (MWP IA) and 9500 yr BP (MWP IB) (*Fairbanks* [1989]).
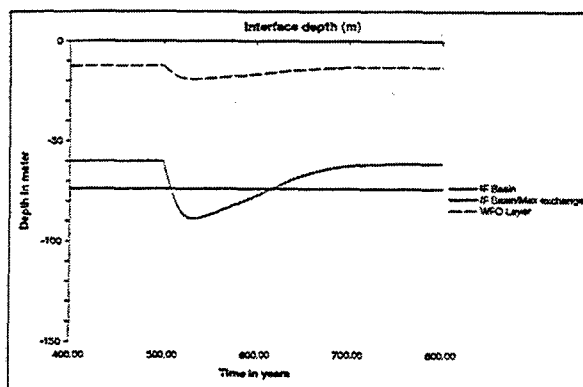

Figure 2. Interface depth for the evaporation-reduction experiment. The thin line is the interface in the basin; the thick line is the interface depth necessary for maintaining the maximal regime in the Strait.
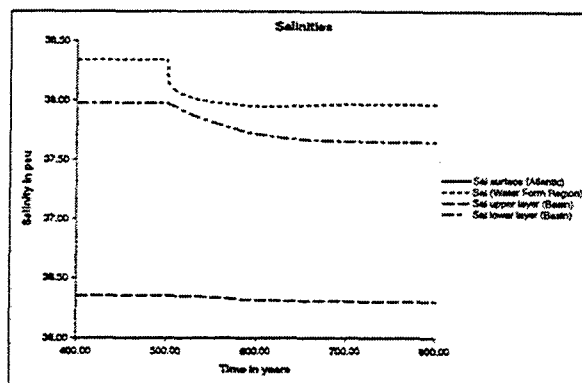

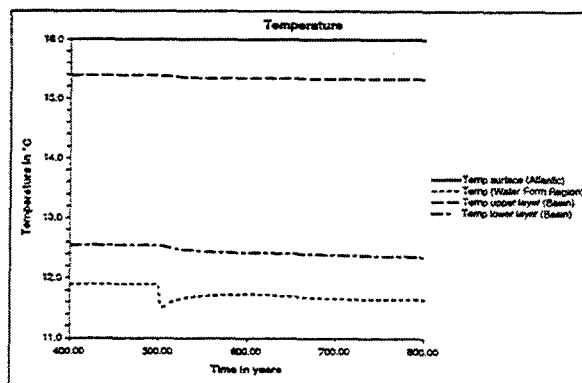**Figure 3.** The salinity for the evaporation reduction experiment.

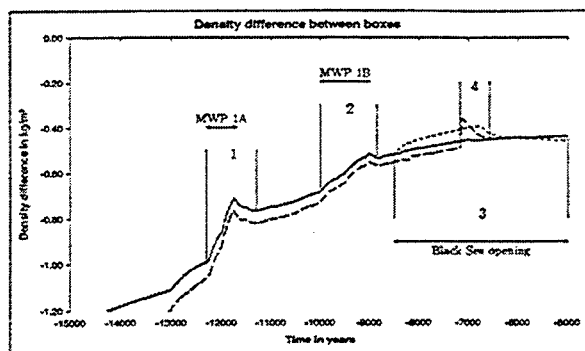**Figure 4.** The temperature for the evaporation reduction experiment.

Figure 5. Stratification $(\rho_L - \rho_F)$ for the deglaciation experiments. Solid line: Experiment with constant $E - P$. Dotted line: Gradual Black Sea opening. Dashed line: Catastrophic Black Sea opening.

As the sea level rises, the strait cross-section and therefore the transport increases, making the basin fresher. However, the salinity in the lower layer can considerably lag behind the steady state values, so that the stratification may increase during the meltwater peaks. The HYCOBOX model was used to estimate the size of this effect by performing an experiment with constant present day precipitation and river runoff, but changing sea level in the Atlantic following the reconstruction by *Fairbanks* [1989]. For comparison, we also model the effect of additional freshwater influx at the time of the opening of the Black Sea with two competing scenarios. In the gradual experiment, the connection to the Black Sea is established slowly between 8500 yr BP and 5000 yr BP, leading to an additional freshwater input which increases linearly in the first half of this period and decreases again in the second half, as suggested by *Lane-Serff et al.* [1997]. The catastrophic experiment is based on the dam break scenario presented by *Ryan et al.* [1997] and has a sudden increase in freshwater influx to present day values at 7150 yr BP. The freshwater events in both scenarios are expected to reduce the circulation.

Figure 5 shows the density difference between boxes F and L for the three experiments. For both Black Sea scenarios, the curves show peaks (labelled 3 and 4 in the figure) at the respective freshwater events, confirming that this quantity is an indicator of the stratification in the basin. All three scenarios also show noticeable peaks (1 and 2) during and a few centuries after the global meltwater events. It should be emphasised that these peaks are purely a result of the reservoir effect, as the meltwater peaks in the model do not affect the Atlantic salinity or change the river runoff inside the basin. The effect of meltwater peak 1A is comparable in size to the Black Sea events, while meltwater peak 1B has a smaller but non-negligible effect.

The timing of sapropel layer S1 at 9600 − 6400 yr BP (*Aksu et al.* [1995]) is towards the end of MWP 1B or at the beginning of the gradual Black Sea opening, and it is possible that the increased stratification following MWP 1B
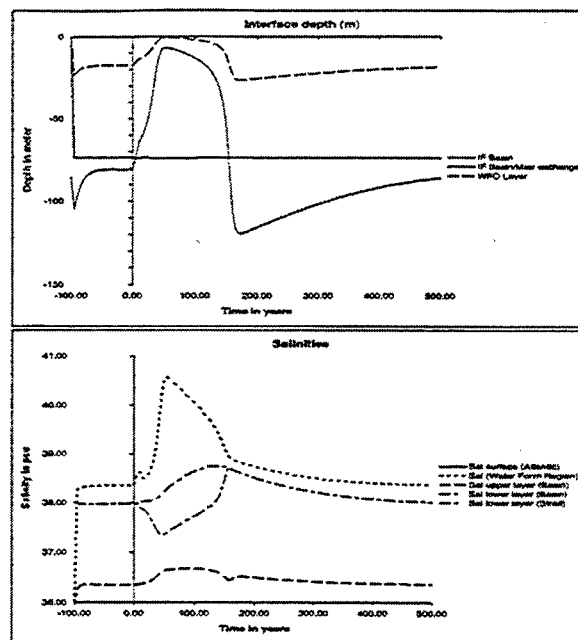

Figure 6. The evolution of the interface depth and the salinity for an entrainment experiment.

contributed to a collapse of the circulation.

Mixing in the Hydraulic jump

In the maximal regime, the supercritical flow at the entrance to the strait has to revert to subcritical inside the Mediterranean basin in a hydraulic jump or smoother hydraulic transition. We tested the idea that this turbulent process entrains some of the inflowing fresher water into the lower layer. This reduces the density of the outflowing water in the strait and therefore reduces the strait transport. The HYCOBOX model was modified so that a proportion of the inflowing water is entrained into the outflow without entering the basin, and the amount is proportional to the depth difference between the interface in the strait and the basin. For submaximal situations, there is no entrainment.

A large number of experiments were performed with different entrainment rates. Fig. 6 shows the interface depth and the salinity for a typical experiment. In year 0 a dry event (the evaporation increases by 20% for 10 years, but goes back to the initial value afterwards) pushes the system from the steady state into an unstable situation, in which the water formation collapses, the interface gets very shallow, and the salinity reaches extreme values. After 125 years the water formation starts again, and the system rebounds into a submaximal situation, with the return to the steady state more than half a millennium after the event. The system therefore exhibits two states:

Weak mixing/strong circulation: The normal situation with no (or a small) hydraulic jump, high strait transport

and low basin salinity.

Strong mixing/weak circulation: Mixing in the hydraulic reduces the transport into the basin directly, but also indirectly through reduced density difference in the Strait.

A more detailed stability analysis shows that for timescales shorter than the salinity timescale, both states are stable equilibria. On longer timescales, however, the salinity adjustment increases the strait transport again, so that the strong mixing state is metastable.

It is unclear if this mechanism is or has been relevant in the Mediterranean or other marginal seas. Possibly the dynamics of the Alboran Gyres provide a mixing mechanism with essentially similar effects. However, we believe that we have identified this behaviour in GCM runs (*Myers and Haines* [2001]), so that this result may help to improve understanding of GCM results.

Conclusion

The investigations with the HYCOBOX model have shown that the feedback between basin and strait processes lead to different types of dynamical behaviour which have not received much attention before.

References

Aksu, A. E., D. Yaşar, and P. J. Mudie, Paleoclimatic and paleoceanographic conditions leading to development of sapropel layer S1 in the Aegean Sea, *Palaeogeography, Palaeoclimatology, Palaeoecology, 116*, 71–101, 1995.

Dalziel, S. B., Two-layer hydraulics: a functional approach, *J. Fluid Mech., 223*, 135–163, 1991.

Fairbanks, R. G., A 17,000 year glacio-eustatic sea level record: Influence of glacial melting rates on the Younger Dryas Event and deep ocean circulation, *Nature, 342*, 637–642, 1989.

Lane-Serff, G. F., E. J. Rohling, H. L. Bryden, and H. Charnock, Postglacial connection of the Black Sea to the Mediterranean and its relation to the timing of sapropel formation, *Paleoceanography, 12*, 169–174, 1997.

Matthiesen, S., The feedback between basin and strait processes in the Mediterranean Sea and similar marginal seas – a process study, Ph.D. thesis, The University of Edinburgh, 2001.

Myers, P. G., and K. Haines, Stability of the Mediterranean's thermohaline circulation under modified evaporative fluxes, *J. Geophys. Res., submitted*, 2001.

Rohling, E. J., and H. L. Bryden, Man-induced salinity and temperature increases in Western Mediterranean deep-water, *J. Geophys. Res. – Oceans, 97*, 11,191–11,198, 1992.

Ryan, W. B. F., et al., An abrupt drowning of the Black Sea shelf, *Marine Geology, 138*, 119–126, 1997.

Stephan Matthiesen, Institute for Meteorology, The University of Edinburgh, James Clerk Maxwell Building, Edinburgh EH9 3JZ, United Kingdom

Keith Haines, Environmental Systems Science Centre (ESSC), Reading University, 3 Earley Gate, WhiteKnights, Reading RG6 6AL, United Kingdom

Theoretical calculations of maximum deep-water overflow based on real topography

Anna Nikolopoulos[1] and Karin Borenäs[2]

[1] Department of Meteorology/Physical Oceanography, Stockholm University, Stockholm, Sweden.
[2] Swedish Meteorological and Hydrological Institute, Göteborg, Sweden.

Abstract. Within the framework of rotating hydraulics, a method of establishing transport estimates for real bottom topographies is presented for flows of zero as well as finite (but constant) potential vorticity. The technique is applied to the deep-water flows through the Anegada-Jungfern Passage and the Denmark Strait.

Introduction

Theoretical estimates of the maximum flow rates through passages between neighbouring deep basins can be obtained in a convenient way by applying the theory of rotating hydraulics [Whitehead et al., 1974; Gill, 1977]. For a number of straits in the world ocean, however, the idealized rectangular or parabolic bottom profiles commonly used in the calculations, cf. Whitehead [1998] and Borenäs and Lundberg [1986], do not represent the bottom topography sufficiently well.

A solution method incorporating the real bathymetry has consequently been developed and applied in the modeling of the deep-water overflow through two contractions with somewhat complicated bottom topographies; the Jungfern Passage in the Caribbean Sea and the Denmark Strait in the northern North Atlantic.

Theoretical considerations

The analysis is based on the formulation of Gill [1977] for a rotating channel, with the overflow taken to be an inviscid fluid layer of uniform density ρ, flowing beneath a passive upper layer of density $\rho - \Delta\rho$. The cross-sectional topography of the strait, $T(x)$, is shown in Figure 1, as well as the position of the interface $\eta(x)$.

For topographies which vary slowly in the along-channel direction, the downstream velocity v may be regarded as geostrophically balanced:

$$v = \frac{g'}{f}\frac{\partial\eta}{\partial x}, \tag{1}$$

where $g' = \frac{\Delta\rho}{\rho} \cdot g$ is the reduced gravity, and f is the Coriolis parameter.

The potential vorticity (PV) of the flow is conserved along streamlines, and for the important case of uniform PV the flow is characterized by D_∞, the upstream depth where the

relative vorticity is zero:

$$PV = \frac{f + \frac{\partial v}{\partial x}}{D} = \frac{dB}{d\psi} = \frac{f}{D_\infty}. \tag{2}$$

Here $D(x) = \eta(x) - T(x)$ is the depth of the lower layer and ψ the transport streamfunction. The Bernoulli function $B(\psi)$ becomes:

$$B(\psi) = \frac{v^2}{2} + g'\eta = \frac{f(\psi - \psi_i)}{D_\infty} + g'\eta_\infty, \tag{3}$$

where ψ_i specifies the flow distribution between the two boundary layers in the upstream reservoir, and η_∞ denotes the upstream interface height above the threshold level. Using (1) and (2), a governing equation for $\eta(x)$ is obtained:

$$\frac{\partial^2\eta}{\partial x^2} - \frac{1}{\lambda^2}\eta + \frac{1}{\lambda^2}[D_\infty + T(x)] = 0, \tag{4}$$

where $\lambda = (g'D_\infty)^{1/2}/f$ is the Rossby radius of deformation.

For the case of zero PV ($D_\infty \to \infty$, i.e. $dB/d\psi = 0$) the analysis becomes more straightforward since the terms involving D_∞ in equations (2) and (3) vanish. Direct integration of a simplified version of the governing equation yields a second-degree polynomial depending on the prescribed topography $T(x)$ and the intersection points a and b. Once η_∞ has been specified, the Bernoulli equation (3) provides a relationship between a and b, and the cross-channel distribution of $\eta(x)$ may be obtained. For all possible interface solutions the volume flux Q can hereafter be calculated as a function of the left-most intersection point a. The maximum value of Q yields an estimate of the flow capacity of the passage.

The case of finite PV is computationally more demanding, since hydraulically consistent solutions must be determined from a numerical integration of the governing equation (4). To obtain the initial values for this procedure we start with prescribed Q-values, which in turn are linked to the streamfunction by equation (3). (When the total transport is assumed to take place as a boundary-layer flow on the
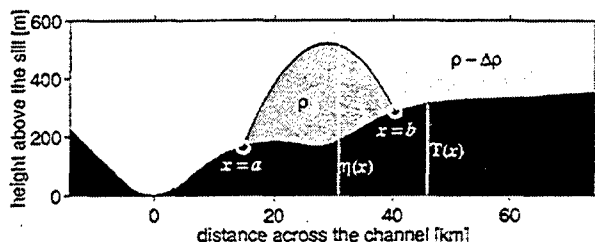
Figure 1. Definitional sketch of the analytical variables as defined in a coordinate system with its origin at the deepest point on the sill. Circles mark the points a and b where the interface $\eta(x)$ coincides with the bottom $T(x)$. (Shown here is the bathymetry of the Denmark Strait sill, looking in the downstream direction).

left bank of the upstream reservoir, $\psi_i = Q/2$. Consistent solutions are found from the criterion that the total transport must be Q at $x = b$, viz. $\psi(b) = Q/2$.) The integration is repeated in an iterative fashion until a unique solution, yielding the maximum volume flux estimate, is obtained.

Wide straits

For passages wider than the Rossby radius of deformation, the solutions comprise flow reversals on the right-hand side of the channel (when looking downstream). The cause of these negative-velocity regions is most readily understood by examining the zero-PV case, for which the calculated interface has a fixed parabolic shape with a maximum height occuring somewhere within the channel, cf. Figure (1).

In the theoretical work by *Killworth* [1994] it was demonstrated that the zone of reversed flow can be replaced by an area of stagnant water extending from the point of maximum interface height (where $\partial\eta/\partial x = 0$, and consequently $v = 0$) to the right-hand boundary of the passage. As will be recognized in what follows, this procedure implies an increase of the calculated flux.

Some applications

As examples of applications of the solution technique for real bottom topographies, two straits connecting the North Atlantic to marginal basins have been considered.

In both cases hydrographic along-channel transects reveal a pronounced dip of the isopycnals at the sill, i.e. a typical feature of topographically controlled flows. It thus appears likely that hydraulic theory may be applied in order to quantify the maximum deep-water volume flux through these straits.

The Anegada-Jungfern Passage

Situated south-east of Puerto Rico, the Jungfern Passage links the Caribbean Sea to the North Atlantic by the overflow of North Atlantic Deep Water. Based on the hydrographic

observations reported by *Frantantoni et al.* [1997] the solution method for zero potential vorticity, as described above, was applied.

A number of the solutions obtained for an upstream interface level of 165 m (representing the 4°C isotherm) are shown in Figure 2. Here the interface configuration A represents a flow that spans the entire passage, in contrast to the flows for C and D, which are found in the subchannels. The B-solution is a special example of a formally possible, but unphysical, solution with disconnected end-points.

The maximum transport of $0.8 \cdot 10^5$ m³/s for $\eta_\infty = 165$ m was found for solution A as shown in Figure 3. However, the interface associated with this solution indicates a narrow zone of reversed flow on the right-hand side of the passage, see Figure 2. By considering only the positive flux the maximum flow rate increases to $0.85 \cdot 10^5$ m³/s. This minor difference in transport reflects the fact that the passage is slightly broader than the Rossby radius of deformation. The calculated values of the deep-water flow agree very well with estimates based on hydrography and current meter data, cf. *Borenäs and Nikolopoulos* [2000].

The Denmark Strait

Located between Greenland and Iceland, the Denmark Strait constitutes one of the main paths of the cold outflow from the Northern marginal seas into the Atlantic Ocean. The analysis is based on hydrographic data from a field survey in August-September 1997 conducted by the Finnish R/V Aranda. The calculations of the volume flux were made for zero as well as finite potential vorticity and for two overflow situations; an overflow composed of only deep-water ($\eta_\infty = 370$ m), and an overflow also incorporating intermediate water masses ($\eta_\infty = 520$ m).

The sill cross-section is around 60 km wide, viz. considerably larger than the Rossby radius of deformation for the upstream heights discussed here. The calculated solutions are hence found to comprise regions of reversed flow, why the procedure suggested in section 3 is applied. Figure 4a shows the estimated transport for all a-points in the zero-PV case, for which the maximum unidirectional volume flux Q_{max} is found to be 1.83 Sv for $\eta_\infty = 370$ m and 4.47

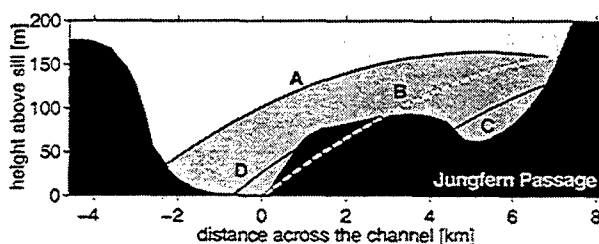**Figure 2.** Examples showing different configurations of the interface across the Jungfern Passage, when $\eta_\infty = 165$ m. (The dashed formal solution B crosses the topography and is thus unrealizable.)
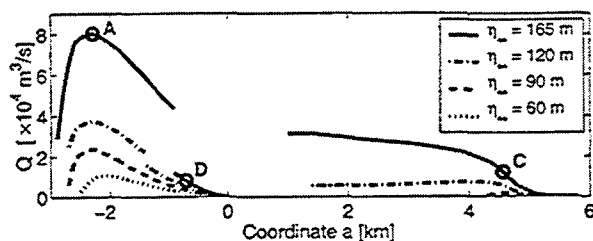
Figure 3. The flow rate through the Jungfern Passage as a function of a for various interface heights (η_{∞}=165 m represents the transport of water below the 4°C isotherm). Circles indicate the transport values associated with solutions A, C and D in Figure 2.
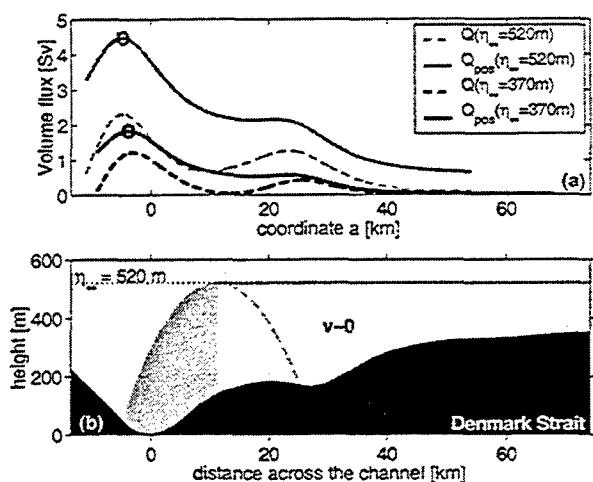

Figure 4. (a) The calculated net and positive flow rates for the Denmark Strait as a function of a for both flow situations (PV=0 and circles indicate Q_{max}). (b) The solution associated with the maximum flux Q_{max} when η_{∞}= 520 m, and the region of reversed flow is replaced by passive fluid.

Sv when η_{∞} = 520 m (1 Sv= 10^6 m^3/s). The lower panel (Figure 4b) shows the interface configuration associated with Q_{max} when η_{∞} = 520 m.

The solutions calculated for a non-zero PV are reminiscent of those obtained for zero PV, but the estimated (uni-directional) flow rate is decreased slightly to 1.79 and 4.35 Sv for η_{∞} = 370 m and η_{∞} = 520 m, respectively. For the Denmark Strait no direct comparison with transport estimates, based on hydrography and current meter data, could be undertaken, but the calculated flow rates are in the range of those cited in literature.

Discussion

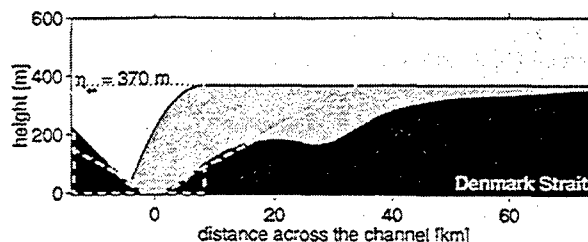In a review by *Whitehead* [1998] it was concluded that the ratio between the theoretically calculated transports (using

Figure 5. The zero-PV overflow associated with Q_{max} for η_{∞}= 370 m, in relation to three idealized bottom geometries (rectangular, triangular and parabolic).

a rectangular cross section) and those observed was in the range of 1.3-2.7. By using real topography the theoretical values are reduced and should, hence, conform better to observations. This feature is especially evident for the Jungfern Passage, with its rather complicated bathymetry. The use of a rectangular cross-section in the theoretical calculation would have overestimated the transport by more than 50%.

Figure 5 shows the Denmark Strait overflow in relation to the idealized topographies considered by *Whitehead* [1989] and *Killworth* [1994]. For this passage, with the complicating topographical features located outside of the flowing region, the parabolic cross-section adheres best to the sill geometry, and yields transport estimates most similar to those obtained for the real topography. If a mathematically straightforward procedure for estimating the flow rate is desired, the parabolic cross-section is thus proposed as the better approximation to the true one.

Killworth [1994] showed that for an arbitrary but "simple" bottom topography (with no multiple mimima) the zero-PV flow yields the largest possible transport. This result is not immediately applicable for the Jungfern Passage, since the bottom topography here does not obey the criterion of being simple. For the Denmark Strait, however, it was shown that the zero-PV solutions did give the largest transports. The difference between these values and those obtained for a constant PV flow were modest, though. The reason is that the ratio of the sill height to the upstream depth is large enough for the zero PV solution to be a very close approximation to the constant PV case.

References

Borenäs, K., and P. Lundberg, Rotating hydraulics of flow in a parabolic channel, *J. Fluid Mech.*, *167*, 309–326, 1986.

Borenäs, K., and A. Nikolopoulos, Theoretical calculations based on real topography of the maximal deep-water flow through the Jungfern Passage, *J. Mar. Res.*, *58*, 709–719, 2000.

Frantantoni, D. M., R. J. Zantopp, W. E. Johns, and J. L. Miller, Updated bathymetry of the Anegada-Jungfern

Passage complex and implications for Atlantic inflow to the abyssal Caribbean sea, *J. Mar. Res.*, *55*, 847–860, 1997.

Gill, A. E., The hydraulics of rotating-channel flow, *J. Fluid Mech.*, *80*, 641–671, 1977.

Killworth, P. D., On reduced-gravity flows through sills, *Geophys. Astrophys. Fluid Dynamics*, *75*, 91–106, 1994.

Whitehead, J. A., Internal hydraulic control in rotating fluids - Applications to oceans, *Geophys. Astrophys. Fluid Dyn.*, *48*, 169–192, 1989.

Whitehead, J. A., Topographic control of oceanic flows in deep passages and straits. *Rev. Geophys.*, *36*, 423–440, 1998.

Whitehead, J. A., A. Leetmaa, and R. Knox, Rotating hydraulics of strait and sill flows, *Geophys. Fluid Dyn.*, *6*, 101–125, 1974.

Anna Nikolopoulos (corresponding author), Department of Meteorology/Physical Oceanography, Stockholm University, SE-106 91 Stockholm, Sweden.
(E-mail: anni@misu.su.se)

Karin Borenäs, SMHI, Nya Varvet 31, SE-426 71 Västra Frölunda, Sweden.

The current system of the Bosphorus Strait based on recent measurements

Emin Özsoy, Mohammed A. Latif and Şükrü Beşiktepe

Institute of Marine Sciences, Middle East Technical University, Erdemli - İçel 33731 Turkey

Abstract. A series of measurements in the Bosphorus Strait using ADCP and CTD profiling, current-meter and sea-level recordings are analysed to yield three-dimensional mapping of hydrography and currents as well as the statistical characteristics of sea-level and current variability. The results show time-dependent meandering of currents, with separated eddies formed in sheltered areas along the coast. Spatial correlation along the Strait reflects these changes. Sea-level differences respond rapidly to changes in flows, and sudden change in wind direction leads to blocking conditions.

Introduction

The Bosphorus is a passageway of heavy marine traffic between the two seas, as well as of land traffic between the two continents that it connects. Information on the nature of the currents in the Bosphorus is thus essential for safe navigation and transit through the Strait. Furthermore, the Turkish Straits System (consisting of the Dardanelles, Bosphorus Straits and the Sea of Marmara) is sensitive to climatic changes, and potentially can induce such changes in the adjacent basins [*Özsoy*, 1999]. Acting as the limiting element of the The Turkish Straits System, the Bosphorus Strait controls the exchanges of mass and passive or active materials
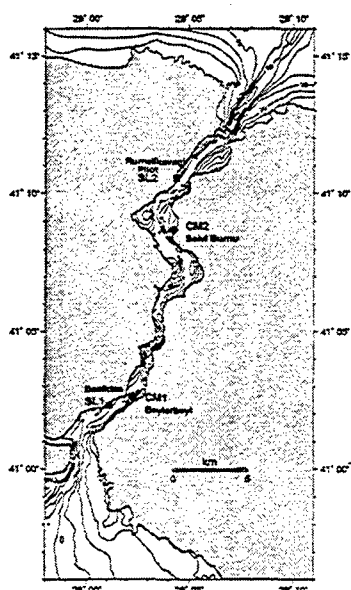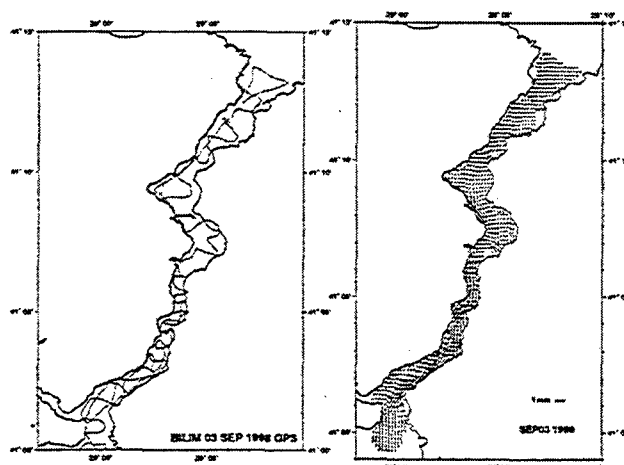

Figure 2. (a) GPS positions of the ship collecting data along the Bosphorus, and (b) interpolated surface currents from continuous ADCP measurements, on 03 September 1998.

transported between the Black and the Mediterranean Seas [*Özsoy et al.*, 1995b; *Polat and Tuğrul*, 1995; *Ünlüata et al.*, 1990].

Based on budgets calculated from average salinity the mass flux of the upper layer flow is about two times larger than that of the lower layer, yielding a net flux of about $300 km^3/yr$ from the Black Sea to the Sea of Marmara [*Latif et al.*, 1991; *Ünlüata et al.*, 1990]. Geometrical features [*Oğuz et al.*, 1990; *Ünlüata et al.*, 1990; *Özsoy et al.*, 1998] make the Bosphorus predisposed to 'maximal exchange', with contraction and sill controls as in *Farmer and Armi* [1986]. Local topographic features have significant influence on the flow, and determine its detailed structure [*Gregg and Özsoy*, 2001]. The exchange flows respond dynam-

Figure 1. Bottom topography of the Bosphorus, and the locations of sea level (SL1, SL2) and current-meter (CM1, CM2) stations.
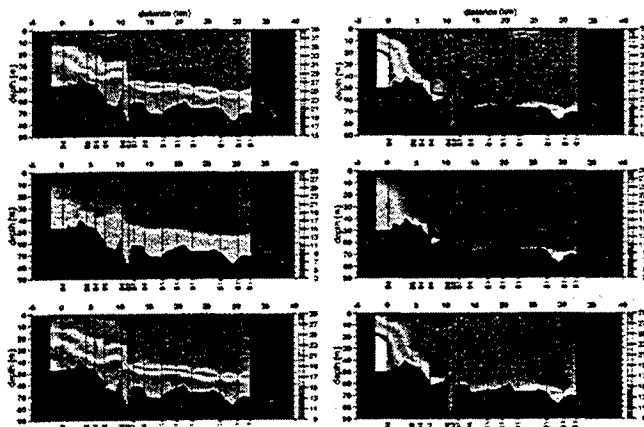
Figure 3. Salinity, temperature, and density cross sections obtained from CTD measurements along the Bosphorus on (a) 15 March 1999 and (b) 18 March 1999.

Figure 4. Interpolated speed of surface currents from continuous ADCP measurements on (a) March 16, 1999, (b) March 18, 1999.

ically to time-dependent meteorological and hydrological forcing in the adjacent basins [*Latif et al.*, 1991; *Özsoy et al.*, 1995a, 1996, 1998; *Özsoy and Ünlüata*, 1997, 1998; *Gregg et al.*, 1999; *Gregg and Özsoy*, 2001]. Observations suggest increased entrainment south of the contraction (upward) and past the northern sill (downward) in the Black Sea [*Gregg et al.*, 1999; *Özsoy et al.*, 2001].

The measurements and data processing

In the present study we have made detailed measurements to observe the fine scale variability in the Bosphorus currents and to determine their time and length scales. The intensive experiments carried out in the Bosphorus Strait included ADCP and CTD data collection during 3-6 September 1998, 4-22 March 1999 and 22 July-3 August 1999. The data were collected simultaneously by two ships (the R/V BİLİM of the IMS-METU, and ATMACA II, a commercial vessel) along repeated criss-cross patterns across the Strait attempting to sample the detailed structure of currents in the main channel and in the various bends and small embayments that line its coasts. A Seabird 911plus CTD profiler and a 150Khz RDI narrow-band ADCP were used on board the BİLİM while a Seabird 25 Sealogger CTD and a 300KHz RDI Workhorse Sentinel broad-band ADCP were used on ATMACA II. Accurate position fixes were obtained using Trimble NT200 GPS and Ensign XL GPS navigation systems on the two ships. In addition, sea level and current-meter measurements were performed respectively at stations near the two ends of the Strait Figure 2, where Aanderaa Instruments water level recorder WLR7 and Aanderaa recording current meter RCM7 were deployed. The current and sea level time series data were recorded at 5 min. interval. Absolute sea level at each station was determined relative to a common datum using leveling to benchmarks.

One of the greatest problems was in processing the navigation data to obtain position fixes and ground referenced
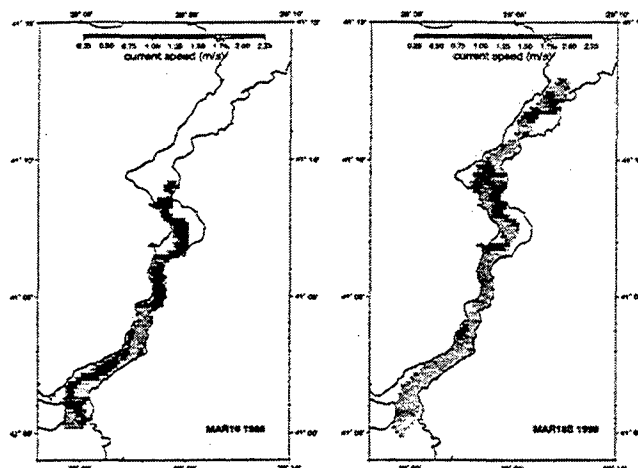
velocity from the GPS and ADCP measurements. Noise in GPS data and magnetic deviations caused by the ship's steel hull were first removed by applying despiking filters, correlation techniques and a number of logical tests for ship speed and position. Independent measurements of bottom track and GPS velocity were used together in these corrections.

The ADCP measurements obtained by the broadband ADCP on board ATMACA II covered the Bosphorus in great detail, including the numerous small embayments on its banks, making use of the manaeouverability of the smaller vessel. The current velocity data from the broad-band ADCP started from a depth of 3m. For interpretation of surface currents, the ADCP data were first averaged in the 0-10m depth range, then intepolated on a 0.15° latitude-longitude grid.

The current-meter and sea level measurements were interpreted based on standard time-series analyses, applying correlation and spectral methods. The current velocity data were rotated to maximize along-channnel variance.

Results

Surface currents obtained along the ship track in Figure 2a are shown in Figure 2b. In the numerous realizations as shown in this example, the larger currents followed the main channel of the Bosphorus and affected by its topography (Figure 1). The surface currents intensified in the narrows in southern Bosphorus, and first followed the deep channel on the eastern side, then crossed to the western side following the main channel, forming a jet near the exit to the Sea of Marmara. Temporal changes as well as turbulent meandering accounted for day to day changes in the horizontal structure of the main current. There were numerous eddies and reversals in the currents consistently observed in
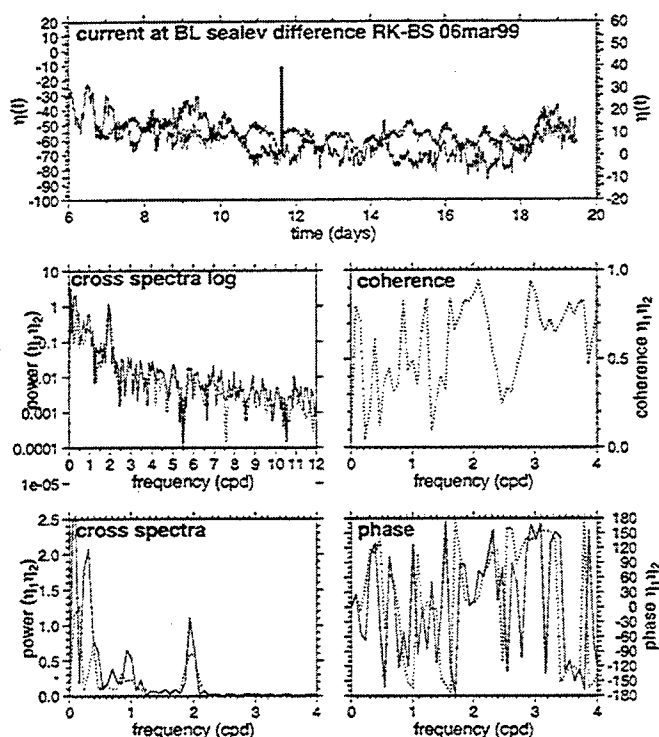
the various shallow banks and embayments.

During March 1999 measurements the winds were generally calm, from the south, when the Bosphorus had its typical two-layer stratiified flow structure shown in Figure 3a. On 18th of March the wind suddenly changed direction and increased in intensity, blowing at full force from the north. The upper layer flow increased and the lower layer flow was then blocked and pushed south of the contraction as shown in Figure 3b, leaving only a small trace of Mediterranean water near the bottom in the upper reaches of the Bosphorus. The magnitude of surface currents on March 16 and 18 respectively are shown in Figures 4a and b to illustrate the great increase in current velocity accompanying the flushing of the Mediterranean water from the Bosphorus following the northerly wind event.The greatest increase in surface currents occurs in the contraction region and in the southern Bosphorus.

Correlation between current components along the Strait and those perpendicular to it were computed (not shown) as a function of distance between pairs of data points to reveal structure relationships of currents. The results indicated lengthwise correlations on distances comparable to the length of the Strait, as expected for the conduit type of flow. There were also correlations at scales characteristic of the coastal features and bends of the Bosphorus channel.

The sea level and current measurements as well as temperature recorded at current-meter sites were individually analysed (not shown), computing correlations and spectra. The current velocity obtained from current-meters indicated reversals in direction, resulting from sheltering effects in the coastal region. The analyses revealed oscillations at diurnal (24h), inertial (18.3h) and semidiurnal (12h) periods, as well as those at periods longer than 2 days.

The time-series of currents at current-meter site CM1 and the sea level difference between stations SL2 and SL1 for the period starting on 06 March 1999 are shown in Figure 5, together with the cross-spectral estimates, coherence and pahse between the two time series. Correlated peaks occur at diurnal, semi-diurnal periods with high coherence. The phase differences indicate the sea level difference is totally out of phase (or has negative correlation) with the northeastward currents at the diurnal and longer than 2d periods; i.e. the sea level difference is positively correlated with southwestward currents. At semi-diurnal periods the phase difference is about $90°$, which is typical for tidal currents.

Figure 5. Time series displays and cross spectra between currents at Beylerbeyi (CM1/BL) and the along-Strait sea level difference between Rumeli Kavağı (SL2/RK) and Beşiktaş (SL1/BS) stations. Dotted lines represent spectral smoothing with a triple point moving average filter.

Conclusions

The Bosphorus currents have fine features that depend on the topography and coastal features on its banks, revealing eddies and revesring currents in various of its embayments, as well as turbulent meandering of the main current. Transience on various time scales in addition to the spatial features make the Bosphorus currents highly variable. Yet the main features of the current system are familiar. Blocking events can flush the Strait almost completely pushing either

the lower or the upper layer back to its origin in the adjacent Seas. The Bosphorus currents have a rapid response to sea level differences between the Black Sea and the Mediterranean.

Acknowledgments. This study has been made possible through a project carried out for the İstanbul Technical University Foundation / Defense Research Center. The authors wish to express their gratitude to the cooperative efforts of the scientists, technicians and graduate students of the IMS-METU who took part in the data collection and processing, and the captains and crew of the ships who were involved in various stages of the work.

References

Farmer, D. M. and Armi, L., 1986. Maximal two-layer exchange over a sill and through the combination of a sill and contraction with barotropic flow, *J. Fluid Mech.*, **164**, 53-76.

Gregg, M. C., Özsoy, E. and Latif, M. A., 1999. Quasi-steady exchange flow in the Bosphorus *Geophysical Research Letters*, **26**, 83-86.

Gregg M. C. and Özsoy, E., 1999. Mixing on the Black Sea shelf north of the Bosphorus *Geophysical Research Letters* **26**, 1869-1872.

Gregg, M. C. and Özsoy, E., 2001. Flow, water mass changes, and hydraulics in the Bosphorus, *J. Geophys. Res.*, (in press).

Latif, M. A., Özsoy, E., Oğuz, T. and Ünlüata, Ü., 1991. Observations of the Mediterranean inflow into the Black Sea, *Deep Sea Research*, **38**, Suppl. 2, S711-S723.

Oğuz, T., Özsoy, E., Latif, M. A. and Ünlüata, Ü., 1990. Modelling of hydraulically controlled exchange flow in the Bosphorus Strait, *J. Phys. Oceanogr.*, **20**, 945-965.

Özsoy, E., Latif, M. A., Tuğrul, S., and Ünlüata, Ü., 1995a. Exchanges with the Mediterranean, fluxes and boundary mixing processes in the Black Sea, In: F. Briand (editor), *Mediterranean Tributary Seas, Bulletin de l'Institut Océanographique, Monaco*, Special Number 15, CIESM Science Series No. 1, Monaco p. 1-25.

Özsoy, E., Latif, M. A., Beşiktepe, Ş. and Gaines, A. F., 1995b. Fluorescent dye measurements of the mixing and transport of wastewater discharge in the Bosphorus, *Wat. Sci. Tech.*, **32**(2), 61-68.

Özsoy, E., Latif, M. A., Sur, H. İ. and Goryachkin, Y., 1996. A review of the exchange flow regimes and mixing in the Bosphorus Strait, in: Briand, F. (editor), Mediterranean Tributary Seas, *Bulletin de l'Institut Océanographique, Monaco*, Special Number 17, CIESM Science Series No. 2, Monaco.

Özsoy, E. and Ünlüata, Ü., 1997. Oceanography of the Black Sea: a review of some recent results, *Earth Science Reviews*, **42**, 231-272.

Özsoy, E. and Ünlüata, Ü., 1998. The Black Sea, in: Robinson, A. R. and Brink, K. (editors), *The Sea: The Global Coastal Ocean: Regional Studies and Syntheses*, **11**, John Wiley and Sons, New York, pp. 889-914.

Özsoy, E., Latif, M. A., Beşiktepe, Ş., Çetin, N., Gregg, N. Belokopytov, V., Goryachkin, Y. and Diaconu, V., 1998a. The Bosphorus Strait: exchange fluxes, currents and sea-level changes, in: Ivanov, L. I. and Oğuz, T. (editors), *Ecosystem Modeling as a Management Tool for the Black Sea*, NATO Science Series 2: Environmental Security **47**, Kluwer Academic Publishers, Dordrecht, vol. 1, 367pp + vol. 2, 385 pp.

Özsoy, E., 1999. Sensitivity to Global Change in temperate Euro-Asian seas (the Mediterranean, Black Sea and Caspian Sea): A review, in P. Malanotte-Rizzoli and V. N. Eremeev (editors), *The Eastern Mediterranean as a Laboratory Basin for the Assessment of Contrasting Ecosystems*, NATO Science Series 2, Environmental Security, **51**, Kluwer Academic Publishers, Dordrecht, pp. 281-300.

Özsoy E., Di Iorio D., Gregg M. and Backhaus J. 2001. Mixing in the Bosphorus Strait and the Black Sea Continental Shelf: Observations and a Model of the Dense Water Outflow, *J.Mar. Sys.*, *31*, 99-135.

Ünlüata, Ü., Oğuz, T., Latif, M. A., and Özsoy, E., 1990. On the physical oceanography of the Turkish Straits, in: Pratt, L. J., (editor), *The Physical Oceanography of Sea Straits*, NATO/ASI Series, Kluwer, Dordrecht, 25-60.

Polat, Ç. and S. Tuğrul, 1995. Nutrient and organic carbon exchanges between the Black and Marmara Seas through the Bosphorus Strait. *Cont. Shelf Res.*, *15*, 1115-1132.

E. Özsoy, M. A. Latif and Ş. Beşiktepe, Institute of Marine Sciences, Middle East Technical University P.K. 28 Erdemli - İçel 33731 Turkey

Stratified shear flow in sea straits of arbitrary cross section

Larry Pratt, Chris Jones*, Jian Deng* and Lou Howard**

Woods Hole Oceanographic Institution, Woods Hole, Massachusetts, USA
*Dept. of Mathematics, Brown University, Providence , Rhode Island, USA
**Dept. of Mathematics, The Florida State University, Tallahassee, Florida, USA

Abstract. A theory for transversely uniform, stratified shear flow in a channel of arbitrary cross section is presented. The presence of nonrectangular topography introduces a new physical mechanism, namely vortex stretching and squashing of *horizontal* columns due to contact with the side walls. Long's model allowing the calculation of nonlinear regimes of steady flow for certain classes of upstream conditions can be generalized. Also, the propagation of linear, long-wave disturbances is governed by an extended form of the Taylor-Goldstein equation. Classical theorems on stability, phase speed bounds, and the enumeration of eigenvalues can be extended. The bounds on the phase speeds of neutral modes is an important aid in the hydraulic interpretation of data. We give several examples of application to the Bab al Mandab.

Introduction

Two-layer models are typically used to asses the hydraulic state of an exchange flows such as those of the Bosphorus and the Strait of Gibraltar (Farmer and Armi, 1987). In some cases, a two-layer formalism may fail to capture certain physical processes (critical layers) or may not satisfactorily resolve the flow. In the case of the Bab al Mandab sill flow (Murray and Johns, 1997; Pratt, et al. 1999, 2000) for example, the velocity and stratification vary smoothly over the from top to bottom and there is a certain amount of ambiguity in fitting a two-layer model to the flow. For these reasons, it may be better to try to assess the hydraulic state of the flow (supercritical, subcritical, or critical) by calculating the speeds of the long internal gravity waves based on the continuously varying density and velocity. To do so, one must solve an eigenvalue problem based on the Taylor-Goldstein equation with homogeneous upper and lower boundary conditions.

A further complication is the nonuniform nature of the cross-sections of all geophysically relevant straits. In the Bab al Mandab, for example, the deep outflow from the Red Sea is confined to a narrow central trough that runs the length of the strait, whereas the shallow inflow is spread out over a much larger width (Murray and Johns, 1997). In an attempt capture some of the rudimentary physics that such topographic variations might introduce, we have developed a theory for a stratified shear flow in a channel of non-rectangular cross section. (The original Taylor-Goldstein formulation requires strictly 2D flow with a rectangular cross section.) The main simplification of our theory is that the stratification and along channel velocity component remain independent of the cross-channel coordinate (y). Such flows can be shown to be dynamically consistent in the long wave limit; that is, when the along channel scale of motion is large compared with both the depth and width of the strait. Although this limit appears quite restrictive, long wave motions are exactly the one of interest in hydraulic theory. It should also be mentioned that dynamical consistency can be shown in the limit of gradual variations in the vertical direction, a case irrelevant to sea straits but of possible interest in engineering applications. In the following development the nonhydrostatic terms (those involving k^2) will be carried along, but their inclusion is only consistent in the second limit. For sea strait applications, k should be set to zero.

Vorticity dynamics

Consider a strait of arbitrary cross section, aligned in the x-direction, and having a width b that varies with x and with the vertical coordinate z. For y-independent density and u, the vorticity balance is given by

$$\frac{d}{dt}\left(\frac{\varsigma}{b}\right) = \frac{\mathbf{j} \cdot \nabla p \times \nabla \rho}{\rho^2 b} \tag{1}$$

where $\varsigma = \dfrac{\partial w}{\partial x} - \dfrac{\partial u}{\partial z}$ is the vorticity of a horizontal fluid column and the other notation is standard. This vorticity can clearly change only by stretching or squashing (the term involving b) or through baroclinicity.

Steady flows

Steady flows are governed by the conservation of the Bernoulli function

$$\rho \frac{u^2 + w^2}{2} + p + \rho g z = B(\psi)$$

and by (1). These relations can be combined and the result cast in terms of a new variable $\delta(x, z) = z - z_o(x, z)$, the elevation of a particular streamline above its elevation z_o at some upstream section. If the flow at the upstream section is parallel and the quantity $q(z_o) = \frac{1}{2}\rho(z_o)U^2(z_o)b_o^2(z_o)$ is constant then it can be shown that δ satisfies

$$\frac{\nabla \cdot [b^{-1}\nabla(\delta - z)]}{b} + \kappa^2(z_o)\delta = 0$$

where $N^2(z_o) = -g\rho(z_o)^{-1}d\rho/dz_o$ and

$$\kappa^2 = \frac{N^2(z_o)}{b_o^2(z_o)U^2(z_o)} = -\frac{g}{2q}\frac{\partial \rho}{\partial z_o}. \tag{2}$$

The boundary conditions are $\delta = 0$ at the rigid top $z = D$ and $\delta = h(x)$ at $z = h$, where h denotes the elevation of the deepest point in the channel. If κ itself is constant then (2) is linear and can be solved by elementary methods (e.g. Miles, 1968). This has not been pursued further, but any conference attendee is welcome to do so! Long's original model (Long, 1953) is obtained by setting b=const.

Linear wave propagation: The extended Taylor-Goldstein equation

If the vorticity equation (1) is linearized about a basic parallel state with velocity $U_o(z)$ and buoyancy frequency $N_o(z)$, and the Boussinesq approximation is applied the result can be written

$$(U_o - c)\frac{\partial}{\partial x}\left(\frac{\tilde{\varsigma}}{b}\right) + w\left[\frac{N_o^2(z)}{b(z)U_o(z)} - \left(\frac{U_o'(z)}{b(z)}\right)'\right] = 0 \tag{3}$$

where $\tilde{\varsigma}$ is the perturbation vorticity. In addition, the continuity equation

$$\frac{\partial(b\bar{u})}{\partial x} + \frac{\partial(bw)}{\partial z} = 0$$

can be written in the form

$$\frac{\partial \bar{u}}{\partial x} + \frac{\partial w}{\partial z} + T(z)w = 0 \tag{4}$$

where

$$T(z) = \frac{b'(z)}{b(z)}.$$

Eliminating the along-channel perturbation velocity $\tilde{u}$ between (3) and (4) yields a single equation for the vertical velocity w. With disturbances of the form $w = \text{Re}\left[W(z)e^{ik(x-ct)}\right]$, the vertical structure function is governed by the following relation:

$$W'' + \left[\frac{N^2}{(U_o - c)^2} - \frac{U_o''}{(U_o - c)} - k^2\right]W + \frac{1}{(U_o - c)}\left[T(U_o - c)W\right]' = 0 \tag{5}$$

subject to

$$W(0) = W(D) = 0.$$

Equation (5) is an extended form of the Taylor-Goldstein equation. The original is recovered if the channel cross section is rectangular ($T(z)$=0). All of the information concerning the topography is contained in the function $T(z)$. An implicit assumption is that the channel bottom has a single minimum in elevation; that is, the channel does not have multiple branches. Some idealized shapes include the triangle ($T(z)$=1/z) and the trapezoid ($T(z)$~1/(α+z)). For rounded cross-sections, the channel width b smoothly approaches a minimum at z=0 and thus $b \sim z^m$, $0 < m < 1$ in the vicinity. Normally m=1/2. In all such cases $T(z) \sim m/z$ near z=0.

Stability

The application of traditional hydraulic principles in the presence of instability is not completely

understood, at least not by us. Nevertheless, it is important to know something about the conditions under which instability can occur. The necessary condition for instability of a 2D stratified shear flow (Miles, 1961 and Howard, 1961) is that the Richardson number fall below 1/4 somewhere in the water column:

$$R_i(z) = \frac{N_o^2(z)}{(U_o'(z))^2} < 1/4$$

for some z.

It can be shown that this condition continues to hold for arbitrary $T(z)$. Although proof can be made along the same lines as the argument used by Howard (1961), we did not originally recognize this. This ignorance led us to develop an alternative proof, one which may suggest an alternative way of proving results about stability.

Let $\phi = (U_o - c)^{-1/2}W$, in terms of which (5) becomes.

$$\left[(U_o - c)\phi'\right]$$
$$-\left[\tfrac{1}{2}U_o'' + k^2(U_o - c) + \frac{\tfrac{1}{4}(U_o')^2 - N^2}{(U_o - c)}\right]\phi$$
$$+\left[(U_o - c)T\phi\right] + \tfrac{1}{2}T\phi U_o' = 0$$

Next, let $\kappa = \dfrac{\phi}{(U - c)(\phi' + T\phi)}$ and assume that the flow is unstable, so that c (and κ) is complex. It can be shown that κ is governed by a Riccati equation:

$$\kappa' = \frac{1}{U_o - c} - T\kappa$$
$$-\left[\tfrac{1}{2}U_o'' + k^2(U_o - c) + \frac{\tfrac{1}{4}(U_o')^2 - N^2}{(U_o - c)} - \tfrac{1}{2}TU_o'\right]\kappa^2$$

with $\kappa(0) = \kappa(D) = 0$.

Since κ satisfies the same homogeneous boundary conditions that W does, a solution must execute a trajectory in the complex κ-plane that begins and ends at the origin. However, evaluation of the imaginary part of the Riccati equation along the real κ axis yields

$$\kappa_i' = c_i\left[k^2\kappa_r^2 + \frac{1 + [N^2 - \tfrac{1}{4}(U_o')^2]\kappa_r^2}{|U_o - c|^2}\right] \quad (\kappa_i = 0)$$

and thus the derivative of κ_i with respect to z is positive if the flow is unstable $c_i > 0$ and if the Richardson number is everywhere $\geq 1/4$. However,

under these conditions a solution trajectory must always cross the real κ axis from the lower to upper half plane and therefore can never begin *and* end at the origin, as required. Thus the flow must be stable if the Richardson number is $\geq 1/4$ for all z.

It can also be shown that the semicircle theorem (Howard, 1961) remains valid regardless of the shape of the cross-section.

It was somewhat surprising to discover that topography does not alter the necessary condition for instability. However, it can be shown that $T(z)$ does explicitly enter in the necessary conditions when stratification is absent. For example the Rayleigh inflection point theorem can be extended, now requiring that $(U_o'/b)'$ change signs for instability to be possible. The Fjørtoft theorem can also be extended. However, it is difficult to develop an general rule regarding the stabilizing or destabilizing effect of topography. Some velocity profiles seem to be destabilized, others stabilized.

Neutral modes and eigenvalues

When $(R_i)_{min} > 1/4$, it is possible to prove that an infinite number of discrete vertical modes occur, that the nth mode has n-1 zero crossings in $W(z)$, and that associated with each mode are two waves whose phase speeds are bounded as follows:

$$U_{min} - \frac{N_{max}D}{(\pi^2 + \tfrac{1}{4}T_{min}^2 D^2)^{1/2}}$$
$$\leq c_{-1} < c_{-2} < \cdots < U_{min} < U_{max} < \cdots c_2 < c_1 \quad (6)$$
$$\leq U_{max} + \frac{N_{max}D}{(\pi^2 + \tfrac{1}{4}T_{min}^2 D^2)^{1/2}}.$$

It can also be shown that $c_n \uparrow U_{min}$ as $n \to -\infty$ and $c_n \downarrow U_{max}$ as $n \to \infty$.

Equation (6) shows that a wave speed cannot lie in the range of the basic velocity. (Were this to occur, a critical level would exist.) The outer bounds suggest that propagation relative to the min and max of the basic velocity is diminished by the presence of topography. It can be shown that the outer bounds exactly give the speed of a wave propagating in a channel with constant T and a flow with constant N and U.

Discussion

The bounds (6) are extremely helpful in evaluating the hydraulic character of an observed flow. For

example, it can often be shown without direct calculation that the flow is supercritical or subcritical with respect to a certain mode or set of modes. Examples based on data from the sill region of the Bab al Mandab will be given in the poster presentation. However, an immediate implication is that an exchange flow ($U_{min}<0$ and $U_{max}>0$) with Richardson number $>1/4$ is subcritical with respect to all modes! People may want to stop by the poster and debate the implications of this result.

References

Farmer, D. M. and L. Armi, 1988. The flow of Atlantic water through the Strait of Gibraltar. *Progress in Oceanography.* **21**, Pergamon, 1-105.

Howard, L.N. 1961. Note on a paper of John Miles. *J. Fluid Mech.* **10**, 509-512.

Long, R. R. 1953. Some aspects of flow of stratified fluids. III. Continuous density gradients. *Tellus*, **1**, 341-357.

Miles, J. W. 1961. On the stability of heterogeneous shear flows. *J. Fluid Mech.* **10**, 495-508.

Miles, J. W. 1968. Lee waves in a stratified flow. Part 2. Semi-circular obstacle. *J. Fluid Mech.* **33**, 803-814.

Murray, S. P. and W. Johns 1997: Direct observations of seasonal exchange through the Bab al Mandab Strait. *Geophys. Res. Let.* **24**, 2557-2560.

Pratt, L.J., Johns. W. Johns, S. M. Murray and K. Katsumata 1999. Hydraulic Interpretation of Direct Velocity Measurements in the Bab al Mandab. *J. Phys. Oceanogr.* **29**, 2769-2784.

Pratt, L.J., H. E. Deese, S. P. Murray, and W. Johns 2000. Continuous Dynamical Modes in Straits having Arbitrary Cross Sections, with Applications to the Bab al Mandab. *J. Phys. Oceanogr. (accepted)*

Rotating exchange flows through straits with multiple channels: Preliminary results of laboratory studies

B. Rabe, and D.A. Smeed

Southampton Oceanography Centre, United Kingdom

Abstract. The basin exchange flow via a rotating strait with an island separating part of the strait into two channels is investigated. Significant cross-channel or even reverse flow can be expected and no solution may easily be found using existing theoretical approaches usually based on semi-geostrophic theory. Our laboratory experiments have so far confirmed previous findings that rotation reduces the exchange flux and increases across channel slope of the two-layer interface in constant depth channels. Furthermore, significant differences in those parameters to equivalent width channels with an island have been found. Other qualitative differences, such as an influence of the island on the evolution of the initial gravity current, have also been observed. Qualitative results and plans for future comprehensive quantification will be presented.

Introduction

Non-uniform bottom topography across a strait or channel connecting two large basins becomes important when rotation is introduced, or in other words, the Strait is wide relative to the internal Rossby deformation radius. Examples include the Sicily Channel, the Strait of Hormuz and the Cretan Arc Straits, where multiple deep channels are separated by ridges.

Flows around islands or complex topography have been studied in the context of homogeneous or continuously stratified, often atmospheric, fluids [e.g. *Boyer and Davies*, 2000; *Alessio et al.*, 1992] but not for exchange fluxes. Some work on single layer, rotating, zero potential vorticity flow through uniformly sloping channel cross-sections by *Shen* [1981] showed that semi-geostrophic theory for all cross-channel slopes agreed well with experimental results for non-separated flows; however, a stagnation region predicted in the separated case [c.f. *Borenas and Whitehead*, 1998] was observed to break down. Theory not bound to the semi-geostrophic assumption, includes the linear Rossby adjustment problem in a rotating finite width, constant depth channel by *Gill* [1976]; however, information about the steady state is limited. [*Killworth and McDonald*, 1993] developed a maximal flux bound for multi-layer reduced gravity flows in rotating channels of arbitrary topography with non-negative potential vorticity and agrees with *Whitehead et al.* [1974]'s single layer flux for a rectangular, zero potential vorticity and constant depth channel. It is applicable to the island problem but not likely to give additional insight. Although some rotating hydraulic theory for arbitrary topography exists [*Killworth*, 1995], no application to en-

vironmental flows has been made as an exact consideration of very complex topography would likely have an infinite amount of virtual controls, making a hydraulic model impractical. To my knowledge, no work has been published regarding the effect of an island on the exchange flow hydraulics through a rotating channel. Such flow will have an additional wall to lean on; in particular, regions near the ends of the island may introduce significant changes in the flow pattern not present in a flat bottom channel. Existing semi-geostrophic theory on rotating two-layer exchange flows, e.g. *Dalziel* [1990], thus cannot easily be applied as the assumption of small cross-channel velocities is violated. However, hydraulic control has been found to occur in many situations, even if specific hydraulic theory is not applicable [*Dalziel*, 1988; *Killworth*, 1995].

We investigate the simplified case of a horizontally contracting (narrows), constant depth, rotating Strait with a full-depth island in the centre (figures 1a and 1b). As a suitable non-dimensional parameter for our problem we define a Rossby number, $R_o = \frac{R}{W}$, based on the Rossby Radius of deformation, $R = \frac{\sqrt{g'H}}{f}$, where f is the Coriolis parameter, $g' = \frac{g\Delta\rho}{\bar{\rho}}$ is the reduced gravity, $\Delta\rho$ the initial density difference between both reservoirs, $\bar{\rho}$ the mean density, W the constricted channel width (subtracting island width) and H the total depth.

Experimental Setup and Scaling

A rotating table-mounted tank was divided into two reservoirs connected by a symmetrically contracting, constant depth channel with a movable island aligned along the channel in the centre. A barrier between the reservoirs, filled with
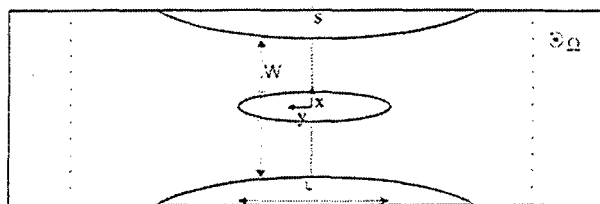
Figure 1a. Plan view of principal geometry and important hydraulic parameters. The coordinate origin is in the centre of the channel with y and x axes as shown. W is the minimum channel width, accounting and $\Omega = 0.5*f$ is the rotational vector. The dotted line denotes the ends of the channel bordering on the large reservoirs.
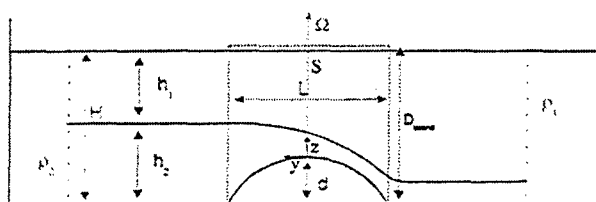

Figure 1b. Side view of figure 1a with coordinate axes as shown. $h_{1(2)}$ and $\rho_{1(2)}$ are the upper (lower) layer depth and density, respectively, and H the total water depth; d is the sill height (d=0 in our experiments to date) and D_{island} the island height; $\Omega = 0.5*f$ is the rotational vector.

different saline solutions, was removed for a time period sufficient to allow steady lock-exchange at near-initial reservoir conditions. We chose $g'' 9.81$ cm s^{-2} based on the our apparatus and previous experiments by *Dalziel* [1988]; *Munday* [2000].

Our flows are considered largely inviscid but laminar based on Reynolds number arguments [e.g. p 31 *Tritton*, 1988]. Close to the boundaries, however, viscosity still plays a role giving rise to rotating boundary layers: Ekman layers [e.g. p 228 *Tritton*, 1988] near the floor and interface and Stewartson shear layers near the walls. The former are negligibly small but Stewartson layers cause the interface to flatten near the sidewalls, especially at low rotation. This decreases the channel cross-section available to the exchange flow and increases R_o due to the reduced cross-section available for the exchange: $R_{oeff} = R_o \frac{W}{W - n_S \delta_S}$, where δ_S is the thickness of a single Stewartson Layer, proportional to the Ekman number [p 217 *Tritton*, 1988], and n_S the number of Stewartson layers present in the vicinity of the contraction ($n_S = 2$ for rectangular channel and 4 with an island). Since we have no comprehensive theory at hand to describe the dynamics within the channel and thus the adjoining Stewartson layers the actual Rossby number will be bound by the values of R_o and our R_{oeff}.

Data acquisition

No measurement probes have been used due to known problems with Taylor columns [p 238 *Tritton*, 1988] in homogeneous rotating fluids [e.g. *Boyer and Davies*, 2000]. Instead, fluxes out of each reservoir are calculated from reservoir volumes and initial and final density measurements [see *Whitehead et al.*, 1974]. Density is inferred from temperature measurements and salinity analysis of water samples to an accuracy of $2.3*10^{-5}$ g cm^{-3}. To study the position of the interface Red food colouring is used as dye in the dense fluid, back-lit from the channel bottom and recorded by a camera and PC based frame grabber. Theory by *Holford and Dalziel* [1996] to make quantitative estimates of interface height is adapted and optimised for our setup. The lower layer thickness, h, can be approximated by assuming an exponential attenuation of the light passing through the fluid from channel bottom; the attenuation coefficient in a uniformly dyed fluid [see p 517 *Apel*, 1987] is $k = \frac{-1}{h} ln(\frac{I}{I_c})$, where I/I_0 is the background corrected absolute light intensity and the path-length of the light through the fluid approximately the same as h (parallax was found to be negligible). A colour filter is used to select that part of the spectrum where the absorptivity function of the dye is linear, i.e. k(c) = Ac, where A is a constant and c the dye concentration. Using the attenuation approximation the layer thickness was directly calibrated allowing h to be accurately measured to within 6% of channel depth.

The two fluids are considered to be immiscible at the interface. Any light scattering effects are included in the dye attenuation and are considered to be negligible. The processing software was DigiImage V1.5 (DL Research Partners, Cambridge) and MATLAB R12.1.

Preliminary Results and Discussion

Treatment of environmental exchange flows often assumes approximately constant reservoir conditions, i.e. well mixed [*Bryden and Stommel*, 1984]. In the lab, finite reservoir volumes lead to a change in reservoir interface heights with time. We have to thus compromise between the timescales underlying our exchange to select data representing the most steady-state flow at nearest to initial reservoir conditions, where hydraulic jumps still isolate the reservoirs from the channel: as soon as the gravity current has passed the end of the channel after approximately $\frac{(g'H)-0.5}{channellength}$, steady flow will begin to set up within approximately f^{-1}. The experiments have thus been taken over an extended time period to find the most ideal observation period and sample spacing using the evolution of cross-channel interface slope in time to detect any passing internal bores.

The exchange flux is defined as, $Q_x = | Q_1 + Q_2 |$ where $Q_{(1,2)}$ are the fluxes out of each of the reservoirs with an associated error of $Q_n = Q_2 - Q_1$, assumed to be zero, so that the inferred flux is $Q_x \pm Q_n$; Q_n was usually similar to the error in Q associated with the density measurements.
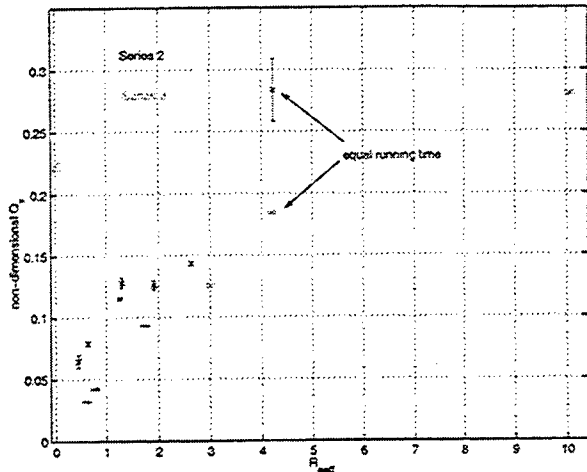
Figure 2. Exchange fluxes (Q_x) vs. effective Rossby number (R_{oeff}). Q_x is non-dimensionalised with respect to internal gravity (Kelvin) wave speed, channel depth and minimum channel width; errors are from net flow Q_n. Series 2 has a uniform cross-section and 3 has a centred island. $R_{oeff}=0$ represents no rotation.
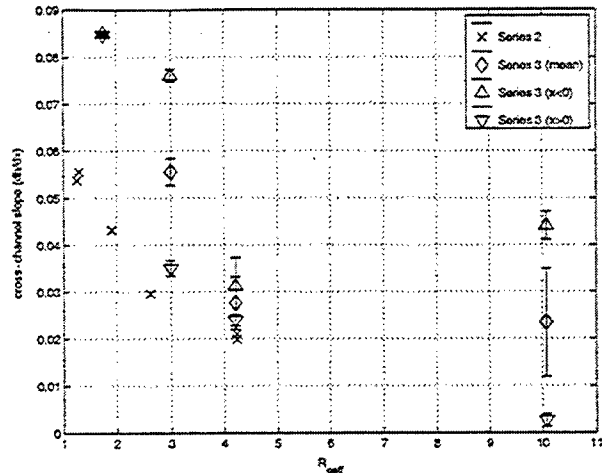
Figure 3. Cross-section slope at the constriction. Series 3 (see figure 2) values for individual channels are also given. Errors from R^2 value of linear fits to slopes.

All Q are non-dimensionalised as described in figure 2. A convenient parameter to compare different fluxes is R_{oeff}, representing the upper bound on the actual Rossby number, as mentioned before. Any difference in Q_x (see figure 2) at the same value of R_{oeff} is likely due to a change in cross-channel geometry, i.e. our island.

The variation of Q_x with R_{oeff} indicates that fluxes generally decrease with increasing rotation. Particularly the island experiments (series 3) show a regularity that appears to be non-linear. Experiments in this series were run for a time period that was scaled by f^{-1} but relatively long compared to the time where initial steady exchange is expected. This means that all experiments can be expected to have reached a time of negligible flux and are thus suitable for an initial comparison.

Running times in non-island experiments (series 2) were not scaled in this way, so that only qualitative observations can be made. However, series 2 shows generally higher fluxes than series 3, which indicates that the presence of an island generally reduces the flux. In particular, two experiments at $R_{oeff} \sim 4$, that both had the same running time, so the remaining difference is almost certainly due to the difference in cross-channel floor geometry, i.e. the island.

The cross-channel slope at the constriction section decreases non-linearly with R_{oeff} (figure 3) as is expected from semi-geostrophic theory (see Introduction). In series 3, the slope on the x>0 side of the island varies similarly to series 2 whereas the slope on the other side, although equal in one experiment, appears to differ significantly at $R_{oeff}>2$. This side is generally associated with a greater slope and a greater error in the linear fit which suggests that it is is more

apt to initial disturbances, less likely to be present in the experiment around $R_{oeff} \sim 2$ due to a longer running time. This emphasises the importance of using the maximum running time at near-initial conditions. The mean of both slopes on each island side is generally of greater magnitude than the series 2 slopes without the island.

For $(R_o, R_{oeff})<1$ we observed a curved interface slope that flattened out toward the x<0 side of the channel, giving a more appropriate parameter in the form of the width of a 'Coriolis boundary layer'; this is not to be mistaken for the rotating (Stewartson) shear layers. However, the presumed intersection of the interface with the channel floor did not occur, which was found likely to be due to Ekman layer transport requirements, further explained in *Dalziel* [1988]. Such separated flow is likely to be associated with a channel crossing [*Dalziel*, 1988], occurring within the two-layer region and possibly recirculation or stagnation within the single layer parts of the channel. Crossing of the flow is though to occur within a length R while oscillating along the channel around the constriction at a frequency of $\sim f$. If R is less than the length of the island, some evidence was found that the crossing occurred in each channel individually with a possible turn around the island tip. Future data also showing these crossing phenomena at high rotation may have to be investigated with respect to frontal dynamics [*Dalziel*, 1988].

We also observed a difference in interface height in the vicinity of the island's sides: the interface on each side did not join but appeared to be lower near the x>0 side than on the opposite one. Even though this agrees with the difference in slope mentioned before, faster rotating experiments did not show this disparity, possibly because they have a different number of Stewartson layers.

Summary and the Future

A laboratory setup and methods for investigating rotating Strait exchange flows with a simple narrows and nonuniform bottom topography has been presented. Methods to attain quantitative flux estimates and interface height measurements have been developed within our setup. Preliminary experiments showed several unique properties for the case of an island centred in the middle of an otherwise flat-bottomed and narrows constricted channel connecting two large fluid exchanging reservoirs. Variation of both interface height and fluxes with respect to the Rossby number suggests the expected influence of rotation but also significant influence by the presence of the island. In particular, maximal fluxes appear to be limited by both increasing rotation and the presence of an island. No direct comparison of fluxes and interface heights to existing theory has been made as the data are not yet sufficient for empirical analysis, but quantitative comparisons with existing work and hydrographic data from the Strait of Sicily are planned for the future.

Future availability of 2-dimensional velocity measurements will allow us to calculate an effective R_o correctly taking the Stewartson layers into account and to investigate variations in potential vorticity. In our setup we expect some finite value, likely constant within each layer and thus related to reservoir depths. Assuming a constant depth channel, the actual value of such potential vorticity is unlikely to affect the flow [*Dalziel*, 1988]. However, this becomes more important if we consider sills as an increase in potential vorticity decreases the critical value of R_o, at which separation occurs. Velocity and h would also allow us to accurately locate hydraulic controls. Some evidence was given by the generally continuous interface slope downward from the dense to the light reservoir. In our setup we would expect a single control to be located at the narrows with supercritical conditions toward the reservoirs, isolated by hydraulic jumps. Only at R_o^{-1} two controls may be expected near the channel exits enclosing a sub-critical interface [*Dalziel*, 1988].

Further experimental work will also incorporate an offset of the island toward either channel wall and possibly use of larger turntable facilities to limit the effect of Stewartson layers, deemed insignificant in the ocean.

References

Alessio, S., L. Briatore, E. Ferrero, A. Longhetto, C. Giraud, and O. Morra, Interaction between atmospheric flows and obstacles: Experiments in a rotating channel, *Boundary-Layer Meteorology*, pp. 235–241, 1992.

Apel, J., *Principles of Ocean Physics*, vol. 38 of *International Geophysics Series*, Academic Press: London, 1987.

Borenas, K., and J. Whitehead, Upstream separation in a rotating channel flow, *Journal of Geophysical Research*, *103*, 7567–7578, 1998.

Boyer, D., and P. Davies, Laboratory studies of orographic effects in rotating and stratified flows, *Annual Review of Fluid Mechanics*, pp. 165–202, 2000.

Bryden, H., and H. Stommel, Limiting processes that determine basic features of the circulation in the mediterranean sea, *Oceanologica Acta*, *7*, 1984.

Dalziel, S., Two-layer hydraulics: maximal exchange flows, Ph.D. thesis, Department of Applied Mathematics and Theoretical Physics, University of Cambridge, 1988.

Dalziel, S., Rotating two-layer sill flows, in *The Physical Oceanography of Sea Straits*, edited by L. Pratt, pp. 343–371, Kluwer Academic, 1990.

Gill, A., Adjustment under gravity in a rotating channel, *Journal of Fluid Mechanics*, *77*, 603–627, 1976.

Holford, J., and S. Dalziel, Measurements of layer depth in a two-layer flow, *Applied Scientific Research*, *56*, 191–207, 1996.

Killworth, P., Hydraulic control and maximal flow in rotating stratified hydraulics, *Deep Sea Research I*, *42*, 859–871, 1995.

Killworth, P., and N. McDonald, Maximal reduced-gravity flux in rotating hydraulics, *Geophysical Astrophys. Fluid Dynamics*, *70*, 31–40, 1993.

Munday, D., Effects of rotation on internal bores, 2000, university of Southampton SOES Honour Research Project Dissertation.

Shen, C., The rotating hydraulics of the open-channel flow between two basins, *Journal of Fluid Mechanics*, *112*, 161–188, 1981.

Tritton, D., *Physical Fluid Dynamics*, 2nd ed., Clarendon Press, 1988.

Whitehead, J., A. Leetmaa, and R. Knox, Rotating hydraulics of strait and sill flows, *Geophysical Fluid Dynamics*, *6*, 101–125, 1974.

B. Rabe, and D.A. Smeed, James Rennell Division, Southampton Oceanography Centre Empress Dock, Southampton, United Kingdom (e-mail: B.Rabe@soc.soton.ac.uk)

Maximum controlled flux in rotating two-layer exchange flows

U. Riemenschneider, P. D. Killworth and D. A. Smeed

Southampton Oceanography Centre, Southampton, United Kingdom

Abstract.
Two-layer rotating hydraulic theory as developed by *Whitehead et al.* [1974] is extended to deepen our understanding of exchange flows. Whiteheads formulation of maximum exchange given as $\frac{1}{6}\frac{g'D_0^2}{f}$ is tested and we find that it overestimates the transport for rectangular channels containing a sill but not for those with a flat bottom. The analytical results will be compared to numerical results from MICOM (Miami Isopycnic Coordinate Ocean Model) by setting it up with an idealised topography similar to that we use in the theory. Preliminary results from a first run of MICOM with a channel obstructed by a sill, have revealed regions of recirculation up- and downstream of the sill.

Introduction

Throughout the global oceans, small scale topographic constraints, such as sills and straits, limit the exchange of water masses between large ocean basins, driven by salinity and temperature differences. It is well established, that these exchanges play a major role in driving the thermohaline circulation and thus determine the developement of global climate. In many climate models however, the resolution is not sufficient to represent these flows realistically [*Roberts and Wood*, 1996]. In order to improve our understanding of overflows we started a modelling study of the dynamics of two-layer exchange flows as part of a PhD project.

A theory for two-layer exchange flows including rotation was first attempted by *Whitehead et al.* [1974] for zero potential vorticity and supported by laboratory experiments. *Gill* [1977] developed a functional approach for the single layer constant potential vorticity case, which was adapted by *Dalziel* [1988] for two layers, equally supported by laboratory experiments. *Whitehead et al.* [1974] found the maximum exchange in the hydraulically controlled two-layer case to be $\frac{1}{6}\frac{g'D_0^2}{f}$, where D_0 is the minimum depth along the channel. However, both *Dalziel* [1988] and *Whitehead* [1989] stated that the energy argument used to obtain this result was ambiguous, which led to findings that this formulation overestimes the flow [*Dalziel*, 1988].

As a first step of the modelling study we set out to investigate the dynamics of the flow using the theory developed by *Whitehead et al.* [1974] and determine how the flux is overestimated. We assume that the flow is hydraulically controlled and we only consider flows for which a solutions can be trace up- and downstream along the channel, a constraint not considered by Whitehead.

The theory

We us the three dimensional inviscid shallow water equations to describe the dynamics of both layers, but reduce these to two dimensions and only investigate horizontal flow along and across the channel.

Taking the curl of the momentum equations we may deduce the conservation of potential vorticity, which we take to be zero.

Including the earth's rotation gives rise to a natural length scale, the radius of deformation or Rossby radius, $a = \frac{\sqrt{g'D_0}}{f}$, which we us to non-dimensionalise the shallow water equations.

Channel geometry

Similar to *Whitehead et al.* [1974] we are considering a rectangular channel connecting two large and deep ocean basins, the cross-section of the channel is shown in Fig. 1. h_1 denotes the thickness of the bottom layer, h_2 the thickness of the top layer, L the width of the channel and D its depth. The axes are set up, such that the x-axis points upstream along the channel (from west to the east), the y-axis lies across the channel, and the z-axis points upward, with $z = 0$ being the surface of the water. Both depth, D, and width, L, are dependent on x.

Solutions

From the assumption of zero potential vorticity we get,

$$u_1 = y + u_{10} \tag{1}$$
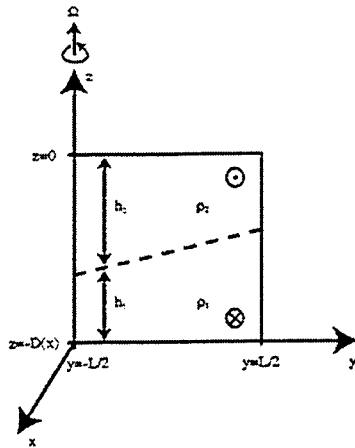
$$u_2 = y + u_{20} \tag{2}$$

189

Figure 1. Cross-section of the rectangular channel. The interface is represented by the dashed line.

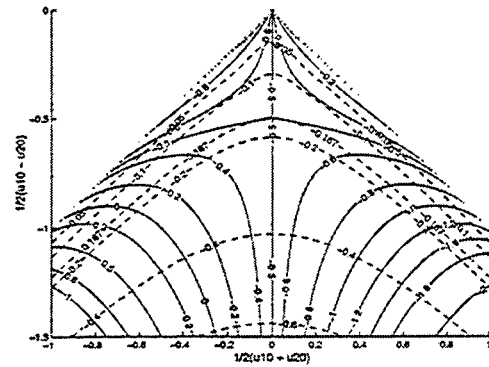**Figure 2.** The dashed lines are constant flux, Q_1, contours, while the solid lines present the different Bernoulli potential differences, ΔE, over a given range of $u_{10} + u_{20}$ and $u_{20} - u_{20}$ at a section of width one Rossby radius and depth D_0. Note the convergence of the $\Delta E = -0.5$ lines at the point $(0, -0.5)$, where the absolute flux is $\frac{1}{6}$.

where u_{10} and u_{20} are the velocities of layers 1 and 2 at $y = 0$ respectively. From geostrophy,

$$h_1 = (u_{10} - u_{20})y + h_{10}. \qquad (3)$$

If we integrate across the channel to obtain the fluxes, Q_1 and Q_2, in the two layers, we find that they are dependent on u_{10}, u_{20} and h_{10}. We may use the **no net-flux** condition,

$$Q_2 + Q_1 = 0 \qquad (4)$$

to find h_{10} in terms of u_{10} and u_{20}.

When integrating across the channel we consider every possible location of the interface, i.e. we allow for the fact that the interface may ground somewhere across the channel or outcrop at the surface, or both. This leads to nine different regimes for the flow geometry, and for each case the expression of h_{10} will be slightly different. In doing so we extend the analysis by *Whitehead et al.* [1974] who do not allow for any other case but that of both layers being present everywhere over the topography, across and along the channel. *Dalziel* [1988] does consider seperation, but only in cases where the interface grounds and not where it outcrops at the surface.

Energies

In addition we assume that the difference between the Bernoulli potentials of the two layers remains constant over the flow up- and downstream. (this is in fact only true if no hydraulic jumps occur anywhere along the channel). The Bernoulli-difference can be expressed as:

$$\Delta E = E_1 - E_2 = \frac{1}{2}(u_{10}^2 - u_{20}^2) + h_{10} - D. \qquad (5)$$

ΔE, may be regarded as a measure of the difference of energy available to the two layers in the upstream and down-

stream basin and hence also represents the interface height difference between the layers in the two basis.

Using (5), we may further reduce the dependence of the fluxes to only one variable, $h_s (= u_{10} - u_{20})$, the slope of the interface, by finding an expression for $u_{10} + u_{20}$ in terms of h_s and ΔE. Therefore Q_1 may be written as follows,

$$Q_1(h_s; L, D) = constant \qquad (6)$$

noting also that the flux is conserved along the channel.

Each controlled flow we attempt to follow is therefore characterised by two values, ΔE, the energy of the system, and Q_1, the bottom layer flux that may arise from the given energy. Fig. 2 showes contour lines of Q_1 (dashed) on top of lines of constant ΔE (solid). In the region between $\Delta u = \frac{1}{2}(u_{10} - u_{20}) = -0.5$ and 0, there are pairs of contours, one of flux and one of energy, which just touch in one point. For any given energy line the fluxline it touches is the maximum controlled flux possible at that particular energy.

Hydraulic control

In order to find the maximum flux in the bottom layer we use the fact that $\frac{dQ_1}{dx} = 0$. Therefore

$$0 = \left(\frac{dQ_1}{dh_s}\right)\frac{dh_s}{dx} + \left(\frac{dQ_1}{dL}\right)\frac{dL}{dx} + \left(\frac{dQ_1}{dD}\right)\frac{dD}{dx} \qquad (7)$$

and assuming hydraulic control at the shallowest or narrowest section in the channel: $\frac{dh_s}{dx} \neq 0$, we find that the condition for determining the flux at the control section is $\frac{dQ_1}{dh_s} = 0$. We procede to compute Q_1 over a range of h_s and find the point at which the flux does not change with respect to the slope of the interface. This is the desired maximum controlled flux for a specific ΔE and a given control section

Table 1. Fluxes for a varying width channel. (y - yes)

ΔE	Tracable	Flux
-0.2	y	-0.026268
-0.3	y	-0.053587
-0.4	y	-0.094592
-0.45	y	-0.122653
-0.5	y	-0.167657
-0.55	y	-0.122654
-0.6	y	-0.094594
-0.8	y	-0.026268

Table 2. Fluxes for a varying depth channel. (n - no)

ΔE	Tracable	Flux
-0.2	n	-0.026268
-0.4	n	-0.094592
-0.5	n	-0.167657
-0.51	n	-0.154215
-0.53	y	-0.136604
-0.55	y	-0.122654
-0.6	y	-0.094594
-0.7	y	-0.053589
-0.9	y	-0.009981

geometry. To trace the solution upstream and downstream we compute the flux Q_1 for a section a small distance, Δx, away from the control section, for a similar range of h_s. Here $L(x_0 + \Delta x) = L(x_0) + \epsilon$ or $D(x_0 + \Delta x) = D(x_0) + \epsilon$, where x_0 is the position of the control section usually choosen to be at the origin. From the results we find the values of h_s for which the flux is equal to that at the control section. For a flux which can be followed up- and downstream there should be two such solution for two different values of h_s. Repeating this process further and further away from the control section we aquire a continous picture of the flow along the channel.

Maximum fluxes

Constant depth, varying width

The first geometry we tested for various values of ΔE was that of a channel with constant depth D_0 and varying width, where the narrowest section is one Rossby radius across. Intuition would suggest that for all values a flux should be found which can be traced up- and downstream. This hunch was confirmed by the runs, the results of which are shown in Tab. 1. At $\Delta E = -0.5$ Whiteheads flux of $1/6$ is acchieved and the interface here extends diagonally across the channel.

Constant width, varying depth

For the second set of tests we varied the depth of the channel, i.e. we introduced a sill of depth D_0 and kept the width constant at one Rossby radius. As the flow has to overcome a vertical obstacle in this case we might suspect that not all values of ΔE present controlled flows which may be traced along the channel; the results in Tab. 2 confirm this. The first flow which may be traced lies somewhere between $\Delta E = -0.51$ and -0.53, where the flux is between -0.1542 and -0.1366 and hence Whiteheads formula overestimates the flow.

Conclusions

In a first attempt to a better understanding of the theory involved in controlled two-layer exchange flows, we find the maximum controlled flux for channels of a constant depth D_0 and a constriction of one Rossby radius to be higher than for channels with constant width of one Rossby radius and increasing depth away from the control section. This confirms, but limits the findings by *Dalziel* [1988] that the flux is overestimated by the Whitehead formulation.

Future work with MICOM (Miami Isopycnic Coordinate Ocean Model)

As the theory we have available is still quite limited in its possibilities, we will use MICOM to model these two-layer exchange flows, using idealised channel topographies as described in Sec. connecting two deep rectangular ocean basins. Hopefully this will tell us about features in the flow which are not immediately obvious from the theory such as hydraulic jumps, which MICOM allows for, and instabilities for example.

Recirculation vs. stagnation

Some preliminary MICOM runs for a rectangular channel with a sill between the basins have shown us that upstream and downstream of the sill a region of recirculation forms in the bottom layer on the righthand and lefthand side of the channel respectively.

This point has only been mentioned in passing by several authors studying maximal controlled flows through channels. Most studies are restricted to the single layer rotating case, and understanding is still quite limited. Upstream recirculation has attracted more attention than downstream recirculation, as it may have some impact on the maximum flux over the sill. *Pratt and Armi* [1987] mention the occurance of a recirculation region upstream while discussing flow separation. Similarly in the context of investigating upstream separation *Borenäs and Whitehead* [1998] compare labora-

tory experiments in a rotating tank to the results from two different theories, one postulating a stagnant region and the other one a region of recirculation. Although the experimental result match neither theory perfectly they clearly seem to resemble the results including circulation more closely. They also find that this recirculation region may have a significant impact on the volume flux across the sill by draining kinetic energy from it and thus reducing the flux. This point is supported by findings of *Straub* [1998]. Laboratory experiments carried out by *Dalziel* [1988] seemed to suggest however that the region forming upstream, to the right of the main current, is stagnant.

We will persue this point further in the future using results from MICOM.

References

Borenäs, K. M., and J. A. Whitehead, Upstream separation in a rotating channel flow, *Journal of Geophysical Research*, *103*, 7567–7578, 1998.

Dalziel, S. B., Two-layer hydraulics: maximal exchange flows. Ph.D. thesis, Department of Applied Mathematics and Theoretical Physics, University of Cambridge, 1988.

Gill, A. E., The hydraulics fo rotating-channel fiow, *J. Fluid Mech.*, *80*, 641–671, 1977.

Pratt, L. J., and L. Armi, Hydraulic control of flows with nonuniform potential vorticity, *Journal of Physical Oceanography*, *17*, 2016–2029, 1987.

Roberts, M. J., and R. A. Wood, Topographic sensitivity studies with a bryan–cox-type ocean model, *Journal of Physical Oceanography*, *27*, 823–836, 1996.

Straub, D. N., Simple models of flow over deep ocean sills: Planetary and semigeostrophic solutions. *Journal of Physical Oceanography*, *28*, 971–983, 1998.

Whitehead, J. A., Internal hydraulic control in rotating fluids–applications to the oceans, *Geophys. Astrophys. Fluid Dymanics*, *48*, 169–192, 1989.

Whitehead, J. A., A. Leetman, and R. A. Knox, Rotating hydraulics of strait and sill flows, *Geophysical Fluid Dynamics*, *6*, 101–125, 1974.

U. Riemenschneider, School of Ocean and Earth Sciences, Southampton Oceanography Centre, European Way, Southamtpon, SO14 3ZH, United Kingdom.
e-mail: url@soc.soton.ac.uk

P. Killworth and D. Smeed, James Rennell Division, Southampton Oceanography Centre, European Way, Southamtpon, SO14 3ZH, United Kingdom

Numerical study of the hydraulics of the mean flow through the Strait of Gibraltar

G. Sannino, A. Bargagli and V. Artale

Global Climate Project -CR Casaccia - ENEA, Rome, Italy

Abstract. The three-dimensional Princeton Ocean Model is used to investigate the hydraulics regime of the mean flow through the Strait of Gibraltar. Model results confirm the presence of a mixing layer between the Atlantic and Mediterranean water. Hydraulic regime is analysed calculating the Composite Froude number for three layers within the strait. Results indicate the presence of a hydraulic control at Camarinal Sill and in the northern part of Tarifa Narrows.

Introduction

Using a 3D general ocean circulation model, Wang (1989) was able to describe most of the aspect of the mean circulation of the Strait of Gibraltar. However, because of the relatively low horizontal and vertical resolutions (~5 Km and 50 m respectively), the model did not reproduce the hydraulic control over Camarinal Sill. Wang found in fact that while the surface flow is supercritical, i.e. hydraulically controlled on the eastern entrance the bottom flow is subcritical, i.e. not controlled on the western entrance, over Camarinal Sill. To our knowledge, Wang's model is the only 3D ocean circulation model applied to the Strait of Gibraltar in the last ten years.

In the present work we describe a numerical investigation of the mean exchange of the Strait of Gibraltar using the Princeton Ocean Model (POM) (Blumberg and Mellor, 1987) in a very high-resolution configuration ($\_x$, $\_y$ < 500 m within the strait) in order to represent well all dominant topographic features of the strait. In particular, the model described in this paper simulates the nature of the mean exchange through the strait, i.e. whether it is maximal or sub-maximal by determining the locations of the hydraulic control.

Model description

The region covered by our model includes the Strait of Gibraltar and the two sub-basins connected to it, the Gulf of Cadiz and the Alboran Sea. The resolution is much higher in the strait (~500 m) than in the eastern (8-15 Km) and western ends (10-20 Km). The vertical model grid is made by 25 sigma levels. The model topography was constructed by

bilinear interpolation of the depth data onto each grid point of the horizontal model grid. The resulting bottom topography and the computational grid in the region of the strait is shown in Figure 1; here are clearly recognizable the dominant topographic features of the strait (from west to east): Spartel Sill (Sp), Tangier basin, Camarinal Sill (Cm) with a depth of 284 m and Tarifa Narrows.
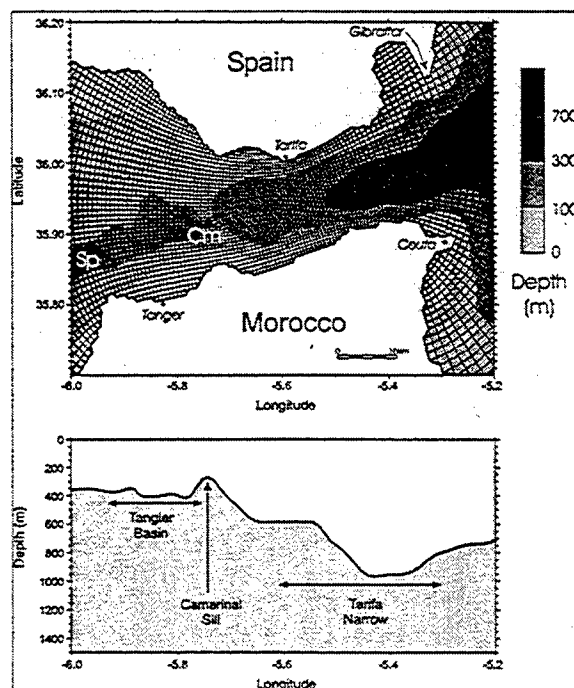

Figure 1. (Upper) Model bathymetry and computational grid for the strait region. The gray levels indicate the water depths. The points Cm and Sp mark the points where are located Spartel Sill and Camarinal Sill

respectively. (Lower) Bathymetry along the longitudinal axis of the strait.

In the vicinity of the eastern and western ends of the computational domain two open boundaries are defined: an Orlanski radiation conditions (Orlanski, 1976) for the depth-dependent velocity, a flow relaxation scheme (Martinsen *et al.*, 1987) for the depth-integrated velocity, and a Newtonian restoring for the two active tracers, with a damping timescale of 5 days.

The model is started from rest; it is only driven by the density difference between the two sub-basin; in particular the initial temperature and salinity fields for the Alboran basin and the Gulf of Cadiz have been obtained by a horizontal average of the spring MODB data and the spring Levitus data (Levitus, 1982) respectively (initial salinity difference $\Delta S = 1.5$ psu).

Model results

After 3 days of integration the flow adjusts to a two-layer circulation in the strait, but only after 200 days of integration the mean transport in both layers reaches a quasi-steady values of 0.72 Sv.

To allow a comparison between the model results and the two layer hydraulic theory, it is necessary to define an interface to discriminate the Mediterranean and the Atlantic flow. To such purpose we have plotted the along-strait steady velocity versus salinity obtaining the scatter plot in Figure 2a; here is evident the intense inflow of Atlantic water with salinities less than 36.5 psu and the strong outflow of Mediterranean water with salinities greater than 38.0 psu. For salinities ranging between 37.0 psu and 37.5 psu we can recognize both inflow and outflow. In Figure 2b the along-strait mean velocity profile versus salinity is shown, it was obtained by averaging the velocities over salinity layers of thickness $\_S = 0.2$ psu. For salinities less than 37.25 psu there is an inflow velocity that reaches a maximum value of 40 cm s$\_$ at a salinity of 36.25 psu. For salinities greater than 37.25 psu there is an outflow velocity that reaches a maximum value of 35 cm s$\_$ at a salinity of 38.4 psu. The transition between inflow and outflow then occurs at a salinity of 37.25 psu, which can be taken to define the interfacial isohaline between the Atlantic and Mediterranean waters. Such definition is in agreement with the choice by Lacombe and Richez (1982), Bormans and Garrett (1989), and Bryden *et al.* (1994).
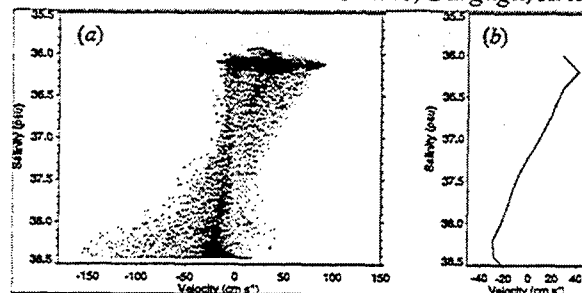

Figure 2. (a) Scatter plot of velocity versus salinity for the strait of Gibraltar. (b) Profile of the along-strait average velocity versus salinity. Velocities are averaged over salinity layers of thickness $\_S = 0.2$ psu.

The resulting value of G^2 is shown in Figure 3. It was calculated averaging the along-strait velocity and density from the surface to the interface depth for the upper layer, and from the interface depth to the bottom for the lower layer $(\overline{u}_i, \overline{\rho}_i)$.
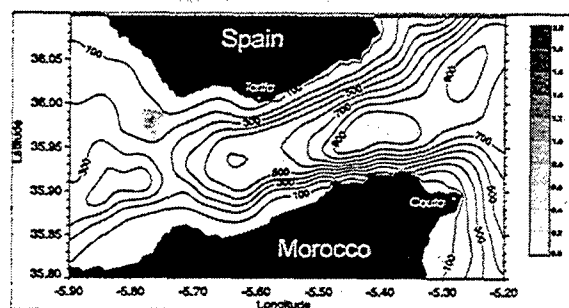

Figure 3. Two layers composite Froude number (gray levels), calculated using mean layer velocities. Contour lines represent the bathymetry.

In Figure 3 one can note that $G^2 < 1$ everywhere, i.e. the flow is subcritical within the strait. However, this result seems to be inconsistent with the simulated character of the flow; in fact, the predicted salinity distribution along the longitudinal axis of the Strait (Figure 4), suggests the presence of a hydraulic jump west of Camarinal Sill. It seems that the direct application of the two-layer hydraulic theory to the Strait of Gibraltar is not obvious. As observed by Bray *et al.* (1995), entrainment and mixing between the Atlantic upper layer and the Mediterranean lower layer are responsible for the creation of a third interfacial layer.
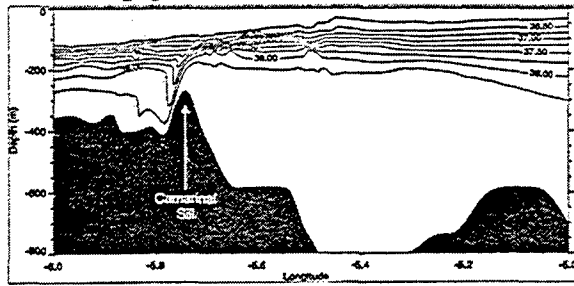
Figure 4. Simulated salinity distribution along the longitudinal axis of the Strait.

Thus, in order to verify the presence of an interface layer, a quantitative method similar to that described by Bray *et al.* was used. Predicted thickness of the interface layer for the whole strait is shown in Figure 5. It is interesting to note that the thickness has the greatest values just west Camarinal Sill, indicating the presence of mixing in that region. The thickness of the interfacial layer obtained is good in agreement with that calculated by Bray *et al.*
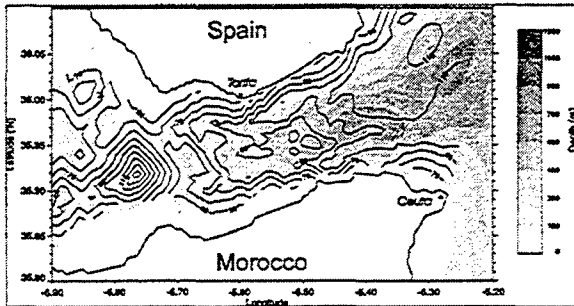
Figure 5. Mixing layer thickness with 10m contour interval. Grey levels indicate bathymetry.

Moreover we have calculated the Bernuolli potential along the strait for the three layers (Figure 6): for the upper layer (Figure 6a) the Bernuolli potential is constant along the whole channel, for the bottom layer (Figure 6c) is constant along Tarifa Narrows as far as Camarinal Sill. Immediately west of Camarinal Sill the Bernuolli potential suddenly decreases because of the presence of the hydraulic jump that, as well-known, is always associated with turbulent dissipation of energy. Only in the interface layer (Figure 6b) the Bernuolli potential shows a weak variation due principally to the mixing.

From the previous discussion about the Bernoulli potential we can conclude that the three-layer

hydraulic theory is applicable to our model. However, to evaluate the effect of more than two layers it is necessary to extend the usual hydraulic control theory to a multi-layer flow (see Appendix A in Sannino *et al.* 2002).
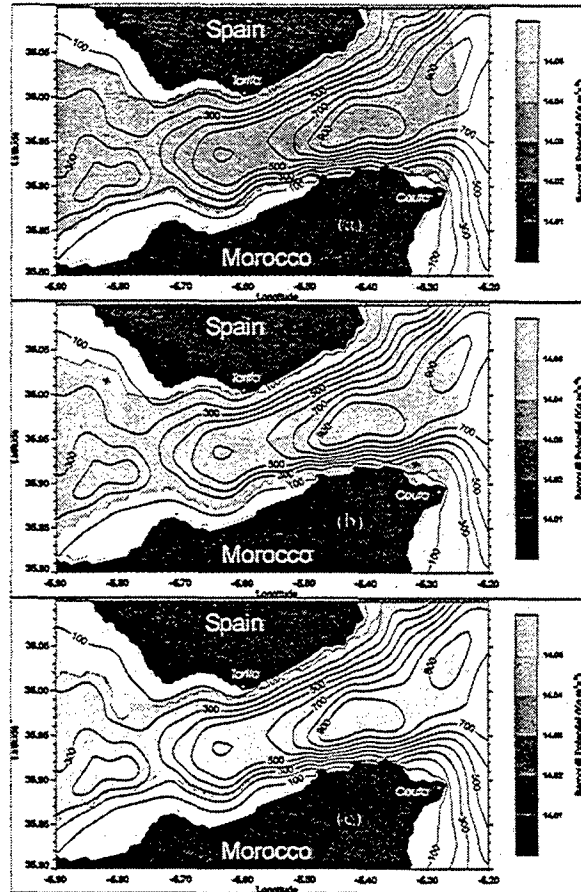
Figure 6. Bernoulli Potential for the upper (a), mixed (b) and lower layers (c).

In particular, in presence of a mixed layer we used the multi-layer formulation for three layers with Froude numbers defined as:

$$F_1^2 = \frac{\overline{u}_1^2}{h_1 g (1 - r_{1,2})}, \quad F_2^2 = \frac{u_2^2 (1 - r_{1,3})}{h_2 g (1 - r_{1,2})(1 - r_{2,3})}, \quad F_3^2 = \frac{\overline{u}_3^2}{h_3 g (1 - r_{2,3})}$$

where $r_{i,j}$ is the density ratio. The composite Froude number is given, to a good approximation, by:

$$G^2 = F_1^2 + F_2^2 + F_3^2 .$$

The predicted composite Froude number within the strait is shown in Figure 7. Critical values of G_- can be observed over the whole cross-strait section west

of Camarinal Sill and in the northeastern part of
Tarifa Narrows. The contribution from the interfacial
Froude number ($F_{2\_}$) is negligible everywhere, i.e., it
can be considered as a stagnant layer, whereas the
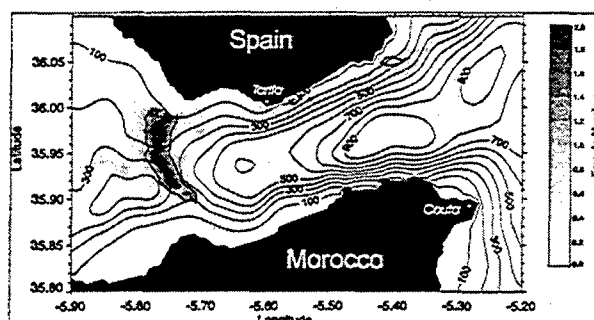upper value ($F_{1\_}$) is essential only for the Tarifa
narrow region.

Figure 7. Three layers composite Froude number (gray
levels), calculated using mean layer velocities. Contour
lines represents (thin) the bathymetry, (bold) limit the
region where $G^2 > 1$.

Thus, model results shown in Figure 7 seem to
indicate the presence of hydraulic control at
Camarinal Sill, whereas there is not a clear indication
for Tarifa Narrows. The uncertainties come from the
application of the two-dimensional hydraulic control
theory to a three-dimensional flow. In an attempt to
remove this uncertainty we formulated cross-strait
mean equations in terms of cross-strait mean quantity
and confined the solution between two upper and
lower limit solutions. This procedure allowed us to
give upper and lower limits for the values of the
composite Froude number for the cross-strait mean
flow (Sannino *et al.* 2002). In particular, at
Camarinal Sill the mean cross-strait composite
Froude number is found in the range 1.2 to 1.5,
whereas at Tarifa Narrows between 0.4 to 0.8 (Figure
8). This result allows us to conclude that the mean
circulation simulated by the model is in a sub-
maximal regime.

We have also performed other three experiments
with different initial conditions. In particular we
have uniformly increased the salinity of the
Mediterranean to have an increased salinity
difference with the Atlantic water. For the new three
experiment ($\Delta S = 2.0$ psu, $\Delta S = 2.2$ psu and $\Delta S = 2.5$
psu) our model predicts a transport in both layers of
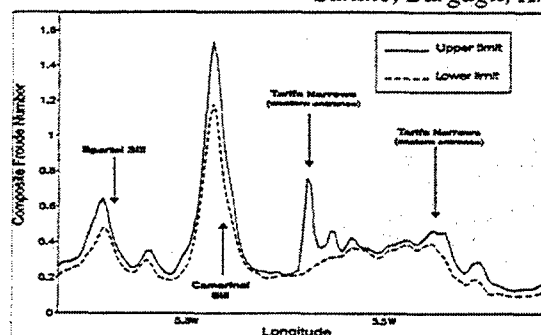0.86, 0.89 and 0.93 Sv respectively (Figure 9).

Figure 8. Upper (solid line) and lower (dashed line) limits
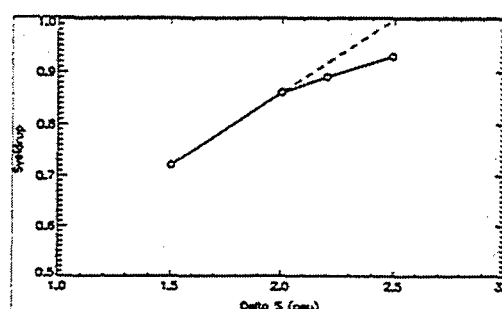for the mean cross-strait composite Froude number.

Figure 9. Predicted transport through the strait for the
three new experiments (a) $\Delta S = 2.0$ psu, (b) $\Delta S = 2.2$ psu
and (c) $\Delta S = 2.5$ psu.

We have also calculated the three-layer composite
Froude number for the three cases (Figure 10).

Here it is very clear that when ΔS increases also the
upper layer Froude number increases, moreover its
range of action extends along the cross-section
located east of Tarifa. In particular, for $\Delta S > 2.0$ the
mean cross-strait composite Froude number is greater
than 1 both at Camarinal Sill then at Tarifa Narrows,
i.e. the flow is in maximal regime.

A connection between the transport through the
strait and the hydraulics regime is quite evident
looking at Figure 9 and Figure 10. In particular in
Figure 9 one notes a discontinuity in the trend of the
transport just at $\Delta S = 2.0$, that corresponds to the
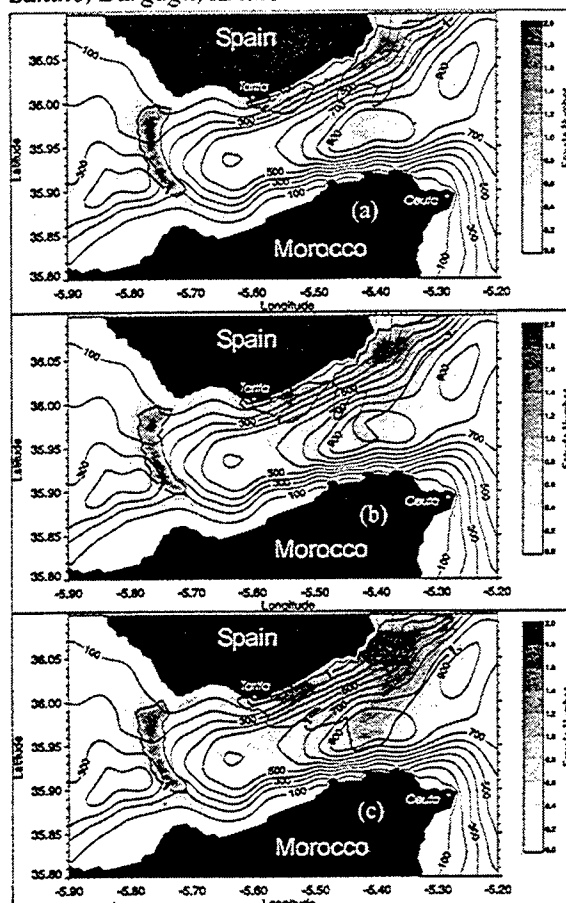transition of the flow regime from sub-maximal to
maximal (Figure 10b).

Figure 10. Predicted three-layer composite Froude number for the three new experiments (a) $\Delta S = 2.0$, (b) $\Delta S = 2.2$ and (c) $\Delta S = 2.5$. Contour lines represents (thin) the bathymetry, (bold) limit the region where $G^2 > 1$.

Conclusions

The purpose of this study was to evaluate, in the frame of hydraulic theory, if there are regions hydraulically controlled and consequently if the Strait of Gibraltar is in a submaximal or maximal regime. It has been stressed that, because of the presence of a mixing layer, three layers structure gives a better representation of the circulation within the strait. For this reason we used a formulation of Froude numbers for three layers indicating in the basic experiment ($\Delta S = 1.5$ psu) the presence of hydraulic control over the whole cross-strait section west of Camarinal Sill and in the northern part of Tarifa Narrows. We have also performed other three experiments with increased ΔS. The results allows us to conclude that the mean circulation simulated by the model is in a sub-maximal regime for $\Delta S < 2.0$ psu and in maximal regime for $\Delta S > 2.0$ psu.

References

Blumberg, A. F. and G. L. Mellor, A description of a three-dimensional coastal ocean circulation model. Three-Dimensional Coastal Ocean Models, *Coastal Estuarine Science*, N. S. Heaps, Ed., Amer. Geophys. Union, 1-16, 1987.

Bormans, M., C. Garrett, The effect of nonrectangular cross section, friction, and barotropic fluctuations on the exchange through the Strait of Gibraltar, *J. Phys. Oceanogr.*, *19*, 1543-1557, 1989.

Bray, N. A., J. Ochoa, T. H. Kinder, The role of the interface in exchange through the Strait of Gibraltar, *J. Geophys. Res.*, *100*, 10755-10776, 1995.

Bryden, H. L., J. Candela and T. H. Kinder, Exchange through the Strait of Gibraltar, *Prog. Oceanog.*, *33*, 201-248, 1994.

Lacombe, H. and C. Richez, The regime of the Strait of Gibraltar. Hydrodynamics of semi-enclosed seas, *J. C. J. Nichol*, editor, pp. 13-74. Elsevier. Amsterdam, 1982.

Levitus, S., Climatological Atlas of the World Ocean, NOAA Prof. Paper, 13, U.S. Govt. Printing Office, 173 pp., 1982.

Martinsen, E.A., H. Engedahl, Implementation and testing of a lateral boundary scheme as an open boundary condition in a barotropic ocean model, *Coastal Eng*, *11*, 603-627, 1987.

Orianski, I., A simple boundary condition for unbounded hyperbolic flows, *J. of Computational Physics.*, *21*, 251-269, 1976.

Sannino, G, A. Bargagli and V. Artale, Numerical modeling of the mean exchange through the Strait of Gibraltar.Model. Accepted on *J. Geophys. Res.*, 2002.

Wang, D.-P., Model of mean and tidal flows in the Strait of Gibraltar, *Deep Sea Res.*, *36*, 1535-1548, 1989.

Reynolds stress measurements in a short tidal inlet

Harvey Seim

Department of Marine Sciences, University of North Carolina at Chapel Hill

Abstract.
A fortnight of ADCP measurements from the throat of a tidal inlet are processed to yield estimates of the Reynolds stress over most of the water column. Ebb currents commonly exceed 1 m/s at 2.5 m above the bottom and generate a 50 cm^2/s^2 stress; flood currents are much weaker and result is a stress less than 10 cm^2/s^2. Estimates of turbulent production exceed 10^{-4} m^2/s^3 and eddy viscosities of 0.1 m^2/s are common. Near bottom mixing lengths on ebb are reasonably well approximated by a parabolic mixing length $l_o = \kappa(z/H)H(1 - z/H)$, where κ is von Karman's constant and H is the water depth. During flood the mixing length is consistently smaller than the predicted length. Enhance near-surface stress may be associated with wave breaking.

Introduction

Sea straits are likely sites of enhanced turbulent mixing owing to the high flow speeds and strong shears that often characterize them. These same qualities make the collection of turbulence measurements difficult. There are relatively few turbulence measurements in sea straits, and almost all have been collected with free-falling microstructure profilers [e.g. Wesson and Gregg , 1994; Gregg et al., 1999] though moored techniques have been used recently [e.g Di Iorio and Yuce , 1999]. These measurements are typically intense in space but rather limited in time. We here present observations of the vertical components of the Reynolds stress collected with an acoustic doppler current profiler (ADCP) in an inlet connecting a small inland sea and the ocean. A different perspective on turbulence variability and its controls is gained from the time-intensive, vertically-resolved but spatially-limited measurements.

The technique of using an ADCP to measure the Reynolds stress has been recently popularized by the work of Lu and Lueck [1999] and Stacey et al. [1999a, b]. Lu and Lueck [1999] provide a brief review of the various techniuqes employed. The "variance" technique used herein relies on the geometry of the system and for a four beam configuration requires a nearly exact upright orientation. Significant tilt leads to smearing of the vertical components of the Reynolds stress tensor into other components of the tensor in the instrument frame of reference. Because the technique only measures the vertical components, there is no simple method to rotate observations collected in a tiltled reference frame into earth coordinates.
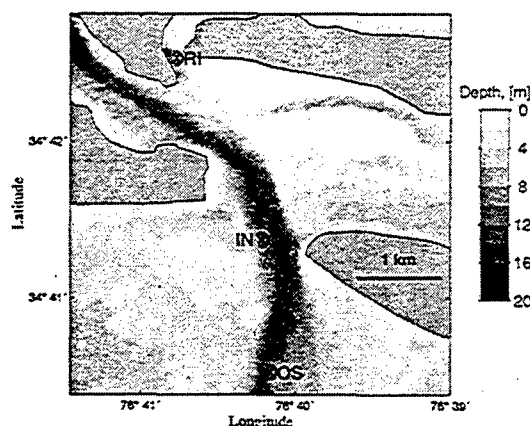

Figure 1. Bathymetry in the vicinity of Beaufort Inlet, NC. The ADCP at the 'IN' position is the one discussed in the text.

Methods

The Reynolds stress measurements were collected as part of a program studying inlet circulation. Three moorings, each consisting of an upward-looking ADCP and a pair of SeaBird microcats, were deployed for approximately 7 weeks around Beaufort Inlet, NC in August and September, 2001, as shown in Figure 1. In addition to the mooring array deployment, 3 anchor stations of 13 or 25 hour duration were occupied, during which time continuous ADCP measurements and CTD profiles at 10 minute intervals were collected. This note focuses on the ADCP observations collected at station"IN" in the inlet throat.

An upward-looking, 4 beam 1200 kHz RDI workhorse

199

sentinel collected the velocity estimates used to form the Reynolds stress. The ADCP was housed in a bottom frame that was anchored by stakes jetted into the bottom by divers. The frame was leveled to within 1-2 degrees of horizontal. The beams were inclined at 20 degrees to the vertical and data were stored in beam coordinates. The instrument pinged once a second and collected 600 samples over 10 minutes every half hour. Mode 1 [RDI , 1998] was used with 30 centimeter bins, resulting in an approximate single ping standard deviation of 10.9 cm/s according to RDI software. The instrument stored the observations internally on two PCM-CIA cards that could hold about 396 MB of information. This required recovering and downloading the observations after 17 days. Redeployment resulted in 25 days of valid observations. Observations from the first 17-day deployment are used below.

Means and variances of the along-beam velocities were formed for each 10 minute average of data at each bin location. Unbiased estimators of two components of the Reynolds stress tensor can be formed from the variances as [Stacey *et al.*, 1999a]

$$\overline{u'w'} = \frac{1}{4\cos\theta\sin\theta}(\overline{u_3'^2} - \overline{u_4'^2})$$

$$\overline{v'w'} = \frac{1}{4\cos\theta\sin\theta}(\overline{u_1'^2} - \overline{u_2'^2})$$

where u_n is the velocity along beam n and θ is 20 degrees, the inclination of the beams from vertical. As shown by Lu and Lueck [1999], pitch and roll of the instrument introduce additional terms in the estimators of these shear stress components that cannot be accurately accounted for with a 4 beam system, therefore it is important to insure that the instrument is deployed in as close to a vertical orientation as possible. It is also possible for form estimates of the turbulent kinetic energy

$$\overline{d_u^2} = \frac{1}{2}(\overline{u_3'^2} + \overline{u_4'^2})$$

$$\overline{d_v^2} = \frac{1}{2}(\overline{u_1'^2} + \overline{u_2'^2})$$

however the estimates are biased by system noise; Stacey *et al.* [1999b] outline a procedure for formed corrected estimates of TKE.

Setting

Beaufort Inlet connects Bogue Sound to the Atlantic Ocean (Figure 1). Bogue Sound in turn connects with Pamlico Sound, part of the "Inland Seas" of eastern North Carolina. As one of only 4 connections between the sounds and the ocean, Beaufort Inlet functions in a sense like a sea strait, connecting a relatively large water body with the ocean.

By any classification scheme, the inlet can be considered a short strait [e.g. Helfrich , 1995]. The bathymetry in the region is generally shallow ($< 10\ m$) but complicated by the presence of dredged channels that create relatively deep pathways through the inlet. Tides in the Atlantic are dominated by the 0.5 m M_2 component, but within the sounds tides are difficult to identify, hence the inlets are small enough to choke the tide.

Tidal currents within the inlet are quite strong, regularly exceeding 1 m/s on ebb. Combined with the shallow depths this drives the systems towards relatively well-mixed conditions (vertical density differences seldom exceed 1 kg/m^3) in the vertical. During the sampling period river discharge into the sounds was quite low, the result of an extended moderate drought along the eastern seaboard of the US. The potential for internal hydraulic controls to play a significant role in regulating the rate of exchange through the inlet is therefore limited. If hydraulic responses are present they were not obvious in the station data used in this study.

Surface waves are largest in the inlet when winds are from the south. As will be shown below, strong southerly winds correlate well with greatly enhanced Reynolds stress in the upper water column and are presumed to be a reflection of surface wave breaking.

The coordinate convention used is that of positive currents on flood (approximately to the north) and negative on ebb (approximately to the south).

Results

Currents are tidally dominated and this is reflected in the Reynolds stress variability (Figure 2). Currents typically exceed 1 m/s on ebb but peak at values closer to 0.5 m/s on flood. The figure shows two time periods, one near times of spring tide and one near neap tide. Peak currents on spring ebb are nearly 2 m/s, and exceed 1 m/s 2.5 meters above the bottom (mab) on most tides. Currents on flood exceed 1 m/s only on spring tides and typically reach on 0.5 m/s.

Reynolds stresses exceed 50 cm^2/s^2 on spring ebb tides and typically reach 20 cm^2/s^2 on most ebb tides, but seldom reach 10 cm^2/s^2 during flood tide. Reynolds stress decreases roughly linearly with height above the bottom but during strong southerly winds, and especially during ebb, very large stress is seen in the upper 2-4 m measured by the ADCP.

The remarkable difference between ebb and flood bottom stress persists over the spring-neap cycle. Ebb stress is typically 3-5 times as large as that on flood and reflects the much larger currents on ebb than on flood. This is likely related to the strong mean export in this part of the inlet; mean currents over the measurement period are directed seaward at 0.1-0.2 m/s. Net riverine inflow to the system is small, and unless other inlets to the sounds are importing seawater, there must be net inflow over some part of the inlet.

As in Stacey *et al.* [1999b] the stress measurements are somewhat noisy so composite tidal cycles have been formed by averaging 4 tidal cycles near maximum and minimum tidal range, similar to Peters [1999]. These composites
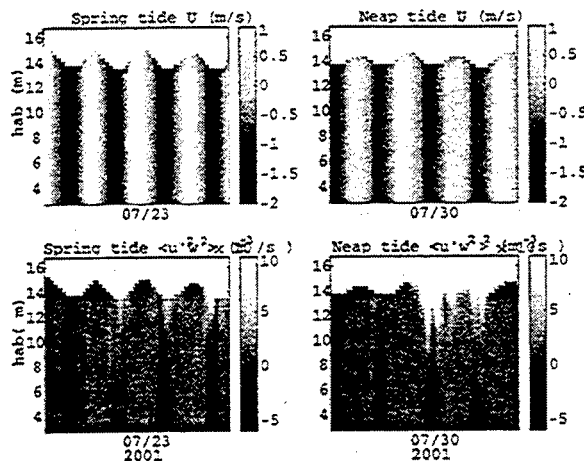
Figure 2. Contoured velocity (top) and stress (bottom) fields for several days near maximum tidal range (left) and minimum tidal range (right). Ebb-directed flows are negative.
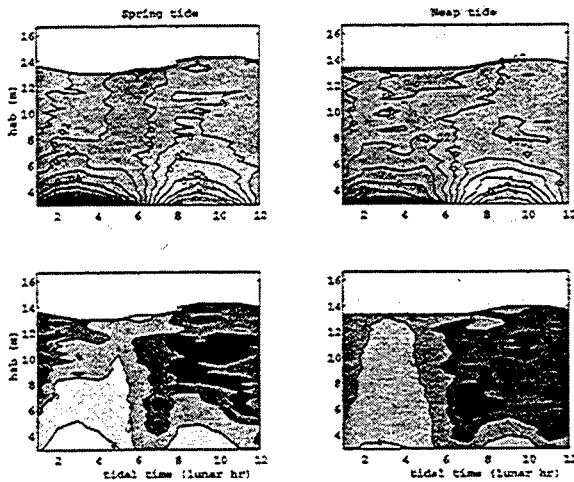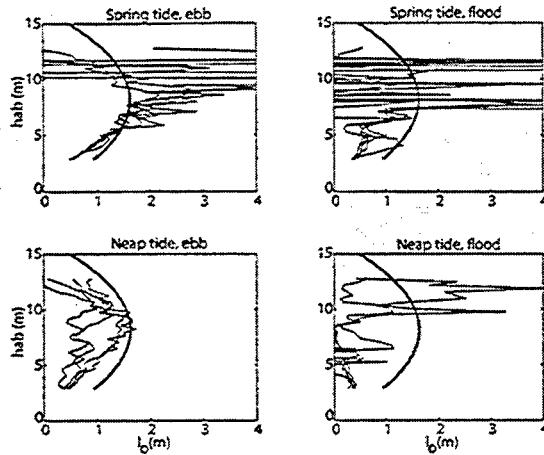

Figure 4. Estimates of the mixing length for the composite conditions as labeled. The bold line on each panel gives a parabolic mixing length for the observed depth.

Figure 3. Contour plots of shear of the along-channel current (in s^{-1}, top) and logarithm of the turbulent production (m^2/s^3, bottom) during spring tide (left) and neap tide (right) conditions from the composite data.

are then used to examine vertical structure of the Reynolds stress, turbulent production and the mixing length.

Vertical shear of the horizontal current is maximum near the bed and decreases to less than 0.02 s^{-1} within 5 mab. Above this height the shear on ebb extends to the surface during low wind conditions and is essentially zero on flood, but can be of either sign in the upper water column when the winds exceed 5 m/s. Southerly winds reinforce flood tide shear and can decrease or reverse shear in the upper water column on ebb. This can be seen in contours of the neap tide composite data (Figure 3) where the shear changes sign in the upper water column.

The strength of the turbulent production can be estimated as $P = - < u'w' > (\partial \overline{u}/\partial z)$; estimates from the composite data are presented in Figure 3. Peak values exceed 10^{-4} m^2/s^3 near the bed. The bottom-generated turbulence can extend to nearly the surface on ebb but is typically trapped within a 4-6 m of the bottom on flood even during spring tides. The exception to this occurs during periods of reasonably strong winds, and presumably breaking waves, and causes production to increase near the ocean surface.

Assuming a local turbulent balance, estimates of the vertical eddy viscosity A_v can be formed as $- < u'w' > /(\partial \overline{u}/\partial z)$. Obviously the formulation can not work where mean shear is near zero, and can not be expected to work in the near surface when wave breaking, rather than mean shear, is the source of energy. Nevertheless, reasonably consistent estimates results at times of non-zero mean shear and give values $10^{-3} - 10^{-1}$ m^2/s. A simple scaling of the eddy viscosity is $A_v = u_* l_o$ where $u_* = sign(- < u'w' >)|- < u'w' >|_{z=0}^{1/2}$ is the friction velocity and l_o is the mixing length. Profiles of l_o for the 4 cases shown in the previous plots are presented in Figure 4. A parabolic mixing length profile $\kappa(z/H)H(1 - z/H)$, where κ is von Karman constant of 0.4 and H is the water depth, is shown for comparison. Only during spring ebb tide does the observed mixing length rise to the theoretical prediction; in all other cases the observed scales are smaller. The difference is greatest during flood tides, and neap tides in particular.

The near bottom Reynold's stress and the depth-averaged tidal currents are highly correlated. Estimates of the drag coefficient $C_d = - < u'w' > /\overline{u}^2$ based on the 10 minute averaged data vary systematically between 0.0021 on ebb and 0.0013 during flood (Figure 5).
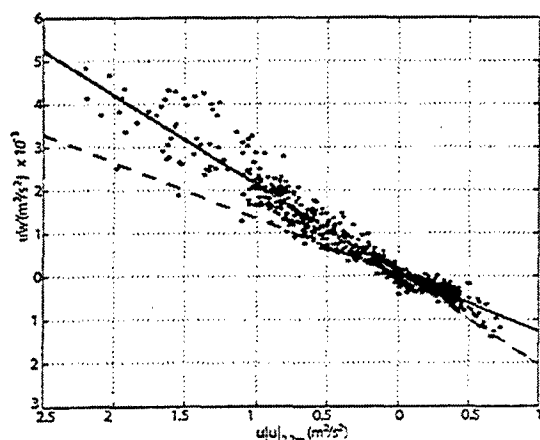
Figure 5. Comparison of squared velocity at 2.7 m above bottom and 10 minuted average — $< u'w' >$ averaged over 2.5-5.5 m above bottom. Linear fits for ebb flow yield a drag coefficient of 0.0021 and fits for flood yield a drag coefficient of 0.0013.

Discussion and Conclusions

The variance technique for measuring Reynolds stress profiles from a bottom mounted deployment would appear to be well-suited to studies of turbulence in sea straits. Continuous estimates of near bottom turbulent production in these energetic flows would nicely complement other measurement techniques. Whereas shear probes are designed to sense the smallest levels of turbulence in the ocean and do not resolve intense turbulence well, the Reynolds stress estimated from the ADCP is noise-limited at low turbulence levels and better suited to measuring very energetic flows.

In the case of Beaufort Inlet bottom-generated turbulence dominates the 15 m deep water column on ebb flows, but its influence is trapped in the lowest 5 m on flood. Preliminary examination of observations of the density field reveal a dense inflow that begins as the tide changes for ebb to flood. The near-bottom stratification it causes may act to suppress overturning as the tidal current changes direction and limit overturning scales throughout the flood. As can be seen from the estimates of C_d the difference in stress between ebb and flood flows is persistent. Quantifying this relationship is being actively pursued.

The near-surface maxima in Reynolds stress associated with southerly winds raises the intriguing possibility of measuring the momentum flux associated with wave breaking. Though Reynolds stress estimates from point measurements of turbulent velocities can be contaminated by surface gravity waves [Trowbridge , 1997], the author is unaware of studies of the susceptibility of the ADCP measurements to contaimination from surface gravity waves. It should be noted that the near surface stress was high only during strong southerly winds and peaked during ebb flow, when currents would oppose wave propagation, consistent with times of en-

hance wave breaking. Obviously simultaneous high quality wave measurements will be required to resolve this issue.

References

Di Iorio, D. and H. Yuce, 1999. Observations of Mediterranean flow into the Black Sea, *J. Geophys. Res.*, 104, 3091-3108.

Gregg, M. C., E. Ozsoy and M. A. Latif, 1999. Quasi-steady exchange flow in the Bosphorus, *Geophys. Res. Lett.*, 26, 83-86.

Helfrich, K. R., 1995. Time-dependent two-layer hydraulic exchange flows. *J. Phys. Ocean.*, 25, 359-373.

Lu, Y and R. G. Lueck, 1999. Using a broadband ADCP in a tidal channel. Part II: turbulence, *J. Atmos. Ocean Tech.*, 16, 1568-1579.

Peters, H., 1999. Spatial and temporal variability of turbulent mixing in an estuary, *J. Mar. Res.*, 57, 805-845.

RD Instruments, 1998. Workhorse technical manual, RD Instruments, San Diego, CA.

Stacey, M. T., S G. Monismith and J. R. Burau, 1999. Observation of turbulence in a partially stratified estuary, *J. Phys. Ocean.*, 29, 1950-1970.

Stacey, M. T., S G. Monismith and J. R. Burau, 1999. Measurements of reynolds stress profiles in unstratified tidal flow, *J. Geophys. Res.*, 104, 10,933-10,9490.

Trowbridge, J. H., 1997. On a technique for measurement of turbulent shear stress in the presence of surface waves, *J. Atmos. Ocean Tech.*, 15, 290-298.

Wesson, J. and M. C. Gregg, 1994. Mixing at Camarinal Sill in the Strait of Gibraltar, *J. Geophys. Res.*, 99, 9847-9878.

H. E. Seim, Dept. of Marine Sciences, 12-7 Venable Hall, CB#3300,University of North Carolina, Chapel Hill, NC 27599

Exchange flow between the Red Sea and the Gulf of Aden.

M. Siddall[1], D.A. Smeed[1], S. Mathiessen[2] and E.J. Rohling[1].

[1]Southampton Oceanography Center, Southampton, United Kingdom
[2]Deptartment of Meteorology, University of Edinburgh, Edinburgh, United Kingdom.

Abstract. A hydraulic model has been developed to simulate the seasonal cycle of the exchange flow in the Strait of Bab el Mandab. To a good approximation the model recreates observed fluxes through the strait. We attribute this success to our use of a realistic channel cross-section. The model results indicate that the summertime intrusion of Gulf of Aden Intermediate Water into the Red Sea has been a feature of the exchange for at least 10 500 years.

Introduction

The Red Sea is a long narrow basin connected with the Gulf of Aden to the south via the Bab el Mandab Strait. The shallowest section of Bab el Mandab Strait consists of Hanish sill and is located 150 km to the north of the narrowest passage, Perim Narrows.
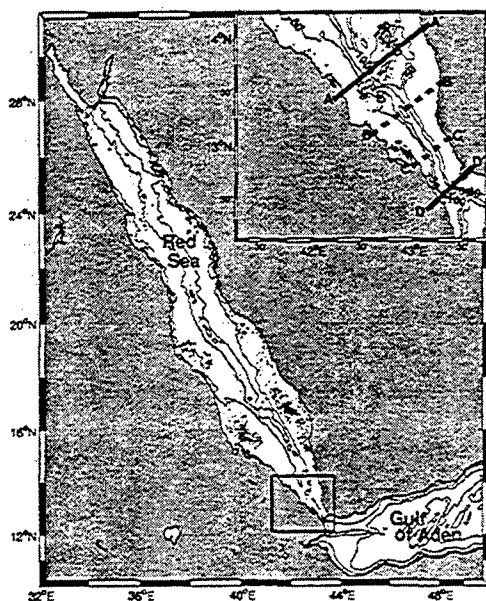

Figure 1: The Red Sea with a detailed projection of the Bab el Mandab Strait (top right). The letters mark the transects used for the mean cross-section in figure 3. AA' is at Hanish Sill and DD' is at Perim Narrows.

The greatest depth at the sill is 137 m (figure 1). The total width of the sill section is about 110 km (Werner and Lange 1975). The sill depth maximum occurs within a deep passage that is 6km wide, outside of which the depth is of the order of 50 m (Murray and Johns 1997). The total width at the Perim Narrows is only about 18km (Murray and

Johns 1997) with a depth of about 300m in the central channel (Maillard and Soliman 1986).

Winds and low freshwater input determine a strong net evaporation over the Red Sea of around 2.06 ± 0.22 m y^{-1} (Sofianos et al. in press). The continual basin wide buoyancy loss due to this evaporation is responsible for the creation of Red Sea Overflow Water (RSOW).

RSOW is observed to flow out of the Red Sea at the Bab el Mandab Strait throughout the whole year (Pratt, Johns et al. 1999; Pratt, Deese et al. 2000). Between November and early June (winter regime) this outflow is balanced simply by an inflow of Gulf of Aden Surface Water (GASW). From June to October the South West monsoon winds provoke an upwelling of Gulf of Aden Intermediate Water (GAIW) to the south of the straits (Smeed 1997). This intermediate layer moves towards the Red Sea as it is upwelled. The flux of GAIW towards the Red Sea eventually becomes greater than the outflow of. The winter surface inflow of GASW is forced to reverse in order to balance the inflowing GAIW and conserve the total volume of water in the basin (figure 2) (Smeed 1997; Smeed 2000; Sofianos et al. in press).

Smeed (2000) attempts to model the seasonally varying two/three-layer annual exchange cycle in the Red Sea. While his work effectively generates the annual cycle in a qualitative sense, it overestimates the fluxes by a factor of two. Smeed (2000) suggests that this poor quantitative reproduction of observations may result from the unrealistic rectangular bathymetry used in the model since Bryden and Kinder (1991) found that realistic bathymetry affected the calculated fluxes (in their case in the Mediterranean) by a factor of three.
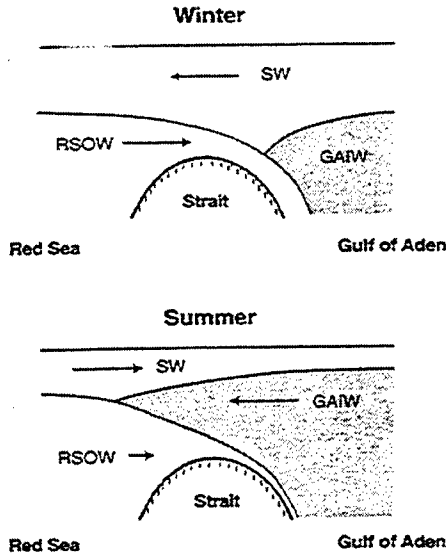
$$b(z) = \exp(kz) \qquad (1)$$

Where b is the non-dimensional width of the channel and z is the non-dimensional depth. The constant k in the exponential function (1) is least squares fitted to the curve of width against depth. The value of k used in the model is 3 ± 0.2. Integrating across the ith layer from $z = d_{i-1}$ to d_i gives a_i, the non-dimensional cross sectional area of layer i.

Bernoulli Functionals

The approach used is to conserve the Bernoulli energy along the strait. Lane-Serff et al (2000) derive the generalized Bernoulli functionals (2) for many layers, using the three-layer case as a specific example:

$$\frac{1}{2}\left(\frac{Q_1}{A_1}\right) - \frac{1}{2}\left(\frac{Q_2}{A_2}\right) + g'_1 D_1 = H_1'$$

$$\frac{1}{2}\left(\frac{Q_2}{A_2}\right) - \frac{1}{2}\left(\frac{Q_3}{A_3}\right) + g'_2 (D_1 + D_2) = H_2' \qquad (2)$$

Where Q is the flux in a given layer (subscripts 1, 2, and 3 denote the upper, middle and lower layer respectively), A is the cross-sectional area of that layer, D is the interface depth below a given layer and H_- the Bernoulli constant for the interface. The reduced gravity, g_-, of the interface is given by $g'_i = 2g(\rho_{i+1} - \rho_i)/\overline{\rho}$ where ρ stands for the density and $\overline{\rho}$ is the mean density of all the layers. Unless stated explicitly upper case letters are used to denote dimensional numbers and lower case letters denote their non-dimensional counterparts.

The Bernoulli functionals (2) assume an inviscid, hydrostatic and Boussinesq fluid in three discrete layers beneath a rigid lid. Since any changes in strait width are small compared to along-strait distance the flow may be assumed to be uni-directional within each layer. The flow is assumed to be non-rotating. The rigid lid assumption forces the fluxes to balance so that: $Q_1 + Q_2 + Q_3 + E = 0$, where E is the net evaporative flux from the Red Sea basin.

For the purposes of the model the equations are non-dimensionalised according to B_S and D_S (the surface width and maximum depth of the channel at the sill) and the total reduced gravity $g' = g_1' + g_2'$. The precise non-dimensionalisations are given in the

Figure 2: Schematic of the summer and winter exchange regimes. Water mass definitions are given in the text.

Model configuration

The model consists of two reservoirs of infinite depth and width joined by a channel of uniform, finite width and non-rectangular cross section. The channel shallows to a minimum depth at the sill.

Figure 3: Mean channel width against depth calculated from the transects labeled in figure 1 (dashed line) and the best fit of the exponential function (1) (full line) plotted symmetrically.

To establish width against depth for the channel four cross sections were taken along the strait. These sections were non-dimensionalised with the maximum depth (D) and surface width (B) of the channel at each transect. A mean was generated for the non-dimensional widths at respective depths. Exponential function (1) was fitted to this curve.

equations set (3). The subscript S denotes values for the sill.

$$Q_i = A_S(g'D_S)^{1/2}q_i \,, \; H_i' = g'D_S H_i \,, \; g_2' = (1-r)g'$$
$$D_i = D_S d_i \,, \; B_i = B_S b_i \,, \; A_i = a_i A_S \,, \; g_1' = rg' \,, \quad (3)$$

For a hydraulic control to be present at a given position the flow must suit the critical condition (6), the Bernoulli constants must be conserved (4,5) and a regularity condition met (below). The Bernoulli functionals in three layers turn out to be quartics so that the correct solution branch for a given set of driving parameters should be selected. The solution branches are chosen to satisfy the control conditions. The non-dimensional Bernoulli Functionals are:

$$J = \frac{1}{2}\left(\frac{q_1}{a_1}\right) - \frac{1}{2}\left(\frac{q_2}{a_2}\right) + rd_1 - H_1 = 0 \quad (4)$$

$$K = \frac{1}{2}\left(\frac{q_2}{a_2}\right) - \frac{1}{2}\left(\frac{q_3}{a_3}\right) + d_2(1-r) - H_2 = 0 \quad (5)$$

Criticality or control is defined as the point downstream from which the flow is such that one or more of the internal wave modes are swept downstream and cannot communicate with the upstream reservoir. In three layers with non-uniform cross section the control condition is:

$$F_2^2\left(F_2^2 \frac{b_1}{b_2}\right) - \left(r - F_1^2 - F_2^2 \frac{b_1}{b_2}\right)\dots$$
$$\dots\left(1 - r - F_2^2 - F_3^2 \frac{b_2}{b_3}\right) = 0 \quad (6)$$

We define F_i as the layer Froude number where $F_i^2 = b_i q_i^2 / a_i^3$.

The regularity condition requires that the solution at the control is realizable (Dalziel 1991). Given basins of infinite depth and width, connected by a channel with parallel sides, the regularity condition can only be satisfied, and hence controls exist, at the sill or either of the two 'exits' (Killworth 1992). Thus the simplification of parallel isobaths allows us to determine the location of the controls and so the degrees of freedom (unknowns) in the problem are reduced. In reality the 'exit' controls move along the straight as a function of the driving parameters of the flow.

When necessary hydraulic jumps are assumed present but not calculated explicitly. The only condition applied to them is that the total energy is higher upstream of them than downstream. Note that if the intermediate layer is not present all equations become identical to those for the two-layer case (Dalziel 1991).

Assuming that layers 2 and 3 reduce to zero thickness at the Red Sea and Gulf of Aden exits respectively there exists a total of eight variations on equations (4-6). A solution type is defined by the position of the controls with respect to the sill and two exits (Smeed 2000). Depending on the solution type a combination of the eight variations on equations (4-6) is solved simultaneously using numerical methods.

Driving Parameters

The net evaporative flux over the basin is taken from Sofianos et al. (in press) which gives a maximum of $2.8 \pm$ m yr^{-1} in mid-winter and a minimum of $1.4 \pm$ m yr^{-1} in mid-summer. The reduced gravity used is that used for Smeed's (2000) model. The ratio of the density change across the upper interface to the density change across the two interfaces, r, varies with g_1', the reduced gravity for the upper interface (g_2' is constant throughout the year (Smeed 1997)): a value of $r = 1/2$ is used found in mid-winter, which increases to $r = 2/3$ in mid-summer. The evaporative flux and r are made to vary sinusoidally with maxima in June and July respectively .

Pratt et al (1999) have made monthly mean current meter readings at the Hanish Sill and Perim Narrows. The velocity zero crossing which represents the base of the upper layer in their data occurs at an isopycnal of 1024.7 kg cm^{-3}. The interface depth in the Gulf of Aden used to drive the model is given by the depth of the 1024.7 kg cm^{-3} isopycnal from Levitus data, and varies approximately sinusoidally between 20 ± 5 m in mid-July and 110 ± 5 m in March. For the purposes of the model we fit a sine curve to this signal with a maximum in mid-July.

The coverage of Levitus data in the Red Sea is too low to be used to generate similar values in the Red Sea. The 1024.7 kg cm^{-3} isopycnal resides at approximately 40 ± 10 m depth in the June observations of Neuman and McGill (1962). Maillard and Soliman's (1986) October observations are disrupted by the presence of a meso-scale eddy but still show the 1024.7 kg cm^{-3} isopycnal at about the same depth of $\sim 40 \pm 10$ m. The Red Sea interface

depth is therefore taken at a constant depth of 40 ± 10 m.

Discussion and conclusions

Results are shown in figure (4). This work represents the first quantitative model reproduction of the Red Sea exchange flux. The model successfully predicts the transition from two to three-layer exchange in the form of an inflowing layer of GAIW. The transition of the surface layer from inflowing GASW to outflowing RSSW is also predicted. The solution types agree with those found in previous generations of the model.
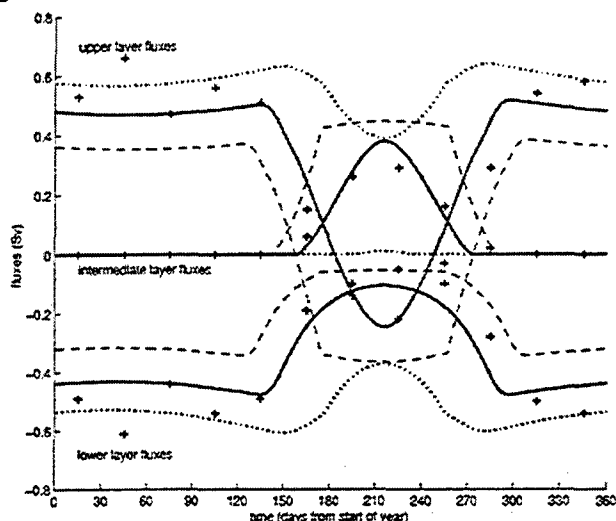

Figure 4: Modeled fluxes in the at the Strait of Bab el Mandab. According to uncertainties in the values used to force the model _ is the best estimate, —— is the minimum estimate and _____ is the maximum estimate. Observations are marked by a + (Sofianos et al in press)

The intrusion of the third layer (GAIW) into the Red Sea appears to be a robust feature of the exchange. It currently intrudes into the Red Sea when the driving interface height in the Gulf of Aden is < 40 m or ~ 0.3 times the sill depth. In the model the shallowest interface depth in the Gulf of Aden used to force the GAIW intrusion is 20 m. Ignoring any variation in monsoonal strength, Red Sea interface depth, change in the channel width with depth, a tentative first approximation can be made of the sea level position at which the intrusion commences. This is carried out by considering when the total depth at the sill = $^{20}/_{0.3}$ m. This would suggest that the total sill depth would need to be about 70 m, and sea level would therefore be 65-70 m lower than today, a condition achieved around 10500 years before present (Fairbanks 1989). This method

predicts gives a minimum age of the three-layer exchange since the channel thins with depth. The upper layer flow reversal would also first occur at around that time.

References

Bryden, H., L. and T. Kinder, H. "Steady two-layer exchange through the Strait of Gibraltar." *Deep Sea Res. 38*: 445-463, 1991.

Dalziel, S., B. "Two-layer hydraulics: a functional approach." *J. Fluid Mech. 223*: 135-163, 1991.

Fairbanks, R., C. "A 17 000 year glacio-eustatic sea level record: influence of glacial melting rates on the Younger Dryas event and deep ocean circulation." *Nature 342*: 637-642, 1989.

Killworth, P., D. "On hydraulic control in a stratified fluid." *J. Fluid Mech. 237*: 605-626, 1992.

Lane-Serff, G., F., D. Smeed, A., et al. "Multi-layer hydraulic exchange flows." *J. Fluid Mech. 416*: 269-296, 2000.

Maillard, C. and G. Soliman. "Hydrography of the Red Sea and exchanges with the Gulf of Aden in Summer." *Ocean. Acta 9(3)*: 249-269, 1986.

Murray, S., P. and W. Johns. "Direct observations of seasonal exchange through the Bab el Mandab Strait." *Geophys. Res. Lett. 24(21)*: 2557-2560, 1997.

Neuman, A., Conrad and D. McGill, A. "Circulation of the Red Sea in early summer." *Deep-Sea Res. 8*: 223-235, 1962.

Pratt, L., J., W. Johns, et al. "Hydraulic interpretation of direct velocity measurements in the Bab el Mandab Strait." *J. Phys. Ocean. 29*: 2769-2784, 1999.

Smeed, D., A. "Seasonal Variation of the flow in the strait of Bab el Mandab." *Ocean. Acta 20(6)*: 773-781, 1997.

Smeed, D., A. "Hydraulic control of three-layer exchange flows: application to the Bab-al-Mandab." *J. Phys. Ocean. 30*: 2574-2588, 2000.

Sofianos, S., S., W. Johns, W., et al. "Heat and frehwater budgets in the Red Sea from direct observations at Bab el Mandab." *Deep Sea Res., in press*.

Werner, F. and K. Lange. "A Bathymetric Survey of the Sill Area between the Red Sea and the Gulf of Aden." *Geol. Jahrb. D 13*: 125-130, 1975.

A three-dimensional model of Bosphorus Strait dynamics

Adil Sözer and Emin Özsoy

Institute of Marine Sciences, Middle East Technical University, Erdemli - İçel 33731 Turkey

Abstract. Bosphorus Strait exchange ows are studied based on SCRUM, a 3-D ocean model with alternative parameterisations of mixing, advection and eddy diffusion, as well as free-surface dynamics. The response of the Strait is investigates with respect to the choices of open boundary conditions and mixing parameters, under idealized geometrical and hydrographical conditions. The selection of open boundary conditions is shown to be crucial, and depends on the direction of net ow. Blocked ow conditions for both ow directions are successfully simulated. The results of sensitivity tests are reported.

Introduction

The exchange flow through the Bosphorus Strait is principally determined by geometry and stratification, and exhibits a complex nonlinear response to forcing by the net water budget, pressure and wind setup effects in adjacent basins [Ünlüata et al., 1990; Özsoy et al., 1998; Gregg et al., 1999; Gregg and Özsoy, 2001]. Time-dependent forcing creates daily to interannual variability in the currents and extreme conditions result in temporary blocking of the flows in either direction [Özsoy et al., 1996, 1998].

The development of realistic numerical models of strait exchange flows has to resolve difficulties imposed by parameterization of mixing, as well as the need to implement physically relevant boundary conditions. Reduced order models based on the two-layer approximation have been used by [Oğuz et al., 1990; Brandt et al., 1986]. Recent developments by [Winters and Seim, 2000; Hogg et al., 2001] utilize a three-dimensional model with rigid-lid dynamics and parameterized vertical mixing.

The present study aims for a better understanding of the behaviour of Bosphorus Strait flows based on a realistic three-dimensional model of its dynamics. As a first step before considering the application of the model to actual conditions of the Bosphorus Strait, the response of the Strait is investigated with respect to open boundary conditions corresponding to idealized geometrical and hydrographical conditions. As opposed to earlier studies, we use a model with free-surface dynamics. Although the rigid-lid assumption would be appropriate for long-term dynamics, the presence of a free surface is essential to predict short-term changes and relate them to sea-level variability in the Strait and the adjacent basins.

Model description

The free-surface primitive equation model, SCRUM, is used for numerical simulations of the idealized Bosphorus
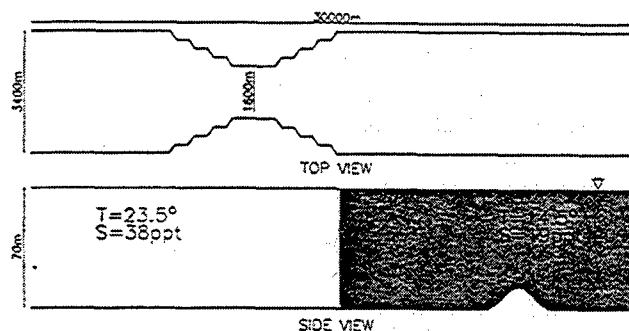

Figure 1. Model geometry: top and side views of the channel

Strait flows. The model has terrain-following coordinates, optional mixing parameterizations and various choices for the bottom, solid or open boundary conditions []. Idealized model geometry of a straight channel with a contraction and a sill, as shown in Figure 1, is considered. A contracting channel, $3.4km$ in width and $30km$ in length, is overlaid on a 17×100 rectilinear grid for numerical simulations.

The initial conditions for tracers consist of water masses with contrasting temperature and salinity values (Figure 1) typical of Marmara and Black Sea waters, meeting at mid-channel. In all runs, free slip boundary conditions are used on the side walls and the bottom. The Smolarkiewicz tracer advection scheme is used to escape the overshooting effect of centred advection, while dealing with sharp gradients. Laplacian diffusion is assumed in the horizontal and vertical directions, with typical diffusion coefficients in ranges of $K_h = 150 - 350m^2/s$ and $K_v = 10^{-6} - 10^{-3}m^2/s$ respectively, for tracers and momentum. To ensure stable integrations, a time step of 5 seconds for the baroclinic modes have been used in all model runs, with a barotropic time step that is 20 times smaller.
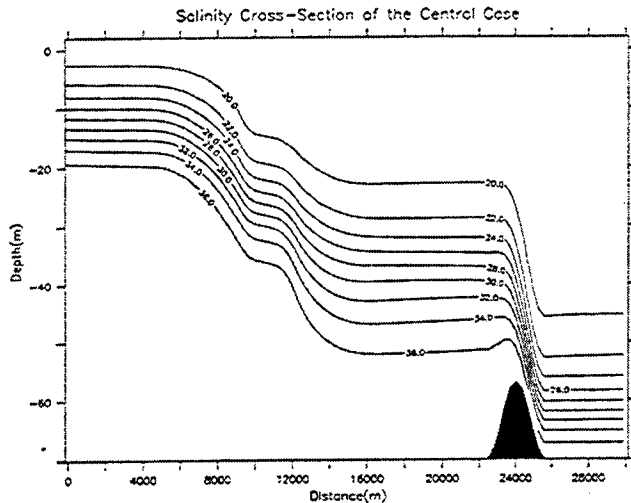
Figure 2. Salinity cross-section for the central run

Figure 3. Salinity cross-sections for cases in which (a) the upper layer or (b) the lower layer is blocked

Results

Open boundary conditions

In order to test the model behaviour, trials were made using various types of initial and boundary conditions. The choice of initial conditions were critical in reaching physical solutions. Because radiation boundary conditions were used for tracers at both ends, the tracer advection by inflowing waters tended partially to carry back into the model domain the properties of outflowing waters from the counter-flowing current. Instead, the 'lock-exchange' initial conditions were used as they avoided this behaviour.

Various types of free surface and velocity boundary conditions were tested at the two open boundaries. Because the cases tested were symmetrical along the long axis, and because free slip conditions were assumed, the normal velocity at solid boundaries and the tangential velocity at open boundaries were respectively always set equal to zero. The mixing coefficients were varied in the range mentioned earlier until more robust results were obtained in terms of free surface response and mass conservation. The mixing coefficients for momentum and tracers determined from this exercise were $K_h = 250 m^2/s$ and $K_v = 10^{-4} m^2/s$, which were then used for the central run.

A special case with radiation boundary conditions for all variables (free surface elevation, velocity and tracers) on each side, started from a lock-exchange initial condition (with water properties in Figure 1), reached a stable solution shown in Figure 2. This result was remarkable, and confirmed the existence of a maximal exchange solution supported by the special geometry of a sill placed on the denser side of a contraction as shown by *Farmer and Armi* [1986]. The mean velocity corresponding to this case was calculated to be $\bar{u} = 0.065 m/s$. For a single sill or a single contraction with the same boundary and initial conditions such stable solutions could not be obtained. The two-layer composite
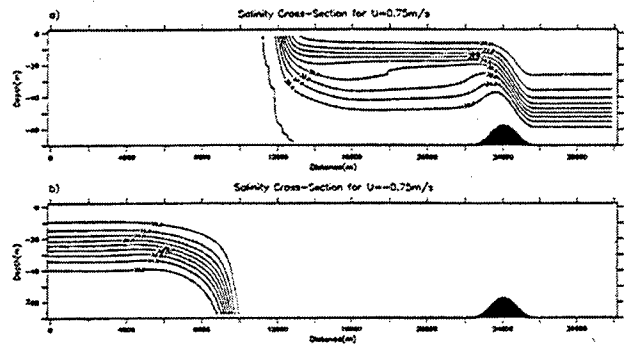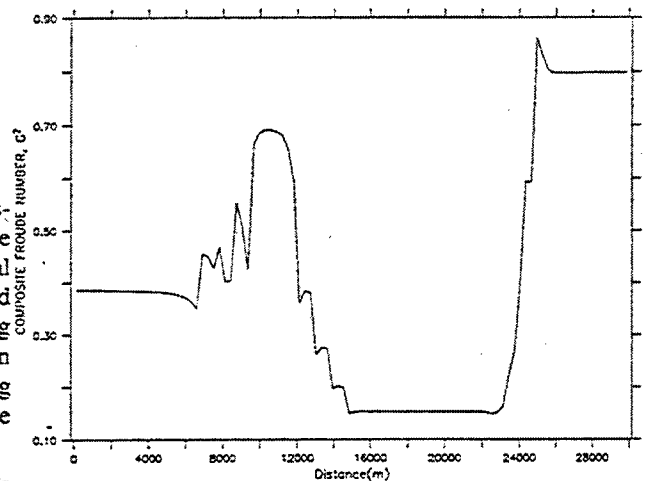

Figure 4. Composite Froude Number for the central run

Froude number $G^2 = F_1^2 + F_2^2$ (where $F_i^2 \equiv \bar{u}_i^2/gh_i$ are the individual Froude numbers of the layers i each with depth h_i and mean along-strait velocity $\bar{u}_i$, delineated by an interface where the horizontal velocity vanishes $\bar{u} = 0$) shown in Figure 2 indicates hydraulic controls established at the sill (where the lower layer is controlling) and at the contraction (where each of the layers contribute comparably to the control). The number G^2 peaks up, but fails to reach a value of 1 at the contraction, mainly because of the two-layer approximation used, as also the case in the observations [*Gregg et al.*, 1999; *Gregg and Özsoy*, 2001].

For most configurations, including the all-radiation case described above, the model had a robust response whenever stable solutions could be reached. There was a deficiency of the model in creating smooth sea level variations near the open boundaries under certain conditions. For such cases, the free surface fields produced by the model often were discontinuous exactly at the open boundary, while being continuous in the rest of the domain. This effect was minimized by appropriate choices of open boundary conditions and mixing
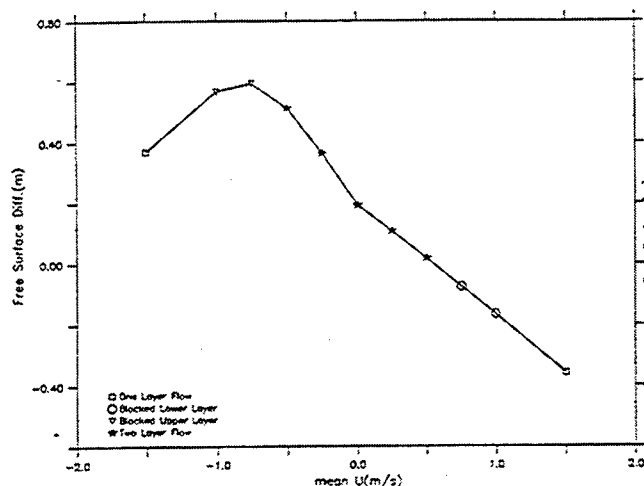
Figure 5. Sea level difference $\Delta\eta$ versus the mean current $\bar{u}$

Figure 6. Along-channel variation of the free surface elevation η for different values of mean current $\bar{u}$. The dotted line corresponds to Figure 2, while the others correspond to the blocked cases in Figure 3

coefficients.

In order to seek solutions corresponding to a specific value of the barotropic flow through the Strait, a strategy had to be found for specifying open boundary conditions. The first case tested used radiation boundary conditions for the normal velocity components u, and specified free surface elevation η at open boundaries at the two ends of the Strait. This type of boundary conditions failed to create stable solutions, because the pressure difference between the two ends of the Strait could not set into motion the water masses in the Strait to generate a corresponding net flux. It was therefore required to specify barotropic velocities at the open boundaries, in order to produce a net flux and a corresponding pressure difference across the Strait.

Specifying the sea-level η and cross-sectional mean velocity $\bar{u}$ at the two ends of the strait did not produce stable results when it was left arbitrary on which side to apply these boundary conditions. It was apparent after many trials that the model produced reliable results only when the mean velocity $\bar{u}$ was specified at the outflowing boundary, together with the free surface η specified at the other (inflowing) end of the Strait. In addition, experiments were carried out in which the specified values of η or $\bar{u}$ were either applied alone or together with a radiation term. In general, the results were similar; however, the specified value of $\bar{u}$ at the southern end of the Strait resulted in stable solutions only if there was no additional radiation term applied.

Although the above specification of η and $\bar{u}$ at opposite ends depending on flow direction consists of a complete set of boundary conditions, steady solutions were also possible if only $\bar{u}$ was specified at the outflowing side, applying radiation boundary conditions for η on both sides of the Strait. In these cases, the solution converged to an absolute sea level value that corresponded to the specified net flow. However, to get consistent results corresponding to different flow rates, the free surface was specified to be $\eta = 0$ at the inflowing open boundary, so that the level was adjusted at the opposite
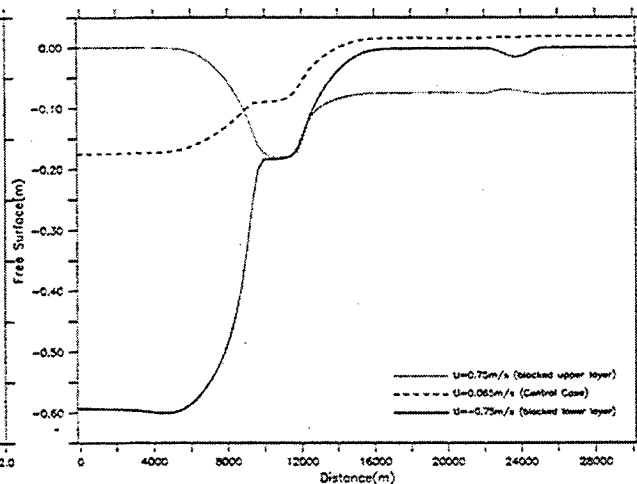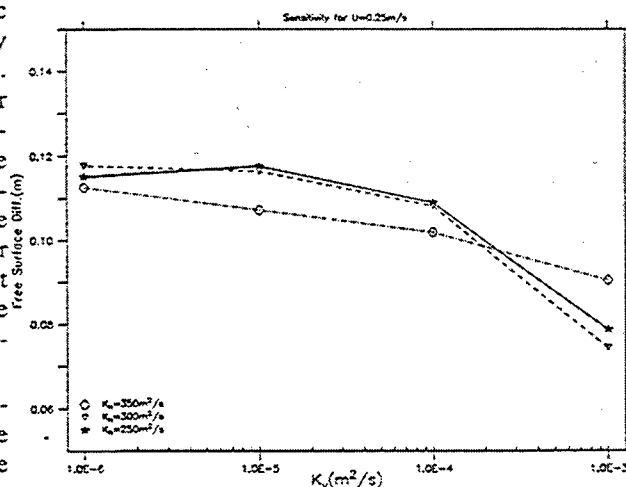

Figure 7. Sea level difference $\Delta\eta$ as a function of horizontal (K_h) and vertical (K_v) diffusion coefficients

side of the Strait.

A series of runs were performed with the above boundary conditions, while varying the net flow $\bar{u}$ from $-1.5m/s$ to $1.5m/s$. Figure 3 shows salinity cross-sections along the centerline of the Strait, for selected net flows producing blocking of the upper and the lower layers. Figure 4 shows the variation of the free surface elevation along the Strait, and Figure 5 shows the free surface difference between the two ends of the Strait as a function of the mean flow. The sea level variations in Figure 6 correspond to the the central run and the two blocked cases in Figures 2 and 3.

Parameter sensitivity

Sensitivity tests were carried out, by varying parameters about the central run with $\bar{u} = 0.25m/s$. In general,

these sensitivity runs produced similar steady solutions with little change in behaviour. Yet, it was observed that the vertical diffusion coefficients controlled the sea level difference along the Strait, decreasing by about 30% when K_v was increased by three orders of magnitude between $K_v = 10^{-6} m^2/s$ and $K_v = 10^{-3} m^2/s$, as shown in Figure 7.

Discussion and conclusions

A three-dimensional dynamical model has been demonstrated to be applicable to the special case of strait exchange flows. The selection of open boundary conditions is a nontrivial first step for succesful applications of the model. The results obtained from tests with idealized cases corresponding to the Bosphorus Strait indicate the need for judicious choices of boundary conditions, which depend on the flow direction. However, the results obtained with these choices and even the case with purely radiation boundary with purely radiation boundary conditions started from 'lock exchange' initial conitions, support the existence of maximal exchange with controlled flows first pointed out by *Farmer and Armi* [1986], and exemplified by observations in the Bosphorus.

The results encourage us to use the model for a better understanding of the dynamis of the Bosphorus. While the simple cases reported here provide confidence in the combined use of observations of and modelling, the extensions of the model application to transient cases and realistic Bosphorus geometry through the use of curvilinear coordinates are the next few steps we are currently working on.

References

Brandt, P., A. Rubino, W. Alpers, and J. O. Backhaus, 1997. Internal Waves in the Strait of Messina studied by a numerical model and synthetic aperture radar images from the ERS 1/2 satellites, *J. Phys. Oceanogr.*, 27, 648-663.

Farmer, D. M. and Armi, L., 1986. Maximal two-layer exchange over a sill and through the combination of a sill and contraction with barotropic flow, *J. Fluid Mech.*, 164, 53-76.

Gregg, M. C., Özsoy, E. and Latif, M. A., 1999. Quasi-steady exchange flow in the Bosphorus *Geophysical Research Letters*, 26, 83-86.

Gregg, M. C. and Özsoy, E., 2001. Flow, water mass changes, and hydraulics in the Bosphorus, *J. Geophys. Res.*, (in press).

Hedström, K. S., 1997. Draft User's Manual for an S-Coordinate Primitive Equation Ocean Circulation Model (SCRUM) Version 3.0, Institute of Marine and Coastal Sciences, Rutgers University, Rutgers University.

Hogg, A. McC., Winters, K. B. and G. N. Ivey, 2001. Linear Internal Waves and the Control of Stratified Exchange Flows, *J. Fluid. Mech.*, 447, 357-375.

Oğuz, T., Özsoy, E., Latif, M. A. and Ünlüata, Ü., 1990.

Modelling of hydraulically controlled exchange flow in the Bosphorus Strait, *J. Phys. Oceanogr.*, 20, 945-965.

Özsoy, E., Latif, M. A., Sur, H. İ. and Goryachkin, Y., 1996. A review of the exchange flow regimes and mixing in the Bosphorus Strait, in: Briand, F. (editor), Mediterranean Tributary Seas, *Bulletin de l'Institut Oceéanographique, Monaco*, Special Number 17, CIESM Science Series No. 2, Monaco.

Özsoy, E., Latif, M. A., Beşiktepe, Ş., Çetin, N., Gregg, N. Belokopytov, V., Goryachkin, Y. and Diaconu, V., 1998a. The Bosphorus Strait: exchange fluxes, currents and sea-level changes, in: Ivanov, L. I. and Oğuz, T. (editors), *Ecosystem Modeling as a Management Tool for the Black Sea*, NATO Science Series 2: Environmental Security 47, Kluwer Academic Publishers, Dordrecht, vol. 1, 367pp + vol. 2, 385 pp.

Ünlüata, Ü., Oğuz, T., Latif, M. A., and Özsoy, E., 1990. On the physical oceanography of the Turkish Straits, in: Pratt, L. J., (editor), *The Physical Oceanography of Sea Straits*, NATO/ASI Series, Kluwer, Dordrecht, 25-60.

Winters, K. B. and H. Seim, 2000. The Role of Dissipation and Mixing in Exchange Flow through a Contracting Channel, *J. Fluid. Mech.*, 407, 265-290

A. Sözer and E. Özsoy, Institute of Marine Sciences, Middle East Technical University P.K. 28 Erdemli - İçel 33731 Turkey

The path of the overflows from the sills in the Sicily Strait

Kate Stansfield [1], D. A. Smeed [1] and G. P. Gasparini [2]

[1] Southampton Oceanography Centre, University of Southampton, European Way, Southampton. UK
[2] Istituto per lo studio dell'Oceanografia Fisica, Forte Santa Teresa, 19036 Pozzuolo di Lerici (SP), Italia

Abstract. High-resolution velocity and hydrographic measurements are used to provide a description of the path of the deep and intermediate overflow waters in the north-west region of the Sicily Strait. The net transport is estimated to be 1 Sv which is consistent with other studies. Evidence of short-term variability in the overflow transport is also presented.

Introduction

The water mass properties of the deep ocean are strongly affected by the entrainment and mixing that occurs where the circulation flows across shallow sills and through straits. By observing the circulation and it's properties at sills and straits one can determine the features of the water exchange between the adjacent sub-basins. Six major sill and strait systems are found within the Mediterranean Sea *Astraldi et al.* [1999]. The two most important of these are the Strait of Gibralter, which connects the basin to the Atlantic Ocean, and the Sicily Strait (the focus of this study) which forms a natural barrier to the passage of the deep waters from the eastern to the western sub-basins of the Mediterranean.

The Sicily Strait (hereafter SS) has a complicated bathymetry (Figure 1) with two near-parallel channels separated by a central bank which rises to within 100 m of the sea surface. In the top 150 m of the SS there is an eastward flow of Modified Atlantic Water (MAW) below this, Levantine Intermediate Water (LIW) flows westward. An energetic vein of LIW passes through the narrow eastern channel (sill depth 430 m) and a weaker, slightly cooler and fresher, vein flows through the broader western channel (sill depth 360 m) [*Astraldi et al.*, 1996, 1999].

Figure 1. Bathymetry of the sills region of the Sicily Strait showing contours at 100, 300, 500, 700 and 900 m. The path of AUTOSUB-2 is shown by the black tracks and the locations of the CTD and LADCP stations are shown by black circles. Current meter mooring positions are shown by the white triangles. The inset map shows the study area in relation to the central Mediterranean region.

Observations

In June 2000, a survey of the sills region was carried out from the R/V *Urania*. The main objectives of the survey were to: 1) make high resolution measurements of the spatial distribution of the overflow from the sills using a combination of velocity and hydrographic data collected from the ship and by AUTOSUB-2 an Autonomous Underwater Vehicle (AUV) [e.g., *Millard et al.*, 1998; *McPhail and Pebody*, 1998], 2) map the path taken by the overflow immediately downstream of the sills and measure the along stream change in the properties of the overflow and 3) quantify the turbulent mixing and dissipation in the overflow and relate these processes to changes in the bulk properties of the overflow.

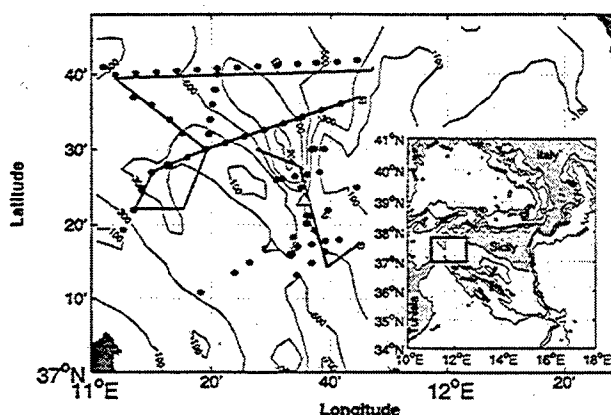Figure 1 shows the mission tracks of the AUV, and the

position of the hydrographic stations occupied by the ship. In addition to data collected during the ship-based survey, velocity data are also available from current meter moorings which were located at the eastern and the western sill (mooring positions are shown in Figure 1).

During each mission, AUTOSUB-2 controlled its altitude above the seafloor profiling between 30 m and 100 m above the sea-bed. AUTOSUB-2 carried two RDI 300 kHz Acoustic Doppler Current Profilers (ADCP)s, one upward and one downward looking, which collected data in 4-m bins at a range of up to 108 m from AUTOSUB-2. AUTOSUB-2 also carried 2 SBE 911plus Conductivity-Temperature-Depth sensors (CTD)s which sampled at a rate of 24 samples a second. A set of shipboard CTD and lowered ADCP (LADCP) profiles were made concurrently with some missions at the stations shown in Figure 1. The CTD was a SBE
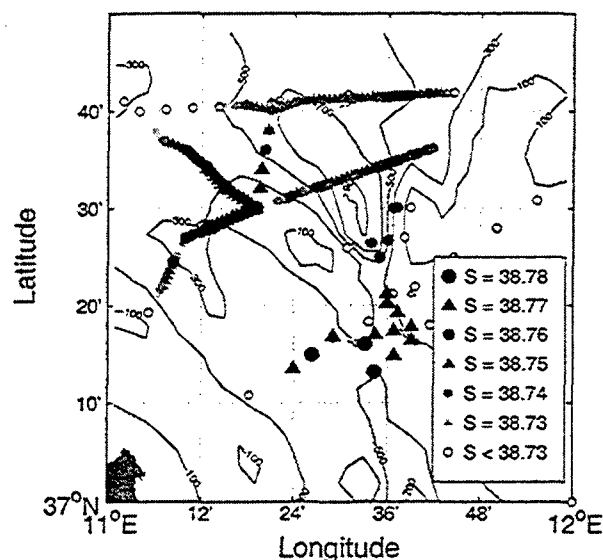
Figure 2. Salinity maximum from the CTD stations and along the path of AUTOSUB-2. The range is from 39.73 to 38.78 psu in steps of 0.01 psu.

911plus CTD and sampled at a rate of 24 Hz, the LADCP was a RDI 150 kHz broadband ADCP which collected data in 16-m bins. Further details of the data collection and data processing are given in *Stansfield et al.* [2001]. The current meter moorings, which were recovered and redeployed on June 3rd and 4th, carried Aanderra-RCM7 current meters at 53, 93, 287 and 390-m and 46, 289 and 390-m above the bottom on the eastern and westerns moorings respectively and sampled at 30-minute intervals.

Results

The path of the deep and intermediate waters through the sill can be traced by mapping the salinity maximum for each CTD station and along the path of the AUV (Figure 2). The range is from 38.73 to 38.78 in steps of 0.01 psu. The flow is split by the central bank into two branches; the saltiest water flows in the western branch and is seen to circulate around the northern end of the bank before flowing back south-eastwards. The greatest change in the along stream salinity maximum occurs on the north-east flank of the bank and we infer that this is a region of high mixing. or entrainment. of the surface waters into the overflow. Our data show that the eastern branch of the overflow is slightly fresher than the western branch and that mixing and entrainment appear to occur immediately downstream of the eastern sill.

Cross-transect velocity sections, derived from the combined AUV ADCP and LADCP data sets are shown in Figure 3. The velocities measured by the ADCPs were de-tided. rotated to obtain the cross-transect component and then linearly interpolation on to a 1-km horizontal by 1-m vertical grid. The cross-transect component of the tidal velocity at

each station was computed from a linear interpolation of a 1/12 by 1/12 degree barotropic tidal model of the Mediterranean for the M2, S2, O1 and K1 components [*Tsimplis et al.*, 1995]. Sections C and D show the western branch of the overflow reaching a speed of up to 0.45 m s^{-1} between 150 and 400 m depth and to the right hand side of each sub-channel. The re-circulation of this branch of the overflow around the central bank is confirmed by the bottom intensified current at the right hand side of section E and by the strong negative flow between 400 and 900 m depth at section B, with speeds of up to 0.55 m s^{-1} over a distance of 4 km. The eastern branch of the overflow can be seen at section A and the combined overflow on the right hand side of section F where velocities are barely greater than 0.20 m s^{-1}.

Section averages of the overflow transports computed from the direct velocity measurements and from the geostrophic velocities are shown in Figures 4 and 5 respectively. Ship-borne and AUV CTD data were used to calculate potential density which was then linearly interpolated to obtain a 1-km horizontal by 1-m vertical grid. Geostrophic velocities were then calculated from the geopotential anomaly fields using a reference layer which minimized the difference between the depth-averaged section transport from the direct velocity measurements and the transport from the geostrophic velocity for each section.

While there is general agreement between the transports calculated using the two different methods at sections C, D, G, B, and H, the methods disagree at sections E, A and F. In general the direct velocity measurements are more self-consistent and agree with the path of the overflow inferred from the spatial distribution of the salinity maximum, but both methods have the transport going the "wrong way" at section G. The direct velocity measurements are also in better agreement with previous local mean estimates of the LIW transport through the strait of 1 Sv [e.g., *Astraldi et al.*, 1996, 1999; *Manzella et al.*, 1988].

Figure 6 shows the daily average transport during June of deep and intermediate waters estimated from the current meter moorings. The transport at the eastern mooring (solid line) was calculated assuming a constant interface depth between LIW and MAW of 150 m and a triangular cross-section of area 1.7 km^2. The transport at the western mooring (dashed line) was calculated assuming a variable interface depth and cross-section area. The daily transport at the western mooring has a minimum value of 0.35 Sv and a maximum of 0.66 Sv and shows variability on a time scale of 10 to 14 days. The transport at the eastern mooring is generally smaller, between 0.4 and 0.5 Sv, and is less variable. At the time of our survey the overflow transport at the western mooring was 0.55 to 0.6 SV which is similar to the combined transports at our sections C and D (0.2 + 0.4 Sv). At the eastern mooring however, the overflow transport is 0.45 Sv which is much larger than the section averaged transport of 0.1 to 0.3 Sv we found at section H.
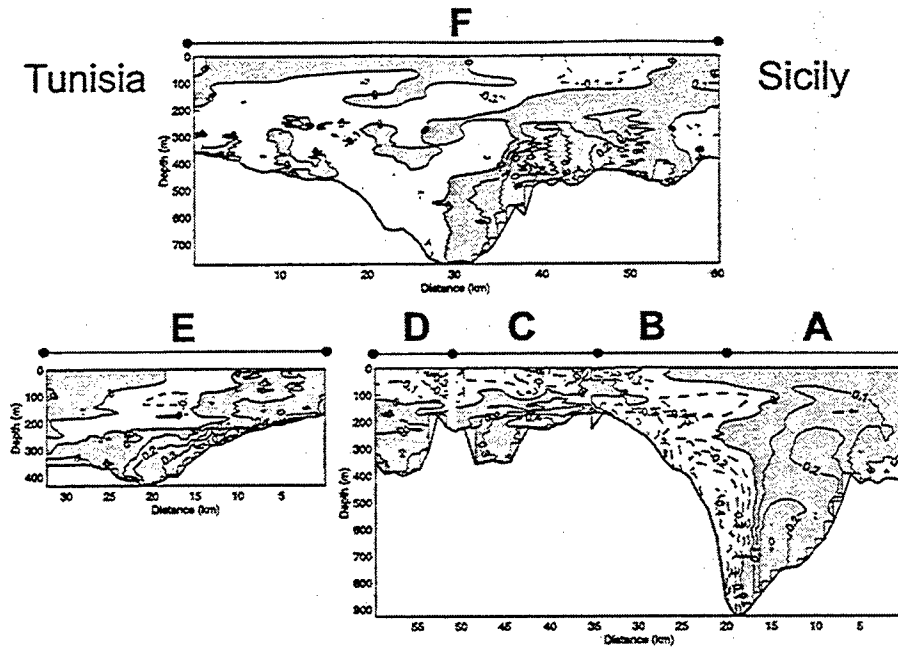
Figure 3. Cross-transect velocity sections derived from the combined AUTOSUB-2 ADCP and LADCP data sets. In each case the observer is standing to the south of the section with Sicily on the right hand side. Positive flow is away from the observer and is shaded grey. Velocities are contoured from -0.6 to 0.6 m s^{-1} at 0.1 m s^{-1} intervals. The position of sections A to F are shown in Figures 4 and 5.

Discussion

The mean monthly transport of the overflow for the two passages in the Sicily Strait and the total transport for the period November 1993 to 1997 are discussed by *Astraldi et al.* [1999, Figure 12]. In contrast to our study they find that the monthly mean overflow transport for June in both passages is about 0.6 Sv, whereas our data indicate that the transport is larger through the western passage. *Astraldi et al.* [1999] also find that the overflow shows more time variability in the western passage, and is more steady in the eastern passage however their results are for seasonal and monthly variations whereas results from this study show sub-monthly fluctuations of the overflow in the western channel over a period of 10 to 14 days.

Our apparent underestimate of the overflow through the eastern passage and to the north of the central bank (section G) may, in part, be due to the poor performance of the barotropic tidal model in a region of complex topography. This in turn may have affected the choice of reference layer
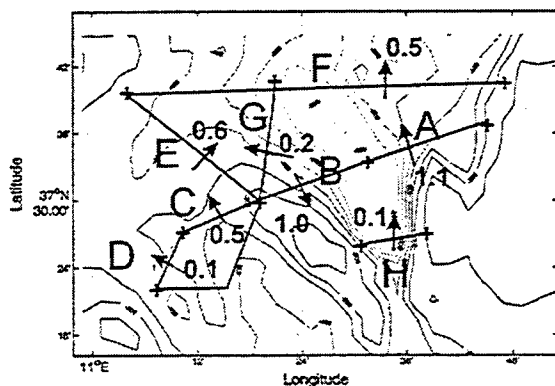

Figure 4. Section average transports (Sv) of the intermediate and deep overflow derived from direct velocity measurements.
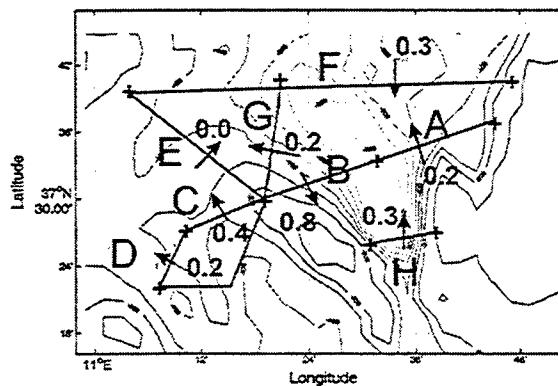

Figure 5. Section average transports (Sv) of the intermediate and deep overflow derived from the geostrophic velocity estimates.
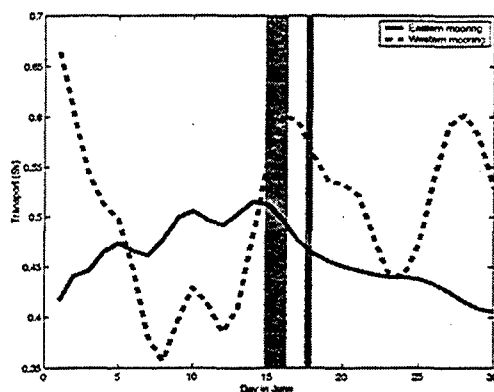
Figure 6. Daily averaged transport (Sv) of intermediate and deep waters for the month of June as calculated from the current meter mooring data. Western mooring (dashed line), eastern mooring (solid line). The two vertical grey bars show the timing of sections A through F and sections G and H.

for the geostrophic velocity calculation due to our method of attempting to match the section average transports. When we compared the predicted barotropic tide from the model against the observed tide at the current meter mooring positions we found that the model predicted the tidal amplitude and phase well at the eastern mooring but over-estimated the tidal amplitude by about a factor of two at the western mooring. Further investigation of the effect of the tide on the outflow and the apparent short-term variability in the outflow is planned.

Conclusions

A combination of AUV and ship-borne CTD and ADCP measurements have allowed us to to identify the path of the overflows through the sills, regions of intense mixing in the sills and short term variability in the overflow. In the near future we hope to quantify the salt and heat fluxes of the overflows and to estimate the turbulent mixing in the region of the sills.

References

Astraldi, M., G. P. Gasparini, S. Sparnocchia, M. Moretti, and E. Sansone, The characteristics of the water masses and the water transport in the Strait of Sicily at long time scales, *Bulletin de l'Institut océanographique, Monaco, no spécial, 17*, 95–115, 1996.

Astraldi, M., S. Balopoulos, J. Candela, J. Font, M. Gacic, G. P. Gasparini, B. Manca, A. Theocharis, and J. Tintore, The role of straits and channels in understanding the characteristics of Mediterranean circulation, *Progress in Oceanography, 44*, 65–108, 1999.

Manzella, G. M. R., G. P. Gasparini, and M. Astraldi, Water exchange between the eastern and western Mediterranean through the Strait of Sicily, *Deep-Sea Research, 35*, 1021–1035, 1988.

McPhail, S., and M. Pebody, Navigation and control of an autonomous underwater vehicle using a distributed, networked, controlled architecture, *J. Soc. Underwater Tech., 23*, 19–30, 1998.

Millard, N., G. Griffiths, G. Finegan, S. McPhail, D. Meldrum, M. Pebody, J. Perrett, P. Stevenson, and A. Webb, Versatile autonomous submersibles - the realising and testing of a practical vehicle. *J. Soc. Underwater Tech., 23*, 7–17, 1998.

Stansfield, K., D. A. Smeed, G. P. Gasparini, S. McPhail, N. Millard, P. Stevenson, A. Webb, A. Vetrano, and B. Rabe, Deep-sea, high-resolution, hydrography and current measurements using an autonomous underwater vehicle: The overflow from the Strait of Sicily, *Geophys. Res. Letters, 28*, 2645–2648, 2001.

Tsimplis, M. N., R. Proctor, and R. A. Flather, A two-dimensional tidal model for the Mediterranean Sea, *J. Geophys. Res., 100*, 16,223–16,239, 1995.

K. Stansfield, James Rennell Division, Southampton Oceanography Centre, University of Southampton, European Way, Southampton. UK

D. A. Smeed, James Rennell Division, Southampton Oceanography Centre, University of Southampton, European Way, Southampton. UK

G. P. Gasparini, Istituto per lo studio dell'Oceanografia Fisica, Forte Santa Teresa. 19036 Pozzuolo di Lerici (SP), Italia.

Modeling archipelago exchange flows

Petter Stenström[1] and Anders Engqvist[2]

[1]Royal Institute of Technology, Stockholm, Sweden
[2]Stockholm University, Stockholm, Sweden

Abstract. A strategy is proposed to model the water exchange in areas with arbitrary but stable stratification, together with complex geometry and topology. The stratification is first approximated by two or three homogeneous layers based on inspection of a density coordinate potential energy diagram. The flow regime is then classified as maximal or submaximal. The two-layer maximal exchange solution may be calculated and tabulated as a function of the imposed barotropic net flow on beforehand for a given strait with full regard to geometric features. For submaximal cases, the solution is also dependent on the interface height in one of the reservoirs. The influence of stratification within the assumed homogeneous layers may be estimated by gradually migrating towards flow cases possible to solve with other methods, e.g contra-flowing multi-layer groups separated by an infinitesimally thin stagnant layer.

Introduction

An archipelago is a collection of coastal basins interconnected by straits with or without sills. Barotropic and baroclinic exchange processes interact over a range of geometric scales to produce a variety of stratification conditions. An archipelago water exchange model must hence strike a balance between sophistication in the representation of the physical exchange mechanisms and geometry on one side, and numerical efficiency and robustness on the other.

Dalziel (1991, 1992) proposed a new formulation of the quasi-stationary, two-layer exchange problem in which the non-dimensional Bernoulli equation is regarded as a functional, the roots of which are traced along the strait. This formulation made possible more efficient numerical schemes to distinguish between fully controlled, maximal exchange cases and partially controlled or uncontrolled submaximal exchange cases, and to determine the corresponding exchange flows.

Smeed (2000) and Lane-Serff et al. (2000) extended the two-layer hydraulic functional theory to three- and multi-layer exchange cases, and demonstrated the solution process for a wide range of three-layer flow situations.

Two- and three-layer theories obviously require that two and three distinct bodies of water, respectively, can be identified. In Baltic archipelagos often a piece-wise linear continuous stratification is a better approximation. Stigebrandt

(1990) took a pragmatic approach to model the strait exchange problem given arbitrary but stable stratification in two adjacent basins interconnected by an infinitely short strait. For a specified net flow this model surprisingly well describes the exchange flow in applied geophysical contexts (e.g. Aure and Stigebrandt, 1996), even though vertical contraction was replaced by horizontal piston-like flow. The main merit of the resulting scheme is its numerical robustness, which is achieved partly by introducing a flow-dependent empirical parameter denoting the fraction of acceleration taking part upstream of the passage of the narrowest section of the strait.

Engqvist (1996) extended the unidirectional multi-layer solutions of Wood (1968) to exchange flows. These solutions are also well suited for implementation in a numerical model, but are restricted to straits with vertical walls and a flat bottom, and cover only maximal exchange cases involving the dominant mode.

We propose an approach to archipelago strait exchange where the density profiles in the adjacent basins are first inspected using a density coordinate, potential energy diagram (PE-diagram, Killworth, 1992) to determine the best approximation to the stratification and the corresponding exchange case (two-, three- or multi-layer). The aim is to find a numerical scheme that, given the basin stratification and the barotropic net flows, can compute the exchange flow with due consideration to strait geometry.

The Stockholm archipelago and the strait Oxdjupet

The inner Stockholm archipelago is a multi-basin estuary with an average of 160 m³/s freshwater discharged from Lake Mälaren at the estuary head. The resulting surface current is split and passes through several parallel straits of which Oxdjupet is the deepest with a depth of 19m, the others having their sills at around 5m. Normally a little less than half of the discharged water passes through Oxdjupet. There are no significant tides, but the sea level varies with the Baltic large-scale fluctuations and with faster wind set-up/set-down locally within the basins. Upwelling events along the Baltic coast produce density variations that eventually reach the Trälhavet basin at the north end of Oxdjupet (Figure 1).
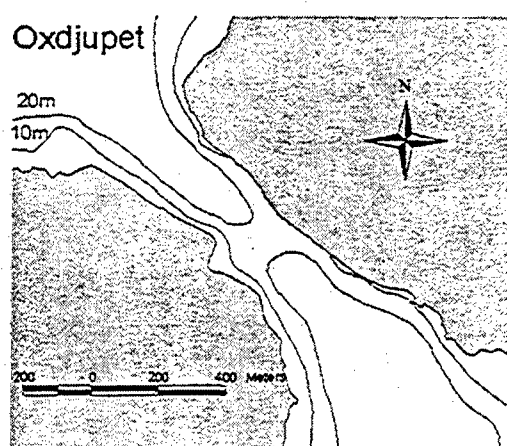

Figure 1. Oxdjupet in the inner Stockholm archipelago.

The normally expected flow regime is two contra-flowing groups of layers, each with vertical density gradients but separated by a distinct pycnocline. However, when the freshwater discharge is weak and/or when significant upwelling events occur in the Baltic Sea, other flow regimes may occur.

High-resolution bathymetric data was available. Equation 1 was fitted to this data to give a realistic geometric description of the along-channel width (B) and depth (H):

$$B(x) = B_{min} + 0.01(x + 100)^2$$
$$H(x) = H_{max} + (H_{min} - H_{max})\exp(-0.003x^2)$$
(1)

The cross-section is described by:

$$B(z) = \frac{1}{2}(1 + \beta)(z/H)^\beta$$
(2)

with $\beta = 0.3$.

There are nine instances of profile measurements 1999 on either side and in the middle of the Oxdjupet strait. For one of these occasions acoustic flow measurements are also available.

Modeling strategy

An archipelago water exchange model should meet several requirements: empirical parameters should be avoided; a prescribed net flow and given density profiles in the reservoirs should yield a unique solution; capability to handle both discrete and semi-continuous stratification is needed; maximal and submaximal exchange cases must be possible to distinguish, and finally; the algorithm must be computationally feasible.

We propose the following procedure (see also Table 1). If the PE-diagram is consistent with a two-layer flow regime, the best two-layer approximation of the density profiles in the reservoirs is determined. The maximal exchange solution is then calculated using the algorithm proposed by Dalziel (1991). Note that the maximal exchange solution is unique for given net flow and strait geometry, i.e. the solution is independent of the interface heights in the reservoirs as long as the interface in the dense reservoir is above, and the interface in the light reservoir is below, the subcritical branch associated with the fully controlled flow. If one of the interfaces should fall below/ rise above its given limit, one control will be flooded and the flow will be submaximal. A new solution must then be computed with the exact location of the interface.

If the PE-diagram is not consistent with a two-layer flow regime, but with a three-layer regime, then the best three-layer approximation of the density profile is determined. The interface heights in the dense reservoir are then compared with those in the light reservoir to determine how many hydraulic transitions are required in the strait, and hence how many controls must be present. The algorithm proposed by Smeed (2000) is used to solve for the flows in the three layers. The solution process is considerably more complex for the three-layer case, and typically requires a good a priori understanding of the basic character of the solution.

H1(DR) < G & H1(LR) > G	2 controls, maximal exchange
H1(DR) < G & H1(LR) < G	xc flooded, subcritical towards SF
H1(DR) > G & H1(LR) > G	xv flooded, subcritical towards TH
H1(DR) > G & H1(LR) < G	xc and xv flooded, subcritical everywhere

Table 1a. Limits for maximal two-layer exchange. H1(DR) is the interface height in the dense reservoir and H1(LR) the interface height in the light reservoir. G is the height in the reservoirs of the subcritical branch associated with the maximal solution. The geometric control is denoted xc, and the virtual control xv.

H1(DR) = H1(LR) & H2(DR) = H2(LR)	Smeed (2000) type a
H1(DR) = H1(LR) & H2(DR) /= H2(LR)	type b
H1(DR) /= H1(LR) & H2(DR) = H2(LR)	type b
H1(DR) > H1(LR) & H2(DR) > H2(LR)	type d or e
H1(DR) > H1(LR) & H2(DR) < H2(LR)	type c or e
H1(DR) < H1(LR) & H2(DR) > H2(LR)	type c or e
H1(DR) < H1(LR) & H2(DR) < H2(LR)	type d or e

Table 1b. The different solution types in the algorithm proposed by Smeed (2000). Type e has one mode supercritical in one reservoir and both modes supercritical in the other, and is analogous to 2-layer maximal exchange.

Results

The PE-diagram for the nine profiles from 1999 is shown in Figure 2. All curves increase monotonically, indicating that the 2-layer approximation should be acceptable. A few cases have been found from other years where the PE-curve has a maximum, and where hence a three-layer approximation is needed (Figure 2). This seems to occur mainly in periods when a weak freshwater discharge from Lake Mälaren has allowed the salinity to increase on the south side of Oxdjupet, combined with a subsequent increase of the sea level and up-welling of the pycnocline on the north side (dense reservoir).

Table 2 gives the two-layer maximal exchange solution for different net flows and for the geometry given in equation 1. The parameter G is the height in the reservoirs of the subcritical branch associated with the fully controlled flow, measured from the sill crest. This is the value
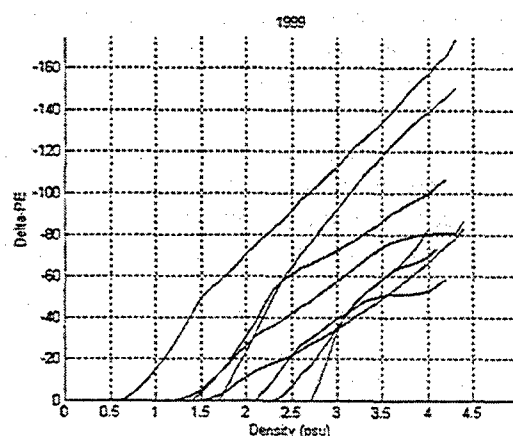
When neither a two-layer regime nor a three-layer regime is consistent with the PE-diagram, then a multi-layer approximation must be used. Stigebrandt (1990) and Engqvist (1996) represent two different such approaches.

Figure 2. PE-diagram for nine profiles from 1999. Each curve represents the difference in potential energy between the light and the dense reservoirs.

with which the actual interface height in the reservoirs should be compared. When the interface in the dense reservoir is above, and the interface in the light reservoir is below, this level, the flow is fully controlled, and hence maximal (Dalziel 1992). Maximal exchange was the most common situation during 1999, although instances occur when the geometric control is flooded.

Qnet	q1	q2	h0	G
316	387	71	12.6	17.3
237	330	93	11.7	15.8
158	275	117	10.9	14.2
79	224	145	10.1	12.6
0	175	175	9.3	10.9
-79	131	210	8.6	9.2
-158	919	24	7.9	7.5
-237	54	291	7.1	5.7
-316	24	340	6.3	3.9

Table 2. Oxdjupet, maximal two-layer exchange solution for different net flows. The geometry given in equation 1 was used with Hmin=19m, Hmax=38m and Bmin=210m. Qnet is positive from south to north. h0 is the height of the interface above the sill crest, G is also measured from the sill crest. The reduced gravity was set to $3.4 * 10^{-3}$ m/s².

The two and three-layer approximations allow for the strait geometry to be adequately treated, but disregard stratification within layers. Multi-layer approximations on the other hand permit better resolution of the stratification, but demands simplification of the geometry. Maximal two-layer exchange corresponds to 2/3-contraction of the contra-flowing groups of layers. For cases with vertical side walls, no sill, and a stratification that permits the groups of contra-flowing layers to be barely decoupled with an infinitesimally thin separating stagnant layer, there is an exact coincidence between the two-layer approach and the self-similar approach (Engqvist, 1996). For all other cases when the pycnoline deviates from a mid-height position at the geometric control, these solutions must thus be negotiated against each other, to find the best compromise that complies with both methods. The free parameter at hand to arrange for such an adjustment is the smallest possible manipulation of the given stratification that yields the same net flow. If a new layer is tentatively created in-between the shearing groups of layers, the ensuing new flow regime may be treated by the three-layer functional approach by Smeed (2000). As this layer is permitted to expand in thickness, eventually the original layers will become decoupled. The departure from the original stratification gives an appreciation of the significant difference between the two-layer and the continuous stratification approaches, the investigation of which goes on.

Conclusions

A strategy is proposed to model the water exchange in areas with arbitrary but stable stratification, together with complex geometry and topology. The two- and three-layer functional approaches allows for different flow regimes to be distinguished and for the flow to be solved for complex geometries. However, the layers on either side of the strait Oxdjupet are rarely homogenous in density but rather continuously stratified. When the stratification is such that the two- and three-layer approximations are in doubt, we attempt to negotiate the functional approach with the self-similar multi-layer approach by manipulating the density stratification in the reservoirs by hypothetical mixing between adjacent layers, while keeping the average density intact.

References

Aure, J. and Stigebrandt, A. "Evidence for hydraulically controlled outflow of brackish water from Holandsfjord, Norway." J. Phys. Oceanogr. 26: 257-266. 1996.

Lane-Serff, G. F., Smeed, D.A. and Postlethwaite, C. R. "Multi-layer hydraulic exchange flows." J. Fluid Mech. 416: 269-296. 2000.

Engqvist, A. "Self-similar multi-layer exchange flow through a contraction." J. Fluid Mech. 328: 49-66. 1996.

Dalziel, S.B. "Two-layer hydraulics: a functional approach." J. Fluid Mech. 223: 135-163. 1991.

Dalziel, S.B. "Maximal exchange in channels with nonrectangular cross sections." J. Phys. Oceanogr. 22: 1188-1206. 1992.

Killworth, P.D. "On hydraulic control in a stratified fluid." J. Fluid Mech. 237:605-626. 1992

Smeed, D. A. "Hydraulic control of three-layer exchange flows: Application to the Bab al Mandab." J. Phys. Oceanogr. 30: 2574-2588. 2000.

Stigebrandt, A."On the reponse of the horizontal mean vertical density distribution in a fjord to low-frequency density fluctuations in the coastal water." Tellus , 42A, 605-614. 1990.

Wood, I. R. "Selective withdrawal from a stably stratified fluid." J. Fluid Mech. 32: 209-223. 1968.

Study of the Yucatan Strait Current with a High Resolution Numerical Model

S. Tanahara*'**, J. Candela** and M. Crépon*

* LODYC/Universite Pierre et Marie Curie, Paris, France
** Oceanografia Fisica, CICESE/Apdo. Postal 2732, Ensenada Mexico

Abstract. A three dimensional Ocean Global Circulation Model (OGCM) was used to study the variability of the Yucatan Current. The model was forced by re-analysis fluxes taken from ECMWF during 20 years. It is found that Yucatan Current has a cycle close to 8 months and that the baroclinic and barotropic transports of the Yucatan Strait Current drive the northward Loop Current intrusion and anticyclonic eddy shedding. A new hypothesis for the generation and westward propagation of eddies in the Gulf of Mexico is proposed according to the numerical results.

Introduction

The Gulf of Mexico is a semi-enclosed basin located in the subtropical zone between 18° to 30° N and 82° to 98° W. The Caribbean Sea is located between 8° and 22° N and 60° to 89° W (Figure 1). The Gulf of Mexico communicates with the North Atlantic Ocean through the Strait of Florida and with Caribbean Sea through the Yucatan Channel. The circulation in the eastern Gulf of Mexico is dominated by the Loop Current, which is a large and variable anticyclonic loop connecting the Yucatan Channel to the Florida Strait. The Loop current is at the origin of the Gulf Stream system (Hamilton, 1990). One of the most interesting features of this current is its variability (Vukovich, 1995). The variability of the Yucatan Current is associated with that of the Loop Current. The goal of the present paper is to study the variability of the circulation in the Gulf of Mexico by analyzing the results of a three-dimensional numerical model with an emphasis on the Yucatan Channel.
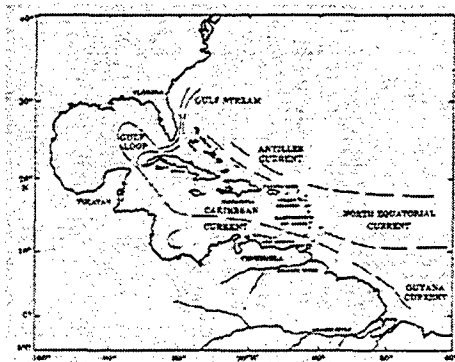

Fig 1 Idealized Pattern Circulation of the Gulf of Mexico

The physical problem

Cochrane (1965) attributes the northward intrusion of the Loop Current to the annual variability of the Yucatan surface current. Molinari and Morrison (1988) argue that the Loop Current intrusion depends of the incidence angle of the current coming from Yucatan channel. Robinson, (1973) and Maul, (1975) showed that maximal intrusion occurs in summer. However, Maul and Vukovich (1993) found a maximal intrusion in winter. The results of these studies suggest that when the Loop Current makes a large northward penetration into the eastern Gulf of Mexico, a portion of the current detaches from the loop, creating an anticyclonic ring.

Cochrane (1965) supports that Loop Current has an eddy shedding cycle due to seasonal variability of the influx coming from Yucatan channel. When the Loop Current retracts, the eddy shedding occurs. Cochrane (1972) also suggested that the separation occurs when a cyclonic meander of the Yucatan Current moves northward and joins a semi-permanent meander off the Florida shelf. Molinari et al., (1978) attributes the eddy shedding to the annual variability of the mass transport through Yucatan channel. Hurlburt and Thompson (1982) explained the eddy shedding mechanism as due to a strangling of the anticyclonic loop by a joint effect of a cyclonic meander in the Florida shelf and a north cyclonic meander of the Yucatan Current occurring when the Loop Current has a maximal Northward penetration (close to 27° N) in the Gulf. Pichevin and Nof, (1996) argued that the momentum associated with the eastward flux (resulting from the penetration and

219

deflection of the Yucatan current) is not in balance (momentum imbalance paradox), so eddies are formed to compensate the eastward jet momentum. Recently Murphy *et al.*, (1999) argue that potential vorticity coming from North Brazil Current retroflection and advected through the Lesser Antilles, mixes the baroclinic and barotropic instabilities and can influence the Loop current structure and consequently the eddy shedding.

The numerical model

The model is an extended version of the primitive equation OPA numerical model (Madec *et al.*, 1998). Boussinesq and hydrostatic approximations, turbulent closure hypothesis, rigid lid and free-slip condition at close boundaries are taken in the present simulation. The model of the Gulf of Mexico is part of a model (CLIPPER, Treguier *et al.*, 2001) covering the whole Atlantic basin with a grid mesh of 1/6°. The numerical model used Reynaud *et al.* (1998)'s climatology and it is forced with climatological data coming from the ECMWF re-analysis (wind-stress, net heat flux, penetrative solar radiation and freshwater budget) the model was run for 20 years after a spin-up of ten years. The physical run starts in 1979.

The results

Seasonal and inter-annual variability of the barotropic transport

The seasonal and inter-annual variability of the transports across the major straits and passages in Caribbean Sea and the Gulf of Mexico are displayed in Figure 2.

The average Yucatan Channel transport is 28.4 Sv from February 1979 to December 1983. This is higher than the 24 Sv obtained from recent observations in the Channel (Sheinbaum *et al.*, 2001), but is in rough agreement with that of Larsen (1992) across Florida Strait of about 30 Sv. The transport through the Lesser Antilles is only 20.5Sv. So, the barotropic transport through Yucatan Channel is influenced by the transport through the little Caribbean passages. The flow through the Windward Passage is 5.4 Sv into the Caribbean Sea during this period, which compares quite well with the observations done by Schmitz and McCartney (1993). The estimated values are 4 to 7 Sv. The mean transport through the Mona Passage is 4.3 Sv southward, flowing into the Caribbean Sea.
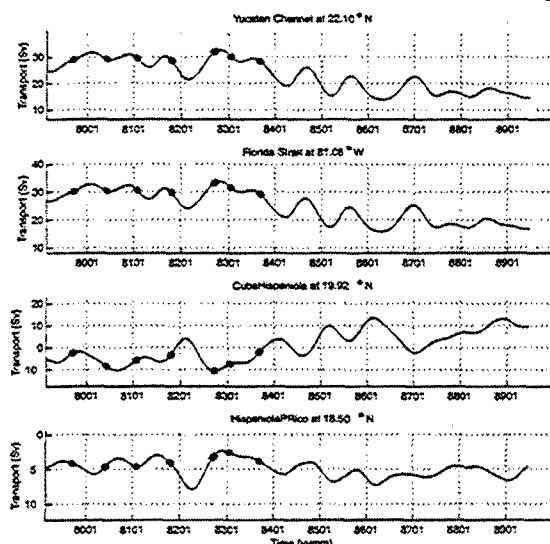

Fig:2   Time series of the barotropic transport through different straits of the Caribbean Sea

During this period of simulation we also found a realistic magnitude and spatial distribution of the eddies in the Gulf of Mexico. The anticyclonic eddies were shed westward in the gulf from meanders of the Loop Current at a rate of 7 to 9 months in the spin-up phase and in the next 4 years of simulation (from 1979 to 1982). A longer shedding period was obtained during the fifth year. Then there was an 18 months period with no shedding and then a last eddy detached. After 1983 a strong stable loop was formed in this region, which persisted until the end of the run affecting the current system of the region. When the eddy shedding is blocked, the barotropic mean transport through the Yucatan Channel and consequently at Florida Current decreased from 28.4Sv to 18.9Sv. The transport through Lesser Antilles remains at the same mean value, but this at the Windward Passage reversed in direction and we observe a 5.7 Sv transport northward. At the Mona Passage the mean transport changed from 4.3 Sv to 5.4 Sv flowing southward. It is obvious that barotropic mean transport through the Yucatan Channel influences the shedding of the Loop Current eddy, but the reason for the absence of detachment of eddies after 1983 is not yet clear. A possible reason could be the parameterization of small-scale turbulence that could dissipate energy unrealistically. Another is the inadequate resolution of the topography in the Caribbean Sea and the absence of Lesser Antilles in the model which may lead to a situation in which the vorticity coming from the North Brazil Current retroflection is not correctly transferred to Caribbean Sea and consequently to the

Yucatan Channel. In that case, the Yucatan Current might remain closer to Yucatan Peninsula affecting the deepening of the anticyclonic eddy. This would lead to an eddy more sensible to topography. In that case, a topographic effect in opposite sense to the β planetary effect would affect the eddy shedding and finally the westward propagation of the eddy (as Pichevin and Nof, 1996 have proposed) would not take place.
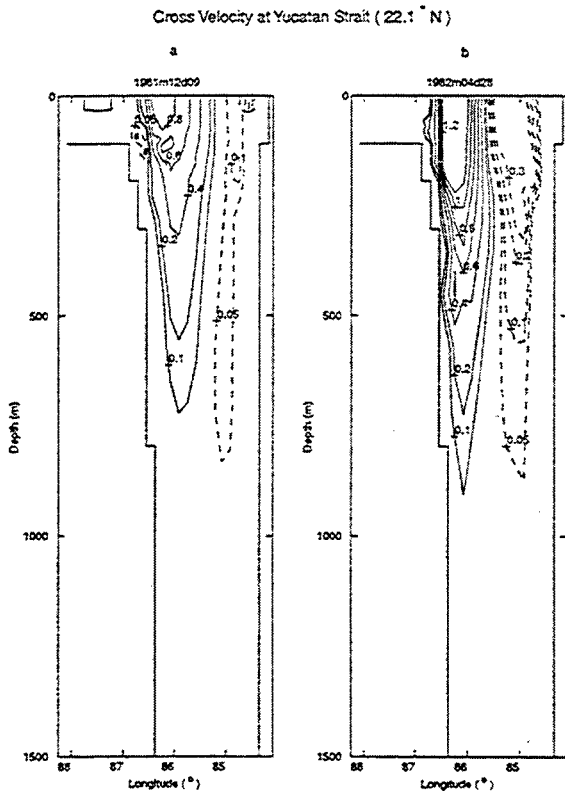

Fig.3 Vertical section of cross Velocity through the Yucatan Strait at two different times a) Dec. 1981, b) April 1982

Variability of the vertical structure

During the first 5 years of the simulation, the vertical structure of the velocity at Yucatan Channel showed a very variable current in time and space with a period of approximately 8 months. Also, the current does not present a seasonal variation. After this 5-year period, the current shows no significant variability.

A zonal vertical section taken at the end of the 3rd year of simulation at 22.1° N across Yucatan Channel (Figure 3a) shows (after a spin-up phase

of 10 years) an incoming flow into the Gulf of Mexico (positive values) close to the Yucatan Peninsula. We can see a slower current flowing out of the Gulf close to the Cuban coast (negative values). This negative flow is as deep as the positive one, but it is also narrower in the horizontal and one order of magnitude slower than the other one. A third slow flow is present in the simulation close to Yucatan Peninsula but at 100 m depth. It has the same magnitude of that confined to Cuban coast but is narrower. This pattern is observed every 8 months. The flow pattern found 5 months later shows a similar geostrophic system (Figure 3b). One observes a positive flow close to the Yucatan Peninsula and a negative flow close to the coast of Cuba. But the negative deeper flow close to Yucatan Peninsula is not present. The speed of positive flow increases and deepens (from 0.8 ms-1 to 1.2ms-1 and from 700 m to 1000 m depth). Another important difference is the westward intrusion of Cuban coast countercurrent and its intensification (from 85° W to 85.5°W and from 0.05 ms-1 to 0.3 ms-1).
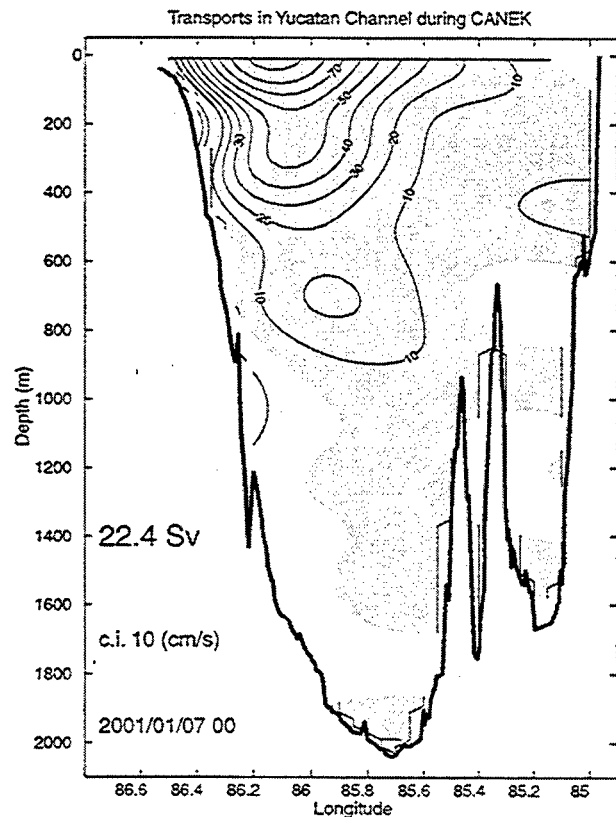

Fig 4 Cross Velocity through the Yucatan Strait from CANEK observations during January 2001
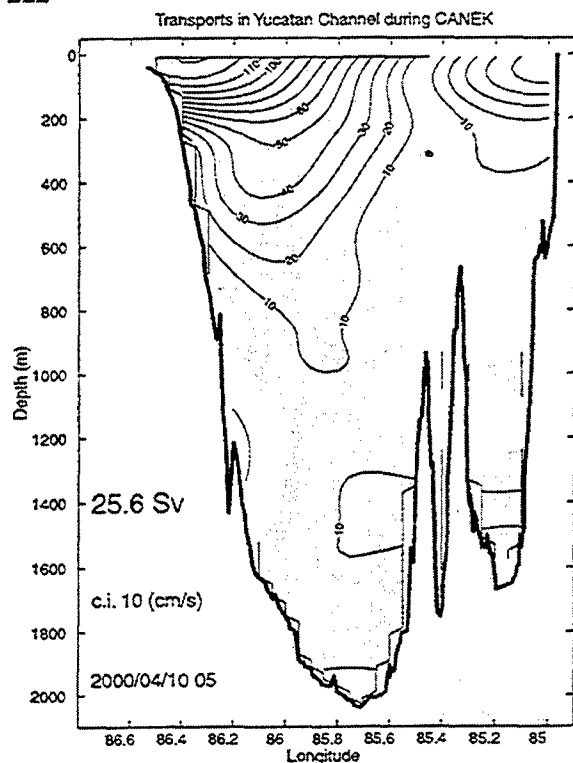
Transports in Yucatan Channel during CANEK

25.6 Sv

c.i. 10 (cm/s)

2000/04/10 05

Fig. 5 Cross velocity through the Yucatan Strait from CANEK observations during April 2000

topography and the momentum paradox of Pichevin and Nof (1996). The analysis of the model deficiency allows us to support this hypothesis.

References

Hamilton P., 1990 : Deep Currents in the Gulf of Mexico, *J. Phys. Oceanogr.*, 20, 1087-1104.

Hulrburt H.E., and J.D. Thompson, 1982 : The dynamics of the Loop Current and shed eddies in a numerical model of the Gulf of Mexico in *Hydrodynamics of semi-enclosed seas*, Elsevier, 243-298.

Larsen J.C., 1992: Transport and Heat Flux of the Florida current at 27oN derived from cross-stream voltages and profiling data: Theory and observations, *Phil. Trans. Roy. Soc.* London, A 338, 169-236.

Madec, G., P. Delecluse, M. Imbard, and C. Lévy, 1998: OPA 8.1 Ocean General Circulation Model reference manual. *Note du Pôle de modélisation, Institut Pierre-Simon Laplace*, N°11, 91pp. (available at: http://www.lodyc.jussieu.fr/opa)

Maul G.A. and F.M. Vukovich, 1993: The relationsip between variation in the Gulf of Mexico Loop Current and Strait of Florida volume transport, *J. Phys. Oceanogr.*, 23 (5), 785-796.

Molinari R.L., S. Baig, D.W. Behringer, G.A. Maul and R. Legeckis, 1977 : Winter intrusions of the Loop Current, *Science*, 198, 505-507.

Murphy S.J., H.E. Hurlburt and J.J. O'Brien, 1999: The connectivity of eddy variability in the Caribbean Sea the Gulf of Mexico and the Atlantic Ocean, *J. Geophys. Res.*, 98 (C1), 1431-1453.

Pichevin T. and D. Nof, 1996: The momentum imbalance paradox, *Tellus*, 49, 298-319.

Schmitz W.J. and M.S. McCartney, 1993: On the North Atlantic Circulation, *Rev. Geophys.*, 31, 29-49.

Sheinbaum, J, J. Candela, A.Badan and J. Ochoa, 2001. Flow structure and transport in Yucatan Channel. *Geophysical Research Letters*, in press.

Tréguier, A. M., B. Barnier, A. de Miranda, J.-M. Molines, N. Grima, M. Imbard, G. Madec, C. Messager, T. Raynaud and S. Michel, 2001: An eddy permitting model of the Atlantic circulation: evaluating open boundary. *J. Geophys. Res.*,106, C10, 22,115-22,114.

Vukovich F.M., 1995 : An updated evaluation of the Loop Current's eddy-shedding frequency, *J. Geophys. Res.*, 100 (C5), 8655-8659.

The variability of Yucatan Current found in the numerical simulation qualitatively corresponds with recently observations carried out by the CANEK Program, Figures 4, 5.

Unfortunately, the model results are not in phase with the observations to do a closer comparison. Another important remark is that when the Yucatan Current is slower and has a maximal eastward intrusion (Figure 3a), the Loop Current has a maximal northward intrusion and then an anticyclonic eddy is detached from the loop in very good agreement with observations carried out before. This shows the importance of the baroclinic component of the Yucatan Current on the Loop Current variability and eddy shedding.

Conclusions

The transport and the vertical structure of Yucatan Current obtained by a high-resolution numerical model have been analyzed. The main features of the circulation in the Gulf of Mexico and Yucatan Channel are very well reproduced by the CLIPPER model between 1979 and 1983. These features are in agreement with those of the CANEK Program. The blocking of the eddy shedding found in the numerical experiment can be explained by a joint effect of

Observations of wind effects on exchange flows in a channel constriction of the Chilean Inland Sea

A. Valle-Levinson[1], J.L. Blanco[1], and J.J. Fierro[2]

[1]Center for Coastal Physical Oceanography, Ocean, Earth and Atmospheric Sciences Department, Old Dominion University, Norfolk, Virginia, USA; [2]Servicio Hidrográfico y Oceanográfico de la Armada, Valparaiso, Chile

Abstract. A >100 day-time series of velocity profiles, sea level and wind velocity at a channel constriction in the Chilean Inland Sea was analyzed to examine the effects of wind forcing on the two-layer exchange. The study area typically shows a net surface outflow and net bottom inflow. Northerly winds that exceed 10 m/s reverse the flow of the upper and lower layers or produce three-layer exchange flows with the surface layer opposing the density-induced outflow. The exchange flows were thus weakened by northerly winds. The depth-integrated dynamics were well represented by the linear balance between sea level slope and friction from surface and bottom stresses.

Introduction

The exchange flows over sills and through constrictions dictate the water properties of the basins separated by such morphological features. The studies on exchange flows have established a hydraulic exchange two-layer theory that has been described in *Farmer and Freeland* (1983). Many of the studies on hydraulic exchange have been summarized by *McClimans* (1990), and by *Bryden and Kinder* (1991). Additional studies have focused on the modifications produced by barotropic forcing (e.g. *Farmer and Armi*, 1986; *Hibiya and LeBlond*, 1993; *Helfrich*, 1995). Despite the substantial body of literature on exchange flows, little effort has been dedicated to study the effects of wind forcing on such exchange. In contrast to studies on barotropic forcing, the wind-induced flows are expected to be depth-dependent as the surface water moves with the wind and the bottom water moves against the wind (e.g. *Wong*, 1994). In particular, if the wind blows against the surface layer of the exchange flows, notable modifications should be expected. The purpose of this study is to document the wind-induced effects on the two-layer exchange at a channel constriction in the Chilean Inland Sea, the Meninea Constriction in the Moraleda Channel.

Study Area

The Moraleda Channel (Figure 1) features two basins >300 m separated by the Meninea constriction

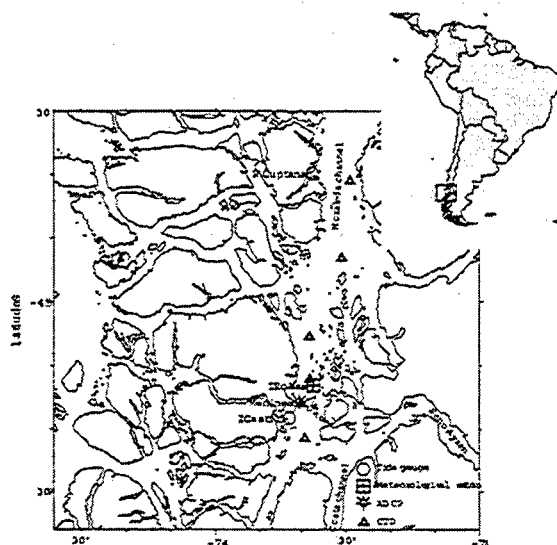where the depth rises to 40 m. The constriction/sill restricts the exchange of waters at depths >50 m

Figure 1. Study area in the Chilean Inland Sea showing the location of the water and wind velocity measurements as well as the sea level and CTD stations.

(*Silva et al.*, 1995). The water of the southern basin is less saline and more oxygenated than that of the north basin. The deep water of the northern basin originates from the Equatorial Subsurface Water (*Silva et al.*, 1997). On the basis of hydrographic information, *Silva et al.* (1998) propose a conceptual two-layer exchange for the area of the Meninea constriction. The less dense water flows northward at surface and the denser water flows southward over

·'·e sill. The inflow through the Meninea constriction .:!ows the ventilation of the southern basin. The .des in the Moraleda channel are mixed with semidiurnal dominance and maximum amplitude in spring tides of 2.8 m. The propagation of the tidal waves is southward (*Fierro et al.*, 2000).

Data Collection and Processing

Time series of current velocity profiles, wind velocity and sea level were obtained at intervals of 10 minutes during more than three months (September 25, 1998 to January 8, 1999) in the area of the Moraleda Channel. A series of CTD casts along the channel were obtained during and at the end of the deployment. The current velocity profiles were obtained with an upward looking 307.2 Khz ADCP. The instrument was deployed in the Meninea Constriction (Fig. 1) at a depth of 50 m and recorded bins of 2 m at a rate of 30 pings per ensemble (10 min). Sea level was recorded at two locations: Cuptana, to the north of the constriction with an Aanderaa sensor, and Castillo, immediately to the south with an Ott Orpheous sensor. Wind velocity was recorded at Islote Rosas with an Aanderaa AWS 2700 sensor at a height of 30 m and transformed to 10 m.

All time series were filtered with a Lanczos low-passed filtered that had a half-power of 34 hours. This eliminated high frequency (greater than diurnal) variability. Therefore, this study concentrates exclusively on the subtidal variability of the exchange flows with an emphasis of those produced by wind forcing.

Results

Profiles of temperature, salinity and sigma-t obtained in 1995, and also during and 1.5 months after the deployment show that salinity and density increased toward the north in this area of the Chilean Inland Sea (Fig. 2). This makes sense as the source of oceanic water is found to the north and the sources of fresh water are located to the south, at the head of the fjords and inlets. Worth noting in every distribution is the increase in slope of all isotherms, isohalines and isopycnals over the shallowest area that represents the Meninea Constriction (between 8 and 10 km in Figure 2). This change in isolines slope suggests the influence of hydraulic effects that result from advective accelerations nearly balancing the pressure gradient. Additional influences from vertical mixing near the bottom are apparent from the

isolines intersecting the bottom at sharp angles. This corresponds with theoretical expectations (e.g. *Pratt*, 1986; *Johnson and Ohlsen*, 1994) and observations in other environments (*Valle-Levinson and Wilson*, 1994). Also, mixing effects are apparent from the general spread of the isolines throughout the water column in contrast to the sharp pycnoclines observed elsewhere in the channels and inlets of the region (e.g. *Silva et al.*, 1995). Increases in vertical mixing will tend to break a hydraulic control and represent subcritical conditions in the exchange flows relative to the propagation of an internal perturbation (e.g. *Valle-Levinson et al.*, 2001).

Figure 2. Along-channel sections of temperature, salinity and density anomaly in Moraleda Channel. The Meninea Constriction appears between 8 and 10 km. Looking from

east to west.
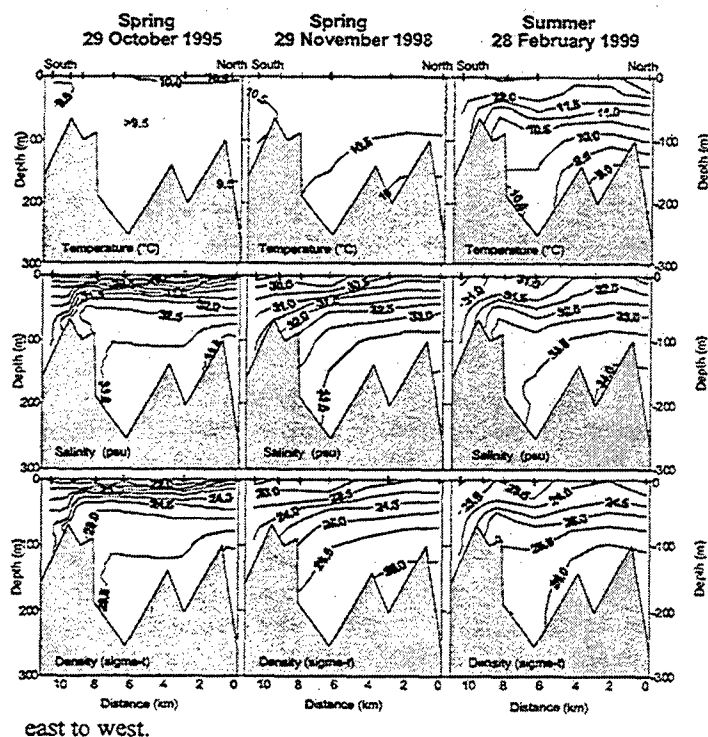
The flow observations obtained with the ADCP show different orientations for whether the flow was flooding (toward the south) or ebbing (toward the north). Ebb flows were toward ~10°T and flood flows were toward ~180°T if their magnitude were <40 cm/s (Fig. 3a). Greater magnitudes in the flood direction were directed toward ~125°T. Because of these changes in flow orientation, which were dictated by the morphology of the region, the direction of the principal axis of the flows was selected according to the magnitude range (Fig. 3b). The mean flow obtained throughout the deployment period for the principal-axis component shows outflow (flow to the north) at surface with values of

up to 0.17 m/s and inflow (flow to the south) at depth at 0.13 m/s (Fig. 3c). This is the typical two-layer exchange flow expected for estuarine environments of this type and agrees with the hydrography obtained at different times of the year. The distribution of the mean flow and the along-channel sections of salinity and density suggest that the dynamic balance at the observation point should be dominated by frictional influences that balance the pressure gradient established by the density differences in the Inland Sea.
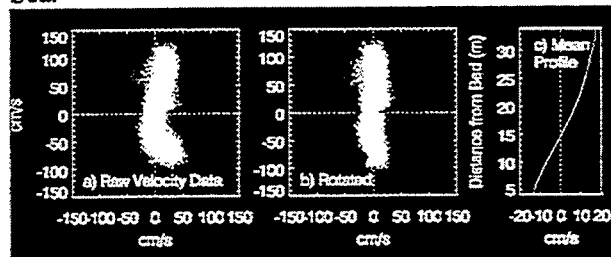

Figure 3. Velocity measurements.

The low-passed principal-axis flow shows that the water exchange is strongest during periods of weak wind forcing (Fig. 4), from days 315 to 325 and from days 345 to 357. The surface outflows and bottom inflows reverse only in a few occasions throughout the 103 days of the record (Fig. 4b). These episodes of outflow reversals coincide with weakening of near-bottom inflows and deepening of the interface between inflows and outflows. There are similar events where the surface outflow decreases, rather than reverses. All the events, totaling six and marked in Figure 4, are related to the strongest pulses (>10 m/s) of northerly wind. The six wind pulses also caused a sign reversal of the vertical shears from the surface to almost mid-depth (Fig. 4c). Those are the only periods throughout the record in which such an extended reversal occurs. In addition, these events are identified as the most anomalous in terms of weakened inflows (lightest tones near the bottom in Fig. 4d) and weakened outflows (darkest tones near the surface in Fig. 4d). The flow responses during the six wind pulses are related to the fact that the northerly wind tends to oppose the density-induced surface layer outflow and builds up a negative sea level slope (subtidal sea level decreasing northward). The barotropic pressure gradient associated with the sea level slope drives a near-bottom flow that also opposes the density-induced near-bottom inflow. Therefore northerly wind forcing dampens the two-layer exchange through Meninea constriction and may even produce a weak three-layer exchange flow as in the last three pulses of the record: near-surface

inflow (with the wind), interior outflow, and near-bottom inflow. This three-layer response to winds that oppose the density-induced near-surface outflow corresponds with observations (*Svendsen and Thompson*, 1978; *Cáceres et al.*, 2002) and numerical simulations (*Klinck et al.*, 1981) of other systems.
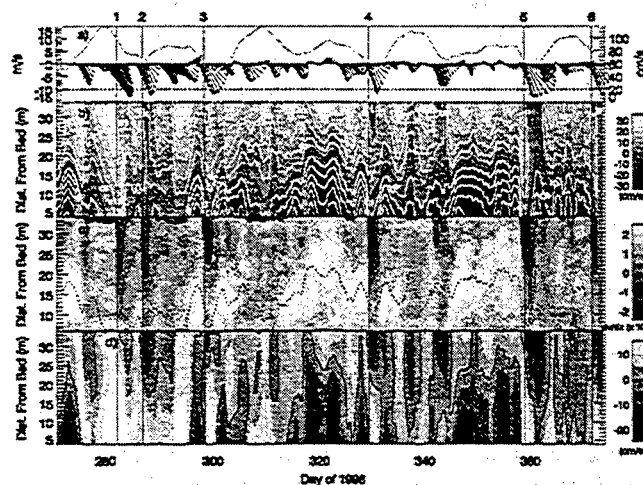

Figure 4. Low-passed variability of a) wind and amplitude of tidal current (to denote spring and neap tides); b) principal axis of flow (dark thick line is the zero contour); c) vertical shear of the principal axis of the flow ($\times 100$ s^{-1}; dotted contour is the interface between the two layers, which coincides with maximum shears; dark contour delineates regions of negative shears); and d) anomalies from the mean for the subtidal flow (negative near the surface means decreased outflow; positive near the bottom means decreased inflow). Numbers 1-6 on top of the figure denote the northerly wind pulses that exceed 10 m/s.

Although the tidal currents in this system exceed 1 m/s in spring tides and decrease by nearly one half in neap tides (Fig. 3), there was no apparent fortnightly modulation in the exchange flows. This modulation would produce enhanced subtidal flows in neap tides relative to springs (e.g., *Griffin and LeBlond*, 1990). Wind forcing is actually masking the potential consequences of such modulation. Interestingly, five of the six northerly wind pulses occurred at or close to neap tides, in close periodicity to the passage of atmospheric pressure systems over the study area.

The relationship among wind forcing, sea level slopes and near-bottom flows that is implied by the observations in Figure 4 is investigated through the principal-axis component of the subtidal, linear, depth-averaged momentum balance:

$$\frac{\partial \langle v \rangle}{\partial t} + f\langle u \rangle = -g\frac{\partial \eta}{\partial y} + \frac{\tau_{sy} - \tau_{by}}{\rho H}$$

where the y axis is positive toward the North; $<u>$ and $<v>$ are the transverse and principal axis components of the subtidal flow, respectively; f is the Coriolis parameter (-1_10^{-4} s^{-1} for 45° S); and g, H, $\_$, $\_$, $\_{sy}$, and $\_{by}$ are the acceleration due to gravity (9.8 m/s^2), water column depth (50 m), density of the water (1027 kg/m^3), sea surface elevation, surface stress and bottom stress, respectively. The surface stresses are calculated as in *Large and Pond* (1981) and the bottom stresses are estimated as $\_{by} = \_C_b\ v_b$ $|v_b|$ using a non-dimensional bottom drag coefficient C_b of 0.0025 and the near-bottom (bin closest to the bottom) flow v_b.

Every term in the momentum balance (1) is calculated with the information available and presented in Figure 5. The barotropic pressure gradient associated with the sea level slope between Cuptana (to the north) and Castillo (to the south; see Figure 1), at a distance of 75 km, is represented by the shaded region of Figure 5 (upper panel). The entire period of observations is remarkably dominated by winds from the north (Fig. 4a). Northerly winds cause negative sea level slopes, i.e., water piling up from north to south. These negative sea level slopes are well explained by the wind stress (negative $\_{sy}$). But when the sea level slopes are positive, the winds from the south (positive $\_{sy}$) are not strong enough to account for the slopes (dotted line in Figure 5, upper panel). Then, for periods of southerly winds the inclusion of bottom stresses improved the match to the pressure gradient. Addition of Coriolis (drawn on Figure 5) and local accelerations (not drawn) produce insignificant improvements. This indicates that sea level slopes respond tightly to the frictional coupling between surface and bottom stresses.

An additional response to wind forcing that is worth noting is the temporal changes of the depth of the interface between the two layers. Figure 4b shows that the changes of the interface, as given by the zero contour of the subtidal flows, follow closely the northerly component of the wind velocity, most notably during the strongest wind pulses. This data set shows that when the wind blows in the same direction as that of the net inflow (from north to south in this application) the interface of the exchange flow deepens. The deepening is a result of the dampening of the net inflow by the wind-induced near-bottom outflow. Analogously, strong winds in the direction of net outflow should contribute to enhance the two-layer exchange. Winds from the south are weak in this time series but such response remains to be explored.
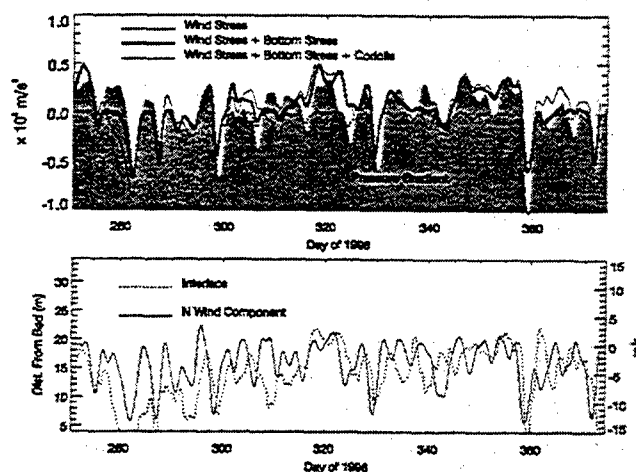

Figure 5. Upper panel shows the terms of the vertically averaged momentum balance (10^5 m/s^2). Lower panel shows the relationship between wind forcing and interface variations.

The wind-induced response contrasts with that of the barotropic tidal flow. Tidal forcing in general contributes to thicken the inflowing lower layer when it is in the direction of the net inflow, i.e., during flood periods (e.g. *Farmer and Armi*, 1986, *Farmer and Armi*, 1988; *Valle-Levinson et al.*, 2001). Therefore, it is hypothesized here that the effects of wind forcing modify the Bernoulli-type exchange hydrodynamics (pressure gradient balanced by advection) to a momentum balance that becomes more frictional. The modified hydrodynamics result in weakened exchange flows and altered layer thicknesses that translate into subcritical conditions. This should be investigated further with concurrent measurements of the density stratification.

Conclusions

The information presented here constitutes one of the few examples that illustrates the fact that wind forcing may significantly modify the two-layer exchange through a channel constriction or over a sill. Strong wind (>10 m/s) directed in the sense of the lower layer inflow hampers the two-layer exchange and should produce subcritical flows. A wind with equivalent speed but blowing in the opposite direction should enhance the two-layer exchange. The observations also represent one of the few examples that illustrate the theoretical result that the surface water flows in the direction of the wind and the bottom water flows in opposite direction.

References

Bryden, H.L., and T.H. Kinder, Recent progress in strait dynamics, U.S. Natl. Rep. Int. Union Geod. Geophys. 1987-1990, *Rev. Geophys., 617-631*, 1991.

Cáceres, M., A. Valle-Levinson, H. Sepúlveda and K. Holderied, Transverse variability of flow and density in a Chilean fjord, *Cont. Shelf. Res., in press*, 2002.

Farmer D.M., and L. Armi, The flow of Atlantic water through the Strait of Gibraltar, *Prog. Oceanogr., 21*, 1-105, 1988.

Farmer, D.M., and L. Armi, Maximal two-layer exchange over a sill and through the combination of a sill and contraction with barotropic flow, *J. Fluid Mech., 164*, 53-76, 1986.

Farmer, D.M., and H.J. Freeland, The physical oceanography of fjords, *Prog. Oceanogr., 12*, 147-220, 1983.

Fierro, J., M. Bravo and M. Castillo. Characterization of the tidal regime and currents along the Moraleda Channel. (In Spanish) *Cienc. Tecnol. Mar, 23*, 3-14, 2000.

Griffin, D.A., and P. H. LeBlond, Estuary-ocean exchange controlled by spring-neap tidal mixing, *Estuar. Coast. Shelf Sci., 30*, 275-305, 1990.

Hibiya, T. and P.H, LeBlond, The control of fjord circulation by fortnightly modulation of tidal mixing processes, *J. Phys. Oceanogr., 23*, 2042-2052, 1993.

Helfrich, K.R., Time-dependent two-layer hydraulic exchange flows, *J. Phys. Oceanogr., 25(3)*, 359-373, 1995.

Johnson, G.C. and D.R. Ohlsen, Frictionally modified rotating hydraulic channel exchange and ocean outflows. *J. Phys. Oceanogr. 24(1)*, 66-77, 1994.

Klinck, J.M., J.O'Brien and H. Svendsen, A simple model of fjord and coastal circulation interaction, *J. Phys. Oceanogr., 11*, 1612-1626, 1981.

Large, W.G. and S. Pond, Open-ocean momentum flux measurements in moderate to strong winds, *J. Phys. Oceanogr., 11*, 324-336, 1981.

McClimans, T.A., Role of laboratory experiments and models in the study of sea strait processes, in *The Physical Oceanography of Sea Straits*, edited by L.J. Pratt, pp. 373-388, Kluwer Academic, Hingham, Mass., 1990.

Pratt, L.J., Hydraulic control of sill flow with bottom friction, *J. Phys. Oceanogr., 16*, 1970-1980, 1986.

Silva, N., H. Sievers and R. Prado, Oceanographic description of chilean austral channel. (41°S – 46°S). (In Spanish). *Rev. Biol. Mar. Valparaiso, 30(2)*, 207-254, 1995.

Silva, N., C. Calvete and H. Sievers, Physical and Chemical features of southern chilean inlets between Puerto Montt and laguna San Rafael (Cimar-Fiordo I Cruise). (In Spanish). *Cienc. Tecnol. Mar, 20*, 23-106, 1997.

Silva, N., C. Calvete and H. Sievers, Water masses and general circulation patterns of some of the southern chilean inlets between Puerto Montt and laguna San Rafael (Cimar-Fiordo I Cruise). (In Spanish). *Cienc. Tecnol. Mar, 21*, 17-48, 1998.

Svendsen, H. and R. Thompson, Wind driven circulation in a fjord, *J. Phys. Oceanogr., 8*, 703-712, 1978.

Valle-Levinson, A. and R.E. Wilson, Effects of sill bathymetry, oscillating barotropic forcing and vertical mixing on estuary/ocean exchange. *J. Geophys. Res. 99(C3)*, 5149-5169, 1994.

Valle-Levinson, A., F. Jara, C. Molinet, D. Soto, Observations of Intratidal Variability of Flows Over a Sill/Contraction Combination in a Chilean Fjord, *J. Geophys. Res., 106(C4)*, 7,051-7,064, 2001.

Wong, K.C., On the nature of transverse variability in a coastal plain estuary, *J. Geophys. Res., 99(C7)*, 14,209-14,222, 1994.

Hydraulically controlled rotating flow - complexities from passage shape

J. A. Whitehead

Woods Hole Oceanographic Institution, Woods Hole MA, USA

Abstract. Velocity, surface height profiles, and volume flux are calculated for critically controlled channel flow of a layer of rotating fluid. A variety of channel cross-stream bottom profiles are considered. The upstream fluid possesses constant potential vorticity. Velocity and surface height distributions, and control criteria are presented for three features that seem to be unique to rotating fluid. These are: sizeable gyres that appear upstream of controlled passages; the existence of more than one critical flow configuration for a single passage (with bottoms of certain special shapes); and strict limits to the value of volume flux for a passage with a sloping wall. In addition, multiple exits allow flux to exceed a rigorous bound for flux out of a single passage.

Introduction

We present a straightforward formulation of the dynamics of nonlinear rotating flow from an upstream channel through an exit passage. It involves only the upstream conditions along the right-hand wall, an equation for geostrophic flow and a simple equation of potential vorticity. The last requires a specification of depth of the fluid in the interior of an upstream region. The approximations are the same as in the well-known formulation of constant potential vorticity by Gill (1977), but the procedure permits simple calculations of critical flows in passages that are more complicated than previously analyzed. Here and in the poster we illustrate a few results of such calculations and will mention some experimental and oceanic considerations.

Theory

Velocity distribution and fluid depth distribution across a constant potential vorticity current obey geostrophy and conservation of potential vorticity.

$$fv = g\frac{dh}{dx}, \qquad \frac{\frac{dv}{dx} + f}{h-b} = \frac{f}{H} \qquad (1a,b)$$

Here, $h(x)$ is elevation of the fluid surface, and $b(x)$ is elevation of the bottom above the deepest point in a controlling passage. A very wide channel lies upstream, H is the fluid depth in the middle there, far away from wall currents, f is the Coriolis parameter

(positive for counterclockwise rotation), g is the acceleration due to gravity (and we could consider this to be reduced gravity $g' = g\Delta\rho/\rho$ if we are studying a layer of fluid of density $\rho + \Delta\rho$, lying below an infinitely deep region of stagnant fluid of density ρ), x is a coordinate at right angles to the direction of flow, and v is velocity. As shown elsewhere, (Whitehead and Salzig, 2002) we assume steady flow and consider the Bernoulli function

$$B = gH_r = \tfrac{1}{2}v^2 + gh \qquad (2)$$

on the right hand wall (always looking downstream), since such a streamline will extend from an upstream point on the right hand upstream channel wall to the right hand wall in the passage. Bernoulli height

$$H_r = \frac{H}{2} + \frac{h_{ur}^2}{2H} \qquad (3)$$

is a known quantity since we consider cases with known H and h_{ur} (surface elevation at the right-hand wall in the upstream channel). The latter is easily related to volume flux of an isolated current on the upstream right-hand wall Q_{ur} that is thereby also known. The current along the upstream left-hand wall is unknown and is set-up by controlled flow in the passage. At the passage, the deepest bottom point is ΔB above the upstream bottom and depth of the fluid in the passage at the right-hand wall (which we take as the origin) is h_0. Velocity there is

$$v_0 = \sqrt{2g(H_r - \Delta B - h_0)} \qquad (4)$$

Using velocity, height, and lateral length scales, $\sqrt{g(H_r - \Delta B)}$, $H_r - \Delta B$, and $\sqrt{g(H_r - \Delta B)}/f$, equations (1a,b) in the passage reduce to

$$\frac{dh'}{dx'} = v', \quad \frac{dv'}{dx'} = \left(\zeta(h' - b')\right) - 1 \quad (5a,b)$$

where the primed are dimensionless variables and the positive dimensionless number $\zeta = (H_r - \Delta B)/H$ expresses elevation of the Bernoulli height over the passage bottom divided by the potential vorticity height H. In the passage, the equations have the boundary conditions $h' = \gamma = h_0/(H_r - \Delta B)$ and $v' = v_0{}' = \sqrt{2(1-\gamma)}$ at $x' = 0$.

For any cross-passage bottom profile it is straightforward to pick values of the two governing dimensionless parameters (γ, ζ) and numerically integrate 5a,b across the passage. We take flow out of the passage to be in the positive direction. The axis for x is positive toward the right, so the integration from the right hand wall must proceed in the negative x direction. Volume flux is scaled by $g(H_r - \Delta H)^2/f$ and the maximum possible value of total flux through a passage with bottom elevation positive everywhere is 0.5 (Killworth and McDonald 1993). This value corresponds to zero potential vorticity ($\zeta = 0$) flow over a wide flat bottom with bottom elevation zero (Whitehead *et al.*, 1974). The value of flux integrated across the passage is a function of γ, ζ, and in addition any other parameters that express the passage shape such as lateral width of the passage w that in dimensionless form is $W = wf/\sqrt{g(H_r - \Delta H)}$.

Following well-known concepts, volume flux can be maximized with respect to γ to determine critical flux that is a function of ζ and passage shape parameters. Surface height profiles are presented here for a variety of bottom configurations.

Upstream gyres

As water flows from a very deep upstream region to a shallower passage, vortex columns shrink and vorticity of the fluid becomes negative. Vorticity amplitude can approach the dimensional value $-f$ for great contraction of vertical columns. This has the value -1 in dimensionless units. The resulting shear can produce sizeable recirculation that signifies gyres upstream of the controlled flow, as described by Borenas and Whitehead 1998. The gyres are most

pronounced for small ζ and possibly are absent for large values. Figure 1 shows profiles for $\zeta = 0.01$. Above the bold line is sketched the profile in the very wide upstream channel that feeds fluid into the passage. We position this current along the left upstream wall, but Whitehead and Salzig (2002) show that a range of upstream conditions might be set. The upstream lateral coordinate $x'_u = x/H$ is scaled by depth of the upstream fluid. Surface elevation $h'_u = h/H$ is scaled by depth of the upstream fluid. Profiles in a narrow passage approaching the control passage are shown below the bold line.
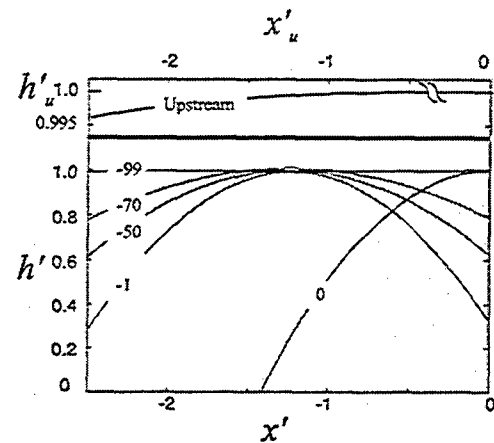

Figure 1. Surface elevation profiles for flow approaching a flat sill for $\zeta = 0.01$. The values of bottom depths are shown for each profile.

Passage floor elevations are set to $b=0$, -1, -50, -70, and -99, respectively which correspond to increasing depth as one progresses upstream from the control section to the deep upstream region.

For the critically controlled flow at the passage we set $b=0$ and select the well-known critical value $\gamma = 1$. The value of shear ranges from -0.99 at the right hand wall to the value -1 at the point where the surface intersects the bottom. This surface is almost perfectly parabolic. Flux has the value 0.5 and at other values of b the values of γ were adjusted to produce this volume flux.

In the upstream passage with depths of $b= -1$, -50, and -70, there are also almost perfectly parabolic profiles. Negative slope denotes a gyre. Fluid reaching the sill is found to the left of the gyre. Values of shear in the regions approaching the controlled passage have values of approximately -

0.98, -0.5, and -0.3 respectively. The surface elevation profile for *b*= −70 visibly extends above the level of the free surface ($h' = 1$) in the upstream basin. Gyres are seen in laboratory experiments (Borenas and Whitehead 1998, Whitehead and Salzig 2002).

The surface height profile in the narrow upstream channel with *b*= -99 is also shown in Figure 1. This bottom elevation is the same as in the infinitely wide upstream channel. The surface profile has almost uniform slope and change of surface elevation between the right and left hand wall is about 0.005. The value of shear is small, about -0.005. There is no recirculation of the fluid. All fluid in this section flows up the slope and through the controlling passage. Separation from the right-hand wall is found downstream of the place where the bottom departs from an elevation of −99.

Multiple extrema

More than one maximum flux is possible as the value of γ is varied. These features have been found for $\zeta > 1$ to date. An example of surface profiles with multiple maxima is shown in Figure 2. The bottom is a parabolic bump extending upward across the passage with an elevation of 0.625 above the deepest point as shown. In this example, we set $\zeta = 1.5$. To produce such a value, either the upstream basin depth is shallow ($\Delta B < 0$) or there is a sizeable current flowing toward the control section along the right-hand upstream wall (Whitehead and Salzig 2002). The volume flux as a function of γ contains two maxima separated by a minimum. The top curve shows the profile for $\gamma = 1.0$. For decreasing γ volume flux increases until the first maximum is reached at $\gamma = 0.9993$. The third interface down is the profile for which volume flux reaches a minimum value. Below this is a second maximum value.

The profile for the top maximum has a gyre. Control of currents with flow reversal introduces numerous unsolved problems. Our calculations show that the counterflow vanishes downstream of this shallowest passage, but clearly the nature of control in such problems requires further study.
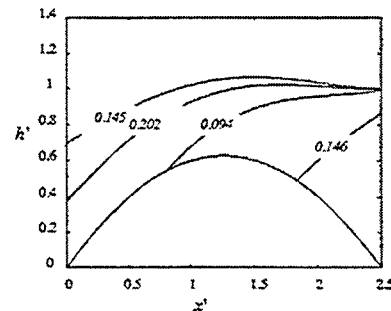

Figure 2. Surface height profiles over a parabolic bump across a passage for $\zeta = 1.5$ and $\gamma = 1.0$, 0.9993, 0.992, and 0.867, from top to bottom respectively. The two volume flux maxima are shown by the second and fourth contours from the top. They are separated by the contour for minimum flux.

Limitations from bottom slope

If the bottom slopes away from the right-hand wall, a sufficiently small slope prevents large velocities. This can produce small values of flux even if the opening is very wide. Figure 3 shows the surface height profiles for three different passage widths with a bottom uniformly sloping away from the right hand side. For all three cases maximum flux is found for $\gamma = 1$. The top profile has $W = 0.675$. The value of critical (maximum) flux is 0.076. The middle profile has $W = 1.25$. The interface adopts a slope very close to that of the bottom slope and the volume flux is 0.210, a value much larger than the top profile but still less than the maximum bound of 0.5. The bottom profile has $W = 1.875$. The current is confined to a layer along the upper part of the slope and volume flux is 0.066. Essentially flux is limited because the fluid velocity cannot exceed a value dictated by the slope of the bottom over a sizeable region Thus with a bottom sloping away from the right-hand wall there is an opening width that admits greatest flux and both narrower and wider openings admit less flux. These results were for $\zeta = 1.0$. Calculations with other values of $\zeta > 1$ gave very little qualitative difference.

These results are in accord with a limitation found by Borenas and Lundberg (1986) to volume flux for a parabolic bottom (deepest in the middle, unlike our example here) with a very wide opening compared to Rossby radius.
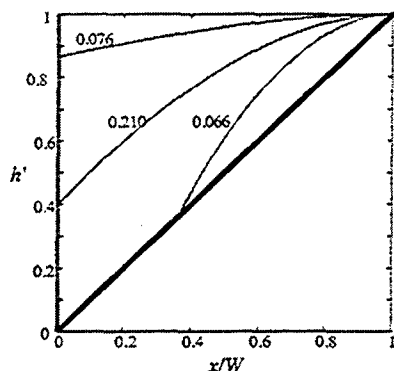
Figure 3. Three surface profiles and their associated values of volume flux for cases with a narrow, moderate, and wide channel, respectively. The top curve has $W = 0.675$, the middle has $W = 1.25$ and the bottom has $W = 1.875$.

Interrupted passages

With more complex bottoms the water surface can be interrupted across the opening. Flows share the same Bernoulli height across the interruption. Figure 4 show surface profiles with two passages coming from the same upstream region. It was shown that the upper bound of flux through a single passage for all upstream values of vorticity and for all passage shapes is 0.5 (Killworth and McDonald 1993). Since the Bernoulli function is almost the same for all streamlines in the limit of a very deep upstream passage (which equals zero potential vorticity) it is easy to exceed this maximum flux with two passages. Figure 4 shows a calculation with $\zeta = 0.1$ where the two passages produce a total maximum flux of 0.931. For greater ζ, the flux in the left-hand passage is smaller since the Bernoulli height decreases to the left across the current. It is not yet known whether multiple passages obey bounding for sufficiently large ζ. We also note in closing that the properties of information propagation with multiple outlets are not well understood.

Implications of the results

Here some effects from fluid rotation with passage bottom configurations.

First is the possibility of recirculating gyres, a known effect but one of great importance to ocean fieldwork. This happens in part because the streamlines in closed gyres do not originate in the upstream region.
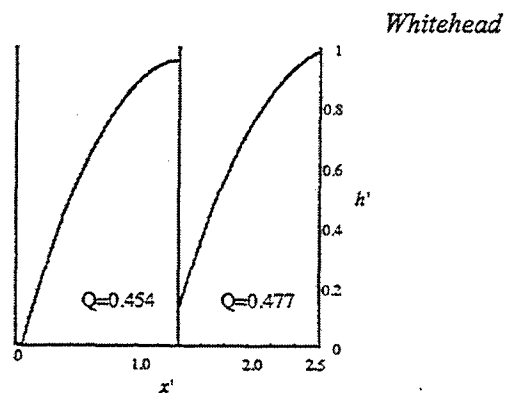

Figure 4. Surface profiles through two passages with flat bottoms. The maximum flux was found first for the right hand channel and then the flux in the left hand channel was maximized. Combined flux of the pair has more flux than the upper bound for a single passage.

More than one local flux maximum is possible. The presence of more than one extremum implies that there is more than one condition with an arrested wave, so there may be more than one stable controlled flow through the passage for the same upstream conditions. In this case the actual flux would presumably be determined by history.

There is a limitation of flow by passage floors that tilt away from the right hand fluid surface with small angles.

Flux out of multiple passages can exceed the value given by upper bounding theory.

More aspects of these four results will be discussed and shown at the meeting.

References

Borenas and Lundburg, 1986: Rotating hydraulics of flow in a parabolic channel, *J.Fluid Mech.* 167, 309-26.

Borenas, K. M. and J. A. Whitehead 1998. Upstream separation in a rotating channel flow. J. Geophys Res. 103, C4 7567-7578.

Gill, A. E., 1977: The hydraulics of rotating channel flow, *J. Fluid Mech.* 80, 641-71.

Killworth, P.D. and N.R. McDonald, 1993: Maximal reduced-gravity flux in rotating hydraulics, *Geophys. Astrophys. Fluid Dyn.* 70, 31-40.

Whitehead, J.A. , A. Leetmaa and R.A. Knox, 1974: Rotating hydraulics of strait and sill flows, *Geophys. Fluid Dyn.* 6, 101-25.

Whitehead, John A. and John Salzig, 2002. Rotating Channel Flow: Control and Upstream Currents, *Geophysical and Astrophysical Fluid Dynamics*, 95, 185-226.